International Journal of Photoenergy

Application of Hybrid Nanostructure for Photo and Bioenergy Applications

Lead Guest Editor: Vinayagam Mohanavel
Guest Editors: Palanivel Velmurugan, Byung-Taek Oh, and Bharath Govindan

Application of Hybrid Nanostructure for Photo and Bioenergy Applications

International Journal of Photoenergy

Application of Hybrid Nanostructure for Photo and Bioenergy Applications

Lead Guest Editor: Vinayagam Mohanavel
Guest Editors: Palanivel Velmurugan, Byung-Taek Oh, and Bharath Govindan

Copyright © 2022 Hindawi Limited. All rights reserved.

This is a special issue published in “International Journal of Photoenergy.” All articles are open access articles distributed under the Creative Commons Attribution License, which permits unrestricted use, distribution, and reproduction in any medium, provided the original work is properly cited.

Chief Editor

Giulia Grancini, Italy

Academic Editors

Mohamed S.A. Abdel-Mottaleb, Egypt
Angelo Albini, Italy
Mohammad Alghoul, Malaysia
Alberto Álvarez-Gallegos, Mexico
Vincenzo Augugliaro, Italy
Detlef W. Bahnemann, Germany
Simona Binetti, Italy
Fabio Bisegna, Italy
Thomas M. Brown, Italy
Joaquim Carneiro, Portugal
Yatendra S. Chaudhary, India
Kok-Keong Chong, Malaysia
Věra Cimrová, Czech Republic
Laura Clarizia, Italy
Gianluca Coccia, Italy
Daniel Tudor Cotfas, Romania
P. Davide Cozzoli, Italy
Dionysios D. Dionysiou, USA
Elisa Isabel Garcia-Lopez, Italy
Wing-Kei Ho, Hong Kong
Siamak Hoseinzadeh, Italy
Jürgen Hüpkes, Germany
Fayaz Hussain, Brunei Darussalam
Mohamed Gamal Hussien, Egypt
Adel A. Ismail, Kuwait
Chun-Sheng Jiang, USA
Zaiyong Jiang, China
Yuanzuo Li, China
Manuel Ignacio Maldonado, Spain
Santolo Meo, Italy
Claudio Minero, Italy
Regina De Fátima Peralta Muniz Moreira, Brazil
Maria da Graça P. Neves, Portugal
Tsuyoshi Ochiai, Japan
Kei Ohkubo, Japan
Umapada Pal, Mexico
Dillip K. Panda, USA
Carlo Renno, Italy
Francesco Riganti-Fulginei, Italy
Leonardo Sandrolini, Italy
Jinn Kong Sheu, Taiwan
Kishore Sridharan, India
Elias Stathatos, Greece
Jegadesan Subbiah, Australia
Chaofan Sun, China
K. R. Justin Thomas, India
Koray Ulgen, Turkey
Ahmad Umar, Saudi Arabia
Qiliang Wang, China
Xuxu Wang, China
Huiqing Wen, China
Weijie Yang, China
Jiangbo Yu, USA

Contents

Contents

Contents

Hindawi
International Journal of Photoenergy
Volume 2022, Article ID 8735562, 11 pages
https://doi.org/10.1155/2022/8735562

Research Article

The Potential Role of PV Solar Power System to Improve the Integration of Electric Energy Storage System

Rajesh Kumar Patnaik,[1] P. Shyamala Bharathi,[2] Sivaramkrishnan Mathiyalagan,[3] Rajesh Thumma,[4] G. Saravanan,[5] Mohana Alanazi,[6] V. Sivaraman,[7] Ashraf Elfasakhany,[8] and Assefa Belay[9]

[1]*Department of Electrical and Electronics Engineering, GMR Institute of Technology, Rajam, Andhra Pradesh 532127, India*
[2]*Saveetha school of Engineering, Saveetha Institute of Medical and Technical sciences, Saveetha Nagar, Thandalam, Chennai-602 105, India*
[3]*Department of Electrical and Electronics Engineering, Karpagam College of Engineering, Coimbatore, Tamil Nadu 641032, India*
[4]*Department of Electronics and Communication Engineering, Anurag University, Venkatapur, Ghatkesar, Hyderabad 500088, India*
[5]*Department of Electrical and Electronics Engineering, KPR Institute of Engineering and Technology, Coimbatore, Tamil Nadu 641407, India*
[6]*Department of Electrical Engineering, College of Engineering, Jouf University, Sakaka 42421, Saudi Arabia*
[7]*Department of Mechanical Engineering, Rajalakshmi Engineering College, Chennai, Tamil Nadu, India*
[8]*Mechanical Engineering Department, College of Engineering, Taif University, P.O. Box 11099, Taif 21944, Saudi Arabia*
[9]*Department of Mechanical Engineering, Mizan Tepi University, Ethiopia*

Correspondence should be addressed to Assefa Belay; assefa@mtu.edu.et

Received 3 February 2022; Revised 1 May 2022; Accepted 4 May 2022; Published 18 July 2022

Academic Editor: V. Mohanavel

Copyright © 2022 Rajesh Kumar Patnaik et al. This is an open access article distributed under the Creative Commons Attribution License, which permits unrestricted use, distribution, and reproduction in any medium, provided the original work is properly cited.

Integration technique is becoming effective due to the world's largest power requirement, which has imposed a considerable need for various techniques by which electricity can be generated or integrated, as well as the assumption that integrating solar energy into nonrenewable source materials is essential to minimize the relative to nonresource consumption and thus reduces fossil fuel consumption. Photovoltaic (PV) systems are at the forefront of this transformation, harnessing the sun's renewable electricity and converting this from DC to AC. Controlling the power grid utilizes power system photovoltaic energy production and the many ramifications of grid-scale PV energy module integration into energy systems. To completely integrate photovoltaic (PV) processes into a network, cost-effective and efficient technologies of energy storage must be used in conjunction with smart energy management systems. Electrical energy storage system (EESS) could have been used to improve a system's stability and the performance, to recent technology improvements and quick efficiency improvements. This research provides an understanding of EESS for the photovoltaic system as well as a complete evaluation of the developing penetration level of PV. As the worldwide photovoltaic solar market is expanding, growing onsite use of PV-generated energy would become increasingly critical to ensure the stability of the grid. This research study was the first one to provide such a comprehensive overview of all forms of energy storage devices which can be used in conjunction with PV, including both thermal and electrical energy storage systems. Finally, a simulation of optimization planning is executed. The result reveals that lowering peak loads and lowering electricity usage lowers the price of electricity.

1. Introduction

Solar-grid connection is a system that allows large amounts of photovoltaic (PV) power to be integrated into the public power system. This is a crucial requirement because integrating standardized photovoltaic systems into grids optimizes increase energy balancing, enhances photovoltaic system economy, lowers operating costs, and adds benefits

to customers and utilities [1]. As there is an increasing desire for alternative renewable power to replace fossil fuels, solar-grid interconnection has become a regular practice in several nations throughout the world. Recent global attempts to reduce energy usage and investigate alternate energy options have been prompted by the shortage of fossil fuels and their detrimental environmental impact [2]. Considering that the construction sector consumes roughly 20–40% of the amount of energy in advanced economies, renewable power technologies represent a potential alternative energy source for addressing the energy problem and issues affecting architecture demand. Solar energy is more suitable as a power source of supply for buildings with constrained installation area, active vibration requirements, and an unpleasant atmospheric condition in an urban setting, so it is important to incorporate structural elements [3]. However, because solar energy is often inconsistent and unexpected and thus does not always match building needs, power storage solutions are required to ensure a steady and reliable electricity supply [4]. The integrated renewable energy storage unit can regulate the speed of the distribution network for on-grid photovoltaic systems, as well as to adapt the solar energy flow to match the structure growth and increase power authority. As a result, it is critical to look into integrating different electrical energy storage (EES) techniques using photovoltaic (PV) devices for an efficient construction power source.

There are some other basic equilibrium solutions. Electric energy storage systems (EESS) can also be utilized to save the energy when there is an excess to utilize it when there is a shortage. The hydroelectric capabilities of specific locations can also be used to balance other regions by linking separate grids [5]. Another sustainable option is bioenergy, which has the advantage of lengthy storability as well as the technological ability to compensate for some of the fluctuations in solar power output. Concentrated solar power (CSP) is a decent selection in some places with strong direct sunrays; it is not a feasible option in others. Solar photovoltaic (PV) generating capacity has expanded substantially over the last century as one of a transition away from fossil fuels more toward reliable, clean, effective, and sustainable energy. To store surplus PV electricity produced for subsequent use when needed, PV technologies with energy production are required [6]. Energy production can serve to promote systems to survive demand spikes and keep transmission and a grid distribution running smoothly. In terms of short storage durations, this can be useful for leveling out transient voltage peaks and irregularities.

As illustrated in Figure 1, the most suitable energy storage media for PV-produced energy is determined by the planned end-use. Global energy production exceeds the world energy need by a large margin. However, owing to the cyclical and unpredictable characteristics of solar energy, integrating it into the power system is difficult. The amount of solar electricity generated is related to the amount of solar irradiation. This means that to avoid swings, dispatchable generators, such as coal-fired or gas-fired power plants, must alter their power production frequently. As a result, calculating a suitable system reserve for stable and safe operations becomes difficult. Increased system adaptability must become a goal for policy and decision-makers if photovoltaic (PV) technologies acquire a bigger percentage of power generation, i.e., as adoption rises [7]. Electrical energy storage (EES) may enhance and give functions for power systems; therefore, it will be widely used. To improve the integration of electric energy storage systems (EESS), stored energy is expected to be a critical element of the smart grid [8]. There is interest in developing enhanced operational techniques for evaluating the integrity and safe functioning of renewable electricity networks with high integration.

2. Related Work

Energy storage is becoming a major player in energy storage systems. The goal of this article is to conduct researches on integrating battery-based energy storing with such a hybrid grid-connected wind-solar electricity system to effectively dispatch wind output by adding peak shaving and ramping speed preventive. The sizing technique is adjusted using a bat optimizing method to reduce a system's development losses from power outages and wind restriction. The integrated system is next put through its paces with a battery control mechanism that protects the battery from being overcharged or discharged. Five main kinds of battery storage are explored and analyzed in the study. They were developed and analyzed depending on techno-economic and ecological indicators in the situation of the Indian electricity markets. Simulation on a planned system of wind-photovoltaic in a wind location in South India supports the battery's techno-economic evaluation. An experimental test is carried out by calculating the cost of emission reductions [9]. An electricity user as being subjected to time-of-use price and a request price uses real-coded evolutionary algorithms to arrange the charging of an energy storage system (ESS) that is utilized in conjunction with sustainable power. Analyses focused on average residential customer demand and production profiles demonstrate that an ESS planned by the method can cut electricity expenditures by about 17% compared to a network without the need for an ESS and by 8% relative to such a scheduling strategy based on average power [10].

The research state of architecture and controlling approach of energy storage grid-connected systems is evaluated in this research, as well as a cascade power electronic transformer (CPET) with a separate Dc converter is considered to improve the operational conditions of a recycled battery. The current supplied isolated bilateral DC-DC converter and a cascaded H-bridge (CHB) working principles are investigated, and a decoupled control method is devised. The repurposed battery energy storage (RBES) grid-connected device is constructed in this study using a centralized control technique based on CPET, which has 3 levels: state of charge (SOC), energy, and power. The resource layer reacts to voltage and frequency management directives, the power completely covered grid-connected electricity, and records voltage level, as well as the SOC layer, corresponds between battery charged states. A three-phase grid-connected model can be tested with a capacity of 3 MVA/12 kV was built, as well as a single-phase system

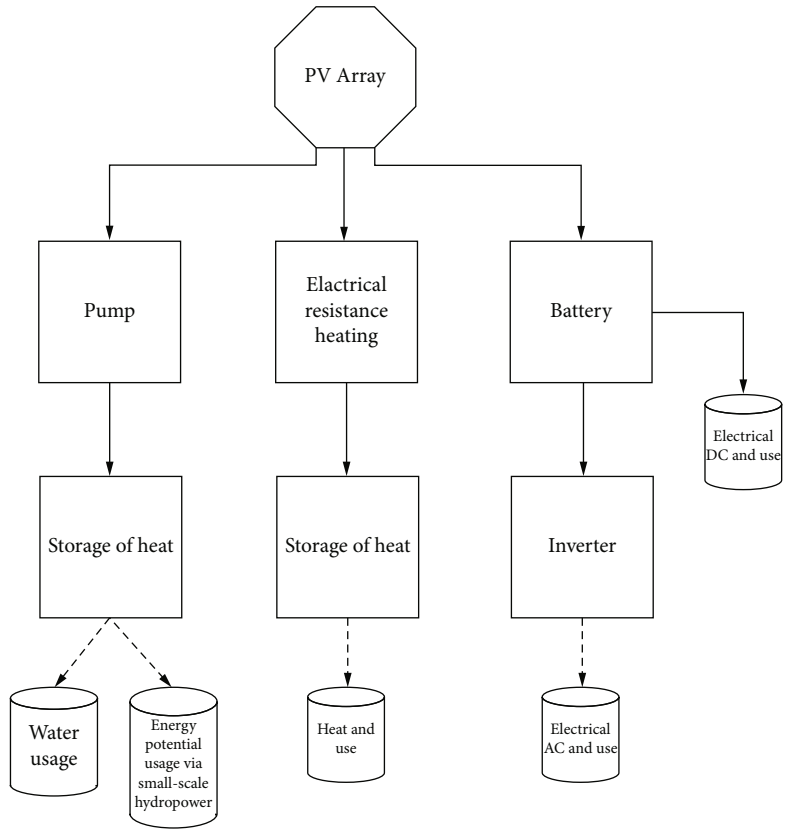

Figure 1: Photovoltaic energy storage system.

experimental platform with a capacity of 1 kW. The simulations and practical data can be used to confirm that the mathematical model is true and that the proposed controller is feasible [11].

This research incorporates a hybrid storage system of super capacitor into a wind-solar hybrid energy harvesting system, allowing the system's power storage space and power output to be significantly increased. This study's approach combines a decentralized power generation system with a hybrid energy system while increasing output power in phases utilizing a static voltage regulation system and a process of developing a dual-mode control scheme. Simultaneously, using MATLAB/Simulink technology, the highest efficiency model of a wind-solar combination power generation is constructed. Simulation is used to determine the microgrid's power output to the wind-photovoltaic mixed power generating system, as well as the optimization method for each system element. To improve the wind-solar hybrid power generating system, this study primarily utilizes the static power factor correction system as well as the conductance-fuzzy dual-mode control scheme. The capability and rationale of the ideal system layout are verified using the MATLAB simulation software [12].

This work reveals that a single energy source typically energizes the entire system and frequently leads to failures. The battery capacity lifetime and excessive regular expense are the primary concerns. Because of its complexity and expertise, the system has been undersized or oversized on occasion. Solar cell restrictions must be optimized. The combination of lead-acid batteries and super capacitors reduces the stress on the batteries and extends their life. To handle the quick input fluctuations across the solar module, an ANN model is used. As a case study, the research uses models of the Nsukka seismic node to better analyze the process. Identifying of PV system factors at a typical remote seismic device via energy transmitter and storage designing, optimal dimensioning of photovoltaic modules as well as a lead-acid charger, and, finally, a combination of energy storage devices to facilitate the energy management system to maximize the accessible atmospheric illuminance are all major contributors of the research. The results reveal that the neural network provided an order to create good switching frequency all across converters and fewer complications, while the capacitors supplemented the lead-acid battery and provided overall effectiveness of roughly 75% [13].

3. Materials and Methods

3.1. Electrical Energy Storage (EES) Technology Global Development for PV Systems. Figure 2 depicts the study's general framework. This research examines the current state of hybrid PV-EES systems for structure power sources, as well as the scope of research and process optimization. To encourage future deployment of PV-EES technology in structures, suitable combination PV-EES systems for building's power source and possible research requirements are detailed. Electrical energy storage (EES) is the conversion of electrical energy in to another condition that can be

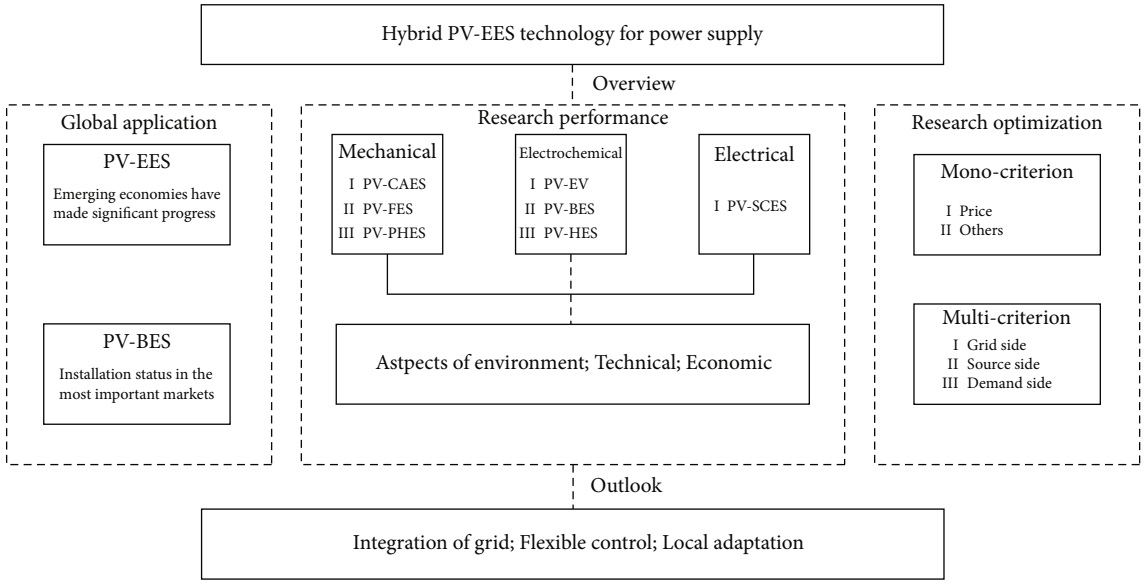

Figure 2: The hybrid of PV-EES technologies' main objective for grid supply.

maintained and transferred back to electricity when required. Photovoltaic systems combined with renewable power can increase the amount of self-consumed PV electricity [14]. The extra PV electricity generated most of the day is retained in such a battery system and utilized at night. Residents with PV-battery systems can lower the amount of electricity they require from the grid and enhance themselves. PV-battery solutions thereby minimize residential customers' reliance on the grid connection while also lowering carbon pollution.

3.2. Using EES for PV. EES is a method which allows energy to generate at a period when prices are low and generating costs are low, or from distributed generation to use when prices increase and production costs are high when another production is unavailable. Such a base load-producing unit can charge storage in the early morning and late at night. this stored energy is being utilized to balance demand during peak hours, which occur about 6 p.m. Furthermore, by utilizing the available resources between 6 : 00 a.m. and 6 : 00 p.m., energy storage preserves frequency and voltage.

Chemical, mechanical, and thermal storages are only a few of the different types of EES. Many of these basic groups have their own set of economic and efficiency considerations. Photovoltaic systems can provide additional social benefits, such as reduced carbon-emissions because PV solar creates power from a solar energy which could have been used to produce electricity from fossil fuels [15]. Although the advantages flow to society as a whole, emission reduction advantages are a major inducement for many who install PV systems. PV-battery systems can also provide grid-level advantages, including enhancing the overall effectiveness of the electrical grid and lowering the cost of the system.

Photovoltaic systems can provide additional social benefits, such as reduced carbon emissions, because solar PV creates power from solar energy which could have been used to produce electricity from fossil fuels. Although the advantages flow to society as a whole, emission reduction advantages are a major inducement for many who install PV systems. PV-battery systems can also provide grid-level advantages, including enhancing the overall effectiveness of the electrical grid and lowering system costs. PV-battery systems have the following grid benefits:

(i) To compensate for the use of more costly generators

(ii) Minimize distribution and transmission network congestion

(iii) Control the flow of electricity

(iv) Regulate voltage variations in the nearby area

(v) Upgrades to transmission and distribution systems can be avoided or postponed

When advantageous regulations, such as tax benefits, specific rate designs, net metering, and feed-in prices are introduced, they can lower the cost of electricity.

4. Proposed Methodology

4.1. EES Generic Model. There are two types of power system analysis and preparing:

(i) Static analysis and preparing

(ii) Dynamic analysis and preparing

The static computations do not employ timing [16]. Only the maximum consumption is being used to size the electronic systems and electricity in terms of balancing power generation over a one-hour or one-day period (24 hr). EES models of varying quality are required to offer computations in the power network strategic planning. The quality and features of the selected EES models for such computation should approximate the average representations of the power system

network, such as transformers and generators. Dynamic models of electric equipment are required for dynamic calculations; these approaches primarily use ordinary differential equations to describe the characteristics of items.

For extensive EES modeling (e.g., inverter dimensioning), more appropriate EES projections depend on, for example, similar networks that are sometimes necessary [16]. The EES methods for dynamic computations will not be treated in this paper because it has already been covered in greater depth in other works. The simulations can be modified dependent on the computation timescale, and then, the calculation includes a very brief time; the constant behavior of the EES model's technology modeling could be considered in a critical condition.

Parameterization of statistically specified models is based on data measured and physical features of the devices. The reliability of the models should be improved to enable extensive evaluations of major channels that take into account the primary parameters and performance of different devices (including EES) without unnecessarily increasing computation time. In terms of modeling needs, the EES can be incorporated into the power system computation as a hybrid generation/load component. If the storage solution has one or more generation devices (generators), they should be fully taken into account.

To meet the above-described requirements, an EES model's section usually should include at least three edges from Figure 3. The initial, the primary surface, is made up of the physical model, which is mostly represented by theoretical descriptions and contains the EES model's central point. This model's physical surface (PhS) is then blended into its specific surroundings, such as the load's electrical and thermal demands, and additional interactions and requirements on the structural model are provided, especially when considering system control simulation. Table 1 highlights the modeling needs for the EES-PhS, taking into account various forms of storage and modeling implementation methods.

4.2. Development of EESS's Perspective Group. An experienced assessment of the vast variety of technically accessible electrical energy storage system (EESS) techniques was conducted to evaluate then associate the systems with a projected data of techno-economic till 2050. Lithium, nickel, and lead are storage-dependent in the short term; redox flow, pump hydro, and high-temperature memory devices are concentrated in the middle period. To obtain data input for such following method, every technique was subjected to a thorough reading of important techno-economic facts.

Simultaneously, the remaining peak demand has to be assessed to increase a total capacity of EESS and the power requirements based on the situation. The analytical hierarchical process (AHP) was used to determine a percentage from each technology depend on a techno-economic information and an EESS capability then the power to generate a network of electrical power storage areas [17]. The goal of this research was to find the best way to use sustainable power. As a result, for low- to midstorage, the capacity of electrical energy storage devices was constructed under the highest negative remaining load of CLASSIC situations, correspondingly. Short-term storage requirements are for negative residual pressures that happen in just a day, whereas midterm storage requirements are for negative residual workloads that occur between a few days and 3 days.

The analytic-hierarchy-process (AHP) utilized in a domain of choice making was modified such a state to construct the fleet of a EESS systems through specifying a contribution of every knowledge for an EESS short- and midterm. The most important component of this procedure is the pairwise assessment of the classes and measures to find the best choice for two pathway situations. The AHP is used to identify a share of every technology inside the short- and midterm cluster, rather than analyzing multiple EESS solutions. EESS grouped essential criteria for describing the technology into three categories: environmental consequences, technical factors, and economic implications. Relevant criteria, as well as their weighting influence of importance, were already discovered within these clusters. The weighting variables for the various criteria are determined mostly through pairwise comparisons of the groups and the criterion within every category. The most important characteristics, according to this strategy, are cycle capability, effectiveness, and prices.

4.3. ESS for Energy Management. By charge/discharge, ESS can lower electricity prices and minimize peak load. As a result, the cost of electricity can be decreased. When run with optimal output scheduling, ESS could be more dynamic in response to peak management than to the solar system load, resulting in significant savings. The demand cost and the cost of energy are two types of electricity costs [18]. The method of minimizing energy usage to identify demand cost and also the method of minimizing power consumption to estimate electricity costs are both organized methodically in this research. The energy management optimization technique employing the ESS is depicted in Figure 4 as flow chart. Phase 1 and Phase 2 of the algorithm are separated. Phase 1 involves power management to reduce peak capacity. Phase 2 is designed to perform energy management to reduce energy costs while not reaching the peak demand set in Phase 1.

Stage 1 involves using the ESS to schedule peak load decreases based on expected monthly data collected. Similarly, the peak load (as determined by ESS) is associated regularly to modify the peak load which defines the monthly consumption cost [19]. When the peak demand that defines a monthly request cost is produced in monthly report, the ESS output is computed based on the peak eliminating unnecessary planning results. The optimal solution and constraint for Stage 1 are as follows:

$$\operatorname{Min}\left\{\rho_d \times L_{\text{peak}}\right\}, \tag{1}$$

$$-L_{ch,\max} \times x(t) \le L_{\text{ESS}(t)} \le L_{dch,\max} \times y(t), \tag{2}$$

$$a(t) + b(t) \le 1, \tag{3}$$

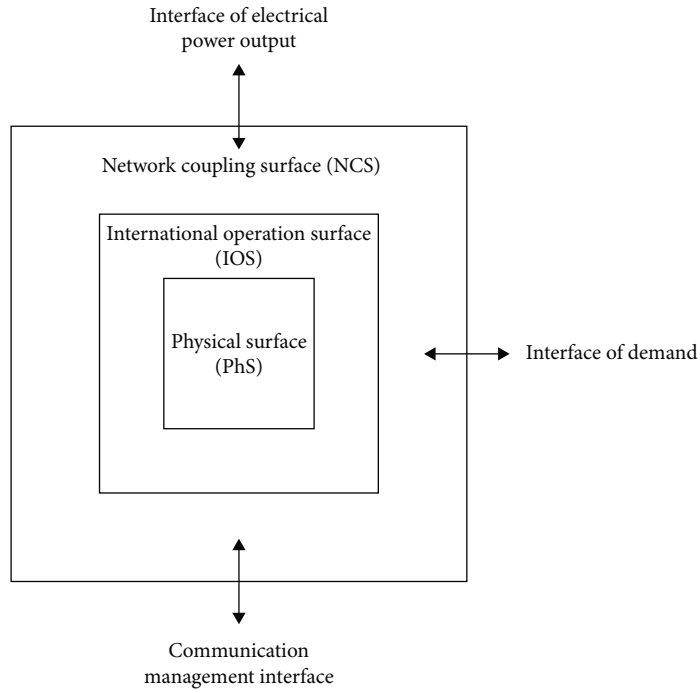

Figure 3: Generic model of ESS.

Table 1: EES physical surface modeling for planning of power network.

Requirement of model	Kind of storage	Used model
Model of static	Independent of storage type, a generic model is used	Model of a reservoir depending on the type of storage, parameters are set
Model of dynamic	Batteries, flywheels, CAES, PHS, storage medium H_2	Advanced model of AC generator

$$\mathrm{SOC}(t) = \mathrm{SOC}(t-1) - \left(b(t) \times L_{\mathrm{ESS}}(t) \times \eta_d^{-1} + a(t) \times L_{\mathrm{ESS}}(t) \times \eta_c\right), \quad (4)$$

$$\mathrm{SOC}_{\mathrm{lb}} \le \mathrm{SOC} \le \mathrm{SOC}_{\mathrm{ub}}, \quad (5)$$

$$\mathrm{SOC}_{\mathrm{last}} = \mathrm{SOC}_{\mathrm{first}}, \quad (6)$$

$$\mathrm{Load}(t) - L_{\mathrm{ESS}}(t) \le L_{\mathrm{peak}}. \quad (7)$$

A functional form, Equation (1) serves as the basic rate. To reduce peak capacity, ESS power management is used. The price per kW of the demanding cost is denoted by d and L_{peak}. Equation (2) is a power restriction for charge/discharge. The discharge energy has a positive number whereas the charging energy is negative. The ESS charging power rating, power of ESS, and ESS discharging power rating are denoted by $L_{ch,\max}$, L_{ESS}, and $L_{dch,\max}$, respectively. Then, one of the charge-discharge modes can function at any given time, according to Equation (3). Furthermore, the ESS charging and discharging states are denoted by a and b, accordingly. Both parameters have binary numbers. The state of charge (SOC) for each cycle of operation is calculated using Equation (4). The ESS charging and discharging efficiency are denoted by d and c, respectively. The operational range of the ESS's SOC is limited by Equation (5), and the ultimate SOC is equivalent to the beginning SOC, as displayed in Equation (6). The lower and upper boundaries of the SOC are denoted by $\mathrm{SOC}_{\mathrm{lb}}$ and $\mathrm{SOC}_{\mathrm{ub}}$ correspondingly. L_{peak} has the greatest value among the discrepancies among the load as well as the ESS power, as shown by Equation (7).

Phase 2 adds the restriction that uses this number after determining the peak capacity which defines the monthly consumption cost in Phase 1. The ESS accomplishes power planning using simply the price of electricity in the goal functional, ignoring the demand cost. The following are the goal function and extra constraint requirement in Phase 2 that minimizes the cost of energy in equation (8).

$$\mathrm{Min}\left\{\sum_{t=1}^{96}\left(\rho_e(t) \times 0.25 \times \left(\mathrm{Load}(t) - L_{\mathrm{ESS}}(t)\right)\right)\right\}, \quad (8)$$

$$L_{\mathrm{peak}} \le L_{\mathrm{peak,limit}}. \quad (9)$$

Considering the cost of electricity, the ESS executes optimization planning to fill at a minimum price of electricity and release at a higher price of electricity, thus according to Equation (8). The energy price is denoted by $\rho_e(t)$. Equation (9) makes the peak demand, which regulates the

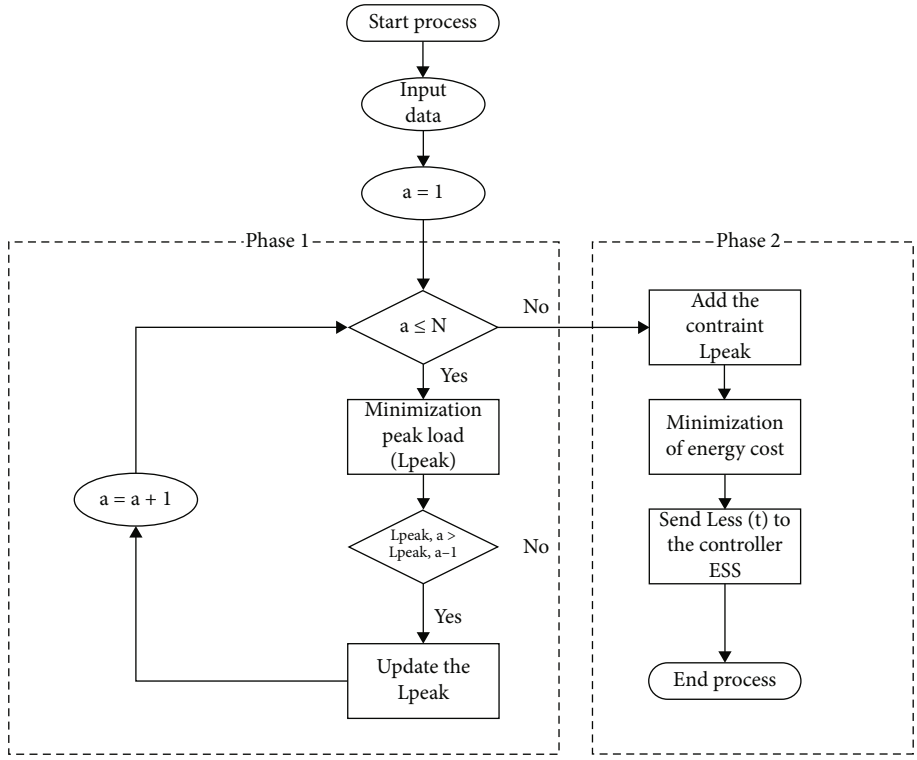

Figure 4: Flowchart of ESS optimization algorithm.

monthly consumption cost, a restriction, and prevents the emergence of original peak usage as a result of the ESS being overcharged based on the power price. $L_{\text{peak,limit}}$ denotes a maximum load limit. The peak-reduction method preferably schedules the day that the peak load happens monthly in Phase 1, then reschedules it to Phase 2.

4.4. Development of an Optimization Method for Fleet Operation Scheduling. The numerical optimization technique created from generic optimization model for energy storage that would be a mixed-integer, linear programming model for a such techno-economic evaluation of a EESS applications, used the generated data from three different previously stated processes. The updated model was used to evaluate the use of various power production technologies in various scenarios, including fossil power stations, adaptable bioenergy facilities, and short-term and midterm EESS. A "reserve" power station (reliant on rapidly steam turbines) was also installed to ensure remaining load coverage within every time interval [19]. The optimization's objective function was to reduce the greenhouse gas emissions as much as possible. Furthermore, a rolling horizon has been used to limit precise vision to two days. On primary day, findings are recorded; the second day was used as a connection to avoid the electrical power storage being depleted after the day, which might contribute to a localized rather than global optimum. The outcomes of this end of the process are utilized to investigate the possibilities and interactions of technological developments for each 12 situations.

The goal of reducing greenhouse gas emissions is selected as an optimization problem since it directly correlates with the overarching goal of producing as much electricity as possible from renewable sources. The equation contains the definition of the goal function (10). Together within rolling horizons, the number of emissions is estimated by adding the pollutants of every plant fossil-fueled for every time step t in each run optimization t. In addition, a cost element for gas-fueled power plants and reserve power plants has been implemented. The component is used to respect individual plants' economic merit ranking, which is determined by their marginal cost of production on the spot price. As a result, the optimization problem prioritizes renewable power feed-ins that will be retained during one surplus condition or flexible biofuel plant feed-ins. Fossil-fueled power stations were now turned on if zero emission-free energy must be generated and delivered.

$$\min \mathrm{CO}_2 = \sum_{T=1}^{365} \sum_{t=1}^{n} \left(\mathrm{CO}_{2,\text{hardcoal}}(t) + 5.\mathrm{CO}_{2,\text{gas}}(t) + 100.\mathrm{CO}_{2,\text{reserve}}(t)\right). \tag{10}$$

Positive remaining load must be supplied for each time interval t, according to every supposed to ensure for assuring the security of supply and grid stability. The residual negative residual stress, on the other hand, is permitted. The left-over negative residual demand, i.e., excess electricity output, is believed to be employed in cross-sectoral equipment [20]. Power-to-heat and power-to-gas appliances are two examples of cross-sectoral devices, although there are several other alternatives. A further constraint ensures that adaptable biomass fuels can provide energy during the year. The

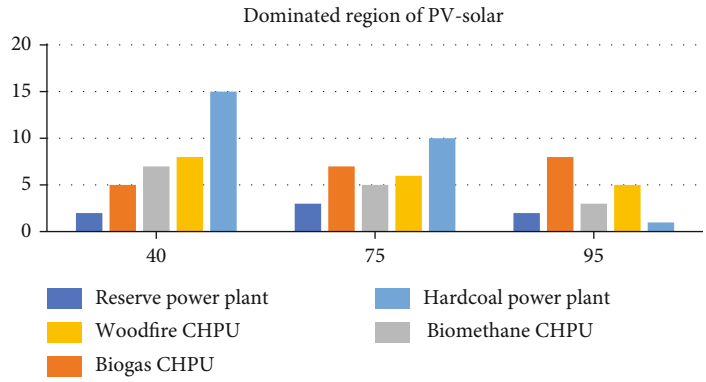

Figure 5: Coverage of the fleet's low residual demand by various facilities or EESS.

Table 2: After addressing the residual load, the remaining extra energy and power.

Region	Share of renewables	Excess of annual energy	Excess of maximum power
Dominated region of PV solar	40%	0	0.2
	75%	0.5	9.6
	95%	4.8	17.3

estimated annual quantity of biomass substrates was subdivided in equivalent to a quantity of positive residual demand throughout each optimization run T for this purpose. Several production process restrictions, such as power rating and capability, capability for part-load operations, rates of receivable ramp, rate of self-discharge, restricted number of attempts each day, the minimum downtime, and less running duration, were also applied for improvement.

5. Result and Discussion

The covering of leftover residual load by various plants or EESS is first demonstrated, and the monitoring impacts are explained. Following that, several key figures are related to the operation of the various plants, and EESS is presented. Finally, the features of leftover excess energy and power are discussed, and EESS optimization technique is also performed. In this section, Figure 5 demonstrates how the interactive activity power stations or EESS handle the remaining positive leftover demand of modeling regions, i.e., the capacity following feed-in renewable generation and must-run power plants. From 2030 to 2050, the percentage of CO_2-free generating electricity for both areas rises. In the solar zone, EESS shifts a greater quantity of renewable power over a period than those in the solar region. This could be for one of two main reasons: On the one side, likely, EESS does not quite fit the leftover positive leftover load's characteristic pattern. The amount of feed-in for the various bioenergy kinds of plants reflects the fraction of power rating. Furthermore, despite the penalty component in the optimization problem favoring coal facilities, there is a zero-electricity formed by a coal power station in the solar zone in 2050. The slower scaling behavior of coal power plants compared to gas-steam power plants helps explain this occurrence. Alternatively, the coal-fired power plant's long minimum power duration or long minimum suspension time could be the origin of this phenomenon. It is also feasible that both factors play a role in the occurrence.

5.1. Excess Power and Energy. Table 2 shows the remaining excess power and energy after addressing the residual demand, while the maximum extra electricity in the solar-dominated region is higher. Contributing to the increase can account for both. The solar-dominated region has a greater annual excess energy due to the block-like occurrences of extra electricity during strong solar phases. EESS can only retain and period a limited portion of this extra wind energy in the short and medium run. When the EESS reaches capacity, the residual extra energy can only be utilized in cross-sectoral applications.

5.2. EESS Optimization. The EESS optimization algorithm's implementation and simulation. After modeling all of the periods using stage 1's technique, it was determined that maximum stress occurs. The EESS has a rated power of 2 MW and maximum storage of 2 MWh. Both the charge-discharge efficiency are adjusted to 90%. The initial and ultimate SOCs are both fixed to 50%, with the SOC control parameter being set to 10% to 90%. Table 3 shows the possibilities for the EESS simulation. The purpose of setting the situation is indicated below so it can present all of the possible outcomes.

5.2.1. Case 1. Case 1's peak demand (with ESS) happens. As a result, phase 1 planning is used to reduce peak load (with ESS). Then, the SOC is set to the highest benefit well before the peak period, and the discharge is sustained from 2 : 00 p.m. to 6 : 00 p.m. since peak usage decrease is the major goal. The ESS reduces 479.4 kW at the initial peak demand, as shown in Figure 6. The peak demand decrease is not significant because the original load distribution is the level just at the peak. Table 4 summarizes the findings of case 1, as

Table 3: Simulation of state EESS.

State	EESS configuration data	Characteristic
Case 1	2 MW/2 MWh Initial SOC-50% Charge/discharge Efficiency-90%	Occurs on peak demand (with EESS)
Case 2		Case 2 occurs on peak demand (without EESS) Case 1 peak demand
Case 3		Case 3 (without EESS) less than peak demand Case 1 (with EESS) peak demand

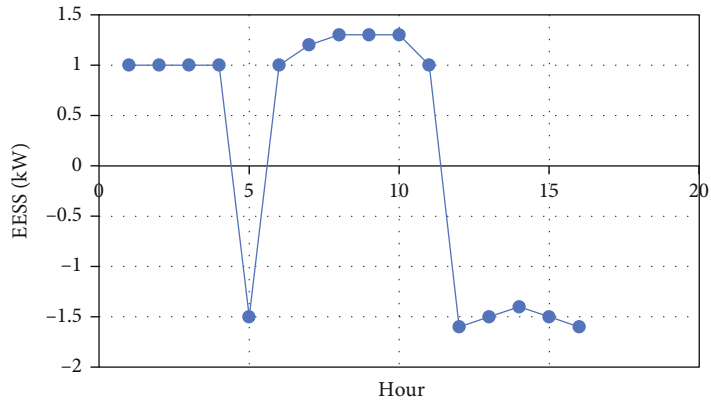

Figure 6: Power of EESS.

Table 4: Case summary of case 1.

State	Original peak demand	New peak demand (with EESS)	Reduction of demand cost	Reduction of regular energy cost
Case 1	5800.3 (kW)	5430.7 (kW)	3096.8 ($)	137.6 ($)

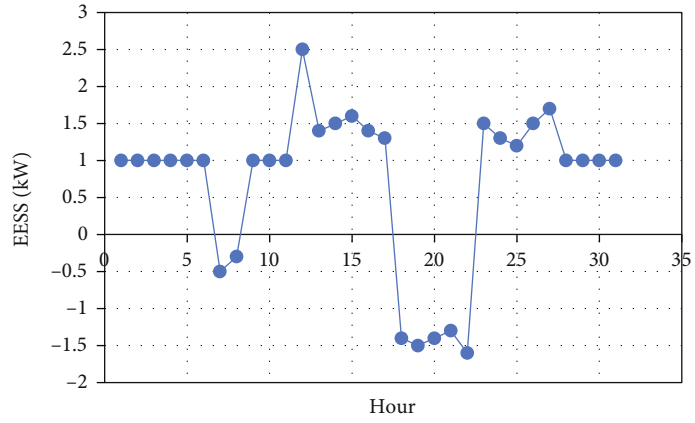

Figure 7: Power of EESS.

well as the peak demand that defines that the demand price is set at 5420.8 kW.

5.2.2. Case 2. Phase 1 is assigned to phase 2 of the flowchart; then, it is not the maximum load that defines the request cost through to the planning of minimizing the peak demand. The goal of case 2's simulations is to verify the EESS's power planning when maximum stress reaches the peak demand which influences demand price. Because consumption cost is not incorporated in the optimization problem in Figure 7, discharge is done when the power price is too high to save energy. As a result of the low price of electricity, the EESS is compensated between 12 : 00 and 1 : 00 p.m. However, due to the peak demand restriction that

Table 5: Case 2 summary.

State	Original peak demand	New peak demand (with EESS)	Reduction of regular energy cost
Case 2	5615.2 (kW)	5420.7 (kW)	150.8 ($)

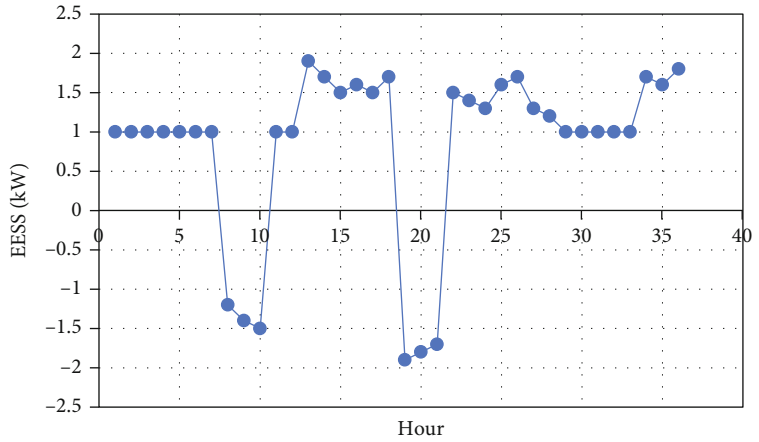

Figure 8: Power of EESS.

Table 6: Case 3 simulation.

State	Original peak demand	New peak demand (with EESS)	Reduction of regular energy cost
Case 3	3247.8 (kW)	4928.7 (kW)	193.2 ($)

affects the cost of demand in case 1, increasing the SOC to the maximum is not achievable. The simulation results indicate that the EESS charged between 12 : 00 p.m. and 1 : 00 a.m. to equalize the ending SOC with a process of being developed. The EESS is collected from 12 : 00 p.m. to 1 : 00 p.m. because a model is only done with one day, and the cheapest cost is presented in the evening. Table 5 contains the findings from case 2.

5.2.3. Case 3. Since case 3 is a weekend demand, the peak is not as high. Simulating case 3 has the goal of confirming the EESS's power planning whenever the peak usage does not exceed the peak load that affects the cost of the demand. The EESS power output and SOC characteristics in Figure 8 are similar to those in case 2. The electricity cost is minimized without breaching the limitations because the original peak demand is modest. When using the EESS, the maximum force is increased by 539.6 kW in comparison to the initial peak demand; nevertheless, the demand cost is unaffected. Table 6 summarizes the findings of case 3.

6. Conclusion

From the work, the following conclusions are made:

(i) Sensitivity analysis revealed only a minor rivalry between EESS and flexible bioenergy in the near and medium run. However, in areas where solar power is abundant, EESS can partially replace adaptable biofuels. Increased storage capabilities would have a diminishing marginal value since only a restricted volume of information electrical power can be integrated into an electricity system because the EESS fleet's capability was a singularity problem giving to the negative residual demand peak

(ii) As a result, flexible bioenergy supports EESS in the cases, and it provides a long-term storage alternative to EESS, which would otherwise be a primary participant. The EESS optimization method was created to arrange the outputs of the ESS in a structured manner in another energy management plan

(iii) This method is divided into two stages: stage 1 was designed to reduce peak load associated with demanding costs, and stage 2 was intended to reduce total energy costs. There are three simulations used to ensure that the schedule was done correctly

(iv) In a single building, the presented algorithms showed power management measures. This paper's contribution is that multiple kinds of technology can be regulated for the similar goal of peak demand decrease and costs of energy reducing

Data Availability

The data used to support the findings of this study are included within the article. Further data or information is available from the corresponding author upon request.

Conflicts of Interest

The authors declare that there is no conflict of interest regarding the publication of this paper.

Acknowledgments

The authors thank the Mizan Tepi University, Ethiopia, for providing help during the research and preparation of the manuscript. This work is also supported by the Taif University researchers supporting project number (TURSP-2020/40), Taif University, Taif, Saudi Arabia.

References

[1] K. N. Nwaigwe, P. Mutabilwa, and E. Dintwa, "An overview of solar power (PV systems) integration into electricity grids," *Materials Science for Energy Technologies*, vol. 2, no. 3, pp. 629–633, 2019.

[2] E. Rakhshani, K. Rouzbehi, A. J. Sánchez, A. C. Tobar, and E. Pouresmaeil, "Integration of large scale PV-based generation into power systems: a survey," *Energies*, vol. 12, no. 8, p. 1425, 2019.

[3] F. Mohamad and J. Teh, "Impacts of energy storage system on power system reliability: a systematic review," *Energies*, vol. 11, no. 7, p. 1749, 2018.

[4] J. Liu, X. Chen, S. Cao, and H. Yang, "Overview on hybrid solar photovoltaic-electrical energy storage technologies for power supply to buildings," *Energy Conversion and Management*, vol. 187, pp. 103–121, 2019.

[5] P. Tafarte, A. Kanngießer, M. Dotzauer, B. Meyer, A. Grevé, and M. Millinger, "Interaction of electrical energy storage, flexible bioenergy plants and system-friendly renewables in wind- or solar PV-dominated regions," *Energies*, vol. 13, no. 5, p. 1133, 2020.

[6] H. Akbari, M. C. Browne, A. Ortega et al., "Efficient energy storage technologies for photovoltaic systems," *Solar Energy*, vol. 192, pp. 144–168, 2019.

[7] C. S. Lai, Y. Jia, L. L. Lai, Z. Xu, M. D. McCulloch, and K. P. Wong, "A comprehensive review on large-scale photovoltaic system with applications of electrical energy storage," *Renewable and Sustainable Energy Reviews*, vol. 78, pp. 439–451, 2017.

[8] J. Liu, X. Chen, H. Yang, and Y. Li, "Energy storage and management system design optimization for a photovoltaic integrated low-energy building," *Energy*, vol. 190, article 116424, 2020.

[9] H. Fathima and K. Palanisamy, "Optimized sizing, selection, and economic analysis of battery energy storage for grid-connected wind-PV hybrid system," *Modelling and Simulation in Engineering*, vol. 2015, Article ID 713530, 16 pages, 2015.

[10] Y. Yoon and Y.-H. Kim, "Charge scheduling of an energy storage system under time-of-use pricing and a demand charge," *The Scientific World Journal*, vol. 2014, Article ID 937329, 9 pages, 2014.

[11] G. Sha, Q. Duan, W. Sheng et al., "A multiport electric energy routing scheme applied to battery energy storage system," *Journal of Engineering*, vol. 2021, Article ID 6637926, 15 pages, 2021.

[12] R. Zhu, A. Zhao, G. Wang, X. Xia, and Y. Yang, "An energy storage performance improvement model for grid-connected wind-solar hybrid energy storage system," *Computational Intelligence and Neuroscience*, vol. 2020, Article ID 8887227, 10 pages, 2020.

[13] D. Duncan, A. M. Zungeru, M. Mangwala et al., "Power-efficient hybrid energy storage system for seismic nodes," *Journal of Engineering*, vol. 2020, Article ID 3652848, 21 pages, 2020.

[14] X. Tan, Q. Li, and H. Wang, "Advances and trends of energy storage technology in microgrid," *International Journal of Electrical Power & Energy Systems*, vol. 44, no. 1, pp. 179–191, 2013.

[15] C. S. Lai and M. D. McCulloch, "Levelized cost of electricity for solar photovoltaic and electrical energy storage," *Applied Energy*, vol. 190, pp. 191–203, 2017.

[16] P. Komarnicki, P. Lombardi, and Z. Styczynski, "Electric energy storage system," in *Electric Energy Storage Systems*, pp. 37–95, Springer Berlin Heidelberg, Berlin, Heidelberg, 2017.

[17] A. Albers, D. Wagner, L. Kern, and T. Höfler, "Adaption of the TRIZ method to the development of electric energy storage systems," *Procedia CIRP*, vol. 21, pp. 509–514, 2014.

[18] D. Tran and A. M. Khambadkone, "Energy management for lifetime extension of energy storage system in micro-grid applications," *IEEE Transactions on Smart Grid*, vol. 4, no. 3, pp. 1289–1296, 2013.

[19] N.-K. Kim, M.-H. Shim, and D. Won, "Building energy management strategy using an HVAC system and energy storage system," *Energies*, vol. 11, no. 10, p. 2690, 2018.

[20] M. Lafoz, L. Garcia-Tabares, and M. Blanco, "Energy management in solar photovoltaic plants based on ESS," in *2008 13th International Power Electronics and Motion Control Conference*, pp. 2481–2486, Poznan, Poland, 2008.

Hindawi
International Journal of Photoenergy
Volume 2022, Article ID 3787141, 12 pages
https://doi.org/10.1155/2022/3787141

Research Article

Performance Development and Evaluation of Solar Air Collector with Novel Phase Change Material

V. Vedanarayanan,[1] J. Dilli Srinivasan,[2] K. Arulvendhan,[2] P. Thirusenthil Kumaran,[3] R. Selvakumar,[4] T. Maridurai,[5] M. Sudhakar,[6] Sami Al Obaid,[7] Saleh Alfarraj,[8] M. M. Raj,[9] and Ishwarya Komalnu Raghavan[10]

[1]*Department of Electronics and Communication Engineering, Sathyabama Institute of Science and Technology, Chennai, 600 119 Tamil Nadu, India*
[2]*Department of Electrical and Electronics Engineering, SRM Institute of Science and Technology, Ramapuram, 600089 Tamil Nadu, India*
[3]*Department of Electrical and Electronics Engineering, Rajalakshmi Engineering College, Thandalam, 602105 Tamil Nadu, India*
[4]*Department of Electronics and Communication Engineering, Koneru Lakshmaiah Education Foundation (K L University), Guntur, 522502 Andhra Pradesh, India*
[5]*Department of Mechanical Engineering, Saveetha School of Engineering, SIMATS, Chennai, Tamil Nadu, India*
[6]*Department of Mechanical Engineering, Sri Sairam Engineering College, West Tambaram, Chennai, 600044 Tamil Nadu, India*
[7]*Department of Botany and Microbiology, College of Science, King Saud University, P.O. Box 2455, Riyadh 11451, Saudi Arabia*
[8]*Zoology Department, College of Science, King Saud University, Riyadh 11451, Saudi Arabia*
[9]*Department of Mechanical Engineering, Seoul National University of Science & Technology, Seoul, Republic of Korea*
[10]*Department of Electromechanical Engineering, Faculty of Manufacturing, Institute of Technology, Hawassa University, Ethiopia*

Correspondence should be addressed to Ishwarya Komalnu Raghavan; ishwarya138@hu.edu.et

Received 22 November 2021; Accepted 12 May 2022; Published 4 July 2022

Academic Editor: Ahmad Umar

Copyright © 2022 V. Vedanarayanan et al. This is an open access article distributed under the Creative Commons Attribution License, which permits unrestricted use, distribution, and reproduction in any medium, provided the original work is properly cited.

Experiments were carried out on an evacuated tube solar air collector connected to intrinsic thermal power storage to provide warm air unless solar radiation was available. As a phase change material, stearic acid was employed (PCM). Water has been used as a base fluid for converting sunlight into electricity gain to warm air, and the solar collector's manifold was connected to the intrinsic thermal energy store. The most significant temperature variation between warm air and ecologic air was 38°C and 22°C, respectively, during direct and indirect solar radiation. A circular fin arrangement was used to achieve a flow rate of 0.020 kg s^{-1}. The efficiency of minimum airflow rates (0.020 kg s^{-1}) was 0.08–0.48 times that of maximum airflow rates (0.04 kg s^{-1}). Because of the PCM's better heat-storing capability, this system has a benefit over sensible storage systems in that it may be used after sunset.

1. Introduction

On the global market, evacuated tube solar collectors (ETCs) are extensively utilized. In 2003, ETC had an 88 percent market share, and in 2009, it had a 95 percent market share. Solar tube collectors (ETCs) convert sunlight into electricity (solar thermal power conversion), making them more suited to operations that require higher temperatures than a none-vacuated system can provide [1]. An evacuated tube solar collector loses minimum heat (UA = 1.2 – 1.67 WK^{-1}) than a flat base solar collector (UA = 2.3 WK^{-1}). When compared to flat base solar collectors, the coupled influence of specialized plating and pressurized shielding in such photovoltaic collectors delivers enhanced heat processing. As a result, solar thermal applications such as solar air heating are increasingly relying on optical evacuated piping systems

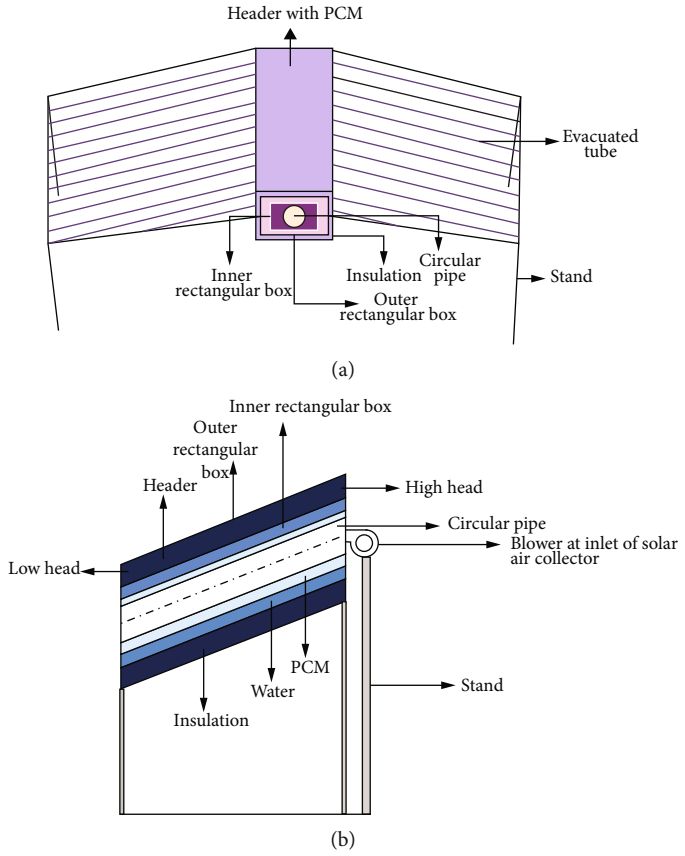

Figure 1: Layout designs of an evacuated tube solar air collector based on a PCM unit and an air heating system.

Table 1: Specifications for the evacuated tube solar air collector and thermal power storage system.

Components	Specifications
The number of collector tubes	36
Tube dimensions	1.8 m
Outer glass tube diameter	0.05 m
Inner glass tube diameter	0.04 m
Vacuum in between outer glass tube and absorber tube	0.05
Collector's inclined angle	20
Rectangular outer box dimension	$1.8 \times 0.25 \times 0.25$
Rectangular inner box dimension	$1.8 \times 0.2 \times 0.2$

[2]. In China, ETCs with a surface area of about 100 m^2 have been deployed and are producing hot air.

According to a survey of the literature, much effort has gone into the research and development of ETCs. The efficiency of series combinations declined as the number of collectors increased, while parallel combinations stayed constant as the number of collectors increased [3–5]. When it comes to the thermal characteristics of a solar cooker, an evacuated tube collector outperformed a flat base collector. According to a quantitative analysis of water flow over long tubes, the occurrence of a static zone near the capped side of the tube could impair the collector's performance [6].

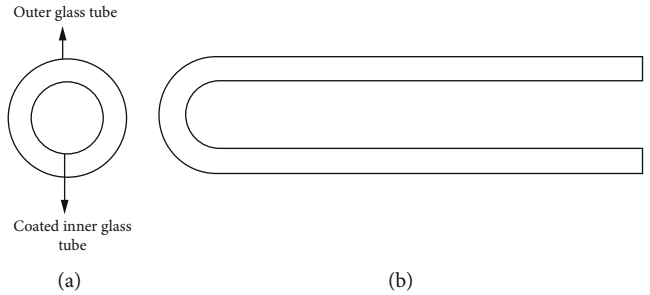

Figure 2: Design of an evacuated tube: (a) from the side; (b) from the front.

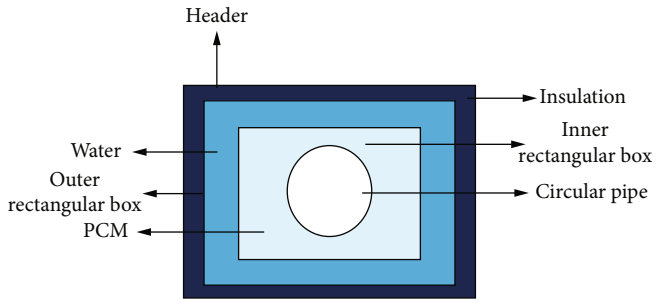

Figure 3: Header schematic figure with PCM unit.

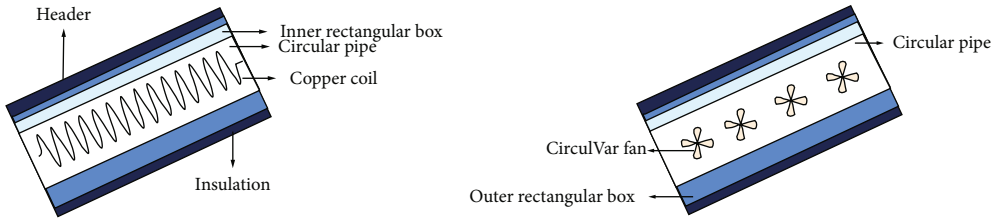

Figure 4: (a) The copper coil in the header's circular pipe. (b) The circular fin in the header's circular pipe.

Table 2: Stearic acid thermophysical characteristics.

Material	Properties	Value
Stearic acid	Melting point	53°C
	Solidifying point	54°C
	Melting latent heat	48°C

High thermal performance was achieved in an experimental collector with opposite evacuated tubes by keeping a 0.2 m gap between the tubes and the collecting chamber [7]: a solar cooker with a container made of phase change material (PCM) and a solar collector made of evacuated tubes (ETSC). Sunset cooking expanded faster than noon cooking when PCM was used as a heat chamber [8, 9]. However, lunchtime cooking seemed to have no impact on evening cooking. The rate of movement through the tubes was influenced by the temperature of the tank. Shortening the tube length resulted in high efficiency. The inlet flow rate had no impact on the flow structure in the glass tubes [10]. Over time, the influence of dust accumulation reducing the tube length resulted in higher efficiency. The inlet flow rate had no effect on the structural flow system in the pipes [11, 12]. Over time, there is impact of dust buildup on the solar collector. An energy flow analysis model was used to develop an evacuated tube solar collector with something like a U-tube. They came to the conclusion that when the collector's heat drop coefficient was high, the impact was clear [13].

In terms of energy and maintenance, compare the behaviour of a flat base solar collector versus an absorber plate evacuated tube collector. The parallel-base collector and thermal pipe evacuated tube collector had yearly collecting accuracy of 46.1 percent and 60.7 percent, respectively, while system efficiencies were 37.9 percent and 50.3 percent [14]. When a mini channel-equipped evacuated tube solar collector was equated to a similar-dimensioned evacuated tube solar collector without mini channels, the mini channel-equipped evacuated tube solar collector outperformed the evacuated tube solar collector without mini channels [15–17]. The two different thermosyphon solar radiation has a better daily and seasonal thermal behaviour than the solitary thermosyphon design. Emphasized monoabsorbers and evacuated tube heat pipes fared better in solar collectors than focused double-sided absorbers and evacuated tube heat pipes. At a reduced rate, a high air temperature variance was obtained in the evacuated tube solar collector. In terms of energy conservation, the evacuated tube collector outperformed the flat base solar collector. The flat base solar collector with PCM obtained the best results at a 10° tilt of inclination, with the effectiveness of 47 percent, 51.1 percent, and 52.0 percent in the instances without PCM, PCM, and Cu-PCM composites, accordingly [18]. Evacuated tube solar air collectors built-in with thermal energy collectors are commonly utilized to achieve high heat fluctuations during sunset hours. Solar energy can be stored using thermal power storage—a form of thermal energy in internal heat storage [19]. PCM-based intrinsic heat storage systems have a higher heat energy capacity for every unit space than conventional storage systems. Because it can store both prudent and intrinsic heat, the PCM is a popular choice in the field of thermal power storage. Because of the solar stove and the PCM storage unit, evening cooking was possible. Over a series of thermal cycles, fatty acids demonstrated proper consistency with fluctuations in melting point and intrinsic heat of reaction [20]. PCMs have many uses, including waste heat recovery, solar energy, building energy-saving, and air conditioning. Because of its excellent energy storage capacity,

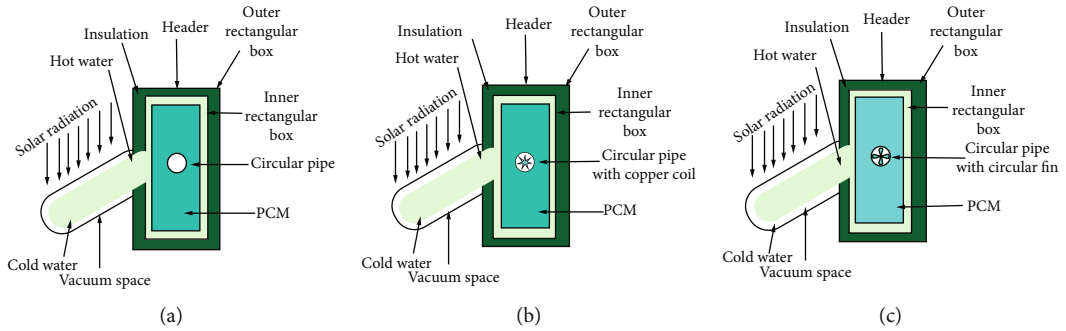

Figure 5: Schematic representation of (a) the normal collector; (b) the normal copper coil collector; (c) the normal circular fin collector.

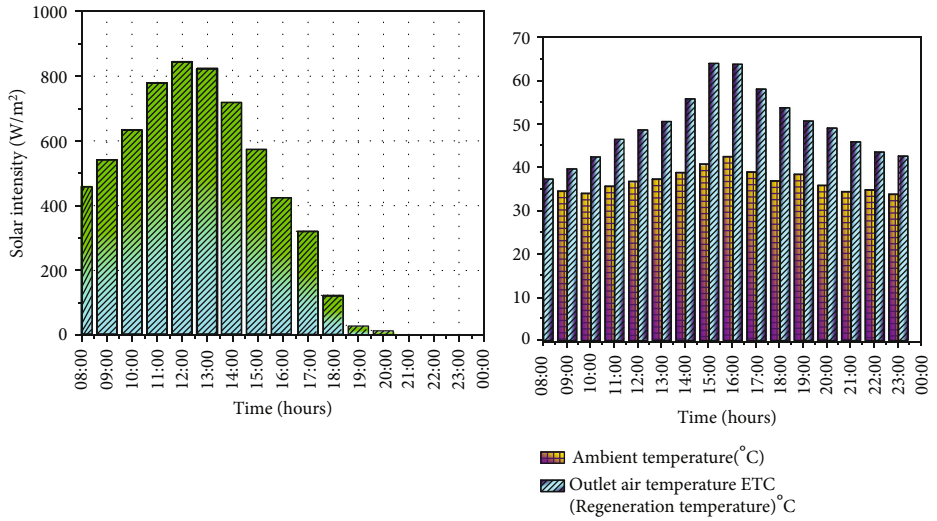

Figure 6: Changes in temperature and solar intensity evolve over time in the case of stearic material as a phase change material for normal collectors at a flow rate of 0.02 kg s^{-1}.

PCM has been extensively employed in various latent heat storage devices. The increased interest in utilizing PCM in building applications is primarily due to the constant growth in building energy consumption. However, PCM leakage and poor thermal conductivity have hindered the use of PCM in buildings on a broad scale.

Inorganic PCMs were found to be unsuitable after a specific number of cycles, whereas organic PCMs could withstand up to 1000 heat cycles. Acetanilide was a promising PCM for indoor cooking since it worked well with aluminium as a restricting material [21, 22]. A direct-contact heat exchanger's heat storage capability was improved using the PCM. Using a PCM storage unit as a cooling system used less electricity than traditional ventilation and air conditioning systems [23, 24]. PCMs were placed near translucent building envelopes because it was desirable to reveal construction methods to direct solar radiation. When a numerous PCM was evaluated as a thermal storage collector, it was revealed that raising the airflow rate during the charging period was more efficient than lowering the incoming air temperature [25]. When stearic acid was employed as the PCM, a quantitative survey of the thermal behaviour of an

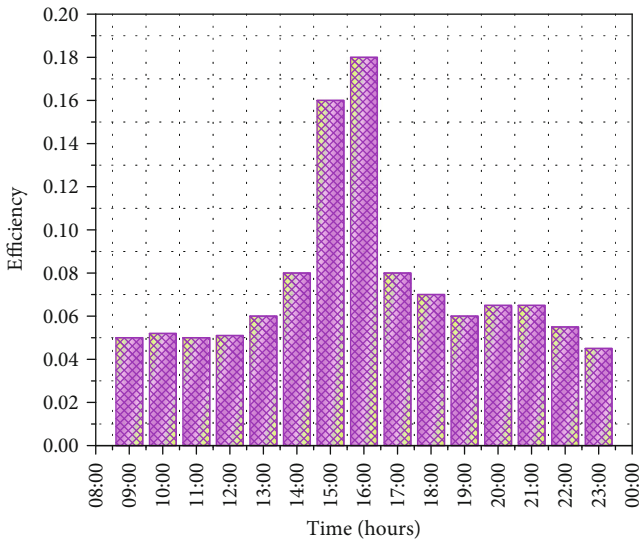

Figure 7: Variation of stearic acid efficiency with time as phase change material at 0.02 kg·s^{-1} in the case of a normal collector.

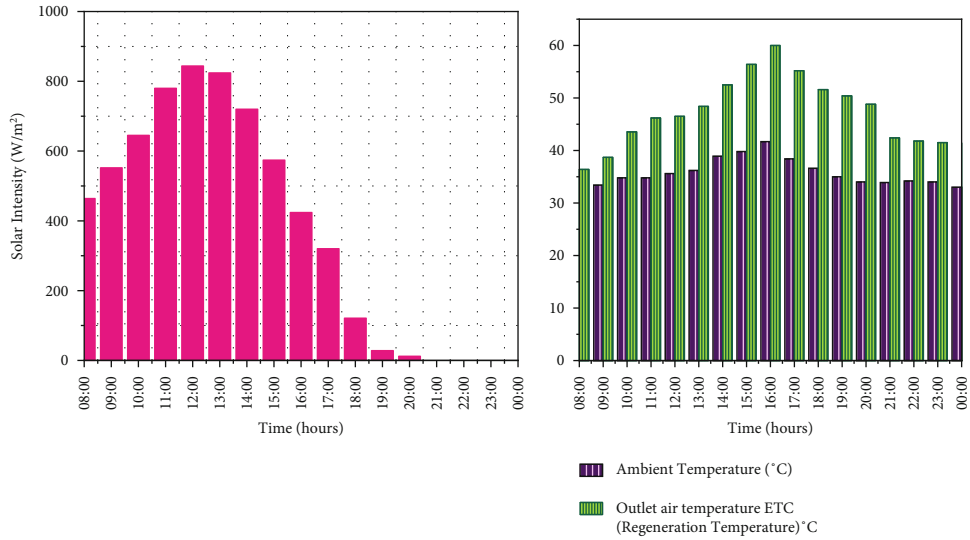

Figure 8: Temperature variation and solar intensity with a flow of 0.04 kg s^{-1} for a normal collector in the case of stearic acid as phase change material.

embedded absorber holding solar heater with a circular reservoir indicated that the behaviour of the intrinsic thermal storage unit was superior to the conventional storage throughout the day. The most extensively utilized technology for energy storage is prudent water heating. Despite its low cost and strong heat transfer properties, water's low energy storage capacity necessitates a big volume. The vast temperature range across which the stored energy is dispersed is another disadvantage of water storage [26]. Stearic, palmitic, and myristic acids can be used to store energy in solar systems for heating and cooling [27]. Integrating solar collectors into the building envelope is advantageous for aesthetic and economic reasons, but it is essential to observe architectural standards and local construction traditions. Solar collection and heat insulation of the building envelope are provided by a collector device integrally incorporated into the façade. The benefits of façade-integrated collectors include cost savings through the shared use of building components, the replacement of the traditional façade, and collectors suited for both new and existing structures. There has been research on evacuated tube solar air collectors, flat base solar collectors, and piping system evacuated tube collectors, but none on an evacuated tube solar air collector with inbuilt thermal storage [28]. A comprehensive study with incorporated PCM is presented of an evacuated tube solar air collector. The goal of this research is to generate heated air at various flow rates while using direct and indirect solar energy [29]. Because it possesses a significant heating value for every unit of weight, a vast melting temperature range, consistent cycling, is noncorrosive, and chemically inert, stearic acid is used as a PCM [30].

2. Experimental Procedure

A pictorial representation of an evacuated tube solar air collector with intrinsic thermal power storage is indicated in Figure 1. The heat exchanger is made up of 36 evacuated tubes, a header (heat transfer) with an incorporated PCM storage container, fins, and a reflector, and it is formed of water. Table 1 shows the experimental setup specific requirements.

Figure 2 depicts a hypothetical design for the evacuated tubes utilized in this mechanism. Each evacuated tube is manufactured by fusing the ends of two borosilicate glass or glass tubes. The air is forced out of the gap between the two glass tubes, generating a vacuum that functions as isolation. The clear outer layer tube passes light to travel along with minimal reflection. The outer layer of the inflatable raft is wrapped with an aluminium nitride (Al-N/Al) coating material that soaks up and gets converted solar radiation to thermal energy. The selective absorption coating has a low emissivity and a high absorptivity.

A header with two squares intra and inter is employed in this arrangement, as indicated in Figure 3. It is made of two rectangular boxes of mild steel. There are 36 holes outside, 18 on each side of the rectangular box. The exposed ends of the evacuated pipes are placed in these pipes, while the frame supports the sealed ends of the pipes. A 0.075 m diameter mild hollow steel tube is in the centre of the inner rectangular box. 50 kg of commercialized stearic acid is put into the internal rectangular box (PCM). Polyurethane isolation is utilized to ensure that temperature distribution from the header to the environment is avoided on the outside of the rectangular box.

At a 20° angle on the horizontal south side, the collector is inclined. To optimize the thermal behaviour of the evacuated tube solar air collector, a variety of designs and reflectors are used. A reflector composed of an aluminium sheet with an 85 percent reflectivity sits beneath the evacuated tubes. The purpose of the arrangements is to enhance the heat of the air by placing the output air concentrically into the circular pipe. As a result, the airflow slows and the air's residence time within the pipe increases, elevating the heat of the outflow air. In the experimental arrangement, two various types of fins are used:

(i) Circular fin

(ii) Copper coil

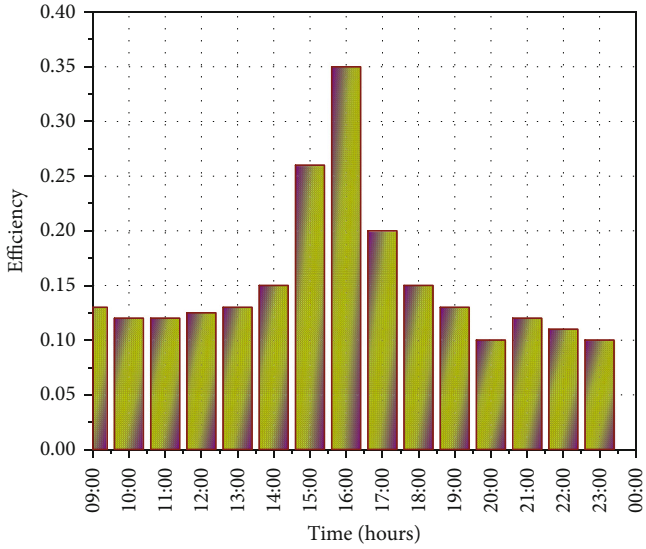

Figure 9: Change in efficiency over day and night in the evacuated tube solar air collector.

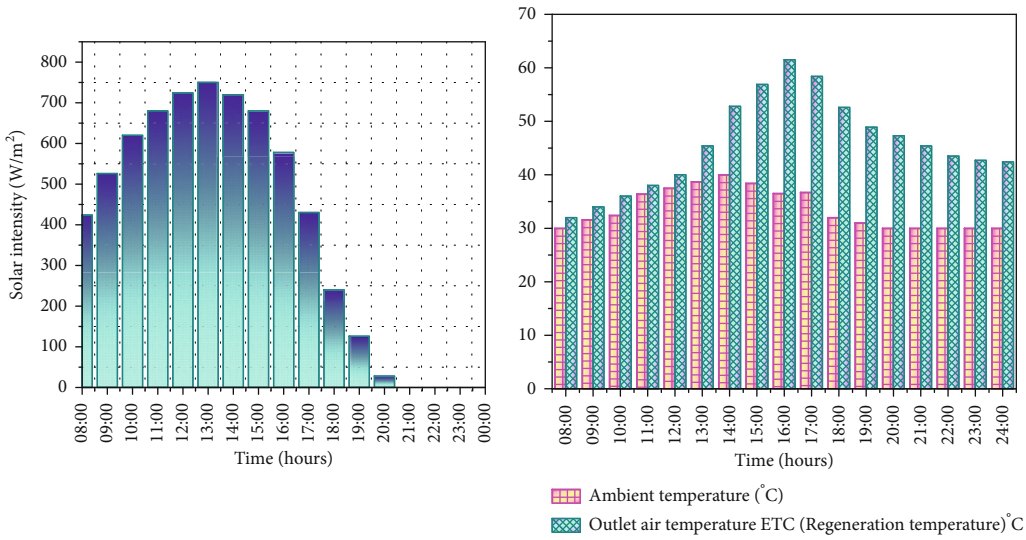

Figure 10: Temperature and intensity variations in a phase change material stearic acid with the time rates of 0.02 kg s^{-1} for normal copper collector devices.

The copper coil used is 1.8 meters long and 0.1 meters in diameter. The copper wire is 0.007 m in diameter. The other fin is 1.5 meters long and has a diameter of 0.085 meters. Mild steel is used for the circular fins. Figures 4(a) and 4(b) show a schematic of a copper coil and a circular fin in a circular header pipe. Reflectors can improve the effectiveness of an evacuated tube solar air collector by minimizing the amount of solar radiation wasted as it goes through the tubes. The liquid within the pipes is heated by sunlight which then passes finally into the air into the thermal storage unit. An extractor blows the solar air collection with a rating of 0.350 KW. A controller regulates the airflow, and an AC provides a power supply for the blower. Two reflectors, one side of the header to emit light on the evacuated pipes, are put beneath evacuated pipes. Each mirror measures 1.56 meters in length and 1.18 meters in width. It is a galvanized mild steel sheet with an aluminium coating for excellent reflectivity. A header with 100 liters of water and evacuated tubes that operate as a convective heat transfer medium is part of the experimental setup. The water present in the tubes is heated by solar radiation and then moved to the thermal storage container and eventually to the air. A capacity with 0.350 KW power blows the air in the solar air collection. The airflow rate is regulated by a regulator, and an AC main supply powers the blower.

Thermal degradation, latent heat of fusion, toxicology, and other properties are used to select phase transition materials. Commercially available stearic acid was utilized in this experiment, and it has the thermophysical parameters listed

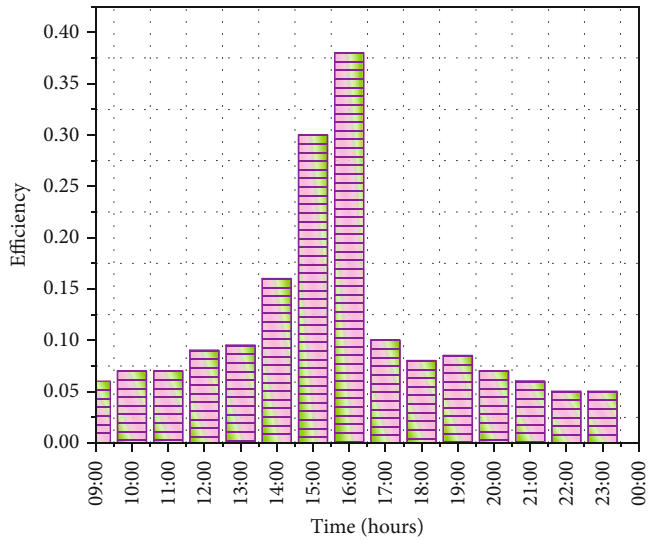

Figure 11: Efficient change in the flow rate 0.02 kg s^{-1} for a normal copper coil collector when stearic acid is the phase change material.

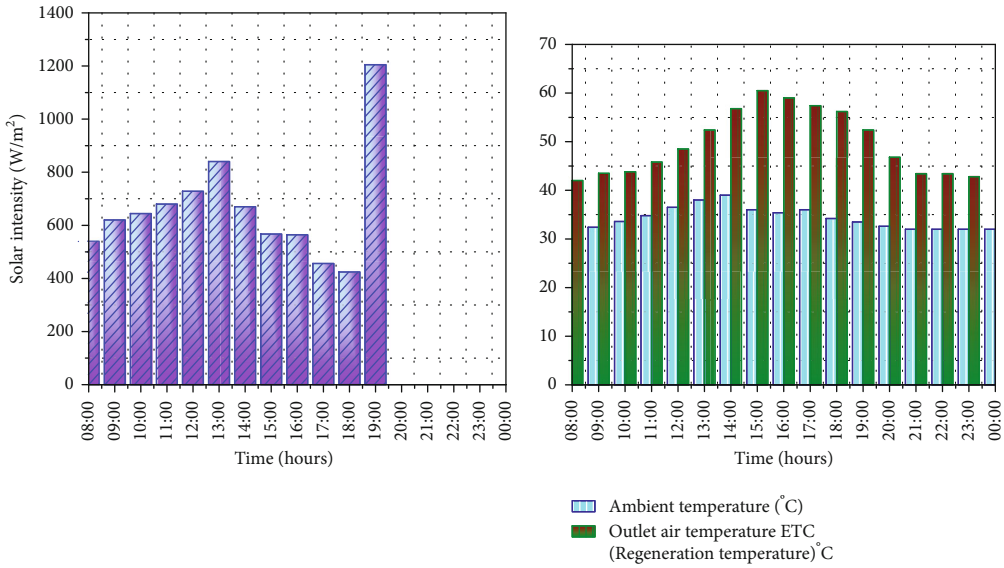

Figure 12: Temperature variation and intensity of time in stearic acid as phase change material at the flow rate of 0.04 kg/s^{-1} for a normal copper coil collector.

in Table 2. 50 kg of stearic acid is added to the rectangular header as a thermal storage component (heat exchanger). It survives as a means of heat transfer and heats up the liquid over the day and releases it into the atmosphere at night.

3. Instrumentation

In these experiments, the following are different parameters:

(i) Fluid temperature, air outlet temperature, and material temperature for thermal storage

(ii) Temperature atmosphere

(iii) The intensity of solar radiation

(iv) Rate of airflow

The following devices measure these parameters.

Temperatures of the working liquid, air ventilation, and thermal storing material are measured using RTD PT100 thermocouples. The temperature indicator is displayed with ±0.3°C exactness and an adjustment of 0.1°C on the digital heat indicator. The dry environmental air temperature with an exactness of ±0.5 percent and an adjustment of 0.5°C is measured by a sling psychrometer. In order to monitor the sun intensity at the test site with an exactness of 2 W/m^2 and an amendment of 1 W/m^2, a pyranometer CM11 in Kipp and Zonen in Holland is used over the day.

At the beginning of the experiment, an anemometer is being used to estimate airflow. An AM-4208 separate sensor

with a 0.1 m/s resolution and a (±2% + dpipe) accuracy is used for monitoring of airspeed. Thanks to digital understandability and the comfort of a remote sensor, it provides fast and precise readings. The roller bearing, minimal friction ensures unrestricted fan motion and thus accuracy at all speeds.

4. Analysis of Experimental Data

All 36 evacuated tubes and the header are full of water at 28°C during the experimental setup. The solar collector is exposed to air every day at 06:30 h to gain solar radiation, and readings are obtained every one hour beginning at 09:30 h. When solar radiation strikes evacuated tubes, the heat is soaked up and converts to water. Now that the water has been heated, the thermosyphon effect, when hot water is raised, but instead cold water comes into evacuated tubes. These evacuated tubes deliver hot water to the outside rectangular box. The thermal power storage container is kept inside the outer rectangular box's internal rectangular box. The thermal power storage device in the interior rectangular box heats up as a result of the heat absorbed from the water. In the interior inside the rectangular box, air flows through a circular pipe. The circular pipe is heated by absorbing heat from the thermal power storage device. The hot working liquid is at the maximum head, and the cold working liquid is at the minimum head in the header (heat transfer), resulting in the same thermosyphon effect.

Three scenarios are examined.

The heat absorbing from the water is responsible for the combined heat and power utilization in the inner rectangular box. The air passes through a circular pipe inside the rectangular box. The circular tube is heated from combined heat and power material by absorbing heat. The high-temperature working liquid is on the upper head, the heat exchanger is on the lower head, and the cold working liquid has the same thermosyphon effect.

(i) Normal collector

(ii) Normal copper-coil collector

(iii) Normal circular fin collector

As illustrated in the schematic picture in Figure 5, a normal collector comprises a collector with reflections (a). Reflectors are utilized beneath the evacuated tubes to reflect solar energy onto the evacuated tubes' bottom surface. A typical collector, as indicated in Figure 5, comprises a copper coil and a collector with reflectors (b). A copper coil absorbs the heat from the PCM inside the circular pipe and transfers it to passing air. The coil is 1.8 meters long and 0.1 meters in diameter. The copper coil diameter is 0.007 m. This type of collector has a reflector and circular fin, as shown in Figure 5(c). The circular fin is used in this arrangement to collect temperature from the PCM and distribute it through the tubing into the air instead of the copper coil inside the circular tube. The circular fin is made from mild steel and has a length of 1.8 meters and a diameter of 0.085 meters.

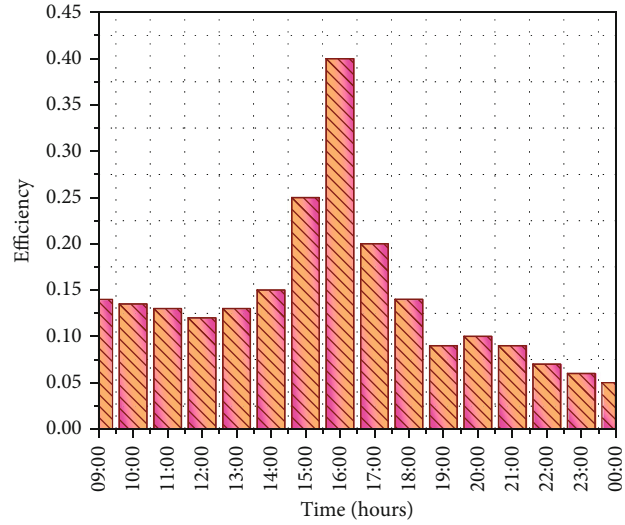

Figure 13: Efficiency variation of 0.04 kg/s^{-1} for the normal copper coil collector with stearic acid as a phase change material.

5. Results

This study will evaluate the efficiency of an evacuated solar air heater tube and examine the air outflow temperature of the evacuated solar air tube with inbuilt PCM during daylight and off daylight hours at various airflow rates. During the months of April and May 2020, the experimental analyses will be carried out. The ambient temperature ranges between 31°C and 41°C for most of the days. The tests were carried out on days when the sky was clear. The measurements were made between the hours of 08:00 and 24:00. The evacuated tube collector was oriented northward.

Figure 6 shows fluctuated air temperatures at inputs and outputs, as well as changes in temperatures at a minimum and maximum head of water and PCMs and sun intensity over time in the evacuated tube collector. At midday, 845 W/m^2 was the highest intensity, while the temperature in the environment was between 30°C and 41.5°C. A maximum difference in airflow temperature of 21.8° C, with air outlets reaching 62.5° C, was achieved. Maximum-head and minimum-head water temperatures of 98.7°C and 94.3°C, respectively, while maximum-head and minimum-head temperatures of PCMs were at 90.4°C and high and lower head temperatures of 64.5°C. A temperature variation of 9.4°C in the air was reached due to a large amount of heat stored by the PCM. Sensitive as well as latent heat can be stored in it.

Figure 7 shows the efficiency of the solar air collector tube, both daytime and nighttime, over time. The maximum efficiency of a conventional collector at a minimal flow rate of 0.02 kg s^{-1} was 18%. During off-sunshine hours, a temperature variation between output air and ecologic air is achieved because of the use of PCM, and effectiveness drops swiftly at first and then gradually with a low beat rate.

Figure 8 demonstrates that at a higher flow rate of 0.04 kg s^{-1}, the maximum intensity was 844 W/m^2 throughout the day, with ambient temperatures varying from 33°C to 42°C. The largest temperature difference measured 18.3°C, with a higher exit air temperature of 60°C. The maximum water temperatures

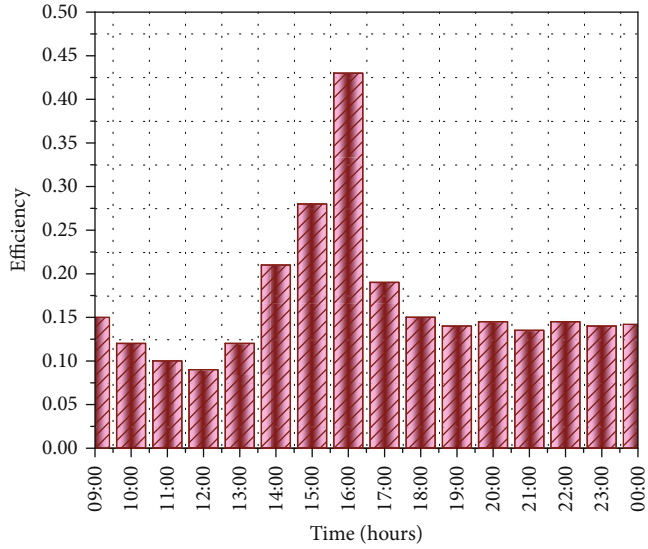

Figure 14: Efficiency in a stearic acid phase change material at a flow rate of 0.02 kg s^{-1} for a normal circular fin collector.

were 98.4°C and 96.5°C at high and low head, respectively, whereas PCM attained maximum temperatures of 94.3°C and 63.5°C at maximum and minimum head, respectively. The air temperature differential was 8.4°C at 24:00 h, which was slightly less than the usual collector at a low flow rate.

The change ineffectiveness in the evacuated tube solar air collector over time, both day and at night, is depicted in Figure 9. At a high airflow rate of 0.04 kg s^{-1}, the highest efficiency in a traditional collector was 35%. The research shows that at a higher flow rate, maximum efficiency is 2.05 times the maximum at a low flow rate. This is due to the high inflow rate that roughly doubled the low airflow rate, while the temperature variation between the environmental and outlet air remained practically constant. Due to rising air resolution time at a low flow rate, the output air temperature progressively increased with a copper coil at a low airflow rate. As for layout in Figure 10, the high intensity over the day was 750 W/m^2, and the environmental temperature ranged from 30°C to 40°C. The highest heat variation between the entrance and outflow air was 25°C, with the outflow air reaching a maximum temperature of 61.5°C. The maximum water temperatures were 105.5°C and 92.4°C at high and low head, respectively, whereas PCM attained the highest temperatures of 99.6°C and 59.5°C at high and low head, respectively. A temperature variation of 12.4°C could be achieved in the air. According to the statistics, the use of copper coils resulted in a higher temperature increase than the previous example. The rate of heat transmission from the surface to the air was boosted with copper coils. Figure 11 shows the evacuated tube solar air collector's efficiency and sun intensity with time, both over daytime and at nighttime. At a modest airflow rate of 0.02 kg s^{-1}, the highest efficiency in a standard collector with the copper coil was 38 percent. The efficiency of a low airflow rate collector was discovered to be 2.25 times that of a high airflow rate collector.

The air output temperature with the copper coil decreased slightly due to a major drop in the resolution time of the air at high rates. Figure 12 indicates that the maximum intensity over the day was 840 W/m^2, with ambient temperatures varying from 32°C to 39°C. The largest temperature variation among the entrance and output air was 24.5°C, with the outlet air reaching the highest temperature of 63.1°C. The maximum water temperatures were 108.5°C and 98.2°C at high and low head, respectively, whereas PCM achieved maximum temperatures of 103.2°C and 65.4°C at high and low head, respectively. A temperature difference of 12.6°C could be achieved in the air.

Figure 13 shows the evacuated tube solar air collector's efficiency with time, over the day and at night. At a high airflow rate of 0.04 kg s^{-1}, the highest efficiency in a normal collector with a copper coil was 40%. The highest accuracy at a high rate of airflow was discovered to be 1.25 times that of a standard copper coil collector at a high rate of airflow. The highest accuracy, in this case, is 1.14 times that of a normal collector at a high rate of airflow.

At low flow rates, the air residence period in the conventional collector with a circular fin was longer than the usual collector with projector headlights and a copper coil. The highest heat variance of exhaust air was obtained in this circumstance.

The highest intensity over the day was 800 W/m^2, and the environment temperature ranged from 31.5°C to 38.5°C. The highest heat variation between the entrance and output air was 38°C, with the outlet air reaching a maximum temperature of 75.5°C. The highest water heats were 107.5°C and 103.2°C at high and low head, respectively, whereas PCM attained maximum temperatures of 104.5°C and 67.5°C at high and low head, respectively. A heat variation of 22°C might be achieved in the air. Figure 14 shows the evacuated tube solar air collector's efficiency and sun intensity with time, both over daytime and at nighttime. At a higher flow rate of air 0.02 kg s^{-1}, the greatest efficiency was 43 percent in a standard circular fin collector. In this illustration, the overall efficiency is 2.6 times that of an airlow normal copper coil collector and 1.25 times that of a low airflow normal copper coil collector.

Table 3: Registered data of ambient conditions on May 25th 2020.

Time (hours)	Sun intensity (W/m^2)	Ambient temperature (°C)	Outlet air temperature ETC (regeneration temperature) (°C)
08:00	456	30	54
09:00	424	31	55.5
10:00	468	32	62
11:00	580	33	64.6
12:00	640	35	67.5
13:00	768	34	68.5
14:00	840	36	64.2
15:00	740	38	61.5
16:00	632	35	59.8
17:00	546	34	58.7
18:00	240	32	56.5
19:00	124	32	54.2
20:00	0	31	52.5
21:00	0	31	50.8
22:00	0	31	46.5
23:00	0	30	44.5
24:00	0	30	43.5

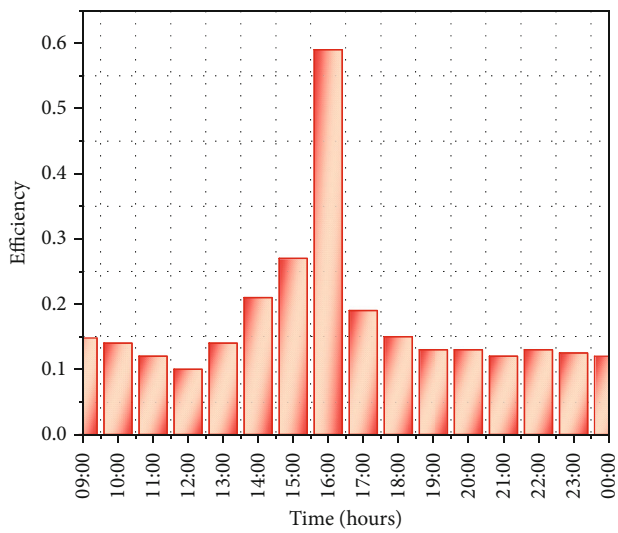

Figure 15: Variations in the efficiency of stearic acid as a phase change material for a normal collector with a circular fin at a flow rate of 0.04 kg s^{-1}.

The intensity over the day was 835 W/m^2 with environmental temperatures between 30°C and 38°C. With outlet air reaching a maximum temperature of 72.2°C, the biggest temperature differentiation between inputs and outputs was 30.5°C. The maximum water temperatures were 108.4°C and 101.4°C at high and low head, respectively, whereas PCM attained maximum temperatures of 103.5°C and 64.5°C at high and low head, respectively. It was possible to achieve a 13.5°C change in air temperature (Table 3). Figure 15 shows the evacuated tube solar air collector's efficiency with time, over the day and at night. In a normal circular end collector at a maximum rate of airflow of 0.04 kg s^{-1}, the highest efficiency was 59%. At a high airflow rate, the highest efficiency is 1.5 times the rate of a normal collector over a circulatory fin at a high airflow rate. In this term, the maximum effectiveness is 1.75 times the effectiveness of a copper-coiled collector with high airflow and 1.5 times the effectiveness of a regular coil-coated collector at an airflow rate. According to the experimental results, the average air temperature difference is 1.5 times higher than the median copper sprocket collector and two times higher than the median copper sprocket collector during incident solar radiation. Furthermore, in a common collector with a circular fin, the mean air temperature difference is 1.5 times that of the normal copper coil collector and 2.25 times the conventional nonsunny time collector method. As a result, the behaviour of the evacuated solar tube collector was raised using a circular fin configuration.

6. Conclusion

This research explored the thermal behaviour of an evacuated tube solar air collector with thermal energy. They built a header with a PCM storage device to store solar energy during solar radiation incidents and generate warm air without solar radiation. It can derive the following conclusions from the findings of the experiment.

The experimental arrangement can generate warm air during nonincident solar radiation. When PCM is employed in a system, it has been discovered that it functions well during the off-sunshine hours. According to the findings, a solar air collector with an evacuated tube and a latent thermal energy store might store enough heat to deliver hot air for up to 24 hours.

Using a circular fin and copper coil inside an evacuated tube, the solar air collector, as such designs, allows a faster heat transmission rate inside the concentrated circular pipe which can significantly increase the air supply. In the case of incident and nonincident solar radiation, the most significant

temperature difference observed between heated air and environmental air was 38°C and 22°C, with a circular fin design and a flow rate of $0.02\,kg\,s^{-1}$.

If a low airflow rate is used, then when a high flow rate is used, the maximum efficiency of the solar air collector is lower. As the working time of the experimental setting extends, the effectiveness of the use of circular fin and copper coils can significantly be increased. The efficiency was 0.035–0.45 times lower in low ($0.02\,kg\,s^{-1}$) and high ($0.04\,kg\,s^{-1}$).

Data Availability

The data used to support the findings of this study are included within the article. Further data or information is available from the corresponding author upon request.

Conflicts of Interest

The authors declare that there is no conflict of interest regarding the publication of this article.

Acknowledgments

The authors appreciate the supports from Hawassa University, Ethiopia, for providing help during the research and preparation of the manuscript. The authors would like to express their gratitude towards Sathyabama Institute of Science and Technology and Seoul National University of Science and Technology for providing the necessary supports to carry out this work successfully. This project was supported by Researchers Supporting Project number (RSP-2021/315), King Saud University, Riyadh, Saudi Arabia.

References

[1] H. H. Al-Kayiem and S. C. Lin, "Performance evaluation of a solar water heater integrated with a PCM nanocomposite TES at various inclinations," *Solar Energy*, vol. 109, pp. 82–92, 2014.

[2] L. M. Ayompe, A. Duffy, M. Mc Keever, M. Conlon, and S. J. McCormack, "Comparative field performance study of flat plate and heat pipe evacuated tube collectors (ETCs) for domestic water heating systems in a temperate climate," *Energy*, vol. 36, no. 5, pp. 3370–3378, 2011.

[3] I. Budihardjo and G. L. Morrison, "Performance of water-in-glass evacuated tube solar water heaters," *Solar Energy*, vol. 83, no. 1, pp. 49–56, 2009.

[4] I. Budihardjo, G. L. Morrison, and M. Behnia, "Natural circulation flow through water-in-glass evacuated tube solar collectors," *Solar Energy*, vol. 81, no. 12, pp. 1460–1472, 2007.

[5] M. Chaabane, H. Mhiri, and P. Bournot, "Thermal performance of an integrated collector storage solar water heater (ICSSWH) with phase change materials (PCM)," *Energy Conversion and Management*, vol. 78, pp. 897–903, 2014.

[6] T.-T. Chow, Z. Dong, L.-S. Chan, K.-F. Fong, and Y. Bai, "Performance evaluation of evacuated tube solar domestic hot water systems in Hong Kong," *Energy and Buildings*, vol. 43, no. 12, pp. 3467–3474, 2011.

[7] A. A. El-Sebaii, S. Al-Amir, F. M. Al-Marzouki, A. S. Faidah, A. Al-Ghamdi, and S. Al-Heniti, "Fast thermal cycling of acetanilide and magnesium chloride hexahydrate for indoor solar cooking," *Energy Conversion and Management*, vol. 50, no. 12, pp. 3104–3111, 2009.

[8] A. M. El-Nashar, "Seasonal effect of dust deposition on a field of evacuated tube collectors on the performance of a solar desalination plant," *Desalination*, vol. 239, no. 1–3, pp. 66–81, 2009.

[9] H. P. Garg and S. Chakravertty, "Thermal analysis of an evacuated tube collector module," *Solar and Wind Technology*, vol. 5, no. 5, pp. 525–531, 1988.

[10] Y. Kim and T. Seo, "Thermal performances comparisons of the glass evacuated tube solar collectors with shapes of absorber tube," *Renewable Energy*, vol. 32, no. 5, pp. 772–795, 2007.

[11] R. Kumar, R. S. Adhikari, H. P. Garg, and A. Kumar, "Thermal performance of a solar pressure cooker based on evacuated tube solar collector," *Applied Thermal Engineering*, vol. 21, no. 16, pp. 1699–1706, 2001.

[12] Y. Kumar and A. Yadav, "Thermal performance comparison of evacuated tube solar water heater with different shapes of flow passage in the tube," *Journal of Energy Research and Environmental Technology*, vol. 2, no. 4–5, p. 8, 2015.

[13] H. Li, Y. J. Dai, Y. Li, D. La, and R. Z. Wang, "Case study of a two-stage rotary desiccant cooling/heating system driven by evacuated glass tube solar air collectors," *Energy and Buildings*, vol. 47, pp. 107–112, 2012.

[14] L. Ma, Z. Lu, J. Zhang, and R. Liang, "Thermal performance analysis of the glass evacuated tube solar collector with U-tube," *Building and Environment*, vol. 45, no. 9, pp. 1959–1967, 2010.

[15] G. L. Morrison, I. Budihardjo, and M. Behnia, "Water-in-glass evacuated tube solar water heaters," *Solar Energy*, vol. 76, no. 1–3, pp. 135–140, 2004.

[16] A. H. Mosaffa, L. G. Farshi, C. A. I. Ferreira, and M. A. Rosen, "Energy and exergy evaluation of a multiple-PCM thermal storage unit for free cooling applications," *Renewable Energy*, vol. 68, pp. 452–458, 2014.

[17] N. Nallusamy, S. Sampath, and R. Velraj, "Experimental investigation on a combined sensible and latent heat storage system integrated with constant/varying (solar) heat sources," *Renewable Energy*, vol. 32, no. 7, pp. 1206–1227, 2007.

[18] D. N. Nkwetta and M. Smyth, "Performance analysis and comparison of concentrated evacuated tube heat pipe solar collectors," *Applied Energy*, vol. 98, pp. 22–32, 2012.

[19] T. Nomura, M. Tsubota, A. Sagara, N. Okinaka, and T. Akiyama, "Performance analysis of heat storage of direct-contact heat exchanger with phase-change material," *Applied Thermal Engineering*, vol. 58, no. 1–2, pp. 108–113, 2013.

[20] M. Pomianowski, P. Heiselberg, and Y. Zhang, "Review of thermal energy storage technologies based on PCM application in buildings," *Energy and Buildings*, vol. 67, pp. 56–69, 2013.

[21] A. Sarı, "Thermal reliability test of some fatty acids as PCMs used for solar thermal latent heat storage applications," *Energy Conversion and Management*, vol. 44, no. 14, pp. 2277–2287, 2003.

[22] L. J. Shah and S. Furbo, "Vertical evacuated tubular-collectors utilizing solar radiation from all directions," *Applied Energy*, vol. 78, no. 4, pp. 371–395, 2004.

[23] L. J. Shah and S. Furbo, "Theoretical flow investigations of an all glass evacuated tubular collector," *Solar Energy*, vol. 81, no. 6, pp. 822–828, 2007.

[24] S. D. Sharma, D. Buddhi, R. L. Sawhney, and A. Sharma, "Design, development and performance evaluation of a latent heat storage unit for evening cooking in a solar cooker," *Energy Conversion and Management*, vol. 41, no. 14, pp. 1497–1508, 2000.

[25] N. Sharma and G. Diaz, "Performance model of a novel evacuated-tube solar collector based on minichannels," *Solar Energy*, vol. 85, no. 5, pp. 881–890, 2011.

[26] S. D. Sharma, T. Iwata, H. Kitano, and K. Sagara, "Thermal performance of a solar cooker based on an evacuated tube solar collector with a PCM storage unit," *Solar Energy*, vol. 78, no. 3, pp. 416–426, 2005.

[27] A. Shukla, D. Buddhi, and R. L. Sawhney, "Thermal cycling test of few selected inorganic and organic phase change materials," *Renewable Energy*, vol. 33, no. 12, pp. 2606–2614, 2008.

[28] R. Tang, Y. Yang, and W. Gao, "Comparative studies on thermal performance of water-in-glass evacuated tube solar water heaters with different collector tilt-angles," *Solar Energy*, vol. 85, no. 7, pp. 1381–1389, 2011.

[29] A. Waqas and Z. U. Din, "Phase change material (PCM) storage for free cooling of buildings–a review," *Renewable and Sustainable Energy Reviews*, vol. 18, pp. 607–625, 2013.

[30] A. Yadav and V. K. Bajpai, "Thermal performance of one-ended evacuated tube solar air collector at different flow rates: experimental investigation," *International Journal of Ambient Energy*, vol. 33, no. 1, pp. 35–50, 2012.

Hindawi
International Journal of Photoenergy
Volume 2022, Article ID 3053953, 8 pages
https://doi.org/10.1155/2022/3053953

Research Article

Designing the Modern Dual-Engine Two-Speed Smart Hybrid Electric Drive Powertrain

Balachandra Pattanaik,[1] **Mukil Alagirisamy**,[2] **V. Karthikeyan**,[3] **Ramesh Babu Nallamothu**,[4] **and G. Giftson Samuel**[5]

[1]*Department of Electrical Engineering, Wisma Lincoln, Lincoln University College, Malaysia*
[2]*Electrical and Electronics Department, Wisma Lincoln, Lincoln University College, Malaysia*
[3]*Department of Electrical and Electronics Engineering, Center for Energy Research, Chennai Institute of Technology, Kundrathur, Chennai, 600069 Tamilnadu, India*
[4]*Department of Mechanical Engineering, School of Mechanical Chemical and Materials Engineering, Adama Science and Technology University, Adama, PoBox: 1888, Ethiopia*
[5]*Department of Electrical and Electronics Engineering, Sir Issac Newton College of Engineering & Technology, Nagapattinam, Tamilnadu, India*

Correspondence should be addressed to Balachandra Pattanaik; pdf.bpattanaik@lincoln.edu.my and Ramesh Babu Nallamothu; ramesh.babu@astu.edu.et

Received 10 February 2022; Accepted 1 April 2022; Published 9 June 2022

Academic Editor: Ahmad Umar

Copyright © 2022 Balachandra Pattanaik et al. This is an open access article distributed under the Creative Commons Attribution License, which permits unrestricted use, distribution, and reproduction in any medium, provided the original work is properly cited.

While potential for battery-powered electric vehicles (BEVs) is increasing as the need to minimise greenhouse gas pollution and the utilization of energy production, the restricted driving range and the uninviting market price constitute BEV obstacles to reliable assessment as a conventional car. This paper suggests a double-motor multispeed direct-drive BEV drivetrain to improve average engine running performance in everyday travelling whilst raising any production or control sophistication, effectively saving minimal battery resources and production costs. The characteristics of the proposed drivetrain are first defined through quantitative and visual measurements, which divide the conventional one-engine propulsion to two with different permanent gears to optimise engine performance. Centred on dynamic powertrain modelling in Simulink, the economic change strategy and circulatory system consisting transfer control were planned and checked. Based on the simulation performance, it is stated that substantial increases in energy quality can be accomplished. Thanks to the optimised torque transfer control technique, the vehicle's incredibly low pull is registered during the shifting phase. Finally, it can be inferred that the suggested dual-motor drivetrain is better than the conventional single-motor equivalent in terms of fuel efficiency, driving range, and expense. There is substantial increase in total machine running areas of affordable to solitary machine performance and megacity driving ages, similar to WLTC, FTP-75, and JP 10-15, with 5 to 8 percentage performance enhancement being achieved.

1. Introduction

Rechargeable hybrid cars are now attracting increasing interest becoming ever more popular. However, compared to conventional cars, the comparatively limited driving range per fee, the prolonged recharge period, and the unfriendly price also pose major obstacles to its large-scale commercialisation [1]. While the improved catalytic and reliability output of the electrical system (engine), including the 100% displacement usable from dead stop and the significantly higher conversion efficiencies relative to the internal combustion engine (ICE), allows direct engine-to-wheel drive by a clutch automatic decrease, the requirement for alternative energy upgrade and better driving output has intensified. In our earlier work on BEV, a multispeed multi-gearbox transmitting structure including a hybrid microgrid

was suggested [2]. Related plans for different microspeed transmitting applications in vehicles, such as automatic gearbox, Advanced Mechanical Transmitting and depending Distribution, can be found in. The findings of the above studies have clearly shown that multispeed transmission not only increases the dynamic and economic efficiency of BEVs, but also lowers high upfront costs by lower operational costs and repair charges in terms of long-term possession.

Additional benefits are also available for electric motors through speed control. However, the dynamic process, e.g. additional gear pairs, the unreliable hydraulic method and the synchronizer for gear shifting and the extra expense of transmission output, provide the obstacles to the effective translation of concepts into practise [3]. Even if some specifically made navigation systems are able to achieve seamless equipment changing by invigorating the throttle application process, the qualifications for rapid and precise motor as well as pneumatic cylinder power require considerable diagnostics and field checking [4]. The dual-engine multispeed direct-drive EV drivetrain has shown the ability to outperform the conventional single-engine fixed-speed drivetrain over perspective of business gain, by sacrificing on the flexibility of the design or management technique. It may be a viable choice for automakers to substitute the existing commonly used single-engine drivetrain throughout the short term [5].

Previously, given the large amount of surplus torque and strength lost in regular driving activities and the poor enhanced success, the planned drivetrain system divided one or two driving motors, addressing various driving trends [6]. Motor power and perpetual gear ratio are deliberately crafted to account for complex and commercial volumetric efficiency, followed by a quick and effective driving motor switching technique. In ensuring smooth propagation of the torque during speed control, the built shift control technique is then evaluated in a dynamic Simulink model.

Hybrid electric vehicles (HEVs), utilising an automobile and one and sometimes more electrical devices, are generally considered as the most suitable option for automobiles in the small to medium term. Battery vehicles automobiles are currently being produced by numerous manufacturers [7]. These cars are actually in service marketed as one way to increase the quality of our traffic process and make growing our reliance on and use of international petroleum. Latest research activities in REV are aimed at creating a fuel-efficient and cost-effective combustion device. Among a multitude of disciplines. Supercharged modes, the two widely recognised classifications are both sequence and parallel. Although the design of the series is effective for high energy requirements, the longitudinal hybrid is more suited for high road capacity requirements [8].

Autonomous driving Emulator (ADVISOR) was first established at the Regional energy technology Facility in November 1994. It was developed as an analysis platform to assist the US Department of Energy (DOE) in advancing HEV (Hybrid Electric Vehicle Propulsion) developments through contracts with Ford, General Motors and Daimler-Chrysler. Its main function is to demonstrate the system-

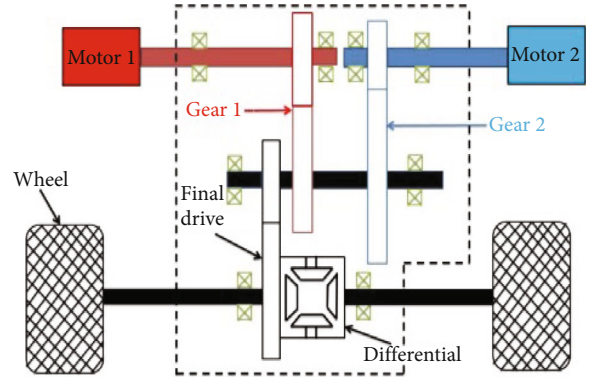

Figure 1: Overview of the hybrid drivetrain model.

level engagement of hybrid and electric vehicles aspects and their effect on vehicle efficiency and fuel consumption. The overview of the drivetrain model which adapts the hybrid electric vehicle has been depicted in Figure 1 [9].

Rather than strengthening BEV engine performance by providing new gears, a number of power splitting systems have been proposed to perform having similar inter-speed drivetrain functions that use engine power to shift directions and exchange acceleration among both gear teeth. Peng and He introduced a dual-engine drivetrain that utilizes multiple cruising engines and a double-input or double-output drivetrain to combine a set of driving configurations, e.g. high-speed four-wheel drive (FWD), low-speed Turbo and legitimate-wheel drive, via the two changing engines. It is an intelligent framework for the Manual transmission EV, but it is not a resource-friendly framework for the common two-wheel EV, taking into account the six-wheel drive, two synchronizers and two constantly changing stepper motors materials. Zhu et al. developed a multispeed two-wheel powertrain with an another-way gear box and a two-way shaft (inner and outer like a DCT). The efficiency of this proposed powertrain is relatively high compared to that of planetary gears, as is the cost of fast transmission regulations and the cost of production [10]. A two-engine drivetrain proposed by Hu et al. claimed about 4 percent enhancement in fuel consumption through some kind of planet-based power splitting system. Shifting of cruising modalities among single-engine train and the consolidated driver circuit in terms of consistency and ground clearance varies depending on a gear reduction unit, a clutch automatic unit, two shackles and a speed controller, making the composition more difficult. A further dual-engine drivetrain was used in the hybrid electric subway car with the new and innovative technologies technique [11].

Around the same moment, to care about saving expense of the engine, Wang et al. boost energy security by reducing this same effect of motor speed mutations on the transmission line. However, the coaxial dual-motor drivetrain structure can only provide an 'add-on' torque, rather than selecting the propulsion engine for efficiency [12]. Compared to the implementation of the significant ones-speed spread in BEV, the benefits of the above-mentioned a double-motor policy idea help reduce the incidence for

transmission control in order to achieve quality shifting, in which the engines are actively engaged in the power splitting system to achieve smooth activation loop and driving product contains. In addition, the constructions increase the capacity of the multipowered torque/speed coupling modes. However, the clutches and/or the controller are still critical parts in the above proposals, which make a significant difference to the conventional BEV distribution service in terms of sector owned and enhanced mechanical performance [13, 14].

In comparison, neither the engine nor the accompanying gearbox of the above solutions was expressly built to have improved logistical and superior craftsmanship. Keeping in mind the different powertrain architectures proposed for multiple power source EVs, it is evident that most of them depend on shackles and synchronizers to accomplish their functions. A novel a double engine Two-Speed direct powertrain is proposed in this study, which seeks to make the most of the excellent engine torque delivery capability while at the same time simplifying the mechanical structure as much as possible, in order to improve engine operating efficiency without increasing the complexity of the control and mechanism [15]. Unlike other conventional BEV multispeed transmitting or energy dividing systems, this policy enforces a parallel osmotic pressure design in BEV, a famous hybrid vehicle drivetrain for engine and engine power flow management. The clear and relevant does have the power to remove the specifications of the clutch, speed controller and centrifugal pump for gear changing or cruising mechanisms switching. The role of the moving curves is realised by the flipping of the propeller engines of continuously joined mechanical parts [16].

The switching system is clearly governed by the engine, inevitably improving the efficiency of the drivetrain and reducing its physical sophistication [17]. In addition, trying to split a single fuselage engine to two raise the likelihood of maximum fuel operating efficiency by improving the design of the distinctive motor torque-speed and gear ratios. The benefit of adopting a two-speed drivetrain, instead of others, is that it can achieve the best balance of improvement in engine efficiency and an additional one through the implemented drivetrain and connected controller design, the testable focus of this article will fill the information gap of established work in the following areas:

(1) A famous 'one-engine yet another-speed' drivetrain is composed of two larger engines with roughly the very same maximum peak output throughout this article to promote better fuel consumption

(2) The method for evaluating the engine torque-speed profile of the conceptual engine and transmission offers the expertise and feedback on the power-efficiency-oriented configuration of the engine specifications

(3) In order to increase performance and facilitate effective transmission of energy, the substitute engine propulsion management method is planned and improved

(4) With the specially developed control approach, the 'multispeed' function is achieved by switching drive motors with persistently available gear pairs, rather than by involving the mechanical shift actuator, i.e. the clutch or actuator [18]

In the following chapters, the drivetrain requirements, which include electric engine and cornering speeds, are committed to even provide equal accuracy to the single-engine drivetrain optimization [19]. Driving vehicle shifting, which include gear trying to shift in this drivetrain, and friction transfer design methods are then suggested. Next, in MATLAB/Simscape R, dynamic simulation is used to replicate automotive output in traditional operating modes and to check the efficacy of the proposed management techniques [20]. Finally, based on a study of renewable energy, friction transmission performance in engine transferring and possibility financial advantages, statements are made that the implemented of double-motor 2-speed direct-drive drivetrain can also provide vehicle with significant quality and cost benefits for both producers and consumers. By increasing the operation speed, the torque requirement for the motor can be reduced, thereby reducing the motor volume and weight, and its power density increased with the speed [21]. The contribution of the work being summarised in Convergent Convertible Electric Vehicle Design with binary machine configuration, incorporating two "lower" effective machines, has the capability to increase machine performance. Also in Hybrid Engine Adaptive Modelling and Regulation Approach, when the speed increases, the energy reduces, owing to the power source of the machine batteries. Eventually in Results and Discussion, necklace comparison and motor effectiveness are being bandied.

2. Convergent Convertible Electric Vehicle Design

For both electric car and the diesel engine collaborate with each other to produce the vehicle's energy in a complementary hybrid car. The simultaneous hybrid can also be used by the engine to recharge packs generally fewer intense driving cycles, such as speeding at cruising speeds. Construction of rotating hybrid car. The connection between the electrical and the mechanical parts is visible. Energy storage connects to the servo motor via the power trolley and the electrical loads [22, 23], then the energy of the automatic transmission and the engine are integrated in the ground clearance coupling. The schematic architecture of the planned novel DMTS direct-drive powertrain shall not follow any clutch or speed controller. Each motor is attached to the final drive shaft by means of a fixed gear pair [24].

Due to the excellent engine torque power of 100 percent of the torque generated from dead stop, all competitive EV markets utilise a single-speed fixed-ratio modulation to minimise engine speed but at the same time boost the power. The rotation speed of the engine was dictated by the state of the vehicle and, as a result, high quality output could not be attained anywhere. As far as the engine output of the standard is concerned, the solid blue line reflects the necessary torque of the wheel at a grade of 30 per cent at 30 km/h, and is generally taken as one of the requirements

for deciding the maximum torque requirement for the engine. If we can see, there is a large difference in these two criteria. In addition, the torque requirements of standard cycles show two simple patterns, namely significantly higher tension-low speed activities and significantly higher speed-low torque events, which could not be catered to a singular gear. Tracking maps show that enough surplus torque/power is seldom utilised in everyday driving, which ensures that most of the service tracks are far from high quality [25].

While a fairly small gear ratio will provide improved engine performance by raising the necessary torque of the engine, the need for a relatively large ratio of acceleration, scrambling and high-speed swerving eliminates the likelihood of a single-speed EV service. In order to increase the low regular running performance of a powerful engine with a high torque capacity, the reduction of the overall usable torque could boost the engine operating area and, as a result, increase the average energy conversion efficiency [26]. In addition, the accompanying set-up gear should be changed to accommodate for the disregarding engine torque.

The design of the two propulsion engines in the designed drivetrain must be carefully applied, as the allocation of existing between the two engines and the characteristics of the torque speed may influence the financial and kinetic efficiency. The overall volumetric efficiency of the standard drivetrain is as follows:

$$U_{max} = 276\,\text{Nm} \times 8.8 = 2423\,\text{Nm} \tag{1}$$

The driving range of 13000 rpm remains unchanged in the proposed approach. The cruising height of the goal of 160 km/h reached throughout the automobile will then be used to calculate the potential utilized to enable:

$$\alpha_{range} \leq \left(\frac{2\pi M_{\max}}{\frac{13000}{60}}\right) \div \left(\frac{W_{\max}}{3}\right) = 13 \tag{2}$$

Extensive simulation findings from standard operating modes, the performance of the engine may be increased by increasing the working leverage and decreasing its rpm. Thus, a dual-engine configuration, incorporating two 'less' efficient engines, has the ability to increase engine performance by restricting the output spectrum to account for everyday driving activities and delivering at least the same overall torque and strength of a single-engine powertrain. Another of the engines is liable for lower turbo/energy moving activities, including such repeated city exits & rests and low-speed cruises. The other engine is used as an auxiliary battery pack during fast torque/power driving incidents, like emergency braking and high-speed trying to overtake. These two engines may operate together if the power of the single engine is inadequate under severe conditions [27, 28].

3. Hybrid Engine Adaptive Modelling and Regulation Approach

Then one microspeed EV drivetrain, that architecture and support programme of the suggested DMTS is clear. The choice to adjust gears, i.e. to turn among 2 propeller engines, is decided mostly by the performance of the engine, and can be accomplished by means of the engine speed controller itself. The basic approach guarantees that the car is still powered by a relatively higher performance engine at all point, unless the necessary torque should not be provided by a single engine [29].

As something of a consultant, the transverse electric assistance management technique utilises the electric motor as an additional power supply and battery capacity in the car. In this technique, the electric engine uses the following methods:

(i) When the speed of the car is below the posted level, the electric engine provides all the necessary torque of the vehicle

(ii) If the automobile torque needed is higher than the average rotational speed, the dc engine shall provide the supplementary kinetic energy

(iii) The electric engine loads the energy recovery electrodes

(iv) If the electric motor requires low driver behaviour and torque needs, the fuel consumption is shut off and the dc engine supplies the car's torque demand

(v) If the SOC is tiny, the diesel engine must generate an additional torque. The parallel electrical assistance management technique for the contractor shall be calculated with six vector values

The electricity source utilises the most essential power suppliers for electrical parts such as traction and auxiliary converters for the provision of electrical power in automobiles. Battery packs have a crucial component to perform in electric vehicles and electric motors. Battery simulation is very complicated and challenging [30, 31]. The power model, then,

The Therapist has been used. Advisor consists of the following design battery cells:

(i) Resilient-capacitive model

(ii) Paradigm of input voltage

(iii) Simple lithium ion model

(iv) Model of the neural network

All of these models separated into other sections, e.g., shock resistant-capacitive framework includes of Li, ni-mh, supercapacitor. Gross domestic product voltage, appropriate monitoring and power capability are needed to pick the battery in HEVs. Even in Planner standby time and rechargeable battery weight are mentioned. Battery simulation in

Advisor requires to provide parameters for the battery. The SOC of the battery reduces at the initial period and rises when the engine is braked. The current of the battery relies on the speed of the car, so increasing the speed of the vehicle allows the SOC to decrease and the current of the battery to rise. If the SOC is the limit, the current of the battery is negative. When the current is positive, the vehicle uses the energy of the battery and when the current is negative, the battery is charged.

Driver circuit has been one of the essential features of HEV. Alluding to various operational ecosystems, such as straight course, downwind, descents, beginning-stop and so on, the engine performance mode must be switched between conditions of load condition, full load or overburden. The major point for the development of the engine as well as its control logic is therefore the improvement of the overall efficiency. Management quality specifications for the HEV engine and the steering system ought to have high systems with minimum loss, long cycle life, elevated torque at low pace, broad frequency adjustment range, high overwhelm capacity, good dependability, and so on. The voltage output of the electric engine is trying to follow the rated speed of the driving cycle. In functional central controls, the engine drive is attached to the VO board and the comparison displacement and rpm of the automatic transmission are calculated.

The acceleration formulas and the graphical diagram of the DMTS are implemented below in order to ensure a seamless transition of torque through gear teeth. A gear pairing continuously connected to the engine 1 comprises of gears 1 and 3; Pairs 2 and 4 reflect the reduction of the gear for engine 2; equipment, i.e. gearing pairs 5 and 6, push the board as shown in Figure 2.

K_{N1}, K_{N2} and K_{1-6} are representing the different power energy for the electrical motor, where as the different gears have been represented. The rotational latency of the motor has been represented by ω. Also, the speed that has been achieved by the rotational latency has been defined with $\dot{\omega}$. j_1 represents the range of gears between gears one and three. j_2 defines the same for the gears two and four. j_{last} represents the range of gears between gear five and six. U_{N1} and U_{N2} are defining the outcomes of the devices one and two and their outputs. U_L and U_{last} represents the outcomes of the shafts represented in Figure 2.So, the model can be derived as follows:

$$\begin{aligned}
(K_{N1} + K_1)\dot{\omega}_{N1} &= U_{N1} - U_1 \\
(K_{N2} + K_2)\dot{\omega}_{N2} &= U_{N2} - U_2 \\
(K_3 + K_4 + K_5)\dot{\omega}_5 &= j_1 U_1 + j_2 U_2 - U_L \\
j_6\dot{\omega}_6 &= j_n U_L - U_{last} \\
\dot{\omega}_5 &= \frac{\omega_{N1}}{j_1}
\end{aligned} \tag{3}$$

$$\begin{aligned}
K_f\dot{\omega}_6 = {} & j_1\, j_{last} U_{N1} + j_2\, j_{last} U_{N2} - j_1\, j_{last}(K_{N1} + K_1)\dot{\omega}_1 \\
& - j_1\, j_{last}(K_{N2} + K_2)\dot{\omega}_2 - j_{last}(K_3 + K_4 + K_5) \\
& \times \dot{\omega}_5 - U_{last}
\end{aligned}$$

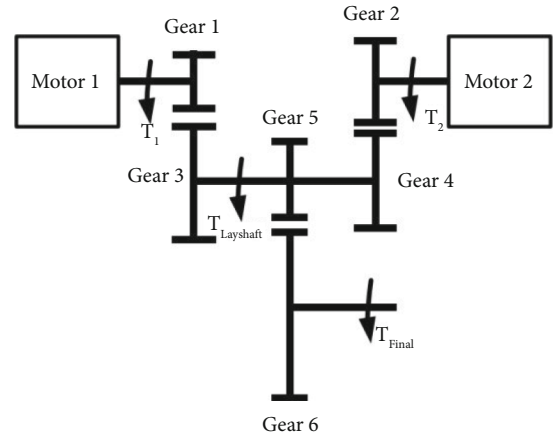

Figure 2: Gear structure.

and also,

$$\begin{aligned}
K_f = {} & (K_{N1} + K_1) j_1^{\,2} j_{last}^{\,2} + (K_{N2} + K_2) j_2^{\,2} j_{last}^{\,2} \\
& + (K_3 + K_4 + K_5) j_{last}^{\,2} + K_6
\end{aligned} \tag{4}$$

Actually, looking at seamless displacement transition avoiding 'displacement crevice ' through spur shafts, the overall production velocity of DMTS on final straight would have been well held unvaried throughout switching phase. The variable speed drive engine is a device wherein the large conductive main source of energy supply a single power generation plant (electric engine) that drives the vehicle. The design that is most widely found in the Counsellor, the ICE would be used to produce energy in the engine. Application provides electricity for the engine and it was either an engine or an energy storage device. Electrical grid transforms the electricity of the motor into electric power. This energy may be contained in batteries or used for electric motors. Regulation technique is used to minimise fuel usage and emissions or to optimise battery life. The technique requires the following framework:

(i) We can turn off the SOC energy generator when growing

(ii) If the SOC is tiny, the electric motor must generate an additional power

(iii) Unless the automobile energy needed is greater than the normal motor speed, the automatic transmission shall provide the supplementary kinetic energy

In the SHEVs, the battery provides electrical strength to the electric motor along with the generator. The charging of the battery is assured either by electric motors or by the compressor. Full output of the electric engine is used where the combined strength of the steam turbine and the battery is greater than the electric motor. Battery energy must have vehicle acceleration capacity even in the toughest of circumstances. There must be certain parameters for emulation of electrodes.

Close to dual hybrids, the energy of the battery, the original contact of the batteries is 0.8 and the full energy for the batteries. When the speed increases, the energy reduces owing to the power source of the engine batteries. Processor is designed to avoid the degradation of energy. Current average energy is provided for the operator since energy is not less than the setting significance. Power of the engine operator in the combination sequence through it's a transformer. Transducer generates electrical power from battery but transformer it's energy. The position of the engine operator in the hybrid sequence is unique as well as an electric hybrid position. The engine is directly related to the powertrain and thus on the gears.

4. Results and Discussion

Focused on any of these approaches and design, the capital accumulation and competitive success of the suggested system is seen in this segment. In order to have greater viewership, the total engine design and resource usage in each standard loop are outlined just at early stages as a reference for more review. Figure 3 shows Torque comparison – 1.

The suggested methods have demonstrated that they are capable of minimising energy usage independently of traveling intervals. That being said, it may not work as well as boost engine efficiency in terms of the probability gain attributable to energy savings (regenerative braking) is omitted from this description, the output of which is heavily dependent on techniques but may also be enhanced by a for double-motor drivetrain. Figure 4 shows Torque comparison -2.

These methods produce substantial increases in total engine running area of affordable to solitary-engine performance. More than 12 percent increase in engine performance can be achieved and planned with the suggested methods in the highway driving trends. For other city driving periods, such as WLTC, FTP-75 and JP 10-15, 5%-8% performance improvement may be accessible. Attempting to compare methods, with the example of HWFET.

Figure 5 shows Shaft torque vs Time. Present comparable results in terms of average engine quality and energy usage. The reasoning for approaches to reasonably high-speed low-torque events offers more chances for the 100 Nm the proposed engine to work in a better energy zone, whereas the two proposed engines have a relatively wide torque capacity. However, in urban bikes, the benefit of a smaller torque capacity may be limited to some degree by a significantly larger torque requirement, particularly when the displacement efficiency of a slower driver in the suggested solution is inadequate.

Allowed to drive motor swapping may be used as a gear change in this analysis since each engine is permanently attached to a set gear ratio. Thanks to the excellent efficiency of the electrical motor (motor), i.e. the swift and precise answer to the challenging torque and pace, the torque is smooth and quick as in Table 1. Transferring from two engines can only be accomplished by regulating the turbine. The amount of the signalling gear does not change before the shifting phase has been finished. The criteria for preferred optimum turgidity of the automobile during conventional gear changes differs across areas. In order to assess the effect of the proposed powertrain on everyday driving for

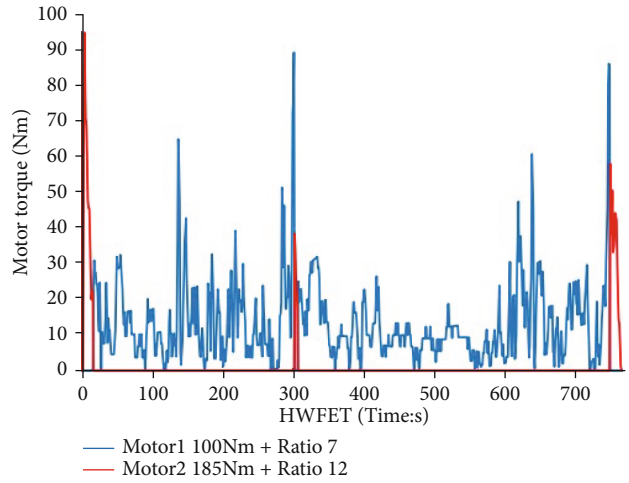

Figure 3: Torque comparison – 1.

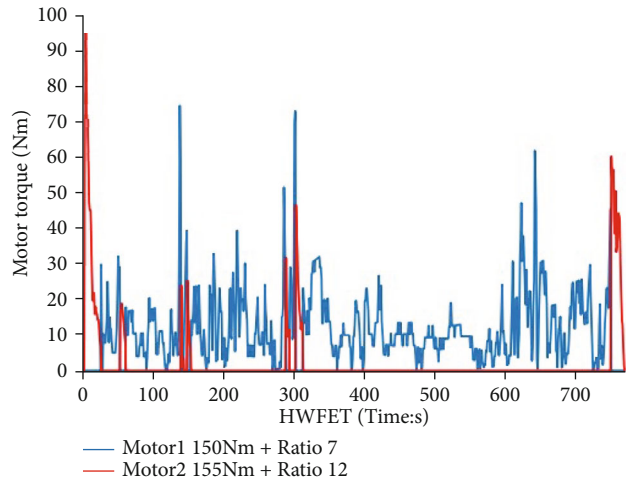

Figure 4: Torque comparison -2.

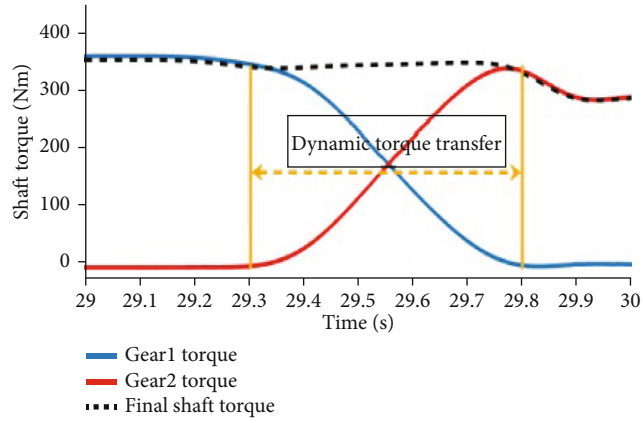

Figure 5: Shaft torque Vs Time.

Table 1: Efficiency estimation and comparison.

	Normal motor efficiency	Proposed system efficiency	Improvement
WLTC	82%	89.20%	7.20%
FTP-75	81.60%	90.40%	8.80%
HWFET	74.80%	81.20%	6.40%
JP10-15	85%	94.20%	9.20%

regular riders, a hybrid driving style is used to analyse the possible expansion of the driving range and the associated cost savings for BEV. The hybrid operating period implemented involves 57% of road driving and 43% of city driving, respectively.

It should be remembered that the aforementioned estimates do not consider losses in other machine systems, such as gear, axle, converter and associated systems, leading to higher than actual energy efficiency relative to the consumer product, e.g. e-Golf. However, because the detrimental variables have an effect on both traditional single-engine drivetrain systems, these statistics also have a strong overview and contrast to demonstrate the superiority of systems to a single-engine drivetrain.

5. Conclusion

Throughout this paper, a double-motor multispeed direct-drive Electric car drivetrain is suggested to enhance engine performance, effectively preserving minimal power consumption and cost of production. Originally, given the large amount of extra displacement and strength lost in regular driving activities and the poor overall performance, the planned powertrain system divided one or two driving motors, addressing various driving trends. Motor power and permanent gear ratio are specially engineered to account for complex and economic efficiency of the vehicle. A quick and effective moving motor swapping approach followed. In order to ensure smooth propagation of the torque through speed control, the built changeover control technique would then be evaluated in a flexible Simulink R model. Modelling of analysis showed that substantial increase in engine performance can be predicted with a pleased vehicle pull during shifting, i.e. less than 5 m = s3. Finally, the proposed dual-engine powertrain reveals the possible advantages for consumers and suppliers in terms of cost reductions in everyday travel and energy output. Overall, the dual-engine multi-speed direct-drive drivetrain has shown the ability to outperform the conventional single-engine fixed-speed drivetrain again from perspective of financial gain, despite sacrificing on the flexibility of the design or control technique. It may be a viable choice for automakers to substitute the existing commonly used single-engine powertrain in the immediate future. Substitute further may be grounded on electric powertrains, traction motor systems, crucial factors, and accoutrements in terms of the time frame by experimenters and masterminds in the unborn strategies in future.

Data Availability

The data used to support the findings of this study are included within the article. Further data or information is available from the corresponding author upon request.

Conflicts of Interest

The authors declare that there are no conflicts of interest regarding the publication of this paper.

Funding

This research work is not funded from any organization.

Acknowledgments

The authors appreciate the supports from Adams Science and Technology University, Ethiopia. The authors thank to *Wisma Lincoln,* Lincoln University College, Malaysia and Chennai Institute of Technology, Chennai for providing assistance to complete this work.

References

[1] J. Peng, S. Shaoyou, H. He, and F. Hao, "Shift control strategy simulation on dual motor driven electric vehicle," in *2014 IEEE Conference and Expo Transportation Electrification Asia-Pacific (ITEC Asia-Pacific)*, pp. 1–4, Beijing, China, 2014.

[2] B. Zhu, N. Zhang, P. Walker et al., "Two motor two speed power-train system research of pure electric vehicle," in *SAE 2013 World Congress & Exhibition*, China, 2013.

[3] M. Hu, J. Zeng, S. Xu, C. Fu, and D. Qin, "Efficiency study of a Dual-Motor coupling EV powertrain," *IEEE Transactions on Vehicular Technology*, vol. 64, no. 6, pp. 2252–2260, 2015.

[4] W. Wang, Z. Zhang, J. Shi, C. Lin, and Y. Gao, "Optimization of a dual-motor coupled powertrain energy management strategy for a battery electric bus based on dynamic programming method," *IEEE Access*, vol. 6, pp. 32899–32909, 2018.

[5] W. Wang, Y. Li, J. Shi, and C. Lin, "Vibration control method for an electric city bus driven by a dual motor coaxial series drive system based on model predictive control," *IEEE Access*, vol. 6, pp. 41188–41200, 2018.

[6] G. Media, "Technical Specifications, G-Class G550 4 MATIC specifications- car specs," 2015, http://www.auto123.com.

[7] J. Ruan, P. D. Walker, P. A. Watterson, and N. Zhang, "The dynamic performance and economic benefit of a blended braking system in a multi-speed battery electric vehicle," *Applied Energy*, vol. 183, pp. 1240–1258, 2016.

[8] M. Goetz, *Integrated Powertrain Control for Twin Clutch Transmissions*, Univ. Leeds, Leeds, U.K., 2005.

[9] I. M. Berry, *The Effects of Driving Style and Vehicle Performance on the Real-World Fuel Consumption of U.S. Light-Duty Vehicles*, Massachusetts Institute of Technology, Cambridge, MA, USA, 2010.

[10] "Worldwide Harmonized Light Vehicles Test Cycle (WLTC)," May 2018, https://www.dieselnet.com/standards/cycles/wltp.php.

[11] "EPA Highway Fuel Economy Test Cycle (HWFET)," May 2018, https://www.dieselnet.com/standards/cycles/hwfet.php.

[12] US Environmental Protection Agency, *Greenhouse Gas Emissions from a Typical Passenger Vehicle*, U.S. Environmental Protection Agency, Washington, DC, USA, 2014.

[13] Y. T. Jang and M. M. Jovanovic, "A contactless electrical energy transmission system for portable-telephone battery chargers," *IEEE Transactions on Industrial Electronics*, vol. 50, no. 3, pp. 520–527, 2003.

[14] B. Pattanaik, R. Balachandran, S. Prakash, and R. D. Haro, "PV-STATCOM based smart inverter for reliable Distrubition system," in *2021 5th International Conference on Intelligent Computing and Control Systems (ICICCS)*, pp. 733–738, Madurai, India, 2021.

[15] P. Meyer, P. Germano, M. Markovic, and Y. Perriard, "Design of a Contactless Energy-Transfer System for desktop peripherals," *IEEEtransactions on Industry Applications*, vol. 47, no. 4, pp. 1643–1651, 2011.

[16] U. M. Jow and M. Ghovanloo, "Design and Optimization of Printed Spiral Coils for Efficient Transcutaneous Inductive Power Transmission," *IEEE Transactions on Biomedical Circuits and Systems*, vol. 1, no. 3, pp. 193–202, 2007.

[17] C. S. Wang, O. H. Stielau, and G. A. Covic, "Design considerations for a contactless electric vehicle battery charger," *IEEE Transactions on Industrial Electronics*, vol. 52, no. 5, pp. 1308–1314, 2005.

[18] J. T. Boys, G. A. Covic, and G. A. J. Elliott, "Pick-up transformer for ICPT applications," *Electronics Letters*, vol. 38, no. 21, pp. 1276–1278, 2002.

[19] H. H. Wu, G. A. Covic, J. T. Boys, and D. J. Robertson, "A series-tuned inductive-power-transfer pickup with a controllable AC-voltage output," *IEEE Transactions on Power Electronics*, vol. 26, no. 1, pp. 98–109, 2011.

[20] J. Huh, E. H. Park, G. H. Joung, and C. T. Rim, "High efficient inductivepower supply system implemented for On Line Electric Vehicles," in *Proceedings of the KIPE Conference*, pp. 105–110, Korea, 2009.

[21] W. Cai, W. Xiaogang, M. Zhou, Y. Liang, and Y. Wang, "Review and development of electric motor systems and electric powertrains for new energy vehicles," *Automotive Innovation*, vol. 4, no. 1, pp. 3–22, 2021.

[22] B. Pattanaik, S. M. Hussain, V. Karthikeyan, G. Giftson Samuel, and G. Samuel, "Energy Storage System with Dynamic Voltage Restorer Integrated for Wind Energy System," *Journal of Physics: Conference Series*, vol. 1964, no. 4, article 042098, 2021.

[23] B. Pattanaik and M. Pattnaik, *Maximum Intermediate Power Tracking for Renewable Energy Service*, Springer Lecture Notes on Data Engineering and Communications Technologies, Springer Nature, Switzerland, 2020.

[24] H. Moghbeli, A. Saleki, and S. Rezazade, "Design and Simulation of electric drive for hybrid vehicle Runna," in *National Conference of Technology, Energy and Data on Electrical & computer engineering*, In Persian, 2015.

[25] T. Markel and K. Wipke, "Modeling Grid-Connected Hybrid Electric Vehicles Using ADVISOR," in *Sixteenth Annual Battery Conference on Applications and Advances. Proceedings of the Conference (Cat.No.0ITH8533)*, pp. 23–29, Long Beach, CA, 2001.

[26] Y. Firouz, M. T. Bina, and B. Eskandari, "Efficiency of three-level neutral-point clamped converters: analysis and experimental validation of power losses, thermal modelling and lifetime prediction," *lET Power Electronics*, vol. 7, no. 1, pp. 209–219, 2014.

[27] Z. Rahman, K. Butler, and M. Ehsani, *A comparison study between two parallel hybrid control concepts*, SAE Technical Paper, 2000.

[28] B. Pattanaik and C. Subramaniam, "Development of safety and dependability aspects for fault tolerant automotive embedded system," *International Review of Electrical Engineering (IREE)*, vol. 8, no. 4, pp. 1218–1230, 2013.

[29] M. J. Mojibian and M. Tavakoli Bina, "Classification of multilevel converters with a modular reduced structure: implementing a prominent 31-level 5 kVA class B converter," *IET Power Electronics*, vol. 8, no. 1, pp. 20–32, 2015.

[30] T. Markel, A. Brooker, T. Hendricks et al., "ADVISOR: a systems analysis tool for advanced vehicle modeling," *Journal of Power Sources*, vol. 110, no. 2, pp. 255–266, 2002.

[31] B. Pattanaik and S. Chandrasekaran, "Predictable dependably fault tolerant model for automotive embedded system," *European Journal of Scientific Research (EJSR)*, vol. 98, no. 1, pp. 16–29, 2013.

Hindawi
International Journal of Photoenergy
Volume 2022, Article ID 5389574, 14 pages
https://doi.org/10.1155/2022/5389574

Research Article

Investigating Rotor Conditions on Wind Turbines Using Integrating Tree Classifiers

Bikash Chandra Saha,[1] Joshuva Arockia Dhanraj,[2] M. Sujatha,[3] R. Vallikannu,[4] Mohana Alanazi,[5] Ahmad Almadhor,[6] Ravishankar Sathyamurthy,[7] Kuma Gowwomsa Erko,[8] and V. Sugumaran[9]

[1]*Department of Electrical and Electronics Engineering, Cambridge Institute of Technology, Ranchi, Jharkhand 835103, India*
[2]*Centre for Automation and Robotics (ANRO), Department of Mechatronics Engineering, Hindustan Institute of Technology and Science, Padur, Chennai, 603103 Tamil Nadu, India*
[3]*Department of Electronics and Communication Engineering, Koneru Lakshmaiah Education Foundation Vijayawada, Andhra Pradesh 522502, India*
[4]*Department of Electronics and Communication Engineering, Hindustan Institute of Technology and Science, Padur, Kelambakkam, Tamil Nadu 603103, India*
[5]*Department of Electrical Engineering, College of Engineering, Jouf University, Sakaka 42421, Saudi Arabia*
[6]*Department of Computer Engineering and Networks, Jouf University, Sakaka 42421, Saudi Arabia*
[7]*Department of Mechanical Engineering, KPR Institute of Engineering and Technology, Arasur, Coimbatore, 641407 Tamil Nadu, India*
[8]*Department of Mechanical Engineering, Ambo University, Ethiopia*
[9]*School of Mechanical Engineering, Vellore Institute of Technology, Chennai, Tamil Nadu 600127, India*

Correspondence should be addressed to Kuma Gowwomsa Erko; kuma.gowwomsa@ambou.edu.et

Received 31 January 2022; Accepted 26 April 2022; Published 9 June 2022

Academic Editor: V. Mohanavel

Copyright © 2022 Bikash Chandra Saha et al. This is an open access article distributed under the Creative Commons Attribution License, which permits unrestricted use, distribution, and reproduction in any medium, provided the original work is properly cited.

Renewable wind power is productive and feasible to manage the energy crisis and global warming. The wind turbine's blades are the essential components. The dimension of wind turbine blades has been increased with blade sizes varying from approx. 25 m up to approx. 100 m or even greater with a specific purpose to increase energy efficiency. While wind turbine blades tend to be highly stressed by environmental conditions, the wind turbine blade must be constantly tested, inspected, and monitored for wind turbine blades safety monitoring. This research presents a methodology adaptation on machine learning technique for appropriate classification of different failure conditions on blade during turbine operation. Five defects were reported for the diagnosis study of defective wind turbine rotor blades, and the considered defects are blade crack, erosion, loose hub blade contact, angle twist, and blade bend. The statistical features have been drawn from the recorded vibration signals, and the important features was selected through J48 classifier. Eight tree-dependent classifiers were used to categorize the state of the rotor blades. Among the classifiers, the least absolute deviation tree performed better with the classification percentage of 90% (Kappa statistics = 0.88, MAE = 0.0362, and RMSE = 0.1704) with a computational time of 0.06 s.

1. Introduction

The increasing impact of fossil fuel energy on global processes such as global warming and the availability of electricity has prompted various countries to explore clean options, like green solar and wind energy, to meet expanding energy demand [1]. The majority of wind turbines have the same essential components: shafts, gearboxes, blades, and generators, both of which giant and small. These sectors work together to turn wind power into electricity. The well-

known fact is that the energy of the wind turbines relies on its propellers [2]. The pivotal parts of the turbine blades and the costs for the blade are approximately 15–25 percent of the cost of generation of wind turbines. The scale of wind turbine blades with blade diameters varies from approx. 25 m to approx. 100 m, or even greater, to improve energy efficiency. The blades may suffer from absorption of moisture, ultraviolet radiation, degradation of the environment, exhaustion, wind or lightning, etc. The use of automated systems becomes troublesome during a traditional approach, as wear and tear vary in the pace for the parts. In the machine-learning method, algorithms will continuously adapt and get to know the changing circumstances [3]. Researchers in the machine learning approach routinely take follow-up on fault diagnosis of mechanical systems.

In specific, economic, social, and environmental influence are the criteria for choosing a maintenance strategy. Even though wind turbines on-shore and off-shore are located remotely from populated areas, there would be little social and environmental concern. The economic dimension is also the key consideration for assessing the annual maintenance strategies [4]. The model proposed in this study can provide a typical approach for the determination of the optimum cost of on-shore and off-shore turbine preventive maintenance. Two key maintenance types are available, namely, corrective maintenance and proactive maintenance. Corrective maintenance measures are based on a strategy of failure [5]. Two common categories of proactive maintenance are condition-based maintenance and time-based maintenance [6]. Predictive maintenance, which can be called a functional method of condition-based maintenance in some fields of research like artificial intelligence and machine learning, is closely related to predictive maintenance [7]. The emphasis of this paper is on condition-based maintenance [8].This study makes an attempt to find five different blade fault conditions by applying an approach through tree-based machine learning classifiers and statistical features. Figure 1 shows the methodology of the work done.

The present study's contributions are as follows:

(i) Five defects were reported for the diagnosis study of defective wind turbine rotor blades, and the considered defects are blade crack, erosion, loose hub blade contact, angle twist, and blade bend

(ii) Statistical features have been drawn from the recorded vibration signals

(iii) For the feature selection, J48 decision algorithm was used

(iv) It is modeled as multiclass problem and aims to examine the state of blade using a tree-dependent classifiers

The organization of the document is prepared accordingly. Section 2 provides the literature review of previous research carried out for the assessment of blade condition via simulation and the machine learning process. Section 3 discusses the experimental setup and procedure. Section 4 includes the procedures of statistical feature extraction. Section 5 illustrates the selection of features through the J48 decision tree algorithm. Section 6 outlines in depth the concept of tree-based machine learning in this research. Section 7 presents the results of the tree-based machine learning classifiers and discussion with their performance. The last section (Section 8) contains conclusions.

2. Literature Survey

Machine learning experiments and wind turbine failure prediction modeling testing were carried out for the most part; they [9] worked on wavelet-based and neural network fault diagnosis by the use of a wavelet transformation process to extract data from the blades collected. The wavelet principle is used to suppress device distortion and to minimize vibration interfering with wind turbine blades defect diagnoses. The processing method shall collect data from the various vibration frequencies of wind turbine blades and insert data into the neural system. The neural networks are used for data analysis and wind turbine blade condition recognition.

This work [10] conducted a work on sparse Bayesian learning through a short-term Fourier transformation to detect errors in wind turbine blades. In this analysis, sparse Bayesian learning (SBL) beam forming (BF) for the identification of blade defects is applied in order to improve signal acoustic information received by a microphone array on the ground. With high-resolution interference, such as noise produced by cooling fans, the path of arrival of the irregular sound can be determined by the low side lobes of the SBL-BF.

Researchers [11] conducted a report on the modeling of failures in large-scale wind turbines and electronic monitoring of blade damage. The study proposes a new approach of the analysis of the wavelet energy spectrum packet and modal operational analytics in the area of wind turbine blades. The first move is to determine the change point of the blades to achieve energy spectrum using the wavelet packet transform. Thanks to the energy change in multiple frequency bands, the harm is observed provisional.

The observed fault tree model for offshore floating wind turbines was suggested by [12]. In this study, the approach for the qualitative and quantitative assessment of semisubmersible offshore wind turbine malfunction components is used in the failure tree study technique. The multiple components include supports, pitch and hydraulics, gearboxes, engines, and other systems. Failure rates are gathered from the previous studies, publications, and reliability records for the related offshore systems.

They [13] have been focusing on the complex reaction of the V-shaped offshore wind turbine to cope with fault states. The dynamic response to different possible fault conditions of the semisubmersible V-form is examined in this paper with different behaviors of the floating wind turbine which were related in the instance of operating and fault conditions of the system. In the different fault situations, a numerical model was developed to provide a fully coupled dynamic analysis of the offshore wind turbine.

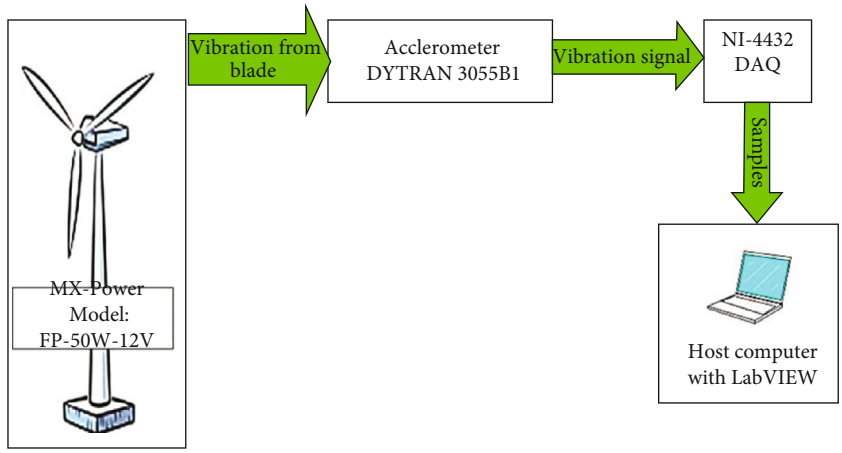

Figure 1: Methodology of the present work.

They have carried out maintenance control studies on artificial intelligence and nonlinear characteristics in wind turbines [14]. This article presents a new scientific solution to delamination research for reliability systems for wind turbine blades. It relies on the abstraction of an exogenous input (NARX) and linear autoregressive process (AR) from a nonlinear self-extraction. Six scenarios were performed using supervised machine learning techniques with various delamination measurements. This involve discriminatory analysis, nearest neighbors, quadratic SVM, ensemble, and tree classifiers.

They [15] have developed a study that uses atmospheric inputs for artificial neural systems to improve the prediction of wind turbine power. The research has a major effect on the calculation of wind farms' financial feasibility by enhancing the precision of monthly energy forecasts. The importance of the analysis is that the wind turbine's performance forecasts take account of ambient equilibrium and air density. A multiparameter input model is used to approximate the power produced by the wind turbine in artificial neural networks (ANN) machine learning method. ANN concept uses the feed forward back propagation (FFBP) algorithm. A 40 percent increase in the mean absolute error (MAE) associated with the density correction indicated an enhancement of the FFBP-ANN model with the density correction techniques.

They [16] have done a research on the rigorous process of detection through acoustic emission and machine learning of wind turbine blade adhesive composite joints. This article provides a framework for clustering method by fast search and find of density peaks (CFSFDP), in an effective detection of various types of damage which can be handled using similarities and differences of AE signals. Based on the clustering study, fatigue cracks and adhesive layer shear failure are, respectively, shown to be critical and characteristic measures of damage. Fiber problems are seen quite close to delamination as a unique damage feature, in comparison to other damage modes in the subspace. In comparison, the effects of the cluster number selection, the spatial similarity metric, and the importance of the cutoff index are seen to be negligible for the cluster performance.

This work [17] carried out adaptive selection for enhancement of blade damage for an operating wind turbine. The proposed works incorporate a structural health monitoring method focused on a semisupervised algorithm for damage detection, using preliminary results to improve the collection of the features of damage detection. The approach suggests a new method of extracting functions by sorting the acceleration values in increasing vibration response. An evolutionary algorithm for choosing applications should be used in order to determine the most appropriate damage prevention. All these technique strengthens the connection of same blade measures and thus the robustness of the proposed structural health monitoring technique.

They [18] conducted an experimental research on passive acoustic detection of damage to structural wind turbine blades health monitoring. The approach uses intrinsic microphones with blades to detect trends, shifts, or spikes in the cavity of the blade by means of a limited network of airborne, natural passive structure amplitude, and recurrent quantification windows. K-means clustering is used to classify the outliers in the calculations and include the feature-spatial representation of the data collection. The system's efficiency is measured on the basis of its capabilities to identify structural events inside the blade detected by manual measurement observation. Novelty of this research work could be identified by Table 1 as discriminant analysis using tree classifiers on wind turbines.

3. Experimental Studies

This research is primarily aimed at assessing whether the blades are in decent or poor shape. The aim is to determine if it is faulty, the form of fault. The following sections describe the experimental and experimental configuration. These were achieved on a wind turbine with varying speeds. Table 2 specifies the basic specifications for the wind turbine. The wind turbine has been fitted opposite to the open-circuit wind tunnel on a stable stainless steel stand. The wind tunnel speed ranges between 5 and 15 m/s and it provides the wind turbine to operate. To mimic the local wind conditions, the wind speed was continuously varying. The diagnostic

Table 1: Comparison of related studies on wind turbine using machine learning algorithms.

Reference number	Year	Literature survey (methods used)																				
		Wavelet	Neural network	Sparse Bayesian learning	Spectrum analysis	Tree classifiers	Dynamic analysis	Autoregressive model	Discriminant analysis	Nearest neighbors	Support vector machines	Ensemble classification	Clustering	Evolutionary algorithm	K-means	Genetic algorithm	Fuzzy logic	Interval observer approach	Blade element momentum	Kriging model	Simulator	Damage detection algorithm	Whale optimization algorithm
Bi et al. [9]	2019	*	*																				
Pan et al. [10]	2019			*																			
Gao et al. [11]	2019	*			*																		
Kang et al. [12]	2019					*																	
Karimirad and Michailides [13]	2019						*																
Jiménez et al. [14]	2020					*		*	*	*	*	*											
Nielson et al. [15]	2020		*																				
Xu et al. [16]	2020												*										
Movsessian et al. [17]	2020													*									
Solimine et al. [18]	2020														*								
Kim et al. [19]	2020															*							
Civelek [20]	2020															*	*						
Beale et al. [21]	2020	*																					
Pujol-Vazquez et al. [22]	2020																	*					
Emami et al. [23]	2020										*												
Elgammi et al. [24]	2020																		*				
Awadallah and El-Sinawi. [25]	2020				*															*			
Saleem and Kim [26]	2020															*							
Philippidis and Eliopoulos [27]	2020																				*		
Krause and Ostermann [28]	2020				*																	*	
Liu et al. [29]	2020															*							
Qais et al. [30]	2020																*						*
Current research	2020					*			*														

Table 2: Technical parameters of wind turbine [31].

Model	FP-50W-12V
Power (W)	50
Voltage (V)	12
Current (A)	8
Rotating rate (rpm)	850
Maximum-power (W)	150
Wind velocity during start up (m/s)	2.5
Wind velocity (m/s) (cut in)	3.5
Wind velocity (m/s) (cut out)	15
Wind velocity (m/s) (security)	40
Wind velocity (m/s) (rated)	12.5
Turbine	3Φ PM generator
Diameter of rotor (mm)	1050
Material of the blade	Reinforced plastics (carbon fiber)

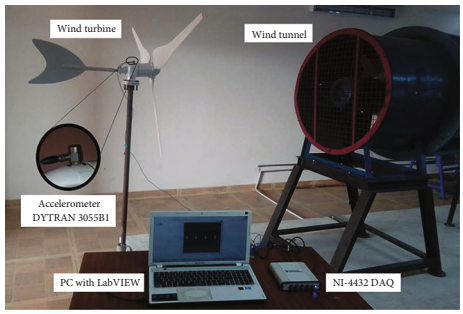

Figure 2: Experimental setup.

test setup is illustrated in Figure 2. As a transducer for the processing of vibration signal, a piezoelectric accelerometer was used. The sensitivity to detect faults is high-frequency. Accelerometers are therefore commonly used for measuring environments. A 500 g range with the sensitivity of 100 mV/g and a 40 Hz accelerometer (resonant frequency) have been used in this case (DYTRAN 3055B1). The DAQ network linked via a wire used was the NI-USB-DAQ-4432 model as data acquisition system. The sample rate of the card is 102.4 kilograms per second, and the resolution of a sample is 24-bit. A signal conditioning device that includes a built-in charge amp and an ADC is attached to the accelerometer. The vibration signal had been received from the ADC. Such vibration signals have been used to disable functionality through the isolation of information. The accelerometer is attached to one end of the cable and the AIO port of the device. The transducer and the computer have been interfaced via NI-LabVIEW.

The three-blade HAWT has been used in this study. At first, the wind turbine (free from faults, new installation) was reasoned to be in good state, and the signals were measured with an accelerometer. Figures 3(a)–3(f) show the faults fabricated on the blade, and Figures 4(a)–4(f) show its corresponding signal, and the following specifications were recorded for these signals:

(1) Sample length: sampling period was chosen appropriately for data accuracy, and the following points were also considered. If the numbers of the sample are sufficiently large, statistical measures are more significant. On the other side, with the amounts of measurements, measurement time decreases. To achieve it, the length of the sample was preferred to be 10000

(2) Sampling frequency: It should be at least twice the maximum signal frequency as set out in the Nyquist theorem. The sampling frequency was calculated using this principle for 12 kHz

(3) Number of trials: 100 measurements (samples) were obtained for each wind turbines blade state

   (i) Blade bend (BB): this defect is caused by high velocity wind and storm-induced dynamic movements. With 10°angles, the blade was made to bend

   (ii) Blade crack (BC-2): it happens during service as a consequence of foreign object disruption to the sword. A 15-mm crack was made on the trailing edge

   (iii) Blade erosion (BE): this failure is caused by high-speed wind on blade's top surface. The smooth blade surface has been eroded with a 320 Cw sheet to erode the blade

   (iv) Hub-blade loose contact: this fault is usually caused by excessive runtime or usage time of a wind turbine. This fault was fabricated by the releasing bolt between the hub and blade

   (v) Blade pitch angle twist (PAT): this failure occurs because of high-speed wind pressures on the surface. It shifts the sound, producing a strong frame vibration. The pitch was twisted around 12° angles in relation to the normal condition to achieve this failure

The turbine was designed to operate at 850 revolutions per minute. The vibration signals are captured at a rate of 12000 Hz with a sample size of 10000. In terms of rotations per second (850/60 ≈ 14 revolutions per second), this equals 14 rotations per second. Besides considering the following factors, the sample length was selected to be long enough to assure consistency in results. When the number of samples is sufficiently big, statistical measures become more relevant. When the number of samples is increased, however, the amount of time spent computing grows. Sample length of around 10000 was selected in order to achieve a good balance. The signal contains data for 14 revolutions, which is good enough to capture the fault information. In this study 100 signal (vibration signatures) were taken for each condition (totally 600 vibration signatures). Each signal, it contain 10000 data points which is very much sufficient in this study.

(a)

(b)

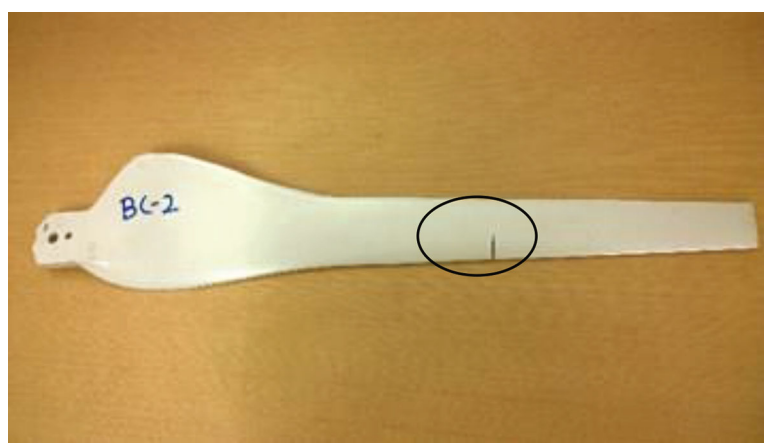

(c)

Figure 3: Continued.

(d)

(e)

(f)

Figure 3: (a) Good blade. (b) Bend fault. (c) Crack fault. (d) Erosion fault. (e) Hub-blade loose fault. (f) Pitch fault.

4. Feature Extraction

Vibration patterns were acquired from the DAQ for different blade fault conditions in this analysis. The feedback to the classifier cannot be explicitly used by vibration signals [31, 32]. Attributes must therefore be determined by statistical methods. In order to explore issues such as fault classification from an objective standpoint, statistical analysis is used by academics to quantify a wide variety of events. It has a propensity to generate overly simplistic solutions to complicated problems when given a complex question. Each of the statistical approaches is categorized according to a set of factors that allows us to do the best analysis possible for the issue and forecast how much error or deviation has occurred for a certain problem. The calculation process is called feature extraction. Some measures represent the

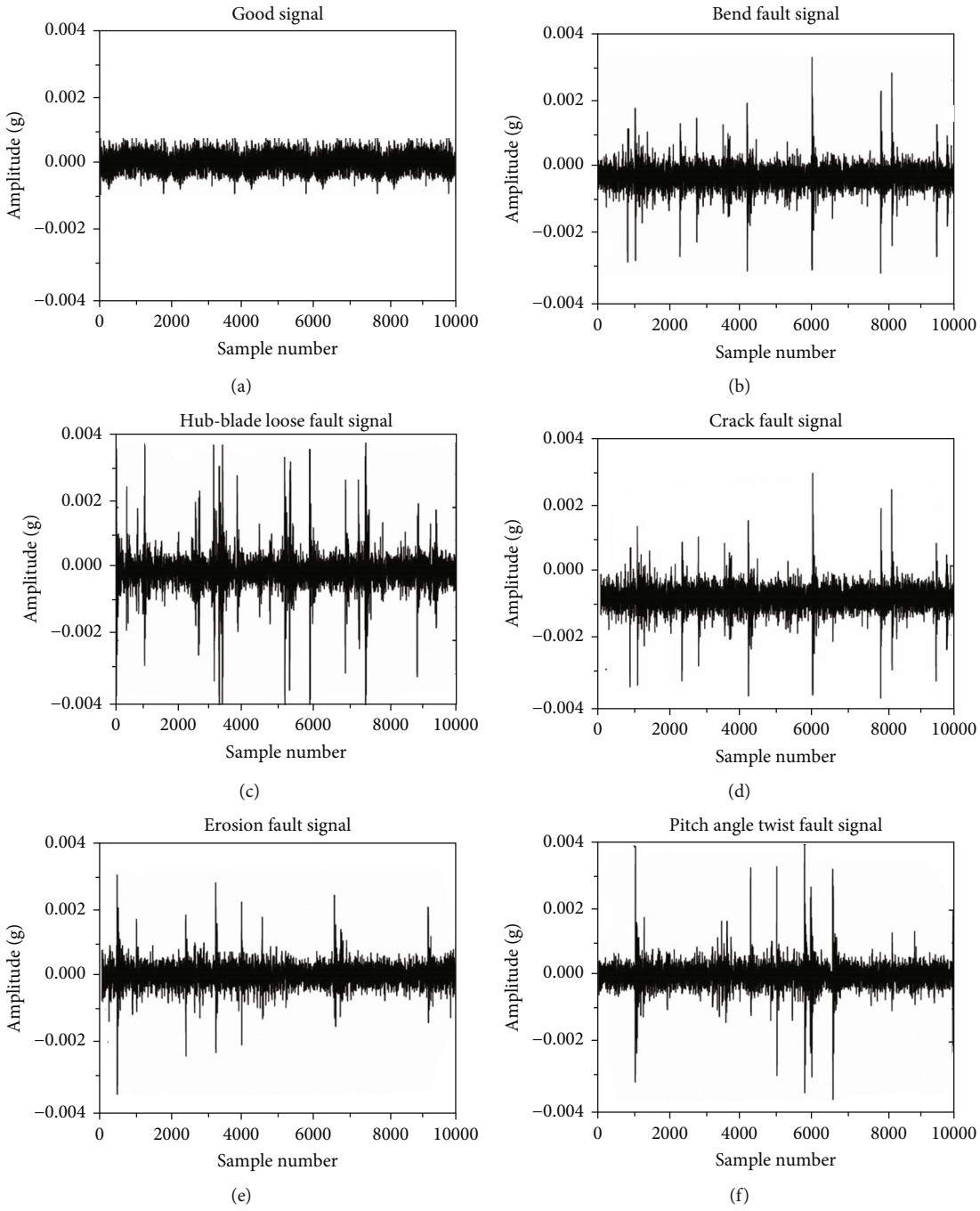

Figure 4: (a) Good condition signal plot. (b) Signal plot for bend condition. (c) Signal plot for crack condition. (d) Signal plot for erosion condition. (e) Signal plot for hub-blade loose condition. (f) Signal plot for pitch angle twist condition.

signal. Vibration signals statistical information provides various parameters [33]. The functions have been taken and the feature collection procedure has been applied once the computational extraction phase has been completed. The most significant characteristics are chosen from the descriptive statistical parameters obtained via the J48 algorithm.

5. Feature Selection

The practice of data mining is commonly used to retrieve useful information structures from libraries utilizing vibration knowledge. An important information framework, which might be produced through the processes of data mining. Decision trees (DT) are recurrently developed after a top-down approach. The regular mediated trees of C4.5 contain a number of branches, roots, many nodes, and leaves. Single branch is a root to a leaf chain of nodes, with one attribute per node. The inclusion of a characteristic in a tree gives information on the importance of the associated feature. Algorithm J48 is a commonly used algorithm to build decision trees (WEKA Application of the C4.5 Algorithm) [34].

J48 decision tree is widely used as a feature selection technique where it uses information gain to select required attributes. This metric assesses how effectively a specific characteristic distinguishes the training instances based on their categorization in the target class. While the tree is being grown, the measure is being used to choose the candidate features at each stage. The projected decrease in entropy as a result of portioning the samples according to this characteristic is referred to as the information gain. The information gain (S, A) of a feature A when compared to a collection of samples S is defined as follows:

$$Gain\,(S, A) = Entropy(S) - \sum_{v \in Value(A)} \times \frac{|S_v|}{|S|} Entropy(S_v), \tag{1}$$

where *Value (A)* is the set of all possible values for attribute A, and S_v is the subset of S for which feature A has value v. It is important to note that the first component in the equation for gain is just the entropy of the original collection S, and the second term is the predicted value of the entropy after S has been partitioned using feature A. The expected entropy described by the second term is simply the sum of the entropies of each subset S_v, weighted by the fraction of samples $|S_v|/|S|$ that belong to S_v. As a result, the predicted decrease in entropy induced by knowing the value of feature A is denoted by the symbol Gain (S, A). Entropy is a measure of the homogeneity of a collection of instances, and it is represented by the expression as follows:

$$Entropy(S) = \sum_{i-1}^{c} - P_i \log_2 P_i, \tag{2}$$

where c is the number of classes and P_i is the proportion of S belonging to class i. The method by which the decision tree is shaped and used for vibration analysis is defined by the following:

(1) The mathematical features from analyses of the blade vibration of the wind turbine are the contribution to the algorithm

(2) DT contains leaf nodes containing class marks and other class nodes (in this case, magnitude level)

(3) The tree branches reflect the parameter node from which they derive with each possible value

(4) One can start from the tree root (top node) and go through a branch to a leaf node by using the decision tree to express structural information

(5) A statistical step is taken within the parentheses in the decision tree to provide the contribution level for each individual parameter (Figure 5). The first parenthesis indicates the amount of data points that can be defined by this set parameter. There are decreasing parameters in the decision tree nodes

(6) Using the appropriate estimation criteria at each decision node of the decision tree, the most useful parameter for classification can be used

The entropy and information gain concept is the principle used to categorize the superlative parameter. Two phases have been developed for the decision tree algorithm (C4.5). The construction phase is also referred to as the "development phase" [35]. The main features of the wind turbine blade descriptors are usually available [36]. With regard to Table 3 (selected features with their accuracy) and Figure 5, four of these leading features can be predictable, (a) sum, (b) range, (c) kurtosis, and (d) standard deviation.

6. Feature Classification

It is a process in which data are grouped into a number of classes. The primary objective of a classification is to define the class of new data. The various tree classifiers are as follows [37, 38].

6.1. Decision Stump (DS). The decision stumbling block is a one-level decision tree machine learning model [39]. It is also known as weak students or basic students. It is an internal hub decision tree linked immediately with the hubs (the leaves) of the terminal. A judgment stump makes a prediction on the basis of the value of a single feature [40]. They are also referred to as 1-rules. The tree may be more complex if the function is numeric and the teaching and boosting methods of machine-learning ensemble [41].

6.2. Extra Tree (ET). The ET [42] is a randomized decision-making technique. It is different from other random decision-making bodies. The split and the chosen attribute for each judgment node would be fully randomized with the last parameter setup, and the tree would be entirely independent from the training data. The additional tree is also referred to as a very random tree [43].

6.3. J48 Consolidated (J48C). Its is also known as the consolidated tree construction (CTC) algorithm (J48C) J48 consolidated (J48C) algorithm [44]. The decision on each split shall be voted on by all the trees rather than building each tree independently. All trees conform to the majority voting and are split equally irrespective of their vote [45].

6.4. J48 Graft (J48G). In view of the grafting of further branches into the tree during a postprocessing phase, the J48 decision tree algorithm is extended [46]. The grafting cycle aims to accomplish some of the strength and stability of ensemble approaches like sacking and boosting of trees. It identifies parts of an instance which include either wrong instances or which are either null or explores those classifications for various tests that could be picked at nodes above the regional leaf [47].

6.5. LAD Tree (LADT). The least absolute deviation tree (LADT) is a multiclass problem-solving alternate algorithm, based on the LogitBoost algorithm [48]. LADT can adapt the

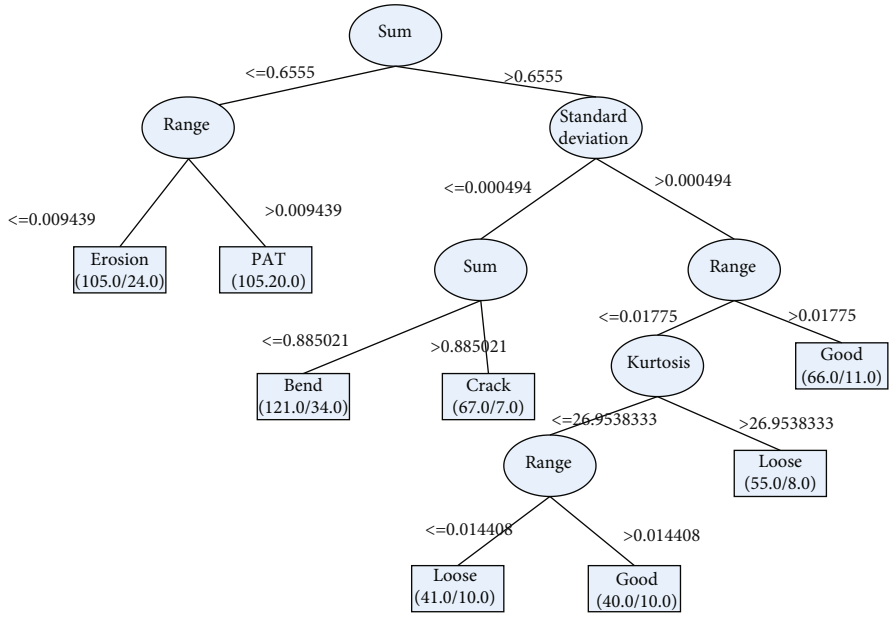

Figure 5: J48 Tree classification for feature selection.

Table 3: Features selected.

No. of features	Name of the features	Classification accuracy (%)
1	Sum	49.33
2	Range and sum	69.17
3	Standard deviation, range, and sum	80.00
4	Standard deviation, range, sum, and kurtosis	86.67
5	Kurtosis, standard deviation, range, sum, and mean	85.83
6	Median, kurtosis, standard deviation, range, sum, and mean	85.83
7	Mode, median, kurtosis, standard deviation, range, sum, and mean	85.83
8	Minimum, mode, median, kurtosis, standard deviation, range, sum, and mean	84.83
9	Maximum, minimum, mode, median, kurtosis, standard deviation, range, sum, and mean	84.83
10	Standard error, maximum, minimum, mode, median, kurtosis, standard deviation, range, sum, and mean	84.83
11	Skewness, standard error, maximum, minimum, mode, median, kurtosis, standard deviation, range, sum, and mean	83.67
12	Sample variance, skewness, standard error, maximum, minimum, mode, median, kurtosis, standard deviation, range, sum, and mean	83.00

amount of boost iterations to the provided data and decide the size of the tree.

6.6. NB-Tree (NBT). The NB-Tree (NBT) hybrid is a hybrid of Naïve Bayes and decision trees. This produces a tree of leaves which are marked as Naïve Bayes for entering the top. Cross-validation is used when constructing a tree to determine if a split node is required or the model of the Naïve Bayes is used in place [49].

6.7. REP Tree (REPT). REP tree (REPT) or REPT builds a decision-regression tree for knowledge gain or variance reduction that is plumed by decreased error pruning. It only speeds up numerical characteristics. This deals, as in C4.5 [50], with missed values by splitting instances into bits. Minimum number of instances can be determined with the root, maximum depth of a tree (useful for boosting trees), and maximum split time (only number groups) as well as several slicing folds.

6.8. Simple Cart Classifiers (SCC). The simple cart classifier (SCC) is a member of a classification decision tree that uses a minimum cost difficulty approach. Similarities do however come to an end here when none of CART's other characteristics are discussed, namely, a CART specialist, a founder of this technique [51]. The overall number of cases per paper can be estimated, the amount of the preparation details used

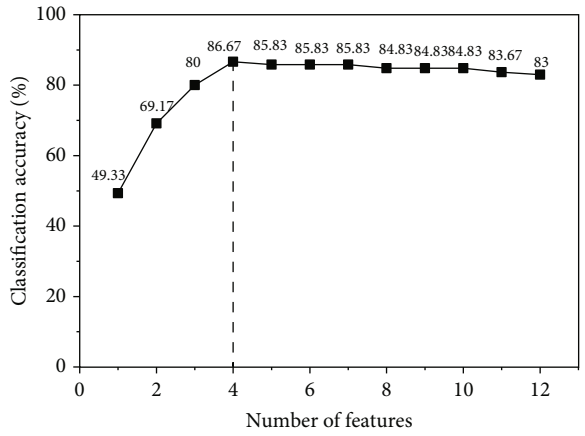

Figure 6: Number of features vs. classification accuracy.

for tree construction and the number of folds used during the cutting process.

7. Result and Discussion

Vibration patterns was obtained with DAQ (total of 600 samples; 100 samples were collected in each condition), in good condition or in bad bladder conditions. 12 concise statistical features were derived from the vibration patterns. Of them, the J48 has selected four best contributing characteristics. In order to select 4 primary features from the J48 method, the minimum number of instances per sheet was set at 50 for reduced-error pruning, and Figure 6 illustrates the number of characteristics vs. precision in classification. The classification performance of the J48 algorithm is 86.67% during the selection process. Other combinations of features were not successful as in Figure 6. The chosen features were then given to the classifier as an input to measure the accuracy of the classification [52].

Table 4 shows the classification precision and measurement time of various classifiers. The purpose of the study is to develop the classification system. It is easy to notice (Table 4) that among classifiers considered, the LADT classification is stronger than other classifiers. This rule is based on high precision (90%) in low time (0.06 s) grouping. The number of iterations increased ranged from 10 to 100 in order to achieve this classification accuracy in the LADT and showed that the optimum classification accuracy was reached in a 90% increase in the number of iterations (Figure 7) [53].

Table 5 shows the LADT confusion matrix. The diagonal components signify the properly categorized occurrences in the confusion matrix, and the other instances are misclassified. For estimating the error rate of a learning process given a single, fixed sample of data, stratified ten-fold cross-validation is the most used approach. At random, the data is split into 10 parts, with each section representing the class in about the same proportion as the overall sample population. It is necessary to train the learning scheme on the remaining nine tenths of each component before calculating its error rate on the holdout set. Because of this, the learning

Table 4: Classifiers accuracy.

Classifiers	Classification accuracy (%)	Computational time (s)
Decision stump (DS)	33.17	0.04
Extra tree (ET)	81.50	0.03
J48 consolidated (J48C)	85.17	0.03
J48 graft (J48G)	79.67	0.09
LAD tree (LADT)	90.00	0.06
NB tree (NBT)	82.33	0.90
REP tree (REPT)	83.83	0.04
Simple cart classifiers (SCC)	85.00	0.32

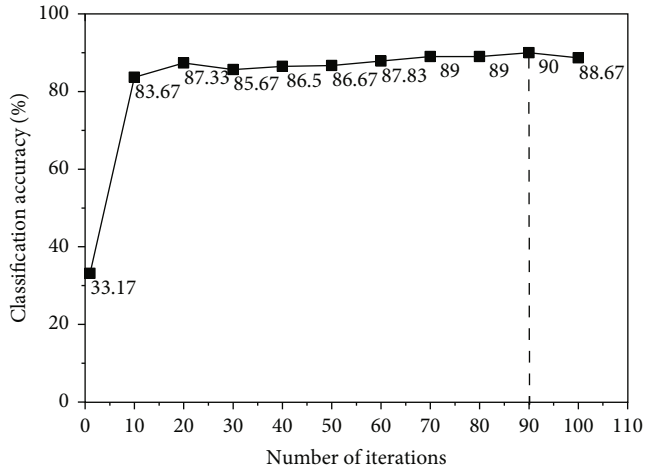

Figure 7: Number of iterations considered for LAD tree.

Table 5: Confusion matrix for LAD tree.

Blade class	Class A	Class B	Class C	Class D	Class E	Class F
Class A	*82*	0	1	0	17	0
Class B	0	*95*	4	0	0	1
Class C	0	5	*91*	4	0	0
Class D	0	4	0	*91*	0	5
Class E	13	0	3	0	*84*	0
Class F	0	0	0	3	0	*97*

Table 6: Class-wise accuracy of LAD tree.

Blade class	TP	FP	PRE	REC	F-M
Class A	0.820	0.026	0.863	0.820	0.841
Class B	0.950	0.018	0.913	0.950	0.931
Class C	0.910	0.016	0.919	0.910	0.915
Class D	0.910	0.008	0.958	0.910	0.933
Class E	0.840	0.042	0.800	0.840	0.820
Class F	0.970	0.010	0.951	0.970	0.960

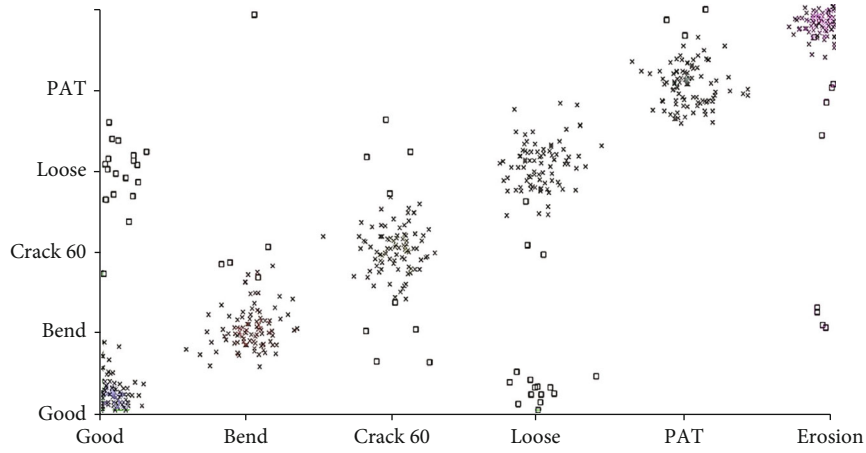

Figure 8: Errors chart.

procedure is repeated 10 times on a variety of practice sets. Finally, an overall error estimate is calculated by averaging the ten error estimates. In this approach, the error rate may be calculated quickly and accurately. The major component (area 1,1) in the first row of the confusion matrix refers to the number of properly categorized items that have a position with the equivalent that reflects good condition (class A). The next component (section 1,2) discusses the number of excellent examples of bent fault that were incorrectly allocated (bend) (class B). The third component (area 1,3) describes the number of excellent crack loss (crack) situations that have been incorrectly delegated (class C). The fourth component (region 1,4) refers to the number of positive occurrences incorrectly referred to as hub-blade (loose) fault situations (class D). The fifth component (area 1,5) refers to the number of good occurrences incorrectly referred to as pitch angle twist fault condition (PAT) (class E). The sixth component (area 1,6) refers to the number of good samples that were incorrectly assigned to the erosion fault condition (erosion) (class F). Kappa was observed to be 0.88 from the LADT. It was observed that the mean absolute error (MAE) was 0.0362. The root mean square error (RMSE) implies that 0.1704 is a square defect. The average error size is processed by a quadratic scoring rule. Table 6 displays the comprehensive class accuracy. The accuracy of the class is shown in terms of the true positive rate (TP), false positive rate (FP), precision (PRE), recall (REC), and F-measure (F-M). [54].The percentage of positive which is accurately labeled as defects is estimated using TP. In a stronger classifier, the TP probability should be about 1 and the FP number similar to 0. Table 6 reveals that the TP average in most groups is below 1 and that the FP rate was below 0 [55]. It ensures the uncertainty matrix provided in Table 5. Figure 8 shows the error classification chart. The squared dots here represent errors, and the "x" corresponds to the right classification. Of the 600 test samples, 540 (90 percent) and the remaining 60 (10 percent) are misclassified. It takes approximately 0.06 seconds to construct the pattern.

8. Conclusion

For harvesting wind energy from the open wind, the wind turbine is a very critical device. The paper presented an algorithmic vibration signal classification for wind turbine blades estimation. Five defects were reported for the diagnosis study of defective wind turbine rotor blades, and the considered defects are blade crack, erosion, loose hub blade contact, angle twist, and blade bend. The collected vibration data has been used to create eight models utilizing tree dependent classifiers. The algorithms were evaluated using the 10-fold cross-validation technique. The following where the findings from this study:

(1) Least absolute deviation tree (LADT) provided the cumulative accuracy of 90% when compared to other tree dependent classifiers with the computational time of 0.06 s (Table 4)

(2) The obtained Kappa statistics is 0.88 for LADT which shows a better fit model

(3) Mean absolute error was found to be 0.0362

(4) Root mean square error was found to be 0.1704

(5) The error rate of 10% is merely less when compared to other classifiers

From the above findings, it could be said with assurance that the least absolute deviation tree (LADT) can be used in real-time to identify blade defects in operating wind turbines. This study can reduce the framework downtime economically, leading to high productivity of wind energy.

Data Availability

The measured data used to support the findings of this study are available from the corresponding author upon request.

Conflicts of Interest

The authors declare that there is no conflict of interest regarding the publication of this paper.

Acknowledgments

The authors thank Ambo University, Ethiopia, for providing help during the research and preparation of the manuscript. The authors thank Vellore Institute of Technology, Chennai; Hindustan Institute of Technology and Science, Chennai; and KPR Institute of Engineering and Technology for providing assistance in completing the work.

References

[1] R. McKenna, S. Pfenninger, H. Heinrichs et al., "High-resolution large-scale onshore wind energy assessments: a review of potential definitions, methodologies and future research needs," *Renewable Energy*, vol. 182, pp. 659–684, 2022.

[2] A. L. Pires, P. Rotella Junior, S. N. Morioka, L. C. Rocha, and I. Bolis, "Main trends and criteria adopted in economic feasibility studies of offshore wind energy: a systematic literature review," *Energies*, vol. 15, no. 1, p. 12, 2022.

[3] A. Chaudhuri, R. Datta, M. P. Kumar, J. P. Davim, and S. Pramanik, "Energy conversion strategies for wind energy system: electrical, mechanical and material aspects," *Materials*, vol. 15, no. 3, p. 1232, 2022.

[4] Z. Zhao, D. Wang, T. Wang, W. Shen, H. Liu, and M. Chen, "A review: approaches for aerodynamic performance improvement of lift-type vertical axis wind turbine," *Sustainable Energy Technologies and Assessments*, vol. 49, no. 49, article 101789, 2022.

[5] T. Asim, S. Z. Islam, A. Hemmati, and M. S. Khalid, "A review of recent advancements in offshore wind turbine technology," *Energies*, vol. 15, no. 2, p. 579, 2022.

[6] Q. S. Ali and M. H. Kim, "Power conversion performance of airborne wind turbine under unsteady loads," *Renewable and Sustainable Energy Reviews*, vol. 153, article 111798, 2022.

[7] N. Hoksbergen, R. Akkerman, and I. Baran, "The springer model for lifetime prediction of wind turbine blade leading edge protection systems: a review and sensitivity study," *Materials*, vol. 15, no. 3, p. 1170, 2022.

[8] C. Jung and D. Schindler, "On the influence of wind speed model resolution on the global technical wind energy potential," *Renewable and Sustainable Energy Reviews*, vol. 156, article 112001, 2022.

[9] J. Bi, C. Zheng, H. Huang, X. Song, and J. Li, "Fault diagnosis of wind turbine blades based on wavelet theory and neural network," *International Journal of Performability Engineering*, vol. 15, no. 7, 2019.

[10] X. Pan, Z. Cheng, Z. Zheng, and Y. Zhang, "Sparse Bayesian learning beamforming combined with short-time Fourier transform for fault detection of wind turbine blades," *The Journal of the Acoustical Society of America*, vol. 145, no. 3, p. 1802, 2019.

[11] F. Gao, X. Wu, Q. Liu, J. Liu, and X. Yang, "Fault simulation and online diagnosis of blade damage of large-scale wind turbines," *Energies*, vol. 12, no. 3, p. 522, 2019.

[12] J. Kang, L. Sun, and C. G. Soares, "Fault tree analysis of floating offshore wind turbines," *Renewable Energy*, vol. 133, pp. 1455–1467, 2019.

[13] M. Karimirad and C. Michailides, "Fault condition effects on the dynamic response of V-shaped offshore wind turbine," *Journal of Marine Science and Technology*, vol. 24, no. 1, pp. 34–45, 2019.

[14] A. A. Jiménez, L. Zhang, C. Q. Muñoz, and F. P. Márquez, "Maintenance management based on machine learning and nonlinear features in wind turbines," *Renewable Energy*, vol. 146, pp. 316–328, 2020.

[15] J. Nielson, K. Bhaganagar, R. Meka, and A. Alaeddini, "Using atmospheric inputs for artificial neural networks to improve wind turbine power prediction," *Energy*, vol. 190, article 116273, 2020.

[16] D. Xu, P. F. Liu, Z. P. Chen, J. X. Leng, and L. Jiao, "Achieving robust damage mode identification of adhesive composite joints for wind turbine blade using acoustic emission and machine learning," *Composite Structures*, vol. 236, article 111840, 2020.

[17] A. Movsessian, D. Garcia, and D. Tcherniak, *Proceedings of the 13th International Conference on Damage Assessment of Structures*, Adaptive feature selection for enhancing blade damage diagnosis on an operational wind turbine, Springer, Singapore, 2020.

[18] J. Solimine, C. Niezrecki, and M. Inalpolat, "An experimental investigation into passive acoustic damage detection for structural health monitoring of wind turbine blades," *Structural Health Monitoring*, vol. 19, no. 6, pp. 1711–1725, 2020.

[19] Y. Kim, G. Bangga, and A. Delgado, "Wind turbine airfoil boundary layer optimization using genetic algorithm with 3D rotational augmentation," in *Design Optimization of Wind Energy Conversion Systems with Applications*, IntechOpen, 2020.

[20] Z. Civelek, "Optimization of fuzzy logic (Takagi-Sugeno) blade pitch angle controller in wind turbines by genetic algorithm," *Engineering Science and Technology, an International Journal*, vol. 23, no. 1, pp. 1–9, 2020.

[21] C. Beale, C. Niezrecki, and M. Inalpolat, "An adaptive wavelet packet denoising algorithm for enhanced active acoustic damage detection from wind turbine blades," *Mechanical Systems and Signal Processing*, vol. 142, article 106754, 2020.

[22] G. Pujol-Vazquez, L. Acho, and J. Gibergans-Báguena, "Fault detection algorithm for wind turbines' pitch actuator systems," *Energies*, vol. 13, no. 11, p. 2861, 2020.

[23] A. Emami, A. Tavana, M. Mahnama, and A. Sadighi, "Model-based data-driven structural health monitoring of a wind turbine blade," *AUT Journal of Mechanical Engineering*, vol. 5, no. 1, pp. 97–108, 2021.

[24] M. Elgammi, T. Sant, and M. Alshaikh, "Predicting the stochastic aerodynamic loads on blades of two yawed downwind hawts in uncontrolled conditions using a bem algorithm," *Renewable Energy*, vol. 146, pp. 371–383, 2020.

[25] M. Awadallah and A. El-Sinawi, "Effect and detection of cracks on small wind turbine blade vibration using special Kriging analysis of spectral shifts," *Measurement*, vol. 151, article 107076, 2020.

[26] A. Saleem and M. H. Kim, "Aerodynamic performance optimization of an airfoil-based airborne wind turbine using genetic algorithm," *Energy*, vol. 203, article 117841, 2020.

[27] T. P. Philippidis and E. N. Eliopoulos, "A progressive damage mechanics algorithm for life prediction of composite materials under cyclic complex stress," in *Fatigue life prediction of composites and composite structures*, pp. 495–537, Woodhead Publishing, 2020.

[28] T. Krause and J. Ostermann, "Damage detection for wind turbine rotor blades using airborne sound," *Structural Control and Health Monitoring*, vol. 27, no. 5, article e2520, 2020.

[29] F. Liu, X. Ju, N. Wang, L. Wang, and W. J. Lee, "Wind farm macro-siting optimization with insightful bi-criteria identification and relocation mechanism in genetic algorithm," *Energy Conversion and Management*, vol. 217, article 112964, 2020.

[30] M. H. Qais, H. M. Hasanien, and S. Alghuwainem, "Whale optimization algorithm-based Sugeno fuzzy logic controller for fault ride-through improvement of grid-connected variable speed wind generators," *Engineering Applications of Artificial Intelligence*, vol. 87, article 103328, 2020.

[31] A. Joshuva and V. Sugumaran, "A lazy learning approach for condition monitoring of wind turbine blade using vibration signals and histogram features," *Measurement*, vol. 152, article 107295, 2020.

[32] X. Meng, P. Zhang, Y. Xu, and H. Xie, "Construction of decision tree based on C4.5 algorithm for online voltage stability assessment," *International Journal of Electrical Power & Energy Systems*, vol. 118, article 105793, 2020.

[33] Y. Cuan, Z. Wang, and J. Han, "Research on TV imaging casing damage detection and classification method based on C4. 5 decision tree," *Journal of Physics: Conference Series*, vol. 1437, no. 1, article 012132, 2020.

[34] R. Hariharan, I. S. Thaseen, and G. U. Devi, "Performance analysis of single- and ensemble-based classifiers for intrusion detection," in *Soft Computing for Problem Solving*, pp. 759–770, Springer, Singapore, 2020.

[35] N. Bhatt, A. Thakkar, N. Bhatt, and P. Prajapati, "Algorithm selection via meta-learning and active meta-learning," in *Smart Systems and IoT: Innovations in Computing*, pp. 169–178, Springer, Singapore, 2020.

[36] D. Lou, M. Yang, D. Shi et al., "K-means and C4. 5 decision tree based prediction of long-term precipitation variability in the Poyang Lake Basin, China," *Atmosphere*, vol. 12, no. 7, p. 834, 2021.

[37] I. H. Witten and E. Frank, "Data mining: practical machine learning tools and techniques with Java implementations," *ACM SIGMOD Record*, vol. 31, no. 1, pp. 76-77, 2002.

[38] Y. J. Chew, S. Y. Ooi, K. S. Wong, and Y. H. Pang, "Decision tree with sensitive pruning in network-based intrusion detection system," in *Computational Science and Technology*, pp. 1–10, Springer, Singapore, 2020.

[39] Y. Qu, B. L. Adam, Y. Yasui et al., "Boosted decision tree analysis of surface-enhanced laser desorption/ionization mass spectral serum profiles discriminates prostate cancer from noncancer patients," *Clinical Chemistry*, vol. 48, no. 10, pp. 1835–1843, 2002.

[40] Y. Zhao and Y. Zhang, "Comparison of decision tree methods for finding active objects," *Advances in Space Research*, vol. 41, no. 12, pp. 1955–1959, 2008.

[41] R. C. Holte, "Very simple classification rules perform well on most commonly used datasets," *Machine Learning*, vol. 11, no. 1, pp. 63–90, 1993.

[42] P. Geurts, D. Ernst, and L. Wehenkel, "Extremely randomized trees," *Machine Learning*, vol. 63, no. 1, pp. 3–42, 2006.

[43] D. Ernst, P. Geurts, and L. Wehenkel, "Tree-based batch mode reinforcement learning," *Journal of Machine Learning Research*, vol. 6, pp. 503–556, 2005.

[44] I. Ibarguren, J. M. Pérez, J. Muguerza, I. Gurrutxaga, and O. Arbelaitz, "Coverage-based resampling: building robust consolidated decision trees," *Knowledge-Based Systems*, vol. 79, pp. 51–67, 2015.

[45] J. M. Pérez, J. Muguerza, O. Arbelaitz, I. Gurrutxaga, and J. I. Martín, "Combining multiple class distribution modified subsamples in a single tree," *Pattern Recognition Letters*, vol. 28, no. 4, pp. 414–422, 2007.

[46] G. I. Webb, "Decision tree grafting from the all-tests-but-one partition," in *IJCAI'99: Proceedings of the 16th international joint conference on Artificial intelligence - Volume 2*, pp. 702–707, Stockholm Sweden, 1999.

[47] V. K. Pachghare and P. Kulkarni, "Pattern based network security using decision trees and support vector machine," in *2011 3rd International Conference on Electronics Computer Technology*, Kanyakumari, India, 2011.

[48] G. Holmes, B. Pfahringer, R. Kirkby, E. Frank, and M. Hall, "Multiclass alternating decision trees," in *European Conference on Machine Learning*, pp. 161–172, Springer, Berlin Heidelberg, 2002.

[49] R. Kohavi, "Scaling up the accuracy of Naive-Bayes classifiers: a decision-tree hybrid," in *KDD'96: Proceedings of the Second International Conference on Knowledge Discovery and Data Mining*, pp. 202–207, Portland Oregon, 1996.

[50] C. Thornton, F. Hutter, H. H. Hoos, and K. Leyton-Brown, "Auto-WEKA: combined selection and hyperparameter optimization of classification algorithms," in *Proceedings of the 19th ACM SIGKDD international conference on Knowledge discovery and data mining*, pp. 847–855, Chicago Illinois USA, 2013.

[51] L. Breiman, J. Friedman, C. J. Stone, and R. A. Olshen, *Classification and Regression Trees*, CRC press, 1984.

[52] C. N. Villavicencio, J. J. Macrohon, X. A. Inbaraj, J. H. Jeng, and J. G. Hsieh, "COVID-19 prediction applying supervised machine learning algorithms with comparative analysis using WEKA," *Algorithms*, vol. 14, no. 7, p. 201, 2021.

[53] G. Zeng, "On the confusion matrix in credit scoring and its analytical properties," *Communications in Statistics-Theory and Methods*, vol. 49, no. 9, pp. 2080–2093, 2020.

[54] C. H. Han, E. Kim, and C. H. Im, "Development of a brain–computer interface toggle switch with low false-positive rate using respiration-modulated photoplethysmography," *Sensors*, vol. 20, no. 2, p. 348, 2020.

[55] S. Suresh and S. Mohan, "ROI-based feature learning for efficient true positive prediction using convolutional neural network for lung cancer diagnosis," *Neural Computing and Applications*, vol. 32, no. 20, pp. 15989–16009, 2020.

Hindawi
International Journal of Photoenergy
Volume 2022, Article ID 6427076, 10 pages
https://doi.org/10.1155/2022/6427076

Research Article

Infrared Thermal Images of Solar PV Panels for Fault Identification Using Image Processing Technique

V. Kirubakaran[1], **D. M. D. Preethi**[2], **U. Arunachalam**[3], **Yarrapragada K. S. S. Rao**[4], **Mansour K. Gatasheh**[5], **Nasrul Hoda**[6] and **Endalkachew Mergia Anbese**[7]

[1]*Centre for Rural Energy, The Gandhigram Rural Institute, Gandhigram, Dindigul, Tamilnadu, India*
[2]*Department of Computer Science and Engineering, PSNA College of Engineering and Technology, Dindigul, Tamilnadu, India*
[3]*Department of Mechanical Engineering, University College of Engineering-Nagercoil, Tamilnadu, Nagercoil, India*
[4]*Department of Mechanical Engineering, Aditya College of Engineering, Surampalem, 533437 Andhra Pradesh, India*
[5]*Department of Biochemistry, College of Science, King Saud University, P.O. Box 2455, Riyadh 11451, Saudi Arabia*
[6]*Department of Neurology, Henry Ford Health System, Detroit MI 48292, USA*
[7]*Department of Civil Engineering, Ambo University, Ambo, Ethiopia*

Correspondence should be addressed to Endalkachew Mergia Anbese; endalkachew.mergia@ambou.edu.et

Received 9 February 2022; Revised 22 March 2022; Accepted 30 March 2022; Published 8 June 2022

Academic Editor: V. Mohanavel

Copyright © 2022 V. Kirubakaran et al. This is an open access article distributed under the Creative Commons Attribution License, which permits unrestricted use, distribution, and reproduction in any medium, provided the original work is properly cited.

Among the renewable forms of energy, solar energy is a convincing, clean energy and acceptable worldwide. Solar PV plants, both ground mounting and the rooftop, are mushrooming thought the world. One of the significant challenges is the fault identification of the solar PV module, since a vast power plant condition monitoring of individual panels is cumbersome. This paper attempts to identify the panel using a thermal imaging system and processes the thermal images using the image processing technique. An ordinary and thermal image has been processed in the image processing tool and proved that thermal images record the hot spots. Similarly, the new and aged solar photovoltaic panels were compared in the image processing technique since any fault in the panel has been recorded as hot spots. The image recorded in the aged panels records hot spots, and performance has been analyzed using conventional metrics. The experimental results have also been verified.

1. Introduction

The usage of renewable energy is increasing daily to give a sustainable and clean form of energy. The recent day's use of solar energy has grown tremendously. Both rooftop and ground-mounted technologies penetrated the market at a rapid phase. In the same way, the operation and maintenance of solar panels also need to be taken care of. Solar PV systems are maintenance-free; however, the system's monitoring is essential to achieve the maximum yield from the plants. Several parameters affect the panel output like dust, humidity, shadow temperature, and moisture. In an extensive power plant, monitoring of individual panels is a cumbersome process. However, any parameters affecting the yield of solar panels will induce internal resistance. Thus, a thermal image of the panels will be able to identify the fault of the panel quickly. Several thermal imagers are readily available in the market; analyzing individual images is a difficult task. Hence, the picture taken in a thermal imager is processed by MATLAB Simulink software for the different steps in the images' layering. The temperature difference is associated with bordering the modules, and hot spots are easily identified.

2. Literature Review

Different types of solution for the fault detection and the analysis by the various steps such as monitoring systems, I and C analysis based on artificial intelligence, and voltage and current measurements and also by power loss measurements analysis process of the different methods have no

precise data and not decentralized in the system for inverters and to fault diagnosis [1–3]. Electrical degradation of old panel and its working defects via IR thermography and VI characteristics and also the simulation in MATLAB and from this study of image processing of the PV panel with the software by an algorithm were discussed [3, 4]. Evaluation of the solar PV system to grid connections and the solar PV system simulation with the MATLAB software the assessment of the full operating power plants were conducted [4, 5]. Comparison between the regular model and expected values of the proposed system by the different types of shading and their output readings for the fault system on PV was performed, and the noise for detection time for these outputs and graph is drawn, and stability curve is also made for respected data [5, 6]. To compare in faulty condition threshold with system operation in nominal condition, there are many approaches and the choice of one technique depends on the following: knowledge of the history of system events, the expert system knowledge, data collected on the system in normal operation conditions, a known model of the system, fault types of the short circuit, open circuit, mismatch of loads, and ground faults by the serious of coding by the data acquired by the control system in the system via MATLAB to indicate which type of defect has occurred on the system [6, 7]. Infrared imager for solar panels provides the data and converts it to the CIELAB (it is 3D color space that enables accurate measurement and comparison of all perceivable colors using three color values), and segmentation by processing the panel of different cells, modules, and dust forming increases the temperature of different sizes and temperature ranges [8, 9]. The relationship between the different panels' dust density and spectral transmittance is determined. The slope angle outcome is rightly linked to the quantity of dirt thickness difference on the outward. Dirt adds to the decrease of PV production by decreasing irradiance in a spectrally reliant manner [10, 11]. This is viewed as the result of the spectral answer data. The outcome is not a similar amount for all sorts of PV technology for spectral conduction that disturbs numerous spectral reply forms [12, 13]. Solar modules are to be viewed as the single cells for the identification of each by the industrial control computer. Then, for the different sets of the problems like the broken grid, fragmented cells, black pieces on solar cells, and cracks on the cells, the different sets of methods are used to identify the fault and analyses with which level of the defects are in it. It provides very accurate and high real processing time [14, 15]. Thermal image processing of the solar PV modules is used. It represents the various steps for the modules' changes for the identification of the fault [16, 17]. They mainly assumed on the three different faults as the heavy, minor, and medium faults. However, this paper deals with thermal imaging technique to detect exact fault in the cells The characteristic curves have been plotted to find out the difference in the spots and healthy ones. This model comprises the electrical and mechanical systems and then provides an optimal solution for the systems' MPPT conditions [18, 19]. Identification of the fault in the solar PV modules is done by the cutting edge technology and by the nondestructive testing methods like the thermal image process. In this paper, a neural network classifier-based algorithm is developed with the different sets of conditions and the collections of the modules to attain the perfectness for the deduction of the fault [20, 21]. After the test algorithm is created, it is verified by the thermal image, which is then converted to the gray image, and then, it is subjected to linear filtering [22]. The intensity gradient is adjusted and then for the hysteresis thresholding, the values at last were identified with the cutting edge technology. The image is then Hough transformed to the binary image, and the Hough lines are peaks on them to identify the faults and the efficiency of the increased than other methods. Solar PV module faults in the only way to show the necessity of the fault detection in the solar modules [23]. The solar modules got fired at California and North Carolina which are showed as the examples of the faults. The EL images are taken for the healthy panels and the spots of the minor cracks, break images, and finger impregnations for fault-finding. Then, by the PCA and ICA for the image to be processed by the component analysis. The differentiation from the healthy panels and finding the exact defects in them for the MATLAB software to find without the exact defects save the faults' cost and reliability [24].

3. Solar PV Panel

3.1. Solar Photovoltaic Cell. The solar PV cell comprises the solar panel. They are made of silicon-based semiconductors and photons of light that transfer electrons to energy when sunlight passes on a PV cell; the PV cell may be reflected and absorbed or pass right through it, converting the light energy into the electrical power. The solar cells are used to make the solar array, which comprises the solar module to generate electricity. This process was explained in the above solar cell figure. The solar cells work high on maximum insolation, making the device work under high-efficient conditions. The solar array is made of solar panels in series and parallel combinations to get the designed voltage and current level. Figure 1 represents a single solar cell.

3.2. Solar Energy Conversion Principles. There are two modes of tapping energy from the sun. The first one is the solar thermal method, and the second one is the solar photovoltaic method. PV modules and arrays are just one part of a PV system. This system includes installing solar panels that convert direct current (DC) to Alternative Current (AC) electricity for appliances in your home. The solar photovoltaic method is used in the experiment; the solar photovoltaic panel is based on the conversion principle that when light falls on the semiconductor, the energy is released and makes electrons flow in the form of the electrical power; this is the primary conversion of the PV system. Figure 2 shows the solar PV panel.

3.3. Thermal Imager. A thermal imaging technique is an image capturing method that converts the original appearance of an object with the heatwave and stores in a digital format without any contact of the item. Figure 3 shows the thermal imaging camera, which will capture any object and give the thermal color coding using infrared techniques. FLIR maker thermal imager is represented in Figure 3.

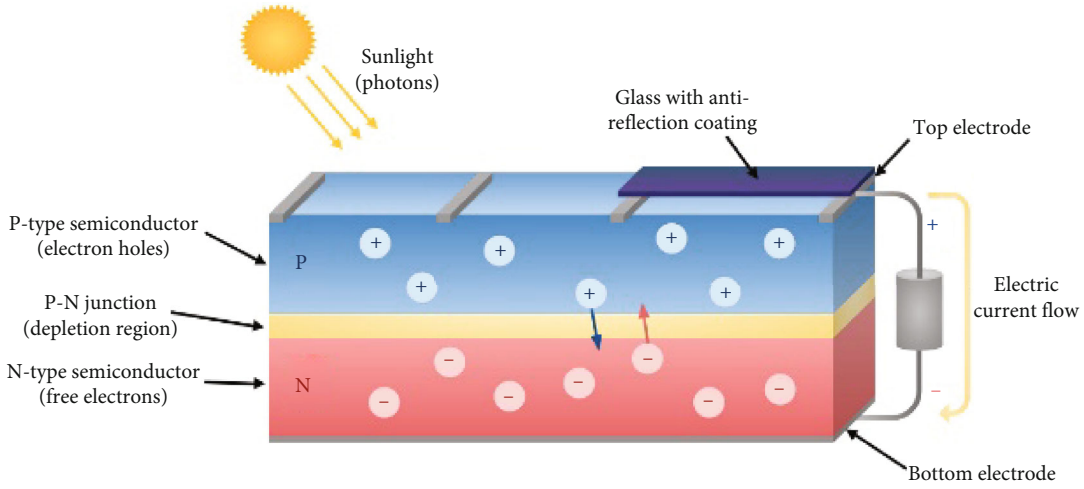

Figure 1: Solar cell.

Figure 2: Solar panels.

Figure 3: Thermal imager.

4. Proposed System

The planned system is aimed at finding out of fault to have occurred in solar photovoltaics in the initial stages. The FLIR's thermal images can do this about the solar PV panels. The thermal images taken are to be processed by MATLAB by the coding. This can be provided with the flow chart process in Figure 4.

5. Methodology

The system comprises the renewable energy source and the fault to be detected by the different images' different sources to change in the product to be carried out by the image processing. The flow chart provides the necessary data and how the things are to be done by the system with the help of MATLAB. As the software plays a significant role in the project which is to make the images be processed by it to provide the difference of the pictures which we were given as the input to make the effective output way to analyze them with the original images so that the fault is found out easily which is shown in Figure 4. At first, in fault-finding, the images provide the absolute image processing of the solar panels. So the experiment is to carry out on a metal plate that is heated in a particular place [25]. It is then taken as the thermal image, grayscale image, and familiar color image by the thermal imager. It is processed under the software, whereas the thermal spikes are getting known to show accurate data. After experimenting with the metal plate, the old panel is subjected to the result's undergoing process to find out the faulty one.

5.1. Preprocessing Unit. Initially, a novel image is converted to a grayscale image. And then, it undergoes the image processing algorithm, which is to differentiate the images.

5.2. Intensity Adjusted Image. It has changed the intensity adjusted of the novel image to get an accurate image in them.

5.3. Morphological Dilated Image. The image then identifies the morphological data to which the unnecessary parts have been removed concerning the original image on the input given for processing the image.

5.4. Cell Structure Removed Image. Then, the image identified the morphological data to which the unnecessary parts have been released concerning the original image on the input given for the processing of the image and the cell structure removing in this stage of the process.

5.5. Mask for Solar Panel. The initial stage is to remove the sections that stake the defects in their features like the hot spot. The subsequent step is to recognize hot spots and cell structure. A hot spot that comes into view in the image can be traced using the Hough transform (HT). The Hough transform is a

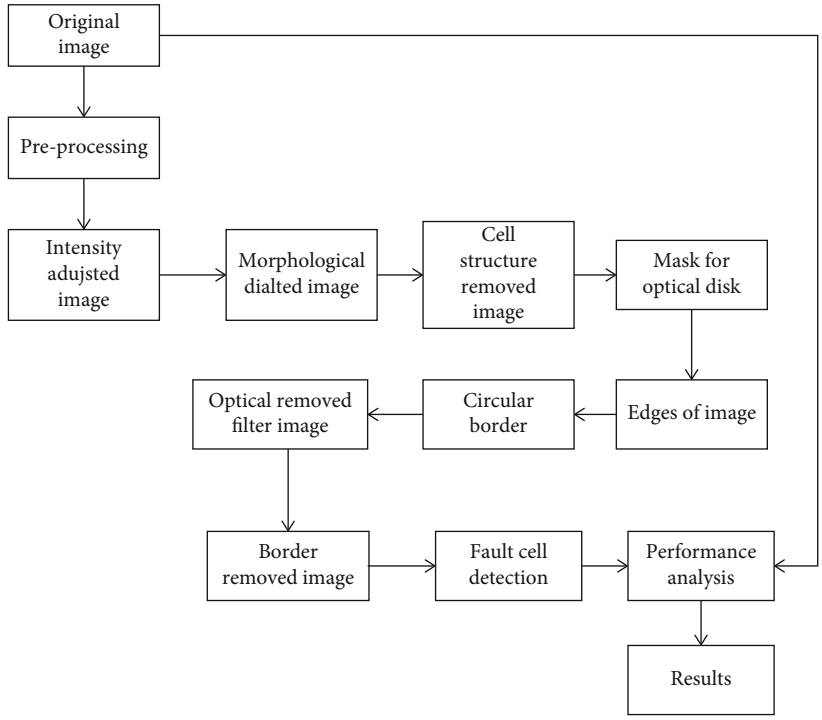

Figure 4: Flow diagram of the proposed system.

technique which can be used to isolate features of a particular shape within an image. Because it requires that the desired features are specified in some parametric form, the classical Hough transform is most commonly used for the detection of regular curves such as lines, circles, and ellipses. The results obtained in the HT are presented in Figure 4.

5.6. Edges of the Image. To make a clear image on the plate system, images are taken to identify the edges of the images sent to the process, the data for the identification. To plot the outer parts, it shows with the structure.

5.7. Circular Border of the Image. The circular border of the image is the different sets of options to provide the circular structure of the data. It is used to identify the edges of the pictures and the spikes from the pixel's variations' input image indifference.

5.8. Hot Spot Identification Image. It provides the hot spots the filtered image on that to make the difference the edges removed, and the visually seen the picture of the input, then it allowed for the processing.

5.9. Border Removed Image. After the hot spots from the circular border image are identified, the border region is removed to get a clear image of the fault's cell structure in the processing data.

5.10. Fault Cell Detection. The Hough transform can identify the fault located on the cell. It is used to remove the border region. The initial point for the transformation is referred to as a marker.

The morphological reconstruction algorithm is to get the final estimate of the hot spot. The MATLAB operations are listed in Table 1.

6. Experimentation and Results

For the experimentation process, the three different images are being taken. In that one is a thermal image of the metal plate, and the other is the grayscale image of the metal plate, and the last one is the color image of the metal plate. These images are being processed on MATLAB with the coding. The experimentation results for the thermal image with the hot spot of metal plate processed with the software are given in Figure 5.

The experimentation results for the metal plate's gray image with hot sport processed with the software are given in Figure 6.

The experimentation results for the normal image with the hot sport of the metal plate processed with the software are shown in Figure 7.

The hot spot is viewed in the thermal image from the above three different sets of image processing data. It is obvious that image processing of thermal images exactly identifies the hot spots. Most of the parameters affecting the solar panels induce internal resistance and give the hot spots which cannot be easily identified. However, the thermal images will detect hot spots. If image processing tools can be employed, the exact hot spots will be easily located.

To ascertain the same, a comparison between aged and new panel thermal images has been analyzed using image processing techniques. It is represented in Figures 8 and 9.

Table 1: MATLAB functions.

MAT LAB functions and their explanations	
Imadjust (I)	Gray image intensity values
Imdilate (IM, SE)	Dilates the grayscale
Imerode (IM, SE)	Sonnet the grayscale
Median (A)	Vectors have assigned for the column "A"
Floor (A)	Converts the number to the nearest integer
Meshgrid (abc, def)	Duplicates the abc and def to arrive final grid
Edge (I, "canny," thresh)	Low and high value considered as a first and second element to get the threshing
Logical (A)	Produces final value from numerical
Adapthisteq (I)	Improve the image

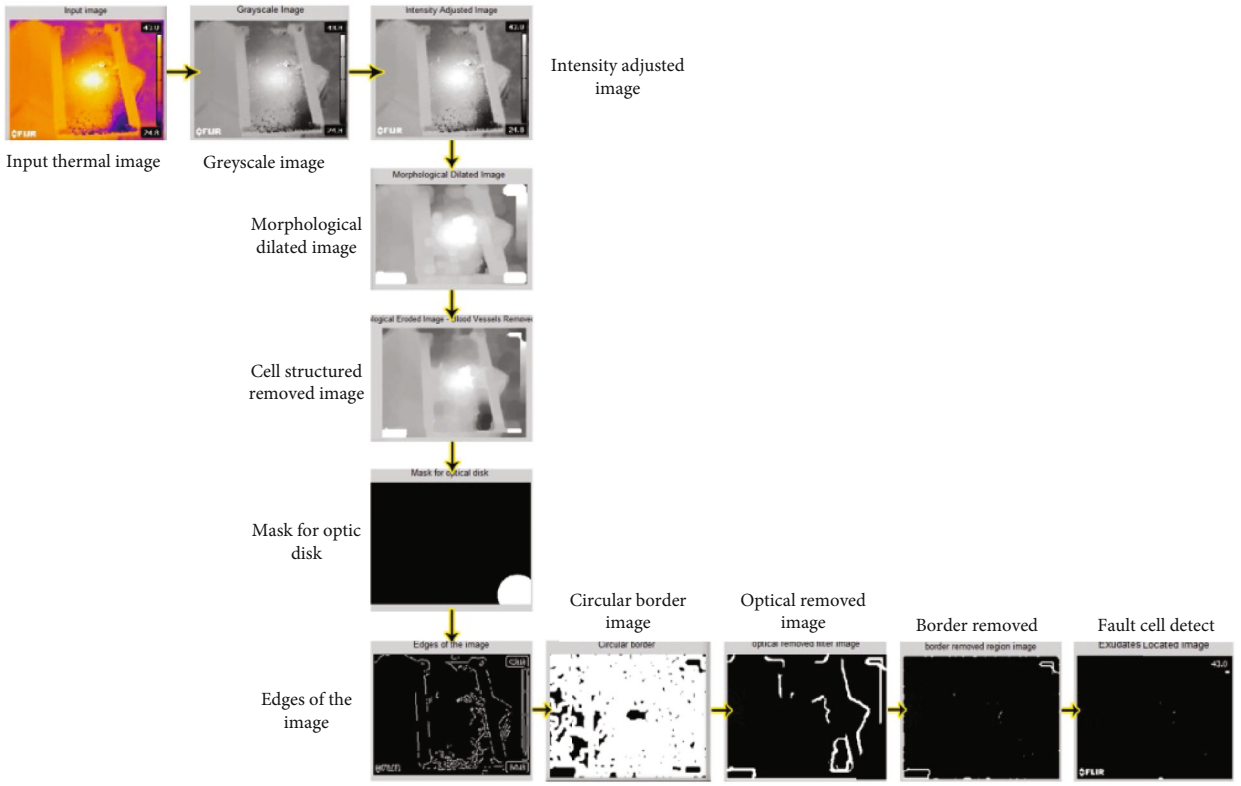

Figure 5: Thermal image processed.

7. Validation

Thermal image of the solar panel quality has been accessed using conventional parameters. New panel thermal image and the aged panel thermal image have been captured using thermal imager with size 300×345 pixels with a resolution of 96 dpi. ANOVA built in MATLAB is used for error analysis.

7.1. Conventional Parameters. Due to aging, the solar cells degraded which increased internal resistance. This may be recorded as hot spots in the thermal images of the solar panel. Hence, the new panel thermal image has been taken as bench mark image. Based on the bench mark image, the quality of the other panel thermal images has been verified using correlation quality (CQ), correlation coefficient (CC), normalized cross-correlation (NCC), image fidelity (IF), normalized mean square error (NM), signal-to-noise ratio (SNR), peak signal-to-noise ratio (PSNR), and mean square error (MSE). Correlation quality (CQ) is a measure of probability indices of measured and calculated quality of images which can be calculated using the following equation:

$$\mathrm{CQ} = \frac{\sum_{p,q} I_{p,q} \sim I_{p,q}}{\sum_{p,q} I_{p,q}}. \tag{1}$$

Correlation coefficient has been obtained from the following equation:

$$\mathrm{CC} = \frac{\sum_{p=1}^{q} I_{p,q} * \sim I_{p,q}}{\sqrt{I_{p,q}^2} * \sqrt{\sim I_{p,q}^2}}. \tag{2}$$

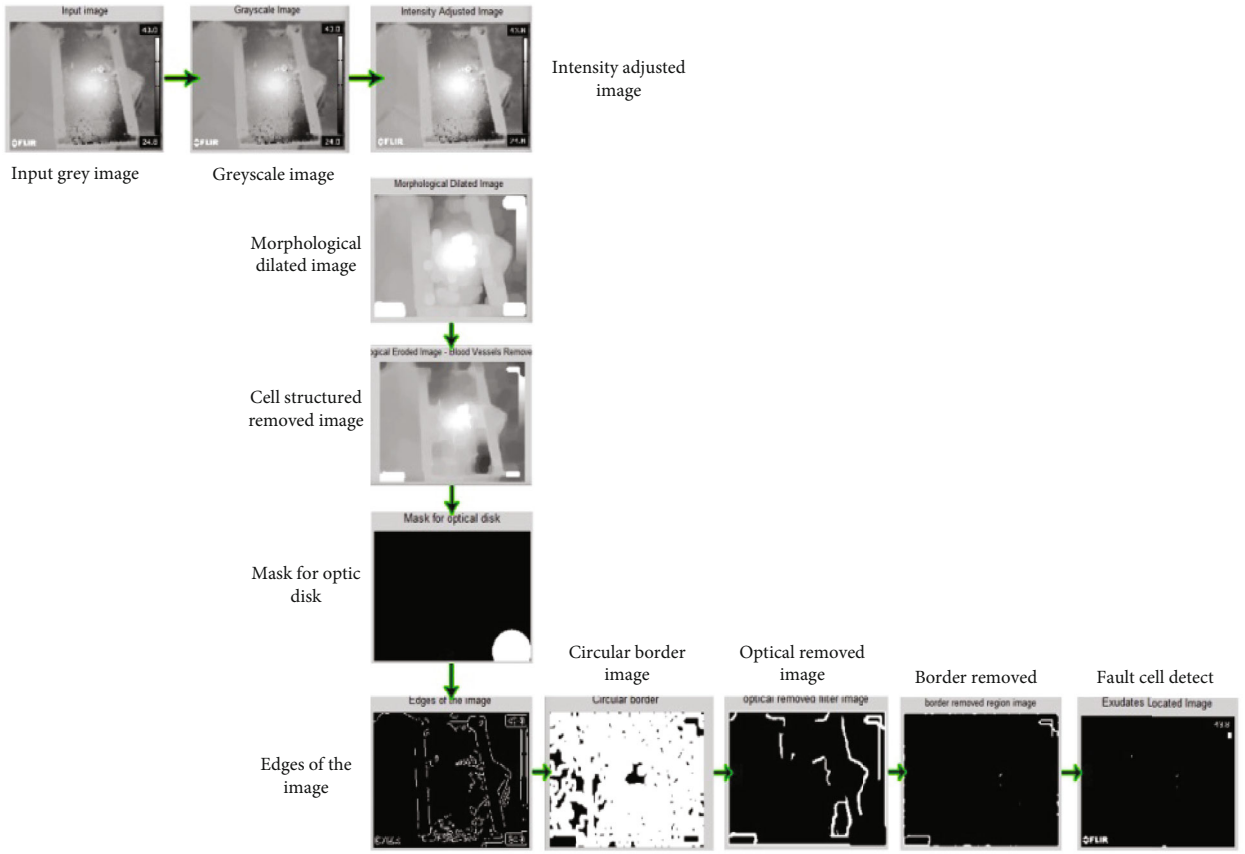

Figure 6: Metal plate's gray image with hot sport processed.

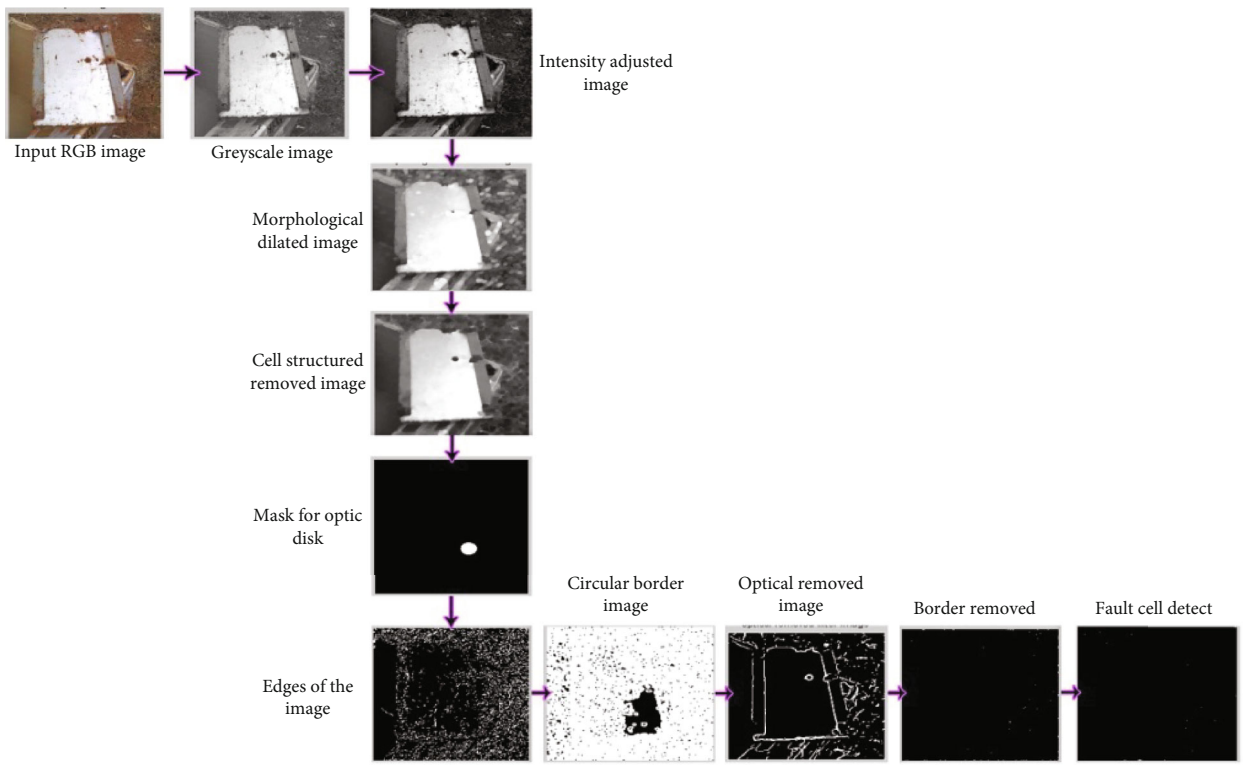

Figure 7: RGB image processed.

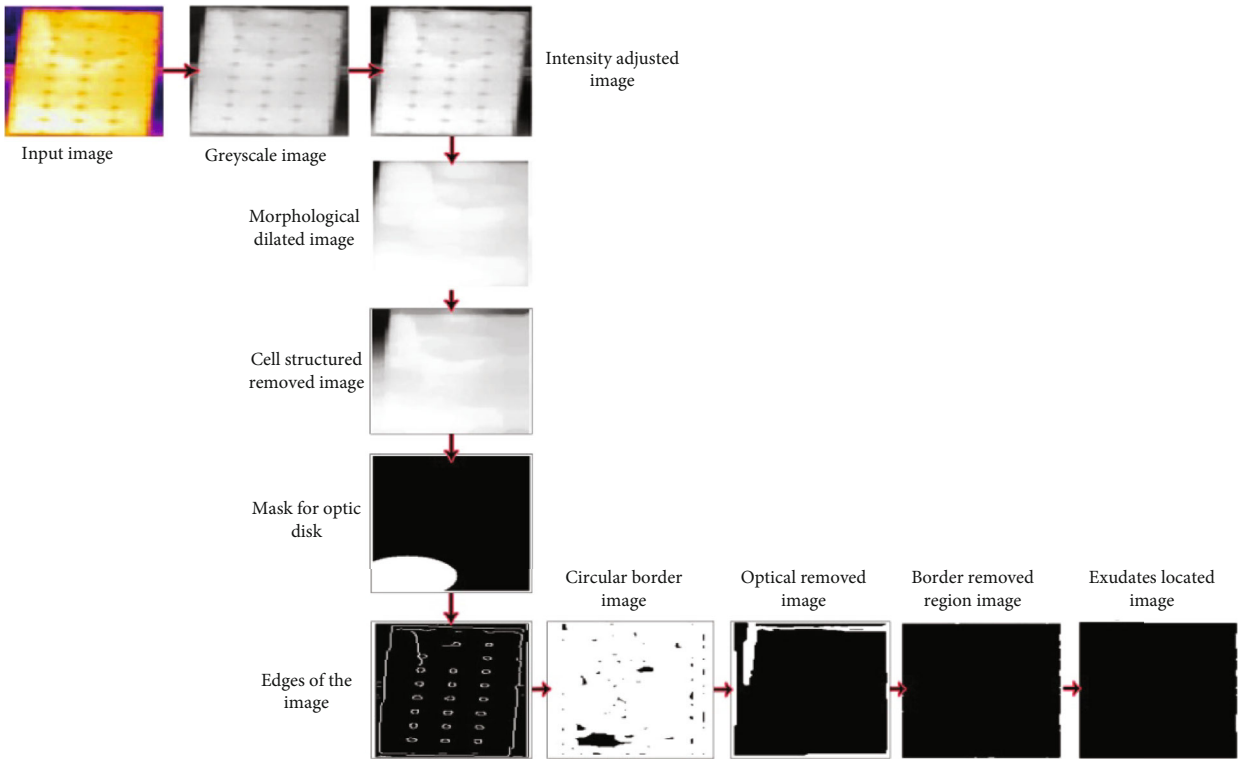

Figure 8: Aged solar panel thermal image processed.

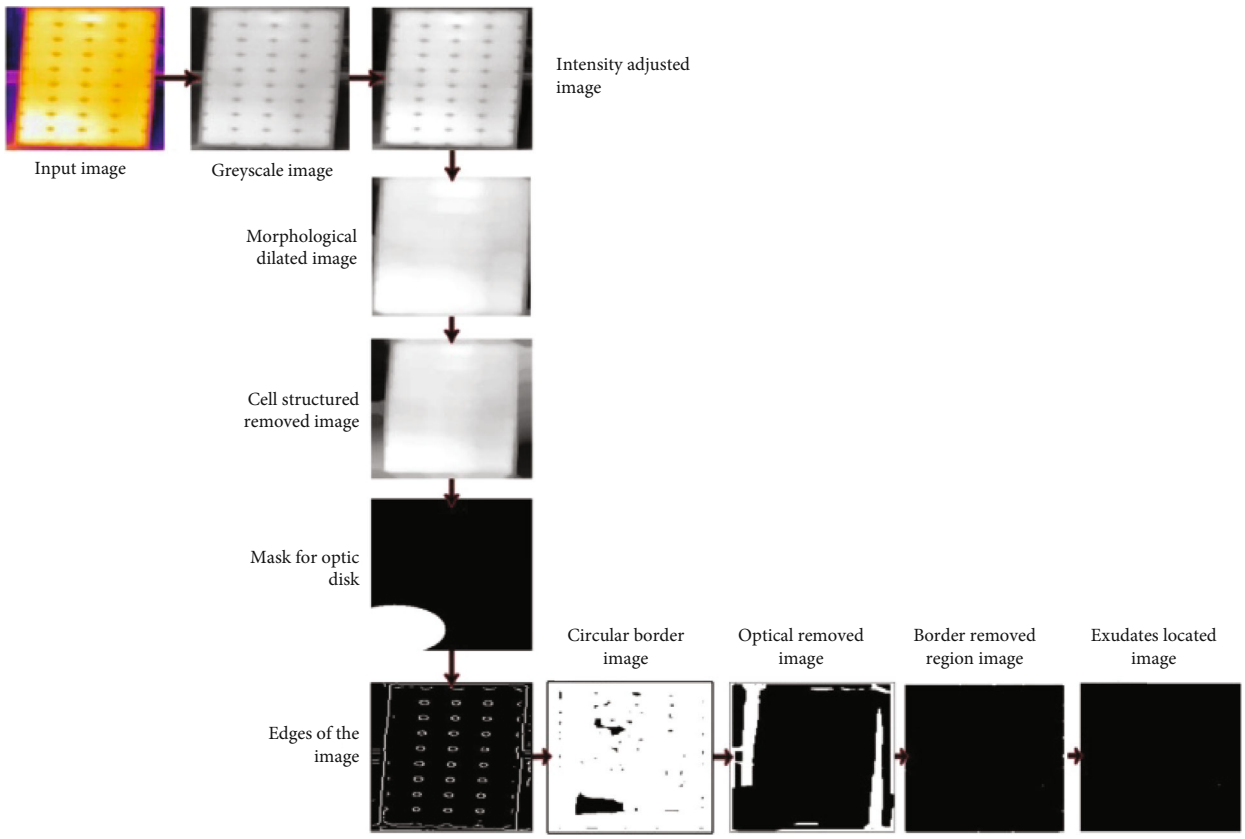

Figure 9: New solar panel thermal image processed.

Table 2: Conventional metric indices.

Thermal image	CQ	CC	NCC	IF	PSNR	SNR	MSE	NMSE
TD1	$7.9818e^{+11}$	0.9993	$1.8305e^{+14}$	$-8.7549e^{+09}$	+20.02db	$8.7549e^{+09}$	0.0100	$4.8645e^{-05}$
TD2	$9.3287e^{+11}$	0.9627	$1.4325e^{+14}$	$-6.1287e^{+09}$	+17.52db	$5.2375e^{+09}$	0.0098	$5.2972e^{-05}$
TD3	$6.2879e^{+11}$	0.9843	$2.8792e^{+14}$	$-4.2789e^{+09}$	+15.42db	$1.5287e^{+09}$	0.0201	$3.2147e^{-05}$
TD4	$9.2234e^{+11}$	0.9332	$2.0078e^{+14}$	$-9.1879e^{+09}$	+27.22db	$3.2489e^{+09}$	0.0096	$5.2278e^{-05}$
TD5	$5.8978e^{+11}$	0.9775	$1.9278e^{+14}$	$-6.1978e^{+09}$	+15.22db	$2.8792e^{+09}$	0.0899	$5.9278e^{-05}$
Quality	Poor	Good	Poor	Poor	Poor	Poor	Poor	Poor

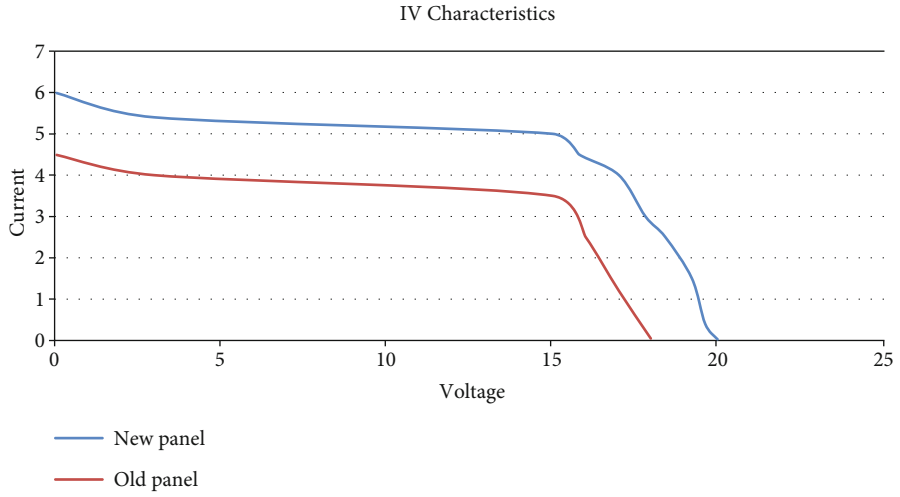

Figure 10: IV characterization of TD1 and bench mark solar panel.

Normalized crosscoordinate (NCC) is identical to the value of CC and computed using the following equation:

$$\mathrm{NCC} = \frac{\sum_{p,q} I_{p,q} \sim I_{p,q}}{\sum_{p,q} I_{p,q}^2} \tag{3}$$

Image fidelity is used to compute the changes in the images which is calculated using the following equation:

$$\mathrm{IF} = 1 - \frac{\sum_{p,q} \left(I_{p,q} - \sim I_{p,q}\right)^2}{\sum_{p,q} I_{p,q}^2}. \tag{4}$$

PSNR indicates peak signal-to-noise ratio of bench mark image which is computed using the following equation:

$$\mathrm{PSNR} = \frac{M \sum_{p,q} I_{p,q}^2 N}{\sum_{\mathrm{p,q}} \mathrm{I_{p,q}} - \sim I_{p,q}\right)^2}. \tag{5}$$

SNR estimates the quality of the degraded images and is represented by the following equation:

$$\mathrm{SNR} = \frac{\sum_{p,q} I_{p,q}^2}{\sum_{p,q} I_{p,q} - \sim I_{p,q}\right)^2}. \tag{6}$$

MSE is used to measure the degradation of image and computed by the following equation:

$$\mathrm{MSE} = \frac{1}{MN} \sum_{p,q} \left(I_{p,q} - \sim I_{p,q}\right)^2. \tag{7}$$

NMSE represents high degradation and is computed using the following equation:

$$\mathrm{NMSE} = \frac{1/MN \sum_{p,q} \left(I_{p,q} - \sim I_{p,q}\right)^2}{\sum_{p,q} \left(I_{p,q}\right)^2}. \tag{8}$$

The CQ and NC must be high, and IF, MSE, NMSE, and SNR must be low for the threshold value for the quality comparison. 20 and 40 db is ideal for PSNR values, and CC should be between 0.8 and 0.98. One-way ANOVA which is inbuilt in MATLAB has been performed for validating the conventional indices. Conventional metric indices are reported in Table 2.

From the above values, it has been inferred that the degraded panels' thermal image quality has been reduced compared with the new panel thermal image. Hence, the proposed thermal imaging technique is an ideal tool for fault identification and quality of the solar cell can be easily monitored, along with the conventional IV characteristics of the aged (TD1) and new panel (bench mark) of 75-watts capacity, which

is carried out and reported in Figure 10. The efficiency of the new panel (bench mark) is about 11.62%, and the efficiency of the aged (TD1) panel is about 6.32%, and the Voc and Isc of the new panels are about 22 V and 6.06 A, and for the aged panels are about 20 V and 5.8 A, respectively, and it is shown in Figure 10. By conventional methods, IV curve is traced.

8. Conclusion

Condition monitoring of large solar power plants is the need of the hour. Analyzing the individual string or panels is a difficult task. Most of the fault in the solar panels are recorded as hot spots due to increased internal resistance. Difference image processing techniques with the different coding in MATLAB have been incorporated to identify the hot spots. From the resultant sets of images of the metal plate with hot sports, it is evident that the thermal image can quickly locate hot spots using the Hough transform technique. The same coding has been tested for aged and new panels, and the hot spots have been recorded in the aged panels since the internal resistance of the aged panels is increased. With the use of conventional metrics, solar panel thermal image quality has been verified. The results obtained from ANNOVA also show the highest correlation coefficient. The same has been experimentally verified that the old panels give less power output compared to the new panels.

Data Availability

The data used to support the findings of this study are included within the article. Further data or information is available from the corresponding author upon request.

Conflicts of Interest

The authors declare that there are no conflicts of interest regarding the publication of this paper.

Acknowledgments

This project was supported by Researchers Supporting Project number (RSP-2021/393) King Saud University, Riyadh, Saudi Arabia. The authors appreciate the supports from Ambo University, Ambo, Ethiopia, for providing help during the research and preparation of the manuscript.

References

[1] A. Mellit, G. M. Tina, and S. A. Kalogirou, "Fault detection and diagnosis methods for photovoltaic systems: a review," *Renewable and Sustainable Energy Reviews*, vol. 91, pp. 1–17, 2018.

[2] P. Raju, K. Raja, K. Lingadurai, T. Maridurai, and S. C. Prasanna, "Glass/Caryota urens hybridized fibre-reinforced nanoclay/SiC toughened epoxy hybrid composite: mechanical, drop load impact, hydrophobicity and fatigue behaviour," *Biomass Conversion and Biorefinery*, vol. 2021, 2021.

[3] E. Kaplani, "Detection of degradation effects in field-aged c-Si solar cells through IR thermography and digital image processing," *International Journal of Photoenergy*, vol. 2012, 11 pages, 2012.

[4] V. Vignesh Kumar, K. Raja, V. S. Chandra Sekar, and T. Ramkumar, "Thrust force evaluation and microstructure characterization of hybrid composites (Al7075/B4C/BN) processed by conventional casting technique," *Journal of the Brazilian Society of Mechanical Sciences and Engineering*, vol. 41, no. 5, p. 228, 2019.

[5] E. M. Natsheh and A. Albarbar, "SSolar power plant performance evaluation: simulation and experimental validation," *Journal of Physics: Conference Series*, vol. 364, article 012122, 2012.

[6] V. Jeyabalaji, G. R. Kannan, P. Ganeshan, K. Raja, B. NagarajaGanesh, and P. Raju, "Extraction and characterization studies of cellulose derived from the roots ofAcalypha indicaL," *Journal of Natural Fibers, Taylor & Francis*, vol. 2021, pp. 1–13, 2021.

[7] M. H. Ali, A. Rabhi, A. El Hajjaji, and G. M. Tina, "Real time fault detection in photovoltaic systems," *Energy Procedia*, vol. 111, pp. 914–923, 2017.

[8] N. Akshaykumar and D. Subbulekshmi, "Online auto selection of tuning methods and auto tuning PI controller in FOPDT real time process-pH neutralization," *Energy Procedia*, vol. 117, pp. 1109–1116, 2017.

[9] A. M. Salazar and E. Q. B. Macabebe, "Hotspots detection in photovoltaic modules using infrared thermography," in *MATEC web of conferences*, vol. 70, pp. 1–5, Spain, August 2016.

[10] D. Subbulekshmi and J. Kanakaraj, "GMC algorithm with IMC and other controllers for a chemical process," *Journal of Advanced Engineering Technology*, vol. I, pp. 18–21, 2012.

[11] G. Radhaboy, M. Pugazhvadivu, P. Ganeshan, and K. Raja, "Influence of kinetic parameters on Calotropis procera by TGA under pyrolytic conditions," *Energy Sources Part A-Recovery Utilization and Environmental Effects*, vol. 2019, 2019.

[12] Y. Hu, W. Cao, J. Ma, S. J. Finney, and D. Li, "Identifying PV module mismatch faults by a thermography-based temperature distribution analysis," *IEEE Transactions on Device and Materials Reliability*, vol. 14, no. 4, pp. 951–960, 2014.

[13] F. A. Khan, B. K. Gautam, and S. Singh, "Detection of defects in solar panels using thermal imaging by PCA and ICA method," *International Research Journal of Engineering and Technology*, vol. 4, no. 6, pp. 1700–1703, 2017.

[14] K. Raja, V. S. Chandra Sekar, V. Vignesh Kumar, T. Ramkumar, and P. Ganeshan, "Microstructure characterization and performance evaluation on AA7075 metal matrix composites using RSM technique," *Arabian Journal for Science and EngineeringArabian Journal for Science and Engineering*, vol. 45, no. 11, pp. 9481–9495, 2020.

[15] S. Guesmi, K. Jamoussi, and M. Ghariani, "Efficiency improvement of PV module using an electrical thermal model," *Journal of Electrical Systems*, vol. 16, no. 2, pp. 246–256, 2020.

[16] V. Yamunadevi, G. Vijayanand, P. Ganeshan, S. Sowmiya, and K. Raja, "Effect on the behaviour of dynamic mechanical analysis for hybrid epoxy nanocomposite," *Materials Today: Proceedings*, vol. 37, pp. 223–227, 2021.

[17] D. M. D. Preethi and V. E. Jayanthi, "Performance analysis of iris-based identification system based on exudates," *International Journal of Biomedical Engineering and Technology*, vol. 29, no. 3, pp. 231–245, 2019.

[18] V. E. Jayanthi, V. Rajamani, and P. Karthikayen, "Performance analysis for geometrical attack on digital image watermarking," *International Journal of Electronics*, vol. 98, no. 11, pp. 1565–1580, 2011.

[19] N. Saravanan, V. Yamunadevi, V. Mohanavel et al., "Effects of the interfacial bonding behavior on the mechanical properties of E-glass fiber/nanographite reinforced hybrid composites," *Advances in Polymer Technology*, vol. 2021, 9 pages, 2021.

[20] Y. Yang, Q. Chen, and Y. Wan, "A fast near-optimum block truncation coding method using a truncated _K_ -means algorithm and inter-block correlation," *AEU-International Journal of Electronics and Communications*, vol. 65, no. 6, pp. 576–581, 2011.

[21] R. Ramkumar, R. Prabu, V. Yamunadevi, P. Saravanan, and P. Ganeshan, "Wear analysis of woven glass / nanofiller fiber reinforced hybrid composites," *Materials Today: Proceedings, Elsevier*, vol. 2020, 2020.

[22] A. Jaiswal, J. Upadhyay, and A. Somkuwar, "Image denoising and quality measurements by using filtering and wavelet based techniques," *AEU-International Journal of Electronics and Communications*, vol. 68, no. 8, pp. 699–705, 2014.

[23] P. Sainath, F. Mohammed Ajmal Sheriff, and P. Ganeshan, "Fabrication of hybrid polyester composites in various combinations and evaluate the mechanical properties," *Materials Today: Proceedings, Elsevier*, vol. 2020, 2020.

[24] M. Kutter and F. A. Petitcolas, "A fair benchmark for image watermarking systems," *Security and Watermarking of Multimedia Contents*, vol. 3657, pp. 25–27, 1999.

Hindawi
International Journal of Photoenergy
Volume 2022, Article ID 4905980, 11 pages
https://doi.org/10.1155/2022/4905980

Research Article

Prediction of Photovoltaic Power by ANN Based on Various Environmental Factors in India

B. Suresh Kumar,[1] Jenifer Mahilraj,[2] R. K. Chaurasia,[3] Chitaranjan Dalai,[4] A. H. Seikh,[5] S. M. A. K. Mohammed,[6] Ram Subbiah,[7] and Abdi Diriba[8]

[1]*Department of Electrical and Electronics Engineering, Chaitanya Bharathi Institute of Technology, Hyderabad, Telangana 500075, India*
[2]*Department of CSE & IT, Kebridehar University, Kebridehar, Ethiopia*
[3]*Department of Electronic and Communication Engineering, ICFAI Tech School, ICFAI University, Jaipur, Rajasthan 302031, India*
[4]*Department of Civil Engineering, Odisha University Technology and Research, Bhubaneswar, Odisha 751029, India*
[5]*Mechanical Engineering Department, College of Engineering, King Saud University, P.O. Box 800, Al-Riyadh 11421, Saudi Arabia*
[6]*Department of Mechanical and Industrial Engineering, Ryerson University, Toronto, Ontario, Canada M5B 2K3*
[7]*Department of Mechanical Engineering, Gokaraju Rangaraju Institute of Engineering and Technology, Nizampet, 500090, Hyderabad, India*
[8]*Department of Mechanical Engineering, Mizan Tepi University, Ethiopia*

Correspondence should be addressed to Abdi Diriba; abdi@mtu.edu.et

Received 2 February 2022; Accepted 6 April 2022; Published 2 June 2022

Academic Editor: V. Mohanavel

Copyright © 2022 B. Suresh Kumar et al. This is an open access article distributed under the Creative Commons Attribution License, which permits unrestricted use, distribution, and reproduction in any medium, provided the original work is properly cited.

Extreme weather conditions, which affect photovoltaic output power, can have a major impact on electricity generated by PV systems. In India, an annual PV power density of 2000kWh/m-2 may be used. Renewable energy (RE) is expected to play a rising part in the nations in coming years. The sun's radiation is the primary source of renewable energy (RE). With the objective of predicting PV output power with the least amount of error in mind, it is vital to analyse the impact of major environmental parameters on it. The researchers looked at a variety of environmental factors in this study, including irradiance, humidity levels, meteorological conditions, wind velocity, PV global temperature and dust deposition. Countries such as India would gain immensely from this since it will increase the quantity of PV power generated in their national networks. ANN-based prediction models and multiple regression models were used to predict PV system hourly power output. There were three ANN models that predicted PV output power with RMSEs of 2.1436, 6.1555, and 5.3551, respectively, utilising all features using the correlation feature selection (CFS) or relief feature selection (ReliefF) approaches. It is possible to reduce bias to enhance accuracy by employing two distinct bias calculation methodologies, which were applied in this study. For example, the ANN model outperforms linear regression, M5P decision trees and GAUSSIAN process regression (GPR) models in terms of performance.

1. Introduction

Global warming and climate change have prompted a slew of national policies encouraging the use of renewable energy sources. Alternatives to fossil fuel-generated power, such as photovoltaic (PV) energy, among the renewable energy as a greatest advantage. You can have as much as you like, and it does not contain any dangerous contaminants [1, 2]. The Arabian Peninsula receives more than 2000kWh/m^{-2} of solar irradiation every year. Compared to other renewable energy sources, PV technology has a lot of potential in this location because of the significant amount of solar irradiation

(e.g., wind energy or tidal energy) [3]. Aside from its environmental benefits, solar energy is becoming increasingly popular due to other factors, like its low maintenance costs and noise and pollution-free technology [4]. However, the PV energy system's power generation is subject to significant uncertainty due to the weather system's chaotic and erratic character [5]. In light of these uncertainties, it will be more difficult to manage and operate the electric power and energy system, and real-time control performance may be affected [6]. Making the most of a solar power plant depends on being able to accurately predict its efficiency. We all know that solar radiation has a direct impact on the power generated by photovoltaic panels. Wind velocity and dirt deposition have also been shown to impact PV system efficacy, as have other climate variables (such as temperature) [7, 8]. Several recent studies have shown that PV panel dust deposition has a negative consequence on the forecast of PV output power [9]. For PV power forecasting, the authors believe that the right meteorological factors in a specific site can be crucial [10]. When multiple sources of energy are combined into a hybrid energy matrix, PV power prediction can be very useful. Intermittent solar electricity causes difficulties in maintaining system stability when too much of it is added [11, 12]. Predicting future solar power generation can help system controllers improve system stability. With this new knowledge in hand, utility companies may more effectively build switching controllers for hybrid energy systems [13]. The switching controller's design parameters may be influenced by environmental factors because of the potential impact on solar power generation.

Solar power forecasting and estimation has recently been the subject of several studies [14]. PV plant power generation can be estimated using a variety of methods, including phenomenological, stochastic/statistical, and even hybrid models. System advisor models (SAM) and other deterministic software programmes like PVSyst can be used to estimate the output of a PV plant based on physical facts [15, 16]. This study used a deterministic method to predict the electrical, thermal, and optical properties of PV modules. Studies on PV power forecasting tend to focus on a single point forecast, which is known as a deterministic forecast [17]. PV power data mistakes can be overlooked by deterministic forecasting systems at times. Recent emphasis has been given to probabilistic PV power forecasting models that can mathematically explain this uncertainty. An ensemble of deterministic forecasters is one of the most common ways to generate probabilistic uncertainty [18–20]. Ensemble-based PV power forecasting models could pose a real-time challenge because of their high computing costs. The shallow learning models employed in deterministic and probabilistic PV forecasting are a downside [21]. It's possible that shallow models will not be able to adequately extract the PV power data's corresponding nonlinear features and static properties because of the weather system's complexity [22]. Improved performance may be achieved with further exploration into the deterministic technique of providing high accuracy through the optimization of an artificial neural network (ANN). Because of their function approximation abilities and structured approach, ANNs are effective data-driven techniques that are frequently utilised for nonlinear system dynamic modelling and detection. [23].

The model has been verified for many types of solar modules using hourly solar resource and meteorological data. Multiple linear regressions, neural inference systems with adaptive neuro-fuzziness and support vector machines, for example, do not require any prior knowledge of the system under investigation to function [24]. To "understand" how inputs and outputs are related, they conduct a thorough analysis of a dataset that includes both the input and output variables they have collected. Backpropagation technique seeks to reduce the computational complexity by modifying both weights and biases of the network. [25]. Numerous advantages of statistical learning algorithms can be cited aside from being able to use incomplete data, they can also learn from it. Second, they can generalise and make predictions after they have been trained [26]. Their characteristics allow them to be employed in a variety of situations. To forecast output power from other renewable sources than solar, many machine learning (ML) algorithms have been tested. Individual qualities in datasets are shown to be important by ML, which provides insights into the properties of data dependency. ANN methods were compared by [27] without displaying the prediction model's features or comparing their relative performance quantitatively. Instead of relying just on PV power, machine learning has been used to estimate solar irradiance [28]. To estimate PV power, some studies used simply a single machine learning algorithm. To model and size a standalone PV plant with a small input dataset, an adaptive ANN was used. In order to represent the PV power system's many components and their output signals, ANFIS was employed. Estimates of worldwide solar radiation were made using a linear regression model and an artificial neural network (ANN) [29]. A hybrid model can mix several models to overcome the constraints of a single technique. As an extra benefit, "ensemble" methods combine several procedures to build prediction models [30].

There has been a great deal of research into machine learning-based prediction models, but there is always potential for improvement [31]. The following new contributions have been made by the authors in this manuscript:

(1) The creation of a test bed for photovoltaic and weather systems, complete with sensors that can be calibrated on-the-fly. The accuracy of the weather data is ensured by this constant calibration of the sensors

(2) Two years of PV system deployment yielded a reasonably large dataset of PV and environmental factors. In order to develop and test the prediction model described in this publication, researchers used a real dataset that can be made available to the public upon request

(3) ANN-based prediction models are compared to numerous other types of multiple regression models

(4) Extensive study of ANNs to discover the most accurate forecasting model with the less Root Mean Squared Error (RMSE). The forecast was also tested to see if it was a biased prediction

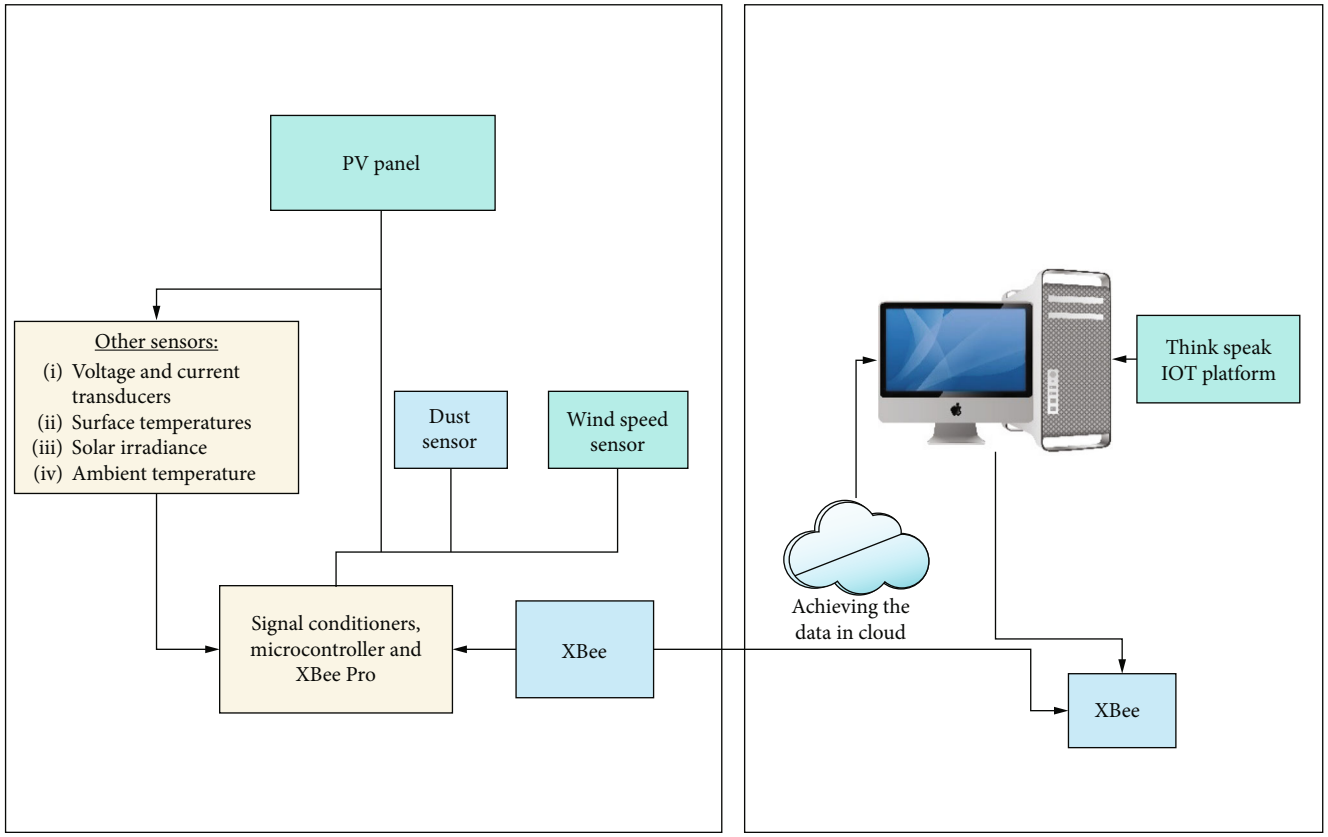

Figure 1: Photovoltaics (PV) system set-up: Rooftop (left) and lab components (right).

Table 1: Features of a PV module made from polycrystalline silicon.

Max power at STC	Area (m^2)	Voc(V)	Isc(A)
80	0.5914	22	5.42

(5) Investigating the best attributes for effectively predicting PV power

2. Experimentation

An in-house PV system was built and operated to study the link between PV performance and environmental variables. Figure 1 shows the experimental set up, which consists of two subsystems. There were two sub-systems: one on the roof, which had sensors for collecting data, and another in the lab, which stored and plotted data in real time.

To control the terrace's solar power system, an Arduino Mega 2560 CPU, an XBee or WiFi transceiver, a DC-DC converter, and a programmable electronic resistive load were needed. MPPT was utilised to create pulse width modulation (PWM) signals that simulated fluctuating current and voltage across the load without modifying its real-life resistive value for the programmable electronic load. Using data from calibrated voltage and current sensors, power and current curves for a simulated electronic load were shown. Solar irradiation was maximised while PV output power was increased by using an MPPT controller to adjust the panel orientation. Wireless XBee/Wifi adapters attached to a workstation were used to capture and log data in the laboratory as part of the rooftop subsystem research. The rooftop sub-system sensors sent data to these wireless adapters on-demand or at fixed intervals. The LabVIEW measurement files recorded from the received data were numerically presented on the workstation screens. An open IoT data platform called Thingspeak was used to make the data accessible to the general audience. The Arduino Mega 2560 microcontroller is used to communicate with an Xbee/EtherMega shield. The PV system's block diagram can be found here. Table 1 shows the specifications of a polycrystalline silicon photovoltaic module.

2.1. Machine Learning-Based Prediction. Data pre-processing, training prediction models, assessing validation accuracy on the training dataset, and evaluating pre-trained models for the test dataset are the three main stages of smearing ML to any dataset in order to anticipate the unidentified output rates. In the beginning, incongruities like missing data, outliers, and specious data values were removed from the dataset. Prior to this, the most relevant traits had already been identified and extracted. It was simpler to complete this sub-task by utilising measurements such as temperature and relative humidity, solar panel surface temperature, irradiance and dust build up. It was necessary to split the training and testing datasets

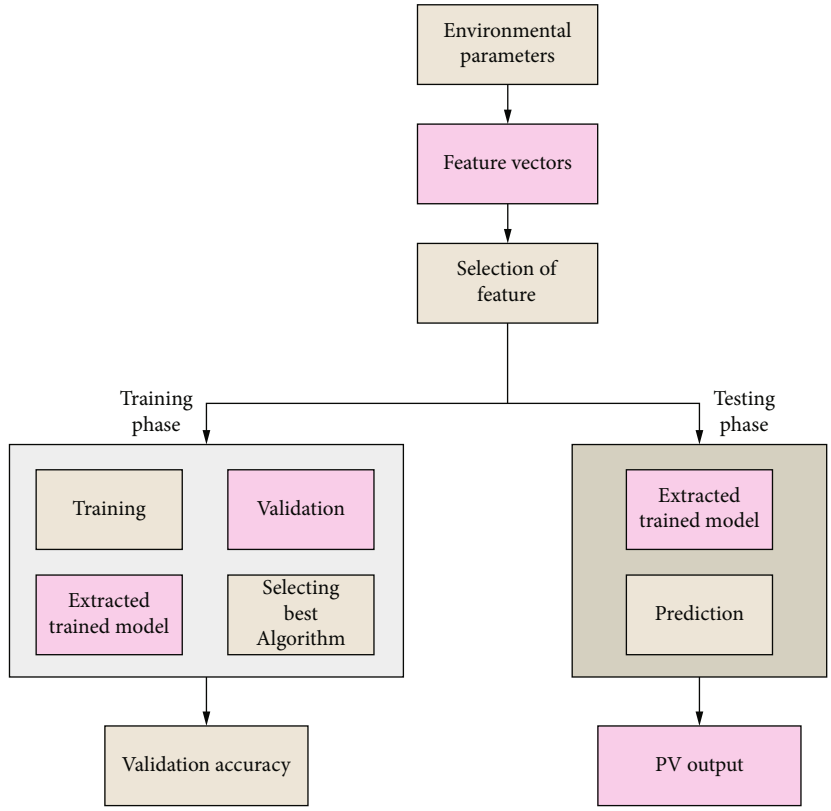

Figure 2: The training and prediction stages of machine learning are depicted in this diagram.

Table 2: Parameters of Neural Networks.

Parameters	Values
No of hidden layer when all features were utilized	70
When CFS filtering was employed	270
When ReliefF filtering was employed	190
Training data	72%
Validation data	14%
Testing data	14%
Number of folding in cross validation	5

Table 3: Information on the predictive model's input conditions.

Environmental parameters	Max	Min
Temperature (°C)	62.04	13.98
Relative humidity (%)	91.83	26.79
PV surface temperature (°C)	75.44	9.410
Irradiance (W/m^2)	1142.46	37.64
Dust accumulation (mg/m^3)	1.24	0.061
Wind speed (km/h)	35.43	0.069
Power (W)	109.11	0.041

into 85 and 15 percent, respectively, using Matlab'scv partition function. There were 380 training and validation cases, and 95 testing cases. Many machine learning algorithms were taught with the Regression Learner and the Neural Network Toolbox in Matlab's Statistics and Machine Learning Toolbox.

The performance of a trained algorithm can be enhanced by using an additional feature selection step as in Figure 2. Sifting through high-quality, non-redundant features is an essential step in constructing more accurate learning models. By means to develop the best prediction model with only the properties we required, we experimented with a variety of feature-reduction strategies. It was necessary to create assessment parameters for pre-trained models that performed the best to ensure that a statistical evaluation could be completed. There are ways to tweak this process to improve model quality as additional data is obtained over time.

2.2. Features Selection. An automated data collection system was used to capture, process, validate and test the PV and ambient parameters as depicted in Figure 1. Consider whether all of the environmental elements are necessary, or whether they can be reduced in order to make more accurate forecasts. Feature selection approaches such as CFS and ReliefF were employed to narrow the field of potential contributors. Subset search methods are used to calculate the level of duplication between features in all subsets using the CFS technique's correlation-based heuristic evaluation function. We then look for subsets having a low connection between them but a high correlation with the desired outcome. It is an instance-based approach called ReliefF that weighs each feature according to how well it can distinguish

between various classes. ReliefF has the ability to recognise interactions that are more than the sum of their parts. With ReliefF, progressively removing the lowest ranked features allowed us to find the best subset from the ranked features.

2.3. Prediction Models. There are a variety of ML-based predictive models, and each performs differently depending on the dataset. Solar panel power output was estimated in this study using a variety of simple regression and prediction models. A few examples include the SLR, GPR, and M5P regression trees, all of which use a simple linear regression model. It is possible to forecast the output response using regression models that employ simple linear regression. An unobserved point's value can be predicted using GPR, which uses a Gaussian process and a evaluate of point resemblance (the kernel function). In addition to providing an estimate, the forecast also provides information on the degree of uncertainty. A Gaussian distribution with only one-dimensional dimensions. Linear regression functions are used to develop a typical that predicts a target value by learning modest guidelines at the ends of each branch in the typical decision tree. "If…then…else…" statements are considered to be powerful.

PV output power was predicted using an ANN, a standard machine learning technique for classifying and regressing variables. Forward propagation and weight adjustment are both a part of the ANN. The ANN aims to mimic the human brain's layered organisation by mimicking machine learning. The models of ANNs are artificial neurons, each of which receives a specific amount of inputs. Using these inputs, the activation function generates the activation level of neurons (the neuron output value), and training inputs and output pairs are used to offer learning information. Distinct datasets require different training functions, each with its own set of pros and downsides. The dataset used in this study necessitated a thorough examination of all of the available training functions. ANN-based PV power prediction network configurations are summarised in Table 2. All features, CFS and ReliefF, had distinct optimal no of hidden layers that provided the better mode.

2.4. Bias Calculation and Correction in Prediction. Forecasting bias can be defined as a predisposition to either overestimate or underestimate the outcome of a given situation. In the presence of bias, forecast accurateness can be improved if bias is correctly recognised. Errors in prediction can be reduced or eliminated by making suitable upward or downward adjustments to the projection, depending on whether it's overly conservative or conservative.

The forecast bias is calculated using two primary techniques in this study:

(i) Tracking signal-based system

(ii) NFM technique

2.5. Signal-based Tracking system. The tracking signal is another typical statistic for measuring forecast accuracy. A forecast's "Bias" can be measured using the "Tracking Signal." A forecast that is heavily skewed cannot be used to plan a product. The first step in determining the accuracy of a forecast is to look at the tracking signal. Each period's tracking signal is calculated:

$$\text{Tracking signal} = \frac{\text{Actual} - \text{Forecast}}{\text{ABS}\,(\text{Actual} - \text{Forecast})} \tag{1}$$

The overall tracking signal is then calculated by adding the figures for each time. Zero is returned for a forecast history that is completely free of bias, and+12 (under predicted) or -12 (over forecast) are the worst possible outcomes for a total of 12 observations (over-forecast). It would be regarded out of control if the predicted history returned a value more than 4.5 or lower than a negative.

2.6. The NFM Method. Bias can be measured with the Normalized Forecast Metric (NFM). NFM uses the following formula to determine bias:

$$\text{NFM} = \frac{(\text{Forecast} - \text{Actual})}{(\text{Forecast} + \text{Actual})} \tag{2}$$

This statistic has a range of 1 to 1, with 0 indicating that there is no bias present. Consistently low levels suggest a proclivity to underestimate, whereas consistently high values indicate a proclivity to overestimate A 12-period forecast is considered skewed toward over-forecasting if the additional values are greater than two. Similar to that, a forecast is deemed biassed towards under-forecasting if the additional values are fewer than 2. Corrective steps are needed on a regular basis to keep a forecasting process that is biassed from going off the rails.

Bias correction and change factor techniques can be used to rectify non-stochastic data. As a result, QM eliminates any systematic bias in the predicted output and corrects for statistical downscaling errors.

2.7. Analysis. A variety of numerical examines were conducted to estimate the behaviour of machine learning procedures for the prediction of Photovoltaic output power. The following are some of the measures that can be used to evaluate a product: A number of measures of linear dependency between two variables, such as correlation coefficient (r), mean absolute error (MAE), and mean square error (MSE), were evaluated and averaged: While RMSE is similar to MAE in that it uses an average of the difference squares to obtain the square root and so gives more weight to larger errors, it differs from MAE in that it uses the square root of the MSE rather than the difference squares to find the square root. Predictor performance can be better described using these factors.

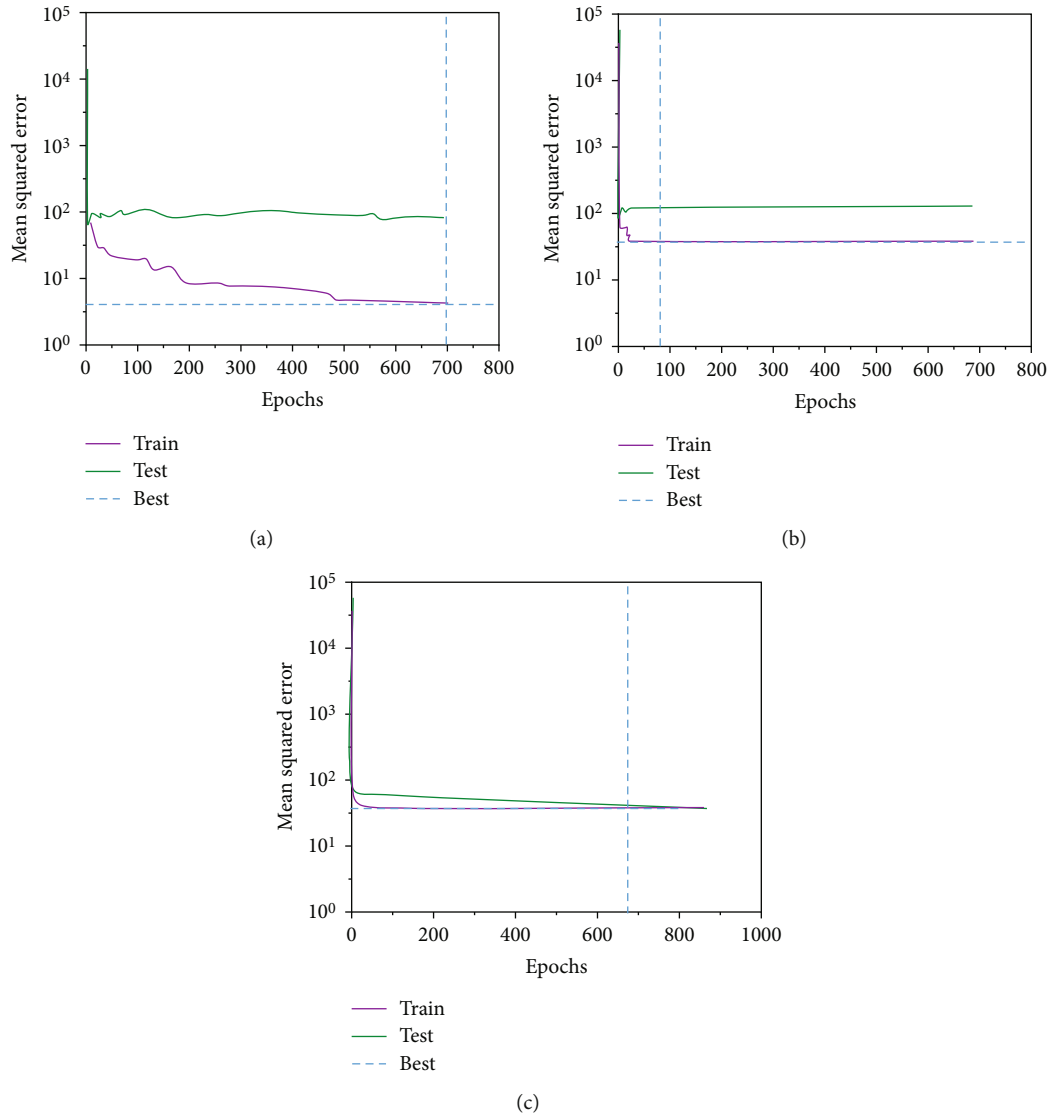

Figure 3: Evaluation of the Mean Square Error for various method: (a) With all features; (b) Correlation Feature Selection; (c) Relief Feature selection method for training and validation.

$$r = \frac{\mathrm{Con}(X, Y)}{\sigma_x \sigma_y}$$

$$\mathrm{MAE} = \frac{1}{\mathrm{n}} \sum_{n} |X - Y|$$

$$\mathrm{MSE} = \frac{\sum |X - Y|^2}{\mathrm{n}}$$

$$RMSE = \sqrt{\frac{\sum |X - Y|^2}{n}} = \sqrt{MSE}$$

$$\text{coefficient of determination, or } R^2 = 1 - \frac{MSE}{\mathrm{MSE\ (Baseline)}} \tag{3}$$

where$X$ is the actual data vector, Y and Y are the predicted and mean of the predicted data vector.

MAE, MSE, RMSE, r-value andR-2. value were used to compare variant ANNs and regression models. Utilizing the neural network toolbox of Matlab, the Bayesian regularisation backpropagation approach was used after a thorough investigation of the ANN training functions that gave the best prediction of the Photovoltaics. Built-in Matlab method for Bayesian regularisation backpropagation builds a network that effectively generalises by minimising the linear amalgamation of squared errors and weights. Levenberg-Marquardt optimization is used to update the weight and bias variables. There were three main situations tested to determine the optimum ANN selection strategy: using all characteristics, using the CFS technique, and using the ReliefF technique.

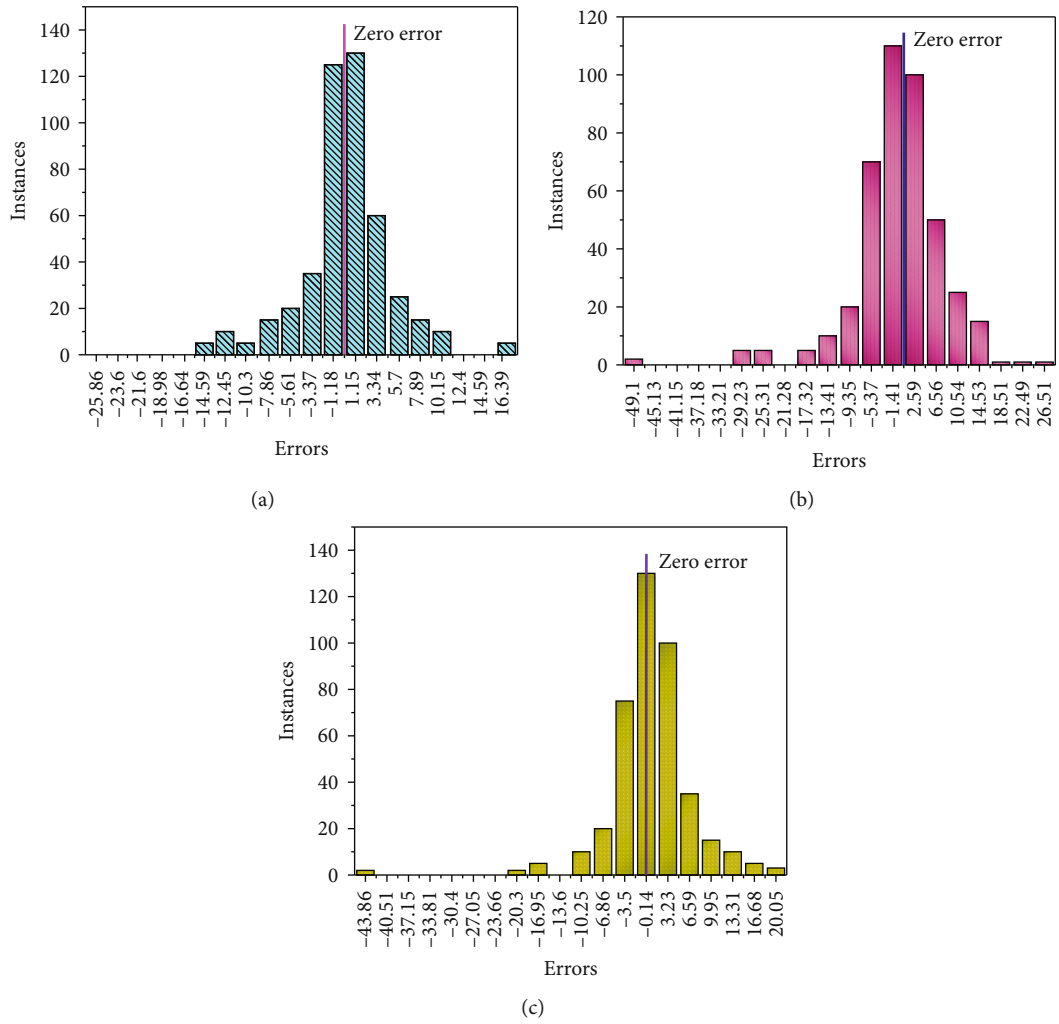

Figure 4: Error Histogram (a) with all features; (b) Correlation Feature Selection; (c) Relief Feature selection method for training and validation.

3. Results and Discussion

To gather data on PV and environmental characteristics, as well as PV power output. Data required to develop a prediction model for PV power generation are summarised in Table 3 .

Results for the three various methods of ANN-based prediction modelling training and validation are displayed in Figures 3 and 4. Different approaches performed well at different epochs of training, as illustrated in Figure 3, which shows the validation performance. The best epochs were 707, 91, and 598, respectively, among the many models established by the ANN using variant sets of structures. A model for estimating PV power could be developed from this data in the future. Bins are represented by the graph's vertical bars in Figure 4, which displays an error histogram with 20 bins. (25.84 to 16.88), (49.08 to 26.43) and (43.83-20.03) are the relative ranges of total error for each of the three neural networks. Samples from the associated dataset are represented by the number of vertical bars in each bin. As you can see, over eighty percent of the errors fall inside a 10-watt range. If an algorithm is able to forecast the output with 80% of the error within 10% of the target value, it is considered to be a Excellent predictive model.

Figure 5 indicates the link among the initial power output and the anticipated power output by the best ANN epochs. The ANN's best linearized predictive model can be used to predict the actual target, and the line shows the better linear relationship between the original output and that model. Correlation coefficient, r, shows the successful linearized model built by ANN employing three distinct strategies, as shown in Figure 5 (dotted line).

After testing a number of properties selection methods, it was discovered that Artificial Neural Network had the least Root mean square error of all of the techniques tested, at 2.1436, while the ReliefF feature selection method came in second with an RMSE of 5.5351 during validation. The same results were found in the testing dataset. It was found that the best RMSE of 5.4784 was achieved using the all features strategy. On the other hand, it is clear from Figure 6 that the expected production was biassed in several cases due to a continuous over- or under-forecasting. It is shown in Figure 6 that all feature-based forecasts have a bias. This shows that tracking

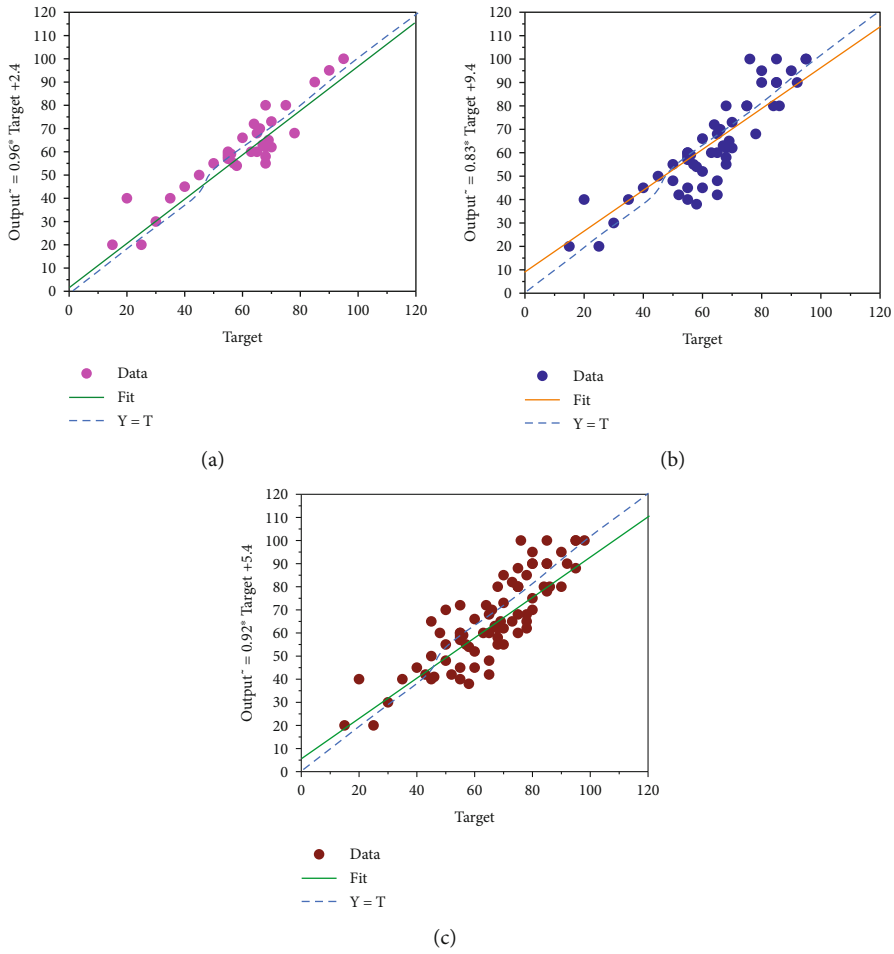

Figure 5: In training and authentication, the relative among the original output power and the Predicted output power: (a) With all features; (b) Correlation Feature Selection; (c) Relief Feature selection.

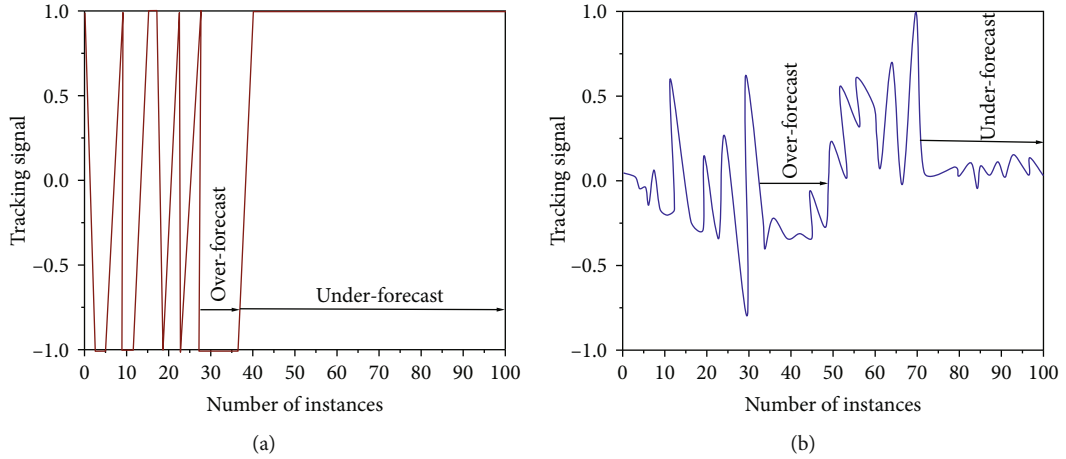

Figure 6: All features-based Photovoltaic power prediction: Bias calculation for a biased forecast (a) Employing tracking signal method; (b) Employing NFM method.

signal-based bias computation is more accurate than NFM in identifying bias.

To see if the ANN-derived models can reliably anticipate the power of a PV system, we utilised assessment data (which was not included in our training data). In order to improve prediction accuracy, The training dataset needs to have more data. The bias correction has been cited in the works by numerous groups, although a different paper demonstrated a

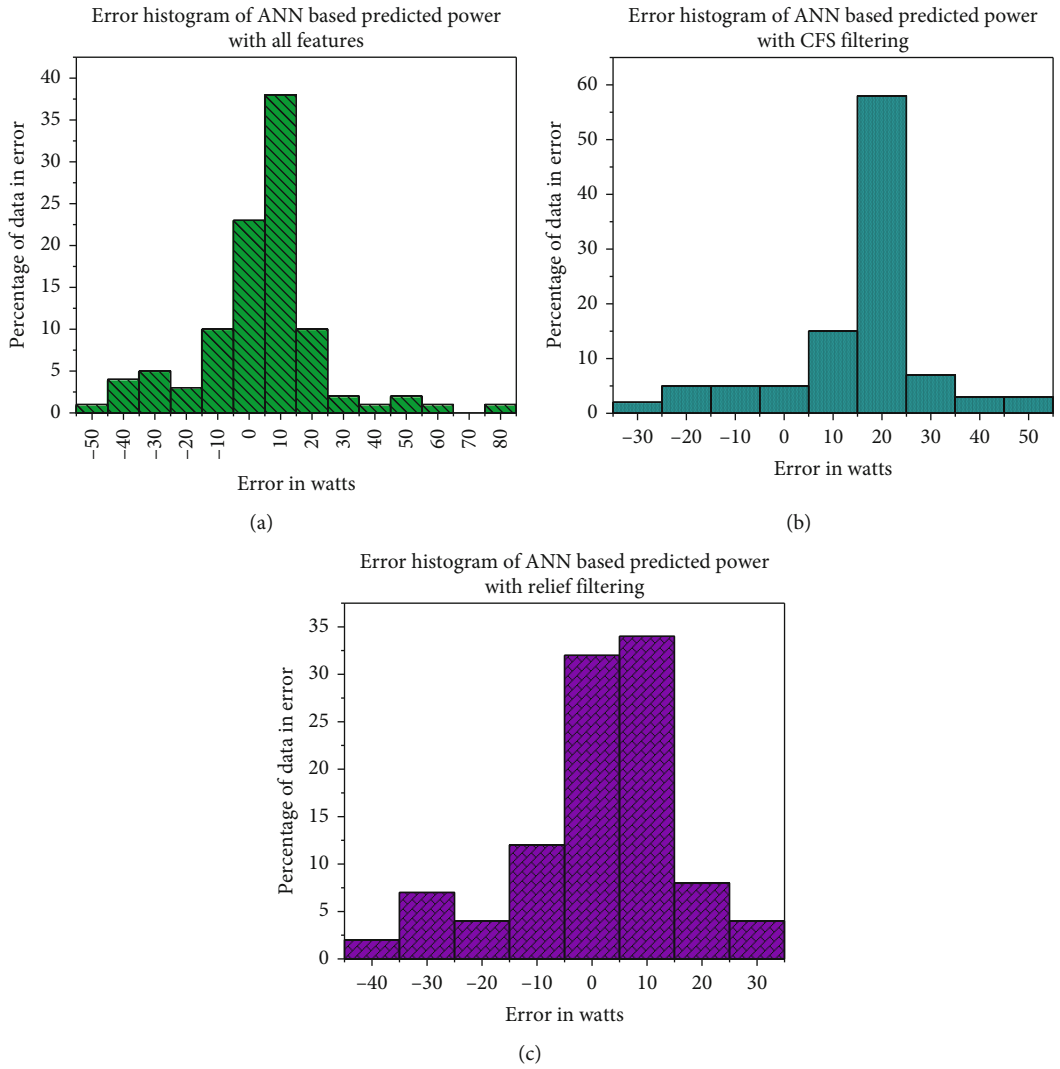

Figure 7: PV Error Histogram using Test Data: Difference between Predicted and Actual: (a) With all features; (b) Correlation Feature Selection (c) ReliefFeature selection method.

different performance. The overall computing complexity and cost will dramatically increase as a result of bias correction being incorporated into the prediction method. A CNN can also be employed to remove PV power forecast bias (CNN). A CNN or deep learning technique may be more computationally intensive for real-time prediction than an ANN. The photovoltaic error histogram using test data for various features of predicted and actual is shown in Figure 7.

4. Conclusions

In order to monitor, analyse, and assess PV performance across a wide range of climatic conditions. We were talented to predict how much PV electricity will be created in the upcoming using the system's PV and environmental data.

(i) Multiple regressions and ANN-based prediction models were built using data from the PV system, in summary. As a means of determining which attributes are most important, we used two feature selection methods (CFS and ReliefF).

(ii) The ANN predicted output power more accurately than the three top regression models with an RMSE of 2.1436. There were reported RMSEs of 6.1555 and 5.5351 when PV power was estimated utilizing feature selection method and the ANN. The output power of PV systems can be accurately predicted using trained ANN models, which are less complex and use less processing effort

(iii) As a result of this effort, Indian researchers can benefit from the improved set of rules and its presentation in forecasting for this section

(iv) As a result of this, we believe that the region's solar industry will gain tremendously. More PV and environmental data is being collected and will be evaluated with the Convolution Neural Network-based technique in the forthcoming in order to train a more accurate predictive model

(v) Reducing dust build-up and increasing efficiency are two possible outcomes of integrating the chilled

PV with the existing PV system. There is still extent for more study in this area, given the five years of system data collected and additional aspects like the cooling and cleaning impacts of the PV system

Data Availability

The data used to support the findings of this study are included within the article. Further data or information is available from the corresponding author upon request.

Conflicts of Interest

The authors declare that there is no conflict of interest regarding the publication of this paper.

Funding

This research work is not funded from any organisation.

Acknowledgments

The authors thank Mizan Tepi University, Ethiopia, for the research and preparation of the manuscript. The authors thank ICFAI University, Odisha University Technology and Research, and Chaitanya Bharathi Institute of Technology, for providing assistance to complete this work. The authors would like to acknowledge the Researchers Supporting Project number (RSP-2021/373), King Saud University, Riyadh, Saudi Arabia.

References

[1] A. Ennaoui, B. Figgis, and D. M. Plaza, "Outdoor Testing in Qatar of PV Performance, Reliability and Safety," *Qatar Foundation Annual Research Conference Proceedings*, 2016no. 1, p. - EEPP2538, 2016.

[2] F. Touati, M. A. Al-Hitmi, N. A. Chowdhury, J. A. Hamad, and A. J. R. S. P. Gonzales, "Investigation of solar PV performance under Doha weather using a customized measurement and monitoring system," *Renewable Energy*, vol. 89, pp. 564–577, 2016.

[3] N. Ahmad, A. Khandakar, A. El-Tayeb, K. Benhmed, A. Iqbal, and F. Touati, "Novel design for thermal management of PV cells in harsh environmental conditions," *Energies*, vol. 11, no. 11, p. 3231, 2018.

[4] M. Benghanem, A. Almohammedi, M. T. Khan, and A. Al-Masraqi, "Effect of dust accumulation on the performance of photovoltaic panels in desert countries: a case study for Madinah, Saudi Arabia," *International Journal of Power Electronics and Drive Systems*, vol. 9, no. 3, p. 1356, 2018.

[5] A. H. Almasoud and H. M. Gandayh, "Future of solar energy in Saudi Arabia," *Journal of King Saud University-Engineering Sciences*, vol. 27, no. 2, pp. 153–157, 2015.

[6] Z. A. Darwish, H. A. Kazem, K. Sopian, M. A. Alghoul, and H. Alawadhi, "Experimental investigation of dust pollutants and the impact of environmental parameters on PV performance: an experimental study," *Environment, Development and Sustainability*, vol. 20, no. 1, pp. 155–174, 2018.

[7] F. Touati, N. A. Chowdhury, K. Benhmed et al., "Long-term performance analysis and power prediction of PV technology in the State of Qatar," *Renewable Energy*, vol. 113, pp. 952–965, 2017.

[8] S. P. Mishra and P. K. Dash, "Short term wind power forecasting using Chebyshev polynomial trained by ridge extreme learning machine," in *2015 IEEE Power, Communication and Information Technology Conference (PCITC)*, pp. 173–177, Bhubaneswar, India, 2015.

[9] P. R. Bevington, D. K. Robinson, J. M. Blair, A. J. Mallinckrodt, and S. McKay, "Data reduction and error analysis for the physical sciences," *Computers in Physics*, vol. 7, no. 4, pp. 415-416, 1993.

[10] S. Netsanet, J. Zhang, D. Zheng, R. K. Agrawal, and F. Muchahary, "An aggregative machine learning approach for output power prediction of wind turbines," in *2018 IEEE Texas Power and Energy Conference (TPEC)*, pp. 1–6, College Station, TX, USA, 2018.

[11] F. Jawaid and K. Nazir Junejo, "Predicting daily mean solar power using machine learning regression techniques," in *2016 Sixth International Conference on Innovative Computing Technology (INTECH)*, pp. 355–360, Dublin, Ireland, 2016.

[12] J. Li, J. K. Ward, J. Tong, L. Collins, and G. Platt, "Machine learning for solar irradiance forecasting of photovoltaic system," *Renewable Energy*, vol. 90, pp. 542–553, 2016.

[13] L. B. Sheiner and S. L. Beal, "Some suggestions for measuring predictive performance," *Journal of Pharmacokinetics and Biopharmaceutics*, vol. 9, no. 4, pp. 503–512, 1981.

[14] A. Khandakar, M. E. H. Chowdhury, M. Khoda Kazi et al., "Machine learning based photovoltaics (PV) power prediction using different environmental parameters of Qatar," *Energies*, vol. 12, no. 14, p. 2782, 2019.

[15] A. Khosravi, R. N. N. Koury, L. Machado, and J. J. G. Pabon, "Prediction of hourly solar radiation in Abu Musa Island using machine learning algorithms," *Journal of Cleaner Production*, vol. 176, pp. 63–75, 2018.

[16] H. Sheng, J. Xiao, Y. Cheng, Q. Ni, and S. Wang, "Short-term solar power forecasting based on weighted Gaussian process regression," *IEEE Transactions on Industrial Electronics*, vol. 65, no. 1, pp. 300–308, 2018.

[17] T. Hiyama and E. Karatepe, "Investigation of ANN performance for tracking the optimum points of PV module under partially shaded conditions," in *2010 Conference Proceedings IPEC*, pp. 1186–1191, Singapore, 2010.

[18] D. O'Leary and J. Kubby, "Feature selection and ann solar power prediction," *Journal of Renewable Energy*, vol. 2017, Article ID 2437387, 7 pages, 2017.

[19] A. Mellit, "Artificial intelligence based-modeling for sizing of a stand-alone photovoltaic power system: proposition for a new model using neuro-fuzzy system (ANFIS)," in *2006 3rd International IEEE Conference Intelligent Systems*, pp. 606–611, London, UK, 2006.

[20] M. Bocco, E. Willington, and M. Arias, "Comparison of regression and neural networks models to estimate solar radiation," *Chilean Journal of Agricultural Research*, vol. 70, no. 3, pp. 428–435, 2010.

[21] P. G. Nikhil and D. Subhakar, "Approaches for developing a regression model for sizing a stand-alone photovoltaic system," *IEEE Journal of Photovoltaics*, vol. 5, no. 1, pp. 250–257, 2015.

[22] Y.-K. Wu, C.-R. Chen, and H. Abdul Rahman, "A novel hybrid model for short-term forecasting in PV power generation," *International Journal of Photoenergy*, vol. 2014, 9 pages, 2014.

[23] A. Mellit and A. M. Pavan, "A 24-h forecast of solar irradiance using artificial neural network: Application for performance prediction of a grid-connected PV plant at Trieste, Italy," *Solar Energy*, vol. 84, no. 5, pp. 807–821, 2010.

[24] J. Yokoyama and H.-D. Chiang, "Short term load forecasting improved by ensemble and its variations," in *2012 IEEE Power and Energy Society General Meeting*, pp. 1–6, San Diego, CA, USA, 2012.

[25] Y. Wang and I. H. Witten, *Induction of model trees for predicting continuous classes*, 1996.

[26] P. P. Ray, "A survey of IoT cloud platforms," *Future Computing and Informatics Journal*, vol. 1, no. 1–2, pp. 35–46, 2016.

[27] I. Guyon and A. Elisseeff, "An introduction to variable and feature selection," *Journal of Machine Learning Research*, vol. 3, pp. 1157–1182, 2003.

[28] H. Wang, T. M. Khoshgoftaar, K. Gao, and N. Seliya, "High-dimensional software engineering data and feature selection," in *2009 21st IEEE International Conference on Tools with Artificial Intelligence*, pp. 83–90, Newark, NJ, USA, 2009.

[29] X. Yan and X. Su, *Linear regression analysis: theory and computing*, World Scientific, 2009.

[30] J. R. Quinlan, "Learning with continuous classes," in *5th Australian joint conference on artificial intelligence*, vol. 92, pp. 343–348, Singapore, 1992.

[31] D. J. C. MacKay, "Cambridge University Press; Cambridge, UK: 2003," *Inf. theory, inference*Learn. algorithms.[Google Sch..

Hindawi
International Journal of Photoenergy
Volume 2022, Article ID 6371182, 8 pages
https://doi.org/10.1155/2022/6371182

Research Article

Deep Learning Model on Energy Management in Grid-Connected Solar Systems

V. Senthil Nayagam,[1] A. P. Jyothi,[2] P. Abirami,[3] J. Femila Roseline,[4] M. Sudhakar,[5] Essam A. Al-Ammar,[6] Saikh Mohammad Wabaidur,[7] N. Hoda,[8] and Asefa Sisay[9]

[1]*Department of Electrical and Electronics Engineering, Sathyabama Institute of Science and Technology, Tamilnadu, 600119 Chennai, India*
[2]*Department of Computer Science and Engineering, Ramaiah University of Applied Sciences, Bengaluru, Karnataka 560058, India*
[3]*Department of Electrical and Electronics Engineering, B.S. Abdur Rahman Crescent Institute of Science and Technology, Tamilnadu, 600048, Chennai, India*
[4]*Department of Electronics and Communication Engineering, Saveetha School of Engineering, Saveetha Institute of Medical and Technical Sciences, Saveetha University, Tamilnadu, 602105, Chennai, India*
[5]*Department of Mechanical Engineering, Sri Sai Ram Engineering College, Chennai 600044, Tamilnadu, India*
[6]*Department of Electrical Engineering, College of Engineering, King Saud University, P.O. Box 800, Riyadh 11421, Saudi Arabia*
[7]*Chemistry Department, College of Science, King Saud University, Riyadh 11451, Saudi Arabia*
[8]*Department of Biochemistry, Henry Ford Health System, Detroit, MI 48292, USA*
[9]*School of Electrical and Computer Engineering, Kombolcha Institute of Technology, Wollo University, Ethiopia*

Correspondence should be addressed to Asefa Sisay; asefasis@kiot.edu.et

Received 10 February 2022; Accepted 28 March 2022; Published 31 May 2022

Academic Editor: V. Mohanavel

Copyright © 2022 V. Senthil Nayagam et al. This is an open access article distributed under the Creative Commons Attribution License, which permits unrestricted use, distribution, and reproduction in any medium, provided the original work is properly cited.

Because of increased electricity consumption and the inherent limitations of fossil fuel ability to replenish themselves in the future, a shift to renewable energy sources is unavoidable. Although renewable energy sources are afflicted by intermittency, this problem can be alleviated by combining them with other sources of electricity. As a result of the above situation, the secondary source will take over if the primary source is unable to match the load demand. In this paper, we develop a hybrid renewable source that is connected with grids in an optimal way for the prediction of energy using an energy management system (EMS). The study is aimed at optimal handling of energy production, grid interaction, and the storage system, all of which must be accomplished simultaneously. The current state information from the battery, as well as control objectives, is used in this study to design control actions that maximise the amount of electricity injected into the grid. During the prediction window, it is assumed that the control inputs received at the start of the window will remain consistent throughout the duration of the window. The results of RMSE show errors lesser than 0.3% that shows improved rate of accuracy using EMS.

1. Introduction

The imported energy source is a major cause of contention for their governments and citizens. A key present challenge [1] is the reliance on imported fossil fuel energy, as well as the availability of freshwater and waste management. As a result of this trend, the share of renewable energy resources in the generation of island-generated electricity has increased dramatically in recent years.

Wind energy is considered as a popular renewable energy sources. As a result of the fluctuating nature and instability of wind energy, it poses substantial operational challenges, particularly for weak or isolated transmission networks. In order to comply with the grid code obligation to assure a controlled power output as well as the provision of additional ancillary services, wind generating installations must meet certain criteria. Because of the unpredictable behaviour of the wind, scheduling becomes more complex,

and the cost of operating the system increases, which necessitates a reduction in frequency [2, 3].

As a result, the number of wind turbines (WTs) being constructed on a global scale is continuously increasing over the years. In wind-powered systems, the output is intermittent due to the variable speed of the wind, which results in lower efficiency [4]. As a result, penalties for failing to comply with day-ahead bids are now unavoidable. While these issues are exacerbated in island networks such as Guadeloupe, it is critical to maintain control over them in order to improve grid efficiency without compromising power quality and reliability [5].

As a means of overcoming these challenges, wind turbines can be integrated with production or storage technology to form hybrid power plants (HPPs). Using a combination of conventional and renewable energy sources [6, 7], wind-thermal hybrid systems [8, 9], wind-hydro hybrid systems [10, 11], and wind-solar hybrid systems [12–15] to manage energy and reduce the variability of wind-generated electricity, HPPs can reduce the cost of energy and the environmental impact of their operation [16]. Additionally, wind energy can be used with energy storage technologies, fuel cells, and hydrogen storage to provide even more renewable energy. Power injection into the grid on-demand and support for traditional power-generating systems are both made possible in this way, and they are both beneficial [17]. Not only are hybrid power plants capable of accepting a wide range of production and storage resources, but their integration into traditional power grids may also improve the efficiency and reliability of the hybrid system, allowing it to fulfil demand more reliably [18–20].

Optimizing control operations is critical for ensuring that high-pressure water-pumped wind-storage activities run smoothly. It is possible to have energy storage units that service the entire wind farm, or they can be distributed such that each wind turbine has its own storage unit in a hybrid wind power system. These configurations can be controlled by an energy management system (EMS). An EMS must find a balance between the multiple objectives of a power plant operation in order to get the most out of its output. When determining the most effective management plan, a variety of considerations must be taken into consideration. Design and operational requirements, as well as control and optimization methodologies, are all included in this category of requirements.

Recent research has focused on the development of EMS for grid-connected microgrid power dispatch, with particular attention paid to HPPs in rural areas and island territories that integrate wind turbines and energy storage systems [17–19]. The purpose of storing extra electricity and releasing it when there is an energy crisis is to deal with periods of high availability of electrical power.

Due to the fact that it is based on assumptions about the future, the wind/storage HPP power dispatch is inherently problematic. Every optimization computation makes use of the hybrid plant real-time WT production and other measures, which are used as input data for each computation. As a result, in order of resolving the entire problem, a reactive optimization is required. In the energy management microgrid community, there has been a substantial surge in interest in model predictive control (MPC). Using forecasts and newly updated information, this control strategy can determine the future trajectories of the system, and it is capable of handling a wide range of constraints successfully.

Although much has been accomplished, there are still a plethora of challenges linked to criteria, such as integrating production sources and storing them in numerous storage technologies, effective load management, and profitability operations, which must be addressed. Optimizing resource utilisation while simultaneously reducing operational expenses, while taking into consideration the global market, applications, and many technical factors, can increase a system performance and efficiency. The main novelty of the article includes the development of a hybrid renewable source that is connected with grids in an optimal way for the prediction of energy using an EMS.

2. Related works

More than one study has looked at energy management [21–23], and they have discovered that different storage systems, energy sources, and whether or not they are connected to the grid all make a difference in how efficiently energy is managed.

The authors of [24] compared an intuitive solution to an optimal solution is worth mentioning. According to the results, the ideal system is more cost-effective than the predictive system when it comes to lowering electricity expenses. The adoption of intuitive approach fails to consider cost constraints or the price per time slot available. The system does not consider the possibility of employing PV energy of an excess of solar energy. Batteries are further restricted by the fact that they can only be in one of two states at any given time: charging or discharging mode.

The authors of [25] developed a hybrid architecture that incorporates solar, wind, and battery technology. It was decided to use parallel resource solutions to manage energy consumption, which may result in losses if the energy can be supplied by renewable sources.

The authors in [26] are concerned about how long the battery will last in their system. The study focuses on countries where power providers distribute their available energy on a predetermined schedule, resulting in intentional blackouts. There is no doubt about it. In order to tackle this, mixed-integer nonlinear programming was applied, and the outcome was a predictive switching, as shown in Figure 1. However, due to the system construction, the electrical current is only permitted to flow in one direction through the system. Because of this, as well as the fact that the grid is still considered a key source of energy, there are limits to how much excess PV can be managed.

In contrast, the authors of [27] conducted a comparative analysis of two distinct energy control systems that included hybrid energy storage. Initially, a rule-based technique is employed, and secondly, a model predictive control strategy is employed. When it comes to the DC bus voltage, the inverter input voltage threshold is not honored, regardless of whether the load is being injected or supplied with alternating current. To make matters worse, the intuitive

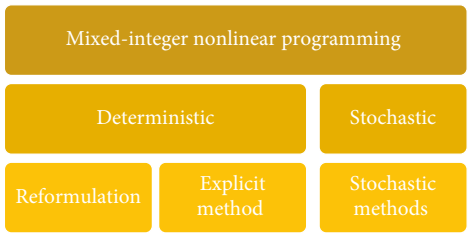

Figure 1: Mixed-integer nonlinear programming.

technique makes use of a decision variable that has no influence on the state of the battery charge, such as voltage, which makes the situation even worse. Although the prior work used dynamic and linear programming, the research presented below used a technique called reduced state number programming.

According to the authors of [28], that authors considered solar system sizing to provide enough electricity for the load while also charging their battery. This technique can be used to track the amount of demand on the power system. Because of the oversizing of the installation, the panels generated an excessive amount of electricity, and the limited mode was employed to reduce the amount of electricity created. Indeed, when sizing, the writers must take into consideration the maximum amount of electricity that may be pumped into the grid. However, on the other hand, the usage of 85% capacity by the EMS is detrimental to the battery general health. As a consequence of this outcome, we investigated how a PV-battery system could share its energy in order to meet the demand in our situation: As a matter of fact, our energy management system mandates that the grid be handled as an emergency line after mathematical modelling is completed for the various components of our hybrid system. At the beginning of each time slot, the output of the PV plant is evaluated; if it is unable to fulfill the load, a battery is used to supplement the PV plant production. In the event of an emergency, the energy that has been sold to the grid will be refunded.

3. Proposed Method

A family of control methods known as model predictive control (MPC) employs the controlled system model as the control signal in order to minimise the user-defined objective function. MPC is a technique for minimising the objective function of a controlled system. Due to the fact that MPC permits constraints to be incorporated into the control design criteria, it is possible to deal with them methodically. MPC capacity to run systems at their constraint boundaries distinguishes it from more classic linear unconstrained approaches such as PID, which operate systems farther away from their constraints. In simple terms, MPC is a method for forecasting future control actions that will result in the intended outcome within a limited time period that is easy to understand. For the purpose of calculating the control signals, a cost function is used as a criterion. The signals are then evaluated in terms of how close they are to the reference trajectory. The current state information from the Li-ION BESS, as well as future control objectives, is used in this study to design control actions that maximise the amount of electricity injected into the grid. During the prediction window, it is assumed that the control inputs received at the start of the window will remain consistent throughout the duration of the window.

Several key performance indicators (KPIs) have been devised to evaluate the EMS predicted wind-storage high-performance power generation performance. While the key performance indicators (KPIs) chosen for this study evaluate performance, they also highlight margins that can be used to optimise the efficient and smart operation of a grid in a way that is both cost-effective and energy-efficient. The objectives and limits of the wind-storage HPP were critical in the development of the key performance indicators in this example.

3.1. Commitment Failure (CF%). Because the output of the wind turbines changes instantly, it is necessary to determine how the storage system should be used (i.e.,which portion of production should be used to charge the BESS and how much power should be discharged) to inject power into the electric grid in accordance with a committed generation schedule (i.e.,how much power should be discharged) (CF%). The commitment profile is then generated based on the data from the day-ahead prediction. It is possible to suffer economic penalties as a result of a violation of the accepted injection area above and below the commitment. The %age of time that the penalty condition was in force is then used to calculate the number of commitment failures, which is expressed as follows:

$$\mathrm{CF\%} = 100 * \frac{\text{penalty triggered time}}{\text{test time}}. \tag{1}$$

3.2. Curtailment Power. It is possible that losses will be incurred as a result of excessive wind turbine production when the BESS is completely charged. These losses can be monitored and measured in order to test a suggested energy management system (EMS) that regulates how battery cycles adhere to the day-ahead commitment while also minimising these losses. This key performance indicator (KPI) is calculated using the following formula:

$$(\text{ifPWECS} > \text{bandceiling}):\ \text{Pcurt} = \text{PWECS} - (\text{PSCHED} + \text{tol}). \tag{2}$$

3.3. Not Supplied Power. It is as follows that in the event of a commitment failure, the complete remuneration injection is made:

$$\text{PINJ} = \text{PWECS} + \text{PBESS} - \text{Pcurt} - \text{Pnotbilled}. \tag{3}$$

3.4. Counting Battery Cycles. Several factors influence the longevity of a battery, and one of these factors is the total charge-discharge cycles each battery undergoes. The most effective strategy to maximise the lifespan and return on investment of your battery is to make an accurate prediction

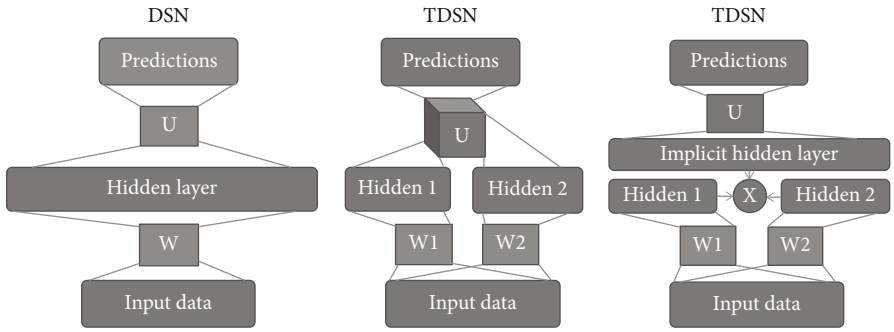

Figure 2: Single module DSN, TDSN, and equivalent TDSN forms.

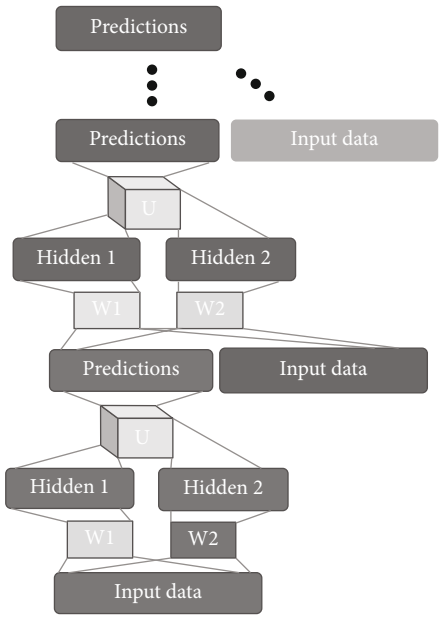

Figure 3: TDSN modules with prediction vector concatenating with input vector.

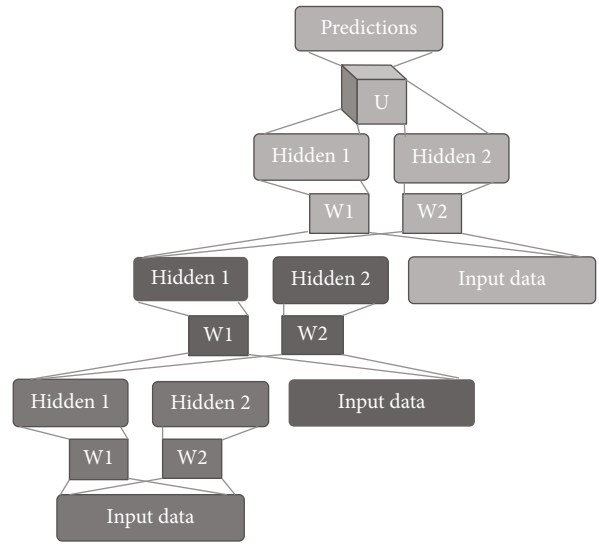

Figure 4: TDSN modules stacking by two hidden-layer concatenating with input vector.

of how quickly it will degrade over time. Here are some things to keep in mind while calculating the storage system utilisation during partial charging and discharging cycles:

$$\text{BESScycles} = \text{BESScycles+}. \tag{4}$$

3.5. Deep Stacking Network for Prediction. Recently, a tensorized variant of the Deep Stacking Network (DSN) architecture, named Tensor DSN (TDSN), was generalized and made available to the public. Although it is not as parallelizable as DSN in learning, it does give higher-order feature interactions that are missing from DSN parallelizability [29].

There are significant similarities between the TDSN and DSN architectures when it comes to stacking operations. A deep architecture may be formed by putting TDSN modules together in the same way that Lego pieces are stacked. TDN and DSN are distinguished by the modules that make up their respective systems. When using DSN, a hidden layer is generated by a single set of hidden units, as can be seen in Figure 2(a). Instead, Figures 2(b) and 2(c) depict two different hidden layers, one labelled hidden 1 and the other hidden 2, for each TDSN module, with the first labelled hidden 1 and the second labelled hidden 2. Consider that the weights of the upper layer, denoted by the letter U in Figure 2 shift from two-dimensional arrays (matrices) in DSN to three-dimensional arrays (tetrahedrons) in TDSN when this difference is taken into consideration.

Figure 2 depicts a comparison between a DSN module (Figure 2(a)) and a tensorized-DSN module (Figure 2(b)) (TDSN). Figure 2(c) displays the TDSN module, which is shown in two different variations. The optimal solutions are attained with the help of DSN, TDSN, and equivalent TDSN forms, where the errors passing through the layers are mitigated.

There are three places where the tensor U is linked: to the prediction layer, to the hidden layers, and output layer. Figure 3 shows how a similar TDSN module can be produced by expanding the two independent concealed layers into their outer products, as seen in the right panel of the figure. All possible pair-wise products of the two hidden layer vector sets contained within the enormous vector are represented by this vector. To put it another way, the size of the prediction layer, as well as the product of the sizes of the two hidden layers, is used to recreate the matrix. Because

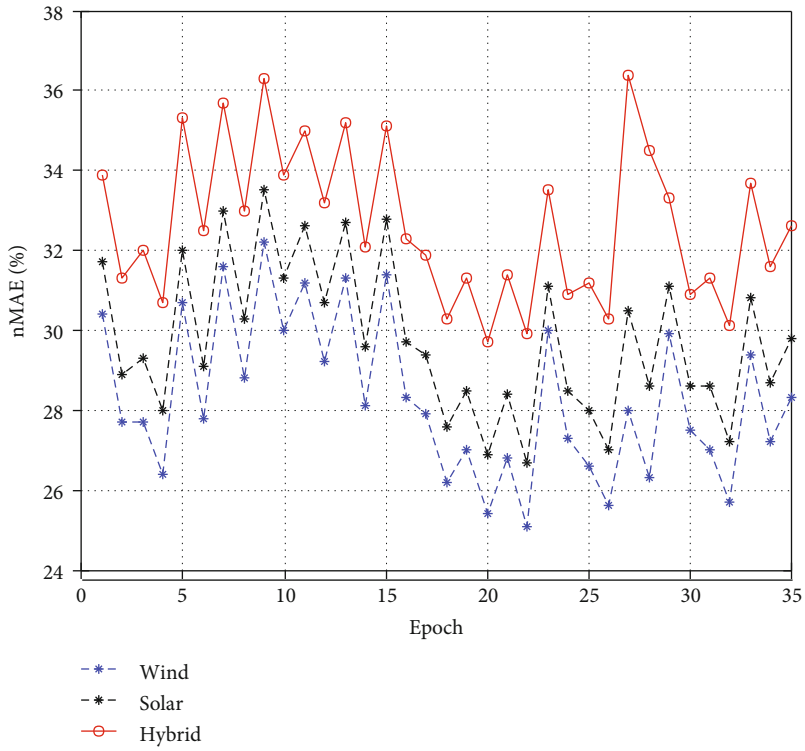

Figure 5: nMAE of all models.

of this equivalence, a convex optimization for learning U can be used to learn tensor U with the same results. Furthermore, the outer product design of TDSN big, implicit hidden layer allows for higher-order hidden feature interactions due to the big, implicit hidden layer implicit hidden layer.

The process of concatenating many vectors in TDSN modules in order to form a deep architecture is similar to that of DSN construction. There are two possible scenarios, as represented in the accompanying pictures. Because of the huge hidden layer in DSN, note stacking by concatenating hidden layers with input (as depicted in Figure 4) is not possible.

4. Results and Discussions

In this section, the validation considered 30 PV plants for one year. There is a plethora of ways available for analysing the success of a single or numerous forecasts. However, in the domain of PV forecasting, there has been no prior study comparing this prediction outcomes. It is also being investigated how wind speed data influences the optimum model selection, as well as the procedures and benefits associated with it.

Because we assume that the fluctuation in power demand is dependent on time slots, this method is logically predictive. Furthermore, it is realistic to anticipate that solar irradiation will vary substantially from one hour to the next. Figure 5 shows nMAE of all models.

Solar energy generation, battery storage, and grid intervention are all given the highest priority possible in this plan. As a result, the usage of switches ensures that this is the outcome. It is noteworthy that when one of the sources intervenes, the switch on the unit alters the unit state, allowing it to participate in the DC bus. During the MATLAB modelling and simulation process, the efficiency of the conversion systems was taken into consideration, which explains the gap between the required power and the actual power used in the experiment. When solar energy is adequate to satisfy the load, excess electricity is delivered back into the grid unless the battery maximum charge level is reached. However, if the power requirements of the load exceed the capacity of the solar system, the battery will step in to make up the difference. Even if the solar panels are unable to keep a minimal charge on the battery, the grid will step in to cover the void left by the solar panels.

Clearly, the separation and transposition models have the greatest impact on prediction accuracy because their average metric differences are so large; this suggests that model selection has the greatest impact on accuracy during the two computation phases of separation and transposition models, respectively. Despite the fact that there is a little difference between the three models of inverters, this difference is insignificant due to the fact that it is so minor. Even after accounting for a large number of unplanned losses in solar power facilities, a 0.3% underestimation of power generation is discovered. Models that are simpler in nature tend to have a lower variance than models that are more complex in nature. In the absence of irradiance measurements, it is hard to determine whether the underdispersion is caused by NWP forecasting or by physical power simulation.

In contrast to their substantial negative correlations with the transposition and cell temperature models, their relationships with the other performance measures are a little more ambiguous. In addition, they have a high correlation

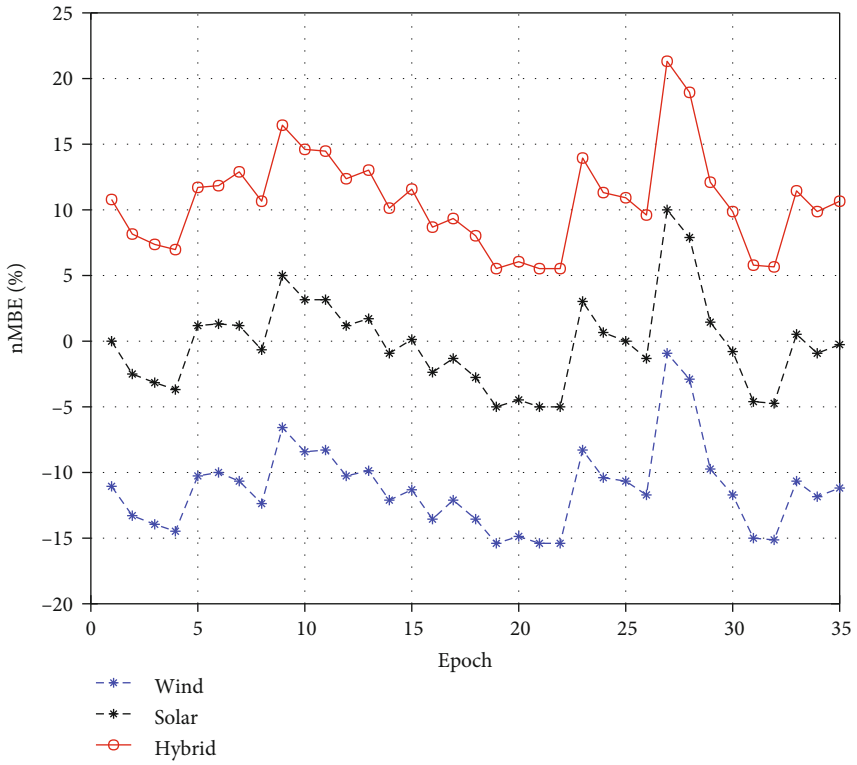

Figure 6: nMBE of all models.

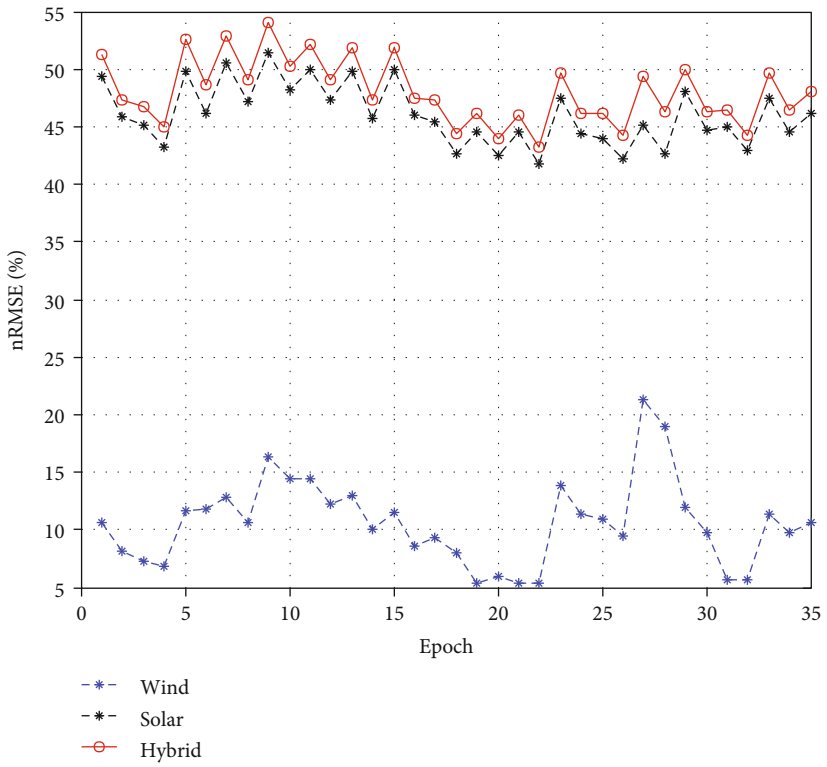

Figure 7: nRMSE of all models.

with the separation, reflection, and shading models. Average errors are reduced in MAE and RMSE directions by utilising the BRL separation model, which includes reflection and shading losses. In contrast, the RMSE and MAE are both at their lowest levels in the Liu-Jordan transposition model. To build skill ratings, the RMSE is used. As a result, these

values provide no further information about the relative performance. As a result, there is a strong relationship between variance and root mean square error, which suggests that forecasts that are less scattered are more accurate. In prior research, it was found that regional averaging can improve the accuracy of forecasts.

When compared to their combined performance, it is only slightly more accurate than the individual best model. As a result, the selection of the physical model may be based on data from other power plants in the same geographical area depicted in Figure 6. Despite having a slightly higher RMSE than the best models, the basic model has an MAE that is 8% higher than the best models.

With respect to a comparison with the best model found in the literature, just 2.8% of the MAE is higher, while the residual mean square error is higher by 6.2%. A basic PV model may outperform a complete one if the RMSE is considered to be the most significant error measure. Furthermore, there is a significant difference in bias and variance between the two groups of participants. The low-MAE model chains, which have a lower nMBE and a higher variance ratios, are related to a higher variance ratio. Even a minor bias can have a considerable impact on the mean absolute error since the absolute error is sensitive to small and large errors of the same magnitude. When comparing high-RMSE model chains to low-RMSE model chains, the variance ratios are both lower than when comparing low-RMSE model chains as in Figure 7.

5. Conclusions

The solar panel, the grid, and battery storage are all components of the energy management algorithm that we have proposed in this paper. In order to function properly, system configuration must be considered at both the scale and management levels. The proposed energy management system, if it does not include a battery storage system, prioritizes the national electrical grid when it comes to solar energy output. In addition, even in the event of an overflow, the solar system energy output is controlled and monitored. Because of resistance losses, our mathematical model of the solar system has been shown to be accurate to within a few watts of the actual system in several experiments. To be certain, a one-day simulation was conducted, and the results revealed that the system fits completely with all of the modelling requirements and adheres to the prioritization orders specified in the preceding section. In future, the RMSE can further be reduced using effective optimistic technique that should constantly work on improving the rate of optimization of target solution.

Data Availability

The data used to support the findings of this study are included within the article. Further data or information is available from the corresponding author upon request.

Conflicts of Interest

The authors declare that there are no conflicts of interest regarding the publication of this paper.

Acknowledgments

The authors appreciate the supports from Kombolcha Institute of Technology, Wollo University, for research and preparation of the manuscript. The work was supported by Researchers Supporting Project number (RSP2022R492), King Saud University, Riyadh, Saudi Arabia.

References

[1] X. Xing, L. Xie, and H. Meng, "Cooperative energy management optimization based on distributed MPC in grid-connected microgrids community," *International Journal of Electrical Power & Energy Systems*, vol. 107, pp. 186–199, 2019.

[2] J. D. Vergara-Dietrich, M. M. Morato, P. R. Mendes, A. A. Cani, J. E. Normey-Rico, and C. Bordons, "Advanced chance-constrained predictive control for the efficient energy management of renewable power systems," *Journal of Process Control*, vol. 74, pp. 120–132, 2019.

[3] S. Leonori, M. Paschero, F. M. F. Mascioli, and A. Rizzi, "Optimization strategies for microgrid energy management systems by genetic algorithms," *Applied Soft Computing*, vol. 86, article 105903, 2020.

[4] R. López-Rodríguez, A. Aguilera-González, I. Vechiu, and S. Bacha, "Day-ahead mpc energy management system for an island wind/storage hybrid power plant," *Energies*, vol. 14, no. 4, p. 1066, 2021.

[5] S. G. Varzaneh, A. Raziabadi, M. Hosseinzadeh, and M. J. Sanjari, "Optimal energy management for PV-integrated residential systems including energy storage system," *IET Renewable Power Generation*, vol. 15, no. 1, pp. 17–29, 2021.

[6] D. Azuatalam, K. Paridari, Y. Ma, M. Förstl, A. C. Chapman, and G. Verbič, "Energy management of small-scale PV-battery systems: a systematic review considering practical implementation, computational requirements, quality of input data and battery degradation," *Renewable and Sustainable Energy Reviews*, vol. 112, pp. 555–570, 2019.

[7] H. Fontenot and B. Dong, "Modeling and control of building-integrated microgrids for optimal energy management–a review," *Applied Energy*, vol. 254, article 113689, 2019.

[8] D. Espín-Sarzosa, R. Palma-Behnke, and O. Núñez-Mata, "Energy management systems for microgrids: main existing trends in centralized control architectures," *Energies*, vol. 13, no. 3, p. 547, 2020.

[9] M. Mohammadjafari, R. Ebrahimi, and V. Parvin Darabad, "Optimal energy management of a microgrid incorporating a novel efficient demand response and battery storage system," *Journal of Electrical Engineering & Technology*, vol. 15, no. 2, pp. 571–590, 2020.

[10] M. M. Morato, P. R. Mendes, J. E. Normey-Rico, and C. Bordons, "LPV-MPC fault-tolerant energy management strategy for renewable microgrids," *International Journal of Electrical Power & Energy Systems*, vol. 117, article 105644, 2020.

[11] M. Alhussein, S. I. Haider, and K. Aurangzeb, "Microgrid-level energy management approach based on short-term forecasting

of wind speed and solar irradiance," *Energies*, vol. 12, no. 8, p. 1487, 2019.

[12] X. Li and S. Wang, "Energy management and operational control methods for grid battery energy storage systems," *CSEE Journal of Power and Energy Systems*, vol. 7, no. 5, pp. 1026–1040, 2019.

[13] A. S. Aziz, M. F. N. Tajuddin, M. R. Adzman, M. A. Ramli, and S. Mekhilef, "Energy management and optimization of a PV/diesel/battery hybrid energy system using a combined dispatch strategy," *Sustainability*, vol. 11, no. 3, p. 683, 2019.

[14] S. Xie, X. Hu, S. Qi et al., "Model predictive energy management for plug-in hybrid electric vehicles considering optimal battery depth of discharge," *Energy*, vol. 173, pp. 667–678, 2019.

[15] B. Benlahbib, N. Bouarroudj, S. Mekhilef et al., "Experimental investigation of power management and control of a PV/wind/fuel cell/battery hybrid energy system microgrid," *International Journal of Hydrogen Energy*, vol. 45, no. 53, pp. 29110–29122, 2020.

[16] V. Marinakis, H. Doukas, J. Tsapelas et al., "From big data to smart energy services: an application for intelligent energy management," *Future Generation Computer Systems*, vol. 110, pp. 572–586, 2020.

[17] U. Zafar, S. Bayhan, and A. Sanfilippo, "Home energy management system concepts, configurations, and technologies for the smart grid," *IEEE access*, vol. 8, pp. 119271–119286, 2020.

[18] O. Ouramdane, E. Elbouchikhi, Y. Amirat, and E. S. Gooya, "Optimal sizing and energy management of microgrids with vehicle-to-grid technology: a critical review and future trends," *Energies*, vol. 14, no. 14, p. 4166, 2021.

[19] M. Afrasiabi, M. Mohammadi, M. Rastegar, and A. Kargarian, "Multi-agent microgrid energy management based on deep learning forecaster," *Energy*, vol. 186, article 115873, 2019.

[20] Y. Zhou, S. Cao, J. L. Hensen, and A. Hasan, "Heuristic battery-protective strategy for energy management of an interactive renewables–buildings–vehicles energy sharing network with high energy flexibility," *Energy Conversion and Management*, vol. 214, article 112891, 2020.

[21] K. Veluchamy and M. Veluchamy, "A new energy management technique for microgrid system using muddy soil fish optimization algorithm," *International Journal of Energy Research*, vol. 45, no. 10, pp. 14824–14844, 2021.

[22] Y. Zhang and W. Wei, "Model construction and energy management system of lithium battery, PV generator, hydrogen production unit and fuel cell in islanded AC microgrid," *International Journal of Hydrogen Energy*, vol. 45, no. 33, pp. 16381–16397, 2020.

[23] F. Weschenfelder, G. D. N. P. Leite, A. C. A. da Costa et al., "A review on the complementarity between grid-connected solar and wind power systems," *Journal of Cleaner Production*, vol. 257, article 120617, 2020.

[24] Z. Wu and X. Xia, "Optimal switching renewable energy system for demand side management," *Solar Energy*, vol. 114, pp. 278–288, 2015.

[25] Z. Sabiri, N. Machkour, K. El Majdoub, E. Kheddioui, D. Ouoba, and A. Ailane, "An adaptative control management strategy applied to a hybrid renewable energy system," *International Review of Modeling and Simulation IREMOS*, vol. 10, no. 4, p. 258, 2017.

[26] M. Alramlawi, A. Gabash, E. Mohagheghi, and P. Li, "Optimal operation of hybrid PV-battery system considering grid scheduled blackouts and battery lifetime," *Solar Energy*, vol. 161, pp. 125–137, 2018.

[27] L. Bartolucci, S. Cordiner, V. Mulone, and J. L. Rossi, "Hybrid renewable energy systems for household ancillary services," *International Journal of Electrical Power & Energy Systems*, vol. 107, pp. 282–297, 2019.

[28] S. Upadhyay and M. P. Sharma, "A review on configurations, control and sizing methodologies of hybrid energy systems," *Renewable and Sustainable Energy Reviews*, vol. 38, pp. 47–63, 2014.

[29] L. Deng and D. Yu, "Deep learning: methods and applications," *Foundations and trends in signal processing*, vol. 7, no. 3–4, pp. 197–387, 2013.

Hindawi
International Journal of Photoenergy
Volume 2022, Article ID 4921153, 6 pages
https://doi.org/10.1155/2022/4921153

Research Article

Improving the Efficiency of Photovoltaic Panels Using Machine Learning Approach

Rashmita Khilar,[1] G. Merlin Suba,[2] T. Sathesh Kumar,[3] J. Samson Isaac,[4] Santaji Krishna Shinde,[5] S. Ramya,[6] V. Prabhu,[7] and Kuma Gowwomsa Erko[8]

[1]*Department of Information Technology, Saveetha School of Engineering, Saveetha Institute of Medical and Technical Sciences, Saveetha University, Chennai, Tamil Nadu 600124, India*
[2]*Department of Electrical and Electronics Engineering, Panimalar Engineering College, Poonamallee, Chennai, Tamil Nadu 600123, India*
[3]*Department of Electrical and Electronics Engineering, Dr. Mahalingam College of Engineering and Technology, Pollachi, Tamil Nadu 642003, India*
[4]*Department of Biomedical Engineering, Karunya Institute of Technology and Sciences, Coimbatore 641114, India*
[5]*Department of Computer Engineering, Vidya Pratishthan's Kamalnayan Bajaj Institute of Engineering and Technology, Baramati, Maharashtra 413133, India*
[6]*Department of Information Technology, M.Kumarasamy College of Engineering, Karur, Tamil Nadu 639113, India*
[7]*Department of Mechanical Engineering, Sri Sairam Engineering College, Chennai, Tamil Nadu 600044, India*
[8]*Department of Mechanical Engineering, Ambo University, Ethiopia*

Correspondence should be addressed to Kuma Gowwomsa Erko; kuma.gowwomsa@ambou.edu.et

Received 29 January 2022; Revised 10 April 2022; Accepted 15 April 2022; Published 28 May 2022

Academic Editor: V. Mohanavel

Copyright © 2022 Rashmita Khilar et al. This is an open access article distributed under the Creative Commons Attribution License, which permits unrestricted use, distribution, and reproduction in any medium, provided the original work is properly cited.

Photovoltaic (PV) solar panels account for a major portion of the smart grid capacity. On the other hand, the accumulation of solar panels dust is a significant challenge for PV-based systems. The accumulation of solar panels dust results in a significant reduction in the amount of energy produced. Because of the country's low wind velocity and rainfall, frequent cleaning of solar panels is necessary either by manual or automated means. Cleaning activities should only be initiated when absolutely essential to reduce maintenance costs and increase the power output of solar panels that have been projected to be affected by dust accumulation. In this paper, we develop a deep belief network model to detect the dust particles in the solar panels installed as a large unit. The study takes into account various input metrics that includes solar irradiance, temperature level, and dust level on the panels. These metrics are used for the estimation of the level of dust present in the atmosphere and how often the panels can be cleaned at regular intervals. The simulation is conducted to test the efficacy of the model in cleaning the panels. The results are estimated in terms of accuracy, precision, recall, and F-measure. The results of the simulation show that the proposed model achieves higher accuracy rate of more than 99% than other methods.

1. Introduction

The use of thermal power plants contributes to the acceleration of global warming. In contrast, the fossil fuels that are used in these plants are getting increasingly expensive and difficult to come by. As a result, the integration of renewable energy sources into power systems has become a global imperative. Solar, wind, biomass, geothermal, and fuel cells are just a handful of the renewable energy sources that can be used to power electric grids and other energy systems.

The demand for natural gas and oil tends to increase dramatically in recent years, causing countries to look for

alternative energy sources. Solar power and renewable energy technology are being actively considered as viable alternative energy sources and other countries across the world. With its favourable temperature and geographical location, it is home to the world's highest solar power generation. As a result, solar energy has become the most widely used renewable energy source.

Photovoltaic panels are made with semiconductor materials, which are employed in the manufacturing process. The inherent properties of photovoltaic materials have an impact on the efficiency of photovoltaic systems. Solar panel output is therefore dependent on the materials used in their manufacture as well as the coating applied to the glass on which they are constructed.

As a result, several impediments to the widespread use of solar energy in underdeveloped countries. The impact of dust is one of the most significant considerations. Because of the country's geographic location, the pace at which dust accumulates is extremely high. A build up of dust on photovoltaic panels causes them to degrade quickly, which results in a significant reduction in their power production. Both the environmental conditions and the qualities of the dust play a role in determining the amount of dust that accumulates in a given area. The weight, shape, and size of the dust particles are all characteristics of the dust, whereas environmental elements include the weather and the particle location [1–3].

Additionally, the wind might have an impact on dust settling. A large amount of dust collects on the surface of solar panels in regions, causing the power output of solar photovoltaic panels to decrease at the fastest rate. Climate factors such as the temperature and humidity of the surrounding air have an impact on dust settlement. Solar panels lose their efficiency as a result of increased dust accumulation on them as the temperature and humidity rise [4].

As a result, solar panels should be cleaned on a regular basis to ensure maximum efficiency. However, if no cleaning procedures are required, this strategy is not cost-effective and may result in a waste of resources [5]. It is critical to determine the quantity of dust on solar panels and to begin cleaning procedures as soon as possible in order to maximise output while reducing maintenance costs. The impact of dust collected on panels varies depending on the weather conditions and the size of the dust particles. The output power of PV panels also fluctuates depending on the location, the properties of the dust, and the temperature of the environment. As a result of this limitation, the outcomes of research undertaken in one country cannot be generalised to other countries.

It is feasible to employ the process described in this paper in other countries, but not the data or findings. As a result, it is vital to continuously monitor the quantity of dust in photovoltaic farms and to take appropriate steps to reduce maintenance costs while simultaneously boosting output. In fact, the generality of the methodology given herein distinguishes it from other approaches as it can be used to detect dust accumulation regardless of where it occurs.

In this paper, we develop a deep belief network model to detect the dust particles in the solar panels installed as a large unit as in Figure 1.

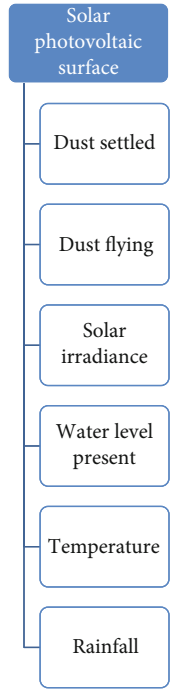

Figure 1: Main sources of data collection on PV panels.

The main contribution of the paper involves the following:

(i) The study takes into account various input metrics that includes solar irradiance, temperature level, and dust level on the panels

(ii) These metrics are used for the estimation of the level of dust present in the atmosphere and how often the panels can be cleaned at regular intervals

2. Background

According to the research literature, solar photovoltaic production can be investigated either via the use of tests or through the development of prediction models.

In [6], the effects of dust, humidity, and air velocity were investigated individually and in combination. Fine particles have a greater impact on the efficiency of solar panels. A greater tilt angle also helped to prevent dust accumulation, albeit wetness accelerated the coagulation of dust particles. Tests were carried out in [7] in order to demonstrate the effect of pollutant type and weight on the output power of solar-powered PV panels.

In [8], it was found that three unique fake contaminants were injected into the solar photovoltaic panel during the experiment. The testing included the use of pollutants as contaminants. The results revealed that solar panels produced substantially more electricity than clean panels. A comparable study into three artificial pollutants, red soil, sand, and ash, was conducted and the results were published in [9].

A 23-day test of self-cleaning coatings on solar panels was conducted [10] to see whether they were effective. When compared to panels that did not have this coating compound, the

performance of the panels with this coating compound was practically equal.

A number of experiments were carried to investigate the dust impact on a solar panel performance. The dust concentrations in solar panel modules ranged from 0.0063 g/m^2 to 0.36 g/m^2, depending on the model. According to the research, a linear link was discovered between dust mass and the fall in solar output power. According to [11], satellite images and an SVM model were used to estimate cloud movement and irradiance. The autoregression model presented in [12] was used to forecast the output over a period of up to 36 hours, and the results were positive.

As reported in [13], the ANN technique provides predictions of global solar radiation based on data from weather stations throughout the world. The hourly diffuse solar irradiance was estimated using a sigmoid function regression model by the authors in [14] for all weather conditions. The model discovered a 25–35 percent relative root RMSE. The output power of a wind turbine in Turkey may be calculated using an ANN model over a variety of time periods and throughout various seasons [13]. A solar panel with a capacity of 750 watts was installed (PV). The RMSE for each season and time period was tallied separately.

In [15], the output power of California PV panels was predicted using four different approaches, one of which being the ANN method. It was decided to use a one-megawatt solar panel field to forecast one hour and two hours in the future. In terms of accuracy, the ANN surpassed all of the other forecasting methods except for one. According to the research, there was an inaccuracy of up to 20% in the other models. In the provided model, the root mean square error (RMSE) was found to be 15%. Neither the study nor the literature made any considerations for how environmental circumstances would affect the output power of the system.

Using solar modules as an example, researchers in Spain conducted a study to determine how rainfall impacts the cleaning of the modules [16]. According to a study, solar photovoltaic power plants lose 20 percent of their energy during dry seasons, compared to only 4.4 percent during wet months, due to dust accumulation on the solar panel surfaces [12].

As part of another study experiment in Morocco, the output of a solar photovoltaic panel and rainfall was measured for four months and then used to determine the accumulation of dust. The information on the amount of rain that fell came from a weather data collection centre.

Studies in [17] looked into how dust collecting affects PV panel performance in the Jazan region, despite the fact that rain occurs seldom and with a low degree of intensity. The efficiency of photovoltaic panels was found to be reduced by 10% as a result of the frequent dust collection. Lower tilt angles, on the other hand, gathered far more dust than higher tilt angles. The authors of this article were inspired to write it because they wanted to share their knowledge with others.

In [18], indications are conducted in order to determine the dust accumulated on photovoltaic surface. Much research has been conducted to determine the dust impact on photovoltaic panels. There have been a few studies conducted to determine the amount of dust that has to be eliminated before the proper cleaning procedure can begin.

3. Proposed Method

Forecasting solar panel dust accumulation accurately is crucial for investors and grid operators alike, as it affects their bottom lines. As shown in Figure 2, the research was aimed at estimating the dust level with various measurements on solar panels. If there is a significant amount of dust, cleaning procedures may be initiated. Machine learning was used in the development of this detector. The first step in developing a machine learning model for photovoltaic panels is to collect all of the data that will be needed. After that, a number of regression models are constructed and tested on the data that has been collected.

3.1. Data Preparation. Analysis of data before it is fed into the model is used to predict dust levels, which is accomplished through the use of regression models. The statistical approach helps to predict the relationship between the response and single output variable, and one or more input variables, referred to as predictors; before entering the model, the predictors and response variables should be grouped in a matrix to make it easier to understand. In this study, three factors are used to predict the value of a single output or response variable. When operating in these conditions, PV power output is influenced by three variables: the amount of solar irradiation received, the temperature of the surrounding air, and a reaction variable termed dust. A comprehensive collection of data was acquired through a series of tests, which will be discussed in further detail in the following paragraphs and which are conducted over a number of days, resulting in an extensive collection of data.

3.2. Model Training. After that, the model is fed with data from the tests, which is then trained on that data to teach it how to predict dust levels based on inputs such as the power output of PV panels, the temperature of the environment, and the amount of solar irradiation. There are two types of data collected (predictor variables and responses). Data sets are used in the model creation and validation process for both the training and testing stages. Data sets are used in both the training and testing stages.

The solar irradiance, temperature, and output power are all included in the regression models as three predictors and one response variable. The regression model predicts the dust present, which is then compared to the actual response. While training, the 5-fold cross-validation method is used. It is often used in regression models to analyse and quantify misclassification errors, which is a common occurrence. During the training phase of this method, five sets of data are picked at random from the training data set to be used in the training phase.

The four groups will be used to train and evaluate the model during the development process. This technique will be repeated numerous times in order to ensure that each group has been examined at least once before moving on. Following the training process, the difference between the actual and projected response is found determined using the data collected. When using different models, it is feasible to estimate solar panel dust collection with a different standard deviation

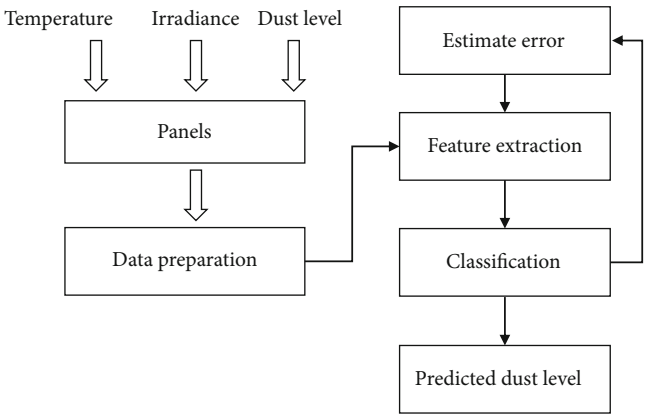

Figure 2: Proposed algorithm.

(RMSE). From among the available regression prediction models, the one that provides the most accurate dust estimation with the lowest RMSE is chosen. The correctness of a model can be tested by using a variety of case studies after it has been narrowed down to the most accurate one through a process of elimination.

When RBMs are trained, they are stacked together to produce a DBN. The following is an explanation of the stacking technique. Using the activation probabilities of its hidden units, a Bernoulli-Bernoulli RBM is trained after learning a Gaussian-Bernoulli RBM or a Bernoulli RBM, which is then used to train another RBM. After that, the activation probabilities of the second-layer Bernoulli-Bernoulli RBM are used as the visible data input by the third-layer Bernoulli-Bernoulli RBM. This is a three-layer RBM with three layers. The layer-by-layer greedy learning improves the training data under the stacking, which provides some theoretical evidence for this effective layer-by-layer greedy learning technique. Thus, the greedy strategy described above achieves a close approximation to the maximum probability distribution. It is vital to remember that this learning process is unsupervised and does not necessitate the use of a class label.

Different learning approaches, often discriminative, that fine-tune the weights together to improve the network performance in classification tasks are used in addition to pre-training. After that, variables reflecting the outputs from the training data are introduced to further fine-tune the performance and accuracy of the discriminative model.

The back-propagation fine-tunes the weights of a feed-forward neural network. What appears in the top layer is determined in this case. HMM-based speech recognition systems employ the top layer, shown in Figure 3 by the letters l1, l2,… lj, lL, to represent syllables, phone calls, subphones, or other speech units, while the lower layers represent additional speech units.

Phone and speech detection were among the tasks on which the generative pretraining described above outperformed random initialization across a broad range of tasks. In addition, the order in which minibatches are formed must be carefully studied prior to being implemented. As a result, it was determined that starting with a simple neural network with one hidden layer and working your way up was the most successful way to learn the DNN. Once the necessary

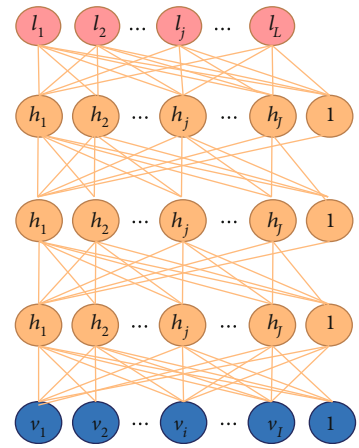

Figure 3: DBN/DNN architecture.

number of hidden layers has been achieved, a complete backpropagation fine tuning procedure is carried out. Using this pretraining strategy has been proven to be effective on the battlefield.

3.3. Dust Estimation Unit. After the model selection with the lowest root mean square error (RMSE), this regression model is extracted. The temperature, output power, and solar irradiance are fed into the system, and it can anticipate the amount of dust that will build up on the solar panel in the future. Those in charge of operating solar photovoltaic systems rely on precise dust estimates to decide the optimal time to clean the modules. When the dust level on solar PV panels surpasses a specified threshold, the amount of energy produced by the system can be considerably reduced. As a result, as soon as the level of dust collection exceeds this threshold, cleaning activities can commence. Solar photovoltaic modules should be cleaned at the most opportune time of year to save on the extra costs associated with cleaning solar photovoltaic modules on a regular basis. In the final stage, a new data set is used to test the dust estimation unit, which helps to minimise bias and evaluate accurately the performance by evaluating its accuracy.

4. Results and Discussions

It has already been stated that a large amount of data is required for both training and testing the model. Using a solar photovoltaic panel in the open air under realistic environmental circumstances, experiments were conducted to determine its performance. Researchers have looked into the impact of dust on the performance of photovoltaic panels in these types of environments. The scientists began by setting up a 400-watt solar photovoltaic panel as a test bed for their experiments.

The dust that was used in the experiment was collected from the same location where the experiment was conducted. The output power of the solar PV panel was tested under a variety of conditions, including different times of the day, varying degrees of solar irradiation, different temperatures, and different dust concentrations. For this experiment, the RS PRO Solar Power Meter ISM400 was utilised to measure solar irradiance.

Table 1: Accuracy.

Panels	ANN	BPNN	Proposed
Series parallel	0.94209	0.94432	0.95687
Parallel	0.94198	0.94357	0.95683
Bridge link	0.94117	0.94355	0.95677
Honeycomb	0.94088	0.94285	0.95664
Total cross tied	0.93368	0.94280	0.95641

Table 2: Precision.

Panels	ANN	BPNN	Proposed
Series parallel	0.87254	0.87307	0.89406
Parallel	0.85895	0.86283	0.89200
Bridge link	0.85859	0.86281	0.88695
Honeycomb	0.83920	0.84169	0.88624
Total cross tied	0.83801	0.84148	0.87110

Table 3: Recall.

Panels	ANN	BPNN	Proposed
Series parallel	0.78337	0.83903	0.94382
Parallel	0.83004	0.84054	0.94434
Bridge link	0.83978	0.84067	0.95362
Honeycomb	0.85972	0.85202	0.95580
Total cross tied	0.86925	0.90605	0.95641

Table 4: F-measure.

Panels	ANN	BPNN	Proposed
Series parallel	0.95449	0.90118	0.94118
Parallel	0.95174	0.89384	0.93457
Bridge link	0.94593	0.89250	0.93276
Honeycomb	0.93495	0.88444	0.93180
Total cross tied	0.86860	0.88444	0.89673

Table 5: MAPE.

Panels	ANN	BPNN	Proposed
Series parallel	0.08574	0.01366	0.00311
Parallel	0.18026	0.02100	0.00201
Bridge link	0.20701	0.02234	0.00192
Honeycomb	0.24857	0.04624	0.00304
Total cross tied	0.23473	0.04091	0.00304

Table 1 shows the results of accuracy between the proposed model and existing machine learning models. The results of simulation on various PV panels show that the proposed model achieves higher accuracy rate with its efficient computation.

Table 2 shows the results of precision between the proposed model and existing machine learning models. The results of simulation on various PV panels show that the proposed model achieves higher precision rate with its efficient computation.

Table 3 shows the results of recall between the proposed model and existing machine learning models. The results of simulation on various PV panels show that the proposed model achieves higher recall rate with its efficient computation.

Table 4 shows the results of F-measure between the proposed model and existing machine learning models. The results of simulation on various PV panels show that the proposed model achieves higher F-measure rate with its efficient computation.

Table 5 shows the results of MAPE between the proposed model and existing machine learning models. The results of simulation on various PV panels show that the proposed model achieves reduced MAPE with its efficient computation.

5. Conclusions

In this paper, deep belief network model is used to detect the dust particles in the solar panels installed as a large unit. The study takes into account various input metrics that includes solar irradiance, temperature level, and dust level on the panels. These metrics are used for the estimation of the level of dust present in the atmosphere and how often the panels can be cleaned at regular intervals. The simulation is conducted to test the efficacy of the model in cleaning the panels. The results are estimated in terms of accuracy, precision, recall, and F-measure. The results of the simulation show that the proposed model achieves higher accuracy rate than other methods. In the future, deep learning models can be used to improve the rate of accuracy.

Data Availability

The data used to support the findings of this study are included within the article. Further data or information is available from the corresponding author upon request.

Conflicts of Interest

The authors declare that there is no conflict of interest regarding the publication of this paper.

Acknowledgments

The authors thank the Ambo University, Ethiopia, for providing help during the research and preparation of the manuscript. The author thank the Saveetha University, Vidya Pratishthan's Kamalnayan Bajaj Institute of Engineering and Technology, Dr. Mahalingam College of Engineering and Technology, M. Kumarasamy College of Engineering, and Sri Sairam Engineering College for providing assistance in completing the work.

References

[1] W. A. Hanafy, A. Pina, and S. A. Salem, "Machine Learning Approach for Photovoltaic Panels Cleanliness Detection," in *In 2019 15th International Computer Engineering Conference*

(ICENCO), pp. 72–77, New Jersey, United States, December 2019.

[2] K. Priyadharsini, A. Srikanth, V. Sounddar, and M. Senthamilselvan, "Elegant method to improve the efficiency of remotely located solar panels using IoT," *Materials Today: Proceedings*, vol. 45, pp. 8094–8104, 2021.

[3] P. Sivagami and N. M. Jothiswaroopan, "IOT based statistical performance improvement technique on the power output of photovoltaic system," *Journal of Ambient Intelligence and Humanized Computing*, vol. 12, no. 5, pp. 5029–5043, 2021.

[4] M. Heinrich, S. Meunier, A. Same et al., "Detection of cleaning interventions on photovoltaic modules with machine learning," *Applied Energy*, vol. 263, article 114642, 2020.

[5] A. Khandakar, M. EH Chowdhury, M. Khoda Kazi et al., "Machine learning based photovoltaics (PV) power prediction using different environmental parameters of Qatar," *Energies*, vol. 12, no. 14, article 2782, 2019.

[6] A. J. Trappey, P. P. Chen, C. V. Trappey, and L. Ma, "A machine learning approach for solar power technology review and patent evolution analysis," *Applied Sciences*, vol. 9, no. 7, article 1478, 2019.

[7] C. G. Haba, "Monitoring Solar Panels Using Machine Learning Techniques," in *2019 8th International Conference on Modern Power Systems (MPS)*, pp. 1–6, New Jersey, United States, May 2019.

[8] Z. Ebrahimi-Khusfi, A. R. Nafarzadegan, and F. Dargahian, "Predicting the number of dusty days around the desert wetlands in southeastern Iran using feature selection and machine learning techniques," *Ecological Indicators*, vol. 125, article 107499, 2021.

[9] M. K. Swain, M. Mishra, R. C. Bansal, and S. Hasan, "A self-powered solar panel automated cleaning system: design and testing analysis," *Electric Power Components and Systems*, vol. 49, no. 3, pp. 308–320, 2021.

[10] G. M. Dantas, O. L. C. Mendes, S. M. Maia, and A. R. de Alexandria, "Dust detection in solar panel using image processing techniques: a review," *Research, Society and Development*, vol. 9, no. 8, pp. e321985107–e321985107, 2020.

[11] M. Altıntaş and S. Arslan, "The study of dust removal using electrostatic cleaning system for solar panels," *Sustainability*, vol. 13, no. 16, p. 9454, 2021.

[12] Y. Natarajan, S. Kannan, C. Selvaraj, and S. N. Mohanty, "Forecasting energy generation in large photovoltaic plants using radial belief neural network," *Sustainable Computing: Informatics and Systems*, vol. 31, article 100578, 2021.

[13] Z. Ebrahimi-Khusfi, R. Taghizadeh-Mehrjardi, and M. Mirakbari, "Evaluation of machine learning models for predicting the temporal variations of dust storm index in arid regions of Iran," *Atmospheric Pollution Research*, vol. 12, no. 1, pp. 134–147, 2021.

[14] B. Gobinathan, M. A. Mukunthan, S. Surendran et al., "A novel method to solve real time security issues in software industry using advanced cryptographic techniques," *Scientific Programming*, vol. 2021, 9 pages, 2021.

[15] I. M. Kirpichnikova and V. Shestakova, "Problems of Using Solar Photovoltaic Panels and Ways to Increase their Efficiency," in *2020 International Conference on Industrial Engineering, Applications and Manufacturing (ICIEAM)*, pp. 1–7, New Jersey, United States, May 2020.

[16] R. Usamentiaga, A. Fernández, and J. L. Carús, "Evaluation of dust deposition on parabolic trough collectors in the visible and infrared spectrum," *Sensors*, vol. 20, no. 21, p. 6249, 2020.

[17] K. Benhmed, F. Touati, M. Al-Hitmi et al., "PV Power Prediction in Qatar Based on Machine Learning Approach," in *2018 6th International Renewable and Sustainable Energy Conference (IRSEC)*, pp. 1–4, New Jersey, United States, December 2018.

[18] B. Yılmaz and R. Yıldırım, "Critical review of machine learning applications in perovskite solar research," *Nano Energy*, vol. 80, article 105546, 2021.

Hindawi
International Journal of Photoenergy
Volume 2022, Article ID 6844853, 7 pages
https://doi.org/10.1155/2022/6844853

Research Article

Energy Management Prediction in Hybrid PV-Battery Systems Using Deep Learning Architecture

Mohamad Reda A. Refaai,[1] Shanmukha Naga Raju Vonteddu,[2] Prasanthi Kumari Nunna,[3] P. Suresh Kumar,[4] C. Anbu,[5] and Mebratu Markos[6]

[1]*Department of Mechanical Engineering, College of Engineering, Prince Sattam Bin Abdulaziz University, Alkharj 16273, Saudi Arabia*
[2]*Department of Electrical and Electronics Engineering, University College of Engineering, Kakinada, Andhra Pradesh 533003, India*
[3]*Department of Electrical and Electronics Engineering, University of Petroleum and Energy Studies, Dehradun, Uttarakhand 248007, India*
[4]*Department of Mechanical Engineering, University of Petroleum and Energy Studies, Dehradun, Uttarakhand 248007, India*
[5]*Department of Mechatronics Engineering, Kongu Engineering College, Perundurai, Tamil Nadu 638060, India*
[6]*Department of Mechanical Engineering, College of Engineering, Wolaita Sodo University, Ethiopia*

Correspondence should be addressed to Mebratu Markos; mebratumarkos@wsu.edu.et

Received 9 February 2022; Accepted 8 March 2022; Published 25 May 2022

Academic Editor: V. Mohanavel

Copyright © 2022 Mohamad Reda A. Refaai et al. This is an open access article distributed under the Creative Commons Attribution License, which permits unrestricted use, distribution, and reproduction in any medium, provided the original work is properly cited.

On-grid predictive energy management using machine learning is presented in this paper. A photovoltaic array considered in this study is one of the kinds of a renewable sources of energy, where the battery bank acts as a technology for energy storage, in order to optimise energy exchange with the utility grid using logistic regression. The model of prediction can accurately estimate photovoltaic energy output and load one step ahead using a training technique. The optimization problem is constrained by the maximum amount of CO_2 produced and the maximum amount of charge stored in a battery bank. The proposed model is tested on dynamic electricity costs. Compared with existing energy systems, the proposed strategy and prediction model can handle more than half of the annual load need.

1. Introduction

Due to the lower installation and operating expenses associated with them, HES (hybrid energy systems) are becoming increasingly popular among residential consumers. The household energy system (HES) is made up of renewable sources of energy including photovoltaic (PV) cells, microturbines, wind turbines, and geothermal. When utilised in combination with the HES, there are a variety of energy storage systems (ESS) available, such as the one seen in Figure 1(a), that can be used to store extra energy.

In the HESS, we are using several types like polycrystalline cells, monocrystalline cells, monocrystalline PERF, and N-Type cells which are described clearly in Figure 1(b) along with its coverage range values. The PV and battery-based high-efficiency solar energy systems (HES) are the most commonly used renewable energy options because of its simpler installation, and it requires initial capital expenditure. As long as the utility grid is connected to the PV-battery HES in grid mode, the surplus energy generated will be able to be traded with the utility grid. Hybrid energy grid systems including PV systems, not only help households decrease their environmental impact, but they also help them save money on their monthly energy bills. It is possible to increase the efficiency of these systems even further by applying energy management strategies.

Model predictive control (MPC) models are a kind of the most frequently utilised in GCHES energy management systems, and they are also one of the most complex. It is typical practice to use MPC for economic optimization in the HES since it combines feedback mechanisms to account for

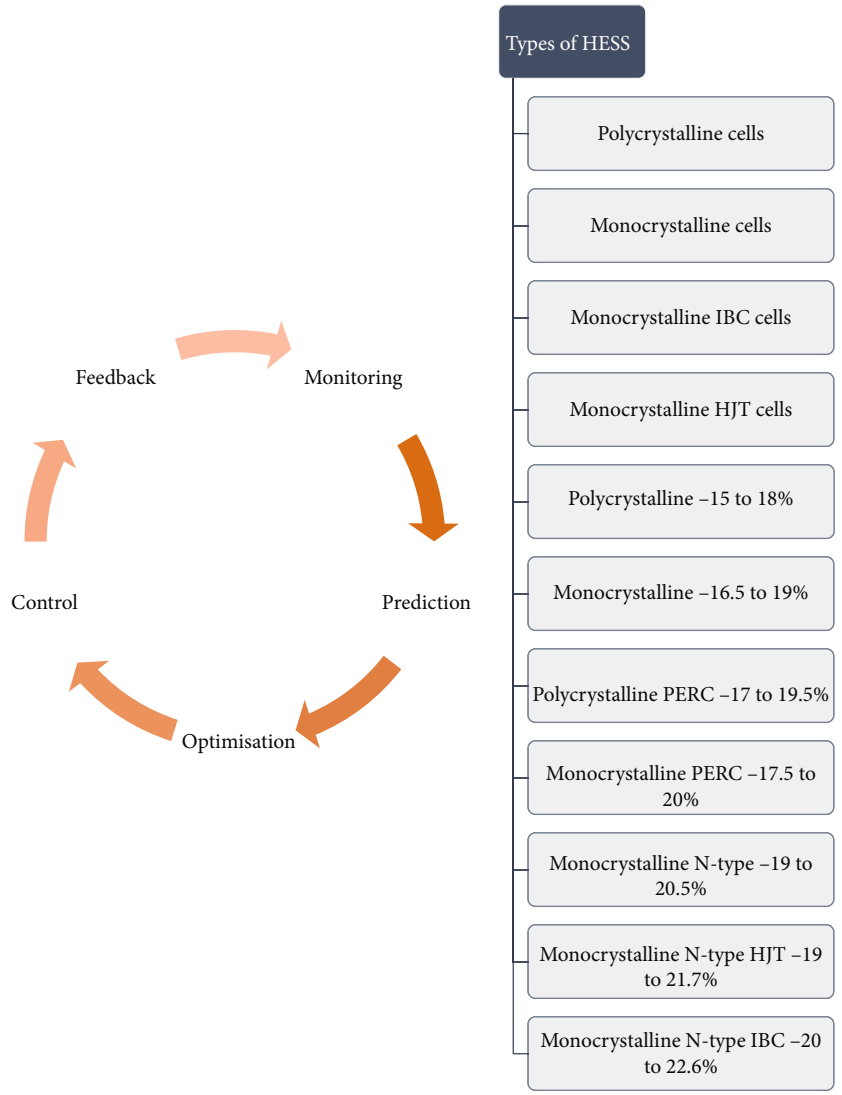

Figure 1: (a) ESS. (b) Types of HESS.

model uncertainty and employs forecasting algorithms to account for future demand and power generation.

The inefficiency of grid-connected HES energy trading, as a result of the inefficiency of HES without the need of EMS and inefficient battery storage in banks, was the impetus for this investigation. Unwanted energy storage can be reduced through more frequent trading of surplus electricity with the utility grid, which will lower the cost of energy. This is an important goal for this research because it will result in less energy being stored than needed.

2. Related Works

The authors in [1] describe a number of characteristics of EMS in MPC and microgrids. In a recent study on microgrid MPC, the topic of economic considerations has been explored in depth. An MPC strategy with various targets, such as that described in [2], can be used to enhance solar grid-connected HES. The study was aimed at managing the multiobjective criterion through linearization of the problem and proving real time traffic into the control unit as its real time input. According to [3], an energy management system has been designed that takes into consideration grid power purchases, electricity bills, and the quality of the power. According to the findings of this study, it is possible to reduce electricity expenditures by 2–6.5%. [4] describes the implementation of a new multiobjective EMS system for a microgrid that makes use of the grasshopper optimization method. This method reduced fuel consumption and CO_2 emissions by 92.4% and 92.3%, respectively, when compared to baseline levels.

Energy management of high-efficiency solar PV, wind turbines, diesel generators, microturbines, and fuel cell systems is presented in [5] in order to achieve optimal PV, diesel generator, wind turbine, fuel cell, and microturbine capacities that consider the major objective fuel costs, energy costs, charging cost, and discharging cost and greenhouse gas penalties. When this technique was used instead of a

normal one, the CO_2 emissions from a single HES were reduced by 51.60% compared to the standard technique.

EMS for microgrids has also progressed in recent years [6–8], with more sophisticated systems now available. The authors of [9] propose that a solar PV system be used in conjunction with an autonomous scheduling system to assist in reducing total electricity use. In addition [7], it has been demonstrated that an energy management technique with supply-demand is superior to a supply-side management strategy when used in off-grid HES in residential construction.

In order to deal with the HES energy management that consists of PV, battery, wind turbine generator, and fuel cell using a hybrid squirrel-whale, a method is designed in [10]. The authors in [11] investigate a number of different energy management optimization methodologies. The particle swarm optimization, genetic algorithm, fuzzy logic, and differential evolution are just a few examples of algorithms that take their cues from the world of nature and apply them to computer programmes. Researchers use genetic algorithms and particle swarm optimization methodologies to find the best potential responses to their questions. In order to function successfully and efficiently, this and other PEMS systems rely on precise projections of future demand and load [12–15]. In order to forecast future PV power generation, several PV power forecasting systems employ advanced machine learning algorithms. A novel LSTM-RNN model is introduced in [16] for solving typical machine learning difficulties such as overfitting and generalisation.

As demonstrated by a study of several experiments described in [17], artificial neural networks are well-suited for forecasting solar energy generation data. The forecasting models developed by [17–19] require a large quantity of prior data in order to provide good prediction accuracy; however, it has been demonstrated that causal and dilated forms of neural network tend to outperform machine learning methods with limited historical data in a variety of fields [20–24].

3. Proposed Method

A form of logistic regression is used to anticipate energy generation and load demand one step ahead of time in order to reduce uncertainty. Because of the intrinsic feature extraction capabilities of logistic regression, time-series prediction is an excellent fit for logistic regression. It is possible to learn about local time series patterns using parallel processing methodologies, and LR integrates information from nearby steps to provide a final result. LR allows smaller-size kernel filters to catch data that exceeds the length of the kernel specified in the specification. As a result, the number of filters is reduced, which allows for a reduction in the total number of trainable parameters. Aside from that, using residual architecture allows data to flow from one convolutional phase to the next that reduces the problem of vanishing gradients via training process.

Because our data is collected at 1-hour intervals, we adjust the number of filters used in this study to match the hours and kernel size used. Because at each residual block, steady rise in dilation of different local and worldwide trends is learned at each convolutional phase, resulting in different local and global trends at each convolutional step. The proposed method of the predictive model is described and shown clearly in Figure 2.

3.1. Grid-PV-Battery System. A residential building with photovoltaic (PV) panels and a battery bank (lead-acid) for energy storage is investigated in this study as a potential source of renewable energy. This system can be connected to the utility grid, allowing for the exchange of energy between the two systems. A predictive EMS (PEMS) controller has been installed in order to connect the battery bank and PV generation system. An electrical circuit breaker is used as an intermediary between the controller and the utility grid in order for energy to be exchanged between the circuit breakers are crucial safety devices because they may be used to manually switch between the grid and the PEMS controller, which is an important safety feature. The PEMS controller regulates the operation of the battery bank, PV system, and utility grid to meet peak demand requirements. This chip also regulates the battery bank (charging/discharging) and maximum limit of SoC in the PV system. The system design is depicted in Figure 3.

For the PV-battery HES energy supply and demand model, the following mathematical equations can be used to represent the model:

$$P_t^r = \frac{P_t^{bt\_r}}{1000}\left(S_t\left(P_t^{load} - P_t^{pv}\right)\right), \tag{1}$$

$$C_t^g = \begin{cases} P_t^r \times C_t^f, & P_t^r \le 0, \\ P_t^r \times C_t^e, & P_t^r > 0, \end{cases} \tag{2}$$

where

P_t^r(kW): Residual battery power at time t,
maxS_t: Maximum limit of PEMS controller.
C_t^g ($): Electricity cost from grid,
C_t^f : Positive electricity cost and,
C_t^e: Negative electricity cost.

3.2. Logistic Regression Model. Logistic regression, like ordinary least-squares (OLS) regression, is a technique for making predictions. When employing logistic regression, it is only possible to predict a binary outcome. In this case, the error variance is not normally distributed, which is contrary to the OLS assumption. Therefore, they have a greater likelihood of being spread in an unplanned manner. In order to obtain the linear regression equation from the logistic distribution, we must first conduct an algebraic conversion on the logistic distribution.

$$\mathrm{Y} = \mathrm{a} + \mathrm{bX} + \mathrm{e}. \tag{3}$$

Because logistic regression does not produce a preprinted result, it is not commonly used. Furthermore, the unstandardized result does not have the same obvious meaning as the OLS regression result, which further complicates the picture even further. A further limitation of OLS and logistic regression is that there is no R^2 to assess the overall fit of the model. An alternative to employing the logistic regression model is to conduct a chi-square test to see how well the data matches the

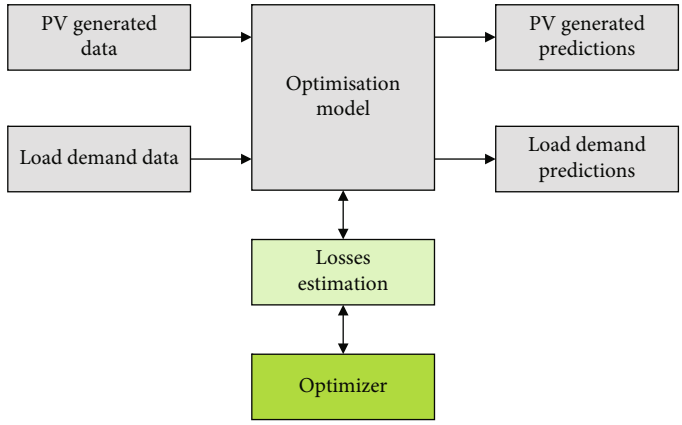

Figure 2: Prediction model.

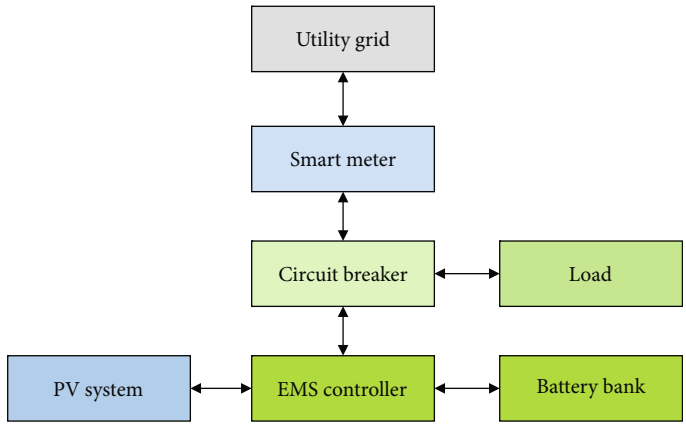

Figure 3: Grid-based PV system.

model. A convoluted formula must be used to go back and forth from the logistic equation to an OLS-type equation in logistic regression, and this formula must be used in both directions. In logistic formulas, the probability that $Y = 1$ occurs is denoted by the letter P. The probability that Y is equal to zero is equal to $1 - P$.

$$\ln\left(\frac{P}{1-P}\right) = a + bX. \tag{4}$$

The regression line equation $a + bX$ is derived from the ln sign, which signifies a natural logarithm and is represented by the letters $a + bX$.

The regression equation can also be used to get the value of P. Thus, only the regression quantity is known, and the study can calculate theoretically the probability that $Y = 1$ for a given number of points in the regression.

$$P = \frac{\exp(a + bX)}{1 + \exp(a + bx)} = \frac{e^{a+bx}}{1 + e^{a+bx}}, \tag{5}$$

where
exp: Exponent function, *e*.

3.2.1. Multiple Logistic Regression. Logistic regression, like ordinary least-squares regression, can be used with more than one predictor in the same way. There are a variety of alternatives for analysing the data, much like there are for regression. There are several ways to input variables: sequentially in a stepwise fashion, continuously, or in blocks. The results are interpreted through the use of OLS regression. The slopes and odds ratios of the dependent variable represent the predicted value obtained through a dependent variable. A slope obtained mainly represents the changes made at unit change in underlying predictor when the effect of the other variable is held constant. To examine whether or not the owner previous business ownership has an impact on the prediction of widget business failure. Using multiple logistic regression, it is possible to examine whether or not years of experience and previous business ownership are predictive of success or failure in a new firm.

4. Results and Discussions

The study presents a description of the simulation findings obtained for the proposed PV-battery EMS multiobjective predictive control system. The data that will be used in the simulation is discussed at the beginning of the simulation.

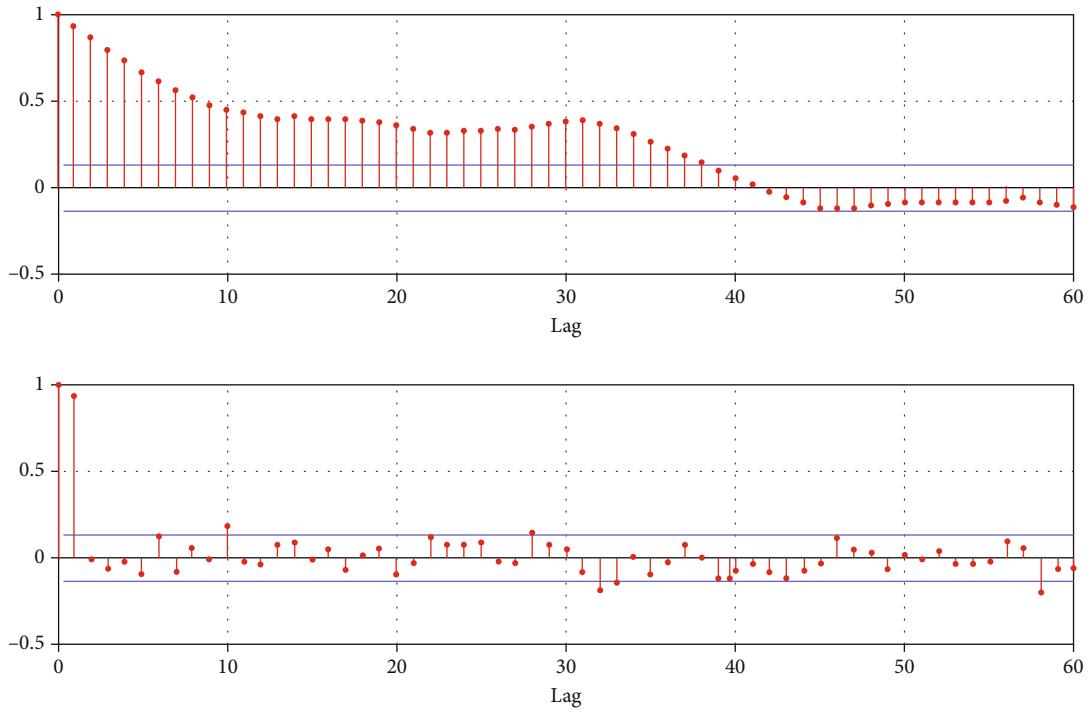

Figure 4: Autocorrelation output.

Following that is the prediction model performance on the displayed test dataset. Finally, dynamic electricity pricing is provided in order to evaluate the success of the proposed methodology.

In this section, the accuracy of the chained prediction model consisting of the LR model is evaluated in light of the hourly statistics and PV energy generation. The 1000 iterations of the prediction model, which is similar to the model that was used to predict the load and PV output datasets, were carried out in the same way. Because the stochastic optimization approach is utilised to train both the LR models, both models have dropout layers, as pointed out by Adam, and the autocorrelation output is given in Figure 4. It is necessary to run the model through multiple iterations in order to make accurate predictions. A single run of LR is performed due to the deterministic nature of the model output results.

For comparison, the normalised absolute error for each model on daily prediction is depicted in Figure 4. As a result, when converting hourly mean absolute errors to one-day spans, a 24-hour average is taken into consideration.

In Figure 4, the neat forecast models are displayed first on the residential load dataset. Our LR model, on average, has the lowest prediction error of all the models tested. The stochastic behaviour, on the other hand, is easily visible, as they exhibit some randomness in their prediction errors, whereas the prediction errors of nave and SVM regression are more deterministic for the same datasets.

The figure shows the PV energy production dataset, which is stochastic. Because of the random PV energy generation dataset, the model is influenced by a range of characteristics, such as solar irradiance and ambient temperature,

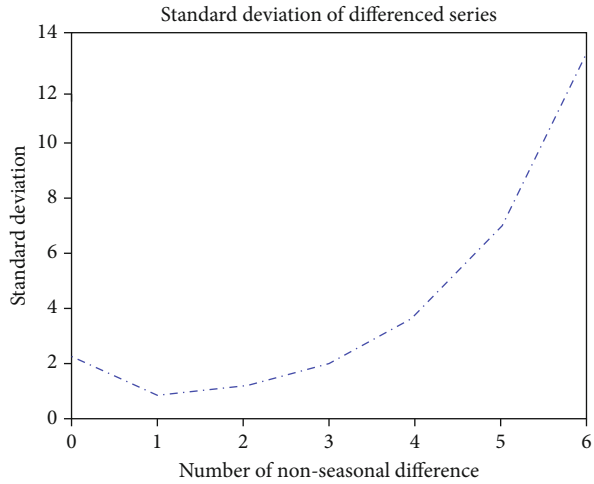

Figure 5: Standard deviation of forecasting.

this is the case. Because PV energy generation data contains a high degree of temporal variability, stochastic prediction using LR is more effective at learning this information.

For quite some time, researchers have been working on novel control and optimization approaches for the efficient management of energy in high-efficiency systems. This system, although simple to install, is focused on making the most of the power provided by the PV array rather than taking advantage of the full range of GCHES features and capabilities. This results as in Figures 5 and 6 in control behaviour that is comparable to that of a stand-alone HES.

Even though the control mechanism itself was straightforward, it was necessary to collect a historical data and it

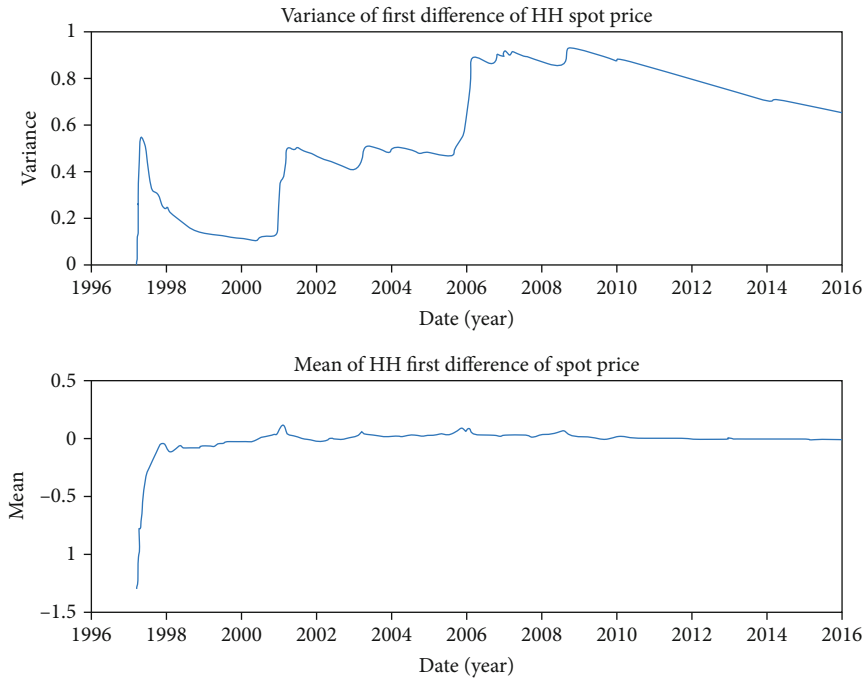

Figure 6: Mean and variance of forecasting.

can computationally run demanding the optimization procedure in order to optimise decision trees. In addition, if the cost of electricity and/or the pattern of solar irradiation change, the control model will need to be revised and updated. When compared with traditional control methods, such as flowcharts and trees, predictive control systems use predicted HES variables to update their respective EMS control parameters, saving time and money.

Because of the sliding window training strategy, our prediction model can adjust the output uncertainties and load pattern even in the absence of large historical data. As a result, our proposed prediction model is capable of identifying high-quality solutions to optimise objectives while requiring no preprocessing or data to be used in its development. The implementation complexity is further lowered by the use of only one control parameter, the maximum SoC limit, which reduces the number of steps required. The authors also provide a hierarchical control system for governing information flows and preventing the prediction model from being trained at night, thereby reducing the processing load.

5. Conclusions

This paper discusses LR-based on-grid predictive energy management for distributed energy resources. When it comes to renewable energy sources, a solar array like the one addressed in this study is one of the types in which the battery bank serves as a technology for energy storage. It is necessary to use LR in order to optimise energy exchange with the utility grid. By employing a training technique, the prediction model is capable of properly estimating photovoltaic energy output and load one step ahead of time. The maximum amount of CO_2 that can be produced as well as the maximum amount of charge that can be stored in a battery bank serve as the constraints on the optimization issue. The proposed approach is put through its paces on a dynamic power cost basis. When compared to existing energy systems, the proposed approach and prediction model can handle more than half of the total yearly load requirement, which is a significant improvement. Achieving the lowest cost of electricity is the economic goal, while lowering emissions is the environmental goal and reaching the greatest possible charge state for battery bank is the technical goal. Sliding window prediction is used to evaluate the performance of the LR model over a 1000-run period, utilising data from PV energy generation and load demand. In future work, the proposed method can improvise the performance, accuracy, and the other metrics using several deep learning mechanisms.

Data Availability

The data used to support the findings of this study are included within the article. Further data or information is available from the corresponding author upon request.

Conflicts of Interest

The authors declare that there is no conflict of interest regarding the publication of this paper.

Acknowledgments

The authors thank the Wolaita Sodo University for providing help during the research and preparation of the manuscript.

References

[1] C. Bordons, F. Garcia-Torres, and M. A. Ridao, *Model Predictive Control of Microgrids*, vol. 358, Springer, Berlin/Heidelberg, Germany, 2020.

[2] A. Maxim and C. F. Caruntu, "Coalitional distributed model predictive control strategy for vehicle platooning applications," *Sensors*, vol. 22, no. 3, p. 997, 2022.

[3] L. Xiong, P. Li, Z. Wang, and J. Wang, "Multi-agent based multi objective renewable energy management for diversified community power consumers," *Applied Energy*, vol. 259, article 114140, 2020.

[4] A. L. Bukar, C. W. Tan, L. K. Yiew, R. Ayop, and W. S. Tan, "A rule-based energy management scheme for long-term optimal capacity planning of grid-independent microgrid optimized by multi-objective grasshopper optimization algorithm," *Energy Conversion and Management*, vol. 221, article 113161, 2020.

[5] V. V. S. N. Murty and A. Kumar, "Multi-objective energy management in microgrids with hybrid energy sources and battery energy storage systems," *Protection and Control of Modern Power Systems*, vol. 5, no. 1, pp. 1–20, 2020.

[6] F. Pilati, G. Lelli, A. Regattieri, and M. Gamberi, "Intelligent management of hybrid energy systems for techno-economic performances maximisation," *Energy Conversion and Management*, vol. 224, article 113329, 2020.

[7] C. Mokhtara, B. Negrou, A. Bouferrouk, Y. Yao, N. Settou, and M. Ramadan, "Integrated supply-demand energy management for optimal design of off-grid hybrid renewable energy systems for residential electrification in arid climates," *Energy Conversion and Management*, vol. 221, article 113192, 2020.

[8] N. Gholizadeh, G. B. Gharehpetian, M. Abedi, H. Nafisi, and M. Marzband, "An innovative energy management framework for cooperative operation management of electricity and natural gas demands," *Energy Conversion and Management*, vol. 200, article 112069, 2019.

[9] M. Martinez-Pabon, T. Eveleigh, and B. Tanju, "Optimizing residential energy management using an autonomous scheduler system," *Expert Systems with Applications*, vol. 96, pp. 373–387, 2018.

[10] M. Durairasan and D. Balasubramanian, "An efficient control strategy for optimal power flow management from a renewable energy source to a generalized three-phase microgrid system: a hybrid squirrel search algorithm with whale optimization algorithm approach," *Transactions of the Institute of Measurement and Control*, vol. 42, no. 11, pp. 1960–1976, 2020.

[11] B. Jyoti Saharia, H. Brahma, and N. Sarmah, "A review of algorithms for control and optimization for energy management of hybrid renewable energy systems," *Journal of Renewable and Sustainable Energy*, vol. 10, no. 5, article 053502, 2018.

[12] M. Dahmane, J. Bosche, and A. El-Hajjaji, "Power management strategy based on weather prediction for hybrid standalone system," *Energy Procedia*, vol. 83, pp. 330–340, 2015.

[13] A. Agüera-Pérez, J. C. Palomares-Salas, J. J. G. De La Rosa, and O. Florencias-Oliveros, "Weather forecasts for microgrid energy management: review, discussion and recommendations," *Applied Energy*, vol. 228, pp. 265–278, 2018.

[14] B. C. Csáji, A. Kovács, and J. Váncza, "Prediction and robust control of energy flow in renewable energy systems," *IFAC Proceedings Volumes*, vol. 47, no. 3, pp. 3663–3669, 2014.

[15] V. M. Zavala, E. M. Constantinescu, T. Krause, and M. Anitescu, *Weather forecast-based optimization of integrated energy systems (No. ANL/MCS-TM-305)*, Argonne National Lab.(ANL), Argonne, IL (United States), 2009.

[16] F. Wang, Z. Xuan, Z. Zhen, K. Li, T. Wang, and M. Shi, "A day-ahead PV power forecasting method based on LSTM-RNN model and time correlation modification under partial daily pattern prediction framework," *Energy Conversion and Management*, vol. 212, article 112766, 2020.

[17] S. Sobri, S. Koohi-Kamali, and N. A. Rahim, "Solar photovoltaic generation forecasting methods: a review," *Energy Conversion and Management*, vol. 156, pp. 459–497, 2018.

[18] H. Wang, Y. Liu, B. Zhou et al., "Taxonomy research of artificial intelligence for deterministic solar power forecasting," *Energy Conversion and Management*, vol. 214, article 112909, 2020.

[19] A. Nespoli, E. Ogliari, S. Leva et al., "Day-ahead photovoltaic forecasting: a comparison of the most effective techniques," *Energies*, vol. 12, no. 9, p. 1621, 2019.

[20] Y. Cheng, Z. Liu, and Y. Morimoto, "Attention-based SeriesNet: an attention-based hybrid neural network model for conditional time series forecasting," *Information*, vol. 11, no. 6, p. 305, 2020.

[21] Z. Shen, Y. Zhang, J. Lu, J. Xu, and G. Xiao, "A novel time series forecasting model with deep learning," *Neurocomputing*, vol. 396, pp. 302–313, 2020.

[22] Y. Cheng and Y. Morimoto, "Triple-stage attention-based multiple parallel connection hybrid neural network model for conditional time series forecasting," *IEEE Access*, vol. 9, pp. 29165–29179, 2021.

[23] W. W. Wei, "Time Series Analysis," *In The Oxford Handbook of Quantitative Methods in Psychology*, vol. 2, 2006.

[24] A. Borovykh, S. Bohte, and C. W. Oosterlee, "Dilated convolutional neural networks for time series forecasting," *Journal of Computational Finance, Forthcoming.*, vol. 22, no. 4, pp. 73–101, 2018.

Hindawi
International Journal of Photoenergy
Volume 2022, Article ID 2881603, 7 pages
https://doi.org/10.1155/2022/2881603

Research Article

Optimal Placement of Hybrid Wind-Solar System Using Deep Learning Model

Sundeep Siddula,[1] G. K. Prashanth,[2] Praful Nandankar,[3] Ram Subbiah,[4] Saikh Mohammad Wabaidur,[5] Essam A. Al-Ammar,[6] M. H. Siddique,[7] and Subash Thanappan[8]

[1]*Department of Electrical and Electronics Engineering, Vignana Bharathi Institute of Technology, Aushapur, Telangana 501301, India*
[2]*Department of Master of Computer Applications, Siddaganga Institute of Technology, Tumakuru, Karnataka 572103, India*
[3]*Department of Electrical Engineering, Government College of Engineering, Nagpur, Maharashtra 441108, India*
[4]*Department of Mechanical Engineering, Gokaraju Rangaraju Institute of Engineering and Technology, Hyderabad, Telangana, 500090, India*
[5]*Chemistry Department, College of Science, King Saud University, Riyadh 11451, Saudi Arabia*
[6]*Department of Electrical Engineering, College of Engineering, King Saud University, P. O. Box 800, Riyadh 11421, Saudi Arabia*
[7]*Intelligent Construction Automation Centre, Kyungpook National University, Republic of Korea*
[8]*Department of Civil Engineering, School of Civil and Environmental Engineering, Ambo University, Ambo, Ethiopia*

Correspondence should be addressed to Subash Thanappan; subash.thanappan@ambou.edu.et

Received 10 February 2022; Revised 23 March 2022; Accepted 31 March 2022; Published 25 May 2022

Academic Editor: V. Mohanavel

Copyright © 2022 Sundeep Siddula et al. This is an open access article distributed under the Creative Commons Attribution License, which permits unrestricted use, distribution, and reproduction in any medium, provided the original work is properly cited.

In this paper, we develop an optimal placement of solar-wind energy systems using restricted Boltzmann machine (RBM). The RBM considers various factors to scale the process of optimal placement and enables proper sizing and placement for attaining increased electricity production from both wind and solar systems. The multiobjective criterion from both solar and wind energy farms simulated on MATLAB simulator shows an increased number of accuracies with reduced mean average error and computation time during training and testing. The results show that the RBM achieves improved rate of finding the optimal placement with a lesser cost and computation time of lesser than 2 ms than other methods.

1. Introduction

The wind velocity and the intensity of solar radiation are the critical renewable energy source like solar energy. Both factors exhibit strong nonlinearity and are highly dependent on the surrounding environment. Due to the fact that they cut greenhouse gas emissions and are environmentally friendly, accurate forecasts are required for a number of applications. Following accurate forecasting of these factors, researchers discovered that machine learning can predict relative moisture, temperature, wind speed, and solar radiation with high accuracy and predictability. For predicting highly nonlinear variables, artificial neural systems are the most effective method of prediction available.

In recent years, it has become increasingly evident that global warming poses a significant threat to human life, with potentially catastrophic effects. As a result of variable fuel prices and the environmental damage caused by excessive use, experts have shifted their attention away from fossil fuels and toward renewable energy (RE) and other kinds of alternative energy. Renewable energy sources such as photovoltaic (PV) and wind power (WP) have played a significant role in the creation of electricity since they are readily available and environmentally friendly [1, 2]. When renewable

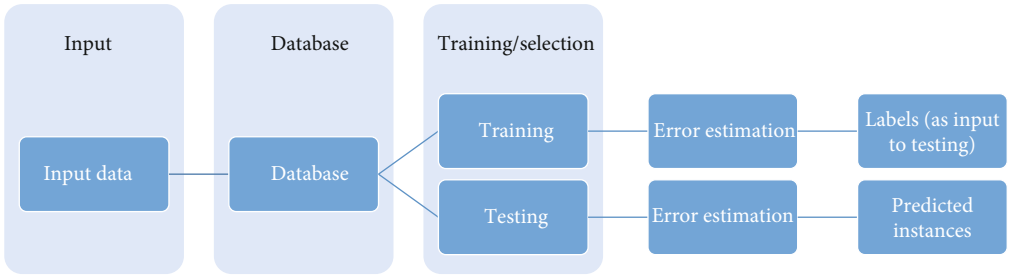

Figure 1: Machine learning approach for optimal placement via features.

energy sources are integrated with power grid, microgrids (MGs) and smart grids (SGs) emerge as a result of the increased use of renewable energy [3–5]. To keep the program costs down, the adoption of greater WT and PV reproduction technologies is encouraged in order to increase the employment of fast-growing renewable sources of energy. In addition, wind turbines and solar photovoltaic technology buildings may be considered to be the most commonly employed and interconnected technologies. Energy derived from renewable sources will soon be more affordable than conventional electricity. Electricity costs are all monetary indicators of power efficiency. The size, features, and WT and PV technology manufacturers can all have a substantial impact on power efficiency.

Hybrid renewable energy technologies, which combine multiple renewable energy sources, are quickly becoming the industry standard. Both wind energy and solar energy are currently considered to be viable renewable energy sources. However, solar energy is considered to be more significant due to the large savings that it provides [6–8], whereas wind energy is considered less significant. It may be difficult to maintain stability in a hybrid system because of some of its disadvantages, such as integration difficulties and the fact that renewable sources are often irregular, unmanageable, stochastic, and exceedingly changeable, which may make it difficult to achieve stability. When dealing with power systems, it is possible to run into a range of troublesome scenarios, including load disparity, voltage unpredictability, poor load following, and poor power quality [9–11].

Because of the transient energy characteristics of multi-WT integration and PV power system adjustment, the OPF problem is made more complicated. When attempting to define and address the OPF that develops in WT and PV technology, the following elements must be considered: an estimation of power output based on dependable wind speed and solar radiation characteristics, a choice of goal functions, an outline of the technical issues, an explanation of how to solve the OPF problem, and a conclusion. Recently, some of the aforementioned functions have been the focus of research into the OPF problem [12–14]. Using new and innovative ideas and technology to increase the usage of renewable energy sources in the power system, these issues can be mitigated to a certain extent. Figure 1 shows the machine learning approach for optimal placement via features.

Our discussion of the many scenarios in which RERs and grid-connected applications can be deployed can be found in [15–18]. As a result of this initiative, photovoltaic (PV) energy storage is being integrated into commercial buildings at a faster rate than ever before. A microgrid grid environment, as well as the technologies that go into microgrid applications with energy coordination [19–25], has one of their key purposes, the stability of the flow of energy. Review the worldwide energy situation as well as the integration of renewable energy sources, especially battery energy storage systems (BESS) and solar photovoltaic (PV). By monitoring and correcting power flow in frequency deviations and neutral lines, the model predictive regulator is crucial in maintaining a healthy balance between active electricity generation and active electricity demand in the microgrid. The main contribution of the paper includes the development of an optimal placement of solar-wind energy systems using restricted Boltzmann machine (RBM).

2. Background

The power of the sun and the wind are the most important renewable energy sources in the United States. A long-term source of energy, renewable energy, can endure the effects of changing climate conditions [1] and is becoming increasingly popular. To avoid financial losses, it is vital to forecast wind speeds on a continuous basis [2, 3]. Solar energy systems rely on accurate estimates of solar radiation to function properly. Accurate estimates of wind speed can help to improve both the safety and the economics of wind energy producing operations. Wind energy, which is a variable and nonlinear kind of energy, is not only cleaner than fossil fuels, but it is also safer and more environmentally friendly [4, 5]. It is also more cost-effective than fossil fuels. It is possible to anticipate wind speed in a variety of timeframes. Short-term forecasting, on the other hand, has a higher degree of precision [6–8].

Wind speed, on the other hand, exhibits a significantly higher degree of nonlinearity than temperature. The temperature, solar panels, and wind all have an effect on sun radiation the majority of the time [8]. When it comes to electricity generation, solar energy is an excellent choice because it is both environmentally friendly and reasonably priced [9]. A variety of models can be employed in order to forecast wind energy and solar radiation. For expressing intricate connections between input and output, neural networks are an extremely powerful tool to have at your disposal [10]. Networks of nodes (NN) outperform other types of networks in terms of generalization.

Because wind and solar radiation are nonlinear, artificial neural networks are the best option. In the future, as a result of this planned research, society and the environment will be better equipped to deal with natural calamities. IIT Delhi, India National Institute of Atmospheric Science, is currently engaged in research on climate change in the country. In the design and deployment of artificial neural networks, MPPT control is the key. India has developed a solar energy business in order to meet the country energy requirements. In India, a target of 20 GW of installed capacity has been set for 2022.

In addition, 42 solar power plants have been built across the country to provide electricity. Large-scale data analysis is a demanding task that machine learning can assist with [13]. Solar energy reduces the amount of money that businesses spend on electricity. Energy from coal and natural gas is available at a cost ranging from 7 to 30 cents per kilowatt-hour, whereas solar energy is available at a cost of between 2 and 12 cents per kilowatt-hour. Those interested in investing in commercial solar energy have a wide range of options when it comes to business strategies. Wind turbines and windmills are employed in a number of applications in the local community. In the world electrical supply, renewable energy sources account for around 26% of total supply. There are 80,000 villages in India that must be connected to the electricity grid. [14] There are a total of 2.1 billion people on the planet who do not have access to electricity. Renewable energy sources will account for 95% of our total energy consumption requirements by 2050. The Ministry of New and Renewable Energy has received critical policy support from the Government of India in order to expand the use of renewable energy sources in the country (MNRE).

A wind turbine may be used to create power by harnessing the speed of the wind. Wind turbines provided electricity to the country to the tune of 11% of total electricity use. According to [16], that ratio will increase to 16.5% in 2020 and 27% in 2030. Wind speed and solar radiation may now be predicted with high accuracy using a range of artificial neural network (ANN) approaches, including different architectures and adjustments to the rules of learning that are currently being researched. Predictions for wind turbines and solar panels can be produced with the help of an energy management system (EMS) [17].

3. Proposed Method

In this study, many methodologies for data visualization were studied as in Figure 2. The study involves data extraction, data preprocessing, feature selection, model training and testing, and evaluation. This project purpose was to identify important patterns that would allow statistical learning models to learn from their own usage patterns. This technique selects the suitable feature (in this case, weather factors) for the procedure in order to develop a robust model. It is vital to remember that in this situation, power or energy may be the ideal characteristic to have.

3.1. Preprocessing. The manipulation of data was used and not used in the processing of the data that was collected.

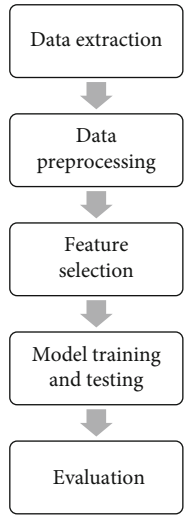

Figure 2: Proposed model.

Data adjustments were carried out with the help of RFECV. To study the data, RBM prediction algorithms were utilised, and correlations between various dataset features were established through the investigation. It was the primary purpose of this study to identify meaningful trends in usage that might be exploited to train statistical learning models.

In step 2, we apply preprocessing and feature engineering to the raw data in order to remove any trash values that could interfere with our model performance. Feature selection is an option in stage 3 in order to reduce computing time and errors, and it is used to do this. Its properties are further refined, and zero padding is applied where necessary to make the model more durable and efficient. During step 4, RFECV is used to separate and train the data in order to remove the repetitive features that could have an impact on the model outputs. Furthermore, the data obtained is evaluated using the seven most commonly used regression models, which are listed below.

3.2. Learning Model. When the estimator runs through each iteration, it takes into account all of the data and all of the features in order to build a set of scores. Each of the scores in this collection will be associated with a characteristic. Consider the following scenario: so we have a total of 20 characteristics to choose from, and we need to select the top five characteristics that will have the greatest impact on the accuracy of the model. Each iteration of the algorithm begins deleting features if and only if the obtained score is less than that predicted by the algorithm in the previous iteration. Cross-validation can be used as an alternative, in which the training and test sets are separated from one another using a k-fold cross-validation procedure. The process of learning and evaluating takes place at the conclusion of every fold.

3.3. Restricted Boltzmann Machine. RBMs are constructed by layering stochastic hidden units on top of visible units, on top of hidden stochastic units, and on top of visible units. RBM bipartite graphs, which can be used to display them,

do not contain any visible-visible or hidden-hidden links, respectively. The illustration of proposed RBM model is given in Figure 3.

The joint distribution function in RBM is represented as $\boldsymbol{p}(\boldsymbol{v}, \boldsymbol{h}; \boldsymbol{\theta})$ that consists of hidden units $\boldsymbol{h}$ and visible units $\boldsymbol{v}$ that takes into consideration the model parameters $\boldsymbol{\theta}$, which is measured as an energy function $\boldsymbol{E}(\boldsymbol{v}, \boldsymbol{h}; \boldsymbol{\theta})$ as given below:

$$p(v, h; \theta) = \frac{\exp\ (-E(v, h; \theta))}{Z}, \tag{1}$$

where

$\boldsymbol{Z}$ is the partition function,

$$Z = \sum_{v} \sum_{h} \exp(-E(v, h; \theta)). \tag{2}$$

The study enables the computation of the marginal probability density function that gets aligned with the visible vector $\mathbf{v}$ as below:

$$p(v; \theta) = \frac{\sum_{h} \exp(-E(v, h; \theta))}{Z}. \tag{3}$$

For a Bernoulli-Bernoulli relation between the hidden and visible RBM, the study computes the energy function as below:

$$E(v, h; \theta) = -\sum_{i=1}^{I} \sum_{j=1}^{J} w_{ij} v_i h_j - \sum_{i=1}^{I} b_i v_i - \sum_{j=1}^{J} a_j h_j, \tag{4}$$

where

$\boldsymbol{v_i}$: visible unit

$\boldsymbol{h_j}$: hidden unit

$\boldsymbol{b_i}$ and $\boldsymbol{a_j}$: bias

$\boldsymbol{I}$: total hidden units

$\boldsymbol{J}$: total hidden units

$\boldsymbol{w_{ij}}$: symmetric interaction between $\boldsymbol{v_i}$ and $\boldsymbol{h_j}$. Finally, the study computes the conditional probabilities as below for hidden unit and then the visible unit:

$$\begin{aligned} p(h_j = 1 | v; \theta) &= \sigma\left(\sum_{i=1}^{I} w_{ij} v_i + a_j\right), \\ p(v_i = 1 | h; \theta) &= \sigma\left(\sum_{j=1}^{J} w_{ij} h_j + b_i\right), \end{aligned} \tag{5}$$

where

$$\sigma(x) = \frac{1}{(1 + \exp\ (x))}. \tag{6}$$

4. Results and Discussions

The assessment is conducted in MALTAB environment, where the ANN was used to compare the mean squared error (MSE), the coefficient of determination (R^2), and the mean absolute error (MAE) of RBM for the annual datasets, with the results being presented below. Weather conditions and the output of the hybrid power system were used to collect and analyse the 77,000 samples that were collected and analysed. RBMs are trained, tested, and verified using the data that has been collected. Outliers, typographical errors, and missing values were removed from the datasets to make them more representative. The validation procedure was employed in order to simplify the network to the point where no more improvement could be detected. Finally, the developed model is put to the test in order to determine its overall effectiveness.

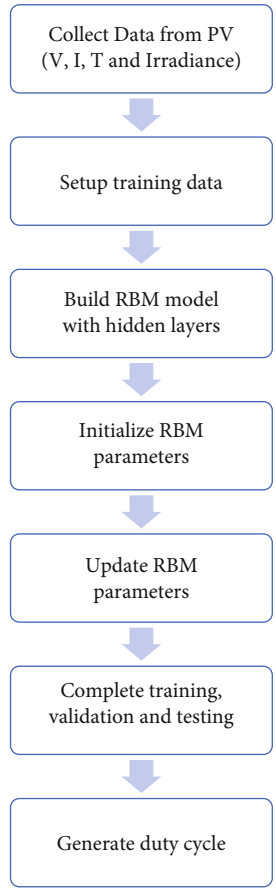

Figure 3: Proposed RBM model.

Specifically, three groups of datasets were created: one for training and validating models, and another for testing models. It is estimated that around 75% of the data was utilised for training, with the remaining 15% being used for testing and validation. Through network training, the output values of MSE and $\boldsymbol{R}$ were tested for the input datasets, and the results were reported. The presence of an error is not shown if the MSE is zero, and the $\boldsymbol{R}$-value is close to one, because zero indicates a weak correlation as in Figure 4.

The dataset was cleaned up at the start of the experiment, and then, the values were scaled between 0 and 1 as the experiment went on. Following the data purification procedure, classifiers were evaluated using the MSE, MAE, R^2, among other metrics as in Figure 5.

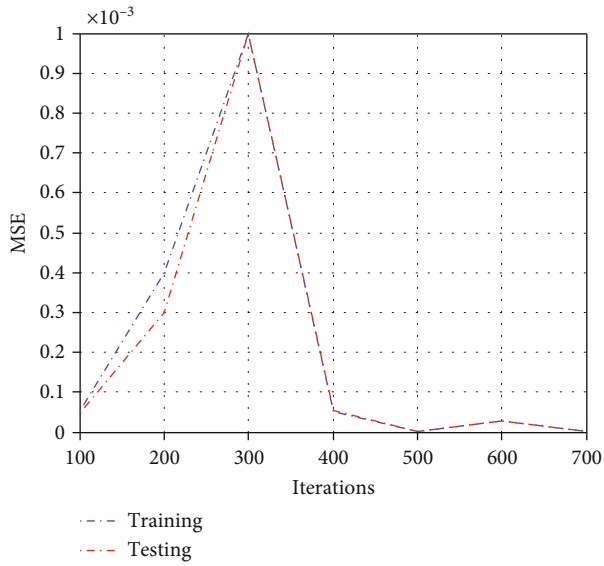

Figure 4: MSE.

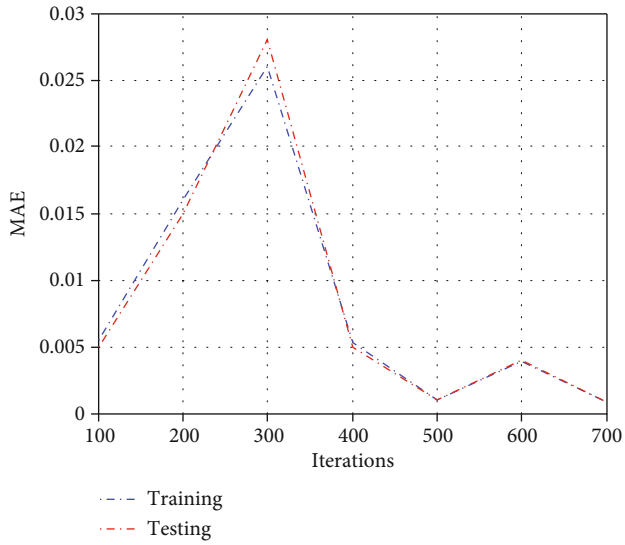

Figure 5: MAE.

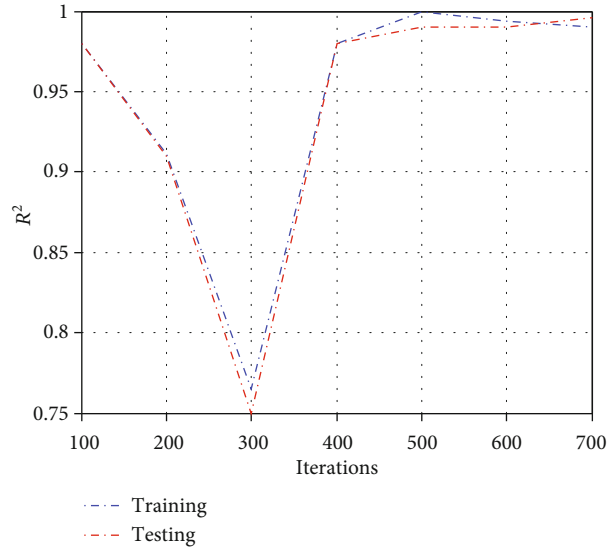

Figure 6: Coefficient of determination.

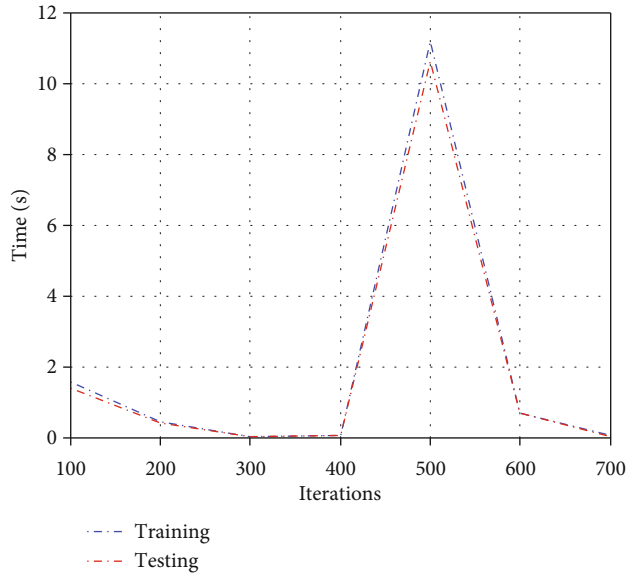

Figure 7: Computational time.

Cross-validation is a technique that is used to score a huge number of features and then select the set of features that scored the highest. The MSE is kept, and fewer features are lost as a result. In addition, the amount of time necessary to train the learning model is significantly decreased as a result of this.

The goal levels of power and energy can be predicted independently of one another. As a result, once the energy has been eliminated, it is possible to regard power as a variable to be targeted. Once the linear regression investigation was done, the researchers found that humidity, temperature, wind direction, air pressure, and precipitation all had relatively small associations with PV production. Although the R^2 values for power and energy were 0.79 and 0.74, respectively, they were significantly linked with solar irradiation and wind, as illustrated in Figures 6 and 7. According to this knowledge, these elements will have an impact on the ability to forecast output variables. It is directly related to changes in solar irradiation and wind speed that the output power of a PV system varies.

5. Conclusion

The results of the simulation are analysed, and the effectiveness of the proposed controller is tested under a variety of weather conditions. A computer programme called MATLAB was used to design and simulate the projected wind and hybrid PV/wind energy systems, which were then connected to a microgrid for operation. The goal is to implement the proposed RBM via a number of simulations of the

proposed system to determine how it would operate in a variety of real-world settings. In the future, the study enables assessment of statistical and deep learning models for predicting the values of optimal nature.

Data Availability

The data used to support the findings of this study are included within the article. Further data or information is available from the corresponding author upon request.

Conflicts of Interest

The authors declare that there are no conflicts of interest regarding the publication of this paper.

Acknowledgments

The authors appreciate the supports from Ambo University, Ambo, Ethiopia, for providing help during the research and preparation of the manuscript. The work was supported by the Researchers Supporting Project number (RSP2022R492), King Saud University, Riyadh, Saudi Arabia.

References

[1] L. Abualigah, R. A. Zitar, K. H. Almotairi et al., "Wind, solar, and photovoltaic renewable energy systems with and without energy storage optimization: a survey of advanced machine learning and deep learning techniques," *Energies*, vol. 15, no. 2, p. 578, 2022.

[2] S. Jamshidi, K. Pourhossein, and M. Asadi, "Size estimation of wind/solar hybrid renewable energy systems without detailed wind and irradiation data: a feasibility study," *Energy Conversion and Management*, vol. 234, article 113905, 2021.

[3] P. A. Adedeji, S. A. Akinlabi, N. Madushele, and O. O. Olatunji, "Hybrid neurofuzzy wind power forecast and wind turbine location for embedded generation," *International Journal of Energy Research*, vol. 45, no. 1, pp. 413–428, 2021.

[4] G. A. Kumar, S. Shankar, and K. Murthy, "Design and control of autonomous hybrid wind solar system with DFIG supplying three-phase four-wire loads," *International Journal of Renewable Energy Technology*, vol. 12, no. 3, pp. 269–299, 2021.

[5] O. Zarrad, M. A. Hajjaji, and M. N. Mansouri, "Hardware implementation of hybrid wind-solar energy system for pumping water based on artificial neural network controller," *Studies in Informatics and Control*, vol. 28, no. 1, pp. 35–44, 2019.

[6] H. Beltran, J. Cardo-Miota, J. Segarra-Tamarit, and E. Pérez, "Battery size determination for photovoltaic capacity firming using deep learning irradiance forecasts," *Journal of Energy Storage*, vol. 33, article 102036, 2021.

[7] L. L. Li, X. Zhao, M. L. Tseng, and R. R. Tan, "Short-term wind power forecasting based on support vector machine with improved dragonfly algorithm," *Journal of Cleaner Production*, vol. 242, article 118447, 2020.

[8] D. Chandola, H. Gupta, V. A. Tikkiwal, and M. K. Bohra, "Multi-step ahead forecasting of global solar radiation for arid zones using deep learning," *Procedia Computer Science*, vol. 167, pp. 626–635, 2020.

[9] E. Han and N. Ghadimi, "Model identification of proton-exchange membrane fuel cells based on a hybrid convolutional neural network and extreme learning machine optimized by improved honey badger algorithm," *Sustainable Energy Technologies and Assessments*, vol. 52, article 102005, 2022.

[10] O. Bamisile, A. Oluwasanmi, S. Obiora, E. Osei-Mensah, G. Asoronye, and Q. Huang, "Application of Deep Learning for Solar Irradiance and Solar Photovoltaic Multi-Parameter Forecast," *Energy Sources, Part A: Recovery, Utilization, and Environmental Effects*, pp. 1–21, 2020.

[11] J. Devaraj, R. Madurai Elavarasan, G. M. Shafiullah, T. Jamal, and I. Khan, "A holistic review on energy forecasting using big data and deep learning models," *International Journal of Energy Research*, vol. 45, no. 9, pp. 13489–13530, 2021.

[12] R. Ahmed, V. Sreeram, Y. Mishra, and M. D. Arif, "A review and evaluation of the state-of-the-art in PV solar power forecasting: techniques and optimization," *Renewable and Sustainable Energy Reviews*, vol. 124, article 109792, 2020.

[13] A. Almadhor, H. T. Rauf, M. A. Khan, S. Kadry, and Y. Nam, "A hybrid algorithm (BAPSO) for capacity configuration optimization in a distributed solar PV based microgrid," *Energy Reports*, vol. 7, pp. 7906–7912, 2021.

[14] S. Aslam, H. Herodotou, S. M. Mohsin, N. Javaid, N. Ashraf, and S. Aslam, "A survey on deep learning methods for power load and renewable energy forecasting in smart microgrids," *Renewable and Sustainable Energy Reviews*, vol. 144, article 110992, 2021.

[15] T. Lan, K. Jermsittiparsert, T. Alrashood, M. S Rezaei, L. Al-Ghussain, and M. A Mohamed, "Application of Deep Learning for Solar Irradiance and Solar Photovoltaic Multi-Parameter Forecast. Energy Sources, Part A: Recovery, Utilization, and Environmental Effects," *Energies*, vol. 14, no. 3, p. 569, 2021.

[16] S. M. J. Jalali, S. Ahmadian, A. Kavousi-Fard, A. Khosravi, and S. Nahavandi, "Automated deep cnn-lstm architecture design for solar irradiance forecasting," *IEEE Transactions on Systems, Man, and Cybernetics: Systems*, vol. 52, no. 1, pp. 54–65, 2022.

[17] S. R. Ara, S. Paul, and Z. H. Rather, "Two-level planning approach to analyze techno-economic feasibility of hybrid offshore wind-solar pv power plants," *Sustainable Energy Technologies and Assessments*, vol. 47, article 101509, 2021.

[18] A. A. Du Plessis, J. M. Strauss, and A. J. Rix, "Short-term solar power forecasting: investigating the ability of deep learning models to capture low-level utility-scale photovoltaic system behaviour," *Applied Energy*, vol. 285, article 116395, 2021.

[19] A. Masoumi, S. Ghassem-zadeh, S. H. Hosseini, and B. Z. Ghavidel, "Application of neural network and weighted improved PSO for uncertainty modeling and optimal allocating of renewable energies along with battery energy storage," *Applied Soft Computing*, vol. 88, article 105979, 2020.

[20] F. Ekinci, T. Demirdelen, I. O. Aksu, K. Aygul, B. Esenboga, and M. Bilgili, "A novel hybrid metaheuristic optimization method to estimate medium-term output power for horizontal axis wind turbine," *Proceedings of the Institution of Mechanical Engineers, Part A: Journal of Power and Energy*, vol. 233, no. 5, pp. 646–658, 2019.

[21] Q. Tian, Y. Wu, X. Ren, and N. Razmjooy, "A new optimized sequential method for lung tumor diagnosis based on deep learning and converged search and rescue algorithm," *Biomedical Signal Processing and Control*, vol. 68, article 102761, 2021.

[22] M. Kiehbadroudinezhad, A. Merabet, A. Rajabipour et al., "Optimization of wind/solar energy microgrid by division

algorithm considering human health and environmental impacts for power-water cogeneration," *Energy Conversion and Management*, vol. 115064, 2021.

[23] Y. Wu, T. Zhang, C. Xu et al., "Optimal location selection for offshore wind-PV-seawater pumped storage power plant using a hybrid MCDM approach: a two-stage framework," *Energy Conversion and Management*, vol. 199, article 112066, 2019.

[24] L. Luo, S. S. Abdulkareem, A. Rezvani et al., "Optimal scheduling of a renewable based microgrid considering photovoltaic system and battery energy storage under uncertainty," *Journal of Energy Storage*, vol. 28, article 101306, 2020.

[25] A. Routray, K. D. Mistry, S. R. Arya, and B. Chittibabu, "Applied Machine Learning in Wind Speed Prediction and Loss Minimization in Unbalanced Radial Distribution System," *Energy Sources, Part A: Recovery, Utilization, and Environmental Effects*, pp. 1–21, 2021.

Hindawi
International Journal of Photoenergy
Volume 2022, Article ID 1123251, 7 pages
https://doi.org/10.1155/2022/1123251

Research Article

Maximum Power Point Tracking of PV Grids Using Deep Learning

K. Rafeeq Ahmed,[1] Farrukh Sayeed,[2] K. Logavani,[3] T. J. Catherine,[4] Shimpy Ralhan,[5] Mahesh Singh,[5] R. Thandaiah Prabu,[6] B. Bala Subramanian,[7] and Adane Kassa[8]

[1]*Department of Electronics and Communication Engineering, School of Engineering, Presidency University, Bangalore, 560064, India*
[2]*Department of Electrical and Electronics Engineering, ACE College of Engineering, Karinkadamugal, Thiruvananthapuram, Kerala 695027, India*
[3]*Department of Electrical and Electronics Engineering, Government College of Engineering, Salem, Tamil Nadu 636011, India*
[4]*Department of Electrical and Electronics Engineering, R.M.K. College of Engineering and Technology, Puduvoyal, Thiruvallur, Tamil Nadu 601206, India*
[5]*Department of Electrical and Electronics Engineering, Shri Shankaracharya Technical Campus, Durg, Bhilai, Chhattisgarh 490020, India*
[6]*Department of Electronics and Communication Engineering, Saveetha School of Engineering, SIMATS, Chennai, 602105 Tamil Nadu, India*
[7]*Department of Biotechnology, Sejong University, Seoul, Republic of Korea*
[8]*Faculty of Mechanical Engineering, Arba Minch Institute of Technology (AMIT), Arba Minch University, Ethiopia*

Correspondence should be addressed to Adane Kassa; adane.kassa@amu.edu.et

Received 29 January 2022; Revised 10 April 2022; Accepted 12 April 2022; Published 25 May 2022

Academic Editor: V. Mohanavel

Copyright © 2022 K. Rafeeq Ahmed et al. This is an open access article distributed under the Creative Commons Attribution License, which permits unrestricted use, distribution, and reproduction in any medium, provided the original work is properly cited.

In this paper, we develop a deep learning model using back propagation neural network (BPNN) that helps to obtain maximum power point. This deep learning model aims to maximise the output power from the solar grids when the panels are connected with the boost converter under different variable load conditions. BPNN-DL enables the prediction of reference voltage at different weather conditions for severing the various output power that ensures maximum power with stable output voltage. The proposed BPNN-DL is tested under different conditions to estimate the robustness of the modules under internal/external interferences. The results of the simulation show that the proposed method achieves maximum output power from each panel compared with existing methods in terms of regression analysis on training, testing, and validation.

1. Introduction

Electricity is a need in our day-to-day lives. Historically, the combustion of fossil fuels for the generation of electricity has resulted in serious environmental and human health issues [1]. Because of this, attempts have been made recently to identify new ways to generate clean energy using sustainable resources. Photovoltaic (PV) systems convert sunlight directly into energy that can be stored or even connected to the grid [2]. PV systems have a high initial implementation cost, which is unfortunate. PV systems have a relatively low energy conversion efficiency [3]. Variations in the weather have an impact on energy output [4]. The effectiveness of a photovoltaic (PV) system can be affected by changes in humidity, temperature, and cloud [5]. This has led to numerous research efforts aimed at figuring out how to maximise the output power of PV panels regardless of the weather.

For a given set of solar insolation and ambient temperature, researchers studying the nonlinear properties of the PV system discovered a single operating point (output voltage)

where the PV system output power is maximised. The PV panel will produce less power than its maximum if the output voltage changes due to the load or for any other reason [6]. Solar radiation and temperature affect the output power [7]. All of the aforementioned make it extremely difficult to keep the system running at its maximum output power level for long periods of time. The goal here is to find a position where the PV panel maximum power output meets the demands of the system [8]. There have been a number of initiatives aimed at ensuring that PV systems operate at their maximum potential. One of the earliest approaches to the problem was the incremental conductance (IC) and the perturb and observe (PaO) [3]. As both strategies are simple to apply, they are frequently utilised in practise [3] [1, 9, 10].

The same problem was addressed in several ways in the literature, all with the goal of improving the PaO outcomes. The usage of machine learning was one attempt to solve the problem. The ability of deep learning to model nonlinear functions allowed for a precise estimate of the reference voltage in adherence with maximum power. Additionally, ANN-based approaches exhibited a rapid reaction in the testing phase, which was a significant advantage. In this paper, we develop a deep learning model using back propagation neural network (BPNN) that helps to obtain maximum power point. This deep learning model aims to maximise the output power from the solar grids when the panels are connected with the boost converter under different variable load conditions.

The main contribution of the work involves the following.

This deep learning model aims to maximise the output power from the solar grids when the panels are connects with the boost converter under different variable load conditions.

2. Background

Reproducing a neural network in association with parameters that connects to individual data points is the goal of the ANN model. There are no sophisticated mathematical equations or equations to mix multiple parameters in an ANN model [11]. When it comes to dealing with large numbers of unknown data points, an ANN technique requires less theoretical work than traditional methods [12]. Imported data is used to train ANNs, a process known as supervised learning or training. Like the human brain, the ANN is made up of many different types of neurons [13]. Weight [14] is the fractional number that connects these neurons. To be able to accurately forecast the results, the weights are adjusted during the training phase. Once the error surpasses a certain threshold, the weights are frozen [15].

It is possible to integrate the inputs into the network at various points. The data sets are divided into two groups based on the percentages of data points in each group. The datasets for training are used to train the deep learning. This data set is used to verify the trained deep learning, which is referred to as a validation data set [16]. The deep learning input-output parameters, as well as their training data, are imported. In this network, an error is acceptable until it is accepted by the system.

Validation data set are associated with the relevant real data set output parameter projections. An optimum deep learning can be recommended if the error exists between actual and projected results is less than the permissible maximum. When the error magnitude falls below the acceptable value, an algorithm combination that has an acceptable error magnitude will be selected as the deep learning. Before a permitted error is attained, the deep learning is loaded with training algorithms, but with the same training methodology for larger error values [17]. Analyses from the ideal deep learning confirm the generalisation capabilities of deep learnings that have been trained.

The MPPT algorithms are also studied in another study [18]. Control variables, techniques of control, and other factors were grouped into categories. Simulink Frameworks were used in this work to perform hands-on evaluations of the most commonly used MPPT algorithms in PV voltage ripple dynamic reactivity [19]. A PI controller has been used to improve the results of classic MPPT algorithms. Simulating MATLAB results with environmental factors such as fluctuating irradiance or rising temperatures has been discussed by the authors in [19]. When irradiance varies unexpectedly, the authors suggest a new way to tighten P&O algorithm constraints [20]. Two algorithms are included in the proposed strategy. A revised P&O algorithm was proposed by the authors in [21]. To test the effects of adaptive measures and regular P&O methods, they conducted research and simulations.

Testing of the INC MPPT algorithm was done in [22]. Using an isolated PV pumping approach, the authors tested the INC algorithm and found that it had an effect on the reference voltage and service speeds. Due to sudden fluctuations in irradiance, the impact on phase and disturbance size for a previous disturbance has been explained here, which typically reveals the algorithm inaccuracy. Finally, the success is linked to the algorithm that was proposed. It is possible to track the PV characteristics. The INC MPPT approach was found to be less affected by noise and device dynamics than other MPPT strategies. Stability at rapidly changing irradiance has been improved by this phenomenon in the suggested device. Faster transitional responses at higher disruption speeds are observed with INC. Due to changes in noise or brightness, the algorithm can be disrupted and the MPP can recover more quickly. The PI controller has been employed in several MPPT algorithms to date.

An ANN controller for PV system construction was unnerving because it was a novel idea. There are various features including higher speed response, nonlinear mapping, and lower estimation delay in the ANN MPPT [23] develop and validate the NN model, we used MATLAB and Simulink to collect data from the P&O system. The proposed NN controllers swiftly shifting insulation showed enhanced monitoring precision, reaction time, and overflow in the simulation results. With artificial intelligence, it can be used to create electronic power networks that are both efficient and reliable.

Data extraction and training for artificial deep learnings are also covered in full. Another ANN in [24] performs in better MPPT than climbing algorithms [25]. The authors used the MATLAB NN-Tool to create a Levenberg-Marquardt backpropagation method to map the maximum highest point. Traditional MPPT algorithms should be used with a NN controller, according to the proposed methodology.

3. Proposed Method

In this section, we present how the BPNN-DL operates to determine the maximum power point and the operation is given in Figure 1.

In Figure 1, it is important to observe with the series of connections in order to obtain maximum power point tracking. The momentary changes in light intensity and temperatures are sent as input to the control and measurement unit. At the first stage, the MPP point is searched, and the obtained value is sent as feedback to the control and measurement unit. Simultaneously, the ANN unit receives the input from the MPP search unit, and this ANN unit helps in finding the maximum MPP value and send it as a feedback to the control and measurement unit. The process involves the control and measurement unit that provides the values to the MPP unit to search an optimal value, however, BPNN-DL interferes with the decision of the MPP unit and provides near-optimal solution of MPP. The local tracking results in a considerable reduction in power. The two-stage maximum power tracking approach provided in this paper identifies the maximum point for two serially connected modules.

Step one involves measuring the array radiation and temperature and calculating the PI curve. Finally, a MPP point search technique is deployed using ANN parameters at MPP. The search is redone if the weather conditions worsen beyond a particular point. If there have been any changes to the performance conditions, then, the actual characteristic curve will begin its MPP search from its previous performance point in step two rather than from its estimated point from the first stage. In the second stage, any of the MPPT process and then a BPNN network is employed.

3.1. BPNN-DL Tracking. The BPNN-DL is briefly described as follows:

Phase 1: the study will calculate the inaccuracy of the MPP output based on the ground truth. The inaccuracy can be traced back to every neuron in each layer of the brain.

Phase 2: The study then updates the weight to find the optimal solution.

In order to get the minimum error, the study defines the cost function:

$$C = \frac{1}{2}\sum_{J\in L}\left\|d_j - y_j^L\right\|^2, \tag{1}$$

where x is the input training data; d_j is the output of each layer; L is total layers, and y_j^L is the neural network output w.r.t x.

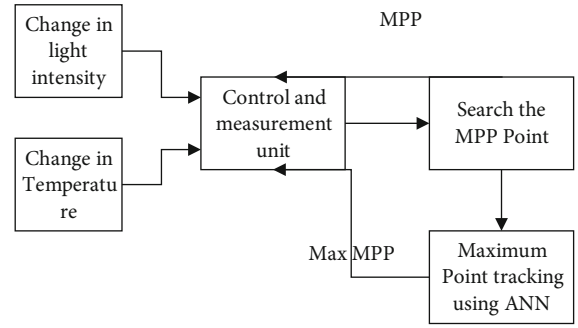

Figure 1: Schematic diagram of the proposed ANN MPPT.

The goal is to find the maximum power value and hence the study uses partial derivative as it helps in attaining minimal cost function w.r.t weights:

$$\frac{\partial C}{\partial W_{ij}^l} = 0. \tag{2}$$

Now, the study considers two cases: the node is an output node or it is in a hidden layer. In output layer, the study first computes the derivative of the difference of the ground truth and the output. That is,

$$\frac{\partial C}{\partial W_{jk}^L} = \left(d_k - y_k^L\right)\frac{\partial}{\partial W_{jk}^L}y_k^L. \tag{3}$$

Node k with weight W_{jk}^L enables the activation function output as y_k^L using sigmoid function as below:

$$\frac{\partial C}{\partial W_{jk}^L} = \left(d_k - y_k^L\right)\frac{\partial}{\partial W_{jk}^L}\sigma\left(x_k^L\right), \tag{4}$$

where x_k^L is the linear combination of inputs.

The sigmoid function derivative is given in the following form:

$$\frac{d}{dx}\sigma(x) = \sigma(x) - \sigma(x)^2. \tag{5}$$

The partial derivative based on the chain rule is defined as below:

$$\frac{\partial C}{\partial W_{jk}^L} = \left(1 - \sigma\left(x_k^L\right)\right)\sigma\left(x_k^L\right)\left(d_k - y_k^L\right)\frac{\partial}{\partial W_{jk}^L}x_k^L. \tag{6}$$

$x_k^L = \sum_{i\in L-1} W_{ik}^L y_i^{L-1}$. Thus, the following expression is given as below:

$$\frac{\partial C}{\partial W_{jk}^L} = \sigma\left(x_k^L\right)\left(d_k - y_k^L\right)\left(1 - \sigma\left(x_k^L\right)\right)y_j^{L-1}. \tag{7}$$

In $i \neq j$ case, $\partial C/\partial W_{jk}^L$ is both linked y_j^{L-1} and unrelated y_i^{L-1}. This equation was used to discover the relationship between the j and k node.

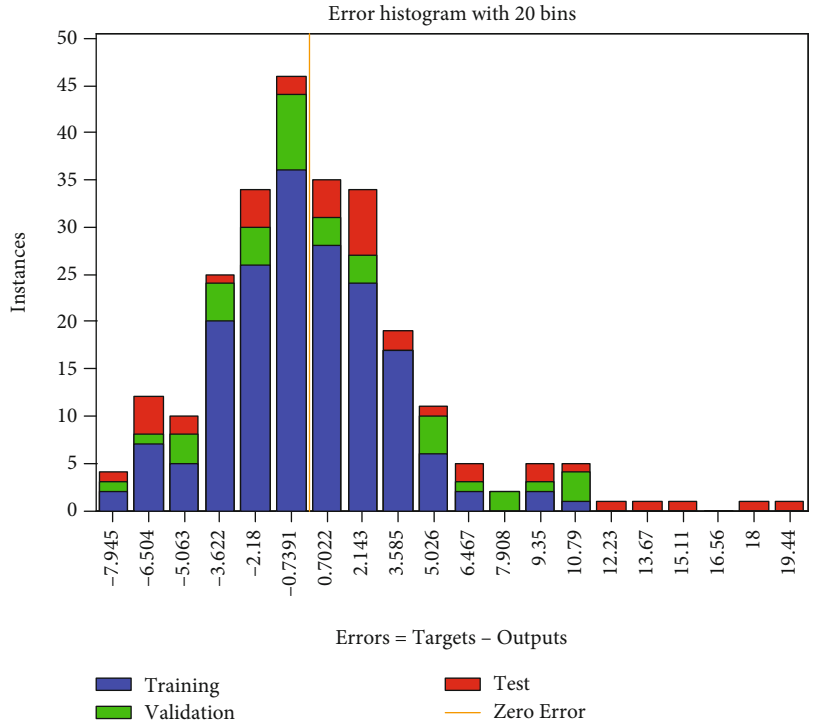

Figure 2: Error of proposed method during MPPT.

$$\delta_k = \sigma\left(x_k^L\right)\left(d_k - y_k^L\right)\left(1 - \sigma\left(x_k^L\right)\right), \tag{8}$$

as a way of representing the L layer k node. The equation is rewritten as below:

$$\frac{\partial C}{\partial W_{jk}^L} = \delta_k y_j^{L-1}. \tag{9}$$

Finally, the hidden node is examined. To begin, the study looks at layer $L-1$, which is shortly before the output layer. It is necessary to use a partial derivative on the cost function as well. Only the hidden layer nodes have been weighted.

$$\frac{\partial C}{\partial W_{ij}^l} = \sum_{k \in L}\left(d_k - y_k^L\right)\frac{\partial}{\partial W_{ij}^l} y_k^L. \tag{10}$$

In the L layer, there is a summation over k, so keep that in mind. So why does it matter if hidden layer weights W_{ij}^l are varied. Because the neural network output y_k^L is affected. The study used the chain rule and came up with the following results:

$$\frac{\partial C}{\partial W_{ij}^l} = \sum_{k \in L}\sigma\left(x_k^L\right)\left(d_k - y_k^L\right)\left(1 - \sigma\left(x_k^L\right)\right)\frac{\partial}{\partial W_{ij}^l} x_k^L. \tag{11}$$

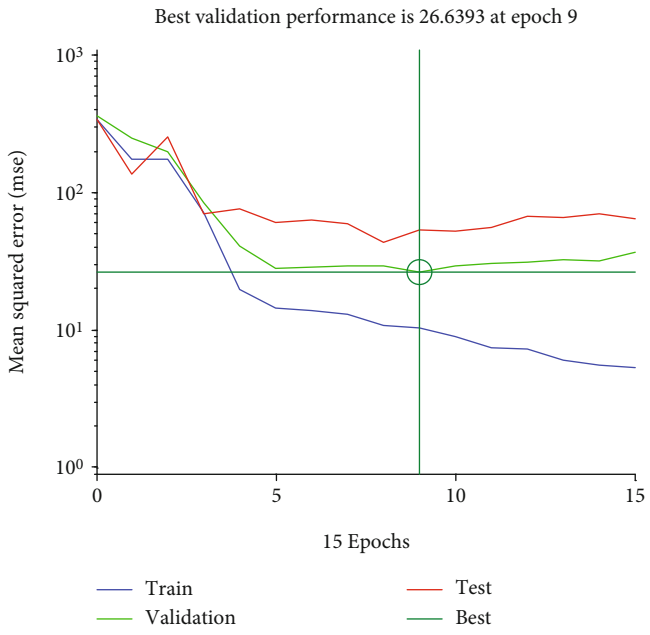

Figure 3: MSE of proposed method during MPPT.

Then, the study uses the chain rule to alter the last derivative term:

$$\frac{\partial C}{\partial W_{ij}^l} = \sum_{k \in L}\left(d_k - y_k^L\right)\sigma\left(x_k^L\right)\left(1 - \sigma\left(x_k^L\right)\right)W_{jk}\frac{\partial y_j^l}{\partial W_{ij}^l}. \tag{12}$$

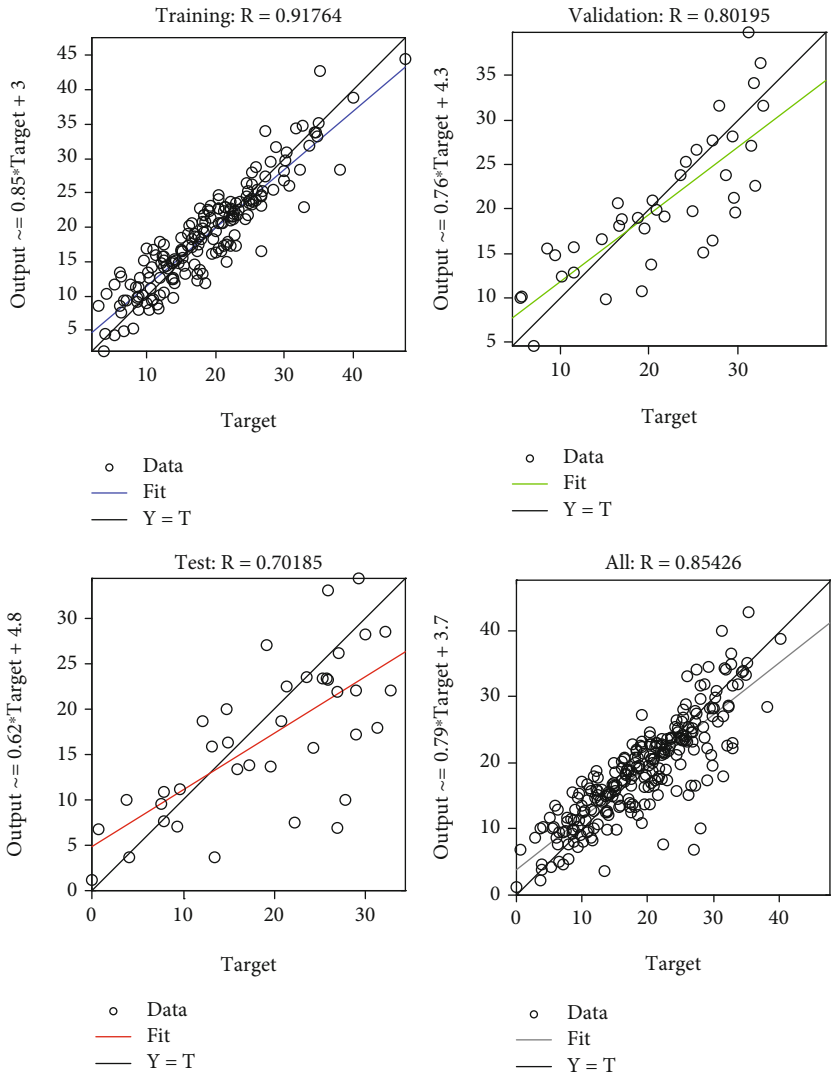

Figure 4: Fitness of proposed method during MPPT at all stages.

Line 2 in Eq. (14) originates from the fact that input is a linear combination x_k^L of the outputs from nodes in the preceding layer with a weight. According to the new findings, the derivative term has nothing to do with the L layer's k node. The chain rule is used again to simplify the derivative term, as seen in the following example:

$$\frac{\partial C}{\partial W_{ij}^l} = \sigma\left(x_j^l\right)\left(1-\sigma\left(x_j^l\right)\right) y_i^{l-1} \sum_{k\in L} \delta_k W_{jk}. \tag{13}$$

Aside from y_i^{l-1} as δ_j, the study is able to define all concepts. As a result, the equation is as follows:

$$\frac{\partial C}{\partial W_{ij}^l} = \delta_j y_i^{l-1}. \tag{14}$$

The equation for the output node of layer k

$$\frac{\partial C}{\partial W_{jk}^L} = \delta_k y_j^{L-1}, \tag{15}$$

where

$$\delta_k = \left(d_k - y_k^L\right)(1-\sigma(x_k))\sigma(x_k). \tag{16}$$

The equation for the output node of layer k

$$\frac{\partial C}{\partial W_{ij}^l} = \delta_j y_i^{l-1}, \tag{17}$$

Where

$$\delta_j = \left(1-\sigma\left(x_j\right)\right)\sigma\left(x_j\right)\sum_{k\in L} \delta_k W_{jk}. \tag{18}$$

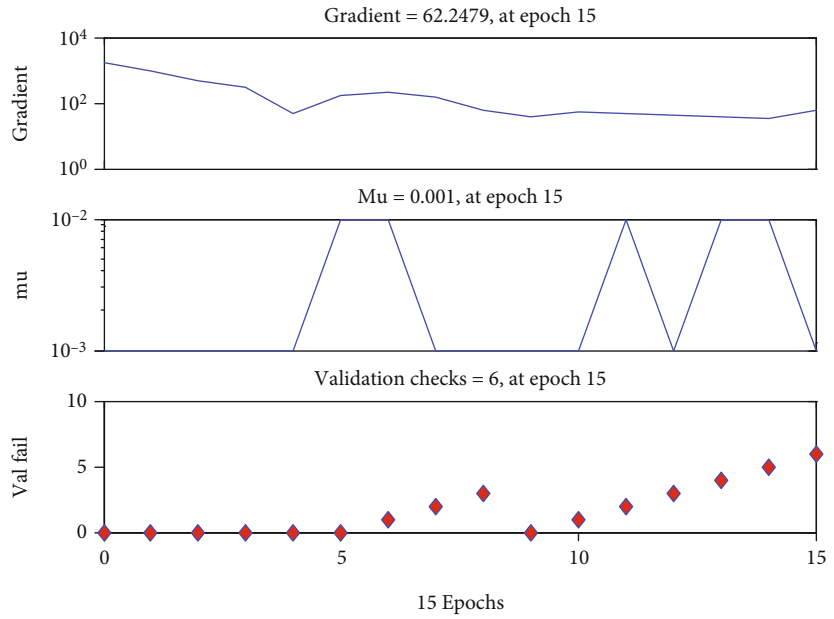

Figure 5: Fitness during training state of proposed method during MPPT.

Faintly, the cost function gradient at bias is given below:

$$\frac{\partial C}{\partial \theta_l} = \left(d_k - y_k^l\right)\sigma\left(x_k^l\right)\left(1 - \sigma\left(x_k^l\right)\right) = \delta_l. \quad (19)$$

4. Results and Discussions

The model is simulated in Simulink to correlate with the input data from PV array. Rather than using a continuous simulation, a discontinuous simulation is performed. ANN ability to accurately forecast the future depends on the size of the training dataset. The ANN predictions are generally accurate because of the enormous amount of data they have been trained on. From the lookup table, a clock synchronises the solar panel input data with the lookup table data. Figure 2 shows error of proposed method during MPPT.

An ANN prediction model is evaluated and validated using one or more specified error metrics. A continuous error matrix is used by the ANN algorithm to complete a function approximation task. No matter how many inputs and outputs are compared, all errors are rounded to the nearest integer.

Figure 3 shows the results of MSE of proposed method during MPPT, where the proposed method achieves reduced rate of error during testing process. The fitness of proposed method during MPPT in Figure 4 shows that the proposed method achieves better fit at all stages of the classifier. The results show that the proposed method moves to zero errors as the number of iterations getting increased, and it approaches towards the targeted solutions.

The average error (Figures 2–5) is the square root of the difference between the estimated and actual values, and this is what the mean square error measures. At each data point, the entire predictive model process is optimised by squaring the loss function and averaging it. Error minimization, or backpropagation, is used by the ANN to alter its anticipated output with respect to its actual output.

5. Conclusions

In this paper, BPNN-DL obtains maximum power point and maximises the output power from the solar grids when the panels are connected with the boost converter under different variable load conditions. BPNN-DL enables the prediction of reference voltage at different weather conditions for severing the various output power that ensures maximum power with stable output voltage. The proposed BPNN-DL under different conditions shows that it is capable of achieving maximum output power (98% accuracy) from each panel compared with existing methods. In future, the reduction of implementation cost can be focused while adopting the machine learning modules.

Data Availability

The data used to support the findings of this study are included within the article. Further data or information is available from the corresponding author upon request.

Conflicts of Interest

The authors declare that there is no conflict of interest regarding the publication of this paper.

Acknowledgments

The authors thank Arba Minch University, Ethiopia, for providing help during the research and preparation of the manuscript. The author appreciates the assistance from Government College of Engineering, Salem, Aditya Engineering College, SIMATS, in completing this work.

References

[1] L. Xia, Z. Ma, G. Kokogiannakis, Z. Wang, and S. Wang, "A model-based design optimization strategy for ground source heat pump systems with integrated photovoltaic thermal collectors," *Applied Energy*, vol. 214, pp. 178–190, 2018.

[2] Y. Chen, J. Wang, C. Ma, and G. Shi, "Multicriteria performance investigations of a hybrid ground source heat pump system integrated with concentrated photovoltaic thermal solar collectors," *Energy Conversion and Management*, vol. 197, article 111862, 2019.

[3] L. Xia, Z. Ma, G. Kokogiannakis, S. Wang, and X. Gong, "A model-based optimal control strategy for ground source heat pump systems with integrated solar photovoltaic thermal collectors," *Applied Energy*, vol. 228, pp. 1399–1412, 2018.

[4] Y. Natarajan, S. Kannan, C. Selvaraj, and S. N. Mohanty, "Forecasting energy generation in large photovoltaic plants using radial belief neural network," *Sustainable Computing: Informatics and Systems*, vol. 31, article 100578, 2021.

[5] B. Xiang, Y. Ji, Y. Yuan, D. Wu, C. Zeng, and J. Zhou, "10-year simulation of photovoltaic-thermal road assisted ground source heat pump system for accommodation building heating in expressway service area," *Solar Energy*, vol. 215, pp. 459–472, 2021.

[6] N. Yuvaraj, K. Praghash, R. A. Raja, and T. Karthikeyan, "An investigation of garbage disposal electric vehicles (GDEVs) integrated with deep neural networking (DNN) and intelligent transportation system (ITS) in smart city management system (SCMS)," *Wireless Personal Communications*, vol. 123, pp. 1733–1752, 2021.

[7] A. James, M. Mohanraj, M. Srinivas, and S. Jayaraj, "Thermal analysis of heat pump systems using photovoltaic-thermal collectors: a review," *Journal of Thermal Analysis and Calorimetry*, vol. 144, no. 1, pp. 1–39, 2021.

[8] Y. Wang, Y. Zhang, J. Hao et al., "Modeling and operation optimization of an integrated ground source heat pump and solar PVT system based on heat current method," *Solar Energy*, vol. 218, pp. 492–502, 2021.

[9] E. I. Sakellariou and P. J. Axaopoulos, "Energy performance indexes for solar assisted ground source heat pump systems with photovoltaic-thermal collectors," *Applied Energy*, vol. 272, article 115241, 2020.

[10] B. Xiang, Y. Ji, Y. Yuan, C. Zeng, X. Cao, and J. Zhou, "Performance analysis of photovoltaic-thermal road assisted ground source heat pump system during non-heating season," *Solar Energy*, vol. 221, pp. 10–29, 2021.

[11] M. Premalatha and C. Naveen, "Analysis of different combinations of meteorological parameters in predicting the horizontal global solar radiation with ANN approach: a case study," *Renewable and Sustainable Energy Reviews*, vol. 91, pp. 248–258, 2018.

[12] Z. Li, S. M. Rahman, R. Vega, and B. Dong, "A hierarchical approach using machine learning methods in solar photovoltaic energy production forecasting," *Energies*, vol. 9, no. 1, p. 55, 2016.

[13] M. Ding, L. Wang, and R. Bi, "An ANN-based approach for forecasting the power output of photovoltaic system," *Procedia Environmental Sciences*, vol. 11, pp. 1308–1315, 2011.

[14] R. Porrazzo, A. Cipollina, M. Galluzzo, and G. Micale, "A neural network-based optimizing control system for a seawater-desalination solar-powered membrane distillation unit," *Computers & Chemical Engineering*, vol. 54, pp. 79–96, 2013.

[15] W. Chine, A. Mellit, V. Lughi, A. Malek, G. Sulligoi, and A. M. Pavan, "A novel fault diagnosis technique for photovoltaic systems based on artificial neural networks," *Renewable Energy*, vol. 90, pp. 501–512, 2016.

[16] C. M. Fernández-Peruchena and M. Gastón, "A simple and efficient procedure for increasing the temporal resolution of global horizontal solar irradiance series," *Renewable Energy*, vol. 86, pp. 375–383, 2016.

[17] A. H. Elsheikh, S. W. Sharshir, M. Abd Elaziz, A. E. Kabeel, W. Guilan, and Z. Haiou, "Modeling of solar energy systems using artificial neural network: a comprehensive review," *Solar Energy*, vol. 180, pp. 622–639, 2019.

[18] B. Subudhi and R. Pradhan, "A comparative study on maximum power point tracking techniques for photovoltaic power systems," *IEEE Transactions on Sustainable Energy*, vol. 4, no. 1, pp. 89–98, 2013.

[19] M. A. G. De Brito, L. Galotto, L. P. Sampaio, G. D. A. E Melo, and C. A. Canesin, "Evaluation of the main MPPT techniques for photovoltaic applications," *IEEE Transactions on Industrial Electronics*, vol. 60, no. 3, pp. 1156–1167, 2013.

[20] S. K. Kollimalla and M. K. Mishra, "A novel adaptive P&O MPPT algorithm considering sudden changes in the irradiance," *IEEE Transactions on Energy Conversion*, vol. 29, no. 3, pp. 602–610, 2014.

[21] M. A. Elgendy, B. Zahawi, and D. J. Atkinson, "Assessment of the incremental conductance maximum power point tracking algorithm," *IEEE Transactions on Sustainable Energy*, vol. 4, no. 1, pp. 108–117, 2013.

[22] L. Hirth, "Market value of solar power: is photovoltaics cost-competitive?," *IET Renewable Power Generation*, vol. 9, no. 1, pp. 37–45, 2015.

[23] T. Dragičević, P. Wheeler, and F. Blaabjerg, "Artificial intelligence aided automated design for reliability of power electronic systems," *IEEE Transactions on Power Electronics*, vol. 34, no. 8, pp. 7161–7171, 2019.

[24] A. Ali, K. Almutairi, M. Z. Malik et al., "Review of online and soft computing maximum power point tracking techniques under non-uniform solar irradiation conditions," *Energies*, vol. 13, no. 12, p. 3256, 2020.

[25] W. Lee, K. Kim, J. Park, J. Kim, and Y. Kim, "Forecasting solar power using long-short term memory and convolutional neural networks," *IEEE Access*, vol. 6, pp. 73068–73080, 2018.

Hindawi
International Journal of Photoenergy
Volume 2022, Article ID 1541938, 8 pages
https://doi.org/10.1155/2022/1541938

Research Article

Prediction of Rooftop Photovoltaic Solar Potential Using Machine Learning

K. Mukilan,[1] K. Thaiyalnayaki,[2] Yagya Dutta Dwivedi,[3] J. Samson Isaac,[4] Amarjeet Poonia,[5] Arvind Sharma,[6] Essam A. Al-Ammar,[7] Saikh Mohammad Wabaidur,[8] B. B. Subramanian,[9] and Adane Kassa[10]

[1]*Department of Civil Engineering, Kalasalingam Academy of Research and Education, Virudhunagar, Tamilnadu 626126, India*
[2]*SRM Institute of Science and Technology, Ramapuram, Chennai, India*
[3]*Department of Aeronautical Engineering, Institute of Aeronautical Engineering, Hyderabad, Telangana 500043, India*
[4]*Department of Biomedical Engineering, Karunya Institute of Technology and Sciences, Coimbatore 641114, India*
[5]*Department of Information Technology, Government Women Engineering College, Ajmer, Makhupura, Ajmer, 305002 Rajasthan, India*
[6]*Department of Electronics and Communication Engineering, Government Women Engineering College, Ajmer, Makhupura, Ajmer, 305002 Rajasthan, India*
[7]*Department of Electrical Engineering, College of Engineering, King Saud University, P.O. Box 800 Riyadh 11421, Saudi Arabia*
[8]*Chemistry Department, College of Science, King Saud University, Riyadh 11451, Saudi Arabia*
[9]*Department of Biotechnology, Kyungpook National University, Republic of Korea*
[10]*Faculty of Mechanical Engineering, Arba Minch Institute of Technology (AMIT), Arba Minch University, Ethiopia*

Correspondence should be addressed to Adane Kassa; adane.kassa@amu.edu.et

Received 29 January 2022; Accepted 5 April 2022; Published 25 May 2022

Academic Editor: V. Mohanavel

Copyright © 2022 K. Mukilan et al. This is an open access article distributed under the Creative Commons Attribution License, which permits unrestricted use, distribution, and reproduction in any medium, provided the original work is properly cited.

Solar energy forecasting accuracy is essential for increasing the quantity of renewable energy that can be integrated into the existing electrical grid control systems. The availability of data at unprecedented levels of granularity allows for the development of data-driven algorithms to improve the estimation of solar energy generation and production. In this paper, we develop a prediction of solar potential across large photovoltaic panels from the roof tops using a machine learning method. The Restricted Boltzmann Machine (RBM) is the machine learning method used in the study to predict or forecast the solar potential in rooftops. The machine learning model is supplied with training dataset to get trained with the dataset for conversion into the model and then tested with the test dataset for validating the model. The results of simulation are conducted on R-package over various libraries to predict the rooftop solar potential. The results of simulation shows that the proposed method achieves higher rate of prediction accuracy than the other methods. The results of the simulation show that the proposed method achieves a higher rate of prediction accuracy of 99% than the other methods.

1. Introduction

Photovoltaic (PV) panels have been developed as a result of the global transition away from fossil fuels and toward sustainable sources of electricity (RES) [1]. Examples include the fact that the cost of producing electricity from solar panels has dropped substantially, while the efficiency of energy conversion has also increased [2]. The power cost of large-scale photovoltaic (PV) panels decreased by 73% between 2010 and 2017. PV panels have emerged as a viable renewable energy source in many countries as a result of their decreasing cost and increasing efficiency [3].

Consequently, the energy production of PV panels is highly changeable as a function of meteorological conditions

such as cloud cover and sun irradiation [4]. The capacity to better assess and manage production unpredictability is of particular relevance to a number of energy market participants [5]. Over and under production of electricity may result in penalty fees, which is why a transmission system operator is interested in the energy output from PV panels in the near future (0–5 hours) [6]. In contrast to this, electricity dealers are more concerned with short-term forecasts, such as those for the following day, because the vast majority of electricity is traded in this manner. Because of this, the profitability of these activities is based on their ability to accurately predict the varied output of solar PV panels [7].

As more countries decide to increase their renewable energy investment, it is expected that the use of solar PV panels will increase. As a result, there will be an increase in the demand for accurate solar PV energy output projections [8]. PV panel energy output projections necessitate accurate and efficient forecasting, but the solution is anything but straightforward. There is a wide range of challenges being addressed by the current research in the field [9]. Because of the inherent instability of weather, it is difficult to forecast specific weather conditions [10].

Recent years have seen an increase in the popularity of machine learning (ML) approaches to forecast PV power, as opposed to traditional time-series prediction models, which have been in use for decades [11]. Despite the fact that machine learning (ML) technologies have been around for a while, increased processing power and better data availability have made them more useful for predicting the future [12].

The major objective of the study is to examine and contrast numerous methodologies for predicting the energy output of solar photovoltaic (PV) panels. With the help of machine learning and time series approaches, it is possible to dynamically determine the relationship between solar PV system output and various weather conditions. Four machine learning algorithms are evaluated in the context of real-world solar power plant installations, and their performance is compared to more traditional time series methods. It was necessary to study several ways of feature engineering in order to increase the overall forecast accuracy.

In this paper, we develop a deep learning model using the Restricted Boltzmann Machine (RBM) which is the machine learning method used in the study to predict or forecast the solar potential in rooftops.

The main contribution of the work involves the following:

(i) The authors develop a prediction of solar potential across large photovoltaic panels from the roof tops using a machine learning method

(ii) The machine learning model is supplied with training dataset to get trained with the dataset for conversion into the model and then tested with the test dataset for validating the model

2. Background

The method in [13] discovered that the RBM was more accurate than the ARIMA in short-term forecasting, indicating that the RBM is superior to the ARIMA. Contrary to popular belief, Coimbra and Pedro anticipated the power output of solar PV panels rather than the amount of solar irradiation. There was no use of exogenous NWP data in this research; instead, the output levels of the panels were used to determine their historical output. Increased accuracy in RBM was achieved by the use of genetic algorithms (an optimization technique based on the natural selection process), which were developed by the authors. When it comes down to it, the different weather regimes [14] have varying degrees of accuracy in terms of forecasting. They advocate splitting data into subsets based on different weather regimes in order to use it for weather modelling. According to the authors of [15], it is feasible that fitting a distinct model to each dataset for a specific weather regime will result in better predictions than using a single fitted model for all possible weather regimes in a single dataset.

The method in [16] examined machine learning approaches and evaluated them in the context of producing characteristics that were predicted to improve the performance of a system. The principal component analysis (PCA) and a feature engineering methodology in combination with a gradient boosting tree model were the two main approaches employed in the research project. The other strategy was a feature engineering methodology in combination with a gradient boosting tree model. In addition, the authors used different smoothing methods to extract features from their NWP data [17], which they shared with the community. A grid of NWP data was used to calculate the average and changes in meteorological factors surrounding the PV installation site. Along with building features from local grid points, the authors also calculated variances for various predictors at varying lead times. The major motivation [18] for constructing variance characteristics based on lead times was to demonstrate the variability of the weather.

It is undeniable that PCA and feature extraction can lead to more desirable results. According to the researchers, there is a two-fold gap in knowledge that will need to be overcome in the future [19]. In order to improve forecast accuracy, it is necessary to understand how to manage features (through feature engineering and feature selection). The second component of this research investigates machine learning modelling strategies that can be utilized in conjunction with informative characteristics. Their conclusion is that the combination of deep learning and feature management will be a fascinating road to travel down in the next few years [20].

The method in [21] predicted solar irradiance using PCA, RBM, and the Analog Ensemble (AnEn), among other techniques. When trying to reduce the dimensionality of a dataset, a technique known as principal component analysis (PCA) was applied. Over the course of eight years, the total daily energy production from solar radiation was gathered and combined into a single dataset for analysis. According to the findings of a study, using PCA in conjunction with RBM and AnEn improves prediction accuracy.

At 15-minute intervals, the method in [22] presents a technique for weather classification and SVM to anticipate

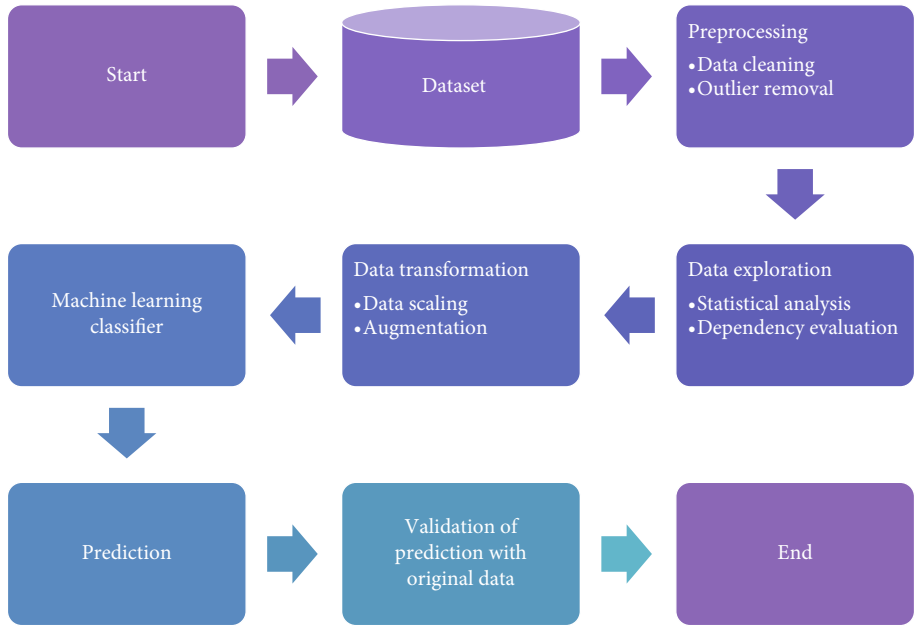

Figure 1: Proposed workflow.

PV power output for the next forecast. The day weather conditions include clear skies, overcast skies, foggy skies, and wet skies, to name a few examples. The classification of sites is based on an analysis of local weather forecasts and PV electricity generation. Once the data has been normalized, it is cleaned up in order to remove any unwanted noise and improve precision while also maintaining data correlation. The four distinct weather classes are then trained with four SVM models with radial basis function kernels, one for each weather type. We come to the conclusion that SVM models can be utilized to train models that are based on specific meteorological circumstances.

According to practically every research study, lag energy output estimations are significant for short-term forecasting, but they become even more important as forecasting horizons increase. Both research studies that supported and rejected the usage of time series models discovered that they were superior to machine learning in the short run. Continuing the comparison between time series models and machine learning approaches, in our opinion, is necessary and worthwhile [23].

When using a regression-based model, the accuracy of forecasting can be increased by using a suitable optimization strategy, as indicated in [24]. As a result, we will not investigate the performance of the RBM across multiple versions because the purpose of this study is to give a generic comparison of different machine learning techniques. It has been discovered in several studies that errors in NWP data have a considerable impact on the accuracy of forecasts [25]. Any model may benefit from the use of NWP data from a number of sources, which may help to ease this difficulty. For this to be possible, data from a large number of credible predictors must be available, which may not be the case in all cases. The overall inaccuracy of the incoming NWP data may be reduced even further if the NWP data were derived from a variety of physical models.

3. Proposed Method

In this section, we present prediction of solar potential across large photovoltaic panels from the roof tops using a machine learning method. The Restricted Boltzmann Machine (RBM) is the machine learning method used in the study to predict or forecast the solar potential in rooftops.

In the beginning, data on solar generation is represented as a matrix with the formula $m * n$, where m signifies the number of features and n denotes the total number of observations. During this stage, the data is sorted into two categories: training data and testing data, as shown in the diagram. Cross-validation with different folds of the same training data is used to train RBM using different folds of the same training data. The results of the k-fold cross-validation approach is completely unaffected by bias.

When it comes to solar photovoltaic (PV) data, the weather has a considerable impact on the seasonal changes. Due to the fact that K-fold cross-validation training is performed on fewer data points, the variance is lower than that of a single hold-out model. With the K-fold method, you can divide your data into k equal-sized parts. Each of the k-folds in the test is taught to the models k times in total.

The models are validated using a five-fold cross-validation procedure. Iteration one employs the first four folds to train models, while the last fold is used to test the models trained in the previous iteration. The model is tested on the second-to-last fold in the subsequent iteration, while the remaining folds are trained in the following iteration. This cycle is repeated until all five test fold predictions have been received, at which point the process is completed as in Figure 1.

3.1. RBM Classification. An RBM, which is a specialized kind of Markov random field, has both stochastic visible units

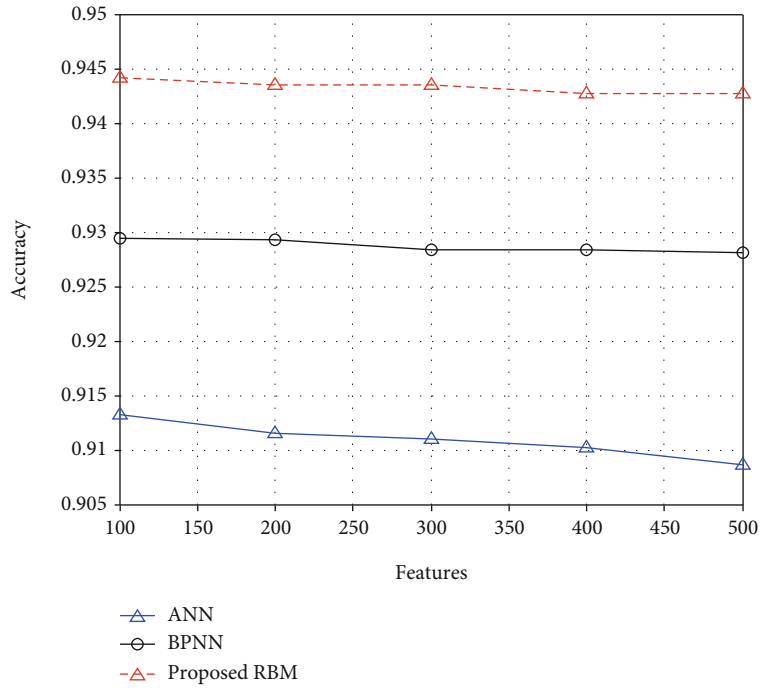

Figure 2: Accuracy.

and hidden units that are both visible and hidden. There are no links between visible and hidden units in RBMs because all of the visible and hidden units are connected to the RBM network. RBMs can be represented as bipartite graphs, which are a type of graph.

Given the model parameters, RBMs use an energy function $\mathrm{E}(\mathbf{v}, \mathbf{h}; \theta)$ to establish a joint distribution $\mathrm{p}(\mathbf{v}, \mathbf{h}; \theta)$ across the visible and hidden units θ:

$$\mathrm{p}(\mathbf{v}, \mathbf{h}; \theta) = \frac{\exp\ (-\mathrm{E}(\mathbf{v}, \mathbf{h}; \theta))}{Z},$$
$$Z = \sum_{\mathbf{v}} \sum_{\mathbf{h}} \exp(-\mathrm{E}(\mathbf{v}, \mathbf{h}; \theta)) \tag{1}$$

where,

Z = normalization factor.

The marginal probability to $\mathbf{v}$ is given as below:

$$\mathrm{p}(\mathbf{v}; \theta) = \frac{\sum_{\boldsymbol{h}} \exp(-\mathrm{E}(\mathbf{v}, \mathbf{h}; \theta))}{Z}. \tag{2}$$

The energy function is given as below:

$$\mathrm{E}(\mathbf{v}, \mathbf{h}; \theta) = -\sum_{i=1}^{I} \sum_{j=1}^{J} w_{ij} v_i h_j - \sum_{i=1}^{I} b_i v_i - \sum_{j=1}^{J} a_j h_j, \tag{3}$$

where w_{ij} = symmetric interaction term between v_i and h_j, b_i and a_j = bias term, I = visible units, and J = hidden units.

The conditional probabilities is estimated as below:

$$p(h_j = 1 | \mathbf{v}; \theta) = \sigma\left(\sum_{i=1}^{I} w_{ij} v_i + a_j\right),$$
$$p(v_i = 1 | \mathbf{h}; \theta) = \sigma\left(\sum_{j=1}^{J} w_{ij} h_j + b_i\right), \tag{4}$$
$$\sigma(x) = 1/(1 + \exp\,(x)).$$

For a visible-hidden RBM, the formulation for energy is given below:

$$\mathrm{E}(\mathbf{v}, \mathbf{h}; \theta) = -\sum_{i=1}^{I} \sum_{j=1}^{J} w_{ij} v_i h_j - \frac{1}{2} \sum_{i=1}^{I} (v_i - b_i)^2 - \sum_{j=1}^{J} a_j h_j. \tag{5}$$

The conditional probabilities is hence modelled as below:

$$p(h_j = 1 | \mathbf{v}; \theta) = \sigma\left(\sum_{i=1}^{I} w_{ij} v_i + a_j\right),$$
$$p(v_i | \mathbf{h}; \theta) = \mathcal{N}\left(\sum_{j=1}^{J} w_{ij} h_j + b_i, 1\right), \tag{6}$$

where v_if ollows a Gaussian with mean $\sum_{j=1}^{J} w_{ij} h_j + b_i$ with unit variance.

Initially, the RBMs can be applied to real-valued stochastic variables, after which they can be processed using the Bernoulli-Bernoulli RBMs, which are a subset of the RBMs. The Gaussian and binomial conditional distributions are

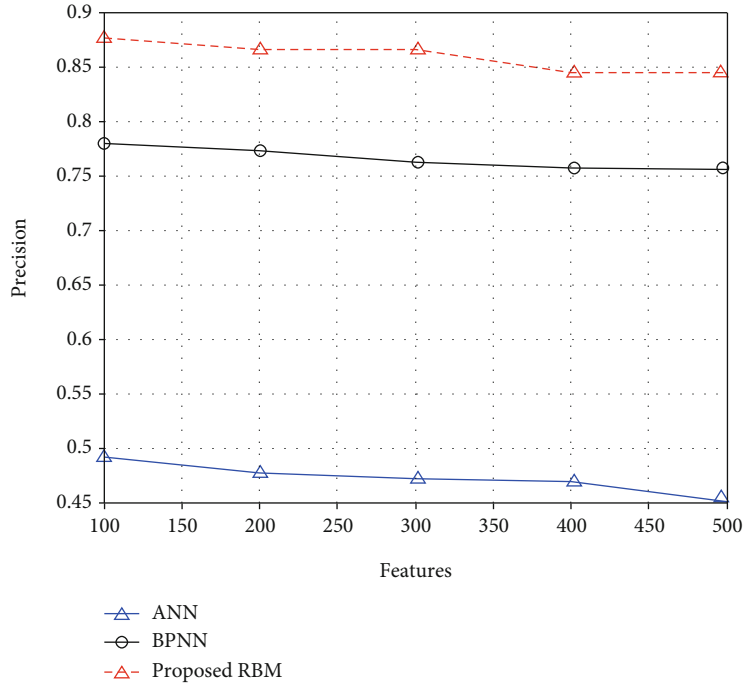

Figure 3: Precision.

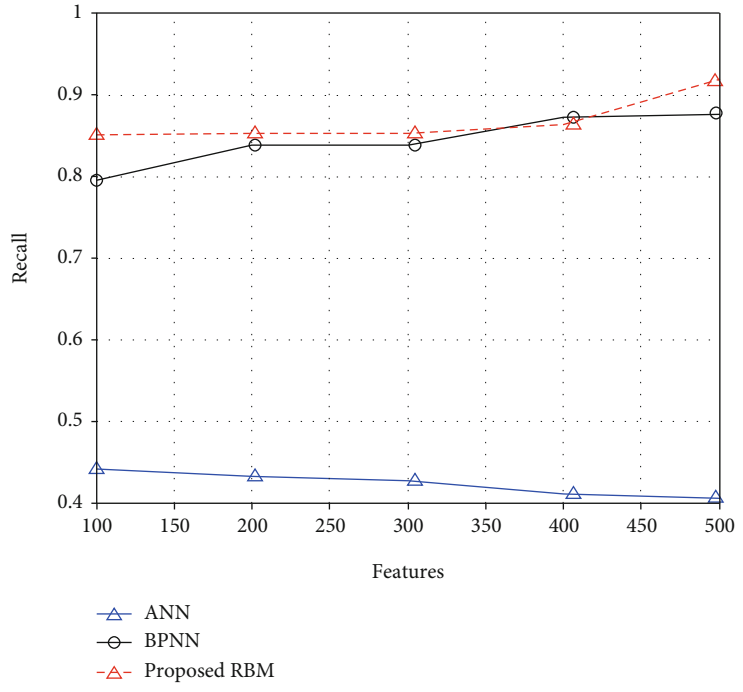

Figure 4: Recall.

the two most common RBM conditional distributions that are used in this discussion.

An RBM performance could be improved by boosting or bagging an RBM with better beginning start weights in order to improve the performance of the RBM in question. There was also discussion of how particular optimization tactics can influence the network ability to converge, and thus the outcomes, in the literature review. We did not apply the genetic optimization strategy to our RBM, despite the fact that it has been shown to improve the performance of RBMs in previous research. When it comes to the RBM, it is critical to compare performance and computation time. A feasible

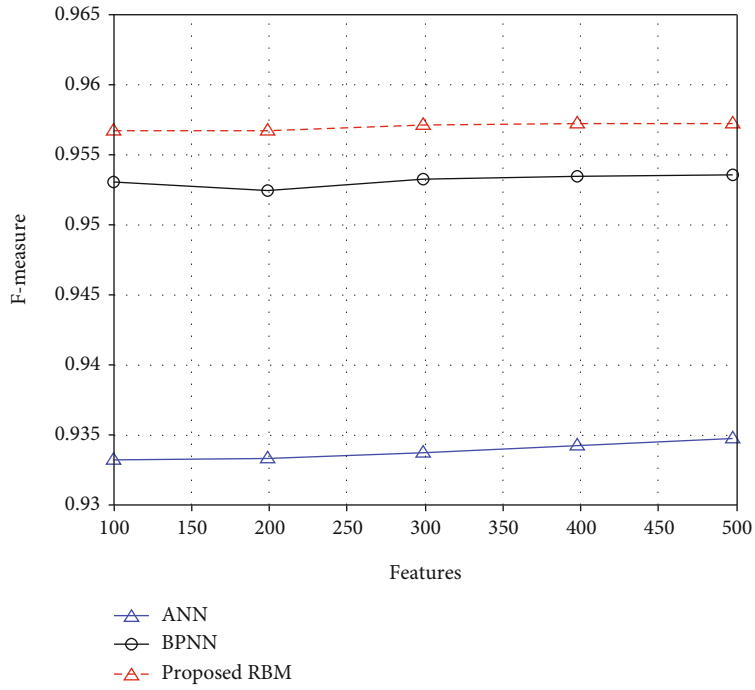

Figure 5: F-measure.

compromise would be to increase forecast accuracy while also increasing computing time. Discussions and conclusions.

4. Results and Discussions

This section of the chapter will include a continuation of the topic of data processing as well as a full treatment of the machine learning methodologies. Through the course of the research, R version 3.4.3 and RStudio have been used to do data processing and mathematical computations. Caret is the most widely used R package, and it is a wrapper that contains tools for speeding up the construction of predictive models and preparing data. Caret is the most widely used R package.

K-fold cross-validation is a technique that can be used to accomplish cross-validation when completing a statistical analysis. The collection is randomly divided into k equal halves, with the number of halves determined by chance. As a result of the validation principle, one of the k-folds is chosen as a test set, and the remaining observations are chosen as a training set. In the following step, the test set is relocated to a new fold, while the remaining dataset is used as training data. An individual performance metric is calculated for each of the k-folds that have been completed. After each metric has been obtained, the average performance of each fold is computed using the information gathered. In order to identify the best performance metric from the cross-validation, it is possible to perform this for a variety of hyperparameters. It is usual for the number k to fall within the range of 5 and 10.

It is crucial to get the weights just right from the beginning. If the weights are set too close to zero, the network may be forced to converge to a linear model. In most cases, zeroing out the initial weights is accomplished by drawing them at random. As a general rule, it is preferable to select lower values rather than larger ones. Initial weights that are both positive and negative are typically preferred. This is due to the fact that they provide greater flexibility in the analysis.

The rate at which back-learning propagation occurs will have an effect on the final result. Training can be time-consuming when the learning rate is either excessively high or excessively low. For example, instead of employing a sophisticated technique, one might simply set a relatively high learning rate and then progressively drop it until, within a reasonable length of computation time, the accuracy of the model degrades to an undesirable level.

Applying penalizing terms to the minimization issue, like in the Lasso example, is a prominent therapy for overfitting in the optimization context. The scale of the input layer can have an impact on the weights of the output layer, which in turn can have an impact on the output results. As a result, it is common practice to standardize all data inputs to ensure consistency. A standard deviation of one is typically used as a starting point for data analysis when dealing with large datasets.

The peak power of these installation ranges between 20 kW and 150 kW, and the data on their energy output was gathered from these installations as well. The data on energy production was obtained from five different places and sampled every 15 minutes. The data was likewise collected from five different locations.

Certain aspects of access to the NWP data have been restricted. In the first instance, because forecasts are created every six hours and cover a time span of six hours in advance, it is not possible to produce longer-term estimates. Because one cRBMot makes use of weather forecasts that are

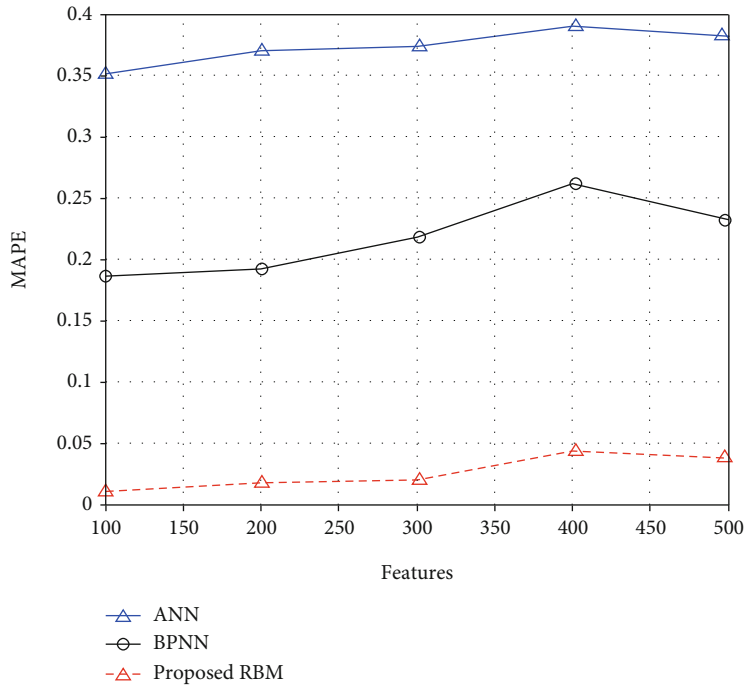

Figure 6: MAPE.

no longer accessible, the training set is reduced for longer time horizons. This means that the precise alignment of the solar PV panel is not represented in the data.

When the forecasts (Figures 1–5) are almost identical, the levels of actual energy output that result can be dramatically different, showing the underlying ambiguity of the data that was used to make the projection in the first place. In some cases, small local errors in the input data can be paired with small local flaws in the forecasting algorithms to produce huge global defects in the model, which can be very difficult to detect. Figure 6 reveal the MAPE.

The inherited patterns in the data may be able to assist in explaining the situation from a data perspective. During the winter months, for example, there was no reported energy generation at the vast majority of the power stations. This occurred occasionally as a result of snow accumulating on the panels for an extended length of time. If the series has a large number of days with zero output in a row, the series will become nonstationary for the remainder of the time period. Keep in mind that because the clear sky normalization does not affect zero-valued variables, it is difficult to maintain a constant state of affairs.

The different RBM parameter configurations did not significantly outperform one another. A greater amount of testing is required because the initial weights were picked at random and only a small number of trials were completed for each arrangement. Additional testing should be conducted. Despite the fact that the RBM outperforms other machine learning models, there is still room for improvement due to the model inherent complexity.

5. Conclusions

In this study, we employ a machine learning method to generate a prediction of solar potential over a large number of photovoltaic panels installed on roof tops. The use of RBMs to anticipate or forecast rooftop solar potential is an example of machine learning in action. In order for the machine learning model to be trained using the training dataset and then tested with the test dataset in order to validate the model, the training dataset must be provided to the model. The results of simulations are run in order to assess the rooftop solar potential, and the results are analyzed using the R-package and a number of libraries. The simulations indicate that the new strategy has a higher accuracy in predicting the future than the previous approaches, which is encouraging news. In future, large-scale real-time PVs can be connected with this model for finding the outcome using machine learning.

Data Availability

The data used to support the findings of this study are included within the article. Further data or information is available from the corresponding author upon request.

Conflicts of Interest

The authors declare that there is no conflict of interest regarding the publication of this paper.

Acknowledgments

The authors thanks the Arba Minch University, Ethiopia, for providing help during the research and preparation of the manuscript. The work was supported by Researchers Supporting Project number (RSP2022R492), King Saud University, Riyadh, Saudi Arabia.

References

[1] A. Khandakar, E. H. M. Chowdhury, M. Khoda Kazi et al., "Machine learning based photovoltaics (PV) power prediction using different environmental parameters of Qatar," *Energies*, vol. 12, no. 14, p. 2782, 2019.

[2] S. Bhavsar and R. Pitchumani, "A novel machine learning based identification of potential adopter of rooftop solar photovoltaics," *Applied Energy*, vol. 286, p. 116503, 2021.

[3] M. Rana and A. Rahman, "Multiple steps ahead solar photovoltaic power forecasting based on univariate machine learning models and data re-sampling," *Sustainable Energy, Grids and Networks*, vol. 21, p. 100286, 2020.

[4] M. Houchati, A. H. Beitelmal, and M. Khraisheh, "Predictive modeling for rooftop solar energy throughput: a machine learning-based optimization for building energy demand scheduling," *Journal of Energy Resources Technology*, vol. 144, no. 1, 2022.

[5] K. Mahmud, S. Azam, A. Karim, S. Zobaed, B. Shanmugam, and D. Mathur, "Machine learning based PV power generation forecasting in Alice Springs," *IEEE Access*, vol. 9, pp. 46117–46128, 2021.

[6] K. Benhmed, F. Touati, M. Al-Hitmi et al., "PV power prediction in Qatar based on machine learning approach," in *2018 6th international renewable and sustainable energy conference (IRSEC)*, pp. 1–4, Rabat, Morocco, 2018.

[7] E. Bacry, D. de Barros Soares, F. Andrieux et al., "Predicting the solar potential of rooftops using image segmentation and structured data," *NIPS Proceedings*, 2021.

[8] M. Mohana, A. S. Saidi, S. Alelyani, M. J. Alshayeb, S. Basha, and A. E. Anqi, "Small-scale solar photovoltaic power prediction for residential load in Saudi Arabia using machine learning," *Energies*, vol. 14, no. 20, p. 6759, 2021.

[9] X. J. Luo, L. O. Oyedele, A. O. Ajayi, and O. O. Akinade, "Comparative study of machine learning-based multi-objective prediction framework for multiple building energy loads," *Sustainable Cities and Society*, vol. 61, p. 102283, 2020.

[10] H. Zarrinkafsh, N. Eslamirad, and F. De Luca, "Classification of the energy production potential of water lens solar concentrators using machine learning," *Journal of Physics: Conference Series*, vol. 2042, no. 1, article 012022, 2021.

[11] S. Rodrigues, H. G. Ramos, and F. Morgado Dias, "Machine learning PV system performance analyser," *Progress in Photovoltaics: Research and Applications*, vol. 26, no. 8, pp. 675–687, 2018.

[12] I. Parvez, A. Sarwat, A. Debnath, T. Olowu, M. G. Dastgir, and H. Riggs, "Multi-layer perceptron based photovoltaic forecasting for rooftop pv applications in smart grid," in *2020 SoutheastCon*, pp. 1–6, Raleigh, NC, USA, 2020.

[13] P. Li, H. Zhang, Z. Guo et al., "Understanding rooftop PV panel semantic segmentation of satellite and aerial images for better using machine learning," *Advances in Applied Energy*, vol. 4, p. 100057, 2021.

[14] A. A. A. Gassar and S. H. Cha, "Review of geographic information systems-based rooftop solar photovoltaic potential estimation approaches at urban scales," *Applied Energy*, vol. 291, p. 116817, 2021.

[15] T. Karthikeyan, K. Praghash, and K. H. Reddy, "Binary flower pollination (BFP) approach to handle the dynamic networking conditions to deliver uninterrupted connectivity," *Wireless Personal Communications*, vol. 121, no. 4, pp. 3383–3402, 2021.

[16] M. Ali, R. Prasad, Y. Xiang et al., "Variational mode decomposition based random forest model for solar radiation forecasting: new emerging machine learning technology," *Energy Reports*, vol. 7, pp. 6700–6717, 2021.

[17] N. Arivazhagan, K. Somasundaram, D. VijendraBabu et al., "Cloud-internet of health things (IOHT) task scheduling using hybrid moth flame optimization with deep neural network algorithm for E healthcare systems," *Scientific Programming*, vol. 2022, 12 pages, 2022.

[18] H. Ren, C. Xu, Z. Ma, and Y. Sun, "A novel 3D-geographic information system and deep learning integrated approach for high-accuracy building rooftop solar energy potential characterization of high-density cities," *Applied Energy*, vol. 306, p. 117985, 2022.

[19] B. Gobinathan, M. A. Mukunthan, S. Surendran et al., "A Novel Method to Solve Real Time Security Issues in Software Industry Using Advanced Cryptographic Techniques," *Scientific Programming*, vol. 2021, 9 pages, 2021.

[20] X. Xu, Y. Xu, M. H. Wang et al., "Data-driven game-based pricing for sharing rooftop photovoltaic generation and energy storage in the residential building cluster under uncertainties," *IEEE Transactions on Industrial Informatics*, vol. 17, no. 7, pp. 4480–4491, 2021.

[21] Y. Natarajan, S. Kannan, C. Selvaraj, and S. N. Mohanty, "Forecasting Energy Generation In Large Photovoltaic Plants Using Radial Belief Neural Network," *Sustainable Computing: Informatics and Systems*, vol. 31, article 100578, 2021.

[22] N. Maitanova, J. S. Telle, B. Hanke et al., "A machine learning approach to low-cost photovoltaic power prediction based on publicly available weather reports," *Energies*, vol. 13, no. 3, p. 735, 2020.

[23] N. Yuvaraj, K. Praghash, R. A. Raja, and T. Karthikeyan, "An investigation of garbage disposal electric vehicles (GDEVs) integrated with deep neural networking (DNN) and intelligent transportation system (ITS) in Smart City management system (SCMS)," *Wireless personal communications*, vol. 123, no. 2, pp. 1733–1752, 2021.

[24] S. Theocharides, G. Makrides, A. Livera, M. Theristis, P. Kaimakis, and G. E. Georghiou, "Day-ahead photovoltaic power production forecasting methodology based on machine learning and statistical post-processing," *Applied Energy*, vol. 268, p. 115023, 2020.

[25] S. Preda, S. V. Oprea, A. Bâra, and A. Belciu (Velicanu), "PV forecasting using support vector machine learning in a big data analytics context," *Symmetry*, vol. 10, no. 12, p. 748, 2018.

Hindawi
International Journal of Photoenergy
Volume 2022, Article ID 6202802, 12 pages
https://doi.org/10.1155/2022/6202802

Research Article

Simulation Model of PV System Function in Stand-Alone Mode for Grid Blackout Area

Bibhu Prasad Ganthia,[1] R. Dharmaprakash,[2] Tushar Choudhary,[3] T. Vijay Muni,[4] Essam A. Al-Ammar,[5] A. H. Seikh,[6] M. H. Siddique,[7] and Abdi Diriba[8]

[1]*Department of Electrical Engineering, Indira Gandhi Institute of Technology, Sarang, Odisha 759146, India*
[2]*Department of Electrical and Electronics Engineering, Panimalar Institute of Technology, Chennai, Tamil Nadu 600123, India*
[3]*Department of Mechanical Engineering, PDPM Indian Institute of Information Technology Design and Manufacturing, Jabalpur, Madhya Pradesh 482005, India*
[4]*Department of Electrical and Electronics Engineering, Koneru Lakshmaiah Education Foundation, Vaddeswaram, Andhra Pradesh 522502, India*
[5]*Department of Electrical Engineering, College of Engineering, King Saud University, P.O. Box 800 Riyadh 11421, Saudi Arabia*
[6]*Mechanical Engineering Department, College of Engineering, King Saud University, P.O. Box 800, Al-Riyadh 11421, Saudi Arabia*
[7]*Intelligent Construction Automation Centre, Kyungpook National University, Daegu, Republic of Korea*
[8]*Department of Mechanical Engineering, Mizan-Tepi University, Ethiopia*

Correspondence should be addressed to Abdi Diriba; abdi@mtu.edu.et

Received 10 February 2022; Accepted 8 April 2022; Published 20 May 2022

Academic Editor: V. Mohanavel

Copyright © 2022 Bibhu Prasad Ganthia et al. This is an open access article distributed under the Creative Commons Attribution License, which permits unrestricted use, distribution, and reproduction in any medium, provided the original work is properly cited.

PV systems are frequently used in a stand-alone configuration. In a solar PV-based energy-producing system, power fluctuation is a natural occurrence. Alternative sources of energy, including such hybrid grid-tied or energy storage systems, could be discovered when solar PV systems run off-grid to satisfy regional power demands for reliable power supply. This research uses an unusual PV system that can function in both grid-connected and stand-alone states to propose an efficient approach for the power generation challenge in the residential segment. A block of storage battery with sufficient dimensions is included in the system to make sure the constant power supply of such a residential building with an average electricity demand of 10 kWh. An atypical 3.2 kWp PV system and a 19.2 kWh storage battery brick was determined to be capable of meeting the house's whole daily energy requirements, as well as the defined electrical shutdown times, to simulate the system, which took into account the day load profile, network cutoff times, and monthly radiation from the sun. The collected simulation results showed that during 9 months of each year, the generated PV energy surpasses the load needs, resulting in a maximum battery state-of-charge (SOC) in the range of 74-85%. The generated PV energy is an approximately proportional requirement as during 3 months of minimum solar irradiance (Dec-Feb), whereas the sequence's SOC differs between 40 and 49%, demonstrating the validity of the proposed photovoltaic system. In January and July, the PV service's daily energy produced ranges between 2.6 and 5.4 kWh/kWp, corresponding to a conversion efficiency of 90% and 66.25%, correspondingly.

1. Introduction

Microgrids are low-voltage networks that include combination of distributed (DG) units, energy storage systems (ESS), and load, controlled demand that can operate either as stand-alone modes [1]. In a state, the microgrid modifies power leveling in free enterprise activities by getting power from the main system or providing electricity to the grid to improve operational benefits. The microgrid is separated from upstream distribution systems in stand-alone operation, to maintain a constant power supply to the customers who use DG. Different types of methods are used as elements of the microgrid to minimize the power swings of nondispatchable DG units, such power dynamic of every

distributed energy generating unit, charge and discharging of ESS, and load variations.

A network-controlled dependent voltage-sourced converter (VSC) or a networking framing agrees to take two modulation techniques utilized in a microgrid. To achieve stable and cost-effective functioning, a microgrid normally requires a powerful platform to enable dynamic referencing power factor, ensuring collaboration among the controlled components. With the quick rise in fossil fuel prices, and also the sharp rise in the construction price of building normalized pattern facilities, there is a renewed focus on alternative generating systems that use energy more efficiently [2]. The electricity sector gets increasingly competitive as a result of activities and reorganization of power networks. Solar, freshwater, air, geological, and wastes generated are the most common alternative energy sources. Solar energy is widely available and may be used in practically anyplace. Many countries have taken major steps in the new millennium to tap into the vast and environmentally benign solar energy supplies. These countries invest much in both development and public awareness campaigns aimed at environmental protection. High-quality studies will lower manufacturing costs while also improving the efficiency of allied solar energy-harvesting equipment [3]. Furthermore, public understanding will raise the demand for these devices in the industry. As a result, the technology will be given out at a cost-effective rate.

Renewable energy systems (RES) present a cleaner solution capable of fulfilling the growing electrical requirements of linked and remote communities. Microgrids (MGs) have piqued the scientific group's interest in recent years, as well as being a possible alternative for future conventional power generation. MGs are being considered as a potential solution for integrating intermittent renewable energy supplies into traditional grids [4]. Many implementations have been applied in SG, notably in the construction of controller and electronic band converters, as a result of the advent of new communications technology such as microprocesses devices and developments in power electronics. Experts had made major contributions that can have a substantial influence in such domains in recent years, particularly in the context of data collecting, mechanization, and management of MGs. MGs not just reliably and cleanly connect electricity renewable to the main grid, as well as provide greater validity in its design to function within the face of natural disasters and interconnected power grids, resulting in lower energy failures in distribution and transmission, as well as reduced building and financial moment.

Connecting terminals with defined and estimated capacities are used to transmit and supply electricity generation. Electrical supply increases in some circumstances, forcing distribution networks to plan electricity supply over multiple periods ranging from 6 to 10 hours each day [5]. Communities and other industries face a serious problem as a result of this situation. This problem has existed for more than ten years, and there are no signs that it will be resolved in the coming years given the political scenario remaining constant [6]. Mounting PV systems on private residences and other privately or publicly facilities with pretty modest minimum fuel use, on either hand, is a viable solution for a wide spectrum of such users, who account for a significant portion of Gaza's overall consumption of electricity. Throughout grid outages, the PV power systems should provide a constant supply of energy, and during the day, this can feed extra produced electricity into the electricity network.

Due to such island operation of the converter, which is a necessary significant aspect with each grid-connected converter to fulfill the safety requirements, grid-connected PV systems may continue to deliver electricity generation during grid shutdown hours [7]. As a result, if the PV system does not have energy storage, the electricity generation produced by the PV system throughout blackout periods would be lost. This results in significant energy waste and lengthens the time it takes for photovoltaic systems to repay for themselves. Stand-alone PV systems are two types of photovoltaic (PV) systems that utilize solar fuel to power electricity. The stand-alone PV system is represented in Figure 1. The grid kind is linked directly to the power grid and operates in comparison only with resource load demand [8]. There is also no requirement for battery storage in this PV system because it does not allow for autonomy. Its size ranges from a small-scale distributed roofing system with a few kW to a large central grid-connected system with an MW capacity, and it uses an inverter to translate DC electricity produced by aPV arrays back AC power that can be delivered into the grid. On either side, a stand-alone or off-grid photovoltaic system does not connect to the power system.

This kind of PV system includes a PV system for producing power, energy storage equipment including such battery, energy ventilation system, or AC or DC electrical demands. A grid-connected PV system reduces electricity and capability inefficiencies in the distribution systems, as well as delays or prevents distribution and transmission systems upgrades [9]. Consumer demands are also unconstrained because energy is delivered to the electric grid. The grid integration service's functioning, on the other side, is contingent on the occurrence of the power scheme. Standalone photovoltaic systems, on either side, have found use in rural places where the grid connection is limited. For instance, rural electricity, telecommunications, and pumping systems are all examples. They demand more upkeep but also give you a great sense of freedom.

The goal of the research is to recommend the solution to these problems by providing a different PV system that includes storage batteries, charging controller, grid-attached, AC/DC bilateral change, and process regulator. That means savings can be saved by the battery. This can prevent excessive energy without wasting. It also helps monitor and categorize the submissions charging through the circuit [10]. The technology was developed to accommodate the advantage of all available network hours, not just for providing the demand but also for recharging batteries. On either side, it will use all of the PV-generated electricity to charge batteries, provide the load, and feed the extra electricity back into the grid. In comparison to another traditional photovoltaic system, the proposed solar system is unique in that it can function in both stand-alone states without compromising the islanding security features. On either side, unlike

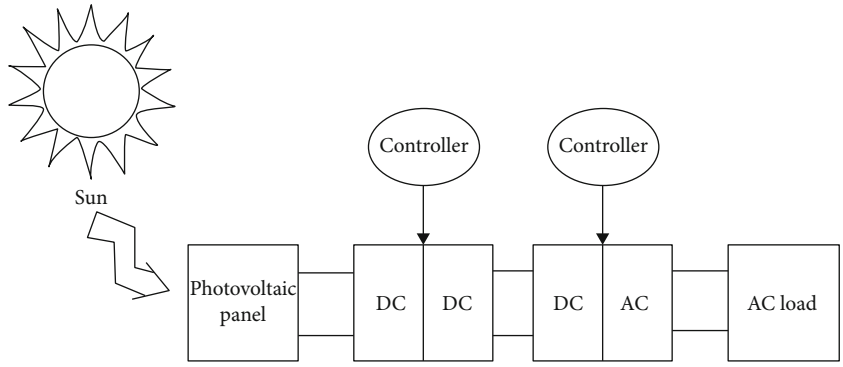

Figure 1: Stand-alone photovoltaic system.

traditional grid-connected photovoltaic system, which typically functions at a voltage source of 400–600 V, the suggested system operates at a drastically reduced voltage source of 48 V, which is safer and allows the required number lithium batteries to be reduced with only 24 cells [11]. The simulation outcomes of this research verify the correctness of the advanced software architecture and demonstrate that its manufactured and preserved electricity generation is fully sufficient to cover overall load requirements throughout the year, indicating that the advanced system design is a viable solution to address the grid outage issue for a huge proportion of a residential market. However, leading to a shortage of papers upon an unusual PV system that is created for a specific scenario, the received testing data could not have been matched to other analogous findings.

2. Related Work

This paper offers a grid-tied photovoltaic (PV) control adaptation topology with a new grid resynchronization mechanism. The goal of this plan is to provide continuous energy to the system while also nourishing control to the network. The control strategy aids in a harmonic compensation and energy quality improvement while obtaining the most generated by the PV array. The suggested arrangement is managed to utilize three ways, characterized as the grid control scheme, points of conventional connection (PCC) voltage regulation, and purposeful transient stability with resynchronization, dependent on the amount of grid energy. Within these modes, a basic error signal controller controls grid frequency, voltage output, batteries, and the direct current (DC) connection amplitude. A control strategy is also presented for rapid and horizontal evolutions between modes. The system's durability in the face of irregular solar irradiance, linear model, and grid supplies interruptions makes it a good fit for a home application. The findings of the controls, architecture, and simulations are given to illustrate that the suggested system operates satisfactorily [12].

Photovoltaic (PV), that could be independent, off-grid linked, or a grid-connected, is viewed as among the most promising alternatives for underdeveloped countries like Rwanda to minimize difficulties associated with energy shortages. Despite developments in renewable technology, Rwanda's present electricity rate is projected to be 59.7%, and hydroelectric maintains the country's principal source of energy. Rwanda's administration has vowed to attain 48 percent of its overall electricity targets through off-grid photovoltaic panels by 2024 to supply inexpensive energy to low-income homes. By constructing an easy and low off-grid photovoltaic system, a comparison of results among a single household as well as a microgrid photovoltaic is undertaken. For a private household, the battery model is 1.6 kWh everyday demand with 0.30 kW peak demand, while for the off PV network, the storage model is 193.05 kWh/day and 20.64 kW peak load. For each of these energy generation representations, the hybrid optimization model for electric renewable (HOMER) software is utilized that estimate a network size or life cycles cost, which includes the net present cost (NPC) and levelized cost of energy (LCOE). The optimal program's LCOE, NPC, electricity generation, and operational cost are predicted to be 1,166,898.0 USD, 1.28 (USD/kWh), 221, and 715.0 USD for the grid and 9284.4 USD, 1.23 (USD/kWh), and 2426.0 USD for an only one stand-alone, correspondingly, according to the analysis. When evaluated to a regional PV network that provides power to a remote county in Rwanda, the LCOE of such a stand-alone PV scheme for individual residence is shown to be charge-effective [13].

Stand-alone mode offers the highest effectiveness of the control of a matrix converter, stand-alone PV converter. Initially, a DC-DC boost converter with quadratic back-stepping regulator was modeled and designed. The suggested converter extracts the maximum power point (MPP) by the properly reacting to variable atmospheric circumstances by using a standard voltage supplied by the perturb and observe (P&O) technique. One purpose of the boost converter is to increase the voltage at the inverter's intake while needing a transformer; proposed system is less small and less costly. Next, the single-phase on H-bridge converter was regulated with back-stepping control to minimize the error among the inverter's voltage level and the target variable; however, there was a significant load variation at the inverter's production. Lyapunov's stable concept was used to verify the boost conversion and H-bridge inverter's reliability. The suggested photovoltaic system using back-stepping controls has a strong recovery of the MPP, with effectiveness of 99.83% and a speed of response of 1 ms, according to simulation findings. Furthermore, the inverter's voltage output is

regulated to 220 V in its sine format, and the overall harmonic component of the output power is little more than 1% [14].

The rapid development in the production of renewable power generation to the power process is due to the use of conventional energy sources and environmental concerns. The reduction of power loss and voltage profile might be significant advantages of distributed energy resources (DG). Nevertheless, studies reveal that inappropriate ESS design and size result in unintended energy losses and risk of voltage stability, particularly in areas where renewable power adoption is strong. To address the issue, this study establishes a microgrid created on IEEE 34-bus distribution network that includes wind power, photovoltaic system, and production of diesel, including energy storage systems about particular types of loads. Furthermore, the research proposes the particle swarm optimization (PSO) technique for minimizing power loss and improving system output voltages by efficiently managing various types of renewable power under the worst-case scenario of renewable power. Case educations were approved out using the well-established IEEE 34-bus system. The thorough simulation results for each example highlight the importance of optimal configuration organizational structure as well as the efficacy of the proposed approach [15].

A single-phase freestanding PV device with two steps of converters is shown in this research. The goal of this project is to track the MPPT so that the extreme possible control can be transferred to the load, as well as to manage the production of current so that the AC load may be fed with a sinusoidal waveform. These objectives are met by designing control rules for the boost DC-DC and an inverter switch utilizing the slipping mode. As a result, a sliding mode MPPT and outputs control technique are presented. The work's unique feature is that it proposes a freestanding PV system using controls based exclusively on adaptive control. Under quick fluctuations of irradiance level, the suggested system is designed and analyzed in MATLAB/Simulink environment. The findings obtained with the proposed MPPT are instead compared with the results with the incremental conductance (IC) approach. These findings show that the sliding manner (SM) MPPT outperforms the fixed mode MPPT in terms of timing velocity, effectiveness, and responsiveness. Furthermore, the current controller produces a high-quality control signal with a THD of 3.47%. Moreover, these controls are assessed under the changes of two daily meteorological patterns and contrasted to the IC approach for valid results. The findings show that the trajectory tracking MPPT can generate more electric power than an IC MPPT, with advantages of up to 13.12% for the bright daily pattern and 27.67% for a gloomy day pattern [16].

3. Materials and Methods

3.1. Characteristics of PV Cell. The majority of solar panel is made up of a series of modules. A p-n connection, which creates small amounts of electricity to the reflected light, can be used to depict this organism. Various analogous circuit designs are provided to investigate the electrical characteristics of the PV cell [17], because of its strong performance concerning substantial fluctuations in temperature and irradiance. The most commonly used designs for PV cell modeling is shown in Figure 2.

A photocatalytic generation source I_{ph} in parallel connection, the connected in series R_s, and also the shunt resistance R_{sh} make up the circuit diagram in Figure 2. The output current I_{pv} is calculated by expression (1) using Kirchhoff's rules:

$$I_{\text{pv}} = I_{\text{ph}} - I_{\text{os}}\{\exp\left[A(V_{\text{PV}} + I_{\text{PV}}R_s) - 1\right]\} - \frac{V_{\text{PV}} + R_s I_{\text{pv}}}{R_{\text{sh}}}, \tag{1}$$

where $A = q/\gamma \text{kTTN}_{\text{cell}}$.

The differences in light-generated current I_{ph} are dependent on the observed and referenced irradiance level parameters as chosen to follow

$$I_{\text{ph}} = \left[I_{\text{SC}} + K_i(T - T_{\text{ref}})\frac{\lambda}{\lambda_{\text{ref}}}\right]. \tag{2}$$

The current is flowing in the diode I_D described by the Shockley equations, as shown in formula (3), where I_{os} indicates the saturation current and is represented by

$$I_{\text{os}} = I_{\text{or}}\left(\frac{T}{T_{\text{ref}}}\right)^3 \exp\left(\frac{qE_G}{k\gamma}\left[\frac{1}{T} - \frac{1}{T_{\text{ref}}}\right]\right). \tag{3}$$

The utilization of series/parallel modules in PV energy systems is dependent on the amount of power required and the voltages employed. The main goal of PV cell mathematical analysis is to obtain precise outputs of current or voltage results for the study to display the I-V and P-V features [18]. In Figure 3, the latter is depicted. The voltages and currents are affected by irradiance and temperature, correspondingly. In addition, the maximum output changes with irradiation and temperature.

3.2. Proposed Method of PV System. The suggested PV scheme can be used in either grid-connected or standalone configurations. Figure 3 displays a structure of a system. The photovoltaic panel, cell battery, power converter devices, and control method are the essential components.

3.3. Photovoltaic Generator. PV modules are connected to the circuit, based on the power and voltage of the DC supply [19]. Monocrystalline or crystalline silicon photovoltaic modules were chosen because of their excellent quality and reduced depreciation over long durations when compared to other PV systems. The photovoltaic module is helpful to improve the quality of the generator. In it, the PV module was connected to the control bus. This control bus carried the control signals from the PV module to the inverter. This module was connected to the battery. The inverter circuit connects with the AC power supply. Then, the input current quality was enhanced by the PV module.

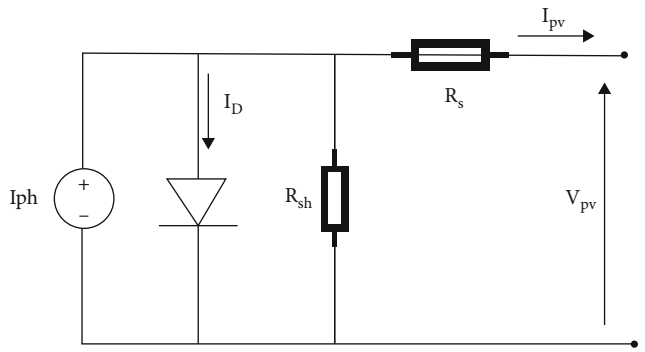

Figure 2: PV cell single diode model.

3.4. Cell Battery Storage. Due to repeated grid shortages, the battery unit includes static cells which can withstand a deep depletion, having a maxima cycle frequency surpassing 1000 times [20]. These lithium batteries offer high amp hour effectiveness of 80-90 percent as well as a high life expectancy of more than ten years. The ability of a battery is the size of the electricity stored within it, and it depends on the size of it. And it is determined by its lifetime depending on the nature of the term. The changes that are stored here are determined by its various standards.

3.5. Regulator of the Battery Charge. It is utilized to keep the battery building's charging rate under control and safeguard it from overcharging and excessive overcharging. The value sensor is used to calculate the voltage levels and open or close switch S2 and per the battery's state-of-charge, as indicated in Figure 3.

3.6. Inverter 1 and Inverter 2. It is a grid-connected converter that converts PV generator DC source electricity to AC electricity exported to the grid. It features MPPT control techniques, management to kind the converter grid-connected, an anti-islanding technique to guarantee protection when a cutoff grid moments [21]. The bidirectional energy conversion can work as a converter to transfer DC to AC and also a radiator to transfer AC to DC electricity. In grid outages, it would deliver AC power to the demand as from battery blocks in the first mode. It functions as a converter in the second scenario; charge the battery component first from the grid throughout its levels of attention [22]. This converter is not intended to provide AC baseload power as from a battery bank. In the event of a grid shutdown, the reference signal (Ig) is primarily utilized to remove inverter 2.

3.7. Power Meter. This pattern is utilized to track how much energy is dissipated from a grid when serving the demand or charge the storage wedge, as well as how much electricity is exported to the grid from aPV scheme. This pattern was connected following the electricity law known as network monitoring.

3.8. PV System Design. The process measures will be considered while evaluating the planned PV system elements depicted in Figure 3:

(i) The daily global solar electricity production on flat surfaces is 5.4 kWh/m^2 day, corresponding to the average maximum sunlight hours [PSH] = 5.4 h/day

(ii) In the city, the everyday consumption of electricity of a residential real estate and one publicly or privately utility is 10 kWh/day; this amount of energy indicates the consumption of a significant number of existing households and modest publicly or privately institutions daily [23]. Furthermore, the required installation surface of the equivalent PV generator is around 25 m^2, allowing for easy deployment on a building roofing

(iii) To choose the right order for a particular voltage for our method, its publishing electronics should be given more than voltage. If so, it will use the stream lord. This may cause the risk of wasting power

(iv) The efficiency (η_{inv}) of inverter 1 and inverter 2 is 94%, whereas the charging agency's CR is 96%

(v) A block current battery maximum current effectiveness is $\eta_{BAh} = 85\%$

(vi) The DC system power is calculated at 48 V to keep the battery's block voltage from exceeding a harmful level. The rate of heat transfer between two surfaces is equal to the temperature difference divided by the total thermal resistance between two surfaces

Tables 1 and 2 show the detailed simulated findings for this position in terms of annual power output and consumption, as well as the quantity of yearly converters inefficiencies.

3.9. Sizing of PV Generator. The highest power of aPV array generator P_{PV} is represented in

$$P_{PV} = \frac{E_d}{\text{PSH} \times \eta_{inv} \times \eta_{CR}}, \tag{4}$$

while E_d seems to be the private house's average power consumption (kWh/day), PSH seems to be the peak solar hours (hours per day), η_{CR} represents charging controller effectiveness, and η_{inv} is converter effectiveness.

This can calculate the peak produced by the PV system in Watt peak (Wp) using the above model parameters represented in

$$P_{PV} = \frac{10000}{5.4 \times 0.93 \times 0.95} = 2096\,\text{Wp}. \tag{5}$$

To ensure constant power is available throughout grid interruption hours and to account for cloudy weather as well as all voltage regulation losses, a PV generating with such a maximum output of 3200 Wp will be chosen [24]. Furthermore, boosting the PV peak output will ensure that the battery block maintains an acceptable state of charge. The PV module will be a polycrystalline module with 72 compartments that are related with such a peak output of 320 Wp. In this example, the PV generator will be made up of five

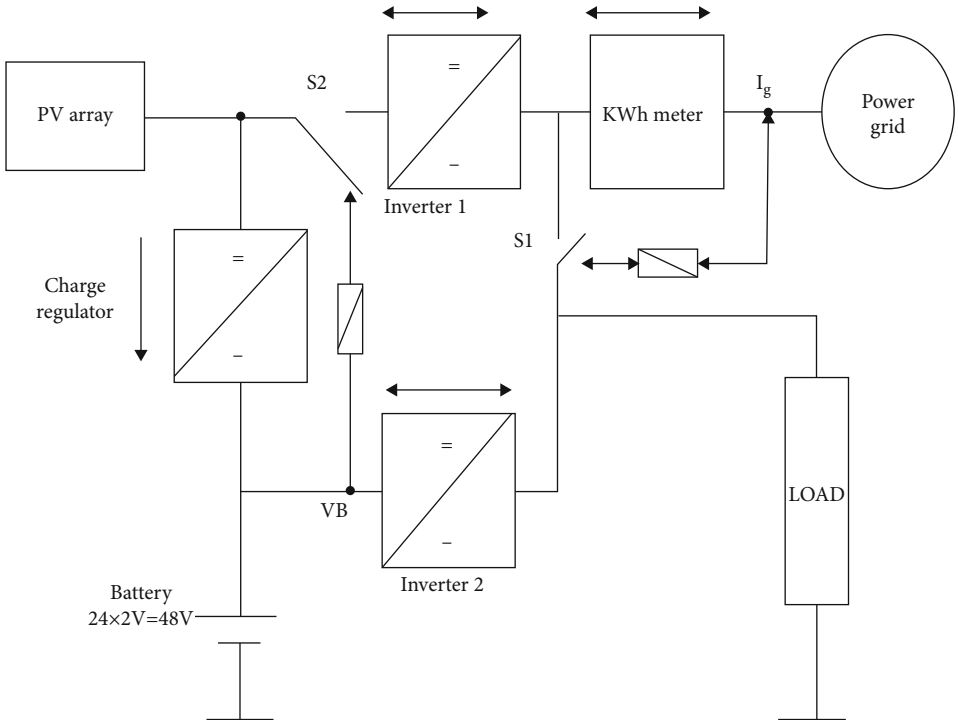

Figure 3: Photovoltaic backup system.

Table 1: Yearly power production and consumption on a stand-alone system.

Construction	kWh/year	Percentage (%)	Consumption	kWh/year	Percentage (%)
Photovoltaic system	1564	100%	AC primary demand	432	100%
Overall	1564	100%	Overall	432	100%

Table 2: Yearly losses in electrical power in a stand-alone system.

Measure	Converter	Rectifier	Component units
Operation hours	6453	0	hrs/year
Power in	463	0	kWh/year
Power out	437	0	kWh/year
Loss	43	0	kWh/year

series connections; that is, each is made up of two PV modules linked in series and has standard DC energy of 47 V, as illustrated in Figure 4 [25]. This energy is chosen to suit a battery storage block's voltage level.

3.10. Storage of Block Battery Design. When mounting the battery block in such an uptown building, the standard cell block power is calculated to be 48 V, which would be acceptable [26]. The storage space of the battery's blocks would be chosen to fulfill the energy load requirements for a couple of days even without sunlight or the electricity supply. C_{BAh} (total ampere hour) is calculated as follows:

$$C_{\mathrm{BAh}} = \frac{E_{\mathrm{db}} \times \mathrm{AS}}{\mathrm{DOD} \times V_B \times \eta_{\mathrm{BAh}}}, \tag{6}$$

where E_{db} is the everyday energy demand from the batteries (Ed/inv), DOD is a allowable penetration of discharge, AS is autonomy times, η_{BAh} seems to be the batteries cell's ampere hourly effectiveness, and V_B seems to be the battery block's chosen minimum DC voltage. The ampere hour load is calculated using actual values for various variables, such as AS = 2.25 days, DOD = 0.8, and $\eta_{\mathrm{BAh}} = 0.85$ and also $V_B = 48$ V.

$$C_{\mathrm{Ah}} = \frac{(1000/0.93) \times 2.25}{0.8 \times 48 \times 0.85} = 741.2 \text{ Ah}. \tag{7}$$

A lead-acid battery block bank classified at 800 Ah/2 V would remain chosen to a construct the loading solution that comprises 24 cells that are associated to offer a DC power supply of 48 V/800 Ah, to improve the battery energy storage stress distribution and to reverence, industry manufactured norm standards. This battery block has a battery performance of $C_{\mathrm{wh}} = 19.2$ kWh, which would be suitable for interior placement in a household residence.

3.11. Regulator Charge Selection. The charge regulators would be evaluated at an input power in the region of 44-86 V and a voltage level of 3.2 kW, whereas its minimum voltage output is 48 V, taking into account the PV battery's amount of voltage and maximum output.

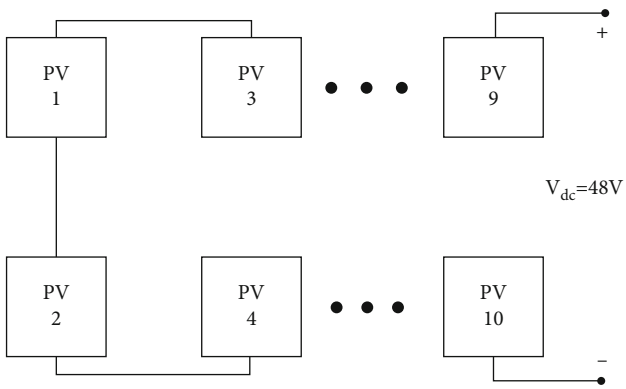

Figure 4: PV generator.

3.12. Inverter Selection. Inverter 1 is still a 4 kVA only one DC/AC inverter that runs at a steady-state operation and has a dynamic performance of 220 V and 50 Hz, respectively [27]. As indicated in Figure 3, it provides the power supply via switch S1 and the power infrastructure with electricity generated by the PV generation via a bidirectional kWh-meter. This convertor is controlled by a system and developed to lock down in the event of a grid outage, ensuring total security.

3.13. Bidirectional Inverter Selection. It is a 5 kVA bidirectional inverter that was chosen to provide AC power from the storage block to demand while also generating electricity from a network when a PV power is restricted for the lengthy time, such as during wintertime.

During conduction, heat is transferred through the vibration of molecules in a substance. As something gets warmer, it begins to increase the vibration and movement of the molecules that it consists of. In solids, particles are closely packed together and are in direct contact.

3.14. System Modes. The solar level of radiation, network disruption periods, the battery's SOC, and autility grid are all variables that will cause the system to function in various modes [28]. Under some of these circumstances, the mechanism in Figure 3 will select the appropriate configuration from Table 3.

3.15. System Evaluation. The system simulations have been carried out using the given system design. Whenever the network is unavailable, the PV scheme and the stored power in the storage blocks were being utilized to fulfill a capacity demands [29]. During network available hours, its electricity would be used to meet power demands and fill the battery blocks, based on its charging condition. The simulation tool examines the energy requirements and PV energy output at every hour cycle and then decides whether to charge or discharge the batteries or infuse additional energy into the network regarding the difference.

3.16. Everyday Demand Curve. The load demand profile displays the load variance that is dependent on customer behavior. The main demands in a typical residential dwelling are lighting, television, computers, and household appliances including fridges, freezers, and dishwashers. As per Black's Law Dictionary, "Residential dwelling means living in a certain place permanently or for a considerable length of time" as per Merriam Webster dictionary.

In the computer simulation, the load profile indicated in Figure 5 is taken into account [30]. The produced annually of PV energy system, the battery SOC, and the thermodynamic efficiency have all been evaluated using computer simulation depending here on everyday load profile illustrated in Figure 5.

3.17. System Component Modeling. The objective of system modeling is to test the state's performance under various settings and seasons. It is carried out utilizing PV array, battery, charge controller, and inverter numerical simulations [31]. Hourly meteorological data, temperature, and humidity and a load demand curve are used as input data. The calculation results give a quick summary of the mathematical methods.

3.18. Estimation of PV Power Output. PV maximum output at standard trial condition (STC), solar irradiance, and module temperatures are all important components in generating DC electricity from a photovoltaic system. This is an example of a simple design.

$$P_{\mathrm{PVout}} = P_{\mathrm{PVPeak}} \times \left(\frac{S}{S_{\mathrm{ref}}}\right) \times [1 + K_T(T_c - T_{\mathrm{ref}})]. \quad (8)$$

From equation (8), where P_{PVout} seems to be the PV array's power factor, P_{PVPeak} seems to be the PV element's power at STC, S seems to be solar energy in W/m^2, S_{ref} is represented as solar energy at STC of 1000W/m^2, KT seems to be the thermal diffusivity of mono- and polycrystalline Si cells, $KT = 3\,7\,103\,1/^{\circ}C$, T_{ref} is the source temperature at STC of 25°C, and T_c represents temperature coefficient estimated using a next econometric model.

$$T_c = T_{\mathrm{amb}} + (0.0256 \times S), \quad (9)$$

where T_{amb} represents the ambient temperature in equation (9).

3.19. Battery Storage Block. In the event of a grid failure or if the operation is performed in a stand-alone operation, a battery is created to gather the extra power generated by PV. They also continue to improve the demand whenever the PV power is insufficient to generate electricity. The following equations are being used to express the efficiency of charging and draining the battery blocks [32]. The rechargeable battery block has two modes of operation: charge and discharge. During charge controller in equation (10), the PV energy increased by the control authority's effectiveness above the bidirectional inverter's input signal (inv2), which represents the power demand divided by inverter 2's effectiveness. This power (P_{charge}) would be increased by the battery's charge effectiveness and then increased by one 60 minutes to contribute to the current battery charge (equation (11)). Since

Table 3: System operating modes.

Configuration	Switch 1	Switch 2	Description
1	0	0	Power cutoff, PV generation storing the batteries, and the cell blocks supplying electricity to the demand.
2	1	0	Grid connectivity is accessible, and load is drawn straight from the network.
3	0	1	The battery's SOC is minimal, and a cellblock is supplied by both the PV system and the network at the same moment.
4	1	1	Grid connectivity, battery charge from the PV system, and surplus generated energy pumped into a network to supply the required. This state is not appropriate for this technology.

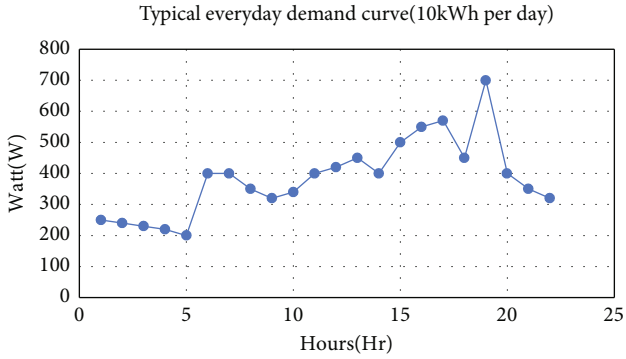

Figure 5: Typical everyday demand curve of a residential.

the simulation duration is one hour, the multiplying is by 60 minutes.

The batteries will discharge power $(P_{\text{discharge}})$ as during discharge mode (equation (12)) to compensate the deficit that occurs when the demand that exceeds a PV power. At cathode or positive electrode, due to oxidation, nickel hydroxide becomes, nickel ox hydroxide releasing water in the electrolyte solution. During charging of battery, the secondary battery turns to its original charged state and is ready for further discharging of battery. The energy released from the batteries is calculated by multiplying the PV power by a charging regulation performance, subtracting the power demand split by the bidirectional inverters effectiveness (inv2), and then dividing everything by the rapid charging effectiveness, as shown in (12). The discharge energy would be increased every 60 minutes, and the energy of a battery's blocks would be deducted:

(i) Charging operation

$$\left(P_{\text{charge}}\right) = \left[\left(P_{\text{PVO}} \times \eta_{\text{CR}}\right) - \left(\frac{P_L}{\eta_{\text{inv}}}\right)\right] \times \eta_{\text{BAh}}, \quad (10)$$

$$E_B(t) = E_B(t-1) + \left(P_{\text{charge}} \times 60 \text{ minutes}\right) \quad (11)$$

(ii) Discharging operation

$$\left(P_{\text{discharge}}\right) = \frac{\left[\left(P_L/\eta_{\text{inv}}\right) - \left(P_{PVO} \times \eta_{\text{CR}}\right)\right]}{\eta_{\text{BAh}}}, \quad (12)$$

$$E_B(t) = E_B(t-1) + \left(P_{\text{discharge}} \times 60 \text{ minutes}\right), \quad (13)$$

where E_B is the current battery energy generated (Wh), P_{PVO} is the PV element's power output (W), P_L is a needed load energy (w), P_{charge} is represented as voltage stimulating to a battery when charge controller (W), and $P_{\text{discharge}}$ is the energy discharge from batteries while discharging state (W). The rate of heat transfer to an object is equal to the thermal conductivity of the material the object is made from, multiplied by the surface area in contact, multiplied by the difference in temperature between the two objects, and divided by the thickness of the material.

3.20. Simulation Algorithm. The numerical methods presented above in this paper make up the system model. Figure 6 depicts the experimental flow diagram. The application determines the MPP dimensions $(I_{\text{mppf}}, V_{\text{mppf}})$ power output produced by the solar generator, or available energy during day and night utilizing weather information (solar insolation and temperatures), modules supplier information, and the condition of the electricity systems. This has used the MPP parameters $(I_{\text{mppf}}, V_{\text{mppf}})$ at STC and the NOCT circumstances supplied by the company to assess the simulation program.

(i) The PV scheme generates enough energy to meet the needs of the household. PV energy will take precedence over draining the battery and using the network if this is capable to satisfy load requirements [33]. If there is extra PV power, it will be pumped into the network or used to charge and discharge block under its state of charge

(ii) The PV power generated is insufficient to meet the load. If grid electricity is supplied, utilize it first; if grid services are not available, empty the maximum load of electricity from storage blocks

(iii) The amount of PV electricity produced is insufficient to meet the demand requirement, and the battery's SOC is low. The grid can then be used to simultaneously charge and discharge blocks and fulfill the capacity demands

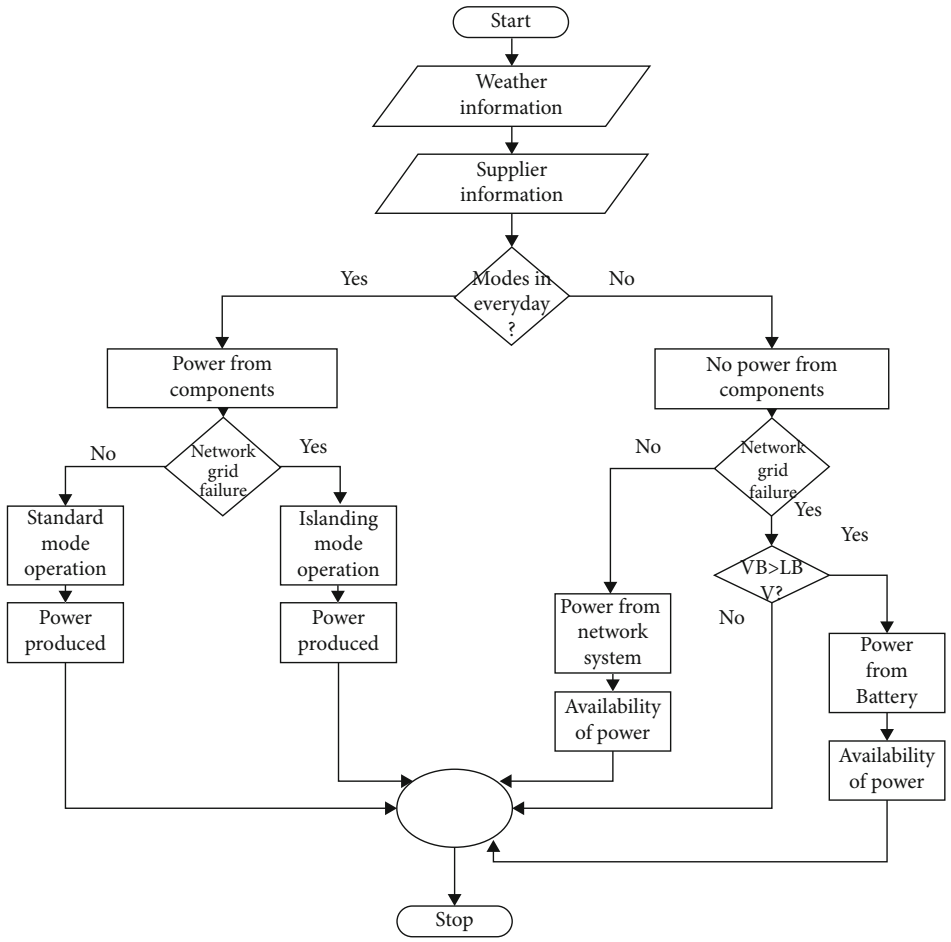

Figure 6: Flow diagram.

(iv) Grid stoppage intervals are, in reality, unpredictable in time and dependent on the state of the energy grid and cannot be determined by the PV user [34]. As a result, the model treats the PV scheme as a stand-alone system, and that is the worst-condition scenario. As a result, a software database depending on the flow chart is shown in Figure 6 is created to assess the network efficiency

4. Result and Discussion

The observed simulation results showed it during 9 months of every year, generated PV power surpasses the demand needs, resulting in a maximum battery state-of-charge (SOC) in an area. The performance of the PV-interfaced power converter's topology functioning in charging mode is verified by simulation. The simulation findings are depicted and detailed in the previous figures.

Figure 7 depicts the PV system's monthly power generation and the load's monthly power usage. As during the 9 months of March to November, the energy generated by the PV outnumbers the energy used. The extra power production will be used to partially recharge the battery block and the remainder to supply the system. The PV electricity generated and the demand electricity demand are extremely close throughout the final three months, which validates the suitability of the executed PV system design, culminating in a PV peak output of 3.2 kW. Figure 8 depicts the system's everyday energy production (kWh/kWp), which fluctuates across 2.6 and 5.4 kWh/kWp among January and July, respectively. This translates to 90% and 66.25% performance ratios, respectively. During the summer season, such as July, the performance index degrades because of better capacity PV power damages caused by relatively high temperatures.

The annual battery SOC ranges among 42 and 86%, as seen in Figure 9. It is worth noting that its minimum price remains above 40% including through the months with a weakest solar energy (Dec-Feb) and fluctuates between 73 and 84% during the remaining nine months, indicating that the battery's design is correct. Figure 10 depicts the excess PV power generated over the connected load over nine months. When additional energy is available, it will either be pumped into the system or used to increase the SOC of a battery block, and it will be discarded then SOC ranges 100%.

Figure 11 depicts an hourly calculation of demand consumption of power, PV energy, and the SOC (percentage) for 3 days in April whenever output of PV is significant due to massive energy from the sun. The battery's SOC remained steady, ranging between 77 and 93%. Figure 12 depicts the same system configuration on three days in

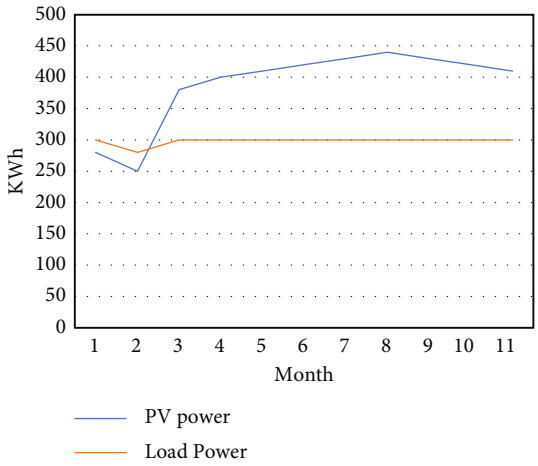

Figure 7: The PV system's regular energy production.

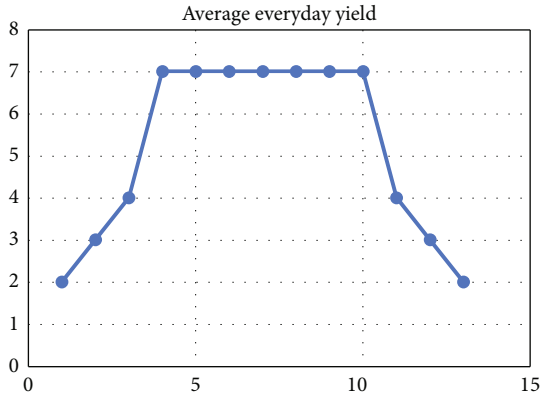

Figure 8: Average everyday yield and load usage.

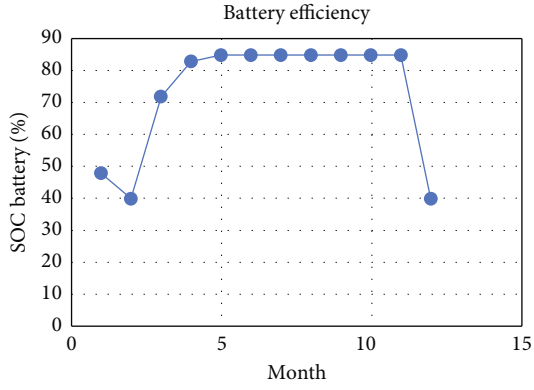

Figure 9: Block of battery SOC.

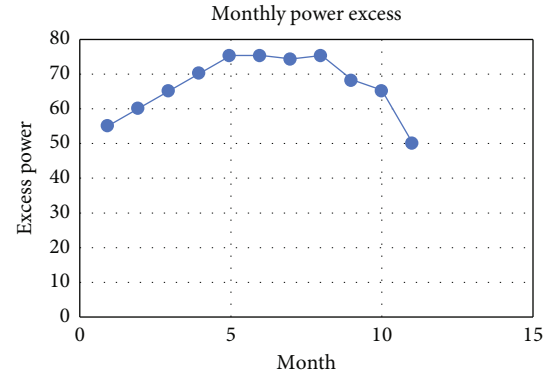

Figure 10: Excess PV power on monthly.

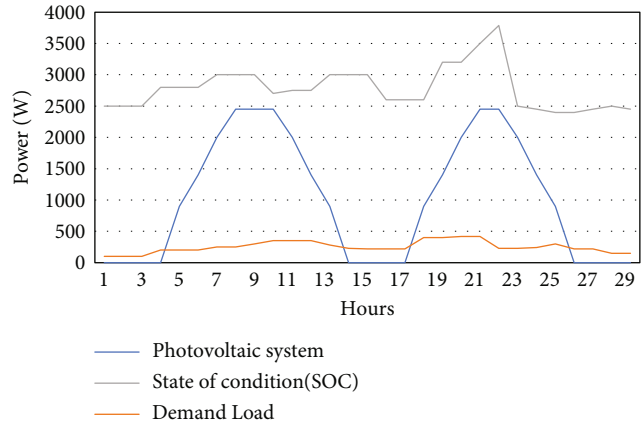

Figure 11: Three days in the month of April.

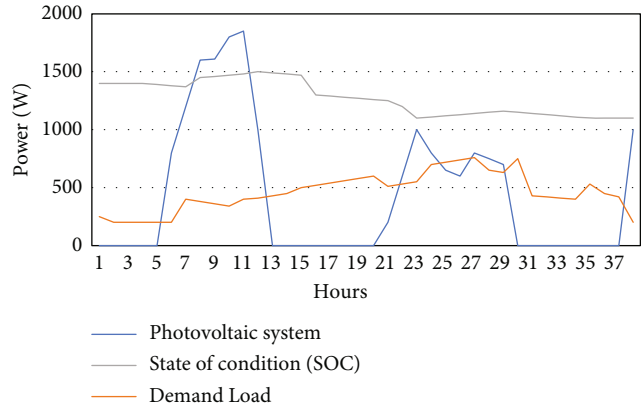

Figure 12: Three days in the month of December.

December when the energy from the sun was minimal. The SOC drops to around 30% on such periods, as can be shown.

The input variables are dependent on the preceding section's predicted design parameters. The discharging cutoff level is the proportion of the fast charger below which the battery cannot be discharged. The discharge cutoff level is 30% since the release depth is 70%. Figure 13 depicts the battery capacity of an intended off-grid device. According to the numerical simulations, the batteries remain powered up about 75% of the time over the year, with just 0.05% of the time having an empty cell, and also the amount of energy not absorbed owing to a set of batteries is 4371 Wh.

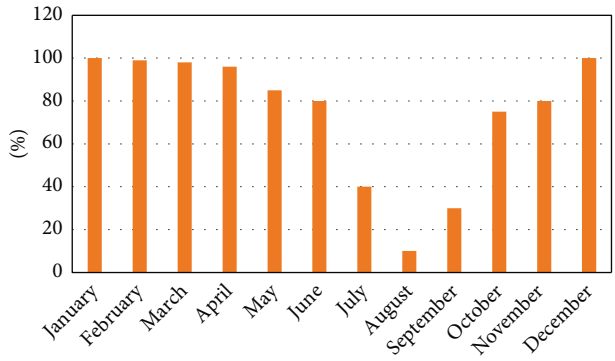

Figure 13: Performance of battery on a stand-alone system.

4.1. Performance Ratio. The energy production to targeted power ratio is shown by the performance ratio (PR). The goal energy is calculated by multiplying total irradiation (kWh/m^2) by a capsule's STC effectiveness and actual implementation area (m^2). PR indicates the losses caused by inverters, cable, shade, cell mismatches, reflections, blackouts, module heating, and other factors. The PR of a photovoltaic system deployed at the study location is measured by the 71.2% and 75% achieved in the preceding sections. According to the PV specifications, a PR of 80% or higher indicates a high-performing PV system, whereas several less than 75% suggest a concern. Nevertheless, in the instance of a building-integrated photovoltaic (BIPV) network, a PR of less than 75% may be considered acceptable. Due to increased temperature applications and the shielding impact, PR below 75% may be considered standard in the situation of a building-integrated PV (BIPV) network.

5. Conclusion

In this research, the residential residence chosen for this research has a daily power consumption of 10k Wh/day, which equates to an everyday power range of 200 to 730 W. Depending on the modeling results, a photovoltaic system evaluated at 3.2 kWp with either a battery block volume of 19.2 kWh could cover the power the most of this residence. Over 9 months of each year (Mar-Nov), the power produces by a PV system surpasses the load requirements, whereas it is nearly sufficient to the power of a charge even through three remaining months (Dec–Feb), when ultraviolet irradiance is at its minimum. These findings support the suggested PV system development's ability to address power supply issues in residential applications. Furthermore, a PR of 71.2% is computed for a building integrating PV system at this location, whereas a PR of 75% is projected for a PV tracking system. The cause for this variation has been determined to be the ability of air circulation behind PV systems that was not constrained in the monitoring system, so increasing conditioning and thus modules effectiveness. The battery block state of charge changes in the area of 73-85% throughout 9 months (March–Nov) and 40-49% percent during 3 months (Dec–Feb), indicating that the suggested PV system can fulfill the demand requirements while retaining the batteries state-of-charge at an appropriate level. In January and July, a photovoltaic service's daily energy produced ranges between 2.6 and 5.4 k Wh/kWp, corresponding to a conversion efficiency of 90% and 66.25%, correspondingly. In July, the decreased performance index shows the high-temperature difference experienced throughout the summer season.

Data Availability

The data used to support the findings of this study are included within the article. Further data or information is available from the corresponding author upon request.

Conflicts of Interest

The authors declare that there are no conflicts of interest regarding the publication of this paper.

Acknowledgments

The authors thank the Mizan-Tepi University, Ethiopia, for providing help during the research and preparation of the manuscript. The authors thank the Kyungpook National University for providing technical assistance to complete this work. This authors would like to acknowledge the Researchers Supporting Project Number (RSP-2021/373), King Saud University, Riyadh, Saudi Arabia.

References

[1] S. Singh and S. C. Kaushik, "Optimal sizing of grid integrated hybrid PV-biomass energy system using artificial bee colony algorithm," *IET Renewable Power Generation*, vol. 10, no. 5, pp. 642–650, 2016.

[2] B. Roy, A. K. Basu, and S. Paul, "Techno-economic feasibility analysis of a grid connected solar photovoltaic power system for a residential load," in *2014 First International Conference on Automation, Control, Energy and Systems (ACES)*, pp. 1–5, India, February 2014.

[3] V. A. Tikkiwal, S. V. Singh, and H. O. Gupta, "Multi-objective optimisation of a grid-connected hybrid PV-battery system considering battery degradation," *International Journal of Sustainable Engineering*, vol. 14, no. 6, pp. 1769–1779, 2021.

[4] J. Zhou, S. Tsianikas, D. P. Birnie III, and D. W. Coit, "Economic and resilience benefit analysis of incorporating battery storage to photovoltaic array generation," *Renewable Energy*, vol. 135, pp. 652–662, 2019.

[5] L. Ortiz, R. Orizondo, A. Águila, J. W. González, G. J. López, and I. Isaac, "Hybrid AC/DC microgrid test system simulation: grid-connected mode," *Heliyon*, vol. 5, no. 12, article e02862, 2019.

[6] M. A. Omar and M. M. Mahmoud, "Design and Simulation of a PV System Operating in Grid-Connected and Stand- Alone Modes for Areas of Daily Grid Blackouts," *International Journal of Photoenergy*, vol. 2019, Article ID 5216583, 9 pages, 2019.

[7] V. Karthikeyan, S. Rajasekar, V. Das, P. Karuppanan, and A. K. Singh, "Grid-connected and off-grid solar photovoltaic system," in *Smart Energy Grid Design for Island Countries*, F. M. R. Islam, K. A. Mamun, and M. T. O. Amanullah, Eds., pp. 125–157, Springer International Publishing, Cham, 2017.

[8] D. Abdoulaye, Z. Koalaga, and F. Zougmore, "Grid-connected photovoltaic (PV) systems with batteries storage as solution to electrical grid outages in Burkina Faso," *IOP Conference Series: Materials Science and Engineering*, vol. 29, article 012015, 2012.

[9] A. A. Alabi, A. U. Adoghe, O. G. Ogunleye, and C. O. A. Awosope, "Development and sizing of a grid-connected solar PV power plant for Canaanland community," *IJAPE*, vol. 8, no. 1, p. 69, 2019.

[10] S. Deshmukh, Y. Baghzouz, and R. F. Boehm, "Design of grid connected-PV system for a hydrogen refueling station," in *Solar Energy*, pp. 171–175, Denver, Colorado, USA, January 2006.

[11] K. A. Makinde, O. B. Adewuyi, A. O. Amole, and O. A. Adeaga, "Design of grid-connected and stand-alone photovoltaic systems for residential energy usage: a technical analysis," *Journal of Energy Research and Reviews*, vol. 8, pp. 34–50, 2021.

[12] N. Saxena, B. Singh, and A. L. Vyas, "Single-phase solar PV system with battery and exchange of power in grid-connected and standalone modes," *IET Renewable Power Generation*, vol. 11, no. 2, pp. 325–333, 2017.

[13] K.-C. Chang, N. Hagumimana, J. Zheng et al., "Standalone and minigrid-connected solar energy systems for rural application in Rwanda: an in situ study," *International Journal of Photoenergy*, vol. 2021, Article ID 1211953, 22 pages, 2021.

[14] O. Diouri, N. Es-Sbai, F. Errahimi, A. Gaga, and C. Alaoui, "Modeling and design of single-phase PV inverter with MPPT algorithm applied to the boost converter using back-stepping control in standalone mode," *International Journal of Photoenergy*, vol. 2019, Article ID 7021578, 16 pages, 2019.

[15] H. Lan, S. Wen, Q. Fu, D. C. Yu, and L. Zhang, "Modeling analysis and improvement of power loss in microgrid," *Mathematical Problems in Engineering*, vol. 2015, Article ID 406545, 7 pages, 2015.

[16] Y. Chaibi, M. Salhi, and A. El-jouni, "Sliding mode controllers for standalone PV systems: modeling and approach of control," *International Journal of Photoenergy*, vol. 2019, Article ID 5092078, 12 pages, 2019.

[17] Y. Jiang, J. A. A. Qahouq, and I. Batarseh, "Improved solar PV cell Matlab simulation model and comparison," in *2010 IEEE International Symposium on Circuits and Systems (ISCAS)*, pp. 2770–2773, Paris, France, 2010.

[18] H. Kawamura, K. Naka, N. Yonekura et al., "Simulation of I–V characteristics of a PV module with shaded PV cells," *Solar Energy Materials and Solar Cells*, vol. 75, no. 3–4, pp. 613–621, 2003.

[19] Y.-K. Wu, C.-R. Chen, and H. Abdul Rahman, "A novel hybrid model for short-term forecasting in PV power generation," *International Journal of Photoenergy*, vol. 2014, Article ID 569249, 9 pages, 2014.

[20] V. A. Ani, "Design of a reliable hybrid (PV/diesel) power system with energy storage in batteries for remote residential home," *Journal of Energy*, vol. 2016, Article ID 6278138, 16 pages, 2016.

[21] H. Mahamudul, M. Saad, and M. Ibrahim Henk, "Photovoltaic system modeling with fuzzy logic based maximum power point tracking algorithm," *International Journal of Photoenergy*, vol. 2013, Article ID 762946, 10 pages, 2013.

[22] N. Onat, "Recent developments in maximum power point tracking technologies for photovoltaic systems," *International Journal of Photoenergy*, vol. 2010, Article ID 245316, 11 pages, 2010.

[23] R. Syahputra and I. Soesanti, "Planning of hybrid micro-hydro and solar photovoltaic systems for rural areas of central Java, Indonesia," *Journal of Electrical and Computer Engineering*, vol. 2020, Article ID 5972342, 16 pages, 2020.

[24] H. A. Kazem and T. Khatib, "A novel numerical algorithm for optimal sizing of a photovoltaic/wind/diesel generator/battery microgrid using loss of load probability index," *International Journal of Photoenergy*, vol. 2013, Article ID 718596, 8 pages, 2013.

[25] M. Engin, "Sizing and simulation of PV-wind hybrid power system," *International Journal of Photoenergy*, vol. 2013, Article ID 217526, 10 pages, 2013.

[26] A. M. Eltamaly and M. A. Mohamed, "A novel design and optimization software for autonomous PV/wind/battery hybrid power systems," *Mathematical Problems in Engineering*, vol. 2014, Article ID 637174, 16 pages, 2014.

[27] A. H. Mutlag, H. Shareef, A. Mohamed, M. A. Hannan, and J. Abd Ali, "An improved fuzzy logic controller design for PV inverters utilizing differential search optimization," *International Journal of Photoenergy*, vol. 2014, Article ID 469313, 14 pages, 2014.

[28] A. Abusorrah, M. M. al-Hindawi, Y. al-Turki et al., "Stability of a boost converter fed from photovoltaic source," *Solar Energy*, vol. 98, pp. 458–471, 2013.

[29] K. A. Alboaouh and S. Mohagheghi, "Impact of rooftop photovoltaics on the distribution system," *Journal of Renewable Energy*, vol. 2020, Article ID 4831434, 23 pages, 2020.

[30] T. Khatib, A. Mohamed, K. Sopian, and M. Mahmoud, "A new approach for optimal sizing of standalone photovoltaic systems," *International Journal of Photoenergy*, vol. 2012, Article ID 391213, 7 pages, 2012.

[31] Y. Sukamongkol, S. Chungpaibulpatana, and W. Ongsakul, "A simulation model for predicting the performance of a solar photovoltaic system with alternating current loads," *Renewable Energy*, vol. 27, no. 2, pp. 237–258, 2002.

[32] S. Lalouni, D. Rekioua, T. Rekioua, and E. Matagne, "Fuzzy logic control of stand-alone photovoltaic system with battery storage," *Journal of Power Sources*, vol. 193, no. 2, pp. 899–907, 2009.

[33] C. Larbes, S. A. Cheikh, T. Obeidi, and A. Zerguerras, "Genetic algorithms optimized fuzzy logic control for the maximum power point tracking in photovoltaic system," *Renewable Energy*, vol. 34, no. 10, pp. 2093–2100, 2009.

[34] K. Chen, S. Tian, Y. Cheng, and L. Bai, "An improved MPPT controller for photovoltaic system under partial shading condition," *IEEE Transactions on Sustainable Energy*, vol. 5, no. 3, pp. 978–985, 2014.

Hindawi
International Journal of Photoenergy
Volume 2022, Article ID 3891881, 13 pages
https://doi.org/10.1155/2022/3891881

Research Article

Design and Implementation of a Floating PV Model to Analyse the Power Generation

Mohamad Reda A. Refaai,[1] Lavanya Dhanesh,[2] Bibhu Prasad Ganthia,[3] Monalisa Mohanty,[4] Ram Subbiah,[5] and Endalkachew Mergia Anbese[6]

[1]*Department of Mechanical Engineering, College of Engineering, Prince Sattam Bin Abdulaziz University, Al-Kharj 16273, Saudi Arabia*
[2]*Department of Electrical and Electronics Engineering, Panimalar Institute of Technology, Chennai, Tamil Nadu 600123, India*
[3]*Department of Electrical Engineering, Indira Gandhi Institute of Technology, Sarang, Odisha 759146, India*
[4]*Department of Electrical and Electronics Engineering, Siksha 'O' Anusandhan, ITER (Deemed to Be University), Bhubaneswar, Odisha 751030, India*
[5]*Department of Mechanical Engineering, Gokaraju Rangaraju Institute of Engineering and Technology, Hyderabad, Telangana 500090, India*
[6]*Department of Civil Engineering, Ambo University, Ambo, Ethiopia*

Correspondence should be addressed to Endalkachew Mergia Anbese; endalkachew.mergia@ambou.edu.et

Received 10 February 2022; Accepted 10 March 2022; Published 20 May 2022

Academic Editor: V. Mohanavel

Copyright © 2022 Mohamad Reda A. Refaai et al. This is an open access article distributed under the Creative Commons Attribution License, which permits unrestricted use, distribution, and reproduction in any medium, provided the original work is properly cited.

The floating photovoltaic (FPV) system is a revolutionary power production technology that has gotten a lot of interest because of its many benefits. Aside from generating electricity, the technology can also prevent the evaporation of water. The electrical and mechanical structures of FPV power stations must be studied to develop them. Much research on FPV technologies has already been undertaken, and these systems have been evaluated from many perspectives. Many problems, including environmental degradation and electricity generation, fertile soils, and water management, are currently limiting societal growth. Floating photovoltaic (PV) devices save a great of land and water resources and have a greater energy conversion efficiency than standard ground power systems. A performance investigation of photovoltaic (PV) installations set on a moving platform is carried out. The paper presents and discusses various design alternatives for boosting the profitability and efficiency of floating photovoltaic (FPV) systems. Especially, FPV systems that take advantage of increasing capabilities like monitoring, conditioning, and attention were included. Although researchers have agreed on the benefits of floating systems, there has been little in-depth research on the parameters of floating photovoltaic systems. The results of this research tests were performed, and these reveal that the beneficial monitoring and conditioning impacts result in a significant gain in performance. The effects of using flat reflections on improvements are also investigated. As a result, this research examines the evolution of photovoltaic systems, then investigates the power generation capacity of floating photovoltaic systems, and then examines the benefits and possibilities of floating PV systems in depth. The concept of developing an integrated air storage system using a floating building on waters is discussed.

1. Introduction

Electricity expenses have a significant impact on farmers' earnings currently. The primary reasons for agriculture's poor predicament include higher productivity expenses, limited farming sizes, competition for worldwide marketplaces, and a water shortage [1]. As a result of increased usage of water supplies and modernization initiatives implemented in recent years, the agricultural industry's power consumption is expected to rise. Water savings have resulted from the construction of more effective irrigated equipment, while energy consumption has increased due to increased filtering

and pumping functions. As a result, while water effectiveness in agriculture has enhanced, electrical energy consumption has increased significantly. Water prices are affected negatively by increased adjustments in electricity tariffs and unclear future situations. The resolution to these challenges comes not just from establishing specialized irrigated electrical tariffs but also from enhancing the irrigated devices' power and water productivity. Renewable power resources appear to be a means to counteract these circumstances [2]. Conventional irrigated methods will be converted to pressurized networks under the novel irrigated designs. In the vast majority of instances, modernization has necessitated the establishment of water reservoirs. World reservoirs waterproofed with geomembranes are the most extensively utilized storing technology among the several options.

Following the implementation of an RPS, the renewable power economy has recently expanded. As a result, much study is being conducted on approaches to the availability of appropriate sites for the installation of highway photovoltaic systems [3]. The floating photovoltaic system shown in this work is a novel technique of renewable electricity that takes advantage of the abundant surface of the water on bridges, lakes, as well as other water bodies. This technology has the benefits of utilizing the available resources use of the country's soil without causing ecological harm, as present photovoltaic systems do when deployed in croplands or woods. Until 2013, Korea gave photovoltaic power installations the same REC value as regular photovoltaic systems. Acknowledging the intellectual importance and necessity of a floating photovoltaic system, on the other hand, a solar panel, a smokestack, and an energy transmitter unit are the three major aspects of a solar power plant. The energy of the sun hits the earth below this one passing through the translucent absorber cap. Heat dispersion warms the air above the bottom as the surface heat increases [4]. As the heat of the air increases, the volume of the gas decreases. The volume differential between both the surrounding atmosphere and the airflow in the solar concentrator is then created. Underneath the water current, the air is circulated toward the center of the solar collector via the chimney. The air passes via the flue and exits through the SCPP just at the peak. The buoyancy event caused the rising air just above the surface as well as the photovoltaic panels to stream into the stack [5]. The solar PV/T technique or equipment was developed to chill the photovoltaic to improve its power usage and collect excess heat to improve the overall performance of the system. It is commonly used in solar heating, thermal, air, and climate control (HVAC), as well as energy from the sun structures. The sizable PV/T technology, on the other hand, has still not been researched. In light of this, the primary goals of this experiment are to mathematical model again for SCPVTPP, examine its effectiveness, and investigate the SCPVTPP with various PV regions.

Due to population and economic growth in underdeveloped nations, an incremental keep rising in levels of comfort in developed nations, the supply for more products and merchandise, and a spike in the proportion of electric cars for public transit and petrol vehicles, electricity consumption has risen dramatically in recent years. As per the Energy Agency, India's energy consumption would rise by 35% by 2041, whereas only a small portion of China's economy will grow its power need by 20%. As the requirement for energy rises, emission levels increase as well [6]. This can be avoided if the electricity is produced utilizing renewable sources of energy. One of the most attractive sustainable energy systems is photovoltaic technologies (PV), which transform solar radiation into electricity. In 2017, 90 GW of new solar PV capacity was produced globally, bringing the total installed PV power to 402 gigawatts per year. The power factor ($P_{\max}$) generated by photovoltaic panels must be increased regularly to secure the required amount of energy [7]. This can be accomplished by following the study findings in the work process, as well as using extrinsic approaches, which are the subject of this work because the users of the panels can make improvements. Maximizing the active area of solar cells is an example of the first type of trial.

The greatest electricity produced by photovoltaics rises in proportion to the amount of solar irradiance falling on it. Sun-tracking devices, which mirror solar energy on photovoltaic panels and solar concentrated structures, can help to alleviate this problem. All of these methods create new issues that must be addressed to achieve genuine progress [8]. One of the most serious issues is that as irradiation grows, the warmth of photovoltaic panels rises, and in concentration devices, the allowable thermal performance for solar devices is readily surpassed, particularly at a high concentrate rate. The maximum output by a crystalline silicon cell reduces by 0.45 percent every degree Celsius, and the lifespan drops as well. To change the temperature of the solar cell, active and passive cool techniques are employed. The thermal consistency of the solar panel area is critical for the photovoltaic to function effectively, and conditioning solutions must guarantee stability. One issue that emerges is that the cooling method is economically viable [9]. The additional lifetime of the photovoltaic panels provided by the cooling system is vital to assess, both economically and environmentally. As a result, in concentrated light sources, the air conditioning system is very essential for photovoltaics.

There have been no PV panels in the upright stack due to regulatory and building financial concerns. Solar energy passes through the lens glass cover before reaching the PV modules. Between both the PV panels and the earth, insulating material and wiring connections are installed. The PV systems receive cosmic rays that pass through the transparent cover. The PV systems produce power on their own. And meanwhile, part radiation from the sun is transformed into latent heat, which is used to warm the PV panels. By heat flow, the elevated PV systems heat up around them [10]. The part of the solar collector that is not covered by photovoltaic panels receives cosmic rays directly, causing the ambient temperature to rise. Thermal conduction causes the earth to warm all air from above. The gravity phenomenon makes the air elevate just above the surface, and the photovoltaic panels stream into the stack. The photovoltaic solar method or equipment was developed to chill the photovoltaic to improve its power usage and collect excess heat to improve the overall device performance.

Based on the foregoing, floating photovoltaic devices could provide synthesized solutions for power generation that do not place a substantial burden on water or land resources. The installation of photovoltaic panels on a floating platform on the water surface is a novel type of solar energy-producing technology. In 2007, the initial research on floating photovoltaic modules was conducted to evaluate their efficiency to that of typical terrestrial photovoltaic facilities [11]. By the end of 2014, 22 solar energy stations had been erected across the globe, with installation capacities ranging from 0.5 kW to 1157 kW, after the first experimental photovoltaic power facility was established in California in 2008. In contrast, Water Resources Incorporated has begun construction on a 500kW floating photovoltaic plant, with plans to expand the framework to 1800 kW by 2022.

A floating photovoltaic power plant (FPPP) device is increasingly being investigated as energy supplying alternatives and also approaches to other concerns such as water evaporating from different lakes and reservoirs. Several floating photovoltaic systems have lately been constructed in oceans, canals, reservoirs, rivers, and ponds with varying degrees of utilization [12]. This looked at the several floating photovoltaic installations that have lately been completed. This describes the impacts of constructing a floating photovoltaic system on the surface of a pit lake for the scenario of an open-pit limestone mining that is gradually being closed [13]. A floating photovoltaic installation on a pit lake of an inactive mining area is regarded to be an effective recycling alternative for abandoned mining, including the economic and environmental benefits from greenhouse emission reductions and power sales. Trapani and Millar examined the viability of integrating a floating photovoltaic energy production with an established conventional energy station in Malta.

Power stability and global warming are two challenges that are emerging in tandem with rising power consumption. Renewable power options have been emphasized in a variety of corporate sectors across the globe because of their potential to improve power safety and reduce greenhouse gas emissions when compared to traditional fossil fuels. Renewable solutions, on the other hand, face a significant obstacle in the form of higher investment expenses, while the price of fossil resources remains cheaper [14]. As a result, when evaluating potential options, not only the ecological viewpoint but also the economic efficiency and social well-being must be taken into account [15]. Even though floating photovoltaic devices have greater initial investment expenses, various considerations could enable the technologies more practical than ground-mounted photovoltaic (GMPV) devices, including the following:

(i) Increased converting performances due to reducing thermally drifting, resulting in increased power outputs

(ii) A zero-land-requirement; land might be important actual estates for farming reasons, as well as in regions where electricity is in high demand, including towns and major cities

(iii) Because there are fewer limits on component spacing in floating photovoltaic technology, greater power efficiencies are possible

(iv) In addition to the preceding argument, many of the world's major towns have been developed on the shore, where there might be a plethora of prospective locations to install on, as well as potentially sufficient grids infrastructure surrounding

(v) Furthermore, protecting the water surfaces could prevent potentially dangerous algae blooms from photosynthesizing

(vi) According to the nearby closeness of water, it is simpler and less expensive to integrate cleaning devices and cooling veil; however, this might be impeded in saltwater regions

Moreover, continuing analysis reveals that the Albedo impact produces increased ambient air temperature changes and unfavourable environmental repercussions for ground-mounted photovoltaic schemes, but the impacts are mitigated for floating photovoltaics.

2. Related Works

The floating photovoltaic system is a novel energy infrastructure proposal for meeting energy demands. Existing territory equipment is combined with recently designed floating photovoltaic panels in the construction plan. The electricity efficiency of solar systems diminishes as the temperature rises. As a result, the solar panel must be chilled by eliminating heat in a certain way to get higher effectiveness. Floating panels are installed on water-resistant high-density thermoplastic polyethylene (HDPE) frames. The effectiveness of floating and land-based energy production was investigated in the present study. The study's goal is to examine and contrast the performance of the original and floating-based PV systems. The system has a 250-watt capability attached. The equipment is put to the test in conditions ranging from 125 W/m^2 to 945 W/m^2. The data were evaluated using the current (I)–voltages (V) and also power (P)–voltages (V) graphs. When compared with the conventional approach, the floating framework has been demonstrated to be more efficient. According to the research, FPV has greater efficiency and complete power increase. Waterways, rivers, wetlands, and water supply all benefit from the FPV systems [16].

The parametric study of a mechanism for extracting groundwater for cultivation utilizing an alternate power source is described in this work. The system was created using data from a previous project in Lalmonirhat, Bangladesh. A 38.4-kWp photovoltaic power panel, converter, AC engine, and pumping set make up the network that can output up to 1930m^3 of water every day. Two forms of energy storage technologies are simulated in MATLAB: (i) electrical energy contained in a power supply and (ii) conserved liquid in a big water reservoir. In the earlier studies, a huge battery bank and a converter are required, which proves to be a

pricey option. Either one, which seems to be a pricey alternative, involves a boost converter and a massive water reservoir to contain roughly 2000m^3 of water. A solution that combines both systems is both efficient and cost-effective. The efficiency of such three technologies is evaluated to that of a traditional diesel generator [17].

A significant proportion of Ethiopians resides in rural areas so rely on woods for their residential energy needs. Domestic usage of wood and fuel causes degradation and health concerns, as well as being highly polluting. The Ethiopian government has indeed been attempting to generate electricity from commonly accessible renewable energy resources. As a result, using a spatial database analysis to predict the surface of the water's high level of energy gathering with a floating photovoltaic system is employed to assist decision-makers in utilizing high-potential locations. Variables that influence usefulness were discovered and evaluated using analytic network procedures to determine suitable locations for floating photovoltaic panels. To create a complete applicability mapping of floating rooftop solar utilizing the ArcGIS software, weighting numbers and unclassified quantities were compounded. The effectiveness of floating solar PV systems is reduced due to their incorrect placement. As a result, the goal of this research was to determine the most useable area of waterways for producing power in Amhara local, state-wide irrigation reservoirs. Angereb, Rib, and Koga agricultural dams had usable water surfaces for floating solar PV power plants of 63.83%, 61.09%, and 57.20%, correspondingly. The bulk of the useful sections was located in the water's midsection. The floating photovoltaic systems and irradiation arriving in the photovoltaic solar module surface are affected by the environmental surface of the water, which is a major component in electricity production [18].

The influence of various impacts posed by shutout collisions (which include affiliated, supplementary, and mixture dangers) and the activating happenings that could cause accidents of the offshore floating nuclear power plant (OFNPP) is formed, with an emphasis on using nuclear power generation in offshore petroleum fields. Blowout incidents in offshore oil resources are summarised and studied in terms of risk origin, entire investment, risk development, and risk management action method. The shutout accidents in offshore oil fields have a wide range of effects on OFNPP, such as injection burning and spilled oil ignition stimulated by good flameouts, wandering, and the blast of heat-release vapor clouds created by good flameouts, saltwater contamination engendered by drubbing oil spillage, etc. The influence of a portable heat source is generated by a flaming oil spill on OFNPP at sea, and also the hazardous gas cloud is generated by a good explosion. For the effects of blowout events on floating production nuclear power stations in offshore petroleum fields, assumptions are as follows, methodologies and associated processes are devised, and a computation example is presented to further demonstrate the methodologies [7].

Photovoltaic power capacity is constantly shifting due to environmental factors such as temperature and other factors, which have a significant effect on the power grid implementation and design. As a result, it is critical to developing an appropriate projection of photovoltaic (PV) system power production in advance. A novel particle swarm optimization method using a multivariable grey theoretical model is adopted in this research for short-term power-generating volume predictions to increase prediction performance. The predictive performance of the grey theoretical model is projected to be greatly enhanced by including the particle swarm optimization technique. Furthermore, for validation of the model, substantial volumes of real information from multiple independent generating stations in Chinese were used. The testing experiments demonstrated that the proposed designer's average relative error has already been decreased from 7.14%to 3.53% when compared to the standard grey paradigm. Both from a conceptual and a pragmatic standpoint, the suggested optimization technique beats the standard parametric approach in practice [19].

Increased amounts of sun irradiation can induce changes in the ambient temperature of photovoltaic (PV) panels, which can reduce their effectiveness and lifetime. The decrease in the ambient temperature of PV panels with such an air-cooled heat sink is investigated in this work using theoretical and analytical analysis. An aluminum plate with punctured fins was designed to be placed to the rear of the PV panel as the suggested heating element. To check that the heat transfer concept operated effectively, a detailed computational fluid dynamics (CFD) model was simulated using the program ANSYS Fluent. The impact of heating elements on energy transfer among a PV panel and also the surrounding air was explored. The study indicated a significant reduction in the temperature range of the PV panel as well as an improvement in its electrical characteristics. The temperature increase of the PV panel was reduced from 85.3°C to 72.8°C using the CFD analysis in passive heat sink simulation with just an air-fluid velocity of 1.5 m/s and a temperate of 35°C under a thermal gradient of 1000 W/m^2. The passive heat sinks raised the voltage open-circuit (VOC) and maximum power point (PMPP) of the PV modules by 10% and 18.67%, respectively, as a result of lowering their temperatures. As a result, the use of aluminum heat sinks could be a viable solution for preventing PV panels from scorching, as well as an indirect decrease in CO_2 emissions due to greater PV system energy output [20].

3. Materials and Methods

Floating photovoltaic is a common solar innovation that includes placing solar modules over natural or manmade water bodies instead of on land. Depending on their supportive components, floating photovoltaic devices are divided into three categories: Permanent tilt panels required rigid pontoons; monitoring patterns could be erected with or without pontoons; and flexibility matrices do not require a supportive framework in the shape of a pontoon because of their low weight. High-scale (MW to GW), small-scale (few kW), and medium-scale (kW to MW) floating photovoltaic could also be characterized depending on the size of

installation. Permanent floating photovoltaic devices cooled FPV devices, and floating-tracking PV systems could be classed depending on the diverse supportive structural architectures of FPV devices. The net investment expenses of floating-tracking photovoltaic devices are higher than permanent floating photovoltaic installations, but they produce more power.

Solar photovoltaic components are often mounted utilizing solid mounted systems on the buildings and ground. Because of a lack of available space, a dense population, and a serious hazard of deforestation, interest in installing photovoltaic panels across reservoirs, oceans, lakes, and canals has grown. Photovoltaic panels are erected above water surfaces by applying appropriate technologies to make them float, and these implementations are known as floating photovoltaic plants. Photovoltaic panels' electrical energy generation is largely dependent on incident solar radiation and panel temperature. In FPV devices, shadowing impacts are minimal or nonexistent, and the temperature of the panels could be reduced by placing water beneath them. Floating photovoltaic modules have an approximately 12.0 percent better performance than rooftop as well as ground-mounting photovoltaic modules. Pontoons/floats, mooring devices, photovoltaic modules, and electrical adapters and cables are the primary elements of floating photovoltaic devices, as depicted in this diagram.

Pontoons are buoyancy-assisted floating structures that include an area for human accessibility as well as photovoltaic modules. Pontoons are usually built of a corrosion-resistant, tensile-strength material, UV-resistant, and high-density polyethylene (HDPE). The mooring device is a structural framework that keeps the pontoons in place and prevents them from shifting. To handle dead loading and lateral pressures, rigid structures in the form of anchorages are established utilizing foundations across the reservoir's circumference. In most floating photovoltaic devices, stiff flat-type photovoltaic modules are utilized. Flexible modules that respond to the movements of the waves, on the other hand, are more appealing. Then, a T3F-PV module-based floating photovoltaic arrays were created. They created a small-scale version of a thin-film-oriented floating photovoltaic device in this example, which was put on an isolated water body. The findings of the 40-day operations revealed a 0.5 percent drop in electrical performance due to silt obstruction on floating photovoltaic components, whereas the water-cooling impact resulted in an estimated electrical enhancement of 5 percent for three months. This is also advocated for the usage of bifacial photovoltaic components in floating photovoltaic devices. They claimed that bifacial components could catch reflecting photovoltaic irradiation from the water's surface, increasing performance. As functioning on the surface of the water, the north-/south-oriented bifacial components could yield a maximum of 55 percent increase in exposure to irradiation whenever compared to traditional components. Figure 1 depicts a wide categorization of different floating photovoltaics that have been documented in the research.

As illustrated in Figure 2(a), a conventional floating photovoltaic module includes a photovoltaic component, a floating framework, and a supporting device. In this form of configuration, strong winds and an uneven surface are two major dangers to rigid photovoltaic modules. Both permanent and monitoring floating devices require mooring to maintain the platforms of position in Figure 2(b). The floating platforms, on the other hand, could be attached to the bottoms or banks of small lakes. The paneling framework is installed on floating structures such as modular rafts, plastic rafts, and pontoons. Because many sources of water include salinity, which can harm photovoltaic panel framing, polymer-based screens and support are preferred for extended panel life. Electrical cabling is used to carry electrical generated by floating photovoltaic modules over water features to the land; therefore, high temperature, waterproof, resistant cabling, and electrical connections are essential for the device's long life. The main reasons for the floating photovoltaic device's poor efficiency are dust collection on the panels as well as an increase in panel temperature. Water cooling reduces radiated reflections and temperatures of floating photovoltaic modules, allowing the device's electrical production to be enhanced by roughly 10 percent to 13 percent. The amount of power used in this process is only about 0.25 percent of the overall power production.

3.1. Structural Design of Floating Photovoltaic (FPV) System. From an architectural standpoint, the structure is made up of the succeeding main components as shown in Figure 3:

(i) Floating platforms (pontoons) ensure the energy-producing service's buoyancy and durability. They are manufactured from rotationally molded medium-density polyethylene (MDPE), and everyone holds two photovoltaic modules

(ii) Photovoltaic component-supporting framework (UF and CF cold-formed metal frameworks) that should be capable to sustain the photovoltaic components' weight while also transmitting wind forces through the pontoons to the perimeter anchored device

(iii) Articulated metal couplings among pontoons (metal linkages or cabling connecting the pontoons, permitting horizontally and vertically migrations, and also gyrations) are used to enable the decks to adjust to concave reservoir patterns

(iv) Flexible connections (MDPE straps or elastic that are permitted to extend before being constrained by nylon ropes or rigid polyester that kick in whenever the maximum movement is achieved) enable the pontoons to shift in connection to one another, enabling the device to adjust to various water stages

(v) Anchors the floated covering and transfers horizontal pressures to the reservoir's sidewalls utilizing a rigid anchorage method (reinforced concrete piles that withstand laterally stresses utilizing the passive pressure of the neighbouring earth)

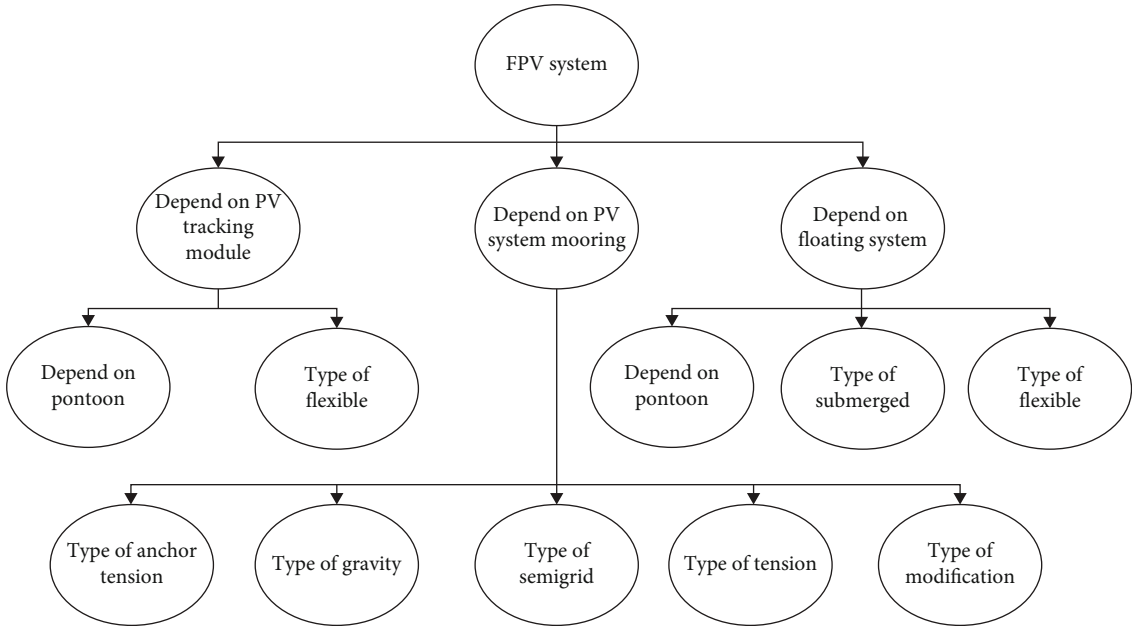

Figure 1: FPV on a different system.

(vi) Cables (nylon nautical and polyester cables) were utilized to secure the floating cover's outermost components to the reservoir's edges

3.2. Finite Element for Floating Photovoltaic Systems. Silica, EVA, glass polycrystalline photovoltaic panels, EVA, and TPT technologies and improvements layer make up the three-dimensional structure of a polysilicon photovoltaic panel. The PV cell is 156×156mm in size, and the heat transmission form is depicted in Figure 4. The designer's values are presented in Table 1.

Dispersion and irradiation are the primary modes of heat transmission in the modules when it is exposed to air. Notton's equation is used to calculate the temperature distribution at the module's edges in Equation (1).

$$h_{\text{front}} = 8.56 + 2.55v, \tag{1}$$

where h_{front} is the front radiative ratio and v is the back radiative factor. In this study, the brightness and wind velocity are considered $1000\,\text{W/m}^2$ and 1 m/s, correspondingly [21]. Because the back of the photovoltaic panel is rarely as well refrigerated as the front, the radiative ratio is considered twice those of the front. The residual energy is used to increase the operating temperature of panels, while a proportion of solar irradiation is transformed to energy. The received solar energy Q is therefore converted to the produced PV cell's heat. The flow numerical solution is based first on the study and is provided on Equation (2):

$$Q = \frac{(1 - \eta) \times G \times \alpha \times A_{\text{panel}}}{V_{\text{cell}}}. \tag{2}$$

This is the PV panel's electricity effectiveness. consists of the panel's front portion. is the PV cell's capacity in liters. The brightness at the front edge of related strata is denoted by the letter G. Its absorption coefficient is the layer's optimum parameters. Table 2 lists the settings of Q and other characteristics utilized in the experiment. The average temperature above the lake surface would indeed be lower than the energy on land depending on the cooling impact of the water. This considered a 30°C temperature and humidity on land and a 25°C temperature difference over the surface of the ocean inside this investigation.

3.3. Floating PV System. The integration of photovoltaic power technologies and float technologies has resulted in a perfected photovoltaic float energy production [22]. This fusion is a novel approach to technological advancement. It can enable new photovoltaic facilities that are erected on top of woodland, agriculture, and buildings as next-generation hardware. A floating system, mooring system, photovoltaic, and submerged cabling make up the PV float facility. Figure 5 represents the flow diagram of the floating PV system: floating device: the model which permits the fitting of the photovoltaic model; mooring device: it can respond to changes in sea levels while remaining in a downward direction; PV device: over the front of the floating network, PV generation hardware, comparable to electric connection points, is placed; and cable underwater: passes produced electricity from the grid towards the photovoltaic system.

3.4. Tracking-Type Floating Photovoltaic Architecture Concepts. A rotational center of the rotating framework is required to rotate the floated framework on the water layer, and anchoring at the rotational center could be efficient. As a result, pillar-like or stake objects should be erected in the direction of the water in an attempt to stabilize the rotating center. Moreover, if the water depths are high, the

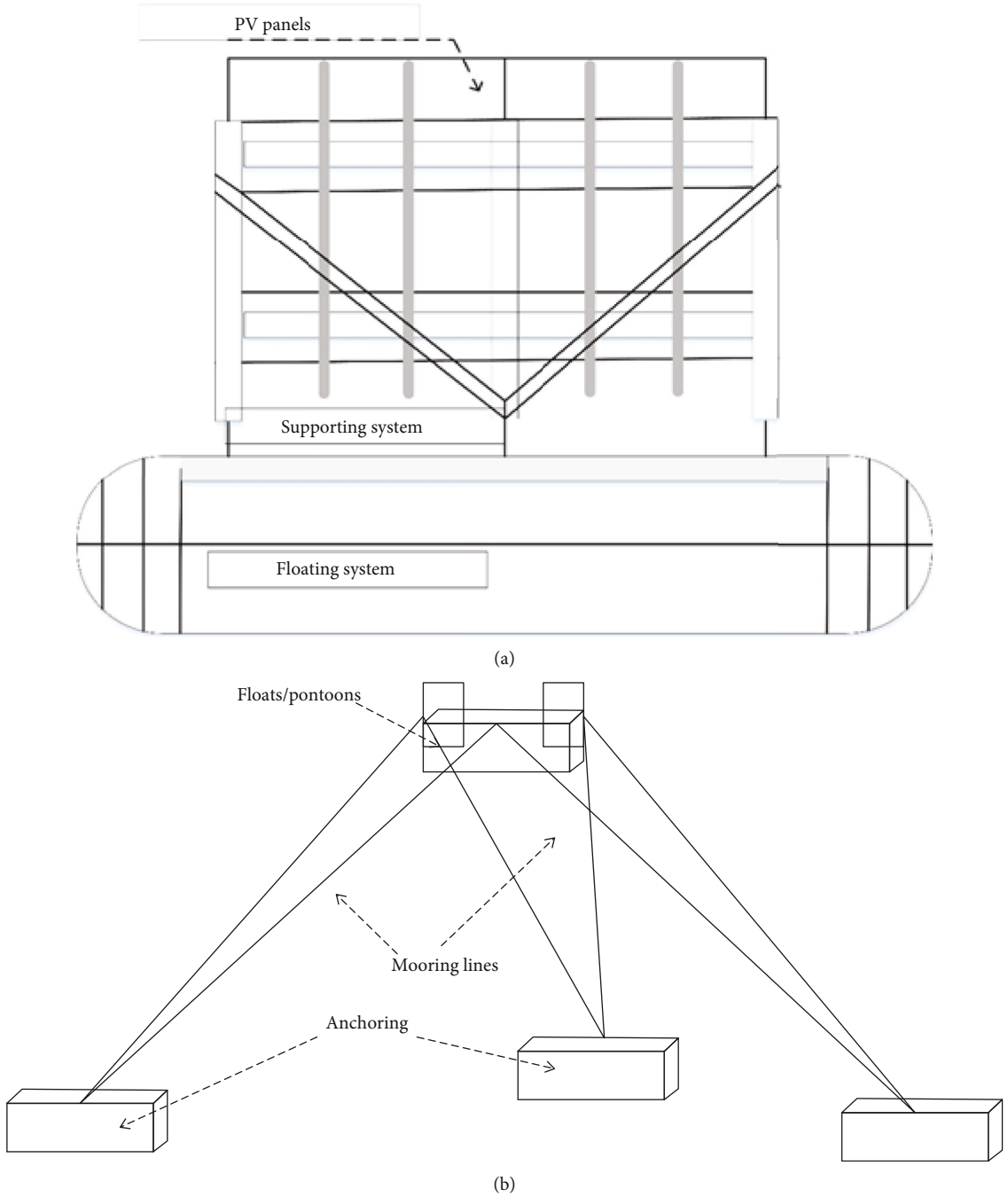

Figure 2: (a) Related mechanism for different photovoltaic systems on FPV module. (b) Mooring system.

framework constructed to maintain the rotating center limits the economic potential of photovoltaic energy stations when compared to the implementation expense, and it is complicated to provide architectural security for the fixing of a big horizontal directional framework at a specific site. Internal rotating structural and exterior static frameworks were therefore used to preserve the rotating center and enable the rotating of the framework [23]. The exterior permanent component serves as a guideline for the inside circular construction to revolve, and it is interconnected to the mooring device to allow the complete framework to be anchored in place.

3.4.1. A Rotating Framework Is Used to Monitor Azimuth. The rotational technique of how the inside rotating component circulates within the exterior permanent framework is significant in tracking-type floating photovoltaic since it includes an internal rotational component and an exterior fixed component. The ropes and reverse/forward rotational technique, the worm and worm gear technique, the chains

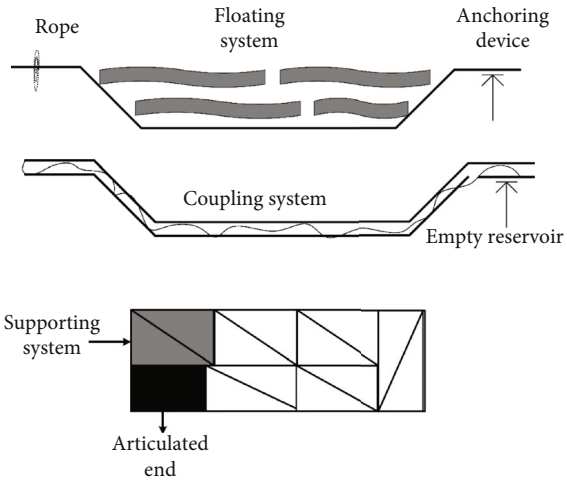

Figure 3: Structural design of floating photovoltaic (FPV) system.

and rolling guidance technique, the constant buoyancy rolling guidance and rope or chain process, and the gearing and rotating ring technique are all examples of rotational processes.

The technique utilizing equipment and orientation circle, for example, spots the equipment at the predefined buoyancy, wraps the sealed rotation circle around the boundary of circular buoyancy, and utilizes the engine; it has the feature of connecting a spherical rolling pin to the commissure of rotating buoyancy and fixed buoyancy to promote rotation while retaining the movable buoyancy to protect motion resulting from water surface flows [24].

3.4.2. Monitoring Tilt Position with a Tilt-Variable Framework. A dual-axis tracking-type floating photovoltaic that monitors the angle of tilt was devised in addition to monitoring azimuth angle by rotating an inner circular framework.

3.4.3. Floating Photovoltaic Implementation. Hybrid projects integrating floating photovoltaic modules with hydropower facilities have the potential to generate a significant amount of the globe's overall energies. For a nation with several hydroelectric facilities and dams, floating photovoltaic is a viable option. If the floating photovoltaic farms are placed near hydroelectric stations, operators could utilize current electricity resources including such transmitting cables. For coastal areas, a novel solution combining floating photovoltaic with battery storing and hydroelectric has been developed [25]. To fulfill peak requirements, the intermittent floating photovoltaic energy is combined with a rechargeable power-storing device. Colocation with hydroelectric facilities would assist to increase the generation of such facilities while also smoothing the production curves. By altering hydroelectric productivity, floating photovoltaic equipment near a reservoir's dam provides for the unsteady productivity of these devices, whereas photovoltaic structures could substitute for the hydroelectric power shortage in the medium to long run. Floating photovoltaic is a versatile and useful technique. Wind turbines are installed in the areas underlying the reservoirs and are interconnected to the general electricity distribution cables in this situation. The installation of a wind turbine could help compensate for the inconsistency of hydropower and floating photovoltaic power output.

(1) Appropriate Locations. Although the number of hydroelectric implementations in typically arid regions (Northern Mexico, the Persian Gulf, Central America, Australia, Sahara, etc.) is notably fewer, they are nevertheless there [26]. Because hydroelectric is a key regional resource, this is the case. Asia has a significant benefit in that it has the maximum density of higher energy dual-power solar/hydro locations in the globe. Tidal flows in Korea and China, canals in Japan, aqueducts in Japan and China are one of the locales, as also rivers in Malaysia, Vietnam, Japan, and Indonesia.

(2) Dry Seasons. Throughout the dry periods, photovoltaic cells have the maximum performance, whereas wet periods have the largest hydroelectric capacity. As a result, both techniques could be used in tandem. Features to consider while evaluating a location for a floating photovoltaic system are shown in Table 3. Dry periods are usually less problematic. The rafts could remain on the dry banks, giving the structure more power till the water levels can be restored. Considering reservoirs' large open-surface region, this is a good approach to obtain the most out of anything that would have been expensive a lot in regards to displacing houses and actual property [24].

4. Results and Discussions

Data was studied from two experimental configurations: a 35 kW framework with monitoring reflections and cooling, also a land-based photovoltaic implementation for comparisons, and a 250 kWp frameworks with monitoring. The FPV device was put in an irrigated reservoir with a surface area of around 5000 m^2 and a depth of 3 meters. This implementation has primarily served as an outside laboratory, allowing for the collection of more information: Polycrystalline photovoltaic components with a capacity of 250 Wp (tolerance 0/+5 W) and 65 cells have been implemented. This component's primary thermal parameters are as follows: NOCT = 50°C + / − 2 K; maximum power thermal, open-circuit voltages, and short-circuit current factors are 0.42 percent/K, 0.08 percent/K, and 0.50 percent/K, correspondingly; measurements $(L \times W \times H$ in mm$)$ are $987 \times 1778 \times 55$; and the weight (kg) is 20 kg. A particular hardened low-iron glass with an antireflex covering is another feature of these modules.

4.1. Enhancement of Performance. The research assessed the energy generating performance under cooling impacts depending on the cooling factors found in the simulations. The cellular effectiveness for terrestrial photovoltaic panels is 15.30 percent, whereas the cell performance for floating photovoltaic panels is 15.61 percent. The generating effectiveness of the floating photovoltaic device is around 2.02 percent better than the terrestrial photovoltaic systems, with

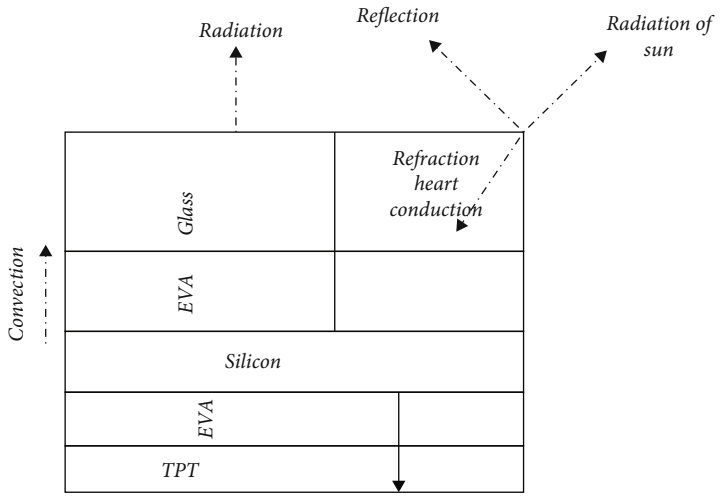

Figure 4: Internal structure of PV cell.

Table 1: Properties of physical material.

Physical material	Layer	Thermal conductivity	Specific temperature	Density	Thickness	Absorptivity
Silica	Silica cell	132	675	2337	0.4	0.7
EVA	Encapsulated	0.321	2084	974	0.3	0.04
TPT	Back-sheet	0.18	1287	1230	0.4	0.12
Glass	Upper cover	0.8	780	2550	3.4	0.05

Table 2: Parameter's result.

Parameter model	Load PV	Floating PV
Average temperature, T_a (°C)	32	28
Generation of heat on PV battery, $Q\left(\mathrm{W/m^3}\right)$	3200	3200
Rear convective coefficient, $h_{\mathrm{front}}\left(\left(\mathrm{W/m^2}\right)\times \mathrm{K}\right)$	5.54	5.54
PV effectiveness, η_{ref}	0.165	0.165
Front and side of convective coefficient, $h_{\mathrm{rear}}\left(\left(\mathrm{W/m^2}\right)\times \mathrm{K}\right)$	5.57	5.57

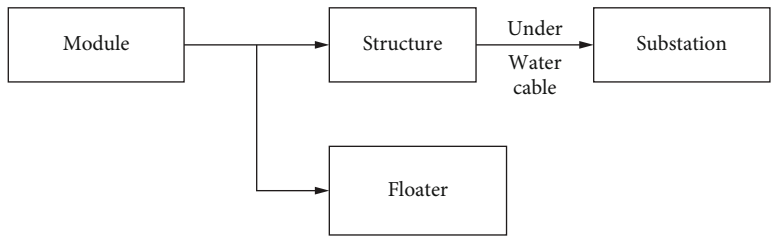

Figure 5: Flow diagram of the floating PV system.

an electrical temperature factor of 0.55 percent and an operational temperature differential of 4.5. The performance of a photovoltaic device is influenced by a variety of factors, including radiation intensity, wind speed, and ambient temperature. Under identical environmental circumstances, the power-generating effectiveness of floating photovoltaic devices would be 2.00 to 2.05% greater than terrestrial devices when various aspects are included.

4.2. The Possibilities of Floating Photovoltaic Panels. With a water surface utilization ratio of 3 percent and a photovoltaic covered area of 20 $\mathrm{m^2/kW}$, the possible capability of floating photovoltaic devices could approach 165 GW, covering around 3000 $\mathrm{km^2}$ of water surfaces. It would generate $2\times 10^{27}\,\mathrm{m^3}$ of water per year from vaporization. If floating photovoltaic devices are combined with hydroelectric plants, yearly energy production from floating photovoltaic devices

Table 3: Features to consider while evaluating a location for a floating photovoltaic system.

	Floating photovoltaic
Advantages of the power network	(i) Capability to adapt to modern electricity networks (for example hydropower systems) (ii) Hydroelectricity has a lot of possibilities for integration
Use of the land/water surface	(i) Ground excavations have a lower environmental impact (ii) Sites near densely developed regions are frequently simpler to come by (iii) A potential alternative for nations with archipelagos
Performances	(i) Generally, a greater starting efficiency ratio (5 to 10 percent, depending on the climate) (ii) Long-term degradation (for example, induced degeneration) is yet unknown
Operational parameters	(i) Low diffused light reflecting from the water surface (ii) The appearance of evaporation cooling and increased wind velocity in generally
Technological	(i) Metal components corrode and oxidize more quickly in humid environments (ii) Cleansing water is simpler to come by (iii) Vandalism and stealing are less likely to occur
Security	(i) The continual shifting of the floating creates a threat for pedestrians (ii) There is a chance that someone will tumble into the water
Losses	(i) Less dusty soiling, but possibly more from bird excretions (ii) Temperature misalignment and inhomogeneity in component facing could cause mismatches

will exceed 250 TWh, resulting in additional indirect water savings of $1.35 \times 10^{12} m^3$. As originally stated, finding land for photovoltaic energy stations has become a major difficulty, despite the government's strong support for the establishment of distributed photovoltaic networks. Floating photovoltaic plants, with a capacity of 2500 km^2, could substantially reduce land resources rivalry, particularly in the eastern areas. The advancement of floating photovoltaic energy production technologies has the potential to make a significant contribution to the long-term energy transitions.

4.3. Analyses the Differences among Overland Photovoltaic and Floating Photovoltaic Modules. The efficiency of a 250 W floating photovoltaic device was contrasted to 250 W overland photovoltaic systems implemented for a comparable examination. The study lasted one month, and efficiency information from clear weather circumstances was utilized for comparison. The maximum energy and effectiveness of the overland photovoltaic network were estimated at maximum photovoltaic radiance and evaluated with the maximum energy and performance of the floating photovoltaic device to evaluate the two devices with similar capacities. Overland photovoltaic and floating photovoltaic had maximum energy and performance of 166.95 W and 12.74 % and 168.83 W and 13.52%, correspondingly, indicating that the energy and effectiveness of the floating photovoltaic network have grown by 3.25% and 0.99%. The properties of floating photovoltaic and overland photovoltaic are compared in Figures 6 and 7.

When compared to overland photovoltaics, testing data show that floating photovoltaics have been effective in enhancing energy production. During the daytime, the temperature of the floating photovoltaic component was lesser than that of the overland photovoltaic component. This is calculated because of the cooling impact of freshwater caused by the water layer, which maintains the temperature of the reduced photovoltaic component. The effectiveness of the overland photovoltaic and floating photovoltaic systems are compared. The highest energy of the 250 W land-based photovoltaic systems and the 250 W floating-based photovoltaic device is compared in Figure 8. The performance of the solar module 250 W is analyzed in Figure 9.

4.4. Comparison between Floating System and PV Land System. The production efficiency of the Hapcheon floating photovoltaic was evaluated to a megawatt terrestrial photovoltaic built-in Hamangun for a similar evaluation. The Haman 1-megawatt overland PV strategy was found as a setting clear goal because it is located 60 kilometers south of Hapcheon, in which the solar radiation and heat are comparable, and it has been built on the same day (2012). The Haman 1-megawatt terrestrial photovoltaic system has a constant 30° inclination and a capability of 936 megawatts. It is comprised of 4000- and 255-megawatt modules.

To begin, days with interruptions, repair, and data error are excluded from the comparison between the rated power float PV system and the terrestrial photovoltaic for a much more effective assessment. The study timeframe was one year long, from February 2012 and ending in January 2013, and data spanning 185 dates of that period was considered. The monthly production quantities of Hapcheon 100 kW and Haman 1 MW were 423 kWh/day and 3487 kWh/day, respectively.

The "average daily output quantity from Haman 936 kW terrestrial photovoltaic system that transformed to 99.35 kW " was obtained and compared with the "average daily electricity production of Hapcheon 99.36 kW floating P4V system" to contrast the two power stations with various capacities. As just an outcome, the coefficients of utilization for the 100 kW and 1 MW installations were 17.5% and 15.6%, correspondingly, implying that now the Hapcheon 100 kW floating photovoltaic system is 13.5 percent more valuable than that of the Haman 1 MW system. The daily electricity production of the 100 kW and 1 MW systems is shown in the graph Figure 10.

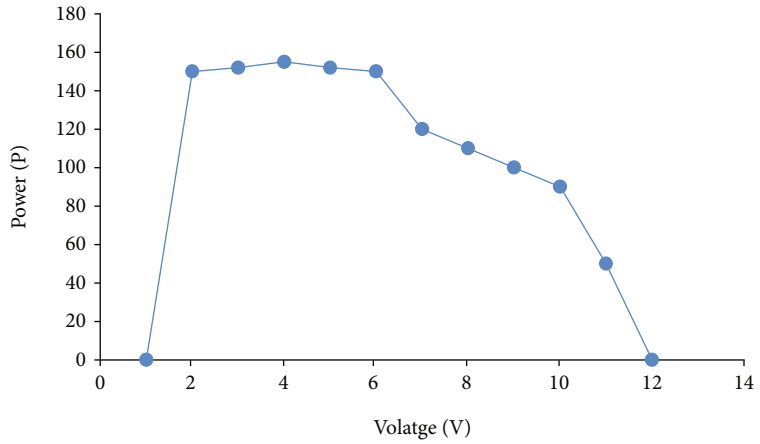

Figure 6: Floating PV on the P-V curve.

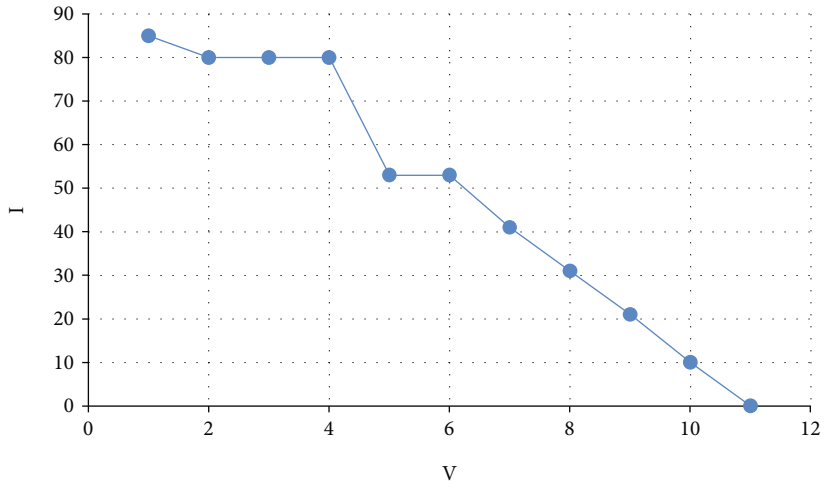

Figure 7: Overland PV on the I-V curve.

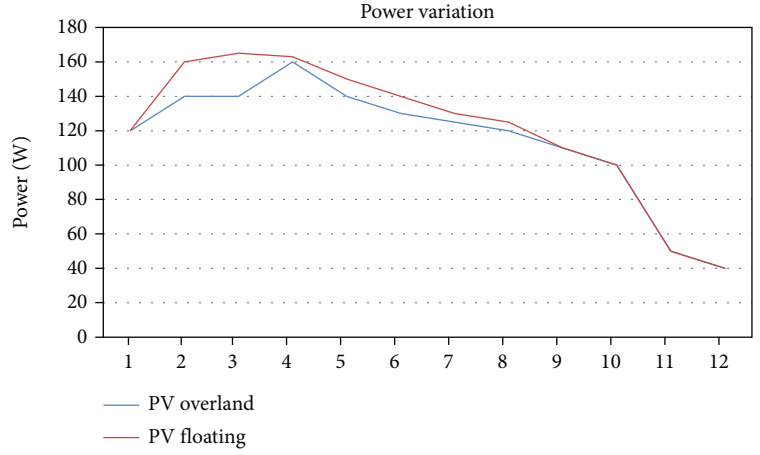

Figure 8: Comparison of power.

Second, the same strategy is used to evaluate the efficiency of 500 kW and 1 MW generators. The data for this research was collected during a six-month timeframe, from October 2012 to March 2013, and was based on 121 days of data. The daily production quantities of Hapcheon 500 kW and Haman 1 MW were 2044 kWh/day and 3491 kWh/day, respectively. The "daily average production volume of Haman 935.9 kW overland photovoltaic when

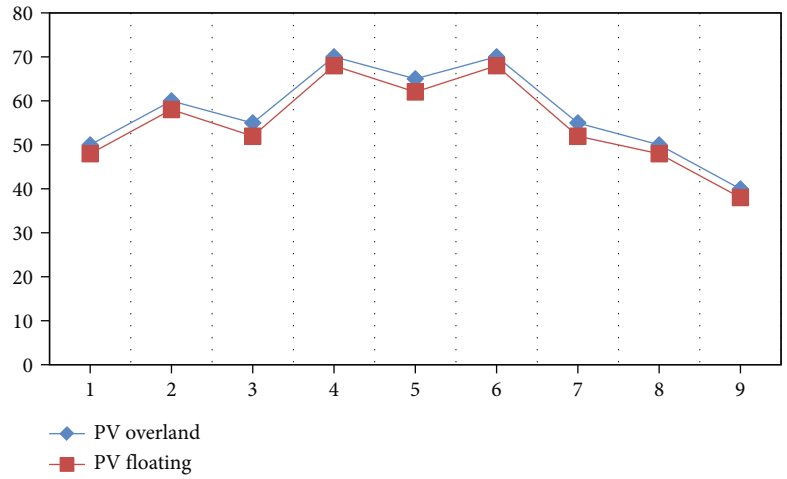

Figure 9: Module temperature variation.

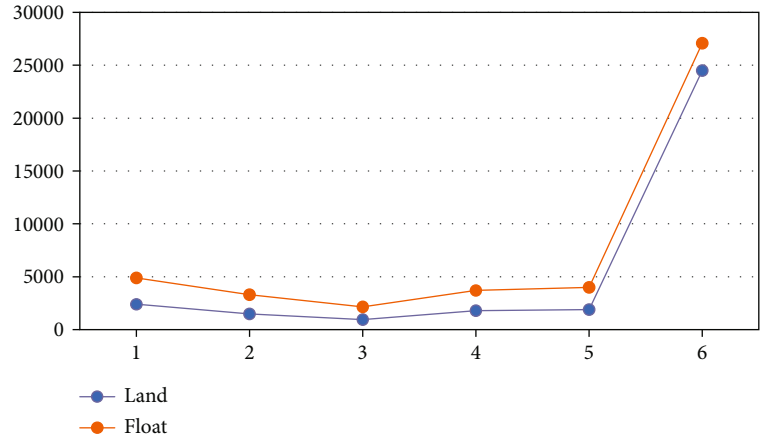

Figure 10: Comparison of land and floating PV systems.

transformed to 496.8 kW" was obtained and compared with the "average daily electricity production of Hapcheon 496.8 kW floating photovoltaic system" to evaluate the different power stations with differing capacities. As a result, the coefficients of utilization for the 500 kW and 1MW plants were 17.1% and 15.5%, correspondingly, indicating that the utility of the Hapcheon 500 kW floating PV system is 10.3 percent greater than the rate of the Haman 1 MW systems. The chart shows the daily production.

5. Conclusion

Floating PV systems have the advantage of promise. The following are the particular findings: Like all other equal variables, the mean average temperature in the water is around 5 times cooler than it was on land depending on the cooling properties of water. The operational temperature range among a floating photovoltaic panel and a grounded cell was found to be 3.5 degrees in this publication's numerical model. According to the study, the performance of drifting photovoltaic systems can rise by 1.58 – 2.00% when compared to standard terrestrial PV systems due to the water evaporative cooling. Floating photovoltaic systems can generate 160 GW of electricity, covering around 2500 km^2 of the sea surface. This will save $2 \times 1027\ m^3$ of water per year from vaporization. If the conserved water could be used for hydroelectric, an additional $1.25 \times 1012\ m^3$ of indirect water savings can be achieved. Furthermore, floating PV technology can effectively reduce competition over land resources, particularly on the eastern side. Since the mean temperature with floating PV is lower than that of regular PV modules, floating photovoltaics have a higher efficiency than conventional photovoltaic modules. Floating photovoltaics have the potential to greatly boost electric power generation. In actuality, the production of floating photovoltaic systems entails more intricate elements than just those examined in this research. The impact of floating photovoltaic systems, for instance, on the natural surroundings, including such groundwater resources, should be thoroughly investigated. Furthermore, in addition to allowing the growth of floating photovoltaic systems, infrastructures must be planned and implemented. In actuality, floating PV power production

equipment is indeed a novel form of power generation sequencing with a lot of challenges to investigate.

Data Availability

The data used to support the findings of this study are included within the article. Further data or information is available from the corresponding author upon request.

Conflicts of Interest

The authors declare that there are no conflicts of interest regarding the publication of this paper.

Acknowledgments

The authors appreciate the support from Ambo University, Ambo, Ethiopia, for providing help during the research and preparation of the manuscript.

References

[1] C. Ferrer-Gisbert, J. J. Ferrán-Gozálvez, M. Redón-Santafé, P. Ferrer-Gisbert, F. J. Sánchez-Romero, and J. B. Torregrosa-Soler, "A new photovoltaic floating cover system for water reservoirs," *Renewable Energy*, vol. 60, pp. 63–70, 2013.

[2] W. Zhou, H. Yang, and Z. Fang, "A novel model for photovoltaic array performance prediction," *Applied Energy*, vol. 84, no. 12, pp. 1187–1198, 2007.

[3] H. Yang, L. Lu, and W. Zhou, "A novel optimization sizing model for hybrid solar-wind power generation system," *Solar Energy*, vol. 81, no. 1, pp. 76–84, 2007.

[4] D. Friel, M. Karimirad, and W. J. Doran, "A review of floating photovoltaic design concepts and installed variations," in *International Conference on Offshore Renewable Energy*, UK, 2019.

[5] Y.-K. Choi, N.-H. Lee, A.-K. Lee, and K.-J. Kim, "A study on major design elements of tracking-type floating photovoltaic systems," *Journal of Smart Grid and Clean Energy*, vol. 3, no. 1, pp. 70–74, 2014.

[6] V. Durković and Ž. Đurišić, "Analysis of the potential for use of floating PV power plant on the Skadar Lake for electricity supply of aluminium plant in Montenegro," *Energies*, vol. 10, no. 10, p. 1505, 2017.

[7] Z. Lan, "Blowout accident impact analysis method for the siting of offshore floating nuclear power plant in offshore oil fields," *Science and Technology of Nuclear Installations*, vol. 2019, 7 pages, 2019.

[8] R. Cazzaniga, M. Cicu, M. Rosa-Clot, P. Rosa-Clot, G. M. Tina, and C. Ventura, "Floating photovoltaic plants: performance analysis and design solutions," *Renewable and Sustainable Energy Reviews*, vol. 81, pp. 1730–1741, 2018.

[9] E. Solomin, E. Sirotkin, E. Cuce, S. P. Selvanathan, and S. Kumarasamy, "Hybrid floating solar plant designs: a review," *Energies*, vol. 14, no. 10, p. 2751, 2021.

[10] G. Tina, S. Gagliano, and S. Raiti, "Hybrid solar/wind power system probabilistic modelling for long-term performance assessment," *Solar Energy*, vol. 80, no. 5, pp. 578–588, 2006.

[11] E. E. van Dyk, E. L. Meyer, F. J. Vorster, and A. W. R. Leitch, "Long-term monitoring of photovoltaic devices," *Renewable Energy*, vol. 25, no. 2, pp. 183–197, 2002.

[12] B. S. Borowy and Z. M. Salameh, "Methodology for optimally sizing the combination of a battery bank and PV array in a wind/PV hybrid system," *IEEE Transactions on Energy Conversion*, vol. 11, no. 2, pp. 367–375, 1996.

[13] H. Yang, Z. Wei, and L. Chengzhi, "Optimal design and techno-economic analysis of a hybrid solar-wind power generation system," *Applied Energy*, vol. 86, no. 2, pp. 163–169, 2009.

[14] M. Redón Santafé, J. B. Torregrosa Soler, F. J. Sánchez Romero, P. S. Ferrer Gisbert, J. J. Ferrán Gozálvez, and C. M. Ferrer Gisbert, "Theoretical and experimental analysis of a floating photovoltaic cover for water irrigation reservoirs," *Energy*, vol. 67, pp. 246–255, 2014.

[15] S. Gorjian, H. Sharon, H. Ebadi, K. Kant, F. B. Scavo, and G. M. Tina, "Recent technical advancements, economics and environmental impacts of floating photovoltaic solar energy conversion systems," *Journal of Cleaner Production*, vol. 278, p. 124285, 2021.

[16] N. Yadav, M. Gupta, and K. Sudhakar, "Energy Assessment of Floating Photovoltaic System," in *2016 International Conference on Electrical Power and Energy Systems (ICEPES)*, pp. 264–269, Bhopal, India, Dec. 2016.

[17] S. Biswas and M. T. Iqbal, "Dynamic modelling of a solar water pumping system with energy storage," *Journal of Solar Energy*, vol. 2018, 12 pages, 2018.

[18] A. H. Nebey, B. Z. Taye, and T. G. Workineh, "GIS-based irrigation dams potential assessment of floating solar PV system," *Journal of Energy*, vol. 2020, 10 pages, 2020.

[19] Z. Zhong, C. Yang, W. Cao, and C. Yan, "Short-term photovoltaic power generation forecasting based on multivariable grey theory model with parameter optimization," *Mathematical Problems in Engineering*, vol. 2017, 9 pages, 2017.

[20] Z. Arifin, D. D. D. P. Tjahjana, S. Hadi, R. A. Rachmanto, G. Setyohandoko, and B. Sutanto, "Numerical and experimental investigation of air cooling for photovoltaic panels using aluminum heat sinks," *International Journal of Photoenergy*, vol. 2020, 9 pages, 2020.

[21] A. Farooq, Z. Malik, Q. Dongchang, Z. Sun, and G. Chen, "A three-phase interleaved floating output boost converter," *Advances in Materials Science and Engineering*, vol. 2015, Article ID 409674, 8 pages, 2015.

[22] A. Iqbal and M. T. Iqbal, "Design and analysis of a stand-alone PV system for a rural house in Pakistan," *International Journal of Photoenergy*, vol. 2019, Article ID 4967148, 8 pages, 2019.

[23] Y. Song, D. Wu, A. W. Mohamed, X. Zhou, B. Zhang, and W. Deng, "Enhanced success history adaptive DE for parameter optimization of photovoltaic models," *Complexity*, vol. 2021, Article ID 6660115, 22 pages, 2021.

[24] M. Masili and L. Ventura, "Local tilt optimization of photovoltaic solar panels for maximum radiation absorption," *International Journal of Photoenergy*, vol. 2019, Article ID 3254780, 10 pages, 2019.

[25] Y. Mallal, L. El Bahir, and T. Hassboun, "High-performance emulator for fixed photovoltaic panels," *International Journal of Photoenergy*, vol. 2019, Article ID 3951841, 11 pages, 2019.

[26] M. Elshafei, A. Ibrahim, A. Helmy et al., "Study of massive floating solar panels over Lake Nasser," *Journal of Energy*, vol. 2021, Article ID 6674091, 17 pages, 2021.

Hindawi
International Journal of Photoenergy
Volume 2022, Article ID 9625564, 9 pages
https://doi.org/10.1155/2022/9625564

Research Article

Design and Analysis of ANFIS – Based MPPT Method for Solar Photovoltaic Applications

S. R. Revathy,[1] V. Kirubakaran,[1] M. Rajeshwaran,[2] T. Balasundaram,[3] V. S. Chandra Sekar,[4] Saad Alghamdi,[5] Bodour S. Rajab,[5] Ahmad O. Babalghith,[6] and Endalkachew Mergia Anbese[7]

[1]*Centre for Rural Energy, The Gandhigram Rural Institute-Deemed to Be University, Gandhigram, 624302 Tamil Nadu, India*
[2]*Department of Mechanical Engineering, Mother Terasa College of Engineering and Technology, Pudukkottai, 622102 Tamil Nadu, India*
[3]*Department of Mechanical Engineering, Medak College of Engineering and Technology, Siddipet, Telangana, India*
[4]*Department of Mechanical Engineering, University College of Engineering Dindigul, Dindigul, 624622 Tamil Nadu, India*
[5]*Laboratory Medicine Department, Faculty of Applied Medical Sciences, Umm Al-Qura University, Makkah, Saudi Arabia*
[6]*Medical Genetics Department, College of Medicine, Umm Al-Qura University, Makkah, Saudi Arabia*
[7]*Department of Civil Engineering, Ambo University, Ambo, Ethiopia*

Correspondence should be addressed to Endalkachew Mergia Anbese; endalkachew.mergia@ambou.edu.et

Received 9 February 2022; Accepted 31 March 2022; Published 19 May 2022

Academic Editor: Palanivel Velmurugan

Copyright © 2022 S. R. Revathy et al. This is an open access article distributed under the Creative Commons Attribution License, which permits unrestricted use, distribution, and reproduction in any medium, provided the original work is properly cited.

The solar photovoltaic energy is becoming popular in the modern-day distribution networks due to the clean energy factor. The photovoltaic modules exhibit a nonlinearity in the output power concerning the environmental conditions. This work suggests an adaptive neuro-fuzzy inference system- (ANFIS-) based maximal power point tracker (MPPT) for the optimization of the solar photovoltaic system (SPVS). The controller modelled is utilized to optimize the output power of a DC-DC converter connected to a 400 W PV array. The entire model is analysed employing MATLAB/SIMULINK using primary features provided by the technical data. The behavior of the controller modelled is tested for various weather conditions and partial shading conditions. The findings show the controller's tracking speed effectiveness and dynamic response in PSCs.

1. Introduction

The solar photovoltaic modules depend on irradiance and temperature for the power generation, but these two factors vary with varying atmospheric conditions like weather, climate, and seasons. Other conditions like partial shading due to cloud cover, nearby trees, buildings, and dust also have adverse effects on PV-based power generation [1–3]. This introduces the need for power optimization in solar photovoltaic power generation, which will keep track of the maximum power point and optimize the power accordingly. A maximum power point tracker can be defined as a technique employed in renewable energy-based power generation units like solar photovoltaic or wind turbines to extract maximum power output at uncertain conditions [4, 5].

The commonly used maximum power point tracking methods like hill climbing methods (perturb and observe method and incremental conductance method) have more and recurrent oscillations around the maximum power value tracked. Hence, they are inaccurate in foreseeing the MPP during adverse atmospheric conditions. However, they are easy to design and implement. These techniques involve less hardware, and hence, they are highly cost effective. [6, 7].

Artificial neural networks employ learning based on the behavioral or operational pattern of the concerned application, which enables speed and independence over the applications where it is employed. ANN-based MPP tracking gives good outputs in ordinary environmental occasions but is unable to follow MPP in shading conditions [8]. The training method has a significant impact on its performance.

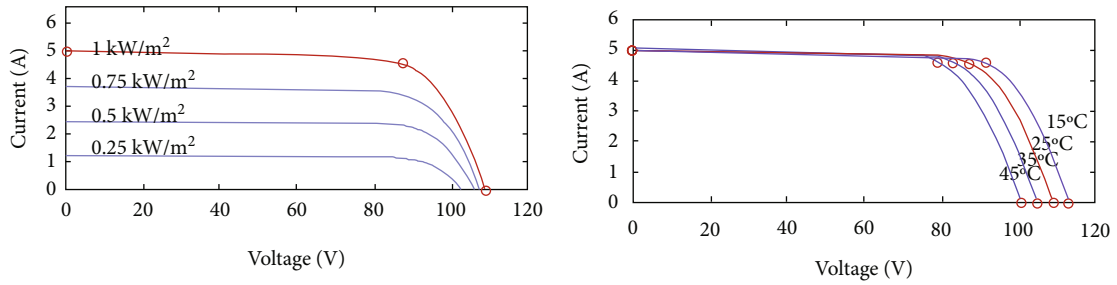

(a) *V-I* characteristics for various irradiances (b) *V-I* characteristics for various temperatures

Figure 1: *V-I* characteristics of the PV array.

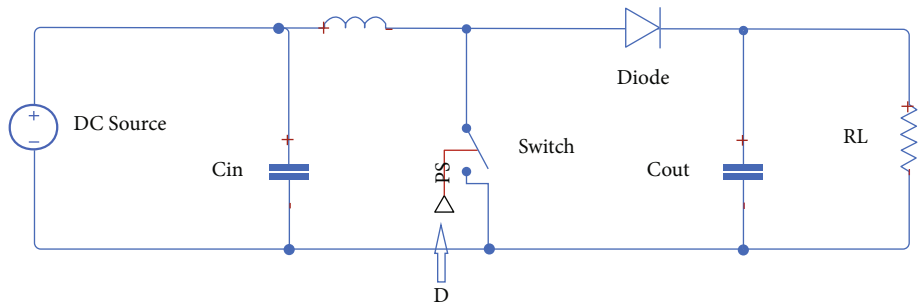

Figure 2: Boost converter.

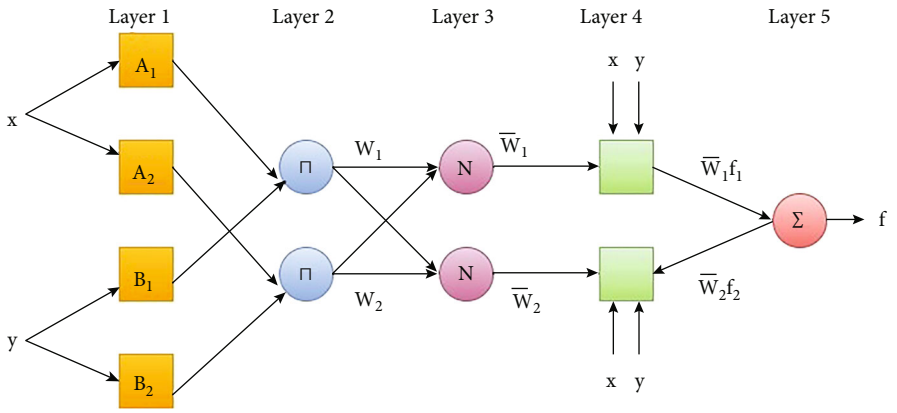

Figure 3: Architecture of an ANFIS.

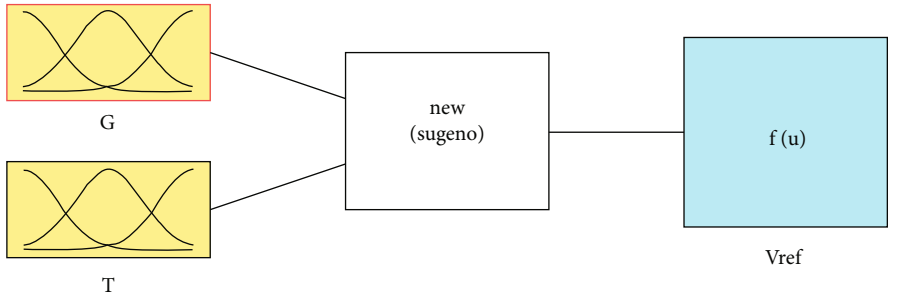

Figure 4: Proposed ANFIS MPPT model.

ANN trained for a specific capacity of the PV system is not employable again, and this makes it exclusive and unsalable. Also, periodic tuning of the nodes is required to keep up with the present operating conditions of the PV system as it ages with time [9]. Fuzzy-based MPPTs show better performance as given in Section 1. However, designing the

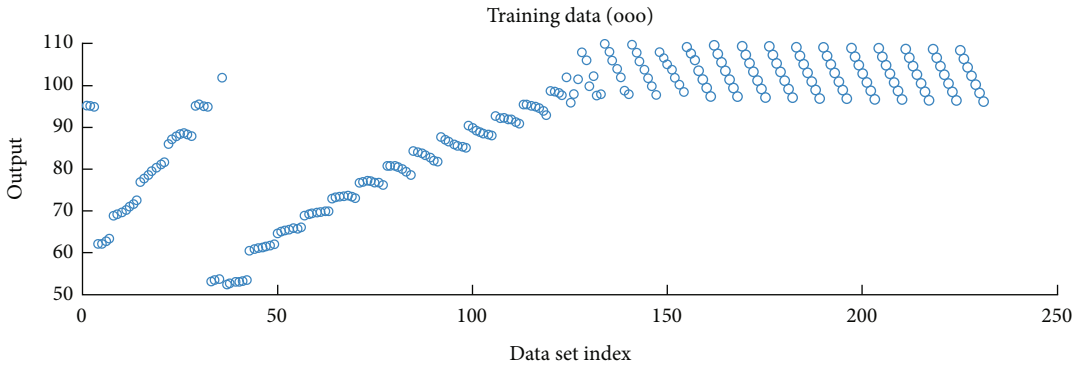

Figure 5: Training datasets.

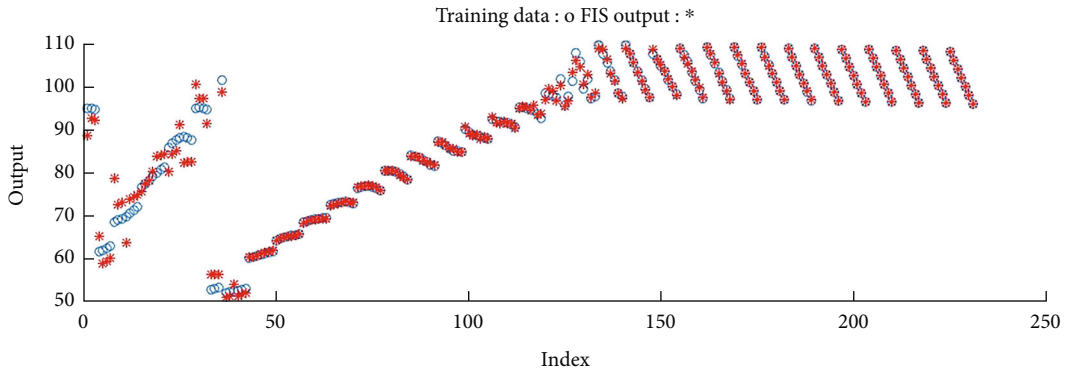

Figure 6: Training output.

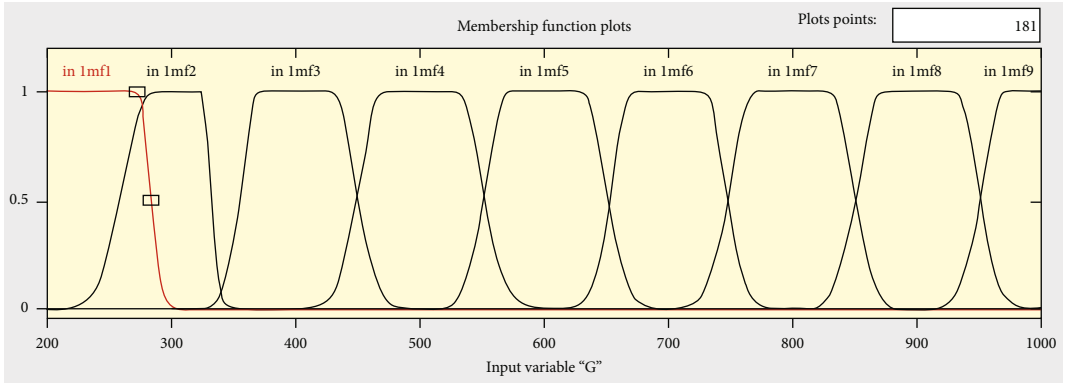

Figure 7: Membership functions of input *G*.

membership functions and the rules are a complex process. Also, the precision of the entire system depends on this design; any manual flaw can affect the output. But in the case of the ANFIS controller, all the MFs and rules were based on the data obtained from the specifications of the PV array. So, it increases the accuracy and eliminates the complexity in the design.

The ANFIS controller combines the merits of neural networks and fuzzy logic together. These controllers exhibit fast response with good efficiency at all weather conditions making it more suitable for nonlinear systems like SPV modules. The rules and the membership functions for the ANFIS controller are autodesigned through the learning/training process, which brings down the design complexity in the fuzzy controller [10–13]. Solar PV modules function by converting the light energy in the photons into electrical energy, so irradiance is an unrulable input. The performance of the solar modules is affected by the operating temperature. Since humidity and wind velocity influences the temperature, there is no need for additional emphasis on it.

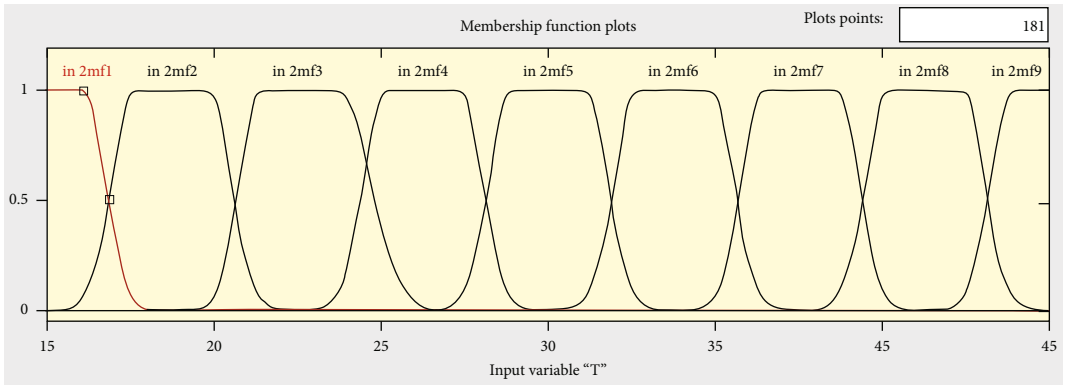

Figure 8: Membership functions of input T.

2. Modelling of the Solar Photovoltaic System

The solar module can be expressed as a mathematical equation as in equation (1). The current of the photovoltaic module under uniform irradiance is derived from equation (1).

$$I = N_p I_{ph} - N_p I_o \left[\exp\left\{\frac{q\left(V_{pv} + I_{pv}R_s\right)}{N_s AKT}\right\} - 1\right], \quad (1)$$

where I_{ph} is the photocurrent of the module, N_p is the number of parallel module connections, N_s is the number of series module connections, I_o is the diode saturation current, k is the Boltzmann constant, q is the elementary charge of electron, A is the quality factor of the diode, R_s is the series resistance, V_{pv} is the module voltage, and I_{pv} is the current. The solar array designed for the study has five Canadian Solar CS5C-80M modules serially connected. The maximum power of a single module is 80.15 W with an open-circuit voltage (V_{oc}) of 21.8 V and a short-circuit current (I_{sc}) of 4.97 A. The voltage-current characteristics of the designed array under various irradiances and various temperatures are given in Figure 1.

2.1. Boost Converter. The boost converter is a DC-DC converter used to increase the DC voltage produced by the solar PV array. The circuit of the boost converter is given in Figure 2.

The rate of conversion is usually determined by duty cycle D. It is obtained on the basis of maximum power value tracked by the MPPT. The connection among the input voltage V_i, output voltage V_o, and the duty cycle D of the boost converter is given in equation (2).

$$\frac{V_o}{V_i} = \frac{1}{1-D}. \quad (2)$$

The optimum D value to remove the mismatch among the resistance of PV module R_{PV} and load resistance R_L is given in equation (3).

$$R_{PV} = R_L(1-D)^2. \quad (3)$$

The inductor value in the T_{ON} state is given in equation (4).

$$L = \frac{VD}{\Delta I_L F}. \quad (4)$$

The boost converter performs better in the continuous conduction mode $\Delta I_L \geq 2\,I_i$, so equation (4) becomes

$$L \geq \frac{D(1-D)^2 R_L}{2F}. \quad (5)$$

The value of the output capacitor in the TON state is given in equation (6).

$$C_O = \frac{DI_o}{\Delta V_o F}. \quad (6)$$

The ripple value of the output voltage V_o should be considered while calculating the output capacitor value. For a desired output capacitance value, the $\Delta V_o = 0.02V_o$. So, equation (6) becomes

$$C_O \geq \frac{D}{0.02FR_L}. \quad (7)$$

The value of the input capacitor can be calculated from equation (8).

$$C_{in} = \frac{V_i D}{8FL\Delta V_i}. \quad (8)$$

The input capacitor reduces the input voltage ripple, so for the desired input capacitance, $\Delta V_i \geq 0.01V_i$. This makes equation (8) as follows:

$$C_{in} \geq \frac{D}{0.08F^2 L}. \quad (9)$$

The parameters of the 1 kHZ, 100 V boost capacitor with R_L of 10 Ω include a 0.625 mF inductor, 0.01 C input capacitor, and 2.5 mC output capacitor. All the component values are calculated with a duty value of 0.5.

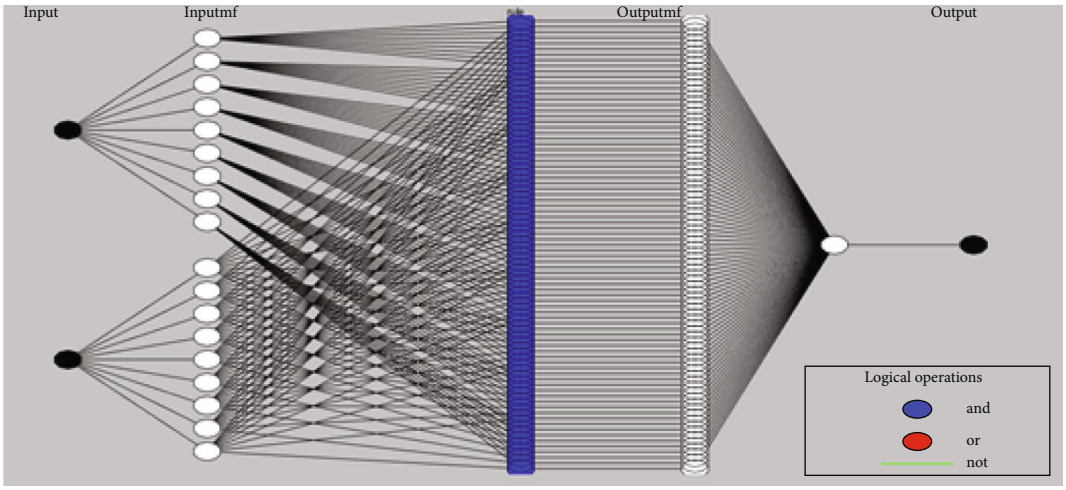

Figure 9: Architecture of the proposed ANFIS MPPT.

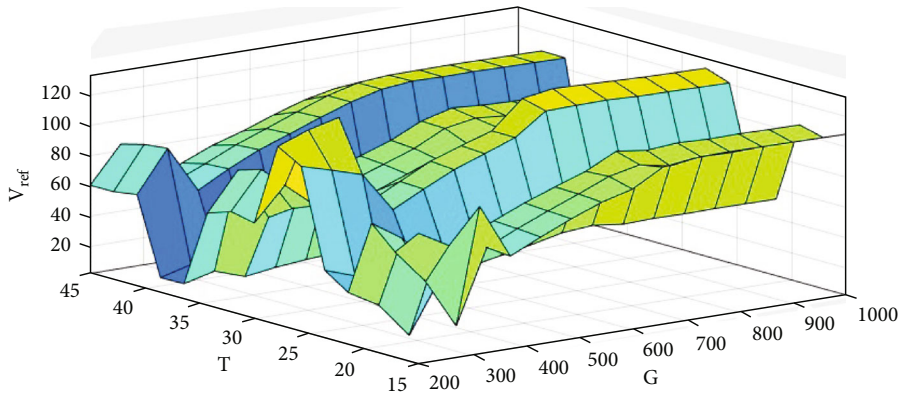

Figure 10: Rules of the ANFIS MPPT.

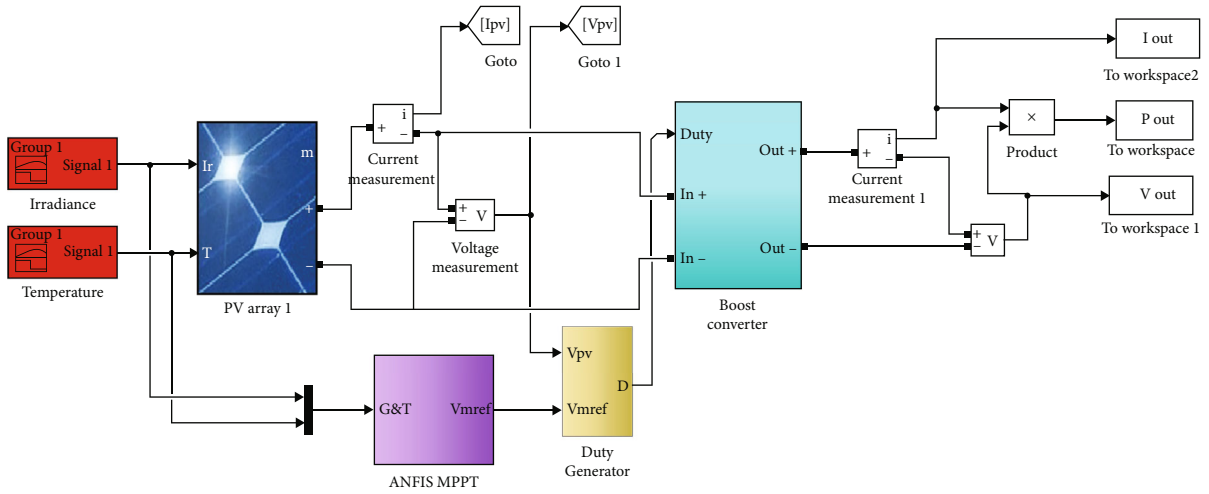

Figure 11: Simulink model of the power optimizer with ANFIS MPPT.

3. ANFIS-Based MPPT

Adaptive neuro-fuzzy inference system ropes in functionalities of ANN and fuzzy logic. The Sugeno fuzzy controller can be trained by an ANN to derive the precise membership functions for the variables based on their interrelatedness [14, 15]. The weights of the nodes involved also can be derived to make up a complete rule base. The solar irradiance and ambient temperature or the PV array voltage and PV array current can be used as inlet of the model. The

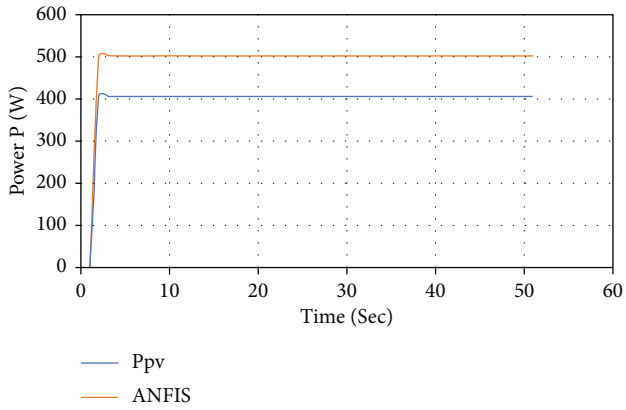

Figure 12: Output power of the optimizer with ANFIS MPPT at STC.

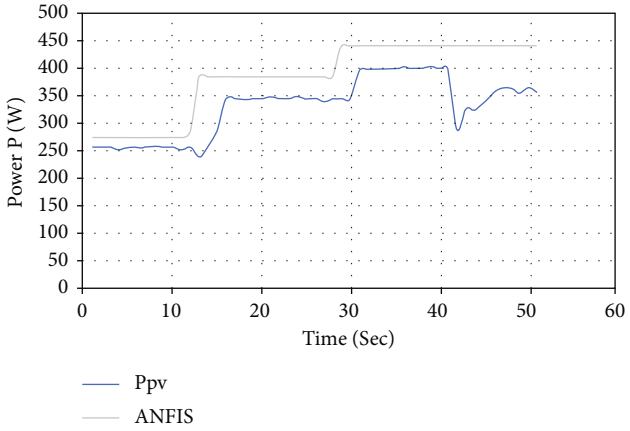

Figure 13: Output power of the optimizer with ANFIS MPPT at VWC.

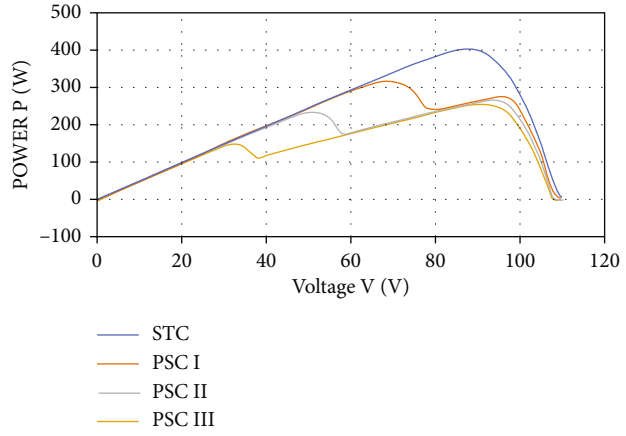

Figure 14: PV curve under PSCs.

ANN helps to easily tune the membership function and rule table [16, 17]. The inference system of the ANFIS controller matches to a set of fuzzy rulebooks with learning fitness for the optimization of nonlinear functions. The fuzzy rule sets for a two-input (x, y)–one output (z) FIS can be given as follows:

The 1st rule is that if x is A_1 and y is B_1, then,

$$f_1 = p_1 x + q_1 y + r_1. \tag{10}$$

The 2nd rule is that if $x$is$A_2$and$y$ is B_2, then,

$$f_2 = p_2 x + q_2 y + r_2. \tag{11}$$

And the output function is given by equation (15).

$$f = \frac{w_1 f_1 + w_2 f_2}{w_1 + w_2} = \overline{w_1} f_1 + \overline{w_2} f_2. \tag{12}$$

The architecture of the ANFIS with two inputs (x, y) and one output (z) is given in Figure 3.

3.1. Layer 1. All the nodes are usually adaptable. In the output of node i in this layer O_1, i depends on the input of the membership functions of the respective node I.

$$\begin{aligned} O_1, i &= \mu_{Ai}(x), \quad \text{for } i = 1, 2, \\ O_1, i &= \mu_{Bi-2}(y), \quad \text{for } i = 3, 4. \end{aligned} \tag{13}$$

Here, x and y are the inputs and Ai and Bi are fuzzy sets in the parametric form associated with node i. In this work, membership functions used for the inputs x and y are Gaussian.

3.2. Layer 2. Nodes are fixed and the output of the node i is the result of input functions. This layer acts as a multiplier and is called a neural network layer.

$$O_2, i = w_i = \mu_{Ai}(x) * \mu_{Bi}(y), \quad \text{for } i = 1, 2. \tag{14}$$

3.3. Layer 3. All the nodes are fixed and characterized by N. In the output of layer 3, O_3, i is called standardized firing strengths since it is the sum of the firing strengths of rules from the previous layer.

$$O_3, i = \overline{w_i} = \frac{w_i}{w_1 + w_2}, \quad \text{for } i = 1, 2. \tag{15}$$

3.4. Layer 4. The characteristics of the nodes are adaptable and the parameters are consequent. This is a fuzzy logic node with a parameter set $\{p_i, q_i, r_i\}$. The output of the node is shown in equation (16)

$$O_4, i = \overline{w_i} f_i = \overline{w_i}(p_i x + q_i y + r_i), \quad \text{for } i = 1, 2. \tag{16}$$

3.5. Layer 5. It has only one node fixed and its output is computed as a total of every incoming signal. The output function of this node is shown in equation (17).

$$O_5, i = \sum_i \overline{w_i} f_i = \frac{\sum_i w_i f_i}{\sum_i w_i}, \quad \text{for } i = 1, 2. \tag{17}$$

The architecture of an ANFIS is not a unique design; different layers can be combined as required by the application. The training algorithm of the ANFIS tunes the alterable

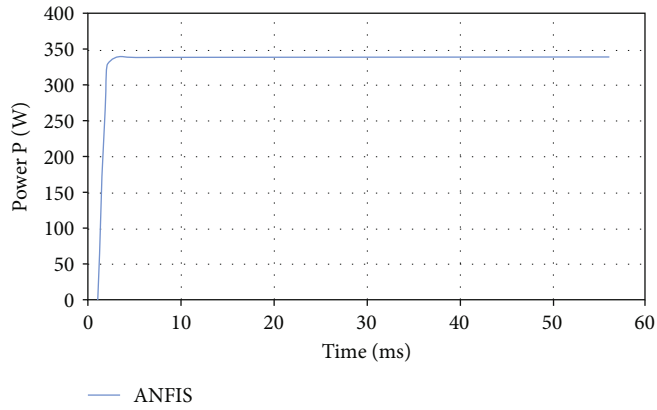

Figure 15: Output power of the ANFIS MPPT at PSC I.

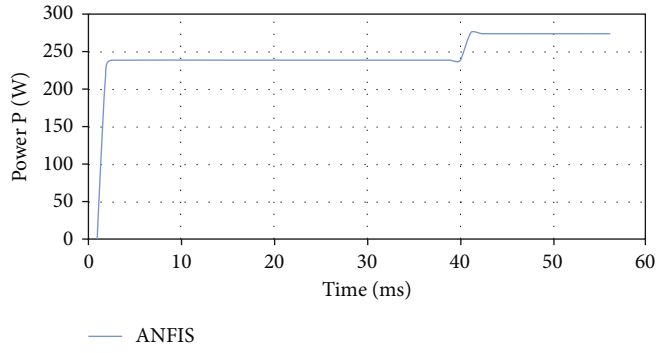

Figure 16: Output power of the ANFIS MPPT at PSC II.

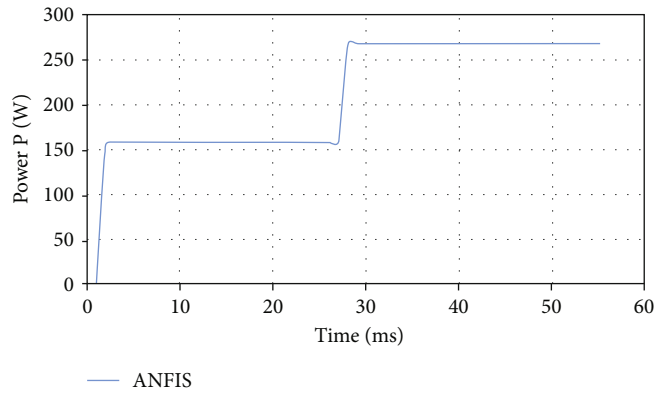

Figure 17: Output power of the ANFIS MPPT at PSC III.

Table 1: Output values.

Evaluation parameters	P_{max} (kW)	Tr (ms)	η (%)	Oscillations	Sensors
ANFIS	0.502	3	30.23	No	G, T

parameters in the adaptive layers (layer 1—A_i, B_i; layer 4—p_i, q_i, r_i) to match the output of the training datasets. The datasets were generated through simulation of the solar PV array under various weather conditions by randomly altering the solar irradiance and temperature values.

The ANFIS model proposed depends on the zero-order Sugeno fuzzy model. The Sugeno fuzzy model has built-in features for training the fuzzy controller. It is time efficient and less complex. The output of the PV array implies two main factors—irradiance hitting over it and temperature. The relationship between the output power and these two factors are studied through correlation analysis. Where Pearson's coefficient of correlation between the power and irradiance and power and temperature are 0.97264 and 0.78435,

respectively. Hence, irradiance G (W/m^2) and temperature T (°C) are considered the inputs for the ANFIS controller. The maximum voltage (V_m) generated at a given instance is considered as the output and is fed into a duty generator. The duty cycle generator is a basic pulse width modulator which compares the ANFIS output with the measured voltage V_{pv} and produces the duty pulse for the boost converter based on the difference between the two voltages. The Sugeno fuzzy model with two inputs and one output is given in Figure 4.

The ANIFIS is trained with 231 datasets acquired from the *I-V* and *P-V* characteristics of Canadian Solar CS5C-80M modules at various weather conditions. The datasets were simulated based on the real-time data of Canadian Solar CS5C-80M modules. And the best sets were selected for training the ANFIS. The datasets employed in the training are shown in Figure 5, and the output of the training are shown in Figure 6. The membership functions of the corresponding input variables are shown in Figures 7 and 8.

The architecture of the proposed ANFIS is shown in Figure 9.

The proposed controller has 81 rules and they are plotted in three dimensions as in Figure 10. There are 81 rules in the proposed controller. These rules were obtained by training the controller with the datasets. The rules are depicted in the pictorial form in Figure 10.

The ANFIS generates a reference duty value, based on which the duty generator creates the duty signal to control the boost controller output. The ANFIS-based maximal power point tracker is simulated in MATLAB/SIMULINK for the proposed solar PV array of five Canadian Solar CS5C-80M modules serially connected to a boost converter for optimizing the output power. The SIMULINK design is portrayed in Figure 11.

4. Results & Discussion

The proposed optimizer is tested under different conditions as presented as follows.

4.1. Standard Test Condition. The standard test conditions indicate that the SPV array works using an irradiance of 1000 W/m^2 and temperature of 25°C. The controller boosts the input voltage level to match the load voltage; hence, the values are higher. The output power of various maximum power point techniques at STC is compared with the output power of the PV array and it is shown in Figure 12.

4.2. Under Rapidly Varying Weather Conditions. The PV array was tested for rapidly varying atmospheric conditions, which was achieved by varying the irradiance and temperature pattern. The inlet signals of the SPV array for varying weather condition VWC is given in Figure 13.

4.2.1. Partial Shading Conditions. The partial shading condition I is influenced in the PV array by reducing the irradiance input of one module by half (500 W/m2). In this condition, two modules out of the five in the PV array are partially shaded with irradiance values of 400 W/m^2 and 500 W/m^2. In this condition, three modules out of the five in the PV array are partially shaded with irradiance values of 400 W/m^2, 500 W/m^2, and 600 W/m^2. Figure 14 describes the effect of partial shading condition III on power-voltage characteristics of the array.

Figures 15–17 represent the output power of the ANFIS MPPT at PSC I, PSC II, and PSC III, respectively. The ANFIS controller responds faster at all PSCs and shows no power fluctuations. The fuzzy controller converges at the same speed as the ANFIS controller in PSC I and II but shows a remarkable response delay under PSC III. Moreover, the fuzzy controller exhibits a little fluctuation under PSC I.

The efficiency is given by equation (18), where P_{max} is the maximum power produced in Watts, G is irradiance in W/m^2, and A is the area of total array $A = 1.6864$ m^2 as in Table 1.

$$\eta = \frac{P_{max}}{GA} \times 100. \tag{18}$$

5. Conclusion

Soft computing approaches are well suited to handling nonlinear issues due to their aptitude and inimitability. Depending on the problem type, almost every technology has certain inadequacies. ANFIS technology proves better convergence and efficiency over the fuzzy technique. Yet, the performance of the ANFIS controller depends on the eminence of the training datasets. Nature-based algorithms like genetic algorithms can be employed to optimize the datasets employed in training the ANFIS controller to further improve its efficiency.

Data Availability

The data used to support the findings of this study are included within the article. Further data or information is available from the corresponding author upon request.

Conflicts of Interest

The authors declare that there are no conflicts of interest regarding the publication of this paper.

Acknowledgments

The authors appreciate the supports from Ambo University, Ambo, Ethiopia, for providing help during the research and preparation of the manuscript. The authors thank The Gandhigram Rural Institute, Umm Al-Qura University, Mother Terasa College of Engineering and Technology, for the support in completing the work.

References

[1] L. Bouselham, M. Hajji, B. Hajji, and H. Bouali, "A new MPPT-based ANN for photovoltaic system under partial shading conditions," *Energy Procedia*, vol. 111, pp. 924–933, 2017.

[2] D. Mlakić, L. Majdandžić, and S. Nikolovski, "ANFIS used as a maximum power point tracking algorithm for a photovoltaic system," *International Journal of Electrical and Computer Engineering*, vol. 8, no. 2, pp. 867–879, 2018.

[3] S. Motahhir, A. El Ghzizal, S. Sebti, and A. Derouich, "Modeling of photovoltaic system with modified incremental conductance algorithm for fast changes of irradiance," *International Journal of Photoenergy*, vol. 2018, 2018.

[4] D. Saravana, J. Mohammed, V. Umayal, and M. Indumathi, "Simulation of fuzzy logic control based MPPT technique for photovoltaic system," in *International Conference on Inovations in Engineering and Technology*, pp. 10–14, Penang (Malaysia), 2014.

[5] B. Bendib, F. Krim, H. Belmili, M. F. Almi, and S. Boulouma, "Advanced fuzzy MPPT controller for a stand-alone PV system," *Energy Procedia*, vol. 50, pp. 383–392, 2014.

[6] M. Azaharahmed, K. Raja, M. K. Patan, C. D. Prasad, and P. Ganeshan, "Invasive weed optimized area centralized 2 degree of freedom combined PID controller scheme for automatic generation control," *Journal of Electrical Engineering & Technology*, vol. 16, no. 1, pp. 31–42, 2021.

[7] A. M. Noman, K. E. Addoweesh, and A. I. Alolah, "Simulation and practical implementation of ANFIS-based MPPT method for PV applications using isolated Ćuk converter," *International Journal of Photoenergy*, vol. 2017, Article ID 3106734, 15 pages, 2017.

[8] V. Jeyabalaji, G. R. Kannan, P. Ganeshan, K. Raja, B. Nagaraja Ganesh, and P. Raju, "Extraction and characterization studies of cellulose derived from the roots of Acalypha indica L," in *Journal of Natural Fibers*, pp. 1–13, Taylor & Francis, 2021.

[9] A. A. Aldair, A. A. Obed, and A. F. Halihal, "Design and implementation of ANFIS-reference model controller based MPPT using FPGA for photovoltaic system," *Renewable and Sustainable Energy Reviews*, vol. 82, pp. 2202–2217, 2018.

[10] D. Subbulekshmi and J. Kanakaraj, "Decoupling and linearizing of a pH plant using Hirschorn's and genetic algorithms," *Journal of Computer Science.*, vol. 8, no. 8, pp. 1422–1427, 2012.

[11] M. K. Patan, K. Raja, M. Azaharahmed, C. D. Prasad, and P. Ganeshan, "Influence of primary regulation on frequency control of an isolated microgrid equipped with crow search algorithm tuned classical controllers," *Journal of Electrical Engineering & Technology*, vol. 16, no. 2, pp. 681–695, 2021.

[12] L. L. Jiang, D. R. Nayanasiri, D. L. Maskell, and D. M. Vilathgamuwa, "A hybrid maximum power point tracking for partially shaded photovoltaic systems in the tropics," *Renewable energy*, vol. 76, pp. 53–65, 2015.

[13] C. Ben Salah and M. Ouali, "Comparison of fuzzy logic and neural network in maximum power point tracker for PV systems," *Electric Power Systems Research*, vol. 81, no. 1, pp. 43–50, 2011.

[14] S. Lyden and M. E. Haque, "Maximum power point tracking techniques for photovoltaic systems: a comprehensive review and comparative analysis," *Renewable and Sustainable Energy Reviews*, vol. 52, pp. 1504–1518, 2015.

[15] A. A. Kulaksiz, "ANFIS-based estimation of PV module equivalent parameters: application to a stand-alone PV system with MPPT controller," *Turkish Journal of Electrical Engineering & Computer Sciences*, vol. 21, pp. 2127–2140, 2013.

[16] R. K. Kharb, M. F. Ansari, and S. L. Shimi, "Design and implementation of ANFIS based MPPT scheme with open loop boost converter for solar PV module," *International Journal of Advanced Research in Electrical, Electronics and Instrumentation Engineering*, vol. 3, no. 1, pp. 6517–6524, 2014.

[17] N. Akshaykumar and D. Subbulekshmi, "Online auto selection of tuning methods and auto tuning PI controller in FOPDT real time process-pH neutralization," *Energy Procedia*, vol. 117, pp. 1109–1116, 2017.

Hindawi
International Journal of Photoenergy
Volume 2022, Article ID 1296822, 13 pages
https://doi.org/10.1155/2022/1296822

Research Article

Thermal Storage for the Analysis of Hybrid Energy Systems Based on Geothermal and Solar Power

K. U. Aravind,[1] N. Muthu Mekala,[2] N. P. Muthuraju,[3] N. B. Soni,[4] Essam A. Al-Ammar,[5] A. H. Seikh,[6] M. H. Siddique,[7] and David Christopher[8]

[1]*Department of Mechanical Engineering, East West College of Engineering, Yelahanka, Bengaluru, Karnataka 560064, India*
[2]*Department of Mechanical Engineering, College of Engineering, Guindy, Chennai, Tamil Nadu 600025, India*
[3]*Department of Mechanical Engineering, Vidyavardhaka College of Engineering, Mysuru, Karnataka 570002, India*
[4]*Department of Electrical Engineering, University of Petroleum and Energy Studies, Dehradun, Uttarakhand 248007, India*
[5]*Department of Electrical Engineering, College of Engineering, King Saud University, P.O. Box 800, Riyadh 11421, Saudi Arabia*
[6]*Mechanical Engineering Department, College of Engineering, King Saud University, P.O. Box 800, Al-Riyadh 11421, Saudi Arabia*
[7]*Intelligent Construction Automation Centre, Kyungpook National University, Daegu, Republic of Korea*
[8]*Department of Mechanical Engineering, College of Engineering, Wolaita Sodo University, Ethiopia*

Correspondence should be addressed to David Christopher; david.santosh@wsu.edu.et

Received 10 February 2022; Accepted 5 April 2022; Published 18 May 2022

Academic Editor: V. Mohanavel

Copyright © 2022 K. U. Aravind et al. This is an open access article distributed under the Creative Commons Attribution License, which permits unrestricted use, distribution, and reproduction in any medium, provided the original work is properly cited.

Thermal degradation of geothermal energy occurs even during the duration of geothermal energy facilities. The enormity and efficiency of thermal energy available for electric transformation, as well as plant performance and power production, are both affected by the decrease in geofluid heat. Additionally, due to the generally increased turbine exhaust temperatures, the efficiency of geothermal energy based upon air-cooled organic Rankine cycle devices (ORCs) degrades considerably at hot room temperatures. A newly designed Geothermal-Concentrator Solar Power (GEO-CSP) station is simulated in this work, which allows for greater geothermal power use and enhances the effectiveness of the geothermal ORC system over the power plant's lifespan. The geothermal fluid entering the ORC's heating element is heated using the sun's radiation. The CSP facility is fitted with a thermal energy storing unit that stores excess energy from the sun accessible throughout the day and releases it at nighttime whenever the energy system's performance is better. When the storage facility is included in the concentrator CSP technology, the incremental yearly energy generation from solar increases by 19 percent, from 5.3 percent to 6.3 percent, similar to the geothermal-only plant. As a result, adding a TES unit to the hybrid unit could be quite beneficial.

1. Introduction

Since economic implications of the operating of the frequency and economic growth projects are dependent on the functioning of the frequency and economic development activities, the energy problem has piqued the general public in the latest generations. The entire world is scrambling to develop renewable technologies now, as the nation's political position has long relied on its control and domination over energy [1]. As the company continues to expand, more power is available, the majority of which is presently provided by energy sources; as a result, the excessive usage of fossil conventional fossil fuels has made the whole thing world oblivious of the consequences, and the surroundings have become engulfed in a circle of never-before-seen occurrences, such as changing climate, global climate change, and

ozone depletion. Considering their detrimental effects on mankind as a whole, coal and oil remain the primary source of energy and are extensively applied in all countries worldwide, mainly in developing countries. Since the price variations, oil and gas prompted significant the global economy to recover, making import and export nations apprehensive regarding their absolute reliance on petroleum as the unique and distinct form of energy [2].

This level of power generation uses sun intensity to increase the intrinsic aerobic energy system. The radiation from the sun raises the temperature in the collectors, which is open across its peripheral, creating a greenhouse gas, and because warmed air is lighter than cool air, it rises to the top of the chimney, which is placed in the collector center. At the foot of the fireplace, a wind farm is placed in the course of the flow in order to transform thermal energy into motion, which is then transformed into electrical by the wind farm combine and turbines [3]. Solar energy is among the most important renewable energy sources since it is pure, limitless, cost-effective, and free of geographical restrictions. It also has good quality. Photovoltaic solar screens can convert this energy into electrical energy, the solar concentrator can convert it into heat, or the photovoltaic-thermal solar concentrator can convert it into each. Solar farms can be used in conjunction with a heating scheme to effectively use solar energy for air conditioners in residential areas during both the cooling and heating seasons. Solar energy, on the other hand, varies substantially depending on temporal, geographical, and climatic factors. As a result, a backup source of heat is essential to keep such systems running smoothly and reliably [4].

The most difficult aspect of using renewable energy systems is maintaining continuousness and dependability over long periods while meeting the required power load. Intensive study has been performed to create adequate and sustainable alternatives, including geothermal resources that can be integrated with enhanced geothermal systems (GSHP). GSHP systems are a promising technology that uses the earth as a heat source as well as a heat sink for energy storage. Because heat pump schemes are impacted by air temperature, it is suggested that constant neighboring circumstances be achieved to create more consistent heat recovery system performance with minimum environmental impact [5]. The term "solar energy" relates to power generation directly derived from direct sunlight. It is not to be conflated with some other sources of renewable radiation that are harvested in different ways, including air and biofuel. PV systems and heat transfer gathering are the two most common ways to use energy from the sun. The photovoltaic module collects rays first from sunshine and uses them to instantly stimulate a transfer of electrons, resulting in power generation. Solar thermal energy can be condensed into a heat transfer medium, which works like a law of conservation of energy to transfer energy into heat, or it can be utilized for basic room cooling and heating. The strategies for converting solar thermal power into electric power will be examined in this research. Because solar thermal and geothermal energy is either in the heat produced, they are indeed transformed to power using the heat exchanger. Due to the general immensity of their heat, it turns out that these two sources are best exploited through one Brayton cycle. Different forms of Rankine cycles, on the other hand, are more relevant to specific thermal variables. Water is commonly employed as the working medium for the refrigeration system at temperatures exceeding 200°C. Organic fluids are commonly employed at relatively low heat [6].

This sort of energy station uses sun strength to increase the inherent energy of sunlight. The energy from the sun warms the air in the collecting, which is exposed along peripheral, creating an effect on the greenhouse, and because warmed air is denser than airflow, it rises to the topmost of the tower, which placed in the detector focus. At the foot of the chimney, a wind turbine is placed in the course of the wind in order to transform thermal power into electricity, which is then connected to a generator by the wind turbine combinations and turbines [7]. Power and heat are the major source of energy for social progress and development, yet fossil fuels make for the vast bulk of annual power use, resulting in serious atmospheric emissions to the environment. Boosting sustainable energy use and penetration, which includes geothermal power, geothermal panels, bioenergy, and wind power, is one viable approach for the long-term objective of carbon reduction. Renewable has a great future, but while difficulties of utilization accuracy and greater costs are also major obstacles, more advanced technologies must be studied urgently to contend with traditional fossil fuel consumption.

Geothermal energy is usually kept in the subsurface ground and contributes to sustainable usage. It is been extensively used for home use or central heating by heat pumps, as well as for energy production through the refrigeration system. Geothermal assets can be divided into two classes created on their storage characteristics: hot dry rock (HDR) and hydropower. For HDR, the improved geothermal framework technology is employed, in which heat exchange solutions (water or CO_2) first were pumped to shatter the interior deep hot stone, and used as a heat transporter to recover elevated geothermal for any further usage. The correlating geothermal energy techniques are differed by determining the various phase condition and specific heat [8]. The generated dry vapor of gaseous mixture could be straightforwardly used to drive a turbine; the single- or double-flash cycle is usually used to use the fluid from geothermal fluid, and more competent steam can be generated by lowering the hydrostatic flow; furthermore, the organic Rankine cycle (ORC) is appropriate to use the reduced tepid geothermal fluid. The security of power generation is essential for economic growth, mechanization, and digitalization. World energy consumption is rapidly increasing, and the globe is currently concerned about how to meet future requirements. According to long-term estimates, consumption of electricity will significantly rise. Coal and oil have indeed been employed as primary energy resources to fulfill this need. Coal and oil produce greenhouse gas emissions that have a great impact on the environment and future generations.

The smart grid, when combined with distributed power generation, creates a new platform that dramatically

improves electric energy security and quality. As more energy sources become available, such as solar, wind, biomass, and hydropower, this approach becomes more feasible and trustworthy. Renewable and nonconventional sources of energy are required to access a smart grid-connected distributed generation connection. As a result, the importance of alternative energy sources in generating power, as well as their interaction with the smart grid infrastructure for energy security, is considered in this chapter [9]. Changing climate and a scarcity of natural resources for generating power, along with rising energy consumption, present a difficult picture for transmission and distribution. In this setting, countries around the world must search out efficient and clean methods to meet their long-term energy needs. The capacity of changed renewable energy sources (RES) has been anticipated to great, and will also be available to satisfy a significant portion of future combined electric power. Radiation from the sun reaches the Earth in the amount of 880 million TWh per year. Solar energy's availability makes it a potential option for producing renewable energy.

The hunt for power from solar has become unavoidable due to the depletion of petroleum and energy supplies, as well as increasing worries about emissions to the atmosphere [10]. As per contemporary standards, they are endless. Throughout most nations, a wide range of technical possibilities are accessible, and social acceptability is strong. Even if the capability is low, rural families in both developed and emerging nations value a constant supply of energy. Billion people in the world live in rural communities in underdeveloped nations that do not have access to grid-based power. Grid connection is sometimes impossible due to scattered communities, rough terrain, or a combination of the two. As a result, tiny off-grid stand-alone renewable energy technologies are a viable option for closing the power gap in remote regions of emerging countries, where the grid connection is lagging behind population expansion. It is virtually incapable of meeting tiny energy requirements in isolated places far off the grid, either via a long-distance transmission network or with traditional generating [11].

A hybrid energy system can be built using a variety of various sources of energy and storage technologies. The impact of incorporating a considerable quantity of wind output into an isolated power system with many generating units is examined. The possibility of photovoltaic panels partially replacing generating units is addressed. The Amazon Basin confronts two significant challenges when it comes to energy policy. An SPV-diesel system generates more energy with more dependability than an SPV-only system. For the same energy produced, this delivers cheaper prices, greater flexibility, and higher efficiency. The implementation of control techniques for photovoltaic-combined power generation, as well as their efficiency and power improvement possibilities, is discussed. If wind and solar power resources are unavailable, the controllers are given to ignite a diesel engine and acquire a feed from a large battery. If alternative sources and power saved in the battery system are unavailable, the diesel engine is becoming the major source of power [12].

2. Related Work

Renewable power applications, particularly for big systems, give a possibility to replacing the principal supply of energy. The heat recovery technique is an excellent way to reduce fossil fuel usage. This article offers a case report of a combination hybridization PV/T sun-aided pumping system for heated water generation in a field house. The very first step in the construction process was given. The system design was then modeled using the TRNSYS 16 computation framework, as well as the overall efficiency was assessed using the numerical model over a year. The findings show that the COP of the system can achieve 4.1 in Hong Kong's tropical environment, with a significant component factor of energy efficiency of 67 percent when compared to the traditional heat pump. The thermal efficiency of the same device was analyzed and compared in three additional French cities under various environmental circumstances. This research will discuss the economic consequences as well. Thus, a research study on estimating the hybrid solar-based PV/Thermal heat pump system was proposed by [13].

A prototype combination geological thermal power network was erected at the Gümüşköy Geothermal Power Power Station is developed to investigate the contribution of the observable universe to the plant's overall energy capacity and to empirically validate created to anticipate hybrid system efficiency. The results of tests on a 200 kWh parabolic dish solar collector are reported. Heat loss of geothermal occurs during the lifespan of geothermal energy facilities. The photovoltaic energy industry is advancing fresh concepts for a variety of uses, including structures, processing plants, and farming. The restricted building for solar technologies has spurred a desire for hybrid photovoltaics for the belief that is in order of proactive electricity and/or solar passive gadgets, particularly in the construction industry. With the international trend toward the creation of limited structures, the significance is growing. Following the testing results and doing a financial study, a post preliminary report for integrating a 1 Mw capacity sunlight sector to the current 5.5 MWe, there is a geological network with combined cycle is conducted out. Thus, a manual approach to the strategy and employment of geothermal and solar thermal control devices is developed.

By incorporating geothermal liquid as an extrasource of heat, this research intends to contribute to the solar thermal power plant (SCPP) agency continuation. An occurrence of the incident institute, a model of the i^{th} and 8-meter elevation and a 12-meter collectors circle was developed. Within the collection, a hydrothermal water spiraling pipe is constructed. The ambient temperature recorded the accumulator, the heat of the chimney's entrance, and the airspeed in all circumstances, including at nighttime with geothermal heating systems and throughout the day with solar output combined with thermal heating water. In the best condition, where thermal fluid passes at the collection point and departs at its perimeter, night warming using water released raises the temperature of the collector center and the air velocity, according to tests done in winter 2019. During the day, whenever the collector center is heated only by solar

irradiation, the temperatures exceed and the air velocity reaches. Moreover, when solar radiation is combined with water released, the heat of the hoarder center rises to 80°C, and the air velocity rises. Hence, an investigation on the hybrid thermal and geothermal wind power plant is developed by [14].

For a hybrid solar-binary geothermal power plant, an integrative design is produced. A preexisting ORC (Rankine cycle circuit) using reduced geothermal saltwater and a photovoltaic troughs process of software up the whole system. The hybrid structure is predicated on a newly created parallel connection. This outperforms individual systems when used together. The combination state's functioning is tuned to maximize net energy production and assessed for typical days in 2013. The goal of the solar trough state's architecture is to maximize the hybrid state's total energy at normal incidence. This design yields a sun contribution of the total output power of 7%. In comparison to the baseline, the optimized constant flow and variable-flow solar systems result in a 5.5% and 6.3% increase in net power output, respectively. The measure for evaluating the hybridization game's performance of the economy when contrasted to a stand-alone geothermal power plant, LEC, for the combination can be reduced by 2%, according to the study. At this moment, optimizing the stand-alone on geothermal ORC leads to an 8% decrease in LCE, indicating that it is a better alternative than hybridizing the hydrothermal plant. Based on the above-mentioned systematic feature, a novel approach to the thermo-economic estimation of the hybrid system in the geothermal plant is proposed by [15].

In the wintertime, apartment structures in Ontario demand significant thermal requirements. Many households can adopt solar cells to substitute fossil energy electricity. It, though, may not even be productive since many towns are subjected to low levels of solar irradiation, leading to solar cells with a big surface size. As a result, for a residential house of $325m^2$ floor space area in the town of Ontario, a hybrid power system plant combining five PVT photovoltaic power, a 300 m geothermal circuit, and a 9463.54 kg liquid of PCM heat battery bank is constructed. The highest cooling and heating loads for the construction correspondingly. Throughout the year, a thermodynamics evaluation is carried out in parallel. Photovoltaic arrays may offer 8 W of heat energy and electricity generation in January, while geothermal and heat store power might provide throughout each year, accordingly. The hybrid version necessitates an extraheat capacity from the furnaces of 1.86 kW. In the wintertime, the overall device energy and exergy COPs are anticipated to be 54.60 percent and 3.38 percent, correspondingly, while in the summertime, 42.7 percent and 4.48 percent. This research was based on the thermodynamic estimation of hybrid energy by utilizing geothermal and solar energy systems in residential apartments [16].

3. Proposed Methodology

3.1. The Hybrid Model of the Solar-Geothermal Energy System. The power station and the parabolic trough solar system are indeed the two primary elements of the hybrid Stillwater power station. The hybrid power station architecture depicted in Figure 1 is a conceptual flowchart. The geothermal liquid is retrieved at various temperatures from many wells drilled. The geofluid generated at lower temperatures is warmed more in an excessive solar converter before being blended with the rest of the geofluid in the primary manufacturing line [17]. An "improved" geofluid is also utilized to vaporize the hydraulic fluid in two matching energy devices to create power and afterward reinjected into the watershed. The geothermal energy device was established for the geofluid form of flow 915 kg/s at a heat of 154.6°C as well as weather conditions of 12°C, which is the yearly thermal gradient in Fallon, Nevada, in which the operations are based. The fluid flow is unclean iC_4, which has a massive pressure of around 30 bar and a condensation temperature of around 4.5 bar. The iC4 velocity of the fluid per device was around 200 kg/s at operation conditions, and each unit's total electricity production was 16.9 MWe. However, at a temperature of 145°C, the saline flow rate presently retrieved from the wells is 586 kg/s. Nevertheless, as previously stated, it is evenly split into 2 ORC divisions. The sunlight area is made up of parabolic trough collectors that use distilled water to transfer heat (HTF). Heat energy is transported from a HTF towards the vapor phase in the excessive solar exchangers. The saline is warmed before reaching the dual-phase when concentrated solar electricity is provided to maintain the temperature as close to the specified product as possible. This research analyzed the implementation of temperature storing energy in a solar model to enhance photosynthetic rates by efficiently converting energy from the sun [18].

3.2. Solar and Geothermal Power Integration. Geothermal and solar power can be combined in a variety of orders to make a hybrid power system. Solar thermal catchers, for instance, can be utilized to provide supplementary excess heat to compensate for any geothermal network shortage. The solar-based pump system is a popular hybrid solar-geothermal pairing. While numerous applications may exist, the fundamental goal of this pairing is to lower yearly running expenses and carbon intensity. Thermal sun detectors can also be utilized for subsurface heat exchange and geothermal network stabilization. A geothermal exchange, on either hand, could be utilized as a backup heat source for a solar energy collector. When contrasted to a separate unit, this mix must boost total efficiency by 3.6 percent [19]. Another reason for combining geothermal and solar thermal scheme could be a requirement to boost the geothermal cycle's flow rate. Using a sun-aided ground source heat exchanger to lower the essential hole heat transfer scope of the field, investigators decrease the initial expenditures involved with a geothermal power plant. To enhance load demand for sensor determines, a supercritical ORC built on a geothermal power plant combined with such a concentrating solar energy scheme can be used. Whereas most hetero structures are intended for heating purposes, a subsurface exchanger can be integrated with a concentrating solar way of enhancing its effectiveness. Concentrated solar

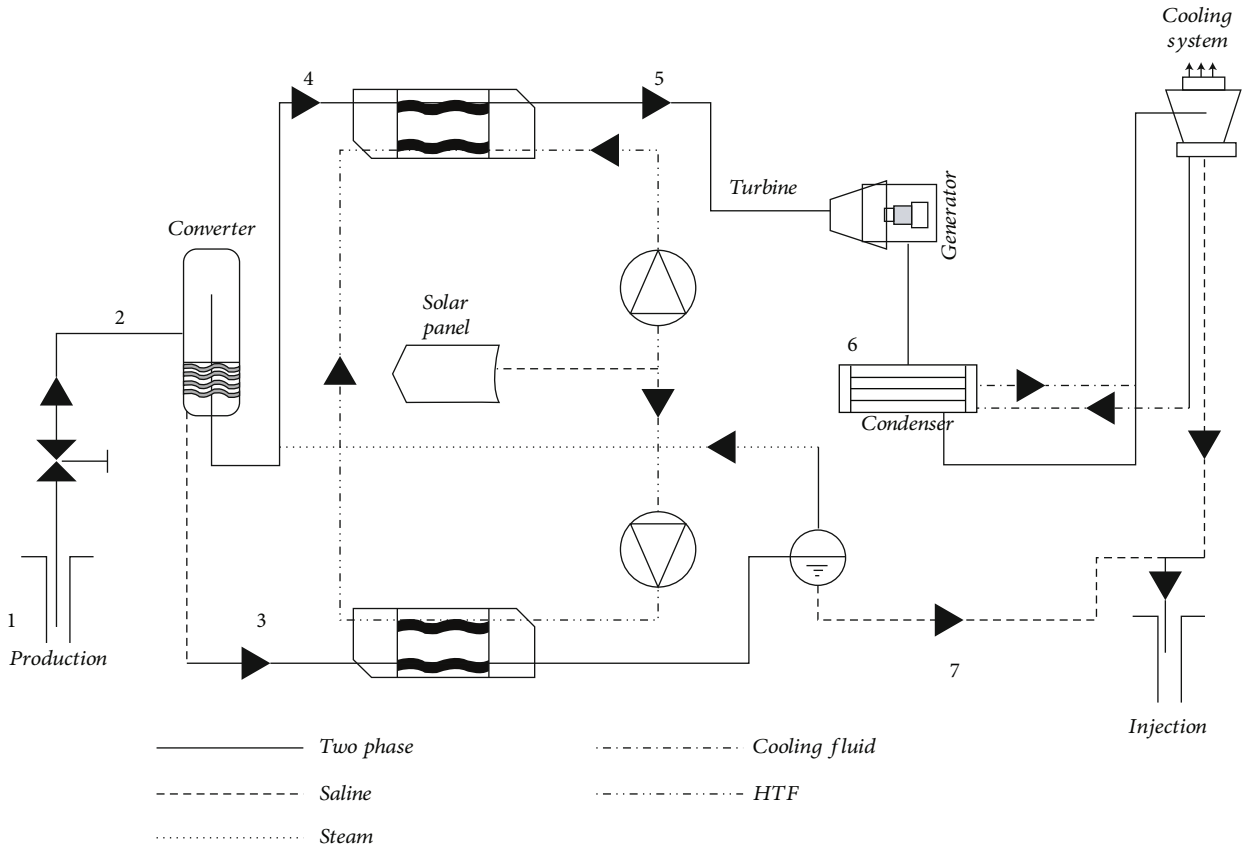

Figure 1: Schematic model of geothermal and solar power.

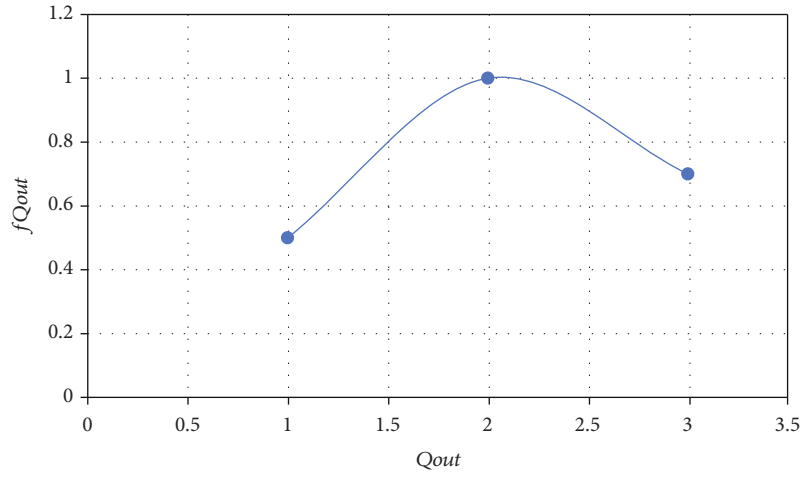

Figure 2: Turbine volume flow rate at outlet.

systems' energy output varies seasonally based just on a sun's location and ambient air conditions [20].

Figure 1 shows schematic model of geothermal and solar power. Using the geothermal scheme as a seasonal energy storing device becomes a technique to increase the seasonal factors of efficiency. A solar thermal game's seasonal extraenergy can be stored in a vertical and lateral heat transfer. A solar concentrator, short-term heat transfer equipment, a heating system, and a subterranean exchanger for prolonged storage would make up the whole system. To eliminate temperature changes and preserve the storage device's efficacy over time, a staged sequence of ground heat transfer might have been used [21]. The primary stumbling block to implementing such an interconnection could be the ground flow of water. The site's watershed levels have to be low enough even to prevent the produced thermal plume from

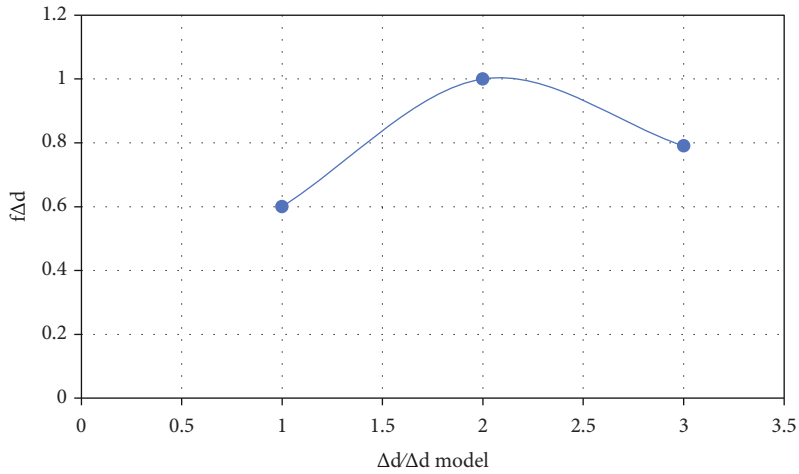

Figure 3: Drop of isentropic enthalpy.

Table 1: Important parameter of cooled condenser.

Data model	
Outline of fan	Tempted
Type of the tube	G-finned
Area or size	489000
GHT coefficient (pure)	460
GHT coefficient (dirty)	446

dissipating. Research showed that if groundwater leakage speed is zero, annual latent heat is ineffective in resolving the temperature imbalance. As shown in the instances above, combining a concentrated solar system with a geothermal power plant can either help produce more power or reduce the amount of geothermal power used. The status of the available ground fluid is an important consideration in the design of solar hybrid devices. A solar PV smart grid PVT will be combined with a GSHP to generate multiple types of energy at a once. While the hybrid power system pulls heat energy from the subsurface, the PVT module creates electrical power from incoming solar light even while collecting heat energy from the sun's radiation. To achieve the optimum results, careful thought of the working medium is required [22].

The primary stumbling block to implementing such an interconnection could be underground water flow. The project's watershed levels have to be low enough just to prevent the produced thermal plume from dissipating. Research indicates that if groundwater recharge leakage speed is zero, annual latent heat is ineffective in resolving the temperature disequilibrium. As shown in the instances above, combining a concentrated solar system with a geothermal system can either help produce more energy or reduce the number of geothermal resources used. The status of the available ground fluid is an essential facet of hybrid solar-geothermal devices. Investigators have been driven to develop novel previous knowledge such as fuzzy logic (FL) controllers and modeling anticipatory management as a result of all this (MPC) [23].

3.3. Turbines. The blades improve the quantity of the heat transfer fluid or convert its power into the effort. The generated power by turbines is given by presuming the transformation is adiabatic and ignoring fluctuations in possible energy and kinetic energy of the occupied gas. The following equation (1) provides the energy generated using the turbines:

$$V_a = u_{vt} \bullet (d_1 - d_2) = u_{vt} \bullet \xi_a \bullet (d_1 - d_{2z}). \quad (1)$$

In the above equation, V_a denotes the output energy of the turbines, and the fluid mass flow rate is denoted as u_{vt}. The enthalpy of the working fluid is denoted by $d_1 - d_2$ based on the outlet and inlet which is represented by ξ_a, and it is termed as isentropic efficiency [24]. Both of these are estimated with the use of the producer's efficiency calculation. The isentropic efficiency reaches a notable rate of 0.869 under operation state, and it is greatly influenced by the departures of the isentropic enthalpy drop and flow velocity at the expander outlet from their design standards under off-design circumstances. To compute the isentropic effectiveness in any situation, two corrections for the venturi flow frequency and isentropic enthalpy decrease, correspondingly, were being used and mentioned in Figures 2 and 3.

As a result, the turbines' off-design isenthalpic performance is the sum of the designed isenthalpic performance (87%) and the following correction factors, and it is illustrated in the following equation (2) [25]:

$$\xi_{it} = \xi_{it,des} \bullet f_{Qout} \bullet f_{\Delta dit}. \quad (2)$$

The generating performance, which is considered to be 0.99, has an impact on the electrical output, which is provided by the following

$$V_e = V_a . \xi_{gn}. \quad (3)$$

3.4. Condenser. Resulting of water constraints in the production plant, the fluid exiting the turbines is desuperheater and condensed in a forced draught air-conditioning system

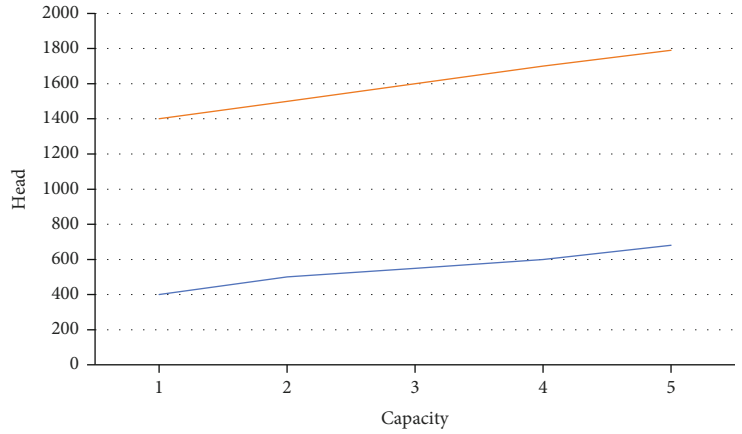

Figure 4: Valve efficiency curve.

Table 2: Preheater model data.

Model data	Preheater (1)	Preheater (2)
Exterior valve area	38676	38674
Diameter of the tube (outside)	16	16
Number tube	7599	7599
Type of tube	Short	Short
Design of tube	30° trilateral	30° trilateral
GHT coefficient (pure)	182.4	355.6
GHT coefficient (dirty)	157.8	272.5

Table 3: Data model of vaporizer.

Data model	
Exterior valve area	5180
Diameter of the tube (outside)	16
Number tube	4418
Type of tube	Short
Design of tube	30° trilateral
GHT coefficient (pure)	1265
GHT coefficient (dirty)	607

condenser (ACC). The energy that is expelled into the atmosphere is provided by

$$Q_{cod} = u_{vt} \bullet (d_2 - d_3) = u_{air} \bullet e_{air} \bullet \Delta F_{air}, \quad (4)$$

the operating fluid's particular enthalpy readings at the outlet and inlet of the condensation, correspondingly. To use the data from the producers' data sheets, the condensation is correctly analyzed utilizing Aspen Exchanger Design and Rating. To recompense for the minimum transfer of air heat rate, low tubes are employed to improve the exterior surfaces. The condensation division's energy consumption is estimated to be 0.13 kW per kg/s of air. Table 1 illustrates the ACC's primary characteristics [26].

3.5. Feed Valves. The feed stream is delivered to the heat exchanger via feed valves after passing through the condensation. The amount of energy required to pump the condensation is demonstrated using the following

$$V_q = u_{vt} \bullet (d_2 - d_3) = u_{vt} = \frac{d_{4z} - d_z}{\xi_q}, \quad (5)$$

where ξ_q is the hydraulic valve efficiency. The actual system has 3 distinct feed valves per module; however, due to the exhausted geothermal energy, only one centrifugal pump is required. A product's multispeed efficiency curvatures are replicated in Figure 4 and applied in Aspen Plus after being tested analytically. For any charge of occupied fluid volume flow frequency and cycle absolute heaviness, the simulation tool determines off-design pump efficiency and pump rotor velocity.

3.6. Heat Transfer Unit. The fluid flow enters the vaporization after passing through two preheaters, where it would be a liquid before being evaporated. Because to prevent liquid particle disintegration at the tip of the nozzle, a 3°C superheating is required. The rate of heat transfer in heat transfer is calculated using equation (6) [27]:

$$Q = G \bullet V \bullet \Delta T_{lm}, \quad (6)$$

where G denotes the total heat coefficient. Based on the data between the two fluids is the exact heat transfer size and is the temperature coefficient. Because the flow rates and temperature differ from the design parameters, the result fluctuates during off circumstances. Aspen Heat Exchange Modeling and Rating was used to simulate the preheaters and purifier, which are barrel heat engines. The heat transfer was sized using the manufacturer's spreadsheets as a guide. Table 2 and Table 3 illustrate the key characteristics of the preheaters and vaporizers achieved during the design approach [24].

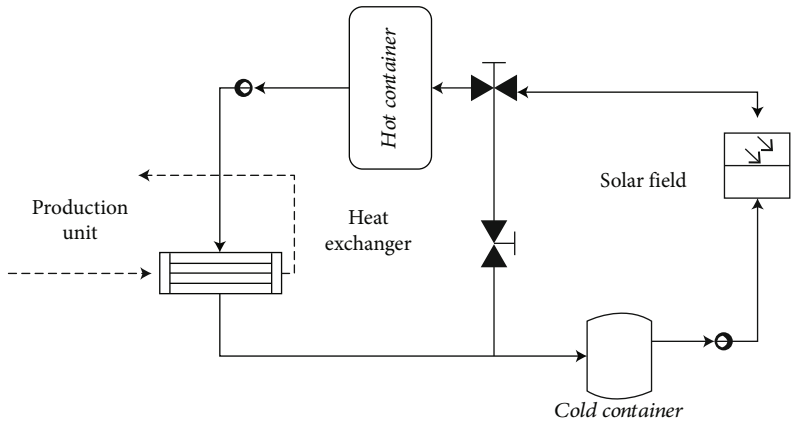

Figure 5: CSP plant.

Table 4: Specification of storage container.

Diameter of the container	18
Height of the container	10
Loss of coefficient	0.5
Volume of the container	2250

4. Solar Energy Site Design

The concentrated solar power plant is utilized to compensate for the geothermal outlet's temperature loss. A recent detailed evaluation of concentrated solar power technologies was conducted. The solar plant in this study is made up of parabolic trough collectors that use distilled water also as a heat transfer medium (HTF). The HTF is preheated in the solar concentrator and then utilized to heat the geothermal fluid using its heat energy [28]. As discussed, a portion of saline from a producing well is preheated in excessive solar exchange before being supplied into the ORC system's major manufacturing line. Figure 5 depicts a conceptual plan of the Stillwater concentrated rooftop solar component. The characteristics of a created solar field reproduction design are described in a subsequent.

4.1. Design on the Storage of Thermal Energy. The current concentrated solar power plant is being upgraded with thermal storing to improve an overall productivity of the device by moving solar energy generation to reduced heat absorption when the geothermal unit is more efficient. The model of CSP plant is mentioned in the following Figure 5. Even though a sensible heat storing method is discussed now, recent developments in latent heat storing utilizing phase modification elements and thermochemical storing employing bidirectional chemical changes, both of which have just been reported, may soon encourage their usage in such devices [29].

The storage system is direct (that is, the heat transfer fluid and the storage device are the same) and comprised of two containers, one at elevated temp and the other at a constant temperature. The solar field heats the distilled water that has been kept in the low-temperature container. The heat transfer achieves different properties at the solar project's output based on the DNI. The solar panel is in "proper functioning mode" when the temperature rises 170°C. As a result, the HTF passes into the high-temperature container before heating the geothermal liquid in the heat transfer.

When the temperature decreases below 170°C, the "recirculating pump mechanism" kicks in. To avoid freezing the liquid in the boiling container, the heat exchanger exiting the solar ground is redistributed to the low-temperature chamber.

To achieve a temperature gradient of 50°C among both the outlet and inlet of every loop, the mass flow degree of the HTF entering the cold container is adjusted as a consequence of the DNI. The volume flow velocity of HTF leaving the hot tank and entering into an excessive solar exchange is determined by the operation mode as well as the temperature difference. The heat transfer fluid again from SF penetrates the hot container throughout normal system operation, as well as its flowrate, which is resolute by the DNI. The heat transfer fluid is also supplied to the excessive solar transporter to preheat the thermal saline before being sent to the cold tank. Inside the heat transfer, the heat transfer rate velocity of the fluid is equivalent to the set point. Whenever the CSP facility is in recycling mode [30], however, the HTF that has collected in a hot tanks is only discharged when the ambient temperature is too low. A threshold temperature difference has indeed been employed for the determination of daily atmospheric temperature variance for every day of the benchmark period. As a result, in recycling operation, the hot container is only drained when the ambient temperature reaches a certain level.

At average sun irradiation, the wastewater facility's useable solar energy output is 17 management and better. This thermal energy can be utilized to warm the geothermal saline to enhance the amount of power produced. The goal of the thermoelectric generator, as outlined in this paper, is to store larger solar energy that can be released at intermediate temperatures, whenever the hydroelectricity is more effective. To recharge the TES technology, a greater solar area is required [31]. The containers are spherical, and the liquid inside can be presumed to be completely mixed.

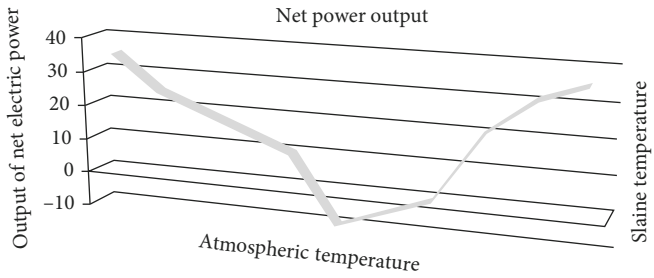

Figure 6: Net power output.

Table 5: Output power variation.

Output power variation	Saline temp					
Atmospheric temp	154	152	150	147	142	140
-10	178%	164%	155%	145%	142%	140%
-5	175%	165%	150%	145%	138%	140%
0	172%	160%	150%	142%	135%	132%
5	165%	155%	140%	130%	125%	119%
10	150%	140%	130%	125%	128%	115%
12	145%	135%	125%	116%	108%	103%
15	135%	125%	115%	110%	105%	100%
20	115%	110%	102%	95%	85%	83%
25	105%	95%	85%	80%	75%	65%
30	85%	80%	75%	65%	62%	55%
35	70%	65%	60%	55%	50%	45%

Because the entering and exiting streams may not be comparable, the fluid level may fluctuate among defined low and high levels. The primary assumption is on the right side of the screen because it is believed that the flow leaving the tank has the same heat as the container. In heat transmission, in general, the tank percentage error per unit of area is a combination of the quantity of liquid in the sample and the factor. The following Table 4 shows the specification of storage container.

5. Result and Discussion

Various fluid inlet values and temperature fluctuations, ranging from 139°C to 156°C and -9°C to 34°C, are used in the geothermal binary cycle computations. To find the plant's maximum output production, the pumping speed of rotation and condensate temperature was changed for both of these variables. The program determines the fluid volumetric efficiency necessary for a 3°C increasing temperature at the tip of the nozzle, as well as the airflow volume flow frequency rate is necessary in the accelerator for a 2°C fluid subcooling. Figure 6 shows the total power plant's net electricity production (both units) as a proportion of saline and atmospheric temps.

The rise in saline temperature from 140°C to 155°C is associated with a significant increase in net electricity production; the magnitude varies with air temperature. It is, in fact, more important at colder temperatures than at warmer ones [32]. The maximal temperature and pressure in the axial compressor are recommended to exceed as the saline heat raises, as is the performance and power production. Improve the ambient temperature from −10°C to 35°C, on the other hand, results in a significant fall in net generating power caused by an increase in contribution to the amount and a decrease in the enthalpy fall in the generator. So, because the condense level is restricted to 2.8 bar at very appropriate temperatures (below 0°C), the energy output is time-invariant. This peak is caused by a restriction on the minimum expansion discharge point, which stops the turbine's temperature drop from increasing higher.

Table 5 illustrates the variance in net electrical efficiency compared with the corresponding condition, which has a saline temp of 140°C (near the current temperature of the reservoir fluids) and a weather condition of 12°C (namely, the annual regular ambient temperature). This table demonstrates that increasing the geothermal temperature difference to the temperature setting of 154.5°C can boost an ORC's net energy production by 42 percent as compared to the comparative scenario.

5.1. Solar Energy. Arbitrary time steps are used to simulate the solar panels over the full reference year. While methodologies for converting worldwide irradiance data are generally available as average temperatures into indirect illumination hourly available in abundance in the research, directly irradiated hour information for the plant location was widely available first from the NREL dataset. The large solar program's total yearly thermal electricity generated with storing and delivered to the geothermal saline is anticipated to be around 41.6 GWh/year. Because the TES process generates inefficiencies due to thermal distribution in the containers, the thermal energy exchange with the saline would be significantly higher if the solar panel did not include the storage container. The advantages of storage, on the other hand, are conversed in greater detailed in the section [19].

Figure 7 depicts heat transferred in the solar heat exchangers either with or without reservoir storage. When a DNI is maximum enough to heat the higher temperature to around 170°C, the thermal heat is dissipated daytime. The implementation of the TES in the photovoltaic system, as illustrated in Figure 7, permits heat energy to be produced at night and when the air temperature is below the earlier in this section threshold.

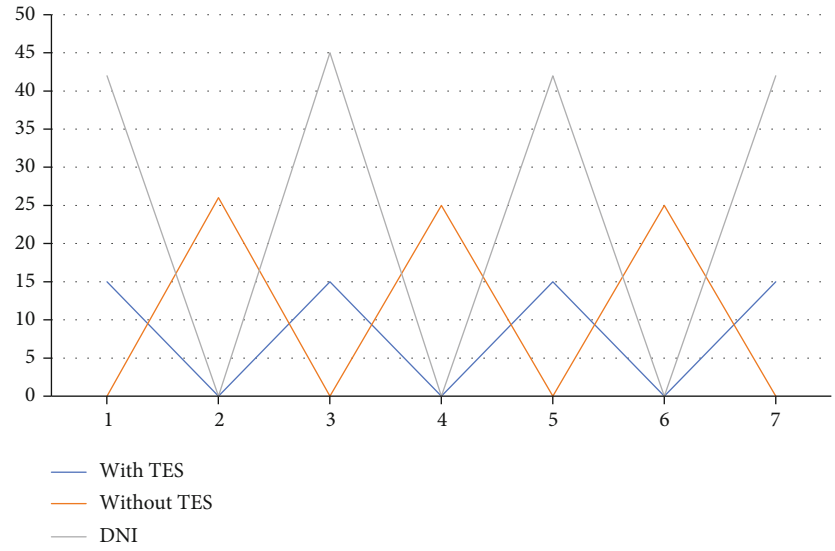

Figure 7: Thermal power exchange between three phases.

Figure 8: Geothermal power with and without thermal power.

At design specifications, the combined heat and power plant's performance is around 11%, but it lowers to 6% at warmer lower temperatures and the relatively low saline temperature. Computed at lunchtime on the position of the sun, the effectiveness of the extraelectricity generation owing to the CSP addition is around 10%. While this figure may seem low as contrasted to other solar-powered power grids, it still is greater than the effectiveness of the geothermal system, and it may be acceptable if low-cost PTC detectors are used.

Nevertheless, the yearly electricity production of the hybrid geo-solar plant with a thermoelectric generator is 171 GWh/year, compared to "only" 170 GWh/year for the same facility without a store. Whenever the TES is incorporated, the power generation process delivers a yearly energy gain of 10.5 GWh, relative to the geothermal system (162 GWh/year), which drops to 8.6 GWh/year without it. As a result, as compared to a hybrid facility without reserve, the TES process allows for an 18.6 percent increase in additional electrical output.

Both the CSP plant and TES unit improve electrically generated power, according to the findings of this study. Whenever the CSP station produces electricity throughout the day and whenever the thermal energy system produces heat during the nighttime, the temp of the geothermal saline approaches the technical solution (154.5°C). Both with storing, the saline temperature is rising at the air-conditioning system input from the real geofluid temp.

In Figure 8, the electrical energy production of the geothermal power plant and the solar hybrid plant is compared

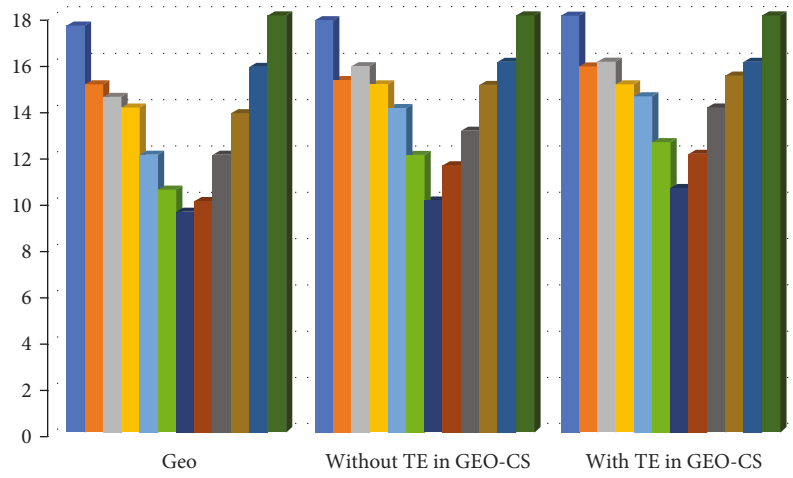

Figure 9: Comparison chart.

for five different. Even though the saline temp is stable on this timeframe, the geothermal-only voltage generated changes throughout the day due to the significant impact of the air temperature on the Exergy output. As a result, the extraconcentrated solar heat is dissipated both throughout the day, while glacial power generation is reduced due to warm atmospheric conditions, and at nighttime, when geothermal effectiveness is greater.

The source reference could not be located. The monthly electric power consumption of a geothermal-only plant, a hybrid facility with TES, and a hybrid plant without TES is compared. During the related results in a year, the hybrid plant with storage generates the most energy. Clearly, because of low illumination rates, the CSP output is minimal during wintertime and it is mentioned in Figure 9 comparison chart on the month (Januray-December).

The thermal storage technology enables for greater utilization of a combined solar plant's excess power generation. The heat power generated by the combined cycle power plant without holding is instantly discharged to warm the geothermal saline, enhancing the hybrid plant's electricity supply production. The TES system, on either extreme, uses a control algorithm to produce extraconcentrated solar energy at night, whenever the atmospheric temperature drops, and the geothermal heat pump system is much more effective. Quarterly, total electric output power is greater, especially in summer when daily temperature fluctuations are considerable.

6. Conclusion

The major elements of a detailed design including off simulation of a realistic hybrid power generation system with a parabolic dish collector solar plant and an aerosol combined-cycle geothermal reactor are shown in this study. The use of renewable radiation to increase the temperature of the geofluid generated from the boreholes is proposed as a way to alleviate the geothermal reporter's temperature exhaustion. This allows the ORC technology to retain greater performance even as the geofluid temperature and mass flow rate decrease below the design levels. Potential advantages derived from the installation of a thermal energy storage (TES) unit inside the network also are assessed. The computational results reveal that both saline and atmospheric temps have a significant impact on the operation of the parched cool geothermal power plant. The photovoltaic mechanism preserves the heat of the geothermal fluid near to the original temperature, assuring that the ORC system is more thermally efficient. Because the net output power area has a nonlinear trend, the additional photovoltaic efficiency fluctuates with solar irradiation and temperature fluctuations. The thermal storage system searches for circumstances that maximize yearly power generation by separating the two factors. When opposed to the geothermal power plant, the introduction of the concentrator CSP system with a practical temperature output of 18 MW^{th} results in a 2.9 percent gain in electricity generated. When the CSP solar field is larger by a solar factor of 1.5, the increase increases to 5.5 percent, and it rises to 6.4 percent when a thermal storage system is added to the oversized field. As a result, the storage system alone boosts the photovoltaic segment's production by 20%.

Data Availability

The data used to support the findings of this study are included within the article. Further data or information is available from the corresponding author upon request.

Conflicts of Interest

The authors declare that there are no conflicts of interest regarding the publication of this paper.

Acknowledgments

The authors appreciate the supports from the Wolaita Sodo University, Ethiopia, for providing help during the research and preparation of the manuscript. The authors thank to Kyungpook National University, East West College of

Engineering, Vidyavardhaka College of Engineering, and University of Petroleum and Energy Studies for providing assistance to complete this work. The authors would like to acknowledge the researchers supporting project number (RSP-2021/373), King Saud University, Riyadh, Saudi Arabia.

References

[1] S. Kuravi, J. Trahan, D. Y. Goswami, M. M. Rahman, and E. K. Stefanakos, "Thermal energy storage technologies and systems for concentrating solar power plants," *Progress in Energy and Combustion Science*, vol. 39, no. 4, pp. 285–319, 2013.

[2] I. Dincer and M. A. Rosen, *Thermal Energy Storage Systems and Applications*, John Wiley & Sons, 2021.

[3] A. Gil, M. Medrano, I. Martorell et al., "State of the art on high temperature thermal energy storage for power generation. Part 1–concepts, materials and modellization," *Renewable and Sustainable Energy Reviews*, vol. 14, no. 1, pp. 31–55, 2010.

[4] D. C. Thomas, "Selection of Paraffin Control Products and Applications," in *International Meeting on Petroleum Engineering*, Tianjin, China, 1988.

[5] S. Hasnain, "Review on sustainable thermal energy storage technologies, Part I: heat storage materials and techniques," *Energy Conversion and Management*, vol. 39, no. 11, pp. 1127–1138, 1998.

[6] K. Pielichowska and K. Pielichowski, "Phase change materials for thermal energy storage," *Progress in Materials Science*, vol. 65, pp. 67–123, 2014.

[7] S. H. Madaeni, R. Sioshansi, and P. Denholm, "How thermal energy storage enhances the economic viability of concentrating solar power," *Proceedings of the IEEE*, vol. 100, no. 2, pp. 335–347, 2012.

[8] N. Ridzuan, F. Adam, and Z. Yaacob, "Evaluation of the inhibitor selection on wax deposition for Malaysian crude oil," *Petroleum Science and Technology*, vol. 34, no. 4, pp. 366–371, 2016.

[9] S. Bell, T. Steinberg, and G. Will, "Corrosion mechanisms in molten salt thermal energy storage for concentrating solar power," *Renewable and Sustainable Energy Reviews*, vol. 114, article 109328, 2019.

[10] J. W. Moon and S.-H. Han, "Thermostat strategies impact on energy consumption in residential buildings," *Energy and Buildings*, vol. 43, no. 2-3, pp. 338–346, 2011.

[11] M. Al-Shawwa, A. A.-R. Al-Absi, S. A. Hassanein, K. A. Baraka, and S. S. Abu-Naser, "Predicting temperature and humidity in the surrounding environment using artificial neural network," vol. 2, no. 9, p. 6, 2018.

[12] S. K. Natarajan, S. K. Sahu, and A. Singh, "Thermal performance of a salt gradient non-convective solar pond in subtropical region climatic conditions," *IOP Conference Series: Earth and Environmental Science*, vol. 312, no. 1, article 012019, 2019.

[13] Y. Bai, T. T. Chow, C. Ménézo, and P. Dupeyrat, "Analysis of a hybrid PV/thermal solar-assisted heat pump system for sports center water heating application," *International Journal of Photoenergy*, vol. 2012, Article ID 265838, 13 pages, 2012.

[14] O. B. E. K. Mokrani, M. R. Ouahrani, M. H. Sellami, and L. Segni, "Experimental investigations of hybrid: geothermal water/solar chimney power plant," *Energy Sources, Part A: Recovery, Utilization, and Environmental Effects*, vol. 2020, pp. 1–18, 2020.

[15] P. Kumar and D. K. Palwalia, "Decentralized autonomous hybrid renewable power generation," *Journal of Renewable Energy*, vol. 2015, Article ID 856075, 18 pages, 2015.

[16] K. Li, C. Liu, S. Jiang, and Y. Chen, "Review on hybrid geothermal and solar power systems," *Journal of Cleaner Production*, vol. 250, article 119481, 2020.

[17] L. Bousselamti and M. Cherkaoui, "Modelling and assessing the performance of hybrid PV-CSP plants in Morocco: a parametric study," *International Journal of Photoenergy*, vol. 2019, Article ID 5783927, 15 pages, 2019.

[18] A. G. Olabi, M. Mahmoud, B. Soudan, T. Wilberforce, and M. Ramadan, "Geothermal based hybrid energy systems, toward eco-friendly energy approaches," *Renewable Energy*, vol. 147, pp. 2003–2012, 2020.

[19] M. Ciani Bassetti, D. Consoli, G. Manente, and A. Lazzaretto, "Design and off-design models of a hybrid geothermal-solar power plant enhanced by a thermal storage," *Renewable Energy*, vol. 128, pp. 460–472, 2018.

[20] A. Egea, J. P. Solano, J. Pérez-García, and A. García, "Solar-driven melting dynamics in a shell and tube thermal energy store: an experimental analysis," *Renewable Energy*, vol. 154, pp. 1044–1052, 2020.

[21] M. Fadl and P. Eames, "Thermal performance analysis of the charging/discharging process of a shell and horizontally oriented multi-tube latent heat storage system," *Energies*, vol. 13, no. 23, p. 6193, 2020.

[22] D. S. Mehta, B. Vaghela, M. K. Rathod, and J. Banerjee, "Thermal performance augmentation in latent heat storage unit using spiral fin: an experimental analysis," *Journal of Energy Storage*, vol. 31, article 101776, 2020.

[23] A. Agrawal and D. Rakshit, "Review on thermal performance enhancement techniques of latent heat thermal energy storage (LHTES) system for solar and waste heat recovery applications," in *New Research Directions in Solar Energy Technologies*, Energy, Environment, and Sustainability, H. Tyagi, P. R. Chakraborty, S. Powar, and A. K. Agarwal, Eds., pp. 411–438, Springer, Singapore, 2021.

[24] L. Mishra, A. Sinha, and R. Gupta, "Recent developments in latent heat energy storage systems using phase change materials (PCMs)—a review," in *Green Buildings and Sustainable Engineering*, Springer Transactions in Civil and Environmental Engineering, H. Drück, R. Pillai, M. Tharian, and A. Majeed, Eds., pp. 25–37, Springer, Singapore, 2019.

[25] M. Ayub, A. Mitsos, and H. Ghasemi, "Thermo-economic analysis of a hybrid solar-binary geothermal power plant," *Energy*, vol. 87, pp. 326–335, 2015.

[26] S. Seyam, I. Dincer, and M. Agelin-Chaab, "Thermodynamic analysis of a hybrid energy system using geothermal and solar energy sources with thermal storage in a residential building," *Energy Storage*, vol. 2, no. 1, 2020.

[27] T. T. Chow, G. N. Tiwari, and C. Menezo, "Hybrid solar: a review on photovoltaic and thermal power integration," *International Journal of Photoenergy*, vol. 2012, Article ID 307287, 17 pages, 2012.

[28] Y. Wang, X. Yang, T. Xiong, W. Li, and K. W. Shah, "Performance evaluation approach for solar heat storage systems using phase change material," *Energy and Buildings*, vol. 155, pp. 115–127, 2017.

[29] M. Rahimi, S. S. Ardahaie, M. J. Hosseini, and M. Gorzin, "Energy and exergy analysis of an experimentally examined latent heat thermal energy storage system," *Renewable Energy*, vol. 147, pp. 1845–1860, 2020.

[30] R. Anish, V. Mariappan, M. M. Joybari, and A. M. Abdulateef, "Performance comparison of the thermal behavior of xylitol and erythritol in a double spiral coil latent heat storage system," *Thermal Science and Engineering Progress*, vol. 15, article 100441, 2020.

[31] D. S. Mehta, K. Solanki, M. K. Rathod, and J. Banerjee, "Influence of orientation on thermal performance of shell and tube latent heat storage unit," *Applied Thermal Engineering*, vol. 157, article 113719, 2019.

[32] H. Abdelrahman, H. Refaey, A. Alotaibi, A. A. Abdel-Aziz, and M. Abd Rabbo, "Experimental investigations on the thermal performance of an ice storage system using twin concentric helical coil," *Applied Thermal Engineering*, vol. 179, article 115737, 2020.

Hindawi
International Journal of Photoenergy
Volume 2022, Article ID 7249109, 7 pages
https://doi.org/10.1155/2022/7249109

Research Article

Optimization of Solar Panel Deployment Using Machine Learning

Shoaib Kamal,[1] P. S. Ramapraba,[2] Avinash Kumar,[3] Bikash Chandra Saha,[4] M. Lakshminarayana,[5] S. Sanal Kumar,[6] Anitha Gopalan,[7] and Kuma Gowwomsa Erko[8]

[1]*Department of Electronics and Communication Engineering, MVJ College of Engineering, Kadugodi, Bengaluru, Karnataka 560067, India*
[2]*Department of Electrical and Electronics Engineering, Panimalar Institute of Technology, Poonamallee, Chennai, Tamil Nadu 600123, India*
[3]*Department of Electrical and Electronics Engineering, Guru Gobind Singh Educational Society's Technical Campus, Bokaro, Jharkhand 827013, India*
[4]*Department of Electrical and Electronics Engineering, Cambridge Institute of Technology, Ranchi, Jharkhand 835103, India*
[5]*Department of Electronics and Communication Engineering, SJB Institute of Technology Bengaluru, Karnataka 560060, India*
[6]*Department of Instrumentation, NSS College, Nemmara, Palakkad, Kerala 678508, India*
[7]*Department of Electronics and Communication Engineering, Saveetha School of Engineering (SIMATS), Chennai, 602105 Tamil Nadu, India*
[8]*Department of Mechanical Engineering, Ambo University, Ethiopia*

Correspondence should be addressed to Kuma Gowwomsa Erko; kuma.gowwomsa@ambou.edu.et

Received 29 January 2022; Revised 23 March 2022; Accepted 25 March 2022; Published 16 May 2022

Academic Editor: V. Mohanavel

Copyright © 2022 Shoaib Kamal et al. This is an open access article distributed under the Creative Commons Attribution License, which permits unrestricted use, distribution, and reproduction in any medium, provided the original work is properly cited.

In this work, we proposed a mechanism for topology reconfiguration or optimization of photovoltaic (PV) arrays using machine learning-assisted techniques. The study takes into concern several topologies that includes series parallel topology, parallel topology, bridge link topology, honeycomb topology, and total cross tied. The artificial neural network-based topology reconfiguration strategy allows for optimal working conditions for PV arrays. With this, machine learning-assisted topology reconfiguration or optimal solar panel deployment enables the proposed mechanism to achieve higher degree of testing accuracy precision, recall, and f-measure under standard ideal condition.

1. Introduction

Researchers are working around the clock to find new ways to generate power that are safe and environmentally friendly, and this effort has global implications. Green energy, often known as renewable energy, is currently a hotly debated scientific topic [1]. Of all the sources of renewable energy, solar power is the well-known and prevalent one as it can be simply purchased and installed, with fewer restrictions on installing [2]. Advances in machine learning and signal processing models employed with the photovoltaic modules [3–6] have made it possible to effectively use data from the PV panels to enable improved control, monitoring, and optimization of power.

They are able to converse with other panels nearby. Additionally, surface mount devices have the ability to act as switching devices, allowing the connection between the panels to be altered in some way [7, 8]. The necessity for connection topology optimization can be alleviated by changing the electrical connections under partial shade situations, which can increase the overall power supplied by the panels with a significant range [3]. Conventional topologies is represented by a line graph showing power output as a function of voltage. The total cross tied topology, which offers the most power, is definitely superior to the SP topology when it comes to delivering power to the array. Therefore, the study is in need to develop a model that should learn in diverse manner from various input data consisting

of irradiance profiles that includes panel partial shadowing and forecasting the configuration for the optimal placement of robust reconfiguration of PV arrays in any type of topologies.

Therefore, the classification is conducted on using irradiance profile on partial shading condition which can be classified accurately by the machine learning model once it has been trained on a considerable amount of training data. For this application, the employment of a machine learning model generates a system that learns via training data in order of relating the irradiance profile that fits with the reconfiguration in an ideal manner. SMDs measure irradiance per panel and communicate it to a local server, where the machine learning helps in predicting the required topology using this information. The server receives the topology selected, and the SMDs are activated to complete topology reconnection.

Several machine learning models including artificial neural network designs find their operations to be successful in many applications [9–13] which can be blamed for the recent surge in supervised machine learning [14, 15]. The PV array irradiance feature is employed to train the machine learning architecture in this study. In order to maximise power output, a PV array system must be reconfigured to the labels used mostly to optimise the weights. Python scikit-learn software was used to train the neural network. The proposed technology is simple and straightforward to apply, requiring no new or external PV panels, and represents a significant advance over the current state of the art in the field.

To ensure that overall radiation on each array row is essentially constant, an irradiance equalisation [16] approach is used for connection reconfiguration. There may be mismatches in the amount of irradiance on a TCT array row that may result in a reduced current output and thus a lower output during the occurrence of the partial shadowing. Solar panels receiving less light energy are switched electronically to the ones that receive increased amount of light. Therefore, the total irradiance on each array rows is nearly identical with the sum of irradiances across every row in an entire PV array.

A simple sorting algorithm [17] may identify the array rows, which are shaded heavily in a location and add dynamic modules to those rows, which is a popular strategy. By decreasing the irradiance mismatch index (IMI) in PV arrays, the authors of [18] show considerable gains in power output when compared to the architecture with no reconfiguration. When the IMI is kept to a minimum, the array total irradiance remains constant across all of its rows, reducing the amount of current and voltage mismatches caused by shade. Based on the limits imposed on frequency inverters, an electrical system that allows the modules in array to get reconfigured and connected with different numbers of modules in each row was proposed by the authors of [19].

The series parallel topology has a variety of options for reconfiguration. In order to create an SP PV array using the SP architecture, a simple reconfiguration technique entails stringing together irradiance levels and joining the strings. Only when more than 15% of the panels are shaded, do the authors of [9] reconfigure the array, based on the current and voltage measurements from each panel.

There exist many algorithm including support vector machine, k-nearest neighbor, and Naïve Bayes to optimise the optimal configuration and placement of panels under different conditions; however, most of the methods fails as it is not supplied with rich set of data, and the proposed method was aimed at determining the solution using machine learning. According to [10], a partial reconfiguration technique employing irradiance characteristics and graph clustering is proposed to merge disparate panels and show considerable performance benefits. Using a neural network-based technique, the authors of [11, 20] have improved performance by learning the irradiance properties and translating them to the appropriate topologies. This research focuses on and elaborates on the use of neural networks to optimise topology. Before we go into the specifics of our approach, the study explains why a similar strategy is needed for photovoltaic (PV) systems [12, 13].

In this paper, we develop a mechanism that enables topology reconfiguration or optimization of photovoltaic array or PV array using a machine learning-assisted techniques. The study takes into concern several topologies that includes series parallel topology, parallel topology, bridge link topology, honeycomb topology, and total cross tied. The strategy for topology reconfiguration using artificial neural network enables optimal working conditions for the PV arrays.

The main contribution of the paper involves the following:

(i) The study takes into concern several topologies that includes series parallel topology, parallel topology, bridge link topology, honeycomb topology, and total cross tied

(ii) The strategy for topology reconfiguration using artificial neural network enables optimal working conditions for the PV arrays

2. Proposed Method

Many modern NN structures and successful applications can be ascribed to the recent rise in ML methods [16]. Learning sophisticated nonlinear mappings between input and output, learning discriminative data representations, and creating generic end-to-end systems are some of the primary advantages of employing neural networks. A model capable of learning diverse irradiance profiles includes partial shading and optimal configuration prediction and automatic reconfiguration of array into topologies.

To maximise output power, the ML model can reliably categorise an arbitrary partial shade irradiance profile once it has been trained on a considerable amount of training data. A machine learning system that helps to map irradiances to the ideal reconfiguration technique is the result of using an ML model for this application. As a result, the study makes use of the data from each and every PV panel. The irradiance feature of PV array on each panel is used to

train the NN method described in the next sections. For the NN to achieve its maximum output, a PV array system must be configured in a specific way. These labels serve as a guide for optimising NN weights.

Using NNs to achieve topology reconfiguration is discussed in length in this portion of the study. Before moving on to describe how to build a neural network model, the paper first explains how to create labelled datasets. For all of our testing, we use a 3×4 PV array. It is possible to extend our approach to work with additional types of array structures by simply scaling up our current implementation.

In Figure 1, the panels with the topology switching include series parallel topology, parallel topology, bridge link topology, honeycomb topology, and total cross tied. These topologies are provided with optimal solution from the trained neural network to reconfigure itself for optimal operation purposes. The classifier is trained with the trained data via features obtained from the panels as inputs for the topologies, and these inputs are the best solutions.

The binary mapping algorithm shown in Figure 1 was used to create synthetic irradiance values for each panel of the 3×4 array in this study. There were two 12 D-4096 irradiance profiles formed when 0 is assigned to an unshaded panel and 1 is assigned to a shaded panel in the experiment. According to the irradiance data connected with the binary integers, the following uniform distribution may be found in equations (1) and (2):

$$0 \longrightarrow \text{irr} \sim U[\alpha, 1000], \tag{1}$$

$$1 \longrightarrow \text{irr} \sim U[50, \alpha]. \tag{2}$$

In this case, the threshold used to determine whether a panel is shaded ($\alpha = 584\,\text{W/m}^2$) is indicated [4]. For a specific binary assignment, all of the panels receive the same irradiance levels, as shown.

For a wide range of partial shading irradiance profiles, the study sampled the uniform distribution for randomly chosen binary assignments and generated more than 14,000 cases. Topology reconfiguration is treated as a learning task that necessitates the use of a labelled dataset (X, y), where X represents the irradiance profile instances in dimensions $(m \times n)$, where $m = 14{,}000$ represents the total number of irradiance profile instances, $n = 12$ represents the total number of PV panels in the array, and y is the label vector that goes along with it. There are 12 irradiance features for each of the 3×4 PV panels. Therefore,

$$y_i = \text{argmax}_i P_i, \tag{3}$$

where P is the global maximum power points for all the topologies.

2.1. Neural Network Optimization. Machine learning approaches use neural networks. Like biological brain networks, they are composed of nodes and connections. There are countless numbers of neuronal connections. Neural networks like the one shown in Figure 1 are an excellent illustration of this. Neurons are shown by the white circles, and

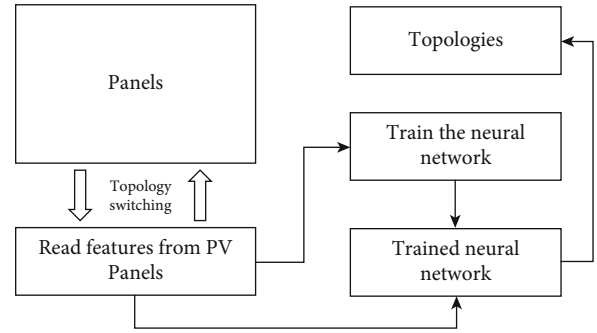

Figure 1: Proposed algorithm.

the arrows show the connections between them. Because the links are directed, arrows are used to symbolise them in the study. The neural network will be explained in this section of the study.

To begin with, researchers need to understand what a neuron is. Inputs, thresholds, and outputs are all defined in biology. The neuron is triggered, and a signal is sent to the output if the input voltage exceeds the threshold. One thing to keep in mind is that even if the neuron has multiple inputs, there is only one signal output from it. Neuron models in machine learning are remarkably similar to those found in biology. The inputs and outputs are also included. Even though there are numerous neurons connecting to the neuron output, the output values are the same. There are, of course, certain differences between the two. The neuron in machine learning uses a function instead of a threshold to convert inputs to outputs. The activation function is available in a variety of ways. It is frequently used as the sigmoid function in research $\sigma(x)$.

$$\sigma(x) = \frac{1}{1 + e^{-x}}. \tag{4}$$

Thresholding in this paper is achieved using a fitness function named sigmoid function that resembles step function. The output of sigmoid function is close to 1 when x is a big positive value. It is impossible to get an output larger than zero when x is 0. The two things are also different in terms of how much they weigh. The weights indicate how much a neuron is affected by a certain stimulus. In other words, the research will not just activate every input. The input value of the activation function is equal to the sum of its inputs, multiplied by a linear formula. The following is a mathematical representation:

$$\sigma(w_1 x_1 + w_2 x_2 + \cdots + w_N x_N), \tag{5}$$

where N is the total inputs, w_i is the weights of x_i, and $\sigma(x)$ is the activation function.

Using only one input and varying the weight, researchers were able to observe the effect of different weightings on the final output. In this example, it is clear that 0 can be used as a threshold to assess if the output is close to 0 or close to 1. A bias is added to the study in order to shift the sigmoid function in this scenario. As a result, the new relationship is as

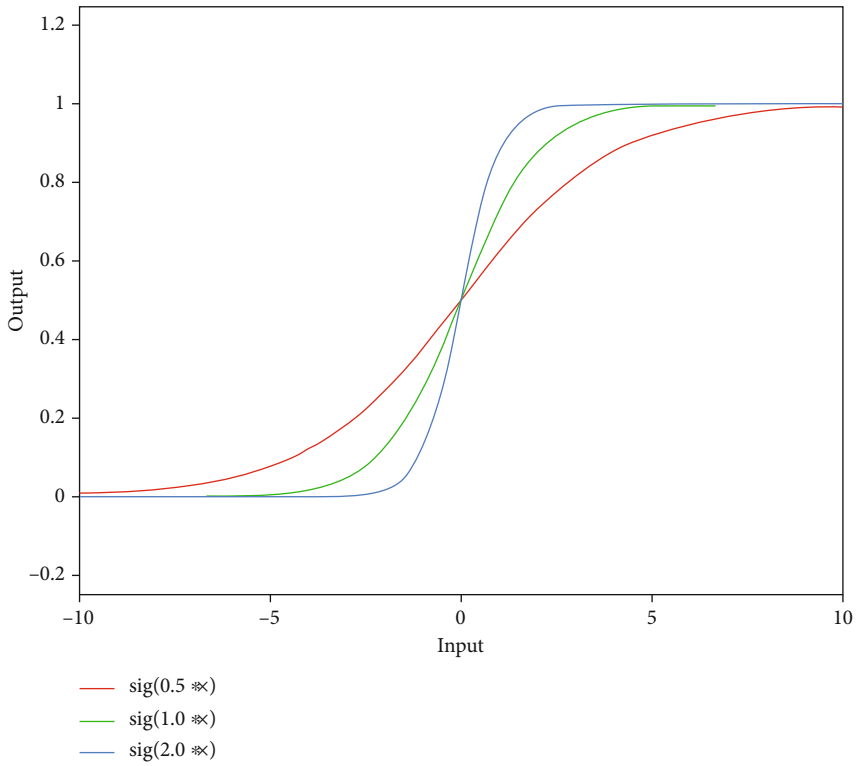

Figure 2: The sigmoid function result with various input weights without bias.

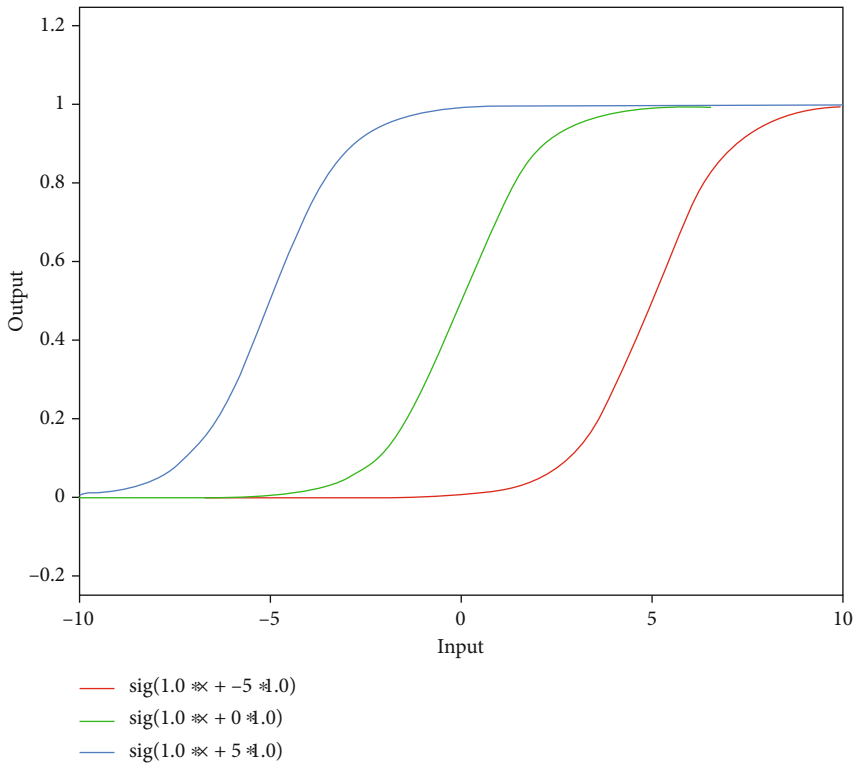

Figure 3: The sigmoid function result with various input weights with bias.

Table 1: Accuracy.

Accuracy	KNN	NB	SVM	ANN
Series parallel	0.9296	0.9421	0.9443	0.9569
Parallel	0.9294	0.9420	0.9436	0.9568
Bridge link	0.9285	0.9412	0.9436	0.9568
Honeycomb	0.9284	0.9409	0.9429	0.9566
Total cross tied	0.9282	0.9337	0.9428	0.9564

Table 2: Precision.

Precision	KNN	NB	SVM	ANN
Series parallel	0.7771	0.8725	0.8731	0.8941
Parallel	0.7703	0.8590	0.8628	0.8920
Bridge link	0.7595	0.8586	0.8628	0.8870
Honeycomb	0.7543	0.8392	0.8417	0.8862
Total cross tied	0.7530	0.8380	0.8415	0.8711

Table 3: Recall.

Recall	KNN	NB	SVM	ANN
Series parallel	0.7843	0.7834	0.8390	0.9438
Parallel	0.8266	0.8300	0.8405	0.9443
Bridge link	0.8270	0.8398	0.8407	0.9536
Honeycomb	0.8609	0.8597	0.8520	0.9558
Total cross tied	0.8648	0.8693	0.9061	0.9564

Table 4: f-measure.

f-measure	KNN	NB	SVM	ANN
Series parallel	0.8291	0.9545	0.9012	0.9412
Parallel	0.7346	0.9517	0.8938	0.9346
Bridge link	0.7078	0.9459	0.8925	0.9328
Honeycomb	0.6801	0.9349	0.8844	0.9318
Total cross tied	0.6663	0.8686	0.8844	0.8967

Table 5: MAPE.

MAPE	KNN	NB	SVM	ANN
Series parallel	0.1878	0.0857	0.0137	0.0031
Parallel	0.1936	0.1803	0.0210	0.0020
Bridge link	0.2194	0.2070	0.0223	0.0019
Honeycomb	0.2628	0.2486	0.0462	0.0030
Total cross tied	0.2334	0.2347	0.0409	0.0030

follows:

$$\sigma(\theta + w_1x_1 + w_2x_2 + \cdots + w_Nx_N), \tag{6}$$

where θ is the bias and the other notations are the same as before.

$\theta, w_1, \cdots, w_n$ is the parameter.

It appears that neural networks exist when several neurons are connected together in a single experiment. Many neurons make up the coloured rectangles, which the study calls rectangle layers. One or more neurons can be found in the layer, but these neurons will not be connected. For the purpose of reconfiguring the network architecture, we provide a six-layered feedforward ANN model with completely linked nodes. These parameters were discovered through a hyperparameter search with the purpose of increasing overall accuracy. Each panel irradiance is represented by an n-dimensional feature vector ($n = 12$) that is fed into the neural network. Figures 2 and 3 display the sigmoid function result with various input weights without bias and with bias.

3. Results and Discussions

Simulink model was used to acquire simulated data for the generation of maximum power points (MPPs). For the Simulink model, Sandia performance model for PV modules was used. There are several topologies available in MATLAB for setting up parameters for the Sandia model, including short-circuit current (I_{SC}), open circuit voltage (V_{OC}), irradiance, and temperature over various topologies like series parallel, parallel, honeycomb, bridge link, and total cross tied. Using the Simulink model, a single PV module may be generated.

Class-wise performance scores provided by the confusion matrix are used to gauge how well NN classifies the test dataset. Generalizability is demonstrated by the fact that more cases are correctly classified than are incorrectly labelled. Then, we ran the algorithm on 10 distinct test splits and found that the average test accuracy was 95%. These methods can simply be incorporated into cyberphysical solar monitoring systems as indicated in the introduction.

Table 1 shows the results of accuracy of predicting the topology configuration of various topologies like series parallel, parallel, honeycomb, bridge link, and total cross tied associated with I_{SC} and V_{OC}, irradiance, and temperature. The results of simulation shows that the proposed ANN achieves higher rate of classification accuracy than the other existing support vector machine (SVM), Naïve Bayes (NB), and k-nearest neighbor (K-NN).

Table 2 shows the results of precision of predicting the topology configuration of various topologies like series parallel, parallel, honeycomb, bridge link, and total cross tied associated with I_{SC} and V_{OC}, irradiance, and temperature. The results of simulation shows that the proposed ANN achieves higher rate of precision than the other existing SVM, NB, and K-NN.

Recall is indeed a criterion of how well our model identifies true positives. Table 3 shows the results of recall of predicting the topology configuration of various topologies like series parallel, parallel, honeycomb, bridge link, and total cross tied associated with I_{SC} and V_{OC}, irradiance, and temperature. The results of simulation shows that the proposed ANN achieves higher rate of recall than the other existing SVM, NB, and K-NN.

Table 4 shows the results of f-measure of predicting the topology configuration of various topologies like series parallel, parallel, honeycomb, bridge link, and total cross tied

associated with I_{SC} and V_{OC}, irradiance, and temperature. The results of simulation shows that the proposed ANN achieves higher rate of f-measure than the other existing SVM, NB, and K-NN.

Table 5 shows the results of MAPE of predicting the topology configuration of various topologies like series parallel, parallel, honeycomb, bridge link, and total cross tied associated with I_{SC} and V_{OC}, irradiance, and temperature. The results of simulation shows that the proposed ANN achieves reduced mean of the absolute percentage errors than the other existing SVM, NB, and K-NN.

4. Conclusions

In this paper, a topology reconfiguration strategy for PV arrays using ANNs is proposed. Using such an approach, we achieve a high test accuracy under ideal conditions. The algorithm can be easily integrated into any cyberphysical system with switching capabilities on every panel. The topologies including series parallel topology, parallel topology, bridge link topology, honeycomb topology, and total cross tied. The strategy for topology reconfiguration using artificial neural network enables optimal working conditions for the PV arrays. The results of simulation show that the proposed mechanism achieves higher degree of accuracy (98%) in finding the optimal topologies to deploy the PV panels under standard conditions. In the future, the method should focus on considering minimal cost consideration while reconfiguring the topology of the panels.

Data Availability

The data used to support the findings of this study are included within the article. Further data or information is available from the corresponding author upon request.

Conflicts of Interest

The authors declare that there is no conflict of interest regarding the publication of this paper.

Acknowledgments

The authors thank the Ambo University, Ethiopia, for providing help during the research and preparation of the manuscript.

References

[1] Z. A. Kudyshev, A. V. Kildishev, V. M. Shalaev, and A. Boltasseva, "Machine-learning-assisted topology optimization for highly efficient thermal emitter design," in *CLEO: QELS_Fundamental Science (pp. FTh3C-2)*, Optical Society of America, 2019.

[2] S. Rao, S. Katoch, V. Narayanaswamy et al., "Machine learning for solar array monitoring, optimization, and control," *Synthesis Lectures on Power Electronics*, vol. 7, no. 1, pp. 1–91, 2020.

[3] S. Rao, A. Spanias, and C. Tepedelenlioglu, "Solar Array Fault Detection Using Neural Networks," in *2019 IEEE International Conference on Industrial Cyber Physical Systems (ICPS)*, pp. 196–200, Taipei, Taiwan, May 2019.

[4] Z. A. Kudyshev, S. Bogdanov, A. V. Kildishev, A. Boltasseva, and V. M. Shalaev, "Artificial-intelligence-assisted photonics (conference presentation)," in *Metamaterials, Metadevices, and Metasystems 2019*, vol. 11080, International Society for Optics and Photonics, 2019.

[5] S. Yuvaraja, G. Arunkumar, B. V. Sai, and P. R. V. Dhinakaran, "Design and development of a compliant clutch fork using topology optimization," *International Journal of Innovative Technology and Exploring Engineering*, vol. 8, no. 11, 2019.

[6] C. Kalogerakis, E. Koutroulis, and M. G. Lagoudakis, "Global MPPT based on machine-learning for PV arrays operating under partial shading conditions," *Applied Sciences*, vol. 10, no. 2, p. 700, 2020.

[7] Z. A. Kudyshev, A. V. Kildishev, V. M. Shalaev, and A. Boltasseva, "Machine-learning-assisted metasurface design for high-efficiency thermal emitter optimization," *Applied Physics Reviews*, vol. 7, no. 2, article 021407, 2020.

[8] J. Rade, A. Balu, E. Herron et al., "Algorithmically-consistent deep learning frameworks for structural topology optimization," *Engineering Applications of Artificial Intelligence*, vol. 106, article 104483, 2021.

[9] S. Preda, S. V. Oprea, A. Bâra, and A. Belciu (Velicanu), "PV forecasting using support vector machine learning in a big data analytics context," *Symmetry*, vol. 10, no. 12, p. 748, 2018.

[10] M. S. Nkambule, A. N. Hasan, A. Ali, J. Hong, and Z. W. Geem, "Comprehensive evaluation of machine learning MPPT algorithms for a PV system under different weather conditions," *Journal of Electrical Engineering & Technology*, vol. 16, no. 1, pp. 411–427, 2021.

[11] W. Ahmed, H. Ansari, B. Khan et al., "Machine learning based energy management model for smart grid and renewable energy districts," *IEEE Access*, vol. 8, pp. 185059–185078, 2020.

[12] Y. Liu, K. Ding, J. Zhang et al., "Fault diagnosis approach for photovoltaic array based on the stacked auto-encoder and clustering with IV curves," *Energy Conversion and Management*, vol. 245, article 114603, 2021.

[13] A. Eskandari, J. Milimonfared, M. Aghaei, and A. H. Reinders, "Autonomous monitoring of line-to-line faults in photovoltaic systems by feature selection and parameter optimization of support vector machine using genetic algorithms," *Applied Sciences*, vol. 10, no. 16, p. 5527, 2020.

[14] G. Muniraju, S. Rao, S. Katoch et al., "A cyber-physical photovoltaic array monitoring and control system," in *Cyber Warfare and Terrorism: Concepts, Methodologies, Tools, and Applications*, pp. 786–807, IGI Global, 2020.

[15] Y. Zhou, S. Zheng, and G. Zhang, "Machine learning-based optimal design of a phase change material integrated renewable system with on-site PV, radiative cooling and hybrid ventilations–study of modelling and application in five climatic regions," *Energy*, vol. 192, article 116608, 2020.

[16] M. Houchati, A. H. Beitelmal, and M. Khraisheh, "Predictive modeling for rooftop solar energy throughput: a machine learning-based optimization for building energy demand scheduling," *Journal of Energy Resources Technology*, vol. 144, no. 1, 2022.

[17] Z. Chen, F. Han, L. Wu et al., "Random forest based intelligent fault diagnosis for PV arrays using array voltage and string currents," *Energy Conversion and Management*, vol. 178, pp. 250–264, 2018.

[18] N. Yuvaraj, K. Praghash, R. A. Raja, and T. Karthikeyan, "An investigation of garbage disposal electric vehicles (GDEVs) integrated with deep neural networking (DNN) and intelligent transportation system (ITS) in smart city management system (SCMS)," *Wireless Personal Communications*, vol. 123, pp. 1733–1752, 2021.

[19] Y. Natarajan, S. Kannan, C. Selvaraj, and S. N. Mohanty, "Forecasting energy generation in large photovoltaic plants using radial belief neural network," *Sustainable Computing: Informatics and Systems*, vol. 31, article 100578, 2021.

[20] Y. Du, K. Yan, Z. Ren, and W. Xiao, "Designing localized MPPT for PV systems using fuzzy-weighted extreme learning machine," *Energies*, vol. 11, no. 10, p. 2615, 2018.

Hindawi
International Journal of Photoenergy
Volume 2022, Article ID 5959443, 8 pages
https://doi.org/10.1155/2022/5959443

Research Article

Battery Energy Forecasting in Electric Vehicle Using Deep Residual Neural Network

Mohamad Reda A. Refaai,[1] Jyothilal Nayak Bharothu,[2] T. V. V. Pavan Kumar,[3] Chodagam Srinivas,[4] M. Sudhakar,[5] and Anirudh Bhowmick[6]

[1]*Department of Mechanical Engineering, College of Engineering, Prince Sattam Bin Abdulaziz University, Alkharj 16273, Saudi Arabia*
[2]*Department of Electrical & Electronics Engineering, AP IIIT-NUZVID, Rajiv Gandhi University of Knowledge Technologies, Nuzvid, 521202 Andhra Pradesh, India*
[3]*Electrical and Electronics Engineering, KG Reddy College of Engineering and Technology, Hyderabad 501504, India*
[4]*Department of EEE, Sri Vasavi Engineering College, Tadepalligudem, 534101 Andhra Pradesh, India*
[5]*Department of Mechanical Engineering, Sri Sairam Engineering College, Chennai-600044, Tamilnadu, India*
[6]*Faculty of Meteorology and Hydrology, Arba Minch Water Technology Institute, Arba Minch University, Ethiopia*

Correspondence should be addressed to Anirudh Bhowmick; anirudh.bhowmick@amu.edu.et

Received 10 February 2022; Revised 27 February 2022; Accepted 1 March 2022; Published 6 May 2022

Academic Editor: V. Mohanavel

Copyright © 2022 Mohamad Reda A. Refaai et al. This is an open access article distributed under the Creative Commons Attribution License, which permits unrestricted use, distribution, and reproduction in any medium, provided the original work is properly cited.

In the recent decade, it is possible to use electric vehicles in a safe, cost-effective, and environmentally friendly manner, but only if accurate and trustworthy state parameter predictions are produced prior to their disposal. The state of health (SOH) of the lithium-ion batteries (LIBs) must be precisely forecasted in order to ensure that the LIB can operate safely. The inability of physical SOH estimators to cope with the dynamic character of SOH when operating in a highly nonlinear environment is a common limitation when operating in nonlinear environments. Traditional SOH estimation techniques have demonstrated that they have limits that can be overcome by data-driven methods. TCN, a new machine learning technique, combines the advantages of residual neural networks (ResNet) with the computing efficiency of neural networks to produce a technique that is both efficient and effective. The results of rgw simulation show that the proposed method has reduced placement cost, and also a TCN can accurately estimate the SOH of a LIB with an MSE error of less than 1% over the LIB lifetime. The performance of an electric car battery, which are numerous and diverse, can be anticipated more precisely using this approach.

1. Introduction

The hybrid electric vehicle (HEV) is one of the most rapidly expanding means of transportation today. As a result of research into green energy and transportation systems, electric vehicles (EVs) will be widely employed throughout the world. When compared to driving a car that is powered by gasoline, driving a battery-powered vehicle produces no hazardous exhaust fumes as a result of its operation. This is why studies that develop effective capacity estimation algorithms [1, 2] are critical to the advancement of EV battery life and range prediction research.

If the users are looking for things that run on batteries, rechargeable batteries are the best example of industrial manufacturing. In recent years, Li-ion batteries have gained popularity over other battery chemistries due to their high energy density and other advantages [3, 4]. Although Li-ion batteries have some intrinsic limitations, such as a limited temperature and voltage operating window and the need to fine-tune the accuracy of capacity estimation, they are no more restrictive than any other cell type in this regard. The performance of lithium-ion batteries is also influenced by a variety of external and internal factors [5]. To put it in another way, all of the factors described above

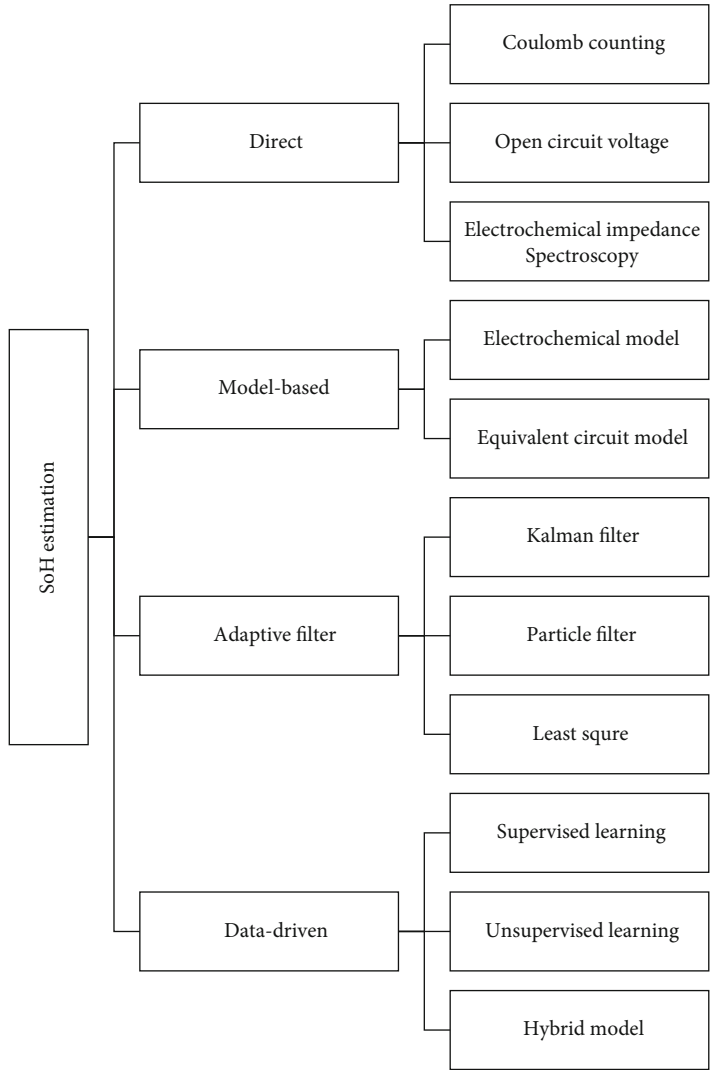

Figure 1: SoH estimation.

have an impact on the stability of an EV battery pack and the estimation of its range. Consequently, it is vital to have an accurate methodology for evaluating the capacity of an electric vehicle battery capacity [6]. Figure 1 shows the SoH estimation for the proposed mechanism.

If it is possible to precisely assess a used battery state of health (SOH) and remaining useful life (RUL) with the least amount of testing possible, given a specific manufacturer and model, it would have huge economic and environmental benefits. Battery management system (BMS) software has the potential to quadruple the cycle life of lithium-ion batteries [7], which implies that fewer lithium-ion batteries (LIB) and that recycles and reuses effectively. Furthermore, because some rechargeable batteries and this can be extensively used in electric vehicles [8], the resale value of older electric vehicles may be more accurately assessed. Consider the scenario of getting a rechargeable battery with increased charge-discharge cycles already in it [9]. A second charge-discharge cycle can be used to collect more I-V data in order to determine the SOH of the battery [10, 11].

The end-of-life (EoL) of a fresh battery can be represented by the integer end-of-life (EoL), in which case

$$\text{EoL} = s + a + \text{RUL}, \tag{1}$$

where

s - ground truth and

a - maximum cycle life.

The use of Residual Neural Network (ResNet) based algorithms in dynamical systems, such as the Kalman filter, is challenging the traditional use of limited-memory calculations in dynamical systems. However, while training a DNN can be computationally costly, modern hardware makes it possible to operate a ResNet in real time [12–15].

The study tests the ResNet to find the RUL with various acquisition cycles in order to determine how well they perform [16]. Other than residual life, we can assign DNNs the task of estimating their own ages and, using analysis tools, evaluate the value of various features in lowering root mean square error, as well as the value of different features

in lowering root mean square error (RMSE) [17]. This is a test to see how well the machine predictions match up with human expert intuition and intuition based on the obtained I(t)-V(t)-T(t) cycle time sequence data [18].

According to the manufacturer, the performance of lithium-ion batteries degrades over time (calendric ageing) and with use [19]. A battery's overall capacity and internal series resistance, which are two of its most distinctive qualities, may be determined by measuring their combined capacity [20–23]. Internal resistance is increasing as a result of unfavourable responses and structural deterioration, among other factors. To put it in another way, a new LIB has the capability of storing more energy and delivering more power than a previous LIB [24]. A time-integrated calculation is used to determine the capacity of the charge or discharge current. In order to determine SOH, it is necessary to first explain and demonstrate how the battery management system measures battery consumption data such as voltage, temperature, and current.

2. Related Works

Using the same regression model, [25] generated even more LIB cell data with even more sophisticated fast-charging rules in order to increase closed-loop fast-charging protocol performance. With the use of a convolutional neural network (CNN) built [12], he was able to reduce the number of charging cycles with increased accuracy.

[15] demonstrated that by using an extreme learning model, they were able to obtain higher accuracy and computational efficiency than the existing models while modelling battery temperatures under external short-circuit conditions. Researchers have developed a multistage model fusion algorithm to estimate the capacity and SOC of an electric vehicle

According to [17], the RUL of acquisition was employed as input data for the dilated CNN design. There are numerous end-to-end training approaches described in the scientific literature, each of which corresponds to a specific set of special features and a distinct set of goal values. As a result, estimating battery EOL when only one cycle is taken into consideration is challenging. When compared to a traditional strategy, the proposed last padding technique is used in the current study. In this technique, numerous groups of characteristics are associated with a single objective value, as opposed to the old strategy.

3. Proposed Method

The four primary phases of the experiment are depicted in Figure 2. The initial stage is the extraction of model parameters, which will be used as inputs to the ResNet network. Several ResNets are trained on a range of hyperparameters during the second phase of the process. Each ResNet would be validated in order to determine which model is the most effective for estimating SOC from the given training dataset.

The battery management system (BMS) is made up of electronics and embedded software that work together to deliver safe, dependable, and application-specific optimal battery system operation. When testing batteries, it is necessary to take readings of the voltage and temperature of individual cells, as well as the current flowing through the entire system. Extra measurement data, like pressure sensors or electrochemical impedance spectroscopy (EIS) readings, can be used to guarantee that a battery system performs at its peak performance level. The battery management system (BMS) is in charge of controlling the electric power contactors in the battery system, ensuring that the battery cells are not used beyond their permitted operating limits when the system is in operation.

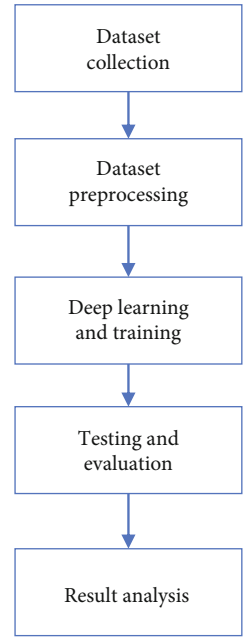

Figure 2: Proposed BMS model.

Battery models at all levels, from cells to modules and up to system models (e.g., equivalent circuit, physical, or heuristics-based models), must calculate battery state parameters, such as the aforementioned SOH, in order for a battery system to operate within an application-specific optimal operating window. This is true for all battery models, regardless of their level of performance. In order for the battery system to function properly, model computations and real-time output projections must be possible. The BMS can employ its own measurement data, as well as application logic and inputs from a higher-level control unit, to ensure safety and optimal battery utilization.

Whenever data on battery utilization is collected for research or commercial objectives, it must be made publicly available outside of the embedded system so that others can take advantage of it and learn from it. The information flow through the data pipeline is depicted in Figure 3.

The measurement data is first collected by the BMS integrated into the application. The ETL (Extract, Transform, and Load) process is used to transport and further process raw data before it is saved in a database, and it is also known as data transformation. For modelling purposes, an ETL procedure is necessary in order to make use of the logged data stream in a low-level system (such as Ethernet). It is therefore necessary to preprocess the output so that it can be used for data analysis as well as model training purposes.

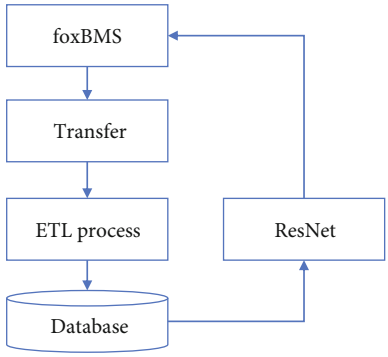

Figure 3: Data pipeline and feedback into BMS.

3.1. Data Extraction. Our battery tester consisted of two components: a continuous current source and an environmental chamber that was used to charge and discharge cells, respectively. It was decided to use a sampling rate of 0.1 Hz, and the results of each of the 40 CAP tests were stored on a host computer in a discrete manner. The charts clearly demonstrate how changing temperatures affect the behaviour of a LiFePO4 cell when performing tests, including voltage and current measurements. This demonstrates the importance of training estimation models at a variety of temperatures.

3.2. ResNet for SOC Estimation. For the purpose of discovering the answers to the study questions, the learning phase for the SOC estimate was painstakingly planned and implemented. Optimization of hyperparameter trends for a ResNet with a simple setup was the objective. As a result, it is possible to develop a SOC estimation model with the lowest possible error metrics. It was discovered that the ResNet design has a tendency to use a small number of neurons and hidden layer configurations, which reduces the demand for high-specification hardware at the time of training.

A ResNet model finds the optimal number of neurons and hidden layers, as well as the appropriate values for the other ResNet hyperparameters. ResNet models were built utilizing all possible ResNet topologies and hyperparameter settings as in Table 1. Training and cross-validation of each model were performed five times using data from six out of eight cells. In order to validate the models, we employed 2 cell data, which accounts for approximately 25% of the total amount of data collected.

3.3. Residual Neural Networks. Consider $\boldsymbol{g}(\boldsymbol{x})$ as one of the important functions that gets learned by the ResNet layers. In this study, we consider the ResNet layer with skip connections:

$$h(x) = g(x) + x, \tag{2}$$

where

$\boldsymbol{x}$ - skip connection.

It is necessary to alter the weights and bias values in order to match the identity function when there are no skip connections. In addition, because of the nonlinearity in the layers, it is even more difficult to learn the identity function from the beginning, leading to degeneration. Let see the

Table 1: ResNet hyperparameters.

Hyperparameter	Values
Hidden layers	5
Neurons	10
Learning rate	0.8
Activation method	Hyperbolic
Epochs	100

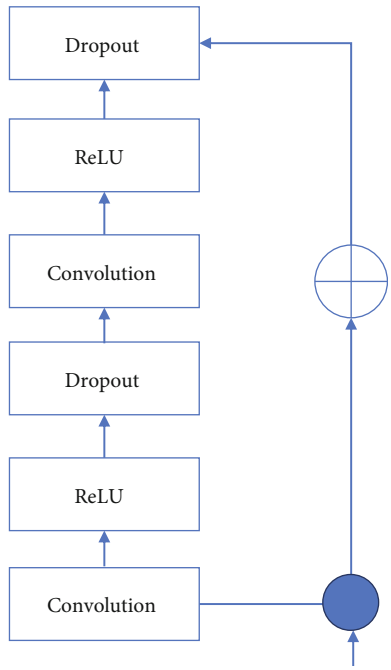

Figure 4: Residual block.

building blocks of Residual Neural Networks or ResNets, the residual blocks as in Figure 4.

The identity function can be elevated to a higher level of sophistication through the use of a skip connection. The residual block is distinguished by the following two characteristics:

(i) Alternatively, if we applied relu before adding the skip connection, all of the residues would have been either positive or zero. As a result of just learning positive identity enhancements, the learning ability has been significantly diminished

(ii) If sin (3/2) = -1, the study needs to include negative residue in our sin function, which is not the case. In contrast, the use of sigmoid has the disadvantage of only producing residues between 0 and 1, which is undesirable. Nonlinearity should be produced by combining the unconstrained response of the weight layer with the activation of the skip layer, as described above

This facilitates the model's ability to learn and adapt to new situations. We might have used a single weight layer

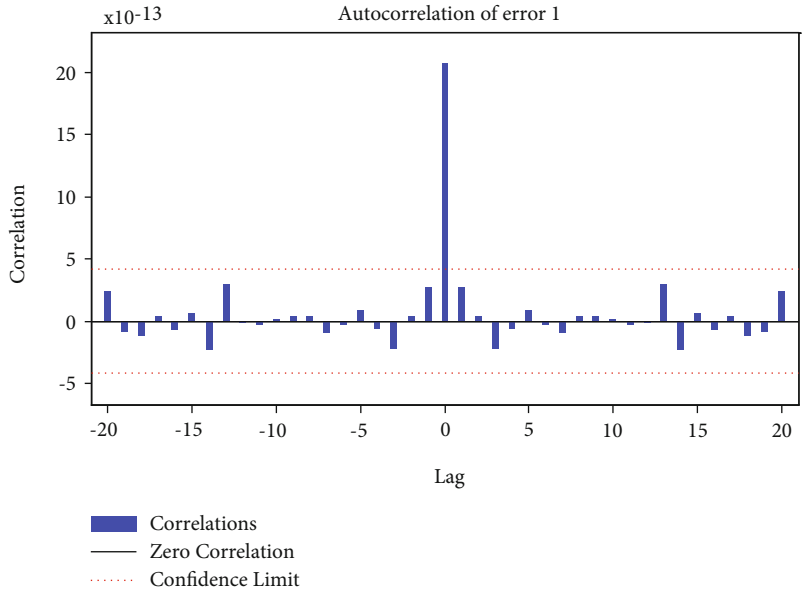

Figure 5: Autocorrelation for the error.

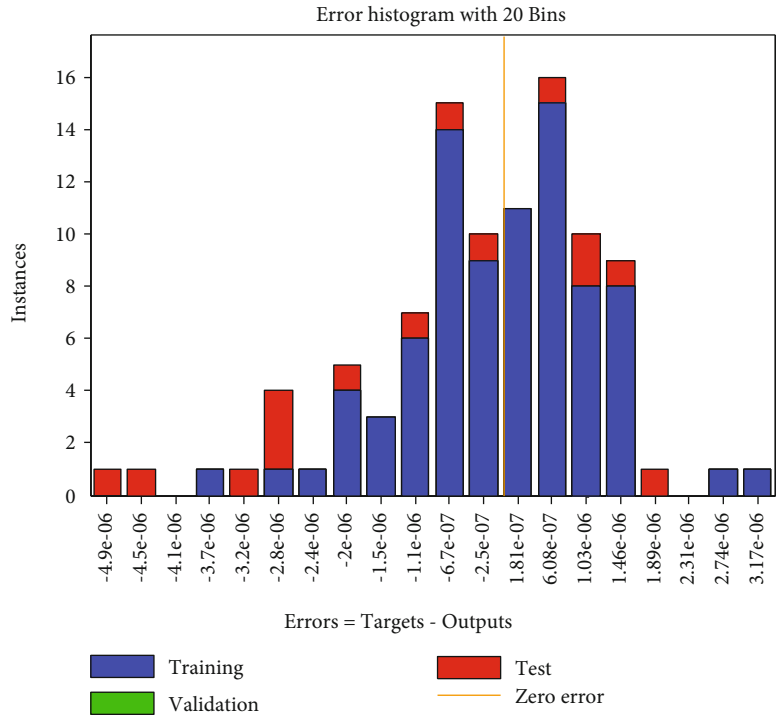

Figure 6: Error histogram.

in the residual block and then added a skip connection before the relu block to obtain a simple linear function:

$$F(x) = W(x) + x. \tag{3}$$

There is no need to include a skip connection because the weight of this is comparable to that of a single layer. We must first introduce at least one nonlinearity into the system before we can introduce a skip link. As we saw in the preceding section, there are learning residuals associated with these blocks. The performance of these blocks will not deteriorate as they are stacked higher and higher in the stack.

As previously stated, the usage of skip connections can also be beneficial in deep networks [13]. A skip connection does not accomplish anything other than provide the input. A residual block is a type of connection that can be used to create a skip connection that is meaningful as well as useful. In order to assure local LIB regeneration, a residual block, which serves as a network layer, is used.

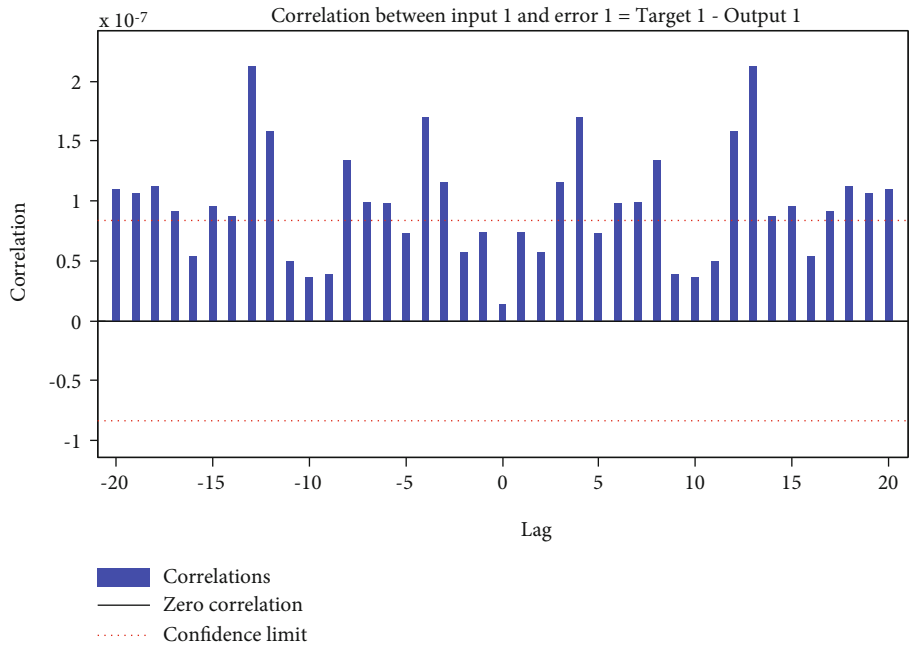

Figure 7: Correlation between input and error.

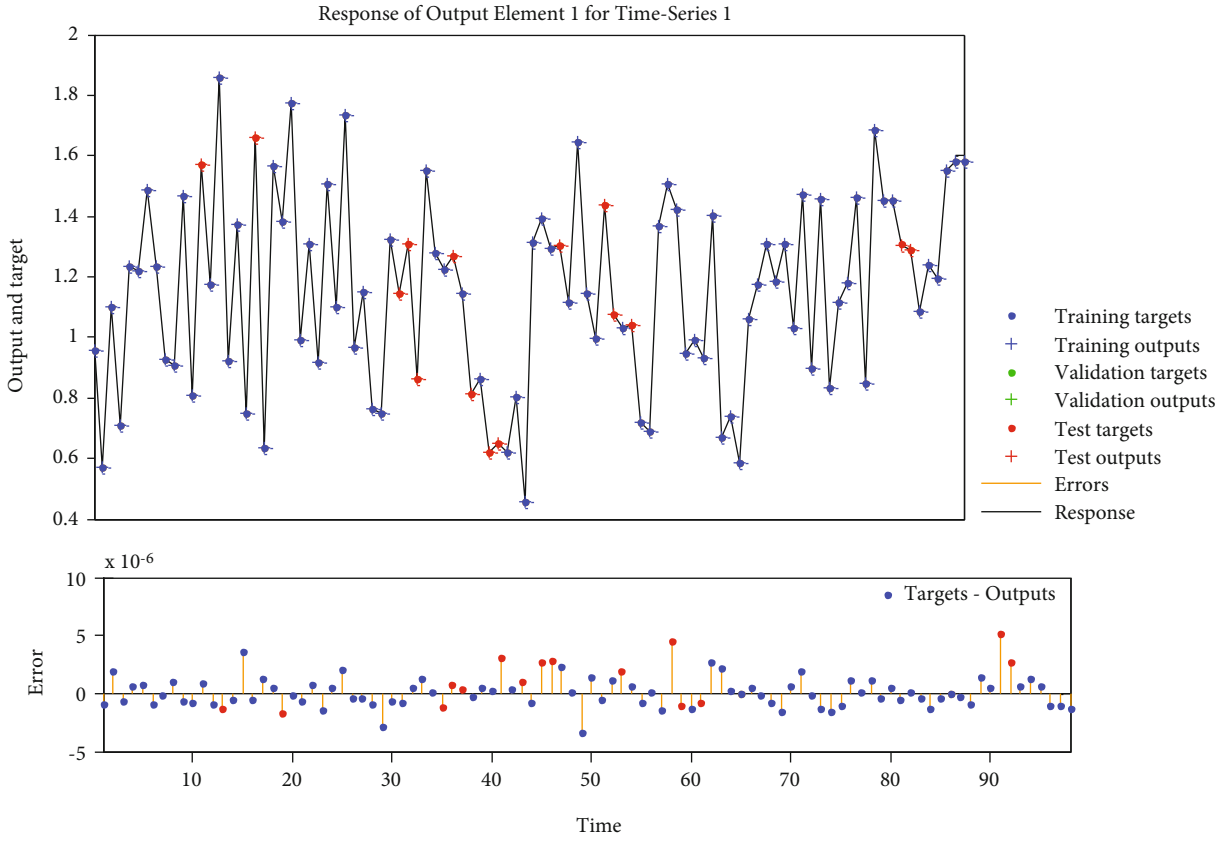

Figure 8: Output of the ResNet model.

4. Results and Discussions

It is expected that the design of our ResNet is trained with the 80% of the input datasets and then it is tested under 20% of the solar datasets. The results of the simulation are considered in terms of performance metrics to validate the efficacy of the entire model.

The performance of ResNet was evaluated by comparing the error between the real SoC and predicted SoC, where the proposed model achieves higher rate of prediction accuracy using the ResNet algorithm. Apart from their epoch counts, the top 20 models selected during the validation phase using ResNet architecture as in Figure 5. Its generalizability is proved by the learning rate of 0.8 for the top ten models, which is higher than the lower learning rates obtained using greedy search, demonstrating that the design is robust.

Additionally, this figure depicts the residual error at the end of each epoch, which is rather interesting. When the number of epochs was reduced by 40%, error metrics increased by less than 0.15 percent, indicating a slight improvement. The performance is assessed using a range of error indicators, including residual error, among others as in Figure 6. Figure 7 depicts the correlation between input and error.

As the model's ability to generalize its conclusions to new datasets increased from validation to testing, the error metric values reduced for each dataset under consideration. As shown in Figure 8, the best model does not overfit the training data and does an excellent job of generalizing to new data. When compared to existing methodologies, MAE on different test data sets ranges from 0.39 to 1.85 to 1.35, indicating that it is superior. Note that while the MAEs in this study had fewer learning epochs (85,500) than the best models, both the lowest and highest MAE is found to be lower than the MAE of other methods.

With increasing age, one capacity and, thus, one SOH diminish. The neural network employed in this study is composed of three layers, each of which has seven neurons. It is also taught using Adam optimizer, which is an adaptive learning rate optimization technique that was developed specifically for deep learning applications.

It is extremely crucial for real-world data in dynamically changing surroundings and operating settings to have the ability to adapt and learn on its own. This is something that neural networks excel at. Consequently, as a result of the TCN, a reliable SOH estimation for LIB is attainable throughout the duration of its existence. Finally, the proposed ResNets may be utilized in real-world applications to continuously update the model to deal with environmental change while increasing the accuracy of forecasts.

5. Conclusions

In this paper, it is shown that a minimal ResNet architecture with numerous configurations of simple designs is required in order to reliably predict the SOC of electric vehicle battery cells while maintaining performance metrics comparable to the current studies. To further reduce the timing and computational cost, the study enables the ResNet to undergo several epochs that reduces the risk of overfitting and has been determined to be significantly smaller than that used in earlier research, to the best of the author's ability to ascertain. The ResNet estimation models can be trained and evaluated using additional battery tests, such as high-performance computing testing at various temperatures and C-rates. Additional drive cycle data acquired from battery cells, both customized and standard, can be added at the training/testing datasets to improve the transfer ability of the ResNet estimation model used to predict the impacts of external influences on the behaviour of electric vehicle batteries. Next-generation research should concentrate on generating batteries with accurate characteristics of their performance and longevity while sacrificing the computational time reductions that would otherwise be achieved. This will be beneficial to both the short-term scheduling and the network planning processes.

Data Availability

The data used to support the findings of this study are included within the article. Further data or information is available from the corresponding author upon request.

Conflicts of Interest

The authors declare that there are no conflicts of interest regarding the publication of this paper.

Acknowledgments

The authors appreciate the support from Arba Minch University, Ethiopia, for providing help during the research and preparation of the manuscript. The authors thank for the support from Rajiv Gandhi University of Knowledge Technologies, KG Reddy College of Engineering and Technology, Sri Vasavi Engineering College for providing technical assistance to complete the work.

References

[1] S. Ansari, A. Ayob, M. S. HossainLipu, A. Hussain, and M. H. M. Saad, "Multi-channel profile based artificial neural network approach for remaining useful life prediction of electric vehicle lithium-ion batteries," *Energies*, vol. 14, no. 22, p. 7521, 2021.

[2] D. Min, Z. Song, H. Chen, T. Wang, and T. Zhang, "Genetic algorithm optimized neural network based fuel cell hybrid electric vehicle energy management strategy under start-stop condition," *Applied Energy*, vol. 306, article 118036, 2022.

[3] C. W. Hsu, R. Xiong, N. Y. Chen, J. Li, and N. T. Tsou, "Deep neural network battery life and voltage prediction by using data of one cycle only," *Applied Energy*, vol. 306, article 118134, 2022.

[4] V. Chandran, K. Patil C, A. Karthick, D. Ganeshaperumal, R. Rahim, and A. Ghosh, "State of charge estimation of lithium-ion battery for electric vehicles using machine learning algorithms," *World Electric Vehicle Journal*, vol. 12, no. 1, p. 38, 2021.

[5] S. Li, H. Zhang, H. Tan, Z. Zhong, and Z. Jiang, "An attention-based model for travel energy consumption of electric vehicle with traffic information," *Advances in Civil Engineering*, vol. 2021, Article ID 5571271, 2021.

[6] M. A. Hannan, D. N. How, M. S. Lipu et al., "Deep learning approach towards accurate state of charge estimation for

lithium-ion batteries using self-supervised transformer model," *Scientific Reports*, vol. 11, no. 1, pp. 1–13, 2021.

[7] R. Chen, C. Yang, L. Han, W. Wang, Y. Ma, and C. Xiang, "Power reserve predictive control strategy for hybrid electric vehicle using recognition-based long short-term memory network," *Journal of Power Sources*, vol. 520, article 230865, 2022.

[8] G. Cheng, X. Wang, and Y. He, "Remaining useful life and state of health prediction for lithium batteries based on empirical mode decomposition and a long and short memory neural network," *Energy*, vol. 232, article 121022, 2021.

[9] X. Wang, J. Li, B. C. Shia, Y. W. Kao, C. W. Ho, and M. C. Chen, "A novel prediction process of the remaining useful life of electric vehicle battery using real-world data," *PRO*, vol. 9, no. 12, p. 2174, 2021.

[10] S. Hespeler, D. Fuqua, and College of Business, New Mexico State University, Las Cruces, NM, USA, "Online state of charge prediction in next generation vehicle batteries using deep recurrent neural networks and continuous model size control," *Journal of Energy and Power Technology*, vol. 3, no. 1, p. 1, 2021.

[11] S. Modi, J. Bhattacharya, and P. Basak, "Convolutional neural network–bagged decision tree: a hybrid approach to reduce electric vehicle's driver's range anxiety by estimating energy consumption in real-time," *Soft Computing*, vol. 25, no. 3, pp. 2399–2416, 2021.

[12] Y. Li, K. Li, X. Liu, and L. Zhang, "Fast battery capacity estimation using convolutional neural networks," *Transactions of the Institute of Measurement and Control*, vol. 2020, p. 014233122096642, 2020.

[13] T. Zhu, R. G. Wills, R. Lot, H. Ruan, and Z. Jiang, "Adaptive energy management of a battery-supercapacitor energy storage system for electric vehicles based on flexible perception and neural network fitting," *Applied Energy*, vol. 292, article 116932, 2021.

[14] C. Chang, Q. Wang, J. Jiang, and T. Wu, "Lithium-ion battery state of health estimation using the incremental capacity and wavelet neural networks with genetic algorithm," *Journal of Energy Storage*, vol. 38, article 102570, 2021.

[15] R. Yang, R. Xiong, W. Shen, and X. Lin, "Extreme learning machine-based thermal model for lithium-ion batteries of electric vehicles under external short circuit," *Engineering*, vol. 7, no. 3, pp. 395–405, 2021.

[16] M. A. Hannan, D. N. How, M. B. Mansor, M. S. H. Lipu, P. J. Ker, and K. M. Muttaqi, "State-of-charge estimation of li-ion battery using gated recurrent unit with one-cycle learning rate policy," *IEEE Transactions on Industry Applications*, vol. 57, no. 3, pp. 2964–2971, 2021.

[17] J. Hong, D. Lee, E. R. Jeong, and Y. Yi, "Towards the swift prediction of the remaining useful life of lithium-ion batteries with end-to-end deep learning," *Applied Energy*, vol. 278, article 115646, 2020.

[18] S. S. Salunkhe, S. Pal, A. Agrawal, R. Rai, S. S. Mole, and B. M. Jos, "Energy optimization for CAN bus and media controls in electric vehicles using deep learning algorithms," *The Journal of Supercomputing*, pp. 1–16, 2022.

[19] Z. Yi, X. C. Liu, R. Wei, X. Chen, and J. Dai, "Electric vehicle charging demand forecasting using deep learning model," *Journal of Intelligent Transportation Systems*, pp. 1–14, 2021.

[20] X. Tang, J. Chen, H. Pu, T. Liu, and A. Khajepour, "Double deep reinforcement learning-based energy management for a parallel hybrid electric vehicle with engine start-stop strategy," *IEEE Transactions on Transportation Electrification*, 2021.

[21] K. Laadjal and A. J. M. Cardoso, "Estimation of lithium-ion batteries state-condition in electric vehicle applications: issues and state of the art," *Electronics*, vol. 10, no. 13, p. 1588, 2021.

[22] L. Yao, S. Xu, A. Tang et al., "A review of lithium-ion battery state of health estimation and prediction methods," *World Electric Vehicle Journal*, vol. 12, no. 3, p. 113, 2021.

[23] H. Abdelaty, A. Al-Obaidi, M. Mohamed, and H. E. Farag, "Machine learning prediction models for battery-electric bus energy consumption in transit," *Transportation Research Part D: Transport and Environment*, vol. 96, article 102868, 2021.

[24] N. Gan, Z. Sun, Z. Zhang, S. Xu, P. Liu, and Z. Qin, "Data-driven fault diagnosis of lithium-ion battery overdischarge in electric vehicles," *IEEE Transactions on Power Electronics*, vol. 37, no. 4, pp. 4575–4588, 2022.

[25] P. M. Attia, A. Grover, N. Jin et al., "Closed-loop optimization of fast-charging protocols for batteries with machine learning," *Nature*, vol. 578, no. 7795, pp. 397–402, 2020.

Hindawi
International Journal of Photoenergy
Volume 2022, Article ID 6428740, 10 pages
https://doi.org/10.1155/2022/6428740

Research Article

Assessment of Bioprocess Development-Based Modeling and Simulation in a Sustainable Environment

R. Satish Kumar,[1] B. Nageswara Rao,[2] M. Prameela,[3] S. Peniel Pauldoss,[4] Amol L. Mangrulkar,[5] Saleh H. Salmen,[6] Sami Al Obaid,[6] S. Sappireamaniyan,[7] and Kibrom Menasbo Hadish[8]

[1]*Namakkal-Department of Medical Electronics, Sengunthar College of Engineering, 637205 Tamilnadu, India*
[2]*Department of Mechanical Engineering, VFSTR Deemed to Be University, Andhra Pradesh, India*
[3]*Department of Electrical and Electronics Engineering, B V Raju Institute of Technology, Narasapur, Telangana, India*
[4]*Department of Mechanical Engineering, Brilliant Group of Technical Institutions, Hyderabad, India*
[5]*Department of Mechanical Engineering, Rajiv Gandhi Institute of Technology, Mumbai, India*
[6]*Department of Botany and Microbiology, College of Science, King Saud University, PO Box-2455, Riyadh-11451, Saudi Arabia*
[7]*Department of Bioenvironmental Energy, College of Natural Resources and Life Science, Pusan National University, Miryang-Si, 50463, Republic of Korea*
[8]*Department of Mechanical Engineering, Faculty of Mechanical Engineering, Arba Minch Institute of Technology (AMIT), Arba Minch University, Ethiopia*

Correspondence should be addressed to Kibrom Menasbo Hadish; kibrom.menasbo@amu.edu.et

Received 8 January 2022; Accepted 26 February 2022; Published 5 May 2022

Academic Editor: V. Mohanavel

Copyright © 2022 R. Satish Kumar et al. This is an open access article distributed under the Creative Commons Attribution License, which permits unrestricted use, distribution, and reproduction in any medium, provided the original work is properly cited.

Modeling and simulation help us gain a better knowledge of chemical systems and develop obstacles and improvement opportunities. In the initial stages of systems integration, the time and money constraints prevent more precise estimates, basic simulation software that provides a reasonable approximation of energy and material usage and procedure exhaust is typically useful. Every next era of technicians will confront a new set of difficulties, including developing new biochemical reactions with high sensitivity and selectivity for pharmaceutical industries and manufacturing lesser chemicals from biomass resources. This job will need the use of operational process systems integration development tools. The existing toolsneed improvement so that they could be used to examine operations against sustainability principles as well as profitability. Eventually, characteristic models for substances that aren't presently in collections will be necessary. In the field of integrated bioprocesses, there will undoubtedly be a plethora of new prospects for process systems engineering. The financial and environmental evaluations were based on a generic methodology for collecting first-estimate stock levels. The time it takes to do the evaluation may be cut in half, and a wider number of choices could be explored. A valuable commitment to sustainability bioprocess modeling and evaluation can be made by using a first-approximation numerical method as the basis for financial and environmental evaluations.

1. Introduction

Renewable resources such as grain production and accompanying leftovers, wood residues, coastal biomass combustion, industrial engineering creeks, and food system side creeks are all used in the manufacturing of bio-based chemicals and polymers. To evaluate the fermentation process synthesis of bio-based chemicals and polymers within a biopolymer matrix, measure feedstock supply as well as the spatial location of important IFSS feedstocks [1]. Traditional fermentation technologies are now widely acknowledged to be less expensive than hydrocarbon processes. As a result, biomass processing should be optimized in comparison to applicable comparisons (e.g., comparable hydrocarbon

byproducts), taking into account the assessment of the innovative, environmental, and social aspects. While the original upstream to downstream relied solely on fungus, germs, and microbes, the inclusion of enzymes and eukaryotic cells eventually expanded industrial output. Other biocatalysts, such as the cells of the insect and plant, as well as transgenic plants and animals, have been introduced to the technology platform, but have yet to be deployed in manufacturing. Simultaneously, the brewing process and downstream methods were improved, and the technology and quality of bioprocess design increased dramatically.

These emphasize the use of abundant renewable inputs in conjunction with sustainable electric power, particularly solar or wind, as an electrostatic field [2]. It is expected that, especially in cities, such electricity will become the main kind of energy, allowing geographically spread biomass should be used more extensively in a descending strategy to provide food, feed, and the essential carbon dioxide concentration for pharmaceuticals while using less energy. The indirect or direct connection of the different sources of carbon and energy is possible. Researchers need to create life-changing, life cycle, systematic problem-solving architectures, tools, and strategies to endorse strategy and regulatory preparation and also company decision - making process in efforts to progress the inter-/cross-/trans-disciplinary conceptions of environmental protection, ecological/evolutionary economics, physical and biological economic, sustainability engineering and science in having to confront advancement issues. Different sustainability-related research has emphasized the importance of establishing these integrated tools and methodologies to support policies, legislation, and practices for environmental sustainability at both the regional and international levels [3]. The bioindustries have grown to a critical level, and they rely on a comprehensive understanding of genomic, proteomic, informatics, genetic transformation, and molecular breeding [4]. Bioprocesses are used in a variety of industries nowadays, as shown in Table 1shows Process Industry vs Microorganisms.

Biorefinery technology should be used to make valuation bio-based goods from different renewable energy sources, including agricultural wastes, forest resources, algal feedstock, and IFSS. Cellulose and lignin biomass is defined as the first two residues. Yellow biomass, which refers to wastes resulting from any growing crops, is one of the biomass feedstocks that is primarily planted for organic material, methane, or other biofuels generation (e.g., corn stover, wheat straw) [5]. Crop residue-related factors are closely linked to the development of industrial units in the best location. Biofuels have a good outlook since they can reduce fossil energy reliance while also reducing environmental consequences and chemical pollutants resulting from reduced utilization of such supplies. There are a few critical characteristics of biofuels that are strongly linked to the selection of biomass resources and the development of biorefinery processes and technologies.

Change is an inherent aspect of natural systems, according to these definitions. Sustainability must be an element of such transition, to induce reasonable human progress rather than protection. The three major aspects of sustainable development, according to the WCED (1987), are the so-called "triple bottom line." These pillars serve as a framework for focusing efforts toward achieving the goal of "responsible human development." Economic feasibility, environmental management systems, and community involvement are the three pillars indicated in Figure 1 Major Aspects of Sustainability Development.

The three aspects of sustainability have frequently been depicted as a mutually beneficial relationship. These parameters can be more precisely described in the context of sustainable process development and design (a central issue of the thesis) [6]. The application of scientific methods to optimize the use of resources and energy localized to the manufacturing process is at the heart of strong sustainability concerns.

As a result, selecting operating pathways for a biorefinery layout becomes a critical issue that must take into account process flow sustainability. As a result, there is genuine interest in developing biorefinery syntheses and enhancement simulations to assist decision-makers in the implementation of construction projects. The primary benefit of using biofuels is that they are more environmentally friendly than traditional fuels (gasoline) throughout their complete lifecycle (resource creation, resource exploitation, product manufacture, and product consumption stages) [7]. The pollutants from farming activities and planting are generally removed or decreased in cellulosic biofuels, especially those made from agro-industrial residues, resulting in a lower ecological footprint than the first decade of biofuels.

Membrane-based, gas-liquid equilibrium and liquid-liquid state of balance are some of the separating concepts used to help with product separation. This research looked into the impact on the environment of biodiesel production, a more appealing gasoline alternative than bioethanol. The need for a pre-concentrate phase before the process of distillation is more crucial for the butanol-water mixture than with the ethanol-water mixture, even though butanol and water form an azeotrope mixture at low butanol concentrations, and the eventual results azeotrope combination has much different boiling points than the ethanol-water azeotrope mixture [8]. Over the next few decades, the use of bioprocesses in various sectors will skyrocket. Bioprocesses could also be used in industries in which they are not currently utilized or where mainly lab-scale procedures are being explored, such as the development of novel substances with new qualities that mimic natural materials. The confluence of biotech, nanomaterials, and information and technology is predicted to result in a significant rate of advancement and expansion. The role of information technology has indeed improved random drug testing and manufacturing, as well as our knowledge of biological systems. It could also lead to bio-chips replacing silicon-based processors in computers.

Sustainable chemical compound manufacturing necessitates a renewable source of carbon, as well as a renewable source of energy if the carbon dioxide is insufficiently energetic. As seen in Table 1, there are several phases of biotechnological processes. The benefits and drawbacks of the early generations are well-known.

Table 1: Process Industry vs Microorganisms.

Organization	Complexity of downstream	Scale	Byproducts	Biocatalyst	Market share biotech
Elementary chemical	Super low	Large	Small organic molecules	Enzymes/micro organic	Super low
Fine chemical	Average	Average	Small organic molecules	Enzymes/micro organic	Low
Cleansing agent	Low	Large	Enzymes	Micro organic	Average
Medical care/ cosmetics	Average - high	Small – Average	Small molecules and proteins	Mammalian cells/enzymes/micro organic	Average
Conventional biopharma	Average - high	Average	Small organic molecules	Mammalian cells/micro organic	Low- average
Food and feeds	Average	Super large	Proteins and others	Enzymes/micro organic	Average
Mining metal	Low	Super large	Metal and metal compounds	Micro organic	Super low
Treatment of waste	Super large	Low	Purified water air and soil	Micro organic	High

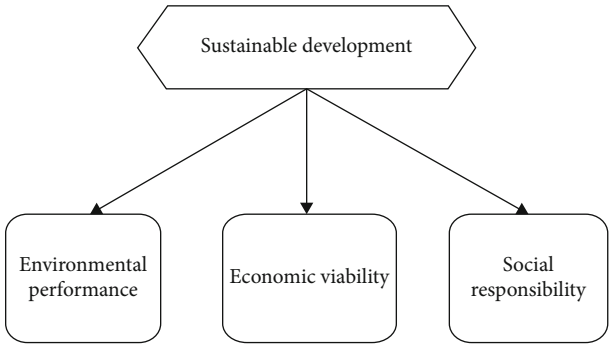

Figure 1: Major Aspects of Sustainability Development.

2. Related Work

The researcher proposed a method for the sustainable production of bio-based chemicals and polymers through integrated biomass refining and bioprocessing based on the circular bioeconomy context. The establishment of feasible bio-refinery models using crude renewable energy sources for the production of varied products is critical for the long-term manufacture of bio-based chemicals and monomers. The accessibility of fractionation co-products and fermentation products that could be obtained from big manufacturing and food distribution network side streams in EU countries is presented in this serious assessment. Fermentable sugars have the potential to be used to make bio-based pharmaceuticals and polymers. Following circular bioenergy principles, the application of bio-refinery ideas in business should be evaluated based on operational success and effectiveness, which includes a techno-economic, environmental, and social impact analysis. Edge possibilities and incorporating sustainability metrics have been provided. A case study of the innovative evaluation of bio-based carboxylic acid secretion from the lignocellulosic biomass waste was provided, with an emphasis on the process efficiency and substrate demand [9].

Synthesis and Sustainability evaluation of a lignocellulosic defines the multifidous biorefinery with the consideration of various technical performance and indicators. This study presents a novel research method for a self-sustaining design process predicated on this motivation, which includes synthesis of a multifidous optimal biorefinery while simultaneously optimizing environmental and economic objectives, while further sustainability assessment that uses the sustainable development balanced return on the capital metric. Researchers performed environmental, safety, economic, and power assessments to examine the system, which is a study conducted for north Colombia after the model synthesized the best biorefinery. The mathematical model provided the data required to create the system assessment process using the Aspen Plus software (expanded material and momentum balances, properties estimations, and downstream modeling). The environmental and economic evaluations revealed that the assumptions used to solve optimization problems were sufficient, resulting in positive financial and environmental consequences [10].

Impact on the environment evaluation is important of biodiesel synthesis since it ensures that emissions are kept to a minimum. The preprocessing and downstream manufacturing phases of a typical cellulosic ethanol manufacturing process were observed to use a lot of chemical products and energy, resulting in a lot of emissions. The biochemical, water, and energy, and wind of cellulosic bioethanol production utilizing low water anhydrous ammonia (LMAA) preparation was projected to be minimal, particularly when the method was paired with more effective downstream processing methods. The life-cycle assessment of various pretreatment and product proposed by the researcher deals with the separation technology for the Butanol Bioprocessing. When contrasted to other predicted pretreatment methods, the analysis indicates that LMAA preparation had commercial viability due to its low energy consumption. LMAA preparation resulted in strong security measures that reduced the chance of anhydrous ammonia leaking into the air [11].

The grand research challenges for sustainable industrial biotechnology proposed by the author define the different issues in the biotechnology process. Unique, enhanced commodities and new, advanced production technologies will be the reference for future production. Recent biotechnological and academic breakthroughs, like as CRISPR-Cas and omics technologies, are paving the way for exciting new biotechnology research, production, and implementation of new sustainable goods. Deeper biologic comprehension and robust in silico biochemical markers will be enabled by mathematically rigorous explanations of microbes and communities. Biological design, which combines model-based architecture and biomedical engineering, will speed up the development of resilient and high-performing microbes. Commercial biotechnology is projected to become strongly incorporated into self-sustaining eras of technology systems based on these creatures and aims toward zero-concepts in terms of greenhouse gas emissions and surplus materials in bioprocess engineering [12].

The author done research on the advancing integrated system modeling explaining the framework for the cycle sustainability assessment. Due to the increasingly multiple environmental systems concerns, the need for integrated conditions stipulated for life cycle assessment has been widely explored and is urgent. These issues affect the environment and human well-being, posing a danger to countries' and enterprises' economic success. The integrated assessment considers several concerns, covers regional and temporal scales, looks forward and backward, and includes input from multiple stakeholders. The goal of this research is to create an integrated technique by combining the capabilities of distinct industrial environmental scientists' and physicochemical economists' methods.

3. Materials and Method

Like other biochemical reactions, bioprocesses require a variety of material and energy inputs, as well as specialized unit activities and supplementary requirements. Bioprocesses are also often divided into three different categories: upstream operations, bioreaction, and downstream operations. All three components, as well as their accompanying operations, must be examined and incorporated into the flowsheet model. It's critical to specify the model's limits and planned use precisely so that all of the components designed to accomplish the model's goals are included [4]. The simulation approach employed is determined by the simulation's goal. Gathering the appropriate process data is the first step in creating a flowsheet model. This is incorporated into a structural model that is tailored to the system for assessment.

3.1. Sustainability in Bioprocess Development. The large assortment of goods and services created by the bioprocessing industry has the potential to generate substantial value. Due to the promoted advantages of functional ingredients, regenerative feedstocks, decrease pollution, and advantageous operational requirements, bioprocess architectures are rapidly being used over conventional chemical production technologies. Furthermore, the economic benefits derived from procedures that use sustainable feedstocks, such as lower emissions costs and higher consumption of natural ingredients, appear to be well justified [13].

Changes to process units and retrofit with new technology can help biomanufacturing plants enhance energy consumption, improve net consumption of water, and minimize waste output in an attempt to enhance the performance of the process. By minimizing greenhouse emissions and natural capital use, this method to better process innovation can assure a more ecologically friendly process. It is, nevertheless, just as critical, if not, even more, to develop more economical and environmentally efficient procedures initially in the process development phase [13]. Changes to process units and retrofit with new technology can help biomanufacturing plants enhance energy consumption, improve net consumption of water, and minimize waste output in an attempt to enhance the performance of the process. By minimizing greenhouse emissions and natural capital use, this method to better process innovation can assure a more ecologically friendly process. It is, nevertheless, just as critical, if not, even more, to develop more economical and environmentally efficient procedures initially in the process development phase.

3.1.1. Process Development Assessment and Designing. This information can be improved by modeling the design process and performing a comprehensive assessment. To realize viable manufacturing processes, a continuous examination is needed [14]. Decisions must be based on accurate assessments of an application's costs and potentials, as well as the identification of 'hot spots in the production timetable. This is known as integrated planning, and it should involve environmental and economic evaluations.

The above Figure 2 Decision in the Process Development is defined based on the basic parameter. The more sophisticated the design of the system, the more the ultimate process of production, including its pricing structure and environmental consequences, is already known. The expense of redesigning to address a previously unnoticed issue climbs as the development stage progresses. End-of-pipe technology, which incurs added expenses, is frequently the only solution to environmental issues at a different stage of development [15].

Gaps in the data and uncertainties in the development phase result in an imperfect image of the predicted production-scale process. Process modeling can bridge this gap as well as provide a solid foundation for evaluation. The following Figure 3 Process development of Bioprocess shows the iterative aspect of designing and developing of bioprocess.

Further data is acquired from trademarks, publications, and other alternative entities, and the models should indeed be produced in close coordination with the design process. The simulation findings are used to assess the process and steer R&D resources toward the most promising avenues and pressing issues. As a result, it's critical to consider the entire process rather than just a single stage, such as the fermentation step, which is separated from the rest of the

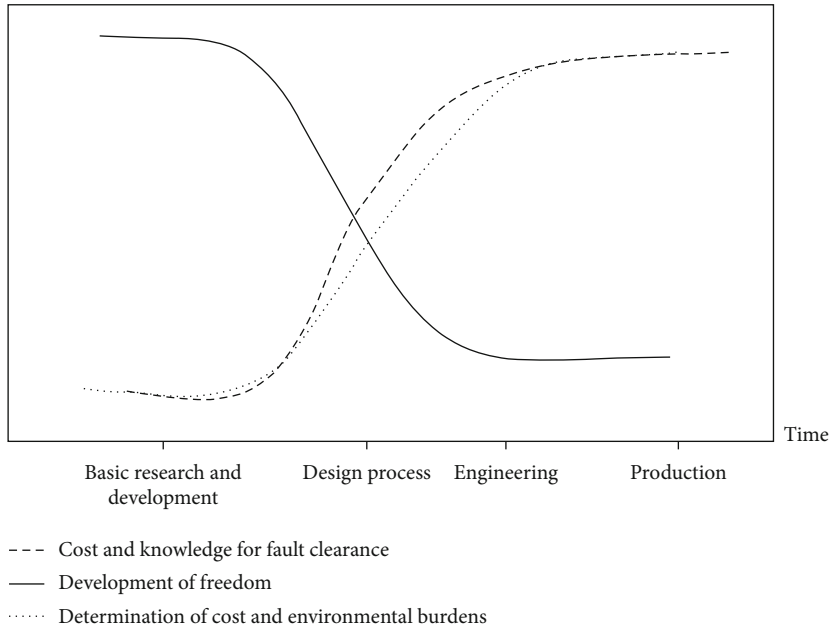

Figure 2: Decision in the Process Development.

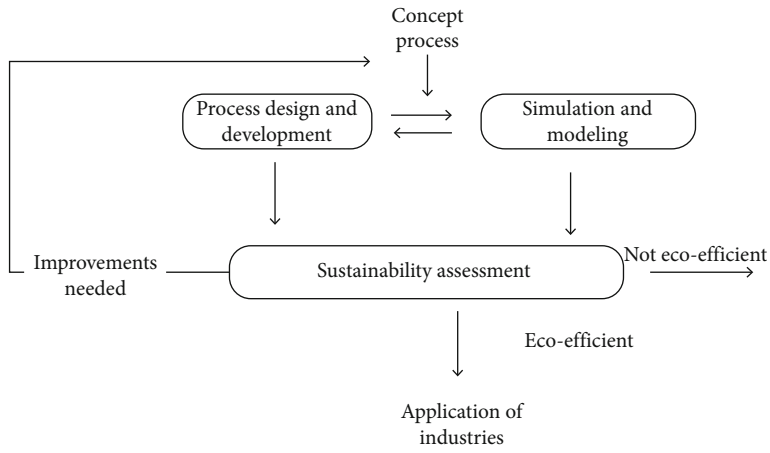

Figure 3: Process development of Bioprocess.

process. The main goal is to create the most competitive and long-lasting process possible [8]. The modeling and evaluation procedure is done iteratively and necessitates a multidisciplinary approach. Important obstacles that may obstruct a successful transfer to an industrial use can be detected sooner using this approach, eliminating R&D waste. Consequently, the predictions that are generated and the assessments that are based on such models have some inherent uncertainty. This inconsistency must be taken into account and quantified.

3.2. Flowsheet Model. For bioprocesses, a basic flowsheet model was created. For Life Cycle Analysis of bioprocesses, the worksheet model was created to generate first-estimate energy and material equilibrium inventory data. The researcher began developing the model on the assumption that these data are often difficult to get or not accessible at all during the initial phases of process development. The model's energy and material equilibrium data can be used to create inventory items for Life Cycle Analysis of particular bioprocesses. The flowsheet was created to address three key requirements for a general initial phase simulation tool:

The flowsheet should act as a first-estimate bioprocess simulation tool

The tool should provide all relevant data for a comprehensive Life Cycle Assessment (LCA).

The flowsheet should require minimum input data to yield a first stage estimate which can be

refined on the availability of more comprehensive data

Produce first-estimate energy and material balance data for specified bioprocess models using the generic flowsheet model. Microsoft Excel is used to create the flowsheet (MS-Office 2008). Model characteristics and calculation processes are mostly based on basic principles and relevant published

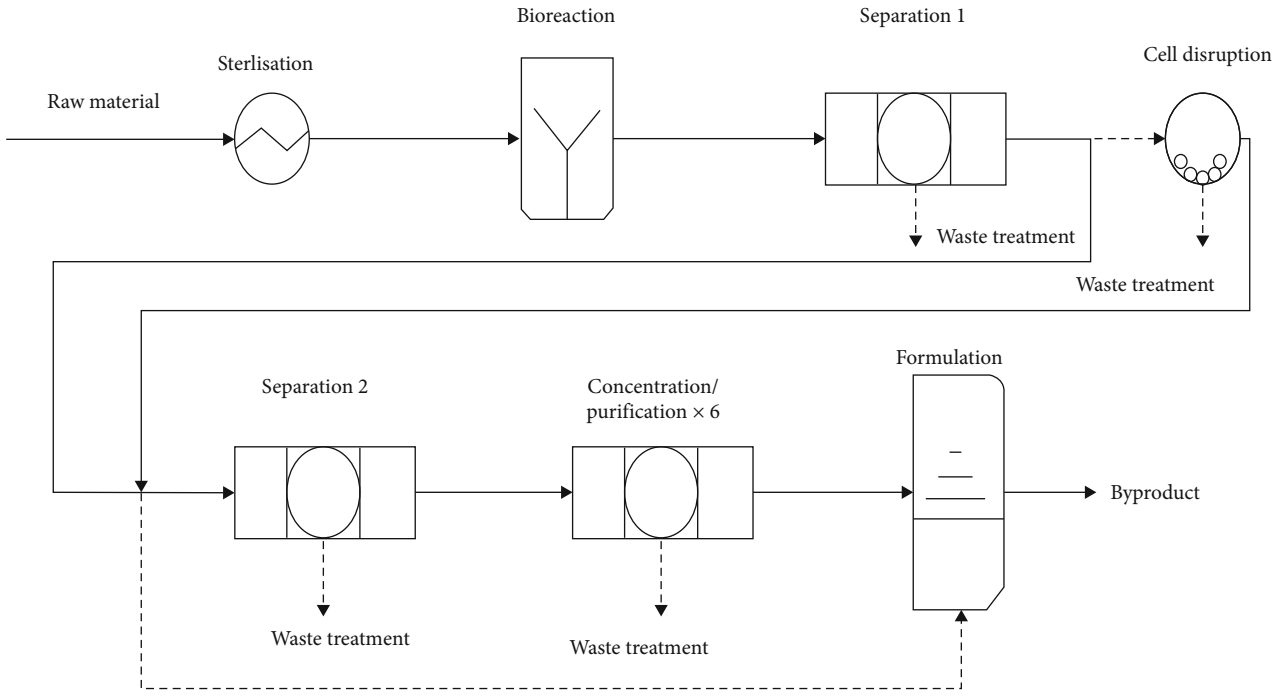

Figure 4: General Process Flow Diagram.

Table 2: Input requirement and simulation.

Procedure	Input of user	Output simulation
Complete process	(i) Selection of batch or continuous operations (ii) Selection of liquid or solid and intra or extracellular products (iii) Selection based on the growth of anaerobic or aerobic biomass (iv) User-defined product quantity	(i) Energy and material requirement (ii) Categorizing the waste material (iii) Recovery and product purity
Sterilization	(i) Media sterilization	(i) Energy and material requirement
Bioreaction	(i) Growth rates, the concentration of biomass, and yield coefficients are required (ii) Maintenance calculation is included for selection	(i) Microbial growth prediction (ii) Requirements of antifoam and agitation
Waste treatment	(i) Waste treatment selection	(i) Chemical oxygen demand
Cooling	(i) Relevant cooling is included	(i) Energy and material requirement
Downstream	(i) From the built-in model, the downstream is specified	(i) Energy and material requirement

information [16]. A typical large-scale bioprocess flowsheet is defined by six successive processes in the model. As the user describes the process, a modified flow process diagram, displayed in Figure 4 General Process Flow diagram shows the sequential selection of potential process units in each stage.

Batch or continuous microbial growth with intracellular or extracellular product production is possible with this technology. The process's energy and material consumption are controlled by the number of products manufactured. Liquid–solid extraction, cell destruction, as well as further filtration precede sterilization, inoculation, microbial growth, and manufacturing of products. Selecting from several unit operations seen in bioprocesses is how downstream treatment is defined. Six concentration or filtration processes are proceeded by a last composition step in the downstream unit. In downstream operations, the recycling of process

Table 3: Material Balance form starch.

Components	Generic flowsheet	
	In	Out
Ammonium nitrate	23.5	—
Biomass	0.356	—
Carbon dioxide	—	157
Citric acid	—	354
COD	—	0.693
Fat	—	1000
Glucose	—	30.5
Hydrogen chloride	0.713	299
Nitrogen	19581	19581
Oxygen	5951	5485
Starch	1201	—
Water	13235	13235

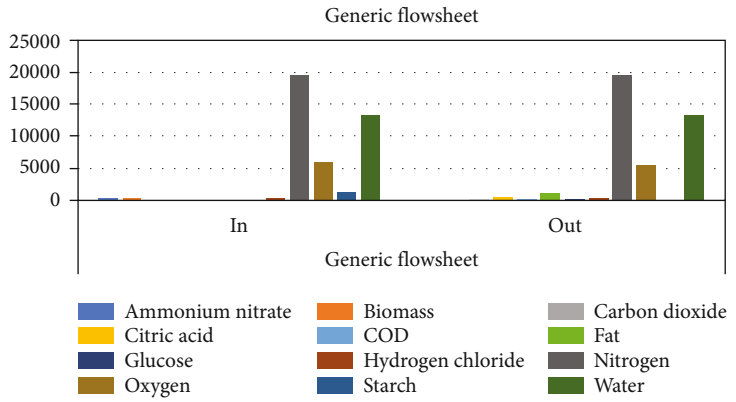

Figure 5: Generic Flowsheet Comparison.

steps is not factored into the equation [14]. Even though the general flowsheet includes attribute values for input variables based on research and production practices, certain essential default values should be checked against procedure research or facility data to guarantee minimal departure from the overall procedure. The parameter estimation for manufacturing found crucial factors. Modifications in these crucial variables have a significant impact on the energy and material balance outcomes of the typical flowsheet. The changes have an impact on the Life Cycle Assessment scores, thus careful evaluation of these factors is required to measure the reliability and validity are as accurate as a first-estimate expense analysis. The following Table 2 displays Input requirement and simulation output based on Flowsheet depicts these six processes as well as the most crucial elements of each.

Selecting from a variety of unit operations seen in bioprocesses is how downstream processing is defined. Six concentration or purification steps are proceeded by a last formulation step in the downstream unit. In downstream operations, the recycling of process steps is not taken into account. Even though process variables for individual component activities can be defined, default settings for chosen units that are typically found in bioprocesses are supplied [17]. Yield ratios, material mixtures, and densities, working pressure and temperature, and enhancing the capabilities are all standard values. The researcher provides a full explanation of the unit operational theory, computation techniques, and default values. The process needs minimum inputs to get precise predictions for material and energy balance data because it was designed for evaluation in the early phases of process development.

Table 4: Energy and Utility Requirement.

Input utility	Generic flowsheet
Electricity	10895
Adsorption	1.84
Aeration	5375
Agitation	2898
Crystallization	39.8
Drying	228
Filtration	565
Ion exchange	1.84
Steam	141005
Bioreactor	1885
Crystallization	11065
Drying	785
Sterilization	380
Cooling water	2235
Aeration	1195
Bioreactor	—
Condenser	995
Sterilization	50
Chilled water	207
Bioreactor	198
Crystallization	8.99

3.3. System Engineering Process and Its Role

3.3.1. Process Option Evaluation. Existing infrastructure, input costs, feedstock availability, and the effectiveness of the necessary (bio)catalyst and (bio)process technology are all economic factors for deployment. Simultaneously, there are environmental and, in a broader sense, sustainability considerations that influence the choice of various process options. The evaluation of the greenhouse effect and the design to reduce or prevent this impact are two examples of current uses of process system analysis. For example, they recently advocated using process systems engineering methods like conservation of mass, thermodynamics, and process work balances to reduce energy use and greenhouse gas emissions [11]. This is an instance of how simulation design and thermodynamics can be used to create measurements and objectives for key elements or consequences. This is also an illustration of current techniques that tend to concentrate on a single effect and its following measure.

Process systems engineering plays a key role in enabling quantitative analyses of such processes, not just from a process standpoint but also from a larger sustainability point of view. Detection and quantification are important because it allows for thorough comparisons and judgments, which boosts decision-making confidence. Rapid computational

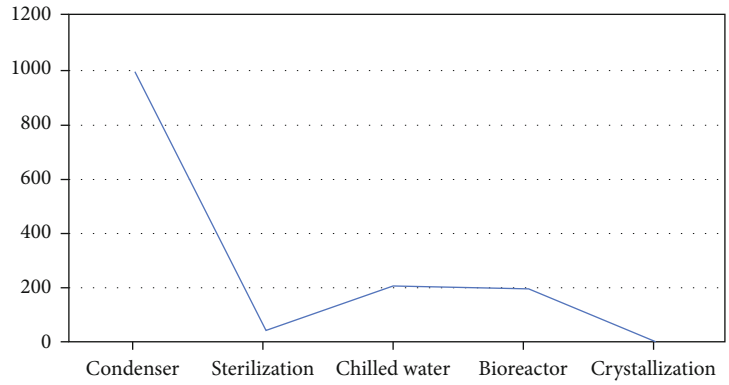

Figure 6: Energy and Utility.

models are also a benefit of process systems engineering. Solutions can be swiftly explored using such simulators. This is critical in allowing tools to be used beginning of the project and product creation. Finally, the response to the challenge posed here will be influenced by regional characteristics in a specific example.

3.3.2. Chemical Platform Evaluation. Aside from biomass, there are several potential options for fuel supply and availability. It's less apparent where the chemicals for the next generation will come from in a world where oil is scarce (or very expensive). There is presently an infrastructure in place that is based on the utilization of the seven well-known platform chemicals. In the medium run, we could investigate repurposing existing infrastructure to make the seven compounds from alternative energy sources. In the long run, new procedures due to a different set of raw materials will be required. A few groups will be dependent on fructose. In a biorefinery, it will be important to create a framework that can handle a variety of feedstocks, methods, and outputs. This poses a significant design and optimization, as well as system integration, problem.

(1) Process Integration. With a few exclusions, water is the principal mediator for most bioprocesses. As a result, the downstream process is typically challenging, which is exacerbated by the requirement to perform breakups at warmer temps. Because of the dilute nature of rivers, the preponderance of the environment and expense, safety, and health implications are typically found in the downstream process [18]. The necessity for energy-intensive segregation has traditionally been driven by the dilute character of the streams. For bigger density estimation, such as petroleum products, evaporation of water becomes a must to cut costs and prevent carrying large quantities of water. In other circumstances, the output may be included in a biorefinery system, however, water will have to be eliminated at some stage.

As a result, incorporating water consumption and recovery via recycling into the design of industrialized bioprocess plants is critical. Furthermore, bioprocesses must be built using processes synthesis and system integration methods to prevent having a procedure that is efficient in one section but wasteful in another. Conventional material and energy integration methods, such as squeeze innovation, will play a key role. In many respects, the problem of water incorporation in a biorefinery is similar to the problem of thermal storage in a traditional refinery.

Table 5: Result of Impact.

Impact	Generic flowsheet	Difference
Abiotic depletion	0.45	0.22%
Ozone depletion	5.81E-08	0.17%
Global warming	4.5	1.5%
Aquatic economy	0.47	-3.3%
Marine economy	1805	0.00%
Human economy	1.85	-0.50%
Acidification	0.025	-1.1%
Eutrophication	0.0099	-4.8%

(2) Design of Biorefinery. Exploitation to produce a variety of sugars (for (bio)catalysis or ferment) as well as oil-based material. In each scenario, the present focus of the biorefinery study is to find that all fractions of a given feedstock are fully used in a given environment. Similarly, the development of downstream goods is currently being investigated. Glycerol, for illustration, can be utilized as a foundation chemical because it is a byproduct of biodiesel manufacturing [19]. Another fascinating case in point is the manufacturing of bioethanol. Although biofuel is widely used as a fuel, there is a solid economic incentive to produce a wide range of different products from it or to use it as a foundation chemical. There seems to be little question that the expanding spectrum of technologies and opportunities available as a result of enzyme- or fermentation-based catalysis will create complicated integration challenges that may necessitate the development of new tools.

(3) Design of Biocatalyst. Bioprocesses are distinguished by their usage of biocatalysts, which come in a variety of forms, as previously mentioned, and can be modified. The alternatives for switching amino acids via protein engineering exist at the most basic level as a protein (isolated enzyme). New enzymes that have been changed may also have better

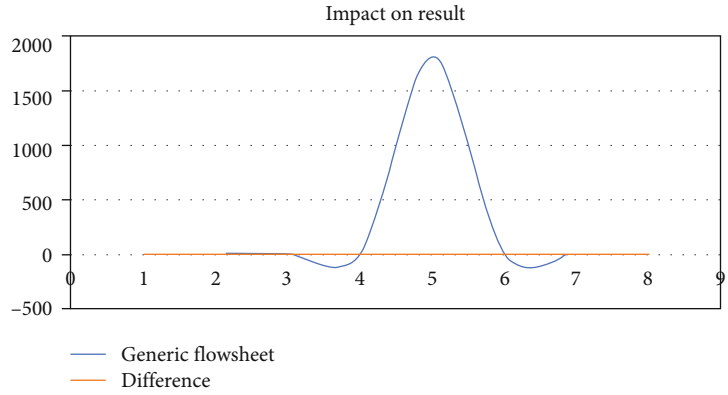

Figure 7: Impact on Result.

selectivity or responsiveness (activity) on a particular (non-natural) target or reaction, as well as new sensitivity to reactors conditions like temperature or pH value [20]. Through a mix of genetic manipulation and de-novo route design, some progress has been made toward the construction of systems in which proteins from many sources are cloned into a host machine to create a novel route. Individuals working in process system design must teach biological designers about what is needed in a given scenario and set appropriate targets in all of these domains.

4. Result and Analysis

Differences in simulation outcomes might also be ascribed to the simulated frameworks' computation methodologies. The bioreaction estimates in the generic flowsheet model were predicated on output to biomass proportion and yield constants, whereas the bioreaction outputs were determined using explicit chemical processes and limiting nutrient content. Because of the inherent differences in the models, the computed values are likely to vary. Variations in computation results can also be caused by default values for non-critical input parameters. The following Table 3 Material Balance form starch shows the in and out model of the generic flowsheet.

The following Figure 5 Generic Flowsheet Comparison is represented. For a variety of material outputs and inputs, the numerical solution outcomes for the various models differ. The presumption that surplus nutrients were provided to the system resulted in higher waste flowrates of glucose, ammonium nitrate, and potassium phosphate in the generic model. The increased yield due to improved process recovery in downstream processing is linked to the generic simulation's lower starch demand.

Table 4 summarizes the energy and utility requirements, which comprise power, steam, cooling water, and chilled water. In terms of energy and utility requirements, the process models contrasted rather well, as shown in Figure 6 Energy and Utility. The bioreactor's air compression and mechanical movement consumed the majority of the electricity in both modeling techniques. The compressor's electrical requirement was dictated by the aeration rate and period of the bioreaction.

Sterilization, medium heating, evaporation in the crystallization unit, and final product drying all required steam. For turbine cooling and isothermal bioreactor operation, cooling water was used. The temperature of the bioreactor was controlled with chilled water, which was also utilized to cool the solution during crystalline structure.

The outcomes of the above analysis suggest that LCA is most useful for method development in the initial stages of process development when decision-making is often based on process designs with drastically different sales data. LCA is likely to reveal significant disparities in effect classifications for processes involving various feedstocks and processing pathways and it is mentioned in the following Table 5 Result of Impact.

The above Figure 7 Impact on Result demonstrates that the generic flowsheet model could be used to create inventory items of adequate quality for use in life cycle impact assessments of large-scale bioprocesses for original decision comparability.

5. Conclusion

New bioprocess chemical and fuel generation technologies are an intriguing endeavor that will keep many process engineers busy in the future. Process systems engineers will play a vital role in this growing industry, thanks to the benefits of quantified decision-making tools and quick modeling and intended to cause and environmental principles. In the future, appropriate models will guide innovations at the infrastructure, process, and catalyst levels (assessment of various solutions and system integration) (evaluation of alternatives for protein and metabolic engineering). More rigorous and consistent life cycle environmental inventory datasets of bio-derived components and better modeling and awareness of social and economic dimensions of sustainability and their connections will be required to assess the sustainability of bioprocesses regularly. Finally, to fully exploit the goals of sustainable development biotechnological processes, increased dialogue among biochemical engineers, biologists, and other professionals with relevant areas of competence will be required.

Data Availability

The data used to support the findings of this study are included within the article. Further data or information is available from the corresponding author upon request.

Conflicts of Interest

The authors declare that there is no conflict of interest regarding the publication of this paper.

Acknowledgments

The authors thank to Sengunthar College of Engineering for providing technical assistance to complete this work. This project was supported by the Researchers Supporting Project Number (RSP-2021/385), King Saud University, Riyadh, Saudi Arabia.

References

[1] A. Halog and Y. Manik, "Advancing integrated systems modelling framework for life cycle sustainability assessment," *Sustainability*, vol. 3, no. 2, pp. 469–499, 2011.

[2] J. Du, B. Kuang, and Y. Yang, "A Data-Driven Framework for Smart Urban Domestic Wastewater: A Sustainability Perspective," *Advances in Civil Engineering*, vol. 2019, 15 pages, 2019.

[3] C. Jiménez-González and J. M. Woodley, "Bioprocesses: Modeling needs for process evaluation and sustainability assessment," *Computers & Chemical Engineering*, vol. 34, no. 7, pp. 1009–1017, 2010.

[4] Z. Usmani, M. Sharma, A. K. Awasthi et al., "Bioprocessing of waste biomass for sustainable product development and minimizing environmental impact," *Bioresource Technology*, vol. 322, article 124548, 2021.

[5] K. Harding, *A Generic Approach to Environmental Assessment of Microbial Bioprocesses through Life Cycle Assessment (LCA)*, 2008.

[6] C. L. Gargalo, P. Cheali, J. A. Posada, A. Carvalho, K. V. Gernaey, and G. Sin, "Assessing the environmental sustainability of early stage design for bioprocesses under uncertainties: An analysis of glycerol bioconversion," *Journal of Cleaner Production*, vol. 139, pp. 1245–1260, 2016.

[7] N. S. Vasile, A. Cordara, G. Usai, and A. Re, "Computational analysis of dynamic light exposure of unicellular algal cells in a flat-panel photobioreactor to support light-induced CO2 bioprocess development,," *Frontiers in Microbiology*, vol. 12,, 2021.

[8] E. Heinzle, A. P. Biwer, and C. L. Cooney, *Development of Sustainable Bioprocesses: Modeling and Assessment*, John Wiley & Sons, 2006.

[9] S. M. Ioannidou, C. Pateraki, D. Ladakis et al., "Sustainable production of bio-based chemicals and polymers via integrated biomass refining and bioprocessing in a circular bioeconomy context," *Bioresource Technology*, vol. 307, article 123093, 2020.

[10] S. I. Meramo-Hurtado, E. Sanchez-Tuiran, J. M. Ponce-Ortega, M. M. El-Halwagi, and K. A. Ojeda-Delgado, "Synthesis and sustainability evaluation of a lignocellulosic multifeedstock biorefinery considering technical performance indicators," *ACS Omega*, vol. 5, no. 16, pp. 9259–9275, 2020.

[11] N. Mahmud and K. A. Rosentrater, "Life-Cycle assessment (LCA) of different pretreatment and product separation Technologies for Butanol Bioprocessing from oil palm frond," *Energies*, vol. 13, no. 1, p. 155, 2020.

[12] A. J. J. Straathof, S. A. Wahl, K. R. Benjamin, R. Takors, N. Wierckx, and H. J. Noorman, "Grand Research Challenges for Sustainable Industrial Biotechnology," *Trends in Biotechnology*, vol. 37, no. 10, pp. 1042–1050, 2019.

[13] P. Tilak and M. M. El-Halwagi, "Process integration of Calcium Looping with industrial plants for monetizing CO2 into value-added products," *Carbon Resources Conversion*, vol. 1, no. 2, pp. 191–199, 2018.

[14] S. Cortina, P. Valoggia, B. Barafort, and A. Renault, "Designing a data protection process assessment model based on the gdpr," *European Conference on Software Process Improvement*, vol. 1060, pp. 136–148, 2019.

[15] D. Petrides, C. L. Cooney, L. B. Evans, R. P. Field, and M. Snoswell, "Bioprocess simulation: An integrated approach to process development," *Computers & Chemical Engineering*, vol. 13, no. 4–5, pp. 553–561, 1989.

[16] A. Bond, A. Morrison-Saunders, and G. Stoeglehner, *Designing an Effective Sustainability Assessment Process*, Routledge, Taylor & Francis Group, 2013.

[17] P. Bergström, "Designing for the unknown: didactical design for process-based assessment in technology-rich learning environments," *PhD Thesis, Umeå Universitet*, vol. 2013, 2013.

[18] C. Mao, N. Zhai, J. Yang et al., "Environmental Kuznets Curve Analysis of the Economic Development and Nonpoint Source Pollution in the Ningxia Yellow River Irrigation Districts in China," *BioMed Research International*, vol. 2013, 7 pages, 2013.

[19] K. H. Zhuang and M. J. Herrgård, "Multi-scale exploration of the technical, economic, and environmental dimensions of bio-based chemical production," *Metabolic Engineering*, vol. 31, pp. 1–12, 2015.

[20] N. K. Tripathi and A. Shrivastava, "Recent developments in bioprocessing of recombinant proteins: expression hosts and process development," *Frontiers in Bioengineering and Biotechnology*, vol. 7, p. 420, 2019.

Hindawi
International Journal of Photoenergy
Volume 2022, Article ID 7797488, 7 pages
https://doi.org/10.1155/2022/7797488

Research Article

Forecasting Solar Energy Production Using Machine Learning

C. Vennila,[1] Anita Titus,[2] T. Sri Sudha,[3] U. Sreenivasulu,[4] N. Pandu Ranga Reddy,[3] K. Jamal,[5] Dayadi Lakshmaiah,[6] P. Jagadeesh,[7] and Assefa Belay[8]

[1]*Department of Electrical and Electronics Engineering, Alagappa Chettiar Government College of Engineering and Technology, Karaikudi, 630003 Tamil Nadu, India*
[2]*Department of Electronics and Communication Engineering, Jeppiaar Engineering College, Semmenchery Raghiv Gandhi Salai OMR, Chennai, 600119 Tamil Nadu, India*
[3]*Department of Electronics and Communication Engineering, Malla Reddy Engineering College, (A) Hyderabad 500100, India*
[4]*.Department of Electronics and Communication Engineering, NBKR Institute of Science and Technology, Vidyanagar, Andhra Pradesh 524413, India*
[5]*Department of Electronics and Communication Engineering, GRIET Gokaraju Rangaraju Institute of Engineering and Technology, Bachupally, Hyderabad 500090, India*
[6]*Department of Electronics and Communication Engineering, Sri Indu Institute of Engineering and Technology, Hyderabad 501510, India*
[7]*Department of Electronics and Communication Engineering, Saveetha School of Engineering, (SIMATS) Chennai, 602105 Tamil Nadu, India*
[8]*Department of Mechanical Engineering, Mizan Tepi University, Ethiopia*

Correspondence should be addressed to Assefa Belay; assefa@mtu.edu.et

Received 8 February 2022; Accepted 24 March 2022; Published 30 April 2022

Academic Editor: V. Mohanavel

Copyright © 2022 C. Vennila et al. This is an open access article distributed under the Creative Commons Attribution License, which permits unrestricted use, distribution, and reproduction in any medium, provided the original work is properly cited.

When it comes to large-scale renewable energy plants, the future of solar power forecasting is vital to their success. For reliable predictions of solar electricity generation, one must take into consideration changes in weather patterns over time. In this paper, a hybrid model that integrates machine learning and statistical approaches is suggested for predicting future solar energy generation. In order to improve the accuracy of the suggested model, an ensemble of machine learning models was used in this study. The results of the simulation show that the proposed method has reduced placement cost, when compared with existing methods. When comparing the performance of an ensemble model that integrates all of the combination strategies to standard individual models, the suggested ensemble model outperformed the conventional individual models. According to the findings, a hybrid model that made use of both machine learning and statistics outperformed a model that made sole use of machine learning in its performance.

1. Introduction

Machine learning approaches have been increasingly popular across a wide range of businesses where data-driven difficulties have been common in recent decades. Machine learning encompasses a wide range of disciplines, including data mining, optimization, and artificial intelligence, to name a few of the more prominent. Machine learning approaches seek to discover connections between input data and output data, whether or not they make use of mathematical models in the process. Following training with the training dataset, the forecasting input data can be fed into the well-trained machine learning models, which can then be used to make predictions [1, 2]. This stage is crucial to machine learning since it has the ability to improve the performance and speed of the algorithm.

Generalizations aside, machine learning relies on three forms of training: supervised training, unsupervised training, and reinforcement training. Clustering criteria are used, and the number of clusters can change depending on the situation.

Figure 1: Fossil fuels.

In order to maximize the intended benefits of reinforcement learning, the learner must interact with their environment in order to obtain feedback from it. This is known as interactivity.

There have been a variety of theories and implementations presented that are based on the three fundamental learning principles [3]. As a result, deep learning is capable of achieving characteristic nonlinear features and invariant high-level data configurations, and as a result, it has been applied in a variety of diverse fields with good results.

According to some studies, a single machine learning model has also been used to anticipate the availability of renewable energy sources [4]. Because of the large range of datasets and time steps, prediction ranges, settings, and performance measurements, a single machine learning model cannot improve forecasting performance on a single dataset or time step. There have been a number of studies in renewable energy forecasting that have resulted in hybrid machine learning models or overall prediction methodologies that are intended to improve prediction performance. Significant attention has lately been drawn to support vector machines (SVMs) and deep learning algorithms [5].

In addition to hastening the depletion of fossil fuel reserves as in Figure 1, overconsumption of fossil fuels has a negative influence on the environment as a whole. Increased health risks as well as climate change threats will result as a result of these issues. Renewable energy, which includes both nuclear power and fossil fuels, is the energy source, surpassing both.

Renewable energy has recently received a great deal of attention as a result of its long-term viability and minimal impact on the surrounding environment. In the near future, the provision of renewable energy will be one of the most critical challenges to be addressed. Alternative terminology: the inclusion of renewable energy sources into current or future electric power generation systems.

Existing energy challenges, such as increasing supply stability and alleviating regional power shortages, can be solved through the evolution of renewable energy technologies. This creation of diverse energy sources, on the other hand, is interrupted and chaotic as a result of the volatility of the energy market as well as the unpredictable and intermittent renewable energy. Dealing with renewable energy fluctuation in an accurate way prevails as a challenge. The energy system efficiency is improved via energy monitoring with high precision. The application of energy forecasting technologies can assist in the creation, management, and formulation of energy policy at all levels of government. As renewable energy sources become more generally available, it is vital to create cutting-edge technologies for storing this energy [6]–[7].

Several studies have discovered that a variety of machine learning algorithms have been employed to estimate the output of renewable energy resources. With the help of data-driven models, it is possible to make more accurate predictions about renewable energy. With the use of hybrid machine learning algorithms, projections for renewable energy sources have also been enhanced. In order to effectively predict the availability of renewable energy sources, it was required to use a number of time intervals. When it comes to renewable energy forecasting, these criteria have been widely used to evaluate the accuracy and efficiency of machine learning algorithms [8].

2. Related Works

Wang et al. [9] investigated deep learning-based renewable energy forecast algorithms in their research. There were four kinds of approaches: stack autoencoder, deep belief networks, recurrent neural networks, and other approaches are lumped together. Certain data processing is employed in order for performance improvement of the predicted results even further.

When it comes to dependability and estimating energy, Bermejo et al. [10] proposed a model using ANN. In this inquiry, potential sources of energy such as solar, hydraulic, and wind power were all taken into consideration. A number of examples are developed to demonstrate the advantages of ANN in the prediction of energy and trustworthiness, among other things. In their study, Mosavi et al. [11] looked at the analysis and classification of ML algorithms used in energy systems. According to the findings of the study, hybrid models outperform standard ML models in energy systems.

According to Ahmed and Khalid [12], they investigated the reliability of renewable power generation systems and optimal reserve capacity in order to better understand forecasting models for renewable power production systems. According to the power industry, this review gave current trends and forecasts for future improvements in system design and operation. In the field of solar and wind energy forecasting, Zendehboudi et al. [13] discovered that support vector machine (SVM) outperformed others. Furthermore, when it comes to forecasting accuracy, hybrid SVM models outperforms single SVM models.

Das et al. [14] conducted an investigation and evaluation of the forecasting methodologies utilized in solar photovoltaic

electricity generation. According to the findings of this study, artificial neural networks and the support vector machine model were found to be particularly prevalent in this field. In their paper, the scientists noted that weather conditions have an impact on the accuracy of solar power forecasts.

Due to the fact that solar radiation is a key source of solar energy, Voyant et al. [15] investigated the application of machine learning algorithms in forecasting solar radiation. Several strategies for forecasting solar radiation have been described. Perez-Ortiz et al. [16] conducted an evaluation of categorization approaches for problems of renewable energy and provided insights for both academics and industry practitioners in this field. In this study, we employed evolutionary approaches and game theory to investigate the feasibility of hybrid renewable energy systems and the obstacles associated with them.

To give a comprehensive survey [17]–[18] of current developments in the field, this paper examines data pretreatment methodologies, machine learning algorithms, parameter selection, and performance assessments of machine learning models in renewable energy projections.

3. Proposed Method

In this section, we validate the forecasting made by the ensemble model for optimal prediction of power generation using PV plants. The study considers two case studies, where the former is simulated for smaller PV farms of 1000 PV cells and larger PV farms of 100000 PV cells. The illustration of training the ensemble model is given in Figure 2. In these proposed methods, the data is classified into a single classifier and another set will act as a training data from which we will classify the samples, classifier, Aggregation was done once it was completed. It will be moved to performance metric evaluation with several comparison techniques.

3.1. Feature Selection. The sun delivers solar energy in the form of solar radiation, which is produced by the photovoltaic effect. Sunlight intensity is the most important factor influencing the output of photovoltaic (PV) solar panels. A PV system output can be affected by a variety of different environmental variables among others. Identifying which parts of PV are valuable and which aspects are not is also essential so that a suitable feature subset may be selected as an input to the model. We propose a hybrid method for feature variable selection that comprises two basic processes, namely, the filter stage and the wrapper stage, as depicted in Figure 3.

Prior to begin the learning process, the filter technique analyzes features based on the inherent attributes of each one of the features. Filter criteria are used to select a subset of features from a dataset based on their relevance.

Because of the characteristics of PV data, the Pearson correlation coefficient (PCC) is employed to assess the relationship between input factors and the target variable. A PCC is a statistical metric that is used to determine the linear correlation between two variables, $\boldsymbol{X}$ and $\boldsymbol{Y}$, in a dataset. Data from time series analysis captures the degree to which a target variable $\boldsymbol{Y}$ correlates with an input variable $\boldsymbol{X}$ over the course of an observation period. When calculating the correlation between two variables, the time series data at

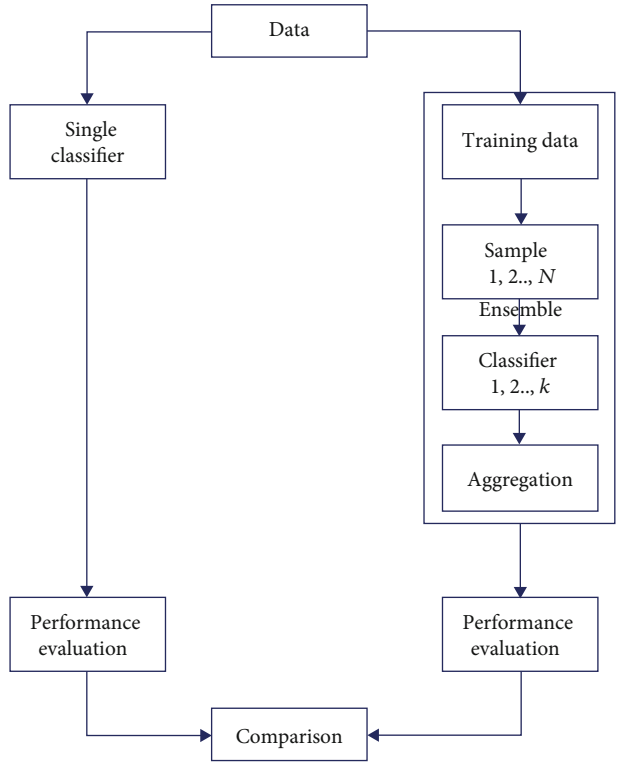

Figure 2: Proposed model.

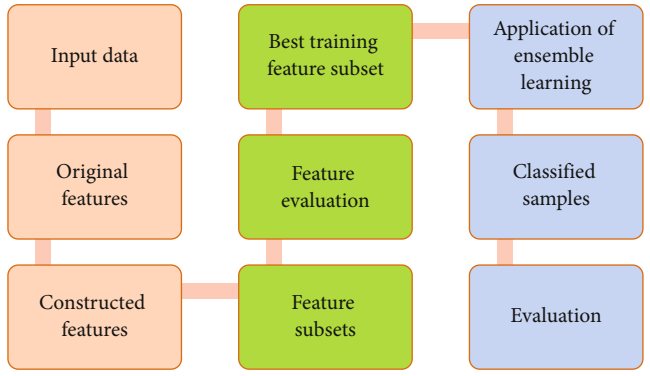

Figure 3: Feature selection.

the points $\boldsymbol{t}$ and $\boldsymbol{t1}$ of the variable are not used. In our example, the meteorological factors that have an impact on PVPG are represented by the letters $\boldsymbol{Y}$ and $\boldsymbol{X}$, respectively. As a result, the PCC may be expressed mathematically as

$$\rho(X, Y) = \frac{\sum_{i=1}^{N}(x_i - \bar{x})(y_i - \bar{y})}{\sqrt{\sum_{i=1}^{N}(x_i - \bar{x})^2}\sqrt{\sum_{i=1}^{N}(y_i - \bar{y})^2}}, \quad (1)$$

where PCC is the value that lies between +1 and -1. PCC is one of the most commonly used criteria for describing the relationship between variables in practice, and it is also one of the most widely studied.

The wrapper approach is utilized to analyze each subset that has been selected. The learning algorithm is integrated into the feature selection process, which in turn makes use

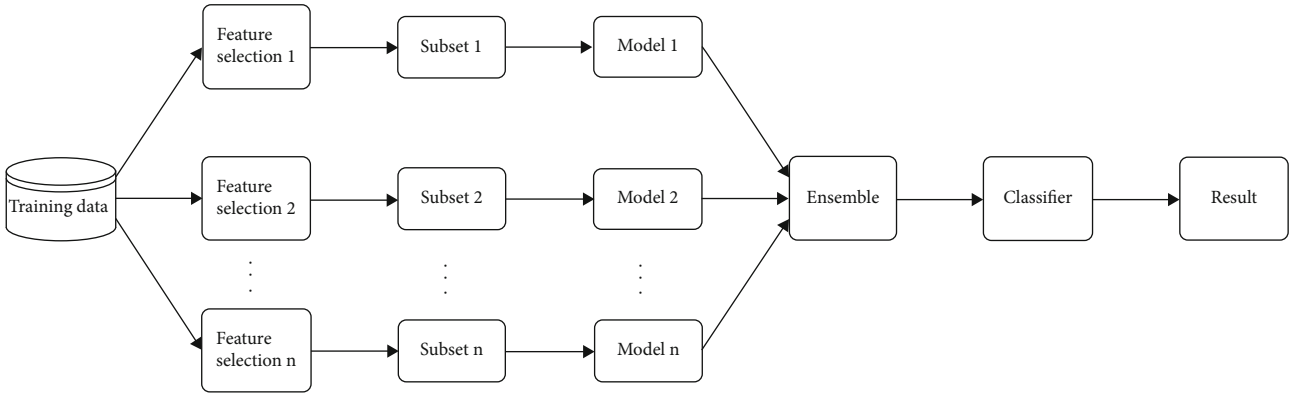

Figure 4: Classification [19].

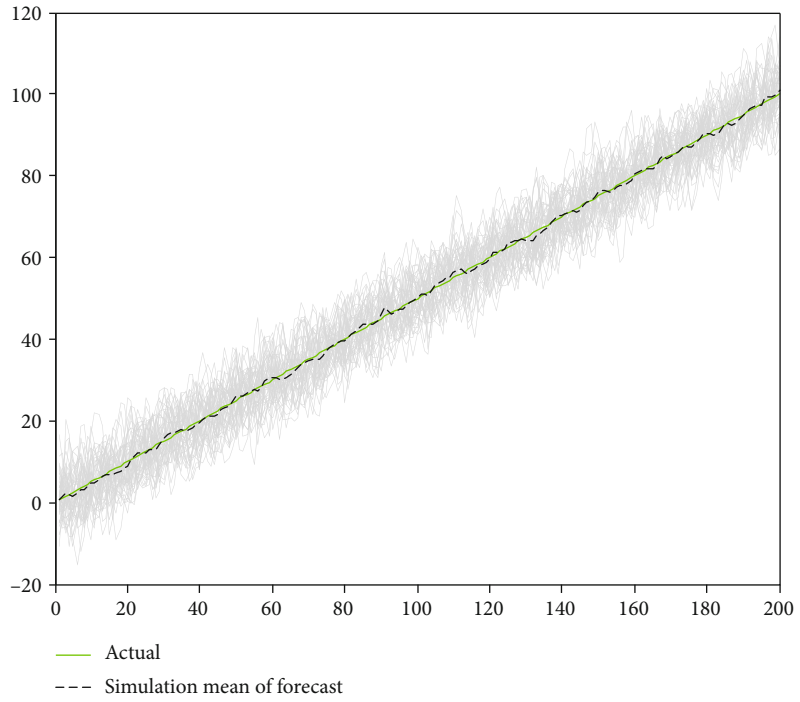

Figure 5: Observations from ensemble model for smaller PV farms.

of the error of a given model to determine which feature subset is most important to the user. It was decided to employ the traditional LSTM model for the analysis of feature subsets in this study because of its capacity to address time series forecasting issues. As a result, the optimal subset of training characteristics may be determined from among all of the subsets that have been investigated.

Through the use of a hybrid approach, the proposed feature selection attempts to integrate the best aspects of wrapper and filter methods into a single method. After examining the correlations between variables using filter criteria, appropriate thresholds are determined in order to reduce the number of feature variables that can be evaluated. The filter technique, in contrast to other learning algorithms, is univariate in nature.

This results in it being significantly more efficient and faster to compute than the wrapper technique, and it is capable of dealing with massive datasets with ease. No consideration is currently given to how features interact with one another or with the learning algorithms, which is a problem. In this case, the wrapper technique is required because coupled features in the single feature evaluation. In order to effectively use an individual wrapper strategy, a significant amount of computer power is required. This is owing to the learning methods used and the enormous number of feature subsets that must be analyzed. Despite this, when the correlation results of the filter approach are utilized as a guide, fewer feature subsets are generated and analyzed than would otherwise be the case. As a result, the hybrid method that has been proposed has the potential to improve the effectiveness of the feature selection.

3.2. Ensemble Feature Classification. In this study, we employed an approach known as multimodel ensemble feature selection, which is an alternative to the methods that have been previously explored. Initially, the training data is

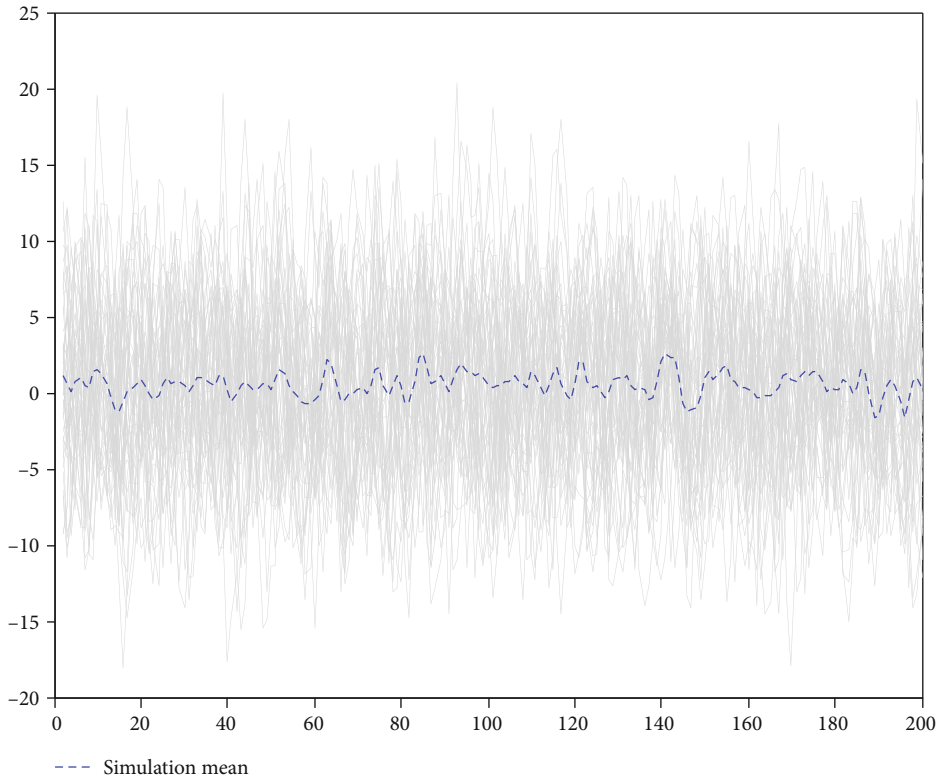

Figure 6: Difference between the smaller and larger PV farms using ensemble model.

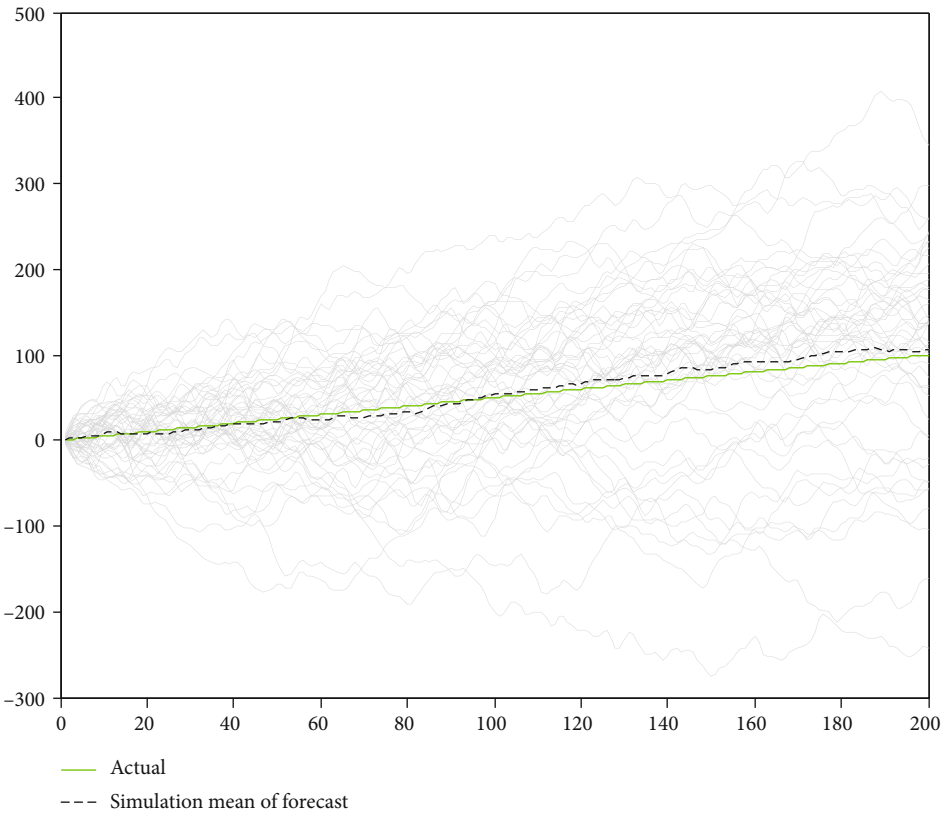

Figure 7: Observations from ensemble model for larger PV farms.

analyzed using a number of feature selection algorithms, each of which generates a subset of the total data. Second, a model is trained using a single subset of data that was previously acquired, as described above. Finally, we compile the results of all of the simulations that we have conducted. Figure 4 depicts the process of selecting ensemble features from a large number of candidates.

4. Results and Discussions

During the experiment, a total of 10 MW of capacity was achieved through the use of polycrystalline solar panels (Poly-SI) and thin-film solar cells (TFSC). The time series dataset can be accessed in a number of different formats. For our research, we used data with a five-minute resolution.

Low-bias machine learning models also reveal that estimates for energy generation are pretty close to the reality. According to the example studies depicted in Figure 5, clear weather conditions outperformed overcast and partly cloudy conditions for each ML model. When the weather is clear, the shift in cloud cover is gradual, which allows for more accurate power predictions. The RMSE of the power forecast for a gloomy day is slightly higher than that of the power forecast for a clear day. It is the actual and forecasted of the predicted power for the partly cloudy day that are particularly bad. The error in a forecast is influenced by the variety of the forecast. It is mostly owing to the greater unpredictability associated with partially cloudy conditions that the abovementioned discrepancies in forecast errors exist. In contrast to the findings in Figure 6, the results in Figure 7 appear to be contradictory.

It is obvious from this dataset that the ensemble model is capable of producing accurate estimates. It is possible that a generalized ML model that can be applied to any PV plant will never be developed. It is possible that the ensemble model, despite its excellent performance in this study, will perform even better on a different dataset. The location and construction of the power plant may have an impact on the weather conditions and the amount of electricity that is generated. Clear data is more abundant in the dataset than cloudy data, which indicates that the data is more reliable. Because the dataset has a higher proportion of clear data than other models for polar regions, the ML model overall performance is superior to that of other models for polar regions.

5. Conclusions

An integrated machine learning model and the statistical approach are used to anticipate future solar power generation from renewable energy plants. This hybrid model improves accuracy by integrating machine learning methods and the statistical method. In order to improve the accuracy of the suggested model, an ensemble of machine learning models was used in this study. When comparing the performance of an ensemble model that integrates all of the combination strategies to standard individual models, the suggested ensemble model outperformed the conventional individual models. According to the findings, a hybrid model that made use of both machine learning and statistics outperformed a model that made sole use of machine learning in its performance. In future work, the proposed method can improvise the performance, accuracy, and the other metrics using several deep learning mechanisms.

Data Availability

The data used to support the findings of this study are included within the article. Further data or information is available from the corresponding author upon request.

Conflicts of Interest

The authors declare that there is no conflict of interest regarding the publication of this paper.

Acknowledgments

The authors thanks to Mizan Tepi University, Ethiopia, for providing help during the research and preparation of the manuscript.

References

[1] I. Jebli, F. Z. Belouadha, M. I. Kabbaj, and A. Tilioua, "Prediction of solar energy guided by Pearson correlation using machine learning," *Energy*, vol. 224, article 120109, 2021.

[2] G. Narvaez, L. F. Giraldo, M. Bressan, and A. Pantoja, "Machine learning for site-adaptation and solar radiation forecasting," *Renewable Energy*, vol. 167, pp. 333–342, 2021.

[3] S. Park, Y. Kim, N. J. Ferrier, S. M. Collis, R. Sankaran, and P. H. Beckman, "Prediction of solar irradiance and photovoltaic solar energy product based on cloud coverage estimation using machine learning methods," *Atmosphere*, vol. 12, no. 3, p. 395, 2021.

[4] K. Mahmud, S. Azam, A. Karim, S. Zobaed, B. Shanmugam, and D. Mathur, "Machine learning based PV power generation forecasting in Alice Springs," *IEEE Access*, vol. 9, pp. 46117–46128, 2021.

[5] A. Nespoli, A. Niccolai, E. Ogliari, G. Perego, E. Collino, and D. Ronzio, "Machine learning techniques for solar irradiation nowcasting: cloud type classification forecast through satellite data and imagery," *Applied Energy*, vol. 305, article 117834, 2022.

[6] F. Rodríguez, F. Martín, L. Fontán, and A. Galarza, "Ensemble of machine learning and spatiotemporal parameters to forecast very short term solar irradiation to compute photovoltaic generators output power," *Energy*, vol. 229, article 120647, 2021.

[7] H. Musbah, H. H. Aly, and T. A. Little, "Energy management of hybrid energy system sources based on machine learning classification algorithms," *Electric Power Systems Research*, vol. 199, article 107436, 2021.

[8] U. Singh, M. Rizwan, M. Alaraj, and I. Alsaidan, "A machine learning-based gradient boosting regression approach for wind power production forecasting: a step towards smart grid environments," *Energies*, vol. 14, no. 16, article 5196, 2021.

[9] H. Wang, Z. Lei, X. Zhang, B. Zhou, and J. Peng, "A review of deep learning for renewable energy forecasting," *Energy Conversion and Management*, vol. 198, article 111799, 2019.

[10] J. Ferrero Bermejo, J. F. Gomez Fernandez, F. Olivencia Polo, and A. Crespo Márquez, "A review of the use of artificial neural network models for energy and reliability prediction A

study of the solar PV hydraulic and wind energy sources," *Applied Sciences*, vol. 9, no. 9, article 1844, 2019.

[11] A. Mosavi, M. Salimi, S. Faizollahzadeh Ardabili, T. Rabczuk, S. Shamshirband, and A. R. Varkonyi-Koczy, "State of the art of machine learning models in energy systems, a systematic review," *Energies*, vol. 12, no. 7, article 1301, 2019.

[12] A. Ahmed and M. Khalid, "A review on the selected applications of forecasting models in renewable power systems," *Renewable and Sustainable Energy Reviews*, vol. 100, pp. 9–21, 2019.

[13] A. Zendehboudi, M. A. Baseer, and R. Saidur, "Application of support vector machine models for forecasting solar and wind energy resources: a review," *Journal of Cleaner Production*, vol. 199, pp. 272–285, 2018.

[14] U. K. Das, K. S. Tey, M. Seyedmahmoudian et al., "Forecasting of photovoltaic power generation and model optimization: a review," *Renewable and Sustainable Energy Reviews*, vol. 81, pp. 912–928, 2018.

[15] C. Voyant, G. Notton, S. Kalogirou et al., "Machine learning methods for solar radiation forecasting: a review," *Renewable Energy*, vol. 105, pp. 569–582, 2017.

[16] M. Pérez-Ortiz, S. Jiménez-Fernández, P. A. Gutiérrez, E. Alexandre, C. Hervás-Martínez, and S. Salcedo-Sanz, "A review of classification problems and algorithms in renewable energy applications," *Energies*, vol. 9, no. 8, article 607, 2016.

[17] S. F. Stefenon, M. H. D. M. Ribeiro, A. Nied et al., "Time series forecasting using ensemble learning methods for emergency prevention in hydroelectric power plants with dam," *Electric Power Systems Research*, vol. 202, article 107584, 2022.

[18] K. Lingelbach, Y. Lingelbach, S. Otte, M. Bui, T. Künzell, and M. Peissner, "Demand forecasting using ensemble learning for effective scheduling of logistic orders," in *In International Conference on Applied Human Factors and Ergonomics*, pp. 313–321, Springer, Cham, 2021.

[19] S. Zhao, Y. Zhang, H. Xu, and T. Han, "Ensemble classification based on feature selection for environmental sound recognition," *Mathematical Problems in Engineering*, vol. 2019, 7 pages, 2019.

Hindawi
International Journal of Photoenergy
Volume 2022, Article ID 5240115, 10 pages
https://doi.org/10.1155/2022/5240115

Research Article

A Novel Optimization Algorithm for Modifying the Parameter Unit of Solar PV Cell

V. Senthil Nayagam,[1] S. Sanal Kumar,[2] V. Thiyagarajan,[3] Neel Kamal,[4] N. Nisha,[5] J. Samson Isaac,[6] and Adane Kassa[7]

[1]*Department of Electrical & Electronics Engineering, Sathyabama Institute of Science and Technology, Chennai, 600 119 Tamil Nadu, India*
[2]*Department of Instrumentation, NSS College, Nemmara, Palakkad, 678508 Kerala, India*
[3]*Department of Electrical and Electronics Engineering, Sri Sivasubramaniya Nadar College of Engineering, Chennai, 603110 Tamil Nadu, India*
[4]*Department of Electrical and Electronics Engineering, Kongu Engineering College, Perundurai, -638060, Erode, Tamil Nadu, India*
[5]*Department of Civil Engineering, Sri Sairam Engineering College, Chennai, 600044 Tamil Nadu, India*
[6]*Department of Biomedical Engineering, Karunya Institute of Technology and Sciences, -641114, Coimbatore, Tamil Nadu, India*
[7]*Faculty of Mechanical Engineering, Arba Minch Institute of Technology (AMIT), Arba Minch University, Ethiopia*

Correspondence should be addressed to Adane Kassa; adane.kassa@amu.edu.et

Received 18 January 2022; Accepted 17 March 2022; Published 15 April 2022

Academic Editor: V. Mohanavel

Copyright © 2022 V. Senthil Nayagam et al. This is an open access article distributed under the Creative Commons Attribution License, which permits unrestricted use, distribution, and reproduction in any medium, provided the original work is properly cited.

Because of the rise in solar electricity, photovoltaic research has increased. A precise model of the PV-based cell/unit is ideal for conceptually examining the capabilities of alternative control approaches. Extraction of precise values for relevant unknown elements of solar photovoltaic models is crucial for modeling PV systems. Optimization strategies for this topic have been increasingly important and dynamic in recent history due to their efficiency in dealing with extremely nonlinear multidimensional optimization challenges. The strategy avoids stalling by deleting the best solution; this keeps the engine diverse and increases global search capacity. Pattern searching, on either side, is a multiobjective approach that has a high convergence speed as well as good stability, which can increase the whale optimization algorithm's traditional optimization ability. As a result, combining these two mechanisms can considerably improve the whale optimization algorithm capacity to find the optimal answer. The modified whale optimization algorithm may also be used to evaluate parameters in single-diode models, double-diode models, and photovoltaic panels, as well as to find independent variables in two distinct methods of PV modules under various light temperature and pressure circumstances. The analytical results show that the modified whale optimization algorithm is both valid and practical for predicting solar cell and photovoltaic unit characteristics. The study goes into great depth on a new optimization approach for changing the parameter unit of solar PV cells.

1. Introduction

Power generation has traditionally become the most approachable, kind of energy, but it must first be generated before it could be utilized. Even though a major part of electric power is still generated from fossil fuels, the global energy mix has changed intensely in recent decades. Several issues have been forced by this kind of shift, including rising costs of conventional energy, resource constraints, and a responsibility to protect the ecosystem [1]. Carbon emissions and the degradation of available substance, especially, have prompted the use of new energy resources. Coal and oil are among the largest and most powerful energy sources, capable of meeting all of humanity's demands. The low price, converting leads, and simplicity of delivery of fossil energy have piqued the interest of all countries, resulting in a growth in their use. The drawbacks of fossil fuels should be weighed against their many benefits. Severely polluted air,

ozone layer depletion, climate change, and other factors have prompted advanced economies to turn to sustainable energy sources such as wind, photovoltaic, hydrothermal, and gravity force.

Those things are happening as a result of the benefits that energy production has over other alternative energy sources. Year-round unlimited type of power, low maintenance requirements, and ease of application, even in household large urban areas, are only a few of the benefits. As a result, there has been an increase in the quantity of study into the solar energy economy. PV panels generate clean, renewable electricity. There are no detrimental greenhouse gas emissions during the generation of power with PV panels, making solar PV environmentally beneficial. Solar energy is energy that comes from the sun. As a result, it is both free and plentiful. The primary goal of the research is to boost the effectiveness of photovoltaic cells/modules, which are the fundamental building blocks for harvesting solar energy [2]. Aside from wind, tidal, and geothermal power, power generation, energy is a major form of renewable energy. In India, for example, the national target of 175 Gigawatts of renewable power was output by 2022, with 100 Gigawatts coming from solar energy. Furthermore, China aspires to be a global leader in the renewable power organization by 2050, with a size of 1300 Gigawatts.

Machine intelligence is known as artificial intelligence. It is described as "the design approach of intelligent agents," where an intelligent agent is a technology that observes its surroundings and acts in a way that increases its likelihood of succeeding. Artificial intelligence investigation is very technical and specialized, and this is separated into numerous subject areas that frequently fail to interact with one another. Statistical modeling methodologies, conventional symbolic, and intelligent systems are currently prevalent artificial intelligent approaches [3]. The researcher said that in the synthetic Intelligence system, the linear combination comparatively straightforward rules. There is no centralized control system in place that dictates how individual agents should act. The genuine behaviors of the agents are local and to some degree chance; nonetheless, relations among such individual's outcome in the conception of "intellectual" global behavior that is unknown to the different agents. Termites, bird flocking, mammal herding, bacterial development, and schools of fish are all examples of synthetic intelligence.

Because solar energy is readily available, substantial inquiry and research on solar energy are carried out to maximize the use of this type of renewable energy. Because the solar energy is a clean source, it helps to lower pollution levels around the world, as well as the constraints on conventional exhaustible power insulation for generating electric power, such as condensation generation and hydroelectric power. As a consequence of this, numerous research investigations have been conducted to solve the challenges that have arisen as a result of greater advancement in the development of solar energy. To achieve optimal performance of photovoltaic panels and solar energy under various process situations, robust manufacturing methodologies must be created in response to such limitations. The solar cell layout approach is primarily based on the comparable physical equation of the solar cell [4]. The solar cell model's importance is seen in its potential to induce all variables that control the enthusiastic behavior of the real SC. Furthermore, the current-voltage (I-V) curve can be easily created by studying the behavior using the computational formula, which aids inefficiently, studying the dynamics of solar cell and photovoltaic systems under various weather circumstances.

In this arena, conventional swarm-based algorithms like PSO and ABC have already worked successfully. Nevertheless, because the challenge of determining the parameters of photovoltaic systems is a heterogeneous problem, there is no method to find the global best solution due to the immaturity of some different algorithms. WOA has been effectively implemented in numerous disciplines such as dynamic planning, artificial neural, image classification and extraction of features, and wind velocity forecasting due to its simple design, few variables, powerful search capability, and simplicity of implementation [5]. Traditional swarm-based techniques like PSO and ABC have already proved effective in this field. Nonetheless, due to the infancy of some distinct techniques, there is no approach to identify the global optimum answer because the difficulty of selecting the characteristics of photovoltaic systems is a diverse problem. Due to its simple architecture, few specifications, advanced search capabilities, and ease of effectuation, WOA has been effectively used in a variety of domains, including dynamic scheduling, machine learning, picture categorization, and features are extracted, and wind speed prediction.

Because photovoltaic systems are environmentally friendly, efficient, and safe power sources, they have played a significant part in sustainable power (RE) technology. PV-based renewable energy solutions have attracted a lot of interest for both standalone and energy systems. The generator should be capable of providing high energy to the load in the SA mode. To attach the demand to the PV, which generates DC electricity, an adapter is necessary. Under the SA operation mode, the inverter's output frequencies, voltage, and flow should be managed compared with the reference values. As a result, a power converter and an appropriate voltage management strategy are necessary [6]. The flexibility of a better power converter to supply amplitude and phase sinusoidal voltage and frequency irrespective of the nature of the load it is attached to is its most important attribute. The voltage transformer must also be able to recover fast from transient conditions caused by the disruptions without compromising power quality. However, the widespread usage of PV systems poses several issues, including harmonic emission, low conversion efficiency, power output variability, and power semiconductor conversion dependability.

PV modeling approaches can be categorized into quantitative, quantitative, and hybrid approaches, based on the literature subject. The alternative is the most straightforward to execute, as well as requiring less calculation time. For the mathematical description of the PV characteristic estimates issued, it uses the power-voltage (P-V) and current-

voltage (I-V) data curves, as well as selected data from the PV cell/unit spreadsheet [7]. The analytical approaches, on the other hand, are based on simplifying assumptions of appropriate quantitative formulas, which will have a substantial impact on reliability. Furthermore, the initial prediction from the I-V curve will very certainly alter this precision. To represent photovoltaic cells, a variety of methodologies have been devised, one of the most prevalent of which is the use of comparable circuit simulations. The double-diode and single-diode types are the most commonly utilized circuit models [8]. The reliability of the components associated with the structural model is critical for modeling, sizing, performance assessment, management, efficient calculations, and maximum power point of photovoltaic systems following choosing an appropriate structural model. The paper provides detail on the approach of parameter identification and its optimization process using the whale optimization algorithm. Section 1 provides the detail on the introduction on the optimization and the approach to the algorithm process in a photovoltaic system. The literature based on the different approaches to optimization and algorithm is defined in Section 2, and the material and method are provided in Section 3. Finally, the optimization technique is provided in Section 4.

2. Related Work

The identification of the parameters of solar cells using artificial bee colonies is proposed by the author, thereby optimizing solar energy. Various studies have focused on the precise prediction of current vs. voltage (I–V) properties of solar cells to enhance the effectiveness of photovoltaic systems. The absence of information about the specific model parameters that do characterize the solar panel is the fundamental obstacle in precise prediction. As these features cannot be derived from sheet requirements, a technique on optimization is necessary to adjust the experimental results to photovoltaic models. The new algorithm is effective and developed that was motivated by honey bees' clever foraging activity. ABC outperforms other optimization techniques when it comes to searching for multimodal optimization methods. The proposed methodology is contrasted to other well-known optimization techniques to show its efficacy. The method performs well in terms of resilience and precision, as evidenced by the experimental outcomes [9].

This research presents a photovoltaic cell input parameter identification approach based on adaptive lion swarm optimization. An improved lion swarm optimization proposed by researcher defines the process of identifying the parameter of photovoltaic cell modes. The lion swarm optimization element method is a numerical intelligence algorithm that has been developed in recent times, although it has issues like a locally optimal and delayed completion. To solve these disadvantages, we may use a combination of the tent chaos map, adaptable variable, and chaos search technique to enhance the individual's suitability and minimize trapping in local optimums. The efficiency of the improved lions swarm algorithm surpasses the other six methods in a simulation of a classic test function. The algorithm is then used to identify the parameters of photovoltaic cells using multiple models and various irradiances. The simulation results indicate that the modified lion swarm evaluation is better and successful in the implementation of photovoltaic cells estimating the parameters [10].

The proposed a method for parameter extraction based on swarm optimization. The photovoltaic specifications were extracted from illuminated current-voltage characteristics using particle swarm optimization (PSO). For single- and double-diode models, the PSO's results are compared to that of genetic algorithms. The suggested technique can get higher variable accuracy with greater computational performance than the GA method, according to synthetic and actual existing information. Relative to traditional diffusion methods, the PSO technique is used to produce photovoltaic characteristics as near to the real values as feasible even without a good initial prediction by specifying a wider spectrum for each characteristic [11].

Relative to conventional diffusion methods, the PSO technique is used to obtain photovoltaic characteristics as near to the real values as feasible even without a good initial prediction by specifying a wider spectrum for each characteristic. The author proposed a method for the variable identification of solar cells, and the researchers used the hybrid firefly and pattern search technique to derive the parameter identification. The firefly method has been a recently developed swarm intelligence-based efficient algorithm that has shown to be very effective in addressing optimization issues. If used alone, this technique is effective for exploring solutions, but it requires a local optimization strategy to increase exploitation. To improve this technique, researchers integrate design search as a local optimization technique with the firefly algorithm in this research. To demonstrate the algorithm's effectiveness, the outcomes are presented to those of other optimization techniques for PV parameters. The findings show that the proposed technique is a competing technique that should be part of the solar panel system modeling [9].

The researcher proposed a method for optimization of solar power panels by identifying the parameter of the energy storage system. The smart grid strategy is designed to take benefit of the extensive current technology on altering the current electrical laws to support all participants in the areas of energy efficiency and conservation integration. Energy storage systems may be able to deal with some of the challenges that arise from the use of renewable energy, such as stabilizing irregular power generation, improving voltage stability, and reducing power peaking. The suggested method is based on an integrated optimization strategy that combines a deterministic and stochastic algorithm, has a limited calculation overhead, and can thus be performed under similar working conditions to account for variable fluctuations owing to battery lifetime and use. The research provides a method for determining the ranges of battery design variables that best suit experimental data and integrating them, together with simulations of forms of energy and electric loads, into a comprehensive structure that reflects a real-time smart grid monitoring system [12].

A method for the variable estimation of the photovoltaic cell model enhances the exploratory shape based on the approach on a chain-based algorithm. Photovoltaic systems (PV) are becoming a more viable solution for future energy systems. As a result, research into the working of PVSs has sparked a lot of interest. Due to the obvious nonlinearity of PV cell properties and their large dependence on climatic circumstances of contamination level and temperature, study into finding PV cell model parameters continues a fluid subject. The resistance-based learning modified salp swarm algorithm is suggested in this study for accurate determination of the two-diode design variables of the PV cell/electrical module's transmission line. The results of the experiment as well as in comparison, investigation show that OLMSSA is very competitive, even much better than the published results of the bulk of previously established parameter identification techniques [13].

2.1. Problem Definition. The difficulty in estimating the parameters for photovoltaic system and solar cells is in estimating the parameters of the model using the voltage and current values that have been observed. Furthermore, SD and DD designs are the most generally used equivalency models to mimic the asymmetric current-voltage relationship of solar cells and photovoltaic panels, with SDM is the most widely used.

3. Materials and Method

3.1. Mathematical Formulation

3.1.1. Solar Cell Model. Photovoltaic, single-diode (SD) model, and double-diode (DD) model designs are the three most common comparable circuit types of photovoltaic cells. In contrast to the double-diode model, the photovoltaic panel takes longer to execute since it needs to retrieve more variables [14]. The estimation methods in the two models change only slightly. The analogous circuit models of SD design, photovoltaic modules and DD models will be deliberated in the following subsections.

3.1.2. Single-Diode Design. In Figure 1, the equivalent circuit of SDM is presented in which the function of the output voltage could be computed from the output current I_o; hence ,the equation could be written as

$$I_o = I_p - I_s \times \left[\exp\left(\frac{V_o + I_o \times R_a}{n \times V_d}\right)\right] - \frac{(V_o + I_o \times R_a)}{R_s}. \quad (1)$$

3.1.3. Double-Diode Design. In contrast to the absorption and combination losses included in SDM, the precision of the PV model can be improved by accumulation an additional diode that reflects space charge loss. Figure 2 shows the equivalent circuit of the double-diode model. The calculation for the DDM is expressed below:

$$\begin{aligned} I_o = I_p - I_{s,1} \times \left[\exp\left(\frac{V_o + I_o \times R_a}{n_1 \times V_d} - 1\right)\right] - I_{s2} \\ \times \left[\exp\left(\frac{V_o + I_o \times R_a}{n_2 \times V_d} - 1\right)\right] - \left[\exp\left(\frac{V_o + I_o \times R_a}{R_s} - 1\right)\right]. \end{aligned} \quad (2)$$

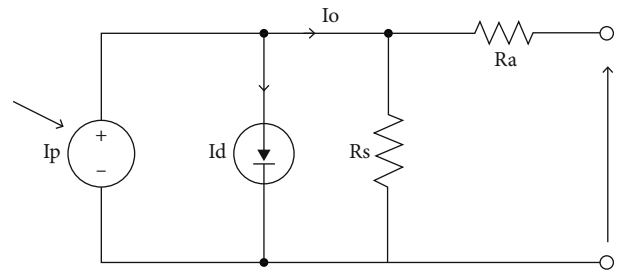

Figure 1: Equivalent circuit of the single-diode model.

In the above two equations, I_o is the output current, I_p denotes the photovoltaic current, V_o denotes the output voltage, and R_a denotes the series resistance and R_s denotes the shunt resistance. In the challenge of estimating the parameters of PV cells and batteries, the information on terminal voltage current is obtained [15]. All that remains to be improved in the recognition process is to determine the best set of unidentified model parameters that minimize the difference between the present predicted value based on the finite element model and the experimentally recorded value.

3.1.4. Whale Optimization Algorithm Background. The basic whale optimization algorithm is a method of artistic intelligence based on a simulation of the humpback whale feeding behavior [16]. The activity of humpback whales is divided into three sections by the method: surrounding prey, bubble-net assaulting, and seeking for prey.

3.1.5. Surrounding Prey. Because the optimal solution to many problems is not planned, it is believed that perhaps the present solution obtained is the intended prey or is near to the prey in WOA. Individual people in humpback whale communities will seek to upgrade their positions in the route of the prey once the prey position has been determined by the following equation:

$$\overrightarrow{A(t-1)} = \overrightarrow{A_{\text{prey}}(t)} - \vec{X}.\vec{Y}. \quad (3)$$

In Equation (3), the number of current iterations is denoted by t and the vector current prey position is denoted by $\overrightarrow{A_{\text{prey}}(t)}$ and the coefficient vectors were denoted by $\vec{X}$ and $\vec{Y}$.

$$\vec{X} = 2\vec{r}.\vec{x} - \vec{x}, \quad (4)$$

$$\vec{Y} = \left|\vec{Z}.\overrightarrow{A_{\text{prey}}(t)} - \overrightarrow{A(t)}\right|. \quad (5)$$

In equation (4), the linearly decreasing parametric vector is denoted as $\vec{x}$ and it starts from 2 to 0 while the random vector is denoted by $\vec{r}$ within $[0, 1]$ and Equation (5); the absolute value of the coefficient is denoted by $\vec{Z}$, and it is illustrated as

$$\vec{Z} = 2\vec{r}. \quad (6)$$

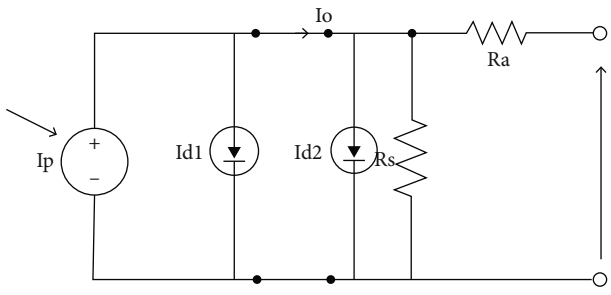

Figure 2: Equivalent circuit of the double-diode model.

3.1.6. Bubble-Net Attacking. A bubble-net attack occurs when humpback whales swim concurrently surrounding their victim in a spiral pattern in a confined circle. Both the expansion wide angle process and the iterative design are used in WOA to replicate their behavior. Elements of the population have the same cases in both methods during the optimization procedure. Aside from that, the precise mathematical design is given:

$$\overrightarrow{A(t+1)} = \begin{cases} \overrightarrow{A_{\text{prey}}(t)} - \vec{X}.\vec{Y}, p < 0.5, \\ e^{bl}\cos(2\pi l) + \overrightarrow{A_{\text{prey}}(t)}, p \geq 0.5. \end{cases} \tag{7}$$

The element b is specified to be constant in the preceding equation, and this is used to determine the spiral's logarithmic shape. The random variable is denoted as l inside the domain $[-1, 1]$, while p is inside $[0, 1]$. A spiral equation is created among the location of the prey and the whale, which aids in the stimulation of a humpback whale's rotating motion.

$$\vec{Y} = \left|\vec{Z}.\overrightarrow{A_{\text{prey}}(t)} - \overrightarrow{A(t)}\right|. \tag{8}$$

3.2. Prey Searching. The whale optimization algorithm updates the population's position during the stage of seeking for prey using the following expression:

$$\overrightarrow{A(t+1)} = \overrightarrow{A_{\text{ran}}(t)} - \vec{X}.\vec{Y}. \tag{9}$$

In Equation (9), $\overrightarrow{A_{\text{ran}}(t)}$ represents the position vector of a random sector in the current population and based on the equation $\vec{Y}$ is computed:

$$\vec{Y} = \left|\vec{Z}.\overrightarrow{A_{\text{ran}}(t)} - \overrightarrow{A(t)}\right|. \tag{10}$$

During this phase, humpback whales are searched at random depending on their relative positions. The constriction wide angles method, in which the component of $\vec{X}$ is higher than 1, indicates that whales in the exploration are forcibly ejected from the prey position, is distinct from the algorithm, which investigates the having the greatest as per the modification of $\vec{X}$. To put it another way, the whale optimization algorithm at this point prioritizes worldwide search.

The mismatch between exploitation and exploration is typically a major issue affecting the success of classic swarm intelligence algorithms. Levy flight, on the other hand, is a non-Gaussian probability distribution method with an indefinite stage duration. This approach is also very unpredictable, with a course that resembles natural metabolic processes, which can aid swarm intelligence systems in balancing exploitation and exploration. As a result, the process is taken into account in this research [17]. In addition, some enhanced WOAs have been developed and implemented to the challenge of evaluating solar model parameters. Therefore, the principle of the no-free lunch dictates that more optimization techniques be developed to improve the problem's solution.

3.3. Proposed Algorithm. Multiple processes will be explained in great detail in this part, as well as the framework for the proposed technique [18]:

3.3.1. Levy Fight. Exploration and exploitation, as well as diversity and development, all benefit from unpredictability. Furthermore, the substance of randomized is chance of walking, which is a stochastic procedure that includes taking a sequence of randomized steps in a row. One of these haphazard procedures is levy flight. Levy flying has also been used as an improvement tool to increase the efficiency of some metaheuristic algorithms.

$$\text{Levy}(s) \sim |s|^{1-\gamma}, \gamma \in (0, 2). \tag{11}$$

In Equation (11), γ represents the exponential function based on the figure of levy distribution and s denotes the accidental step and this could be defined by the following equation:

$$s = \frac{\tau}{|\vartheta|^{(1/\gamma)}}, \tag{12}$$

with ϑ and τ being the elements related to the normal distribution which is defined as $\tau \sim L(0, \sigma_\tau^2)$ and $\vartheta \sim L(0, \sigma_\vartheta^2)$. The derivation for σ_τ and σ_ϑ are given below:

$$\sigma_\tau = \left(\frac{\Gamma(1+\gamma).\sin(\pi\gamma/2)}{\Gamma(1+(\gamma/2)).\gamma.2^{(\gamma-1/2)}}\right)^{(1/\gamma)}, \qquad \sigma_\vartheta = 1, \tag{13}$$

where Γ represents the gamma function.

3.3.2. Pattern Search. Pattern search is widely recognized as a resident derivative-free enhancing approach that is useful to overcome many objective functions that are outside the reach of traditional optimization algorithms. The design search method starts with a set of dots, and the grid is created by adding the associated requirements to a set of integer multiples of a vertex named pattern. Furthermore, among the points on the grid, a point with superior fitness is chosen

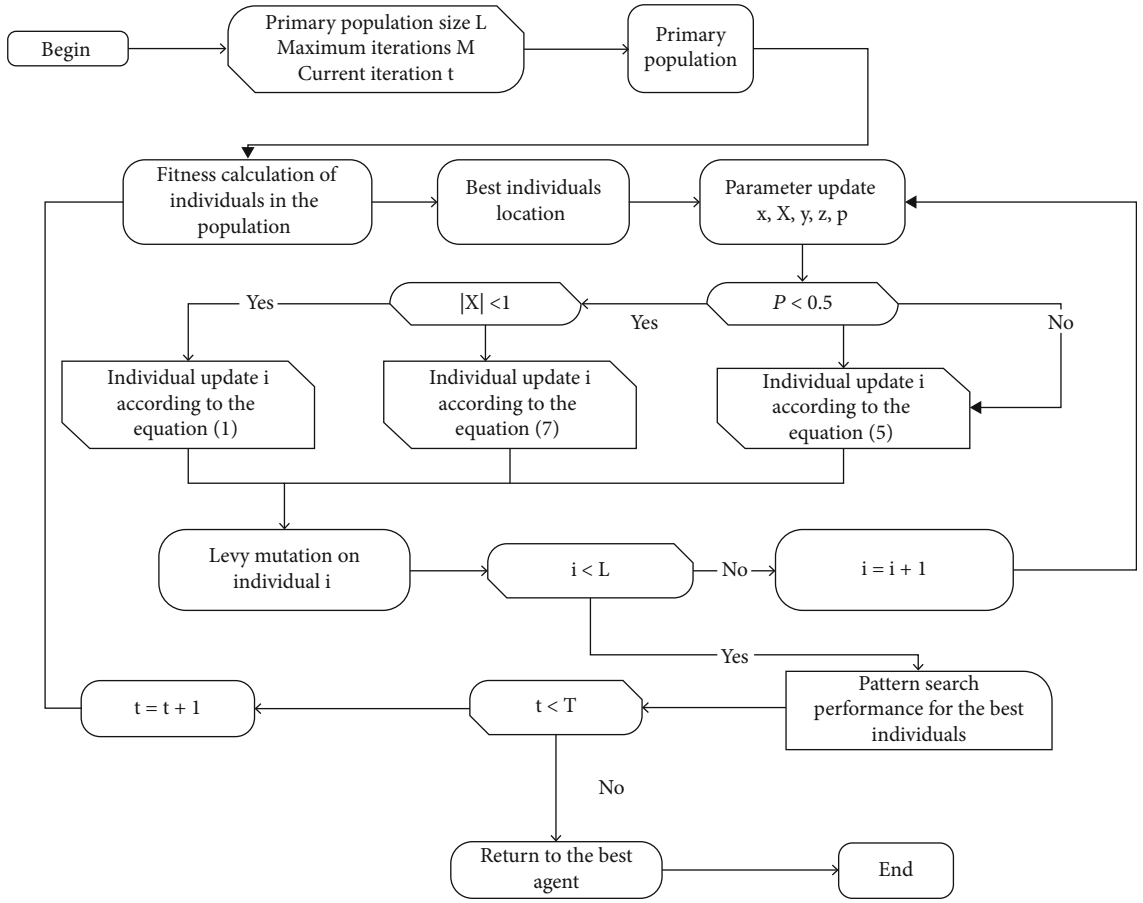

Figure 3: Framework of the modified whale optimization.

Initializing the Whale, A population;
Calculate each search agent's ability:
Lead_position = the best search agent
while (t > maximum no of repetition)
  for each search agent
  Upgrade x, X, Y, z, and p;
    if ($p < 0.5$)
    if ($|X| < 1$)
      Upgrade the current search agent position by Equation (3)
    else if ($|X| \geq 1$)
      Upgrade the current search agent position by Equation (9)
end if
else if ($p \geq 0.5$)
  Upgrade the current search agent position by Equation (7)
    end if
  Carry on the levy flight using Equation (17) for each agent
    end for
With a pattern search to the best agent Lead_ position:
Check that a research officer energy out there the research space and revise it;
Compute the fitness of each search agent;
Upgrade Lead_ position if there is a better solution;
$t = t + 1$
end while
get back Lead_ position:

Algorithm 1: Modified whale optimization

Table 1: Parameter for three different models.

Elements	Double or single diode		Photovoltaic module	
	Inferior border	Superior border	Inferior border	Superior border
I_p	—	1	—	2
I_s	—	1	—	50
R_s	—	0.6	—	2
R_{sa}	—	101	—	2000
L	1	2	1	51
I_{s1}	—	1	—	51
I_{s2}	—	1	—	51
l_1	1	2	1	51
l_2	1	2	1	51

as the starting point for the following iteration. The pattern search is broken down into the following steps:

(i) Stage 1: the primary point a_o was determined and the fitness $f(a_0)$ is computed.

(ii) Stage 2: the other point a_i around the primary point a_o is computed based on the Equation (14) by computing the objective fitness $f(a_i)$. When there is a point better than the a_o, then, stage 3 is performed or else stage 4 is performed.

$$a_o = a_i + u(j).N, \tag{14}$$

where $u(j)$ denotes the vector pattern in which $j \epsilon (1, 2...2d)$ in which d is the dimension of the issue or challenge to be solved and N represents the search stage

(i) Stage 3: based on Equation (15), N has to be updated where $\beta > 1$ and the search space could be extended based on the equation. Stage 5 is executed.

$$N = \beta N \tag{15}$$

(i) Stage 4: according to Equation (16), N has to be updated, where $\zeta < 1$ and this helps to narrow the search space. Stage 5 is executed.

$$N = \zeta N \tag{16}$$

(i) Stage 5: continue with stage 1 if the provided the required is not fulfilled; else, terminate the repetition and display the optimal point

3.4. Modified Whale Optimization Algorithm Design. In this study, the researcher suggested the modified whale optimization algorithm (MWOA). The prototype for MWOA is presented in Algorithm 1, and its flowchart is displayed in Figure 3. In the modified whale optimization algorithm, levy flight is used to increase the computational efficiency and prevent it from slipping into a locally optimal solution too soon [19]. So, to summarize, MWOA initially updates the populations using the core strategy of the classic optimization algorithm.

Then, there is the levy flight, which goes like this. The individuals U_i that has experienced levy variation is produced using Equation (17), and its fitness $f(U_i)$ is determined at the same time.

$$U_i = A_i + \alpha.\text{Levy}(\gamma) \bigoplus (A_i - \text{Lead\_position}). \tag{17}$$

The optimization algorithm in the present inhabitants is chosen as the start position of pattern search after executing levy flight of the overall inhabitants. The optimization algorithm in the present inhabitants is chosen as the start position of pattern search after executing levy flights on the overall population. The pattern search's repetition completion criterion is met to 0.1 times the extreme number of MWOA repetitions, with the outer limits established to standard values [20].

3.5. Time Complexity Analysis. Before examining the suggested technique's temporal intricacy, it must first be classified in the following stages:

(i) Stage 1: Parameter initialization: the generation counter it is initialized, T represent the number of maximum repetitions, L represent the size of inhabitants d represent the dimensionality of the spaced, the searching area edge is defined as $[ib, sb]$

(ii) Stage 2: random whale population initialization

(iii) Stage 3: the fitness of the whale is calculated and the best agent is chosen

(iv) Stage 4: whale update: based on Equations (3)–(15), the whale in the population is updated

(v) Stage 5: if the fitness of U is better than the previous, do a levy flight based on Equation (17) to obtain the variation U, and then upgrade the inhabitants if the fitness of U is better than the original. If one is just outside of the bounds, introduce new whales.

(vi) Stage 6: pattern search: then, upgrade Lead_position if the fitness of the applicant acquired before is greater than that of Lead_position by using the present maximum Lead_position to achieve a pattern search function to create the applicant location and come back if it is over the border

(vii) Stage 7: continue or stop the repetition process: stage 3 to stage 8 is repeated until the exit disorder is met and then get back to Lead_position.

Table 2: SDM result based on different algorithms.

Parameter	Clonal particle swarm optimization	Enhanced Harris Hawks optimization	Local maximal search algorithm	Generalized oppositional teaching learning based optimization	Artificial bee swarm optimization	Chaotic whale optimization algorithm	Levy flight whale optimization algorithm	Modified whale optimization algorithm
I_p	0.7605	0.7612	0.76079	0.760782	0.7609	0.7606	0.7603	0.760773
I_s	0.5	0.3615	0.31850	0.331553	0.30625	0.5045	0.4608	3.24
R_s	0.0355	0.03584	0.03645	0.036265	0.033660	0.0342	0.0350	0.03676
R_{sa}	59.013	53.755	53.32645	54.11545	52.2905	51.4779	75.4619	53.76690
l	1.5034	1.4815	1.47975	1.483825	1.47878	1.52783	1.5177	1.48128
Root mean square error	$1.3901E-03$	$1.0485E-03$	$9.86401E-03$	$9.8744E-04$	$9.9125E-04$	$1.5793E-03$	$1.2353E-03$	$9.8603E-04$

Table 3: Implemented information and related IAE based on MWOA.

Element	Leisurely data		Current information implemented		Power information implemented	
	Voltage	Current	$I_{\text{simulated}}$	$\text{IAE}_I(A)$	$P_{\text{simulated}}$	$\text{IAE}_P(A)$
1	-0.2058	0.7642	0.764082568	$8.25668E-06$	-0.15717179	$1.69840E-05$
2	-0.1292	0.7625	0.762659235	0.006592630	-0.09845932	$8.51067E-05$
3	-0.0589	0.7610	0.761352628	0.000852927	-0.04476754	$5.01346E-06$
4	0.0058	0.7610	0.760152393	0.000347610	0.004332870	$1.98138E-06$
5	0.0645	0.7605	0.759054595	0.009455408	0.049034930	$6.10734E-05$
6	0.1186	0.7592	0.758042628	0.000957376	0.089828055	0.000113450
7	0.1680	0.7573	0.757092745	$9.27410E-06$	0.127040163	$1.55611E-05$
8	0.2135	0.7573	0.755089265	0.000856834	0.161209725	0.000182678
9	0.2925	0.7556	0.753666678	0.000410741	0.192170218	0.000104534
10	0.3270	0.7470	0.751393928	0.000333323	0.220372138	$9.74635E-05$

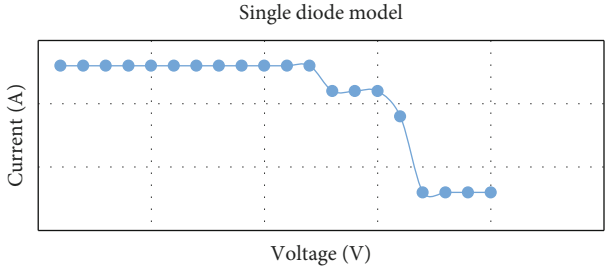

Figure 4: Current-voltage characteristic curve.

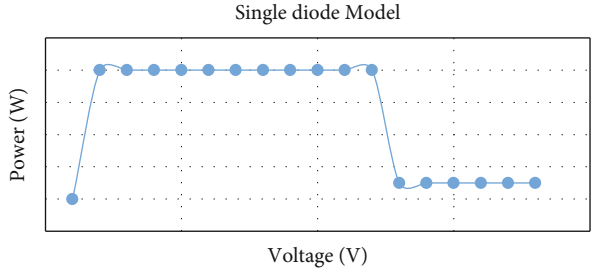

Figure 5: Power-voltage characteristic curve.

4. Result and Analysis

The characterization of solar cell and photovoltaic panel parameters is performed using the various datasets provided in the documentation to validate the functionality of the MWOA. These two sources of information, linked to the RTC solar cell and the PV Photo watt-PWP 201 unit, were extensively used to assess the effectiveness of the new methodologies. The RTC solar cell dataset covers 26 pairs of voltage and current values obtained under standard test settings (34°C, 1000 W/m^{2}powerstrength), whereas the Photo watt-PWP 201 dataset has 26 pairs of measurements obtained under standard operating situations (45°C light concentration).

In this section, MWOA was developed, and each investigation was ended when the number of repetitions (10,000) was reached. Table 1 shows the number of variations to be determined for the SDM, DDM, and PV modules. To verify the significance and durability of MWOA, it was used to determine the parameters for two distinct methods of photovoltaic units: thin-film photovoltaic unit ST40 and monocrystalline silicon photovoltaic unit SM55. Experimental information was acquired from their metadata volume,

Table 4: Comparison of modified whale optimization with three different models.

Design	Technique	Maximum	Minimum	Mean	Standard deviation	Time cost (ms)
Single diode model	MWOA	0.00561032	0.00098610	0.00180882	0.00091695	1309
	LWOA	0.4599370	0.00112372	0.01637348	0.01822289	192
	PSWOA	0.00375843	0.00098645	0.00176644	0.00057629	1285
Double diode model	MWOA	0.0026340	0.00098605	0.00137715	0.00050242	4319
	LWOA	0.04601360	0.00197693	0.00953997	0.01368630	206
	PSWOA	0.00369538	0.00098965	0.00177876	0.00075722	3299
Photovoltaic	MWOA	0.0094305	0.00242788	0.00343323	0.00167525	1818
	LWOA	0.27431198	0.00251423	0.11064790	0.12821915	193
	PSWOA	0.0171528	0.0024509	0.00350585	0.00203755	1694

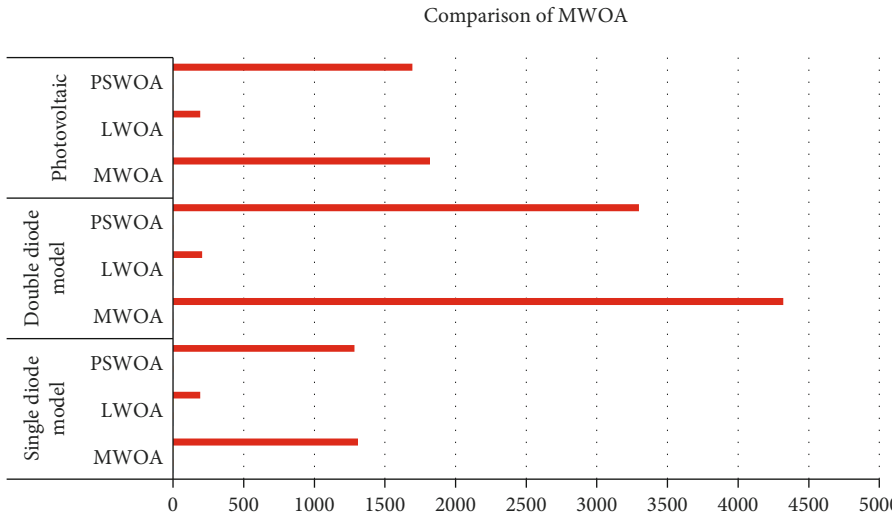

Figure 6: Comparison of the modified whale optimization algorithm.

which included information under various light intensities and temperature and pressure. The maximum repetitions and inhabitants' size were set to 5000 and 30 correspondingly, in this phase of the investigation.

4.1. RTC Solar Cell. The investigational outcomes of MWOA on double- and single-diode solar cells, as well as PV modules, will be detailed in this section. Because some competitive methods perform well on one model, but not for others, they may perform badly on others. As a result, the competitive method chosen for the three variables may vary. Yet, all computation parameters remain constant in the same system to ensure equality.

4.2. Result of SDM. The section presents the results, which include the standards of different variables in RMSE and SDM based on MWOA, as well as the results of the other different algorithms for comparison: ABSO, GOTLBO, LWOA, CPSO, LMSA, EHHO, and CWOA as in Table 2. Table 3 includes the relative errors (REs) and residual error (IAEs) between the experimental and simulated data, the IAE and RE between such information with their definition provided in Equations (18) (1)nd (19), correspondingly, further to reveal the validity of the results. Furthermore, IAE and RE can more naturally assist readers in observing the fault between the actual observed information and the information acquired by the imitation study at each quantity opinion, thereby displaying the suggested individual's efficiency. Figure 4 shows current and voltage characteristics, and Figure 5 shows power-voltage characteristic the best SDM achieved by MWOA.

$$\mathrm{IAE} = |I_{\mathrm{measured}} - I_{\mathrm{simulated}}|, \tag{18}$$

$$\mathrm{RE} = \frac{|I_{\mathrm{measured}} - I_{\mathrm{simulated}}|}{I_{\mathrm{measured}}}. \tag{19}$$

From the foregoing, it is clear that modified whale optimization employs two techniques: levy flight and pattern search. The mean value (mean), standard error (std), minimum (min), and maximum (max) of root mean square error are provided to further demonstrate the significance of these two processes to the suggested approach. Table 4 shows the comparison of modified whale optimization with three different models compares the outcomes of MWOA with variations that solely use one of these processes.

The graphic illustration of comparison is presented in Figure 6. The LWOA is assigned to the approach that only

incorporates levy flight, whereas PSWOA is assigned to the technique that only incorporates pattern search.

5. Conclusion

The unidentified constraints in the best models that characterize solar batteries and photovoltaic units are discovered using a modified whale optimization technique presented in this paper. Combining the levy flying approach with a pattern search tool yields the innovative MWOA method. The current best solution is utilized as the starting point for pattern search by MWOA, which then uses the population update approach of the basic WOA to explore for possible effective alternatives in the domain of this solution. Furthermore, levy flight is utilized to preserve the variety of replies, allowing you to search the entire field. Although MWOA is a population-based probabilistic estimates, it could still experience a community standstill for more complicated datasets. Improving the computational efficiency using other optimization methods is also a worthwhile direction for future research.

Data Availability

The data used to support the findings of this study are included within the article. Further data or information is available from the corresponding author upon request.

Conflicts of Interest

The authors declare that there is no conflict of interest regarding the publication of this paper.

Acknowledgments

The authors thanks AMIT, Arba Minch University, Ethiopia, for providing help during the research and preparation of the manuscript.

References

[1] Y. Fan, P. Wang, A. A. Heidari, H. Chen, and M. Mafarja, "Random reselection particle swarm optimization for optimal design of solar photovoltaic modules," *Energy*, vol. 239, article 121865, 2022.

[2] S. M. Ebrahimi, E. Salahshour, M. Malekzadeh, and F. Gordillo, "Parameters identification of PV solar cells and modules using flexible particle swarm optimization algorithm," *Energy*, vol. 179, pp. 358–372, 2019.

[3] A. A. El-Fergany, "Parameters identification of PV model using improved slime mould optimizer and Lambert W-function," *Energy Reports*, vol. 7, pp. 875–887, 2021.

[4] M. H. Qais, H. M. Hasanien, and S. Alghuwainem, "Parameters extraction of three-diode photovoltaic model using computation and Harris Hawks optimization," *Energy*, vol. 195, p. 117040, 2020.

[5] D. Allam, D. A. Yousri, and M. B. Eteiba, "Parameters extraction of the three diode model for the multi-crystalline solar cell/module using moth-flame optimization algorithm," *Energy Conversion and Management*, vol. 123, pp. 535–548, 2016.

[6] M. Ye, X. Wang, and Y. Xu, "Parameter extraction of solar cells using particle swarm optimization," *Journal of Applied Physics*, vol. 105, no. 9, 2009.

[7] M. H. Hassan, S. Kamel, M. A. El-Dabah, and H. Rezk, "A novel solution methodology based on a modified gradient-based optimizer for parameter estimation of photovoltaic models," *Electronics*, vol. 10, no. 4, article 472, 2021.

[8] H. V. Hultmann Ayala, Coelho, Mariani, and Askarzadeh, "An improved free search differential evolution algorithm: a case study on parameters identification of one diode equivalent circuit of a solar cell module," *Energy*, vol. 93, pp. 1515–1522, 2015.

[9] D. Oliva, E. Cuevas, and G. Pajares, "Parameter identification of solar cells using artificial bee colony optimization," *Energy*, vol. 72, pp. 93–102, 2014.

[10] Z. Wu, Z. Xie, and C. Liu, "An improved lion swarm optimization for parameters identification of photovoltaic cell models," *Transactions of the Institute of Measurement and Control*, vol. 42, no. 6, pp. 1191–1203, 2020.

[11] G. Xiong, J. Zhang, D. Shi, and Y. He, "Parameter extraction of solar photovoltaic models using an improved whale optimization algorithm," *Energy Conversion and Management*, vol. 174, pp. 388–405, 2018.

[12] D. Gallo, C. Landi, M. Luiso, and R. Morello, "Optimization of experimental model parameter identification for energy storage systems," *Energies*, vol. 6, no. 9, pp. 4572–4590, 2013.

[13] A. Abbassi, R. Abbassi, A. A. Heidari et al., "Parameters identification of photovoltaic cell models using enhanced exploratory salp chains-based approach," *Energy*, vol. 198, p. 117333, 2020.

[14] Y.-P. Huang, X. Chen, and C.-E. Ye, "A hybrid maximum power point tracking approach for photovoltaic systems under partial shading conditions using a modified genetic algorithm and the firefly algorithm," *International Journal of Photoenergy*, vol. 2018, 13 pages, 2018.

[15] W. Hou, Y. Jin, C. Zhu, and G. Li, "A novel maximum power point tracking algorithm based on glowworm swarm optimization for photovoltaic systems," *International Journal of Photoenergy*, vol. 2016, 9 pages, 2016.

[16] W.-z. Sun, J.-s. Wang, and X. Wei, "An improved whale optimization algorithm based on different searching paths and perceptual disturbance," *Symmetry*, vol. 10, no. 6, article 210, 2018.

[17] S. Motahhir, A. El Ghzizal, S. Sebti, and A. Derouich, "Modeling of photovoltaic system with modified incremental conductance algorithm for fast changes of irradiance," *International Journal of Photoenergy*, vol. 2018, 13 pages, 2018.

[18] G. Xiong, J. Zhang, D. Shi, L. Zhu, X. Yuan, and G. Yao, "Modified search strategies assisted crossover whale optimization algorithm with selection operator for parameter extraction of solar photovoltaic models," *Remote Sensing*, vol. 11, no. 23, article 2795, 2019.

[19] X. Ye, W. Liu, H. Li et al., "Modified whale optimization algorithm for solar cell and PV module parameter identification," *Complexity*, vol. 2021, 23 pages, 2021.

[20] N. Onat, "Recent developments in maximum power point tracking technologies for photovoltaic systems," *International Journal of Photoenergy*, vol. 2010, 11 pages, 2010.

Hindawi
International Journal of Photoenergy
Volume 2022, Article ID 7756261, 10 pages
https://doi.org/10.1155/2022/7756261

Research Article

Optimization of Solar Hybrid Power Generation Using Conductance-Fuzzy Dual-Mode Control Method

S. Ramesh,[1] **J. Seetha**,[2] **G. Ramkumar**,[3] **Satyajeet Sahoo**,[4] **T. M. Amirthalakshmi**,[5] **A. Ranjith**,[6] **Asiful H. Seikh**,[7] **Sohail M. A. Khan Mohammed**,[8] **and Ram Subbiah**[9]

[1]*Department of Electronics and Communication Engineering, St. Mother Theresa College of Engineering, Vagaikulam-628102 Tamilnadu, India*
[2]*Department of Computer Science, SRM Institute of Science And Technology, Ramapuram, Chennai-600 089, Tamil Nadu, India*
[3]*Department of Electronics and Communication Engineering, Saveetha School of Engineering, SIMATS, Chennai 602 105, Tamil Nadu, India*
[4]*Department of Electronics and Communication Engineering, Vignan's Foundation for Science, Technology and Research (Deemed to be University), Vadlamudi, Guntur, Andra Pradesh-522213, India*
[5]*Department of Electronics and Communication Engineering, SRM Institute of Science And Technology, Ramapuram, Chennai-600 089, Tamil Nadu, India*
[6]*Department of Electronics and Communication Engineering, St.Joseph University in Tanzania, Dar es Salaam, Tanzania*
[7]*Department of Mechanical Engineering, College of Engineering, King Saud University, P.O. Box 800, Al-Riyadh 11421, Saudi Arabia*
[8]*Department of Mechanical and Industrial Engineering, Ryerson University, Toronto, M5B 2K3, Ontario, Canada*
[9]*Department of Mechanical Engineering, Gokaraju Rangaraju Institute of Engineering and Technology, 500090, Nizampet, Hyderabad, India*

Correspondence should be addressed to S. Ramesh; ramembengineer@gmail.com and A. Ranjith; ranjith.arumugam@sjuit.ac.tz

Received 2 February 2022; Revised 15 February 2022; Accepted 19 February 2022; Published 13 April 2022

Academic Editor: V. Mohanavel

Copyright © 2022 S. Ramesh et al. This is an open access article distributed under the Creative Commons Attribution License, which permits unrestricted use, distribution, and reproduction in any medium, provided the original work is properly cited.

The functioning of a solar hybrid power system is investigated in this research using a unique fuzzy control method. Turbines, solar photovoltaics, diesel engines, fuel cells, aqua-electrolyzes, and other autonomous generation products are used in the hybrid renewable energy system. Further energy storage components of the system include the batteries, turbine, and ultracapacitor. This research incorporates a supercapacitor hybrid energy storage system (HESS) into a solar hybrid power generating system, allowing the consumption and energy storage space and power output to be significantly increased. This study's approach incorporates a decentralized power generation system with a HESS while increasing electrical output in phases utilizing a dynamic reactive power compensation scheme and a conductance-fuzzy dual-mode control strategy. Due to a nonlinear behavior of photovoltaic (PV) devices' power output, maximum power point tracking (MPPT) methods must be used to create the greatest power. Infrequently developing atmospheric circumstances, traditional MPPT algorithms do not work adequately. Modeling is used to determine the microgrid's power output to the photovoltaic hybrid power generating organization, as well as the optimization method for each device in the network. The dynamic power factor correction scheme and also the conductance-fuzzy dual-mode control approach are primarily used in this study to optimize the solar hybrid renewable energy system.

1. Introduction

Energy plays a significant role in everyday life, but as the world's population and economic growth grow, so does the demand for it. As the cost of electricity use rises and supply drops, fossil fuel-based energy sources deplete, leading to energy loss [1]. The depletion of oil supplies connected to coal or natural gas-fired power plants is motivating

professionals to look for alternate and ecological sources of energy. However, because the energy industry produces the majority of greenhouse gas emissions, there seems to be a significant link between energy strategy and environmental policy. The usage of sustainable power, often known as the common squares, is a crucial approach for reducing carbon emissions [2]. Synergy around them is a critical element in building energy industry emission reduction paths. Because they are well, it could solve greenhouse gas emission decreases and grid adaptability at the same time. To preserve system reliability, renewable energy can improve power generation including such extra capacity or physical and rotating energies. However, because the grid is the source of electricity for nuclear plants' offsite power systems, international norms emphasizing the need for nuclear plants have yet to be merged. The capability to provide a dependable supply having adequate resources and voltage quality is the fundamental goal of such a connection. This is a result of a variety of factors. With the widespread and widespread use of solar HESS, the influence on the network by these systems cannot be overlooked [3]. The maximum power of solar combined energy storage devices may change arbitrarily and sporadically due to inapplicability and uncertainty. As a result, as compared to traditional power generators like nuclear and coal-fired power plants, renewables can be difficult to distribute on the network [4]. Dispatchable energy storage is used because the power production of a solar ESS has to be as constant as possible. This uses a supercapacitor and battery to create storage of battery in this research. To enhance energy conversion efficiency, an MPPT employs fuzzy set theory. To operate the step-up conversion for MPPT, a fuzzy procedure depends on 25 linguistic variables characterizing the operator's control approach which was used. FLC with coarse and fine modes is used to decrease not just the time it takes to track the MPP, as well as the energy fluctuations. The proposed algorithm requires more memory and does not have the capacity to self-tune. To get the most power out of a solar array, an appropriate MPPT control system with fuzzy control is designed. A modest number of rules are used in the fuzzy system [5]. As a result, this control mechanism is simple to apply to a real-world system. For its effortlessness and ease of application, the perturbation and observation (P&O) approach is a popular MPPT methodology. Unfortunately, this technique produces a lot of variations around the maximum power point (MPP), which leads to a lot of energy loss, particularly in big PV systems. To solve these issues, incremental conductance (INC) approach was devised [6]. This approach employs constant data steps, allowing the MPP to be tracked by comparing the ratio of measured voltage to INC levels of photovoltaic systems power. The development of an appropriate regulator for MPPT has subsequently gotten a lot of attention. For the functioning of the PV-based hybrid energy system, the P&O approach was presented, and theoretically calculated results have been compared [7]. The proposed fuzzy method was utilized to compare several MPPT approaches of frequently used systems such as P&O and INC. Two MPPT approaches, namely, application of fuzzy and neural control systems were described, with the effectiveness of the suggested techniques evaluated. In PV arrays, an INC approach was utilized for MPPT [8]. It was proposed to employ the particle swarm optimization (PSO) technology in a novel MPPT strategy. These technologies control PV arrays with only one pair of sensors, resulting in lower costs, improved overall performance, and ease of deployment. These approaches, on the other hand, do not work well in quickly changing environmental circumstances. To allow the operating point to be nearer to the MPP and minimize oscillations at the maximum power output, the fuzzy control scheme with conductance progressive algorithm is coupled. Furthermore, the maximum power monitoring of a photovoltaic solar device is achieved by combining the conductance increment approach and an enhanced fuzzy control strategy [9]. A thorough design of solar combination energy storage devices comprising a supercapacitor and a battery-integrated energy storage device is proposed in this work. To begin, the battery energy storage program's output power was optimized using a hybrid particle swarm optimization (HPSO) and maximum power point tracking (MPPT) fuzzy-based method [10]. Then, to evaluate the effective accuracy of the solar power source, a simulation result framework has been developed. In terms of energy forecasting, the optimized system is adaptable. The grid-connected solar HESS can be fully utilized solar energies' natural redundancy [11]. The conductance-fuzzy dual-mode control technique also improves productivity of power curve monitoring and dispatched grid curves. Energy saving unit prices have dropped significantly. In addition, it has improved financially and environmentally.

2. Related Works

The investigation of efficiency in partial shade conditions is a vital aspect of a solar photovoltaic (PV) system. A resilient intelligence algorithm (RIA) is being developed in cooperation with the internet of things (IoT) to provide real-time management of solar panels, providing worldwide maximum power point tracking (MPPT). The RIA is made up of a radial basis function (RBF) multilayer perceptron with limited-time terminal sliding-mode control (LTTSMC) and quantum particle swarm optimization (QPSO) neural network. The LTTSMC provides for the avoiding of singularities by allowing for a rapid constrained convergence time. The trembling phenomena or fairly constant error, on the other hand, happens around the LTTSMC if system ambiguity is exaggerated or undervalued. To address plant component fluctuations and external load disturbances, the QPSO-RBF communication system is implemented into LTTSMC, decreasing trembling and steady-state faults. Monitoring equipment in the solar panel system delivers convergence speed to fractional integral points thanks to the combination of the RIA as well as the IoT, but it also provides a neural network approach for even more precise ambiguity estimate. Below passing and steady-state dynamic load, experimental results demonstrated the arithmetical performance evaluation improvement of a sample encryption method solar PV system that depends on digital signal processing. Because the suggested solar power system has

significant tracking performance and robust adaption benefits over traditional terminal-sliding photovoltaic panels, this research should be read by developers of comparative controller design and neural network optimization models [12]. This work presents a novel fuzzy adaptive proportional-integral-derivative (PID) control approach for MPPT in a solar photovoltaic system with continuous set-point monitoring. The relay feedback tuning approach was used to optimize the scope of the attribute values of the fuzzy systems for a continuous PID parameter tuner. Utilizing power, light, and temperature monitoring, the suggested MPPT controller has indeed been constructed which included an online set-point modification technique. For a solar power system including buck-boost converter and load resistance, real-time computations were done on the $MATLAB^{TM}/dSPACE^{TM}$ ds1104 Research and Innovation central control architecture. The suggested methods' performance is in comparison to that of the most widely used MPPT techniques. MPPT approaches are based on perturbing and observation, constant voltage, fuzzy control, Bayesian network, and adaptable neuro-fuzzy inference engine. The tracking effectiveness, time constant, and dynamic characteristics of several approaches have been examined. The proposed method outperformed others in terms of usability maximum power point with rapidly shifting sun radiation, according to the results obtained [13]. This work proposes a novel PV module modeling technique in Simulink using a fuzzy logic-based MPPT algorithm and a power convertor. The work's major components are the reduction of PV modeling techniques and the construction of a fuzzy-based MPPT system to accurately way maximum output. The key highlights of this work are the demonstration of exact duty cycle regulation under varied climatic circumstances, depiction of PV characteristic curves, and conversion methodology uses. Three distinct PV modules have been tested with the proposed system: SOLKAR 36 W, BP MSX 60 W, and KC85T 87 W. Finally, the obtained data was estimated by the following forecast and the number provided by the employer to verify the system's accuracy [14]. A wind-hybrid power system with storage of battery and a dump load is modeled and controlled in this study. The Takagi– Sugeno (TS) fuzzy model, as well as the linear controller, is used in the suggested control method. The local behaviors of a nonlinear function separated into sectors by grammatical rules are expressed by the TS fuzzy model. Based on the given time-series data, a potential autoregression model is proposed that offers ideally divided subsystems. The linear quadratic regulation creates the regulators for each component. The suggested controller is evaluated to a traditional proportional-integral controller in such an experiment and demonstrated to be more successful over disruptions induced by weather conditions and strain fluctuations [15]. The modeling of an interconnected hybrid renewable energy system is described in this paper. Creative product for such hybrid power system includes solar and wind. Photovoltaic (PV) and hybrid renewable energy systems are designed as part of the proposed network. The system is built to withstand continuous wind speeds as well as changes in solar irradiance and solar output. To obtain the most power from such a PV array, the maximum power point tracking (MPPT) technique is utilized. An intermediate outcome (MI) *cuk* conversion is used to combine two input sources. To obtain the maximum power output array, a fuzzy logic controller is employed to adjust the switching frequency of the bidirectional converters [16].

3. Materials and Methods

The system construction of a solar HESS is introduced in this section. In addition, numerical simulations for solar cells, solar farms, supercapacitors, transformer power density, and conversion are provided.

3.1. Structure of System. The design of the solar hybrid renewable energy method is illustrated in Figure 1, as well as converters, DC and AC buses, a PV array, and a combined power system buildup the network. The decentralized power generating system provides electrical energy, which travels along the DC bus to a converter, where it is transformed into an electrical current [17]. Hybrid energy storage systems control objective is to guarantee that demand and network receive extremely steady electricity generation from the power-producing systems.

3.2. A Mathematical Model for Photovoltaic System. In a solar power system, the Photovoltaic system has been the most basic component. Its process is equivalent to that of a P–N junction. The photovoltaic cell production power dynamic is as follows:

$$P = IV = \left(I_{ph} - I_d - I_{sh}\right)V = \left[I_{ph} - I_o e^{\left(\left(V+\frac{IR_s}{A}\right)\right)} - I_o - \frac{(V + IR_s)}{R_{sh}}\right], \tag{1}$$

where I is the discharge current in this calculation. In this similar circuit, Id is the current of the diodes. The current twisted by the PV panel is referred to as the I_{ph}. The current flow remains represented by I_{sh} by the parallel connection. The optimal parameter for the P–N connection is A [18]. The load's reference voltage is denoted by the letter V. The load impedance is R_S. Because R_{sh} is infinite large and R_S is incredibly tiny, this expression can be reduced as follows:

$$P = IV = \left[I_{ph} - I_o e^{((V+IR_s)lA)} - I_o\right]V. \tag{2}$$

A single maximum output power point will arise under the influence of various factors.

3.3. Supercapacitors Mathematical Model. In this study, capacitive constants and voltage relate to both edges of the capacitors, and W in the equivalent circuit reflects the supercapacitor energy transfer (ΔW is the integration of $P_c(t)$

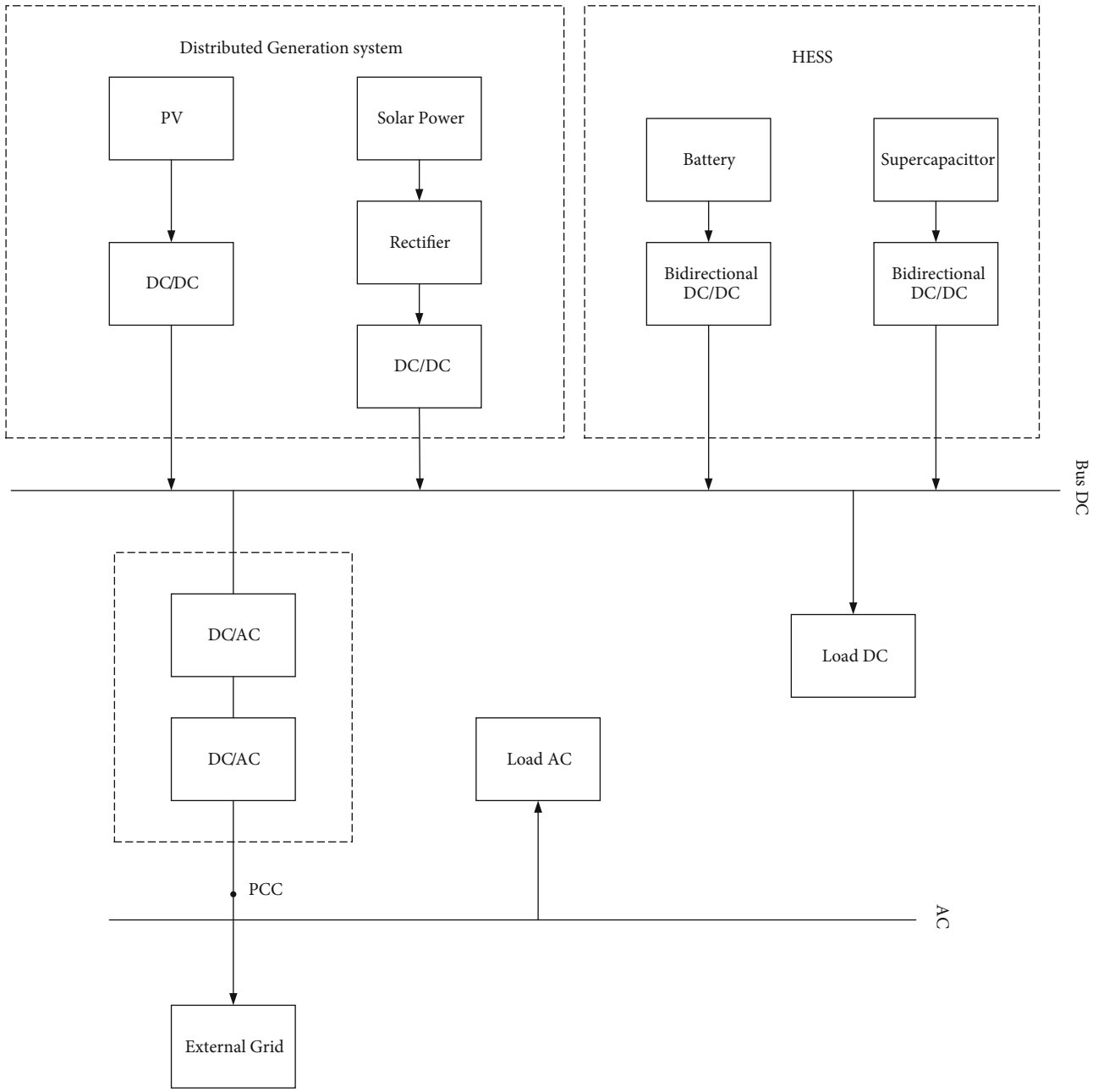

Figure 1: The grid-connected solar hybrid renewable energy production method is depicted in this diagram.

with t) inside the interval $[t(n-1), t(n+1)]$. The capacitor's interaction energy is as follows:

$$\Delta W = \frac{1}{2}U_c^2(t_{n+1}).C(t_{n+1}) - \frac{1}{2}U_c^2(t_{n-1}).C(t_{n-1}) = \int_{I_{n-1}}^{I_{n+1}} P_c(t)\mathrm{dt}. \tag{3}$$

The capacitor voltage is $u_c(t)$. The capacitor's resistance is R_S. The capacitor's determined function is calculated as $c(t)$. The resistance voltage in the series is $u_s(t)$ [19]. The total simultaneous power and the simultaneous energy of the resistor, as shown in Figure 2, are used to represent the capacitor's maximum voltage:

$$P_c(t) = u(t).i(t) - i^2(t) - R_s. \tag{4}$$

The series resistance is R_S, the current flow through capacitance is $i(t)$, and the load demand is $u(t)$. Simpson's Formula is used to determine the integrating.

$$\Delta W = \frac{1}{2}[u_c(t_{n+1}) - R_s i(t_{n+1})]^2.C(t_{n+1}) - \frac{1}{2} \cdot [u_c(t_{n-1}) - R_s i(t_{n-1})]^2.C(t_{n-1}). \tag{5}$$

3.4. Inverter Mathematical Model. The energy on the demand is mostly inverted energy from the battery [20]. The inverter's maximum output is P_{out}, and also the input

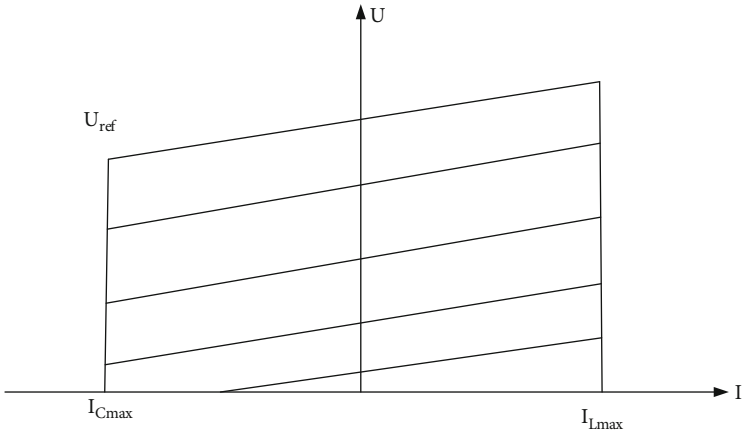

Figure 2: Characteristics of V-I.

power is P_{in}. Thus, the performance which was determined is given as

$$\eta = \frac{P_{out}}{P_{in}} \tag{6}$$

The power input is equal to the power output then the power gets lost as

$$P_{in} = P_{out} + P_{loss} = P_o + K_p^2 \tag{7}$$

Thus, obtain

$$\eta = \frac{P}{P + P_o + K_p^2} = 1 - \frac{P_o + K_p^2}{P + P_o + K_p^2} \tag{8}$$

The expression formula for P_o with k is $p = P_{out}/P_{in}$ (p is inverters and P_{in} is the total energy of inverters); in the earlier calculation for P_o with k as

$$P_o = \frac{9}{11}\left(\frac{10}{9\eta_{10}} - \frac{1}{9\eta_{100}} - 1\right)^2. \tag{9}$$

At η_{10}voltage, the inverter's effectiveness is 10%, and at 100% voltage, the inverter's effectiveness is η_{100}. The continuity formula gives these requirements.

$$k = \frac{1}{\eta_{100}} - p_0 - 1 \tag{10}$$

3.5. Converter Mathematical Models. Power can be converted from an AC bus to a DC bus using converters. Inverting is indicated by a positive integer while rectifying is indicated by a negative sign. R_{rec} represents the maximum electricity while a rectifier is trying to rectify [21], which would be the valued capacity. $P_{con,DC}$ defined as the total electricity upon that Dc link.

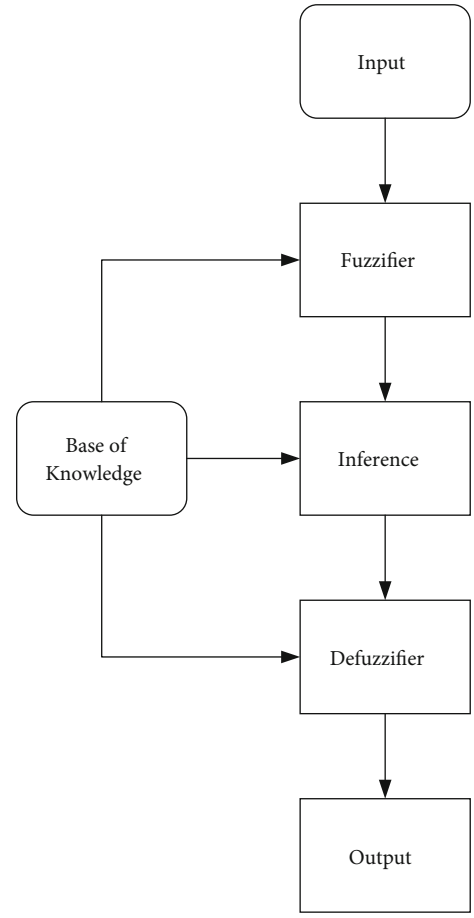

Figure 3: Construction of fuzzy controller scheme.

4. Fuzzy Logic MPPT Control Technique

FLC has already been widely utilized for commercial processes since it does not demand an immediate solution and can handle nonlinearities [22]. As shown in Figure 3, FLC is divided into four areas: the fuzzifier, the level of knowledge, the inference system, and also the defuzzifier.

The error (r) and change of error (Δr) are the two parameters of an MPPT-based FLC, but one productivity is the variation in duty cycle $(\bar{d})$ in two techniques or variation in a DC-link voltage $(\bar{v}_{dcref})$ in even a single-stage system. The productivity of a fuzzy logic system was subsequently combined towards to create an input signal $(d \text{ or } v_{dcref})$. At the kth sampling time, r and Δr are described as follows:

$$r(h) = \frac{\Delta p_{pv}}{\Delta v_{pv}} = \frac{P_{pv}(K) - P_{pv}(K-1)}{v_{pv}(K) - v_{pv}(k-1)}, \Delta r = r(h) - r(h-1). \tag{11}$$

Every fuzzy parameter in the input and output has three of linguistic attributes: False rate, True rate, and zero. As seen in Figure 4, each linguistic model is defined by a

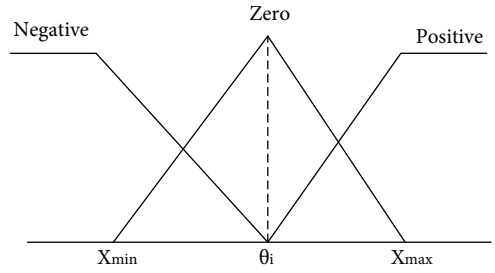

Figure 4: Membership functions.

Table 1: Two-stage scheme of fuzzy rules.

r		Δr	
	False rate	*Zero*	*True rate*
Zero	*True rate*	*Zero*	*False rate*
False rate	*True rate*	*True rate*	*True rate*
True rate	*Zero*	*False rate*	*False rate*

Table 2: Fuzzy rules.

r		Δr	
	False rate	*Zero*	*True rate*
Zero	*False rate*	*Zero*	*True rate*
False rate	*False rate*	*False rate*	*Zero*
True rate	*Zero*	*True rate*	*True rate*

triangle basis function. The input and output signals' maximum and minimum variations are represented by the parameters X_{maz} and $X_{\min}$. These settings are chosen and obtained from the simulation data or an optimization algorithm. To represent the real signal, let $X_{maz} = -X_{\min}$ and the spectrum of each fuzzy variable be normalized between 1 and +1 by providing a scaling factor $(k = 1/X_{maz})$.

The reaction of input parameters under various environmental situations is used to estimate the minimum and maximum values.

The fuzzy controller is represented using symmetrical fuzzy rule set, as shown in Tables 1 and 2. The proper sharp management is then constructed using the center of mass defuzzification. Let θ_i denote the coordinates of the result variable's ith membership degree. As a result, for h parameters, the fuzzy state's output is calculated as follows:

$$\overline{d}, \overline{v}_{\mathrm{dc}} = \frac{\sum_1^h \omega_i \theta_i}{\sum_1^h \omega_i} = \underline{\theta^T} \tau \tag{12}$$

where $\tau_i = \omega_i / \sum_1^h \omega_i$, and ω_i is the power of the ith rule. It is generated by reading the "AND" combination as a sum of the participation values in comparison to e and Δe field measurements.

4.1. Proposed MPPT Controller. Step 1. Describe the input and output scaling factors

Step 2. Specify the perturbation time

Step 3. Define the rules of the fuzzy regulator as shown in Tables 1 and 2

Step 4. Specify the parameter $(K_1, K_2, \cdots, K_{n.})$

Step 5. Use the simulation to tune p_2

Step 6. Validate the equation as Lyapunov is fulfilled: $P\Lambda + \Lambda_C^T P < 0$

Step 7. Determine the vertices of the membership functions values using the adaptation rule.

Step 8. Step size is calculated

Step 9. The MPPT control output is given as $u(K) = u(k-1) + \tilde{u}(k)$ where u is represented by d or v_{dcref}.

4.2. The Conductance-Fuzzy Dual-Mode Controlling Techniques. MPPT optimizing has been improved. The basic premise of the conductance increase approach employing the particle swarm optimization algorithm is initially introduced in this section [23]. Secondly, a short explanation of the fuzzy control algorithm is described. Furthermore, a conductance-fuzzy dual-mode control approach with increased conductance is created.

4.2.1. The Conductance Increment Technique's Fundamental Concept. Particle swarm optimization algorithm is used. The classic conductance enhancement approach works based on a feature of the photovoltaic cell itself, which does not emit any light fluctuate in response to external environmental changes, and after establishing a stable condition, volatility is minimal [24]. The renewable characteristic curve is used to determine whether or not something is true. The particle swarm optimization algorithm works on the following scheme: Assume a K-dimensional search process with n particles. The place and speed of the No.i particle is $x_i = (x_1^i, x_2^i, \cdots, x_k^i)$, $V_i = (V_1^i, V_2^i, \cdots, V_k^i)$. The photon's speed and position also are changed as per (13) and (14).

$$V_k^{j+1} = \rho v_k^i + \theta_1 \mathrm{rend} \frac{P_k^i - X_k^i}{\Delta t} + \theta_2 \mathrm{rend} \frac{P_k^g - X_k^i}{\Delta t}, \tag{13}$$

$$X_k^{j+1} = X_k^i + \mathrm{v}_\mathrm{k}^{\mathrm{j+1}}, \tag{14}$$

where p_{ik} represents the optimal location of a $i-th$ particle during period k, p_{gk} represents the optimal place of the group particle k, ρ is a inertia factor, $\theta 1$ represents the resident assurance factor, and $\theta 2$ represents the component collective's self-confidence variable. The HPSO algorithm's workflow entails employing the neural network's expected power output as a particle swarm and then applying the PSO method to solve inverter substituting at the maximum power point.

The enhanced conductance increment technique depends on the particle swarm optimization algorithm which adjusts the conductance increase product's step length describing the relationship among particle separation and its minimal thresholds to monitor the program's maximum power output

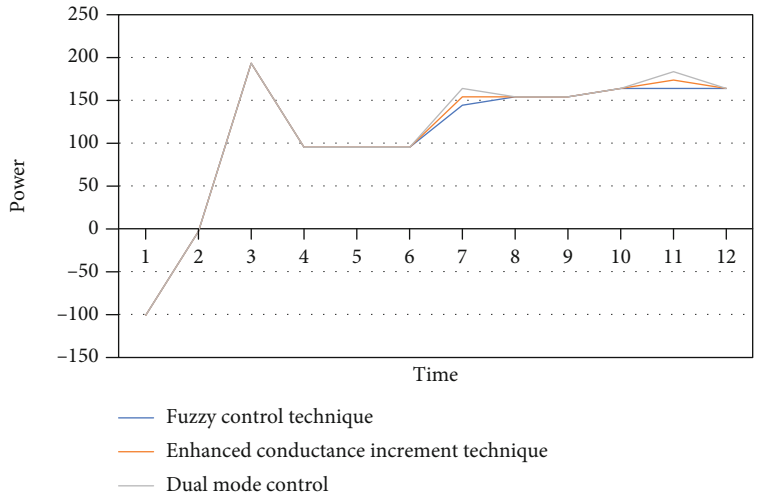

Figure 5: When the environment changes, the balance of power fluctuates.

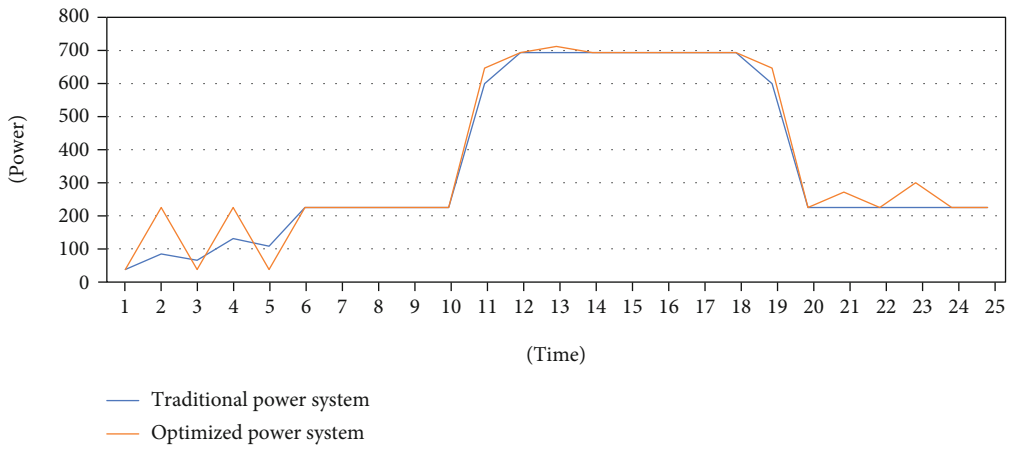

Figure 6: The power output of traditional and optimized power systems is compared.

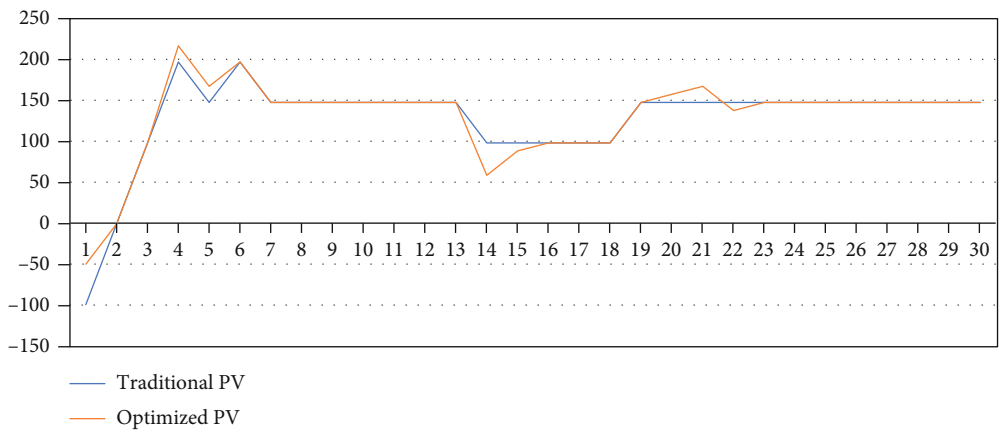

Figure 7: The power output of traditional and optimized PV generated is compared.

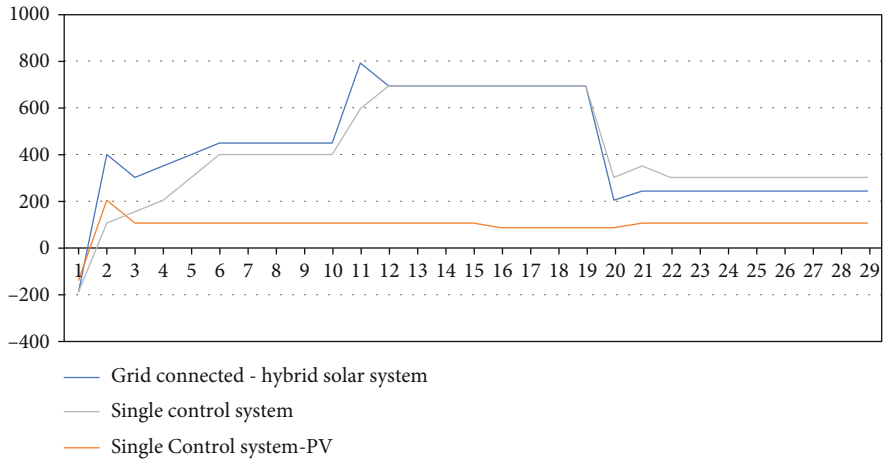

Figure 8: The output power of single-generator systems versus grid-connected solar power systems is compared.

Table 3: Initial rule.

r	Δr		
	False rate	Zero	*True rate*
False rate	0.6	0.6	0
Zero	0.6	0	−0.6
True rate	0	−0.6	−0.6

5. Algorithm of Fuzzy Control

Fuzzy control is a controller that is built based on user interaction. It is not essential to progress a mathematical model. The unique control flow idea is that by entering the quantity and individual characteristics and then choosing the suitable one, the operator's membership function and developing customized are determined [25]. The control strategy has been approved, and the management has been accomplished. The data redundancy of the fuzzy control method can be quite high because it does not demand a precise computational formula. The fuzzy analysis process, on the other hand, causes a reduction in control system accuracy and dynamical efficiency.

5.1. Enhanced Conductance-Fuzzy Dual-Mode Control Techniques. Assuming that such a simple particle swarm optimization (PSO) conductivity increases technique or a fuzzy technique neither assures control system precision or duration to a time constant, the MPPT mixed control approach is presented. The PSO technique was being utilized to improve the system's output voltage characteristic curve worldwide, and the control algorithm is utilized to improve the system's power output curves locally by changing the scale factor in the conductance augmentation process [26]. Whenever the E value is low and the system response is closer to peak power, the fuzzy controller produces a lower period size to increase steady-state precision. The E value increases as the range from the maximum power point increases, and also the fuzzy controller generates a higher scale factor to accomplish maximum power point tracking.

5.2. Environmental Parameters of Linear Variation. Suppose that such environmental variables would not drastically change. As a result, the study's accepted is an increase in the intensity of light after 600 W/m^2 to 1000 W/m^2. The conductivity increment method of particle swarm optimization, the conductance of fuzzy hybrid control method, and the fuzzy control strategy are all modeled. The outcome is depicted in Figure 5. As shown in Figure 5, all three algorithms are capable of improving the power quality in any situation [27]. If the corrected or lose situation seems to have no influence on the outcomes, the conductance-fuzzy dual-mode controller strategy T and ΔT developed in this work have various degrees of decrease compared to the traditional fuzzy control approach, and the duration for getting the optimum power point is reduced significantly. Compared to the particle swarm optimization technique, the enhanced conductance-fuzzy dual-mode control method produces a quicker steady-state rate and increased benefits are realized.

6. Result and Discussion

A model of the massive amount condition of the solar grid-connected complementing system is created to verify the capability and efficiency of the suggested control approach. The following are the variables for the solar array and boost compressor circuits in the simulation: The solar array lighting intensity is decreased from 1000 W/m^2 to 600 W/m^2 before being adjusted to 800 W/m^2, while the rapidity increases from 8$m/s$to 10m/s before being lowered to 8m/s. The upstream and downstream capacitors of the course are 500μF, the inductor is 5 mH, and the load is 25Ω.

The optimized photovoltaic power systems, as well as the power generating system, reach a stable level faster than the traditional generation system, as shown in Figures 6 and 7. Because the variation is reduced, the improved system monitoring is more precise and quicker. The optimized solar complementing is capable of tracking the excessive value for particular energy and achieves the stable equilibrium

for roughly 0.16 s whenever the initial luminous power is $1000\,W/m^2$ and the air velocity is $8\,m/s$, as shown in Figure 8. To obtain a stable level, the photovoltaic systems must be controlled for about 0.05 seconds. Traditional solar systems take about 0.115 seconds to achieve a stable level, but their tracking error is about 0.23%, while the latter two's uncertainty is 1-2 times that of the earlier.

At this point, the solar complementing system's power output has a greater steady-state period but much less curved variability. The atmospheric air frequency is higher from $8\,m/s$ to $10\,m/s$ after 0.3 secs. At about the same time, the levels of variability in the power output levels of the two devices are different. The optimum solar complementing method carries about 0.073 secs to return to steady-state. The curvature variability is reduced and the found significant effect is faster. The classic power generation system takes 0.09 secs to achieve stable equilibrium, and the curve is highly variable. The different lighting brightness is lowered from $1000\,W/m^2$ to $600\,W/m^2$ after 0.6 secs. The time necessary for a solar complementing process to the obtain a steady state during optimizing is around 0.05 s. The duration is around 0.089 secs, and the following inaccuracy is 400% larger than the optimal solar complementing system. The output current waveforms of the two have different variations. Using traditional optimization photovoltaic panels and traditional control, the different lighting strength is enhanced from $600\,W/m^2$ to $800\,W/m^2$, the speed will decrease from $10\,m/s$ to $8\,m/s$, and the time necessary for the solar complementing organization to achieve steady-state is improved. The time it takes for power to achieve a steady-state is similar, but the original's production curve changes significantly less than that of the latter two. The fuzzy control initial rule is given in Table 3. The critical values of e and Δe are shown to improve as solar radiation and modules increased temperature.

The power output curves of the solar complementing achieving significant improvements get gentler as the optimization level develops, according to the entire monitoring stage, that is, twice of a conventional controller solar panel and one-third of a traditional authentication photovoltaic panel. When compared to the other two single-power generating systems, the complementary system's general proficiency time can be enhanced by almost 90%. As a result, the solar complementing system's optimal performance is superior.

7. Conclusion

To handle the issue of reducing emissions and climate change at the same time, it is suggested that such a proportion of the grid's supplies be atomic and renewable in the future. To be effectively safe, fission plants need a reliable and stable network, which necessitates improved advantages of renewable energy sources, particularly solar PV systems. Under varied light intensities, the particles cluster optimization conductance increment method, conductivity-fuzzy dual-mode controller, and standard fuzzy controller are modeled. The results suggest which the conductivity fuzzy dual-mode proposed controller could reach a stable level faster and more accurately than other methods. Furthermore, the algorithm extends battery performance and lowers power usage. Whenever the power distribution model of a photovoltaic power generation system is only used, the demand fluctuation causes inadequate power sources, according to the findings. The local power distribution model is verified by the integration of a hybrid energy storage system (HESS) and a solar complementing power scheme. This control distribution style is among the most effective strategies to assure legal compliance because it supports various sources of energy. Combining advanced algorithms only with MPPT as in the future is a promising avenue for achieving great precision and knowledge.

Data Availability

The data used to support the findings of this study are included within the article.

Conflicts of Interest

The authors declare that there is no conflict of interest regarding the publication of this article.

Acknowledgments

The authors would like to express their gratitude towards St. Mother Theresa College of Engineering, Vagaikulam-628102, Tamilnadu, India for providing the necessary infrastructure to carry out this work successfully. The authors would like to acknowledge the Researchers Supporting Project Number (RSP-2021/373), King Saud University, Riyadh, Saudi Arabia.

References

[1] N. Bigdeli, "Optimal management of hybrid _PV_ /fuel cell/ battery power system: a comparison of optimal hybrid approaches," *Renewable and Sustainable Energy Reviews*, vol. 42, pp. 377–393, 2015.

[2] E. Kandemir, S. Borekci, and N. S. Cetin, "Conventional and soft-computing based MPPT methods comparisons in direct and indirect modes for single stage PV systems," *Elektronika ir Elektrotechnika*, vol. 24, no. 4, pp. 45–52, 2018.

[3] G. Ramkumar, "A short-term solar photovoltaic power optimized prediction interval model based on FOS-ELM algorithm," *International Journal of Photoenergy*, vol. 2021, Article ID 3981456, 202112 pages.

[4] K. Walid, M. Sofiane, and G. Hamza, "Fuzzy logic control to track the maximum power for photovoltaic system," in *in International Conference on Artificial Intelligence in Renewable Energetic Systems*, pp. 277–284, Tipasa, Algeria, November 2021.

[5] Y. Zhang, H. Sun, and Y. Guo, "Research on maximum power point tracking method of photovoltaic power generation," *Journal of Intelligent & Fuzzy Systems*, vol. 37, no. 3, pp. 3149–3162, 2019.

[6] D. Karanjkar, S. Chatterji, and A. Kumar, "Design and implementation of a linear quadratic regulator based maximum power point tracker for solar photo-voltaic system,"

International Journal of Hybrid Information Technology, vol. 7, no. 1, pp. 167–182, 2014.

[7] Amirthalakshmi, "A novel approach in hybrid energy storage system for maximizing solar PV energy penetration in microgrid," *International Journal of Photoenergy*, vol. 2021, Article ID 3559837, 2021.

[8] U. K. Renduchintala, C. Pang, S. V. Pavan, K. Maddukuri, and K. M. Tatikonda, "Comparison of MPPT techniques for SEPIC converter based photovoltaic system," in *in 2016 Online International Conference on Green Engineering and Technologies (IC-GET)*, pp. 1–5, Coimbatore, Tamil Nadu, 2016.

[9] H. Islam, S. Mekhilef, N. Shah et al., "Performance evaluation of maximum power point tracking approaches and photovoltaic systems," *Energies*, vol. 11, no. 2, p. 365, 2018.

[10] G. Shankar and V. Mukherjee, "MPP detection of a partially shaded PV array by continuous GA and hybrid PSO," *Ain Shams Engineering Journal*, vol. 6, no. 2, pp. 471–479, 2015.

[11] A. Harrag and S. Messalti, "Variable step size modified P&O MPPT algorithm using GA-based hybrid offline/online PID controller," *Renewable and Sustainable Energy Reviews*, vol. 49, pp. 1247–1260, 2015.

[12] E.-C. Chang, "Applying robust intelligent algorithm and Internet of Things to global maximum power point tracking of solar photovoltaic systems," *Wireless Communications and Mobile Computing*, vol. 2020, 10 pages, 2020.

[13] D. S. Karanjkar, S. Chatterji, A. Kumar, and S. L. Shimi, "Fuzzy adaptive proportional-integral-derivative controller with dynamic set-point adjustment for maximum power point tracking in solar photovoltaic system," *Systems Science & Control Engineering*, vol. 2, no. 1, pp. 562–582, 2014.

[14] H. Mahamudul, M. Saad, and M. Ibrahim Henk, "Photovoltaic system modeling with fuzzy logic based maximum power point tracking algorithm," *International Journal of Photoenergy*, vol. 2013, 10 pages, 2013.

[15] H.-S. Ko and J. Jatskevich, "Power quality control of wind-hybrid power generation system using fuzzy-LQR controller," *IEEE Trans. On Energy Conversion*, vol. 22, no. 2, pp. 516–527, 2007.

[16] T. Shanthi and A. S. Vanmukhil, "Fuzzy logic based MPPT control of hybrid power generation system," *IJCA*, vol. 86, no. 1, pp. 37–44, 2014.

[17] A. S. Ingole and B. S. Rakhonde, "Hybrid power generation system using wind energy and solar energy," *International Journal of Scientific and Research Publications*, vol. 5, no. 3, 2015.

[18] W. Abd El-Basit, A. M. Abd El-Maksood, and F. Soliman, "Mathematical model for photovoltaic cells," *Leonardo Journal of Sciences*, vol. 23, pp. 13–28, 2013.

[19] M. C. Argyrou, P. Christodoulides, C. C. Marouchos, and S. A. Kalogirou, "Hybrid battery-supercapacitor mathematical modeling for PV application using Matlab/Simulink," in *in 2018 53rd International Universities Power Engineering Conference (UPEC)*, pp. 1–6, Glasgow, Scotland, 2018.

[20] L. T. Scarabelot, C. R. Rambo, and G. A. Rampinelli, "A relative power-based adaptive hybrid model for DC/AC average inverter efficiency of photovoltaics systems," *Renewable and Sustainable Energy Reviews*, vol. 92, pp. 470–477, 2018.

[21] P. Shiyas, S. Kumaravel, and S. Ashok, "Fuzzy controlled dual input DC/DC converter for solar-PV/wind hybrid energy system," in *in 2012 IEEE Students' Conference on Electrical, Electronics and Computer Science*, pp. 1–5, Bhopal, Madhya Pradesh, India, 2012.

[22] A. Jemaa, O. Zarrad, M. A. Hajjaji, and M. N. Mansouri, "Hardware implementation of a fuzzy logic controller for a hybrid wind-solar system in an isolated site," *International Journal of Photoenergy*, vol. 2018, 16 pages, 2018.

[23] S. B. Biswas, *Sizing, dynamic modelling and control of a solar water pumping system for irrigation*, PhD Thesis, Memorial university of Newfoundland, 2018.

[24] M. A. G. De Brito, L. Galotto, and L. P. Sampaio, "Evaluation of the main MPPT techniques for photovoltaic applications," *IEEE Transactions on Industrial Electronics*, vol. 60, no. 3, pp. 1156–1167, 2013.

[25] Z. Chen, Y. Zhu, Y. Di, and S. Feng, "A dynamic resource scheduling method based on fuzzy control theory in cloud environment," *Journal of Control Science and Engineering*, vol. 2015, 10 pages, 2015.

[26] C. Vadim and N. Ilie, "Photovoltaic system modeling with fuzzy logic based incrimental conductance tracking algorithm," in *in 2017 International Conference on Modern Power Systems (MPS)*, pp. 1–7, Cluj-Napoca, Romania, 2017.

[27] M. Abdulkadir, A. Yatim, and S. Yusuf, "an improved PSO-based MPPT control strategy for photovoltaic systems," *International Journal of Photoenergy*, vol. 2014, Article ID 818232, 11 pages, 2014.

Hindawi
International Journal of Photoenergy
Volume 2022, Article ID 3412817, 12 pages
https://doi.org/10.1155/2022/3412817

Research Article

Synthesis of Modified Phase-Changing Material with Latent Heat and Thermal Conductivity to Store Solar Energy Using a Carbon Nanotube

V. Vedanarayanan,[1] J. Dilli Srinivasan,[2] K. Arulvendhan,[2] P. Thirusenthil Kumaran,[3] R. Selvakumar,[4] H. S. Asif,[5] M. H. Siddique,[6] and Jifara Chimdi[7]

[1]*Department of Electronics and Communication Engineering, Sathyabama Institute of Science and Technology, Chennai, 600119 Tamil Nadu, India*
[2]*Department of Electrical and Electronics Engineering, SRM Institute of Science and Technology, Ramapuram, 600089 Tamil Nadu, India*
[3]*Department of Electrical and Electronics Engineering, Rajalakshmi Engineering College, Thandalam, 602105 Tamil Nadu, India*
[4]*Department of Electronics and Communication Engineering, Koneru Lakshmaiah Education Foundation (K L University), Guntur, 522502 Andhra Pradesh, India*
[5]*Mechanical Engineering Department, College of Engineering, King Saud University, P.O. Box 800, Al-Riyadh 11421, Saudi Arabia*
[6]*Intelligent Construction Automation Centre, Kyungpook National University, Daegu, Republic of Korea*
[7]*Department of Construction Technology and Management, Ambo University, Ambo, Ethiopia*

Correspondence should be addressed to Jifara Chimdi; jifara.chimdi@ambou.edu.et

Received 9 February 2022; Accepted 15 March 2022; Published 11 April 2022

Academic Editor: V. Mohanavel

Copyright © 2022 V. Vedanarayanan et al. This is an open access article distributed under the Creative Commons Attribution License, which permits unrestricted use, distribution, and reproduction in any medium, provided the original work is properly cited.

MicroPCMs' excellent thermal capacity and photothermal translation features benefit solar energy storage applications significantly. A successful in situ polymerization procedure was employed to build microencapsulated phase-change materials using n-hexadecanol as the core and melamine-formaldehyde resin as the outer shell, and the thermal characteristics of the microPCMs were evaluated. In terms of micromorphology, the incorporation of hydroxylated carbon nanotubes into microPCMs with a compact shell has little effect on their spherical structure. MicroPCMs' melting heat and latent heat are both 51.5°C with a 0.2 weight percent dose of hydroxylated carbon nanotubes, and n-energy hexadecanol's storage efficiency is determined to be 75.25 percent. Thermal conductivity and photothermal conversion efficiency of microencapsulated phase-change materials engendered with increased hydroxylated carbon nanotube dosage have improved significantly, laying the foundation for improved photothermal storage efficiency. When 0.6 weight % hydroxylated carbon nanotubes are added to the mixture, microencapsulated phase-change materials have a thermal conduction of $0.3597\,Wm^{-1}\cdot K^{-1}$ and $181.5\,J\cdot g^{-1}$. Additionally, all of the improved microPCMs show exceptional thermal stability across 500 heat cycles. Because of their large thermal capability and efficient photothermal conversion, the new microPCMs appear to be an appealing option for solar energy storage in direct-absorption solar collector systems.

1. Introduction

Many people believe solar energy to be among the best energy sources available, both theoretically and practically, because it is both clean and renewable [1]. The usage of solar thermal energy is an efficient approach to harness solar by absorbing radiation, helping to relieve the energy crisis and environmental issues that result from our continued reliance on fossil fuels. Direct absorption of solar light and subsequent thermal energy generation are possible due to the device's internal working fluid composition [2–4]. The physical change of a phase-change material will transform from

the solid state to liquid, culminating in heat absorption, and heat is released whenever the temperature reaches the freezing point during the thermal cycling phase. Working fluid characteristics and photothermal conversion performance are unquestionably linked to DASC efficiency. Microencapsulated phase-change materials (microPCMs) become extensively employed in processing fluids in recent years due to the difficulties of storing considerable amounts of solar radiation energy utilizing the practical means of storing heat [5]. Latent heat storage is a technique used by these materials to retain energy. In order to construct core-shell microPCMs, the phase-change materials are encased in film and their feature sizes range from nanometres to micrometres [6–8]. Because they are employed as the core materials, microcapsule PCMs can collect, accumulate, and subsequently proclaim a significant quantity of thermal inactivity with very minor heat variations during the phase transition method. For example, microencapsulation of PCMs can help prevent leakage, control capacity change, and enhance temperature in a particular surface area during phase transitions [9, 10]. Phase change materials are used in a range of businesses, which include solar plants, photovoltaic energy processes, aviation industry, and preservation of food materials. There has also been a great deal of attention paid to microPCMs' realistic applications for building energy storing and the thermal control of microelectronic parts and heat-altered fabrics [11].

The most typical components of microPCMs with a stable core-shell structure are PCMs and inert organic or inorganic elements [12, 13]. There are a wide range of organic PCM materials that have excellent characteristics such as high chemical stabilization, less supercooling, moderate capacity fluctuations, moderate harmfulness and little abrasion, and low supercooling. With its high purification, low cost, high latent heat, and heat constraints of 22–60°C, n-dodecanol is a popular choice for making microPCMs [14–16]. n-Hexadecanol and n-octadecanol are also commonly employed. A microPCMs' shell is made up of a variety of materials, including organic and inorganic ones. PCMs can be encapsulated using a broad variety of materials, including MF resin, PMMA, UF, polystyrene, polyurethane (PU), silica, TiO_2, and $CaCO_3$.

To preserve the core components throughout the solid-liquid transition process, high molecular polymers offer several benefits over inorganic material, such as easy manufacturing, high compatibility, and superior compactness [17–19]. To create microPCMs with a high-heat storage capacity, researchers have looked into using crosslinked MF resin, which is easy to prepare and stable once it is encapsulated. MicroPCMs' heat absorption and release rates are adversely affected by the poor thermal conductivity of MF resin and other polymer shell materials. The practical implementation of polymer-based microPCMs in temperature management and solar energy storage remains a significant problem. Inorganic fillers with high thermal conductivity, like carbon or metallic oxide, have been included into the core and shell materials in several studies in an attempt to increase thermal conduction, thermal storing capability, and uniform photothermal adaptation. Phase-change microcapsules with capric acid as core and graphene oxide (GO) as shell were created by [20] using in situ polymerization. At ambient temperature, the thermal conduction of microencapsulated phase-change materials with a graphene oxide dosage of 0.9 wt percent was 75.1 percent higher. PCMs and specific heat of the graphene oxide-altered microencapsulated phase-change materials were almost equal in the next 100 thermal cycles, confirming the increased thermal stability of the modified microPCMs. Reference [21] examined the thermal characteristics of microPCMs, synthesizing n-dodecanol/MF resin microcapsules containing GO as part of the process. Addition of 0.6 percent to micro PCMs with the greatest oxidation degree occasioned in an enhanced in thermal conduction by 115%, which considerably improved thermal storage efficiency. Nano alumina was used by Jiang et al. to decorate microPCMs with a paraffin wax core and a poly (methyl methacrylate-co-methyl methacrylate) shell. Heat transmission in microPCMs can be considerably enhanced by the addition of nano-aluminium oxide. Once the nano-aluminium oxide dose was 16 weight percent of the monomer mass, the thermal conduction of the microencapsulated phase-change material was $93.41\,J{\cdot}g^{-1}$. In situ polymerization was used by [22] to create paraffin wax/UF resin microcapsules containing a variety of nanoparticles, including Al_2O_3, CuO, and TiO_2. Using nanomaterials to strengthen polymer-based microPCMs has shown that they can increase their heat conductivity [23]. Carbon nanotubes, a type of 1-dimensional carbonaceous material, are popular reinforcement nanomaterials for composites since, high feature ratio, Excellent thermal conduction (up to $3000\,W\,m^{-1}$ and a higher thermal conduction of $0.586\,W\,m^{-1}\,K^{-1}$), less density, and admirable photographic absorption. CNTs may also be used in conjunction with other materials to improve the thermophysical characteristics and photovoltaic translation behaviour of mixture [24]. As a result, they represent one of microPCMs' most promising thermal-conductive fillers. It is simple for CNTs to aggregate and have less dispersion in the synthetic microcapsule system because of their passive surface. The surface chemical composition of CNTs must be altered. Concomitant acid treatment by [25] increased the hydrophilic characteristics of CNTs, which were subsequently in situ polymerized in order to form CNTs/MF resin microcapsules with CNT reinforcement. To validate the melting heat content of the microencapsulated PCMs, they were subjected to 20 cycles of heating and cooling. The thermal conduction of microencapsulated phase-change materials was improved by 25th percent by the addition of 1.67 weight percent carbon nanotubes. They created an invention of double-walled n-octadecane microcapsule with an inner layer of melamine formaldehyde resin and an outside layer of carbon nanotube-poly Na(4-styrenesulfonic acid), utilizing the self-assembly procedure [26]. There was a considerable increase in the microPCMs' thermal response time, cooling efficiency, and thermal stability. MicroPCMs/epoxy resin composite has a thermal conductivity of $0.30\,Wm^{-1}{\cdot}K^{-1}$.

While [27] used O_2-plasma to produce CNTs, they used CNT-based microcapsules to analyze the electrical and mechanical characteristics of n-octadecane/melamine urea

formaldehyde resins. The thermal conduction and mechanical characteristics of microencapsulated phase-change materials with CNTs added to the polymer arrangement were significantly enhanced [28]. The thermal conduction of microencapsulated phase-change materials was increased by 225% when carbon nanotubes were added to the polymer arrangement. A graphene oxide-carbon nanotube hybrid filler enhanced the thermal characteristics of n-dodecanol/melamine formaldehyde resin microcapsules, which had a synergistic effect [29]. MicroPCMs' thermal conductivity improved by 195% when a hybrid filler was added at 0.6 wt percent, although the latent heat was reduced somewhat. We discovered that the microPCM-dispersed slurry has an excellent light absorption capacity for solar energy storage. Carbon nanotubes with stearyl alcohol (CNT-SA) grafted onto them were used in the experiment devised by [30].

Only 47.7 $J{\cdot}g^{-1}{\cdot}K^{-1}$ of latent heat was released in the microPCMs, but their thermal conductivity was increased by 79.2 percent. The results of the trials clearly show that CNT nanofillers may be employed to greatly boost the thermal conductivity of microPCMs synthesized by various methods [31]. The latent heat of microPCMs, on the other hand, falls significantly with increasing CNT concentration. If the specific heat values of the CNT-changed microencapsulated phase-change materials are not optimized, the thermal storage capacity will be drastically reduced. Research on the photovoltaic translation efficiency of CNT-modified microPCM solar energy storage devices has also been under-researched [32]. Thermal conductivity and photovoltaic translation in microencapsulated phase-change materials have mostly been studied using hydroxylated carbon nanotubes (HO-CNTs). It's still being created MicroPCMs with increased heat storage capacity, like the Hydroxylated-Carbon Nano Tubes-enhanced MicroPCM [33]. In situ polymerization was employed in this investigation to generate n-hexadecanol- and MF resin-coated hydroxylated carbon nanotube-changed microcapsules. In microPCMs, n-hexadecanol was chosen as the primary material owing to its maximum heat storing capability and acceptable phase transition temperature (50°C) (240 $J{\cdot}g^{-1}$).

2. Experimental Section

2.1. MicroPCMs Modified with HO-CNTs Synthesized. Ho-CNT enhances carbon nanotube solubility and dispersibility while decreasing contact resistance. Its applications include energy storage, device modelling, thin-film electronics, and coatings. In situ polymerization was used to create the HO-carbon nanotube-enhanced n-hexadecanol/melamine formaldehyde resin microcapsule. The HO-CNT-modified microPCMs were synthesized in three conventional processes.

2.1.1. Shell Prepolymer Preparation. A tiny beaker was filled with 20 ml of deionized water, and a probe-type ultrasonic oscillator was used to equally scatter a certain amount of HO-CNTs. The aqueous solutions containing 10.0 gM and 21.5 g·F were heated to 70 degrees Celsius in 150 ml bottom flask at a rate of 350 revolutions per minute until the liquid turned transparent. While we waited for this to occur, we added 50% triethanolamine aqueous solution to the HO-CNT water dispersion and gradually transferred it to the flask for pH adjustment to 8–9. To prepare a hydroxylated carbon nanotube-improved prepolymer solution of shell material, the reaction liquid was maintained at the specified temperature and mechanical stirring rate for 3.0 hours.

2.1.2. Phase-Change Material Esterification. Magnetic stirrers were used to mix SMA 1000HNa and water in a 250 ml beaker, which was heated to 75°C and covered with plastic film. Mechanically stirred and condensed n-hexadecanol was added to the flask, which was heated to 75°C in an oil bath, and the flask was stirred at a low rotating speed. It was then added to the core material in order to bring the temperature down to an even level. Forcefully emulsifying the solution at a velocity of 2000 revolutions per minute resulted in a stable oil-in-water (O/W) suspension. A 500 rpm stirring rate of citric acid aqueous solution maintained the pH of the emulsion system after 90 minutes. To prevent the emulsion from burning, the temperature was maintained at 65°C.

2.1.3. The Formulation of Enhanced MicroPCMs. This modified prepolymer solution, 9.6 grammes, was added to the n-hexadecanol in a drop-wise manner within 30 minutes after the temperature of the system had restored to 65 degrees Celsius. Shell prepolymers were polycondensed and cross-linked in a mixed environment at 70°C for 3.0 hours to produce the microcapsules. A vacuum-assisted membrane filter was used to separate the resulting suspension from the aqueous phase and allow it to cool to room temperature on its own. To create microcapsule powders, the microcapsule specimens were dehydrated in void oven at 50 degrees Celsius for 48 h after being rinsed three times with a warm 50-weight percent ethanol-water solution.

Similar to microPCM-0.0, a "blank" microcapsule sample was also created using the same methods, but with no inclusion of HO-CNTs. Each of the six microcapsules had a different proportion of hydroxylated carbon nanotubes comparative to the shell material: microencapsulated phase-change material—0.1, 0.2, 0.3, 0.4, and 0.6, correspondingly. As shown in Table 1, you may create microcapsules using modified nanocrystals and n-hexadecanol/melamine formaldehyde resin.

2.2. Properties and Evaluation. The chemical compositions of dried-out microencapsulated phase-change materials, n-hexadecanol, melamine formaldehyde resin, and hydroxylated carbon nanotubes were determined. The positive aspect of microencapsulation seems to be that the core material is entirely coated and confined from the outside enviro. 5 mg specimens were wrapped in an aluminium pan and verified in a N-atmosphere at temperatures ranging from zero to eighty degrees Celsius at a ten-degree-per-minute heating and cooling rate. In the course of testing, specimens start heating at 20° Celsius to 80° Celsius, detained at 80° Celsius for 3 minutes, then air conditioned to 0° Celsius, maintained at 0° Celsius for 5 minutes, and again heated to 80° Celsius.

Table 1: The experimental protocol for the fabrication of hydroxylated CNTs improved micro-phase-change materials.

Specimens	Emulsion system			Prepolymer system			
	n-Hexadecanol (g)	SMA 1000HNa (g)	Deionized water (ml)	Melamine (g)	Formaldehyde (g)	HO-CNTs (mg, wt%)	Deionized water (ml)
MicroPCM-0.0	14.5	2.9	100	12	22.1	0,0	25
MicroPCM-0.1	14.5	2.9	100	12	22.1	19, 0.1	25
MicroPCM-0.2	14.5	2.9	100	12	22.1	38, 0.2	25
MicroPCM-0.3	14.5	2.9	100	12	22.1	56, 0.3	25
MicroPCM-0.4	14.5	2.9	100	12	22.1	74, 0.4	25
MicroPCM-0.5	14.5	2.9	100	12	22.1	92, 0.5	25
MicroPCM-0.6	14.5	2.9	100	12	22.1	110, 0.6	25

For the NETZSCH Proteus investigation, the next heating and cooling DSC dashes were together after each sample was heated to completely destroy all thermal and processing histories of the materials being investigated. Energy storage efficiency (E), distinct as the mass ratio of PCM to total microcapsule mass, was determined using the following formula when microPCMs were synthesized:

$$E(\%) = \frac{\Delta H_{m,\text{microPCMs}} + \Delta H_{c,\text{microPCMs}}}{\Delta H_{m,n-\text{hexadecanol}} + \Delta H_{c,n-\text{hexadecanol}}} \times 100\%. \quad (1)$$

The constant-temperature heating plate was used to evaluate the thermal stabilization of microencapsulated phase-change materials. On the pad paper, we inserted the microPCMs and n-hexadecanol and heated them simultaneously. All of the samples were heated to 65°C for 0, 30, or 60 seconds before being photographed using a mobile camera. For this investigation, a C5465 probe was used with a hot disc thermal persistent examiner based on the transient plane source (TPS) approach. Using a 15 MPa press for 60 seconds, two cylindrical flat-surface blocks with 10 mm high and diameters of 10 mm each were produced from the powder samples. Afterwards, two cylindrical blocks were placed in between the probe and the blocks. At least three measurements were taken at room temperature for each sample, and the average value was computed and recorded. Thermal cycling tests using an alternate high-low temperature test chamber were used to assess microPCMs' thermal durability. The samples were heated to a temperature of 80 degrees Celsius over their melting point and subsequently cooled to a temperature of 0 degrees Celsius below their crystallization point. There were 500 cycles of the thermal cycling process. The PCM properties of microPCMs were calculated at the millimetre and micrometre scales. MicroPCM photothermal conversion performance may be measured with a self-built test system that contains a thermal isolation device, a sun simulator, and data gathering equipment, as previously shown in our study. The solar emulator was powered by 300-watt sunlit energy, and data was gathered using T-type thermocouple junction sensors and a processor. It was utilized to record real-time temperature measurements of the sample cylinder block using a thermocouple probe with a quantity accurateness of 0.1°C and a procurement break of 1.0 s during the irradiation process.

3. Results and Discussion

It is possible that certain HO-CNTs may not be completely encased in the microcapsules, with a few of the ends protruding. For effective heat transmission external of microencapsulated phase-change material, the outwardly expanded hydroxylated carbon nanotubes of close microPCMs are physically linked together. The hydroxide groups on the surface of hydroxylated carbon nanotubes react with melamine formaldehyde resin prepolymer during shell creation, making them an excellent combination with microPCMs. The n-hexadecanol/melamine formaldehyde resin microcapsules' heat transfer rate is boosted by the movement of hydroxylated carbon nanotubes in and out of microencapsulated phase-change material. Table 1 contains the experimental technique for producing better microPCM using hydroxylated CNTs.

The abundant –OH functional groups of the HO-CNTs significantly interact with the prepolymer of melamine formaldehyde resin. With respect to absorption in the microPCM-0.6 spectrum, the moderate absorption peak at 1465 cm^{-1} is classified as being part of the C–H stretching band. The 723 cm^{-1} absorption peak is caused by the alkyl-(CH2)n-(n 4) group's in-plane rocking vibration band. The unusually sharp absorption peak at 1062 cm^{-1} is caused by the main alcohol's C–O stretching vibration band. Captivation bands of the phase transition substance n-hexadecanol can be clearly seen in all of the vibration peaks. Parallel to this, the absorption peak at 813 cm^{-1}, which is a typical triazine skeleton vibration, is seen in the spectra of

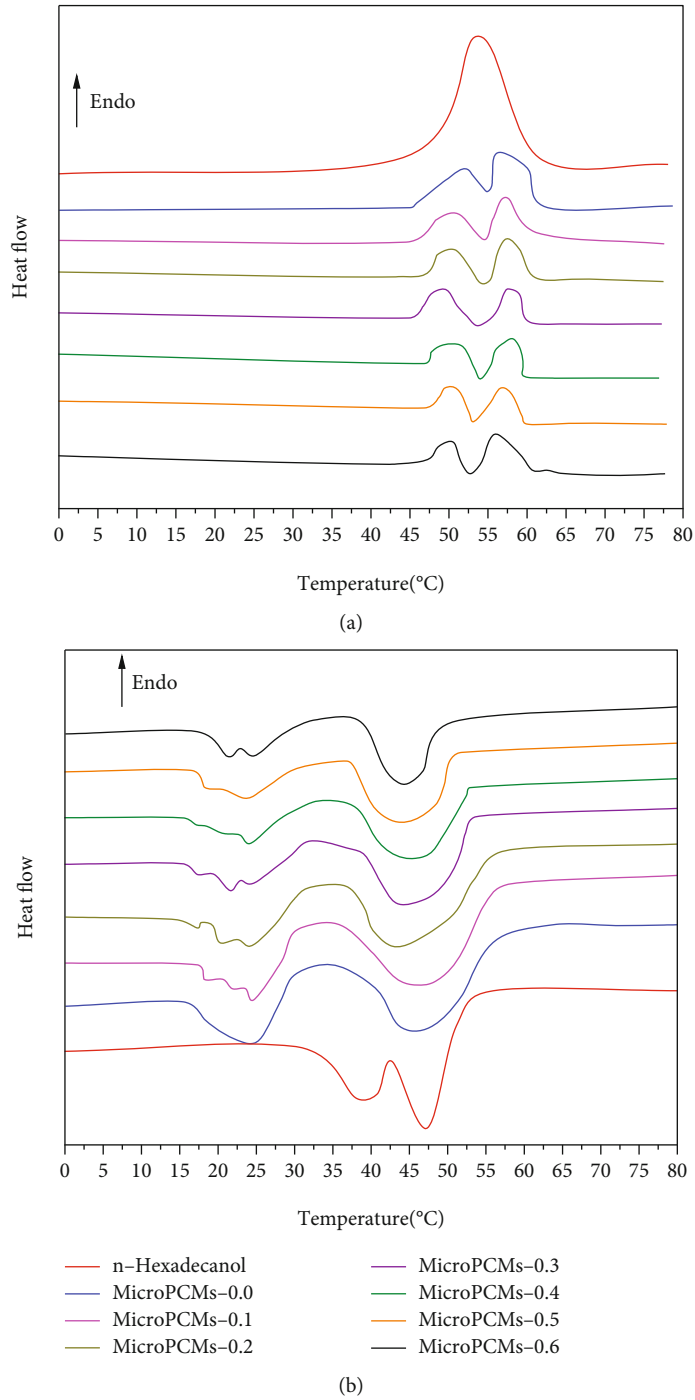

Figure 1: (a) The melting and (b) crystallizing processes in n-hexadecanol and microPCMs, respectively, as depicted by DSC curves.

microPCMs, together with the stretching vibrations at 1564 and 1350 cm^{-1} of the C−−N and C–N groups. O–H and N–H stretching vibrations overlap, mostly owing to n-hexadecanol and MF resin, to produce wide absorbing ability at around 3330 cm^{-1}. Owing to the low loading of CNTs in microPCMs, HO-distinctive CNT's absorption peaks do not show up in their spectra. Based on spectral analysis, it was determined that the in situ polymerization of n-hexadecanol in MF resin was a success.

3.1. MicroPCM Thermal Storage Capability. When evaluating the microPCMs' heat storage properties in a real-world application, the PCM is critical. The DSC was therefore used to evaluate the microPCMs' phase change characteristics. There are DSC results for both unmodified microPCMs and modified microPCMs with varied quantities of HO-CNTs in Figure 1. While the melting process is shown by the upward endothermic peak in Figure 1(a), the crystallization process is shown by the downward exothermic peak

Table 2: Characteristics of the n-hexadecanol and microencapsulated PCM improved with hydroxylated carbon nanotubes in varied quantities.

Samples	Melting process				Crystalizing process					
	T_{mo} (°C)	T_{mp1} (°C)	T_{mp2} (°C)	ΔH_m (J/g)	T_{co} (°C)	T_{cp1} (°C)	T_{cp2} (°C)	ΔH_c (J/g)	ΔH (J/g)	E (%)
n-Hexadecanol	46.2	—	52.1	242.2	47.2	39.2	44.2	240.2	239.6	100.0
MicroPCM-0.0	37.1	43	52.1	183.6	48.5	30.1	44.6	179.8	179.4	73.8
MicroPCM-0.1	37.1	42.4	52.8	178.2	48.4	30.3	44.5	172.8	176.6	71.8
MicroPCM-0.2	38.1	42.9	52.5	183.6	48.6	32.4	44.8	180.4	179.8	74.6
MicroPCM-0.3	38.3	44.1	50.4	174.6	48.5	30.5	44.7	170.6	178.4	73.8
MicroPCM-0.4	38.2	43.6	53.3	170.1	48.6	30.7	44.5	166.6	164.3	71.4
MicroPCM-0.5	38.6	43.4	53.3	159.6	48.4	30.4	44.6	156.6	154.2	66.8
MicroPCM-0.6	38.7	41.8	52.2	158.5	48.6	28.6	44.7	154.9	152.2	63.8

(Figure 1(b)). Table 2 displays the samples' temperatures and latent heat values based on DSC analysis. The transition from a liquid to a hexagonal-filled solid phase is marked by two exothermic peaks, first at high temperature and next at low temperature. For thermal responsiveness and transfer, a lower melting temperature for microencapsulated n-hexadecanol appears to be advantageous due to the huge specific surface areas of microPCMs. The crystallization temperature of microencapsulated n-onset hexadecanol is substantially comparable to the temperature of pure n-hexadecanol. As can be shown in Figure 1, the peak of crystallization at the solid-phase transition for microPCMs moves to a lower temperature range (Figure 1(b)). Because the molecular formation of n-hexadecanol restrained, this resulted in a restricted crystallization behaviour during the freezing process. During the phase shift, the peak area of microPCMs is also shown to be smaller than that of pure n-hexadecanol. For the generation of microPCM phase-change enthalpy in the core shell, only n-hexadecanol may undergo the requisite phase changes.

MicroPCM-0.0 and pure n-hexadecanol both have average enthalpy values of 180.5 $J{\cdot}g^{-1}$, as seen in Table 2. It has also been shown that the phase transition enthalpy of microPCMs decreases as the HO-CNT dose is increased. Whereas the hydroxylated carbon nanotube dose is <0.2 weight percent, the specific heat of microencapsulated phase-change materials is practically constant at 180 $J{\cdot}g^{-1}$ with an equivalent energy storing efficacy of roughly 75%. This suggests that HO-CNT dosages below 0.2 wt percent have no impact on the specific heat of microencapsulated phase-change materials. In the aqueous solution, the HO-CNTs diffused efficiently due to the abundance of –OH groups on their surface at low additions. Thus, the n-hexadecanol core material may be further encapsulated by the HO-CNTs interacting fully with the MF resin prepolymer. MicroPCM latent heat decreases more slowly when the HO-CNT dose is more than 0.2%. This is in accord with experimental outcome stated in the analysis. As a result, it may be possible to hasten the polycondensation of the MF resin prepolymer in order to release the partial shell materials from their packaging with n-hexadecanol, thereby allowing the HO-CNTs to be dispersed. For the microPCMs to lose their latent heat, an excessive amount of HO-CNTs must be supplied. H and E are greatly enhanced to 1 155.7 J·g and 64.52 percent when the HO-CNT dosage is increased to 0.6 percent when microPCMs are used as the energy storage. Because of their apparent capacity to store substantial amounts of heat and energy at low temperatures and their precise phase transition temperature, n-hexadecanol/melamine formaldehyde resin microcapsules treated with HO-carbon nanotubes may be able to store thermal energy. Characteristics of n-hexadecanol and microencapsulated phase-change materials are shown in Table 2.

3.2. Thermal Stabilization of Microencapsulated PCMs. A variety of hydroxylated CNT-filled microPCMs were tested for thermal stability using thermal analysis methodologies in this section. MF resins and microPCMs are shown in Figures 2(a) and 2(b) for the thermogravimetric tests of n-hexane. Table 3 shows the measurement results. At a temperature of 5% weight loss, microPCMs begin to lose weight owing to a little quantity of water and inadequate reactants in the specimens (T5 percent). At 300°C, microPCMs lose W300°C and W165°C of their total weight. The mass % of core materials in microencapsulated phase-change materials can be estimated by subtracting the weight reduction of residual water and imperfect reactants from W300°C to W165°C.

MicroPCMs remain in a very stable, dry powder state even at temperatures considerably beyond the melting point of n-hexadecanol (50° Celsius), even during the heating process. Due to the microPCMs' absence, n-hexadecanol/MF resin microcapsules are form stabilized, whether or not they include HO-CNTs. An effective barrier to leakage is provided by the resin, which is made up of polymethylmethacrylate (MF). Thermogravimetric methods were used to analyze N-hexadecanol, MF resins, and microPCMs at temperatures between 50 and 750 degrees Celsius. Pure n-hexadecanol has a starting weight loss temperature (T1 percent) of 146°C, and by 300°C, there are almost no residues left owing to the evaporation of molten N-hexadecanol. There is just one stage of weight loss. Temperature increases cause the MF shell to slowly and steadily lose mass. Adsorbed water, remaining reactants, and oligomers lose weight at temperatures below 300°C owing to volatility and breakdown, while at temperatures between 300°C and

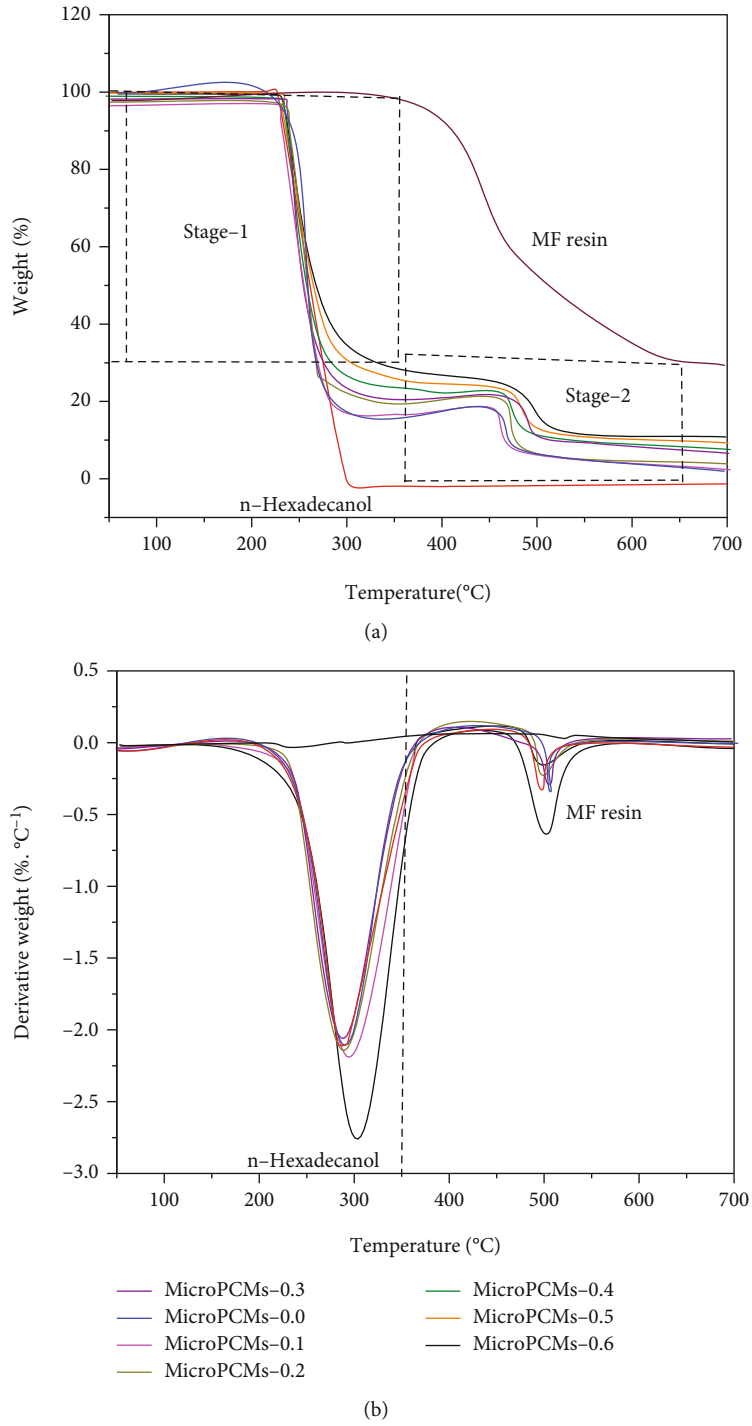

Figure 2: MicroPCMs and n-hexadecanol modified with various concentrations of HO-CNTs are shown in (a) TGA and (b) DTG curves.

600°C, the MF shell undergoes significant pyrolysis. The pyrolysis of MF resin at temperatures of 300–600°C is mostly responsible for the first step, whereas the evaporation of n-hexadecanol, the core material, is primarily responsible for the second stage. As indicated in Table 3, micro-phase-change material improved with various quantities of HO-carbon nanotubes had almost identical beginning weight loss temperatures ($T5$ percent) at 165°C, indicating that these microPCMs may be effectively used at temperatures lower than 165°C without degrading in performance. Calculated core mass percentages are essentially compatible with energy storage efficacy of micro-phase-change materials from DSC analysis. Microencapsulated phase-change materials modified with high n-hexadecanol n-hexadecanol mass % HO-CNTs may be employed in a wide range of practical sectors with operating temperatures below 165°C, as

Table 3: Thermo gravimetric results of the micro-phase-change materials improved with various quantities of HO-carbon nanotubes.

Samples	$T_{5\%}$ (°C)	W_{300-C} (%)	$W_{300-C} - W_{165-C}$ (%)
MicroPCM-0.0	167	81.07	76.04
MicroPCM-0.1	165	75.76	70.81
MicroPCM-0.2	167	83.61	80.12
MicroPCM-0.3	167	75.87	71.87
MicroPCM-0.4	165	75.35	70.42
MicroPCM-0.5	167	72.86	64.72
MicroPCM-0.6	165	69.73	66.12

demonstrated by this study. Results on the enhanced micro-phase-change materials with different amounts of HO-carbon nanotubes are shown in Table 3.

3.3. Thermal Conduction of the Microencapsulated Phase-Change Materials. Thermal conduction is an important property that moves the thermal responsiveness to fascination and removal of PCM enthalpy in microPCM thermal energy storage. These microcapsules' heat transmission capabilities were evaluated by measuring the thermal conduction of the n-hexadecanol/melamine formaldehyde resin with varying quantity of hydroxylated CNT additives. The impact of the hydroxylated carbon nanotube fillings on microPCMs' thermal conduction was also examined and conversed in this study. There is a noticeable enhancement in the thermal conduction of microPCMs when HO-CNTs are added to varied degrees. The unmodified microPCMs have a measured thermal conductivity of just $0.3002\,Wm^{-1}{\cdot}K^{-1}$ due to the weak thermal conduction of natural PCMs and polymeric shells. When HO-CNTs are included in microPCMs, the resulting increase in thermal conductivity is 0.1 weight percent or $0.3181\,Wm^{-1}{\cdot}K^{-1}$. When HO-CNTs are introduced at a weight percentage of 0.6, micro-phase-change materials have the extreme thermal conduction of $0.3597\,Wm^{-1}{\cdot}K^{-1}$. The accumulation of HO-carbon nanotubes considerably boosted the thermal conduction of the n-hexadecanol/melamine formaldehyde resin microcapsule, demonstrating that the microPCM heat incriminating/discharging rate was successfully raised. HO-CNTs may help reduce interfacial heat resistance by creating a bond with the melamine formaldehyde resin shell due to their high aspect ratio and many hydroxylated groups on the outer surface. Additional HO-CNTs, which adhere to the microPCM shell, form thermal conductors between microPCMs and increase the transfer rate of heat between them. After adding HO-carbon nanotubes to the carbon nanotubes, n-hexadecanol/melamine formaldehyde resin microcapsules exhibit a considerable increase in thermal conductivity and keep that level even at a modest accumulation, hence increasing its thermal responsiveness to changes in temperature.

3.4. MicroPCM Thermal Cycle Testing. A 500-cycle thermal cycling experiment was directed to test the thermal consistency of the microPCM-0.0 and microPCM-0.6 that were created. First, fifty-fifth, one hundredth, two hundredth, three hundredth, four hundredth, and five hundredth minutes of melting and crystallizing DSC curves of microPCM-0.0 and 0.6. Next 500 heat cycles, the MicroPCM-0.0's phase change behaviour remains largely constant, but the MicroPCM-0.6's peak phase change profile deviates slightly from the primitive state. Although it is still possible that microPCM-0.6 has a slight departure from its primordial condition, its latent heats at the 500th thermal cycle have been shown to be almost identical to those of microPCM-0.0 and microPCM-0.6. Figures 3(a) and 3(b) are the microPCM-0.0 average latent heat (H), and the microPCM-0.6 latent heat values for microPCM-0.0 and 0.6 were found in this study to be roughly the same as their initial values of 180.5 J·g apiece at 500 cycles of thermal cycling. During repeated heating and cooling cycles, this material does not leak at all. Since the formaldehyde resin encapsulates n-hexadecanol, it is safe to use. The addition of HO-carbon nanotubes has no effect on the PCM cycling behaviour of n-hexadecanol/MF resin microcapsules. For thermal storage applications, the improved microPCMs have excellent thermal dependability due to the incorporation of HO-CNTs.

3.5. The MicroPCMs' Photothermal Conversion Performance. A variety of PCMs with varied levels of enhanced photothermal conversion capability were found to be useful for storing plentiful renewable solar energy based on the literatures that were reviewed. The MF resin and microPCMs were monitored for temperature changes under continuous simulated solar irradiation in terms to assess the impact of HO-CNT inclusion on the photothermal conversion property. The HO-carbon nanotube-improved microPCMs display a comparable heat change mechanism as the unmodified microPCMs when the irradiation period is extended. During irradiation, the temperature of microPCMs increases at an accelerated rate, which is solely dependent on their sensible heat. When irradiated for extended periods of time at temperatures between 40 and 50 degrees Celsius, it is clear that the heat rise degree of microPCMs is slower than that of the MF resin, leading to the formation of a temperature buffer zone, as indicated by the grey-dotted box. n-Hexadecanol microcapsulated in resin shell undergoes solid-liquid phase change as temperature increases, and this is why this phenomena happens. As a result, microPCMs absorb a significant quantity of solar energy and convert it into latent heat. Immediately after melting the n-hexadecanol core material over 50°C, microPCMs must be immediately elevated to the maximum balanced temperature by imitating solar irradiation. For solar thermal storage, unaltered microPCMs maintain a longer buffer at 40–50°C for around 1000 seconds than the HO-CNT-modified microPCMs. When bombarded for an extended period of time, HO-CNT-modified microPCMs have a higher temperature than untreated microPCMs. Filling microPCMs with more HO-CNTs resulted in higher temperatures when heated in the same irradiation setting. Consequently, when irradiation has achieved equilibrium, microPCMs without

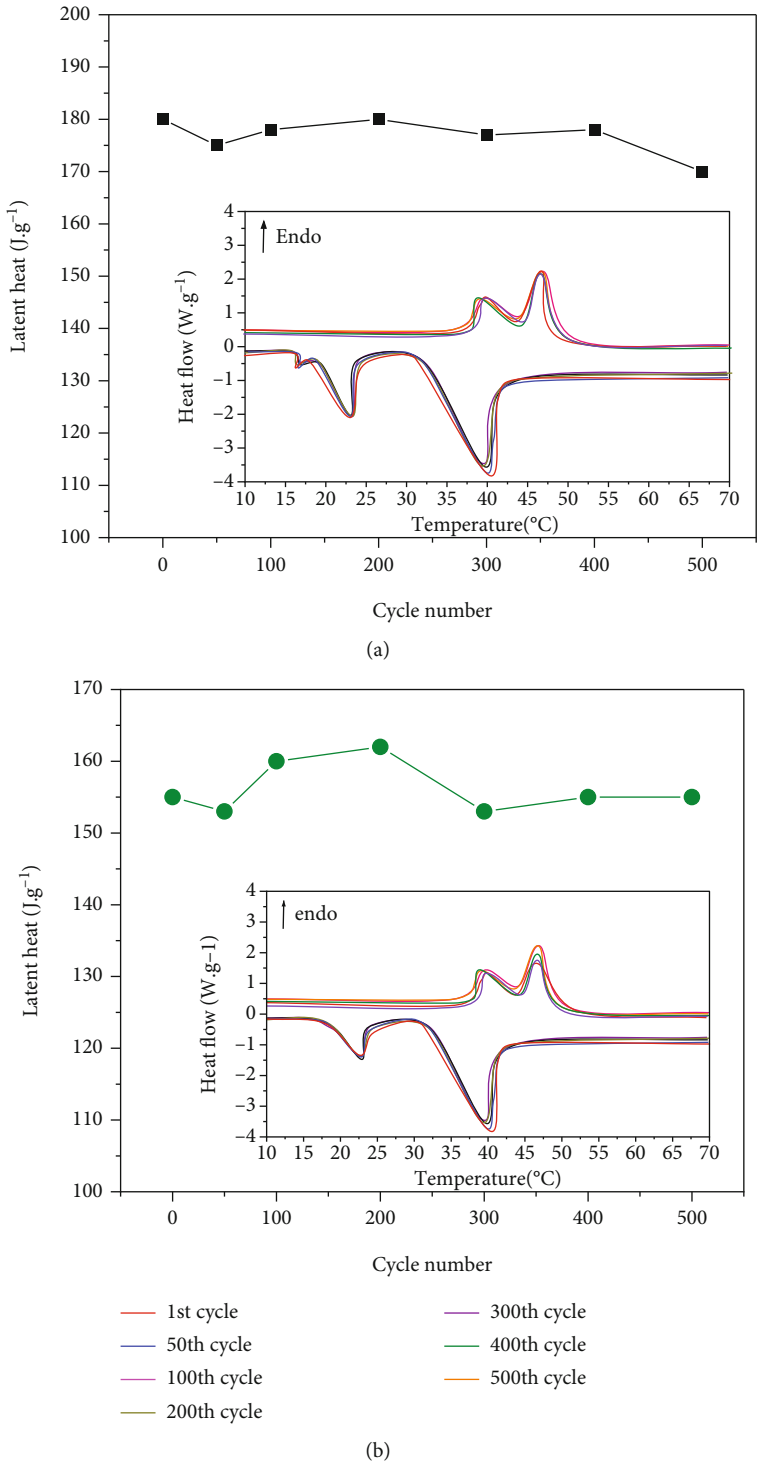

Figure 3: The next 500 thermal cycles and the latent heat of the microencapsulated phase-change materials. (a) 0.0 and (b) 0.6.

HO-CNT additions rise from 28 to 64.0°C in temperature, whereas those with 0.1 and 0.06 percent HO-CNT additions rise from 66.0 to 75.0°C, and it is shown in Figure 4. Due to the strong optical absorption capability of the filler HO-CNTs, the temperature of microPCMs modified with filler HO-CNTs rises significantly. For photothermal energy storage, the microPCMs' temperature buffer of 40 to 50°C is sufficient even at a HO-CNT dosage of 0.6 weight percent. According to the results of this study, all modified microPCMs exhibit stable photovoltaic translation behaviour in solar energy absorption and release. Filler HO-CNTs may significantly increase the photothermal transition efficiency of n-hexadecanol/melamine formaldehyde resin microcapsules with maximum thermal storing capacity, thereby making microPCMs an attractive alternative for use in solar energy storage cells such as the DC-DASC.

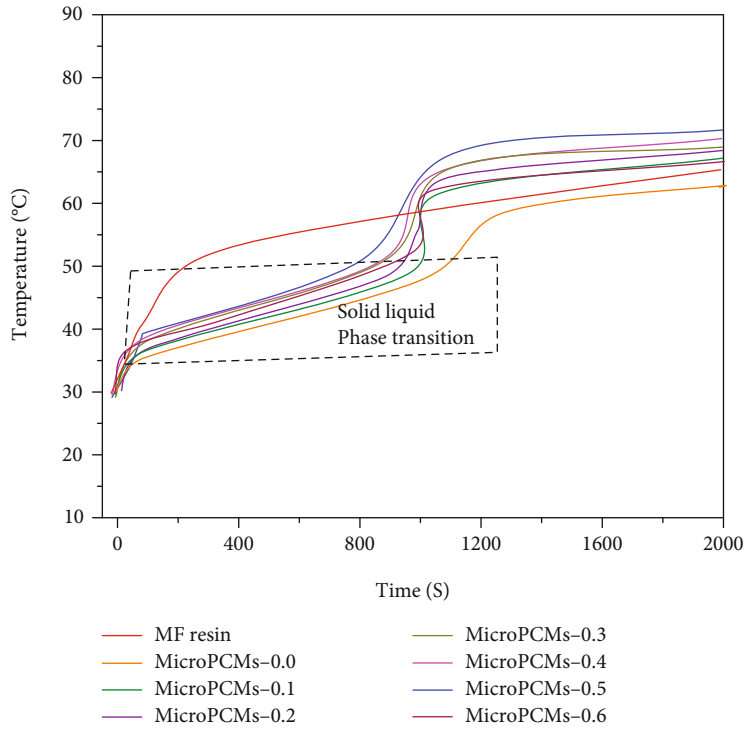

Figure 4: Irradiation time affects both the MF resin and microPCMs' temperature curves.

4. Conclusions

A sequence of hydroxylated CNT-improved microencapsulated phase-change materials with n-hexadecanol cores and melamine formaldehyde resin shells were effectively constructed in this work using in situ polymerization. On the microPCMs' surfaces, there are many HO-CNTs that can be observed. DSC observations from microPCM microparticles show that after the quantity of hydroxylated carbon nanotubes is improved, the latent heat decreases. It is found that the energy storage efficiency of microPCMs at 0.2 weight percent HO-CNTs is 75.25% and the corresponding melting and latent heat temperatures are 51.5°C. After adding an additional 0.6% of HO-CNTs, the average latent heat of the microPCMs stays at $155.6\,J{\cdot}g^{-1}{}^{\circ}C$ and $181.5\,J^{-1}$. This study shows that microPCMs modified with different levels of HO-CNT have excellent thermal stability and form stability throughout the phase shift process. The addition of HO-CNTs to microPCMs has considerably enhanced the thermal conductivity and photothermal conversion efficiency. More light-responsive temperatures were seen in the modified microPCMs than in the unmodified microPCMs, with a maximum thermal conduction of $0.3597\,Wm^{-1}{\cdot}K^{-1}$ and an increase in light-responsive temperature in simulated sunshine. The HO-carbon nanotube-improved n-hexadecanol/melamine formaldehyde resin microcapsules with remarkable photothermal conversion properties, high PCM, and appealing thermal charging/discharging rate are promising materials for solar energy storage.

Data Availability

The data used to support the findings of this study are included within the article. Further data or information is available from the corresponding author upon request.

Conflicts of Interest

The authors declare that there is no conflict of interest regarding the publication of this paper.

Acknowledgments

The authors appreciate the supports from Ambo University, Ethiopia, for providing help during the research and preparation of the manuscript. The authors thank Sathyabama Institute of Science and Technology, SRM Institute of Science and Technology, Rajalakshmi Engineering College, and King Saud University for providing assistance to complete this work.

References

[1] B. S. Moraes, M. Zaiat, and A. Bonomi, "Anaerobic digestion of vinasse from sugarcane ethanol production in Brazil: challenges and perspectives," *Renewable and Sustainable Energy Reviews*, vol. 44, pp. 888–903, 2015.

[2] K. Yuan, H. Wang, J. Liu, X. Fang, and Z. Zhang, "Novel slurry containing graphene oxide-grafted microencapsulated phase change material with enhanced thermo-physical properties

and photo-thermal performance," *Solar Energy Materials & Solar Cells*, vol. 143, pp. 29–37, 2015.

[3] B. Xu, J. Zhou, Z. Ni, C. Zhang, and C. Lu, "Synthesis of novel microencapsulated phase change materials with copper and copper oxide for solar energy storage and photo-thermal conversion," *Solar Energy Materials & Solar Cells*, vol. 179, pp. 87–94, 2018.

[4] N. J. Vickers, "Animal communication: when I'm calling you, will you answer too," *Current Biology*, vol. 27, no. 14, pp. R713–R715, 2017.

[5] A. Sharma, V. V. Tyagi, C. R. Chen, and D. Buddhi, "Review on thermal energy storage with phase change materials and applications," *Renewable and Sustainable Energy Reviews*, vol. 13, no. 2, pp. 318–345, 2009.

[6] X. Y. Xu, J. H. Liu, X. Ouyang et al., "In-situ temperature regulation of flexible supercapacitors by designing intelligent electrode with microencapsulated phase change materials," *Electrochimica Acta*, vol. 334, p. 135551, 2020.

[7] S. Alay Aksoy, C. Alkan, M. S. Tözüm, S. Demirbağ, R. Altun Anayurt, and Y. Ulcay, "Preparation and textile application of poly(methyl methacrylate-co-methacrylic acid)/n-octadecane and n-eicosane microcapsules," *Journal of the Textile Institute*, vol. 108, no. 1, pp. 30–41, 2017.

[8] R. K. Sharma, P. Ganesan, V. V. Tyagi, H. S. C. Metselaar, and S. C. Sandaran, "Developments in organic solid-liquid phase change materials and their applications in thermal energy storage," *Energy Conversion and Management*, vol. 95, pp. 193–228, 2015.

[9] Z. Chen, J. Wang, F. Yu, Z. Zhang, and X. Gao, "Preparation and properties of graphene oxide-modified poly(melamine-formaldehyde) microcapsules containing phase change material n-dodecanol for thermal energy storage," *Journal of Materials Chemistry A*, vol. 3, no. 21, pp. 11624–11630, 2015.

[10] J. Singh, S. Parvate, P. Dixit, and S. Chattopadhyay, "Facile synthesis of microencapsulated 1-dodecanol (PCM) for thermal energy storage and thermal buffering ability in embedded PVC film," *Energy & Fuels*, vol. 34, no. 7, pp. 8919–8930, 2020.

[11] F. Cheng, X. Zhang, R. Wen et al., "Thermal conductivity enhancement of form-stable tetradecanol/expanded perlite composite phase change materials by adding Cu powder and carbon fiber for thermal energy storage," *Applied Thermal Engineering*, vol. 156, pp. 653–659, 2019.

[12] D. Yin, H. Liu, L. Ma, and Q. Zhang, "Fabrication and performance of microencapsulated phase change materials with hybrid shell byin situpolymerization in pickering emulsion," *Polymers for Advanced Technologies*, vol. 26, no. 6, pp. 613–619, 2015.

[13] Y. Zhao, B. Yu, G. Yu, and W. Li, "Study on the water-heat coupled phenomena in thawing frozen soil around a buried oil pipeline," *Applied Thermal Engineering*, vol. 73, no. 2, pp. 1477–1488, 2014.

[14] G. N. Kumar, B. Al-Aifan, R. Parameshwaran, and V. V. Ram, "Facile synthesis of microencapsulated 1-dodecanol/melamine-formaldehyde phase change material using in-situ polymerization for thermal energy storage," *Colloids and Surfaces A: Physicochemical and Engineering Aspects*, vol. 610, p. 125698, 2021.

[15] X. Hu, Z. Huang, and Y. Zhang, "Preparation of CMC-modified melamine resin spherical nano-phase change energy storage materials," *Carbohydrate Polymers*, vol. 101, pp. 83–88, 2014.

[16] M. R. Yeung, P. K. Yuen, A. Dunn, and L. S. Cornish, "Performance of a solar-powered air conditioning system in Hong Kong," *Solar Energy*, vol. 48, no. 5, pp. 309–319, 1992.

[17] A. T. Naikwadi, A. B. Samui, and P. A. Mahanwar, "Melamine-formaldehyde microencapsulated n- tetracosane phase change material for solar thermal energy storage in coating," *Solar Energy Materials & Solar Cells*, vol. 215, p. 110676, 2020.

[18] F. Yu, Z. Chen, X. Zeng, X. Gao, and Z. Zhang, "Poly (methyl methacrylate) copolymer nanocapsules containing phase-change material (n-dodecanol) prepared via miniemulsion polymerization," *Journal of Applied Polymer Science*, vol. 132, no. 31, 2015.

[19] C. Alkan, A. Sarı, and A. Karaipekli, "Preparation, thermal properties and thermal reliability of microencapsulated *n* -eicosane as novel phase change material for thermal energy storage," *Energy Conversion and Management*, vol. 52, no. 1, pp. 687–692, 2011.

[20] S. Sami, S. M. Sadrameli, and N. Etesami, "Thermal properties optimization of microencapsulated a renewable and non-toxic phase change material with a polystyrene shell for thermal energy storage systems," *Applied Thermal Engineering*, vol. 130, pp. 1416–1424, 2018.

[21] Y. Fang, X. Liu, X. Liang, H. Liu, X. Gao, and Z. Zhang, "Ultrasonic synthesis and characterization of polystyrene/n-dotriacontane composite nanoencapsulated phase change material for thermal energy storage," *Applied Energy*, vol. 132, pp. 551–556, 2014.

[22] S. Lu, T. Shen, J. Xing et al., "Preparation and characterization of cross-linked polyurethane shell microencapsulated phase change materials by interfacial polymerization," *Materials Letters*, vol. 211, pp. 36–39, 2018.

[23] I. A. Kinloch, J. Suhr, J. Lou, R. J. Young, and P. M. Ajayan, "Composites with carbon nanotubes and graphene: an outlook," *Science*, vol. 362, no. 6414, pp. 547–553, 2018.

[24] Z. Han and A. Fina, "Thermal conductivity of carbon nanotubes and their polymer nanocomposites: a review," *Progress in Polymer Science*, vol. 36, no. 7, pp. 914–944, 2011.

[25] Z. Xu and M. J. Buehler, "Strain controlled thermomutability of single-walled carbon nanotubes185701," *Nanotechnology*, vol. 20, no. 18, 2009.

[26] V. Pethurajan and S. Sivan, "Fabrication, characterisation and heat transfer study on microencapsulation of nano-enhanced phase change material," *Chemical Engineering and Processing-Process Intensification*, vol. 133, pp. 12–23, 2018.

[27] C. Kwak, H. Park, J. H. Kim et al., "Surfactant-free fabrication of phase change material emulsions (PCMEs) using mineral oxide Pickering emulsifiers," *Korean Journal of Chemical Engineering*, vol. 37, no. 4, pp. 736–741, 2020.

[28] X. Jiang, R. Luo, F. Peng, Y. Fang, T. Akiyama, and S. Wang, "Synthesis, characterization and thermal properties of paraffin microcapsules modified with nano-Al_2O_3," *Applied Energy*, vol. 137, pp. 731–737, 2015.

[29] Q. Wang, M. Wang, J. Miao, W. Bi, H. Yang, and M. Zhang, "Fabrication of SiO 2 aerogel supported C/TiO 2 nanocomposite and Li+ storage performance," *Journal of Materials Science: Materials in Electronics*, vol. 30, no. 16, pp. 14834–14846, 2019.

[30] N. Şahan and H. Paksoy, "Determining influences of SiO_2 encapsulation on thermal energy storage properties of different phase change materials," *Solar Energy Materials & Solar Cells*, vol. 159, pp. 1–7, 2017.

[31] L. Liu, D. Su, Y. Tang, and G. Fang, "Thermal conductivity enhancement of phase change materials for thermal energy storage: a review," *Renewable and Sustainable Energy Reviews*, vol. 62, pp. 305–317, 2016.

[32] J. Shi, X. Wu, R. Sun, B. Ban, J. Li, and J. Chen, "Synthesis and performance evaluation of paraffin microcapsules with calcium carbonate shell modulated by different anionic surfactants for thermal energy storage," *Colloids and Surfaces A: Physicochemical and Engineering Aspects*, vol. 571, pp. 36–43, 2019.

[33] C. Li, G. He, H. Yan, H. Yu, and Y. Song, "Synthesis of microencapsulated stearic acid with amorphous TiO_2 as shape-stabilized PCMs for thermal energy storage," *Energy Procedia*, vol. 152, pp. 390–394, 2018.

Hindawi
International Journal of Photoenergy
Volume 2022, Article ID 3000227, 9 pages
https://doi.org/10.1155/2022/3000227

Research Article

Experimental Investigation on the Effects of Exhaust Emission Reduction in a Single Cylinder CI Engine Fuelled with Diesel and Diesel Plastic Pyrolysis Oil with Zeolite Nanomaterials

S. Jacob,[1] **L. Karikalan**,[1] **and Anirudh Bhowmick**[2]

[1]*Department of Automobile Engineering, VELS Institute of Science, Technology & Advanced Studies (VISTAS), Pallavaram, Chennai, 600 117 Tamil Nadu, India*
[2]*Faculty of Meteorology and Hydrology, Arba Minch Water Technology Institute, Arba Minch University, Ethiopia*

Correspondence should be addressed to L. Karikalan; karilk1972@gmail.com

Received 10 February 2022; Revised 12 March 2022; Accepted 18 March 2022; Published 4 April 2022

Academic Editor: V. Mohanavel

Copyright © 2022 S. Jacob et al. This is an open access article distributed under the Creative Commons Attribution License, which permits unrestricted use, distribution, and reproduction in any medium, provided the original work is properly cited.

The steady-state activity of zeolite 4A and 5A has been investigated experimentally for nitrous oxide and other emission gases in highly oxidizing conditions, typical for lean-burn engine exhaust. Zeolite has been characterized by XRD and FTIR. The CAD model is designed which shows the layout and basic mounting points of the catalytic converter on the Kirloskar TVI engine. Zeolite 4A and 5A substrate has been made using simple molding techniques, further heating it in an electric heater at 650°C for 6 hours. Several fuels such as plastic pyrolysis oil and diesel oil have been used to investigate the effect of NO on zeolite 4A and 5A substrate. The NO conversion has been found to be decreased by 40% using plastic pyrolysis oil. The zeolite powder has been added with 8% of bentonite clay and 5% of carboxymethyl cellulose powder, and 34% distilled water was stirred constantly to form like molding sand. The applied torque was monitored during stirring, signifying even mixing. The mixture has been kept in the prearranged mold design, and uniform pressure has been applied to guarantee no air holes in the shape. The hole pattern has been made using SOLIDWORKS and has been printed to get reliable openings (10 mm) with the assistance of wooden bars; the prearranged mold has been dried for 92 h in the immediate daylight; thereafter, dry pipes have been taken out from the mold. The subsequent form has been kept in the furnace at first at 150°C. Carboxymethyl cellulose is utilized as a fastener which assists with shaping the mold since it has great binding properties. Significant NO_x reduction of 45~50% using zeolite 5A and 27~30% using zeolite 4A mold structure with diesel fuel was observed. Reduction of 35~40% using zeolite 5A and 13~16% using zeolite 4A mold structure with PPO + diesel fuel was observed.

1. Introduction

The main problem today is the emission of harmful gases from automobiles which affects the environment in several ways. Nitrous oxide is the main threat to the environment such as global warming, ozone depletion, and acid rain [1]. The exhaust emissions include nitrogen oxides (NO_x), hydrocarbons (HC), carbon monoxide (CO), carbon dioxide (CO_2), and particulates [2]. Therefore, many countries have emission regulations such as EURO emission standards and Bharat stage emission standards for Indian cars. Currently, there are several techniques which are implemented to reduce the emissions from an exhaust gas including SCR using urea [3]. The conventional catalytic methods used to reduce NO_x automobile exhaust gases are categorized into (i) decomposition reactions, (ii) nonselective catalytic converter, and (iii) selective catalytic converter [4]. The selective catalytic reduction is used to reduce certain emission gases such as NO_x, HC, CO, and CO_2. Emission control of NO_x is less prominent in lean-burn engines such as diesel engines as it operates in highly oxidizing conditions [5]. The conversion of NO_x into less harmful gases such as N_2 is possible with three-way catalytic converters in spark ignition engines because gasoline engines work in rich-burn conditions [6]. The desire to improve fuel consumption and lower emissions of CO_2 is supposed to surge the demand of diesel

Zeolite 4A Zeolite 5A

Figure 1: Photographic view of zeolite in powder form.

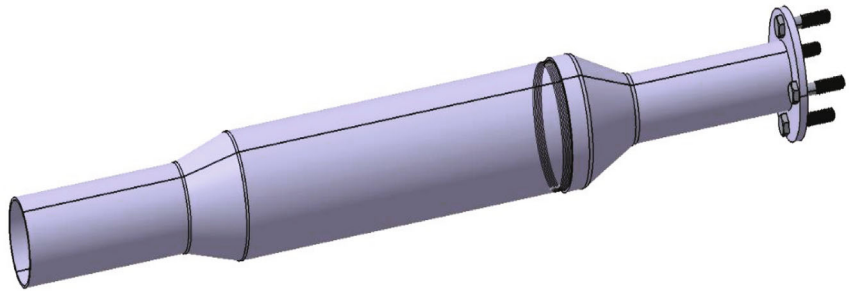

Figure 2: CAD model of catalytic converter casing.

engines [7]. Therefore, it is important to develop a system that can reduce NO emission from lean-burn engines. Though the traditional three-way catalytic converter does not control NO_x emission in oxygen-rich conditions [8], hydrocarbons are generally used to selectively reduce NO_x emissions as it acts as a reducing agent [9]. However, in a lean-burn engine, the hydrocarbon is not present in required quantities to complete decomposition of NO_x. Therefore, there is a need to develop a system that can reduce NO_x emissions from lean-burn engines [10]. Composite honeycomb consisting of microporous zeolite 5A is developed with many potential applications. The cordierite structure of zeolite 5A can be used in diesel engines in order to reduce NO_x emissions in lean-burn conditions [11]. Zeolites are a group of minerals that consists of calcium, sodium, and potassium. One of its properties is that they can be readily dehydrated and rehydrated. They can be used as molecular sieves and powders [12]. They are microporous minerals generally used as catalysts and commercial adsorbents. Zeolite has the property of absorbing impurities [13].

Figure 1 shows the photographic view of zeolite in powder form. The structure of zeolite is porous and thus can trap cations and others of the wide variety [14]. These cations can readily be exchanged with others in a contact solution which is loosely held [15]. These are used as catalysts in several acid catalytic reactions because these ions exchanged zeolite possessing acidity in a wide range. When ash layers and volcanic rocks will react with alkaline groundwater, it results in the formation of natural zeolite [16, 17]. Zeolites which occur naturally are not pure and are polluted by various metals, minerals, and other zeolite. These natural zeolites are not used in some commercial applications where purity and uniformity are important [18]. Compositions of the zeolites consist of Si, O, Al, and other metals like Zn, Sn, and Ti. The word molecular sieve means a particular property of the material and refers to the tendency of selectively sorting molecules based mainly on size [19]. This is because it has a very regular molecular pore structure. For specific separation of gases and removal of NO_2, CO_2, SO_2, and H_2O from exhaust gas streams, zeolites are widely used [20]. The necessity of this research work is to develop an exhaust aftertreatment system which is cost-effective and also optimal to achieve current emission norms of the required. The next level of development in this research is to implement urea injection and analyze and compare the performance and emission parameter results.

2. Experimental Work

2.1. CAD Modeling. CAD model has been designed using SOLIDWORKS 2017 considering all the mounting points. The material chosen for catalytic converter is steel. The dimension of the CAD model has been taken using different mounting points of the catalytic converter casing and length between mounting points, and it is shown in Figure 2.

Figure 3: Zeolite mixture.

Figure 4: Zeolite paste.

2.2. Catalyst Preparation Using Carboxymethyl Cellulose. Zeolite powder has been blended in with 8% of bentonite clay, 5% of carboxymethyl cellulose, and 34% of water by mixing as in Figure 3 continually to form like paste. Bentonite clay helps in converting zeolite powder into paste form, and carboxymethyl cellulose is a good binder. These chemicals do not affect the properties of zeolite after preparing mold. During blending, force applied was checked until it arrived at a uniform value, to have a homogeneous combination as in Figure 4. Zeolite paste has been put in the prepared mold cavity, and uniform pressure has been applied consistently to ensure that there are no air holes in the mold. The hole pattern has been made utilizing SOLIDWORKS and has been printed to get uniform opening diameter (12 mm) with the assistance of pipe as in Figure 5.

The outer casing of the catalytic converter has been made using hollow steel tubes which have been welded in order to prepare the outer case. The inlet and outlet section of the catalytic converter (diameter: 70 mm, length: 170 mm, thickness: 4 mm) has been used for the fabrication and reducer (diameter 1: 70 mm, diameter 2: 106 mm, length: 57 mm, thickness: 4 mm), and the main section (diameter: 106 mm, length: 348 mm, thickness: 4 mm) has been used to make the catalytic converter casing. A billet (thickness: 8 mm, diameter: 100 mm) has been used for fitting by drilling four uniform holes of 8 mm. For catalytic converter casing, TIG welding has been used to ensure proper welding between different parts of the catalytic converter and no gaps has been ensured. To enhance the serviceability of the casing, external threading has been done on one side of the main section and internal threading has been done on the reducer, threading up to 20 mm has been done to ensure proper fitting. The catalysts used nowadays in automotive industries are very expensive; the cost of zeolite powder is cost-effective and zeolite has the property of reducing harmful emission gases; that is the motive in selecting zeolite 4A and zeolite 5A for development. Mold was dried in direct sunlight for 96 hours, and then, mold was kept in an oven for 3 hours from 150°C to 600°C by increasing 75°C for every 30 minutes.

Figure 5: PVC pipes as mold cavity.

Table 1: Characteristics of plastic pyrolysis oil and high-speed diesel.

Fuel properties	Diesel	Plastic oil	Diesel + PPO
Density of fuel (kg/m^3)	832	794	813
Calorific value of fuel (kJ/kg)	45550	42500	43850
Kinematic viscosity (at), 40°C (cSt)	3.50	9.00	6.20
Flash point (°C)	52	60	55

Table 2: Engine specifications.

Specification	Parameter
Engine type	Kirloskar
No. of cylinders	Single cylinder
No. of stroke	Four-stroke
Cylinder diameter (mm)	87.5
Stroke (mm)	110
Compression ratio	17.5 : 1
Powered by	Diesel
Horse power (HP)	6.5 kW @ 1500 rpm
Dynamometer	Eddy current dyno

2.3. Welding of the Outer Case. The welding process used while fabricating the casing has been TIG welding (Tungsten Inert Gas). In this method, nonconsumable electrode is used to direct arc onto the metal surface until it gets to the

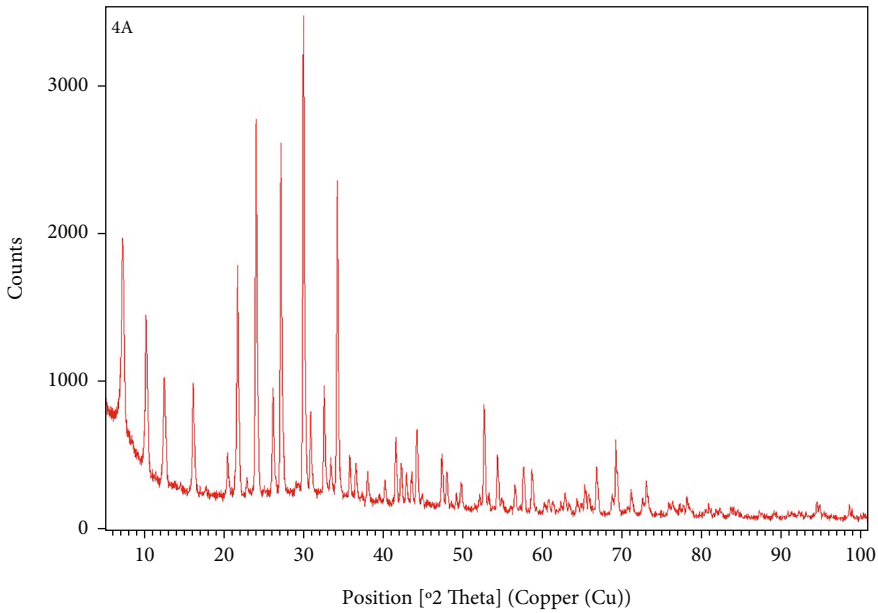

Figure 6: XRD pattern of zeolite 4A catalyst.

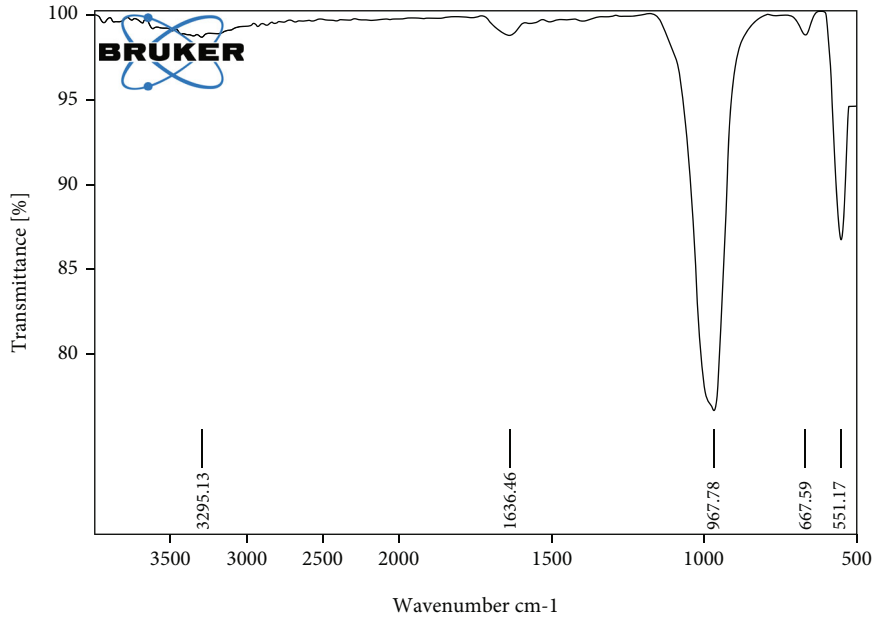

Figure 7: FTIR pattern of zeolite 4A catalyst.

melting point, and then, filler rods are poured in uniform motion to get proper weld with no gaps. This method has been preferred over arc welding because it forms a few blow-holes when compared to arc welding, which prevents gas from passing through the metal surface.

2.4. Threading of Outer Case. Threading at one side of the outer casing is done for the better serviceability, one side of the main section is threaded with external threading, and the larger diameter side of the reducer is threaded internally; threading is done to place the catalyst in the main section with the mesh and the separator supporting the catalyst inside the section. Internal thread on the large diameter side of reducer is done through the lathe machining, the reducer is fixed on the tool post, and after setting the reducer at right angle to the lathe axis, the threading operation is done using a thread gauge; the depth of cut on the reducer is given by the compound slide, and the internal threading is finished on reducer. For the external threading on the main section of the outer case, it has been machined by lathe machining.

2.5. Fabrication of Flange. The flange has been prepared using a billet of thickness 8 mm which has been turned to get the required diameter of 100 mm, four holes have been drilled uniformly of 8 mm diameter, and a center hole was milled of diameter 50 mm. Further, the flange has been

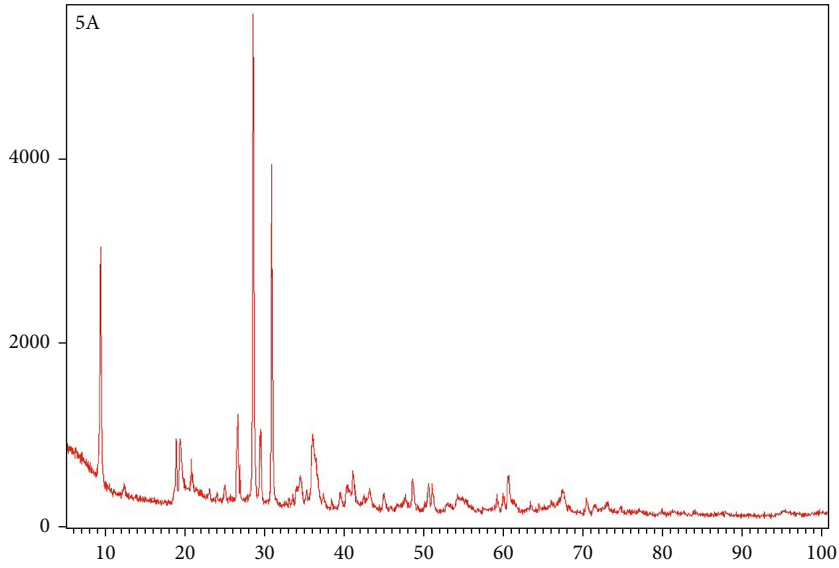

Figure 8: XRD pattern of zeolite 5A catalyst.

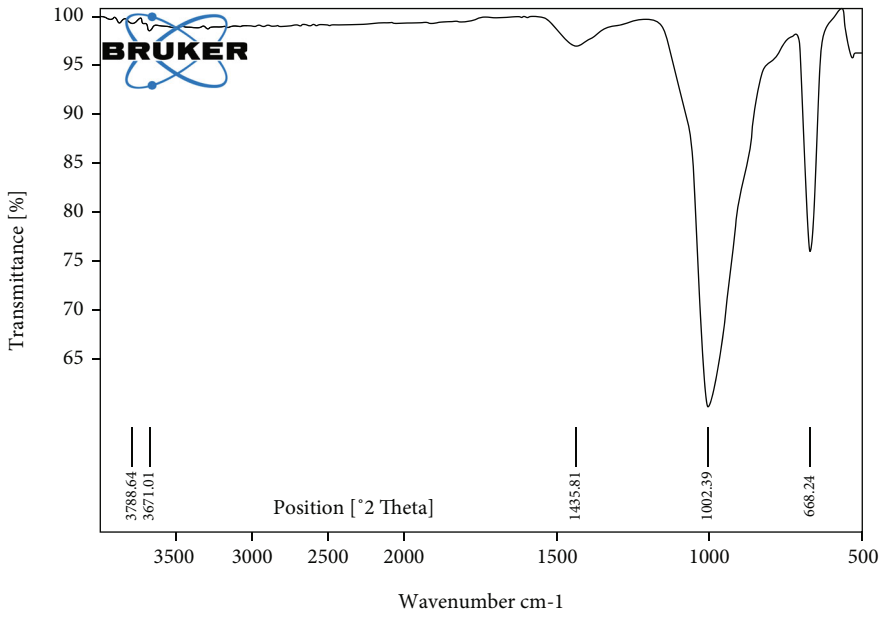

Figure 9: FTIR pattern of zeolite 5A catalyst.

welded to ensure proper fitting on the catalytic converter and mounting points.

2.6. Mesh Preparation with Metal Separators. Wire mesh is used with metal separators to ensure that the mold is kept at 1.5 cm distance between when the exhaust gas is passed through the catalytic converter. Wire mesh has been selected to ensure that the gas flow between the molds is adequate.

2.7. Fuel and Engine Specification. The fuel used for emission analysis is recycled plastic waste oil blended with diesel as shown in Table 1. Diesel with zeolite 4A and 5A catalyst is analyzed for emission of HC, NO_x. Test on diesel and plastic pyrolysis oil blend ratio of 50 : 50 with zeolite 4A and 5A catalyst is carried out on the engine with specification shown in Table 2, and the readings are taken. The major problem with the degradation of plastic is the very wide product range and the necessity of high temperature; to overcome this problem, catalytic degradation is done to reduce the temperature range of the reaction and also to improve the quality of the product.

3. Result and Discussions

3.1. XRD and FTIR Characterization of Zeolite Catalysts. Zeolite 4A X-ray diffraction patterns are shown in Figure 6. Zeolite has the property of observing oxygen from

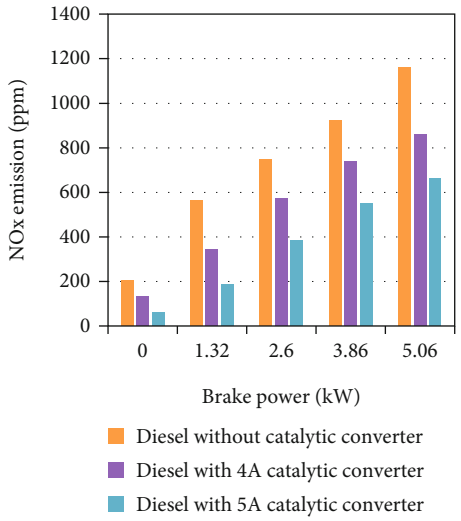

Figure 10: NO_x emission with diesel with zeolite 4A and 5A catalyst.

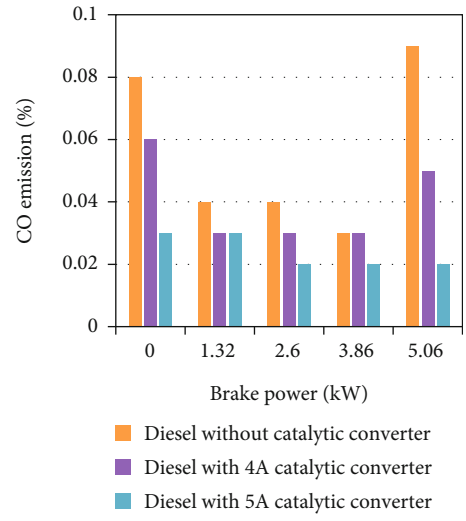

Figure 12: CO emission with diesel with zeolite 4A and 5A catalyst.

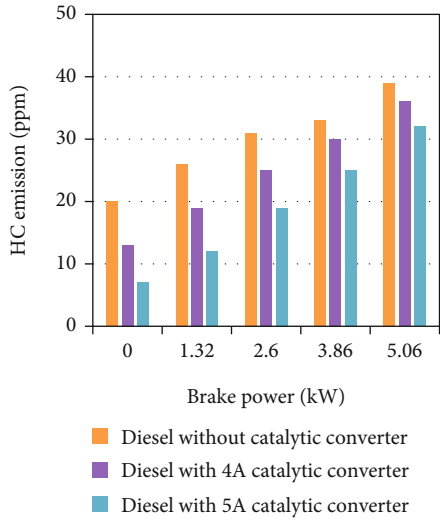

Figure 11: HC emission with diesel with zeolite 4A and 5A catalyst.

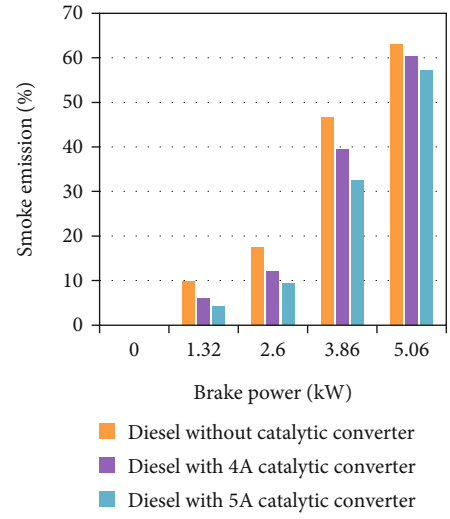

Figure 13: Smoke emission with diesel with zeolite 4A and 5A catalyst.

the harmful gases, it observes oxygen from NO_x and splits it into NO_2 and O_2, and it also converts HC, CO, and CO_2. The characteristic diffraction peak of zeolite 4A appears at 24°, 28°, 30°, and 34.3°. It can be clearly seen that the peaks correspond to those of zeolite 4A. The curve shows the scattered intensity vs. 2θ for a crystal solid is almost 0 everywhere except at certain angles where maximum high peak occurs.

The FTIR spectra of the sample show certain characteristics of absorption bands assigned to zeolite 4A. These spectra are in good agreement with zeolite 4A formed by conventional method, and it is seen in Figure 7.

Zeolite 5A X-ray diffraction patterns are shown in Figure 8. The characteristic diffraction peak of zeolite 5A appears at 9°, 28.10°, and 31.3°. It can be clearly seen that the peaks correspond to those of zeolite 5A. The peaks of the scattered intensity vs. 2θ for a crystalline solid are nearly zero all over apart from those at some angles, where the highest peaks occur maximum; these are deflected beams.

The FTIR spectrum of the sample confirms the characteristic absorption of bands assigned to zeolite 5A. This spectrum is also in good contract with that of zeolite 5A equipped by using conventional gel technique and displayed in Figure 9.

3.2. Emission Test on Diesel Engine. The emission test has been conducted on the Kirloskar single cylinder diesel engine. The test has been performed to analyze emission reduction using zeolite 4A and 5A as catalysts. The emission gases to be measured are nitrous oxides (NO_x), hydrocarbon (HC), carbon monoxide (CO), and smoke, and it is shown in Figures 10–13. First using diesel base engine

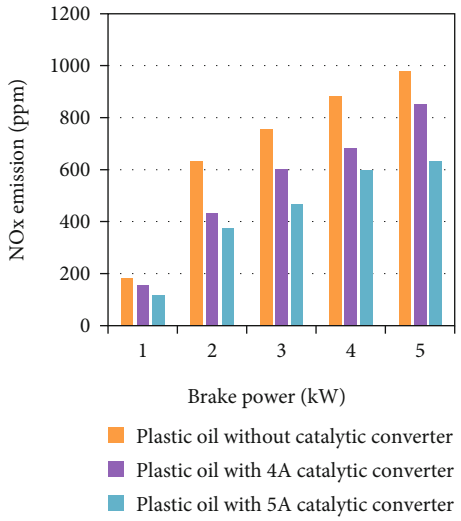

Figure 14: NO_x emission with diesel + PPO with zeolite 4A and 5A catalyst.

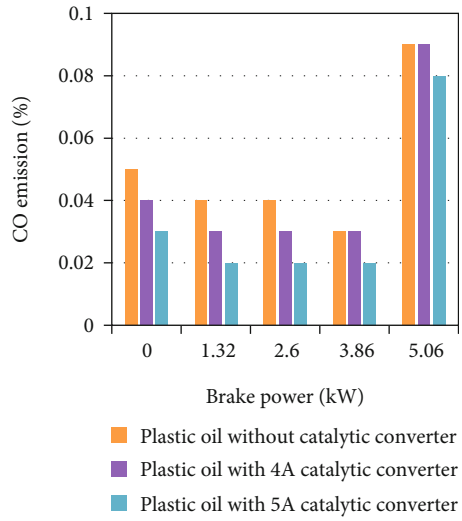

Figure 16: CO conversions with diesel + PPO with zeolite 4A and 5A catalyst.

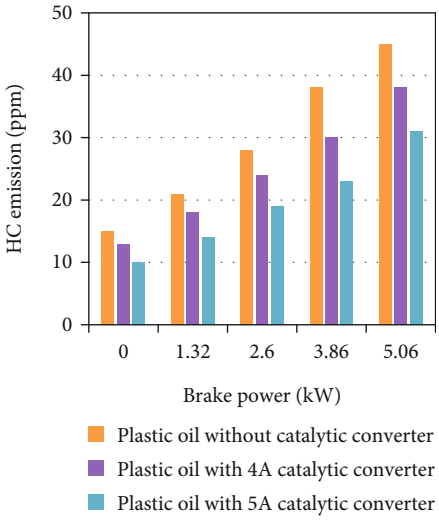

Figure 15: HC conversions with diesel + PPO with zeolite 4A and 5A catalyst.

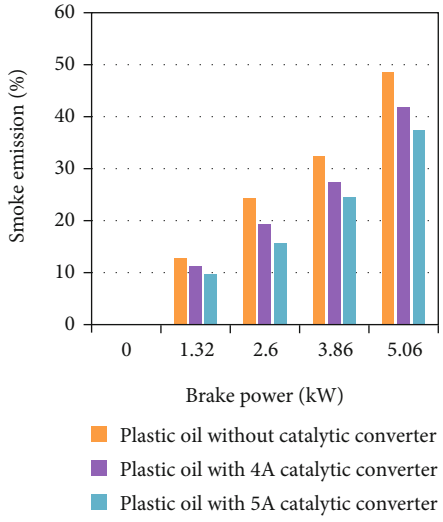

Figure 17: Smoke emission with diesel + PPO with zeolite 4A and 5A catalyst.

performance and emission without and with different catalyst have been tested.

The graph shows NO_x ppm at each load without and with catalytic converter. The graph explains that there is significant reduction in NO_x with each catalytic converter. The graph shows that NO_x reduction is higher with zeolite 5A than zeolite 4A at all loads.

The graph shows HC ppm at each load without and with catalytic converter. The graph explains that there is significant reduction in HC with each catalytic converter. The graph shows that HC reduction is higher with zeolite 5A than zeolite 4A at all loads.

The graph shows CO% at each load without and with catalytic converter. The graph explains that there is significant reduction in CO with each catalytic converter. The graph shows that CO reduction is higher with zeolite 5A than zeolite 4A at all loads.

The graph shows smoke at each load without and with catalytic converter. The graph explains that there is significant reduction in smoke with each catalytic converter. The graph shows that smoke reduction is higher with zeolite 5A than zeolite 4A at all loads.

3.3. Test on Diesel + Plastic Pyrolysis Oil Blend (50 : 50). The graph shows NO_x ppm at each load without and with catalytic converter. The graph explains that there is significant reduction in NO_x with each catalytic converter. The graph shows that NO_x reduction is higher with zeolite 5A than zeolite 4A at all loads, and it is seen in Figure 14.

The graph shows HC ppm at each load without and with catalytic converter. The graph explains that there is significant reduction in HC with each catalytic converter. The graph shows that HC reduction is higher with zeolite 5A than zeolite 4A at all loads and displayed in Figure 15.

The graph shows CO% at each load without and with catalytic converter. The graph explains that there is significant reduction in CO with each catalytic converter. The graph shows that CO reduction is higher with zeolite 5A than zeolite 4A at all loads, and it is displayed in Figure 16.

The graph shows smoke at each load without and with catalytic converter. The graph explains that there is significant reduction in smoke with each catalytic converter. The graph shows that smoke reduction is higher with zeolite 5A than zeolite 4A at all loads, and it is displayed in Figure 17.

4. Conclusion

Zeolite 4A and 5A have been used with conventional casting methods using carboxymethyl cellulose as binder to prepare the catalyst for substrate structure. The substrate has been heated at around 650°C for 4 hours with an increase 75°C for every interval of 30 minutes.

(i) Preparation of mold has been accomplished by using 8% of bentonite clay, 5% of carboxymethyl cellulose, and 34% of distilled water

(ii) The outer casing has been welded using TIG welding, and no gaps has been ensured; it is prepared with several metal parts

(iii) Length and dimension of the casing have been calculated for conventional catalytic converter measurements and space constraints

(iv) Exhaust back pressure created by catalytic converter is 60 mbar. The same back pressure was created in without catalytic converter setup by using electrical motor-controlled flap valve

(v) The gap between the molds has been chosen to be 2 cm in order to ensure proper adsorption on zeolite 4A and 5A

(vi) Reduction of NO_x has been proved using adsorption properties of ZSM 4A and 5A and decomposition reaction

(vii) Significant reduction of 42% in NO_x using zeolite 5A and 27% reduction in nitrous oxide (NO_x) using zeolite 4A mold structure were observed

(viii) Comparing zeolite 4A and 5A, it is observed that zeolite 5A has adequate amount of reduction in nitrous oxide and other harmful emission gases from a diesel engine

(ix) These results indicate that the use of zeolite 4A and 5A mold using bentonite clay and carboxymethyl cellulose as a binder is an effective way of reducing NO_x emissions

(x) Zeolite 4A and 5A molds could be used as catalytic converters after calcination to get an adequate amount of reduction in nitrous oxide and other harmful emissions from a diesel engine, typically lean-burn engines

(xi) Future scope of my study is to implement urea injection system in zeolite catalytic converter and validate the emission reduction

Data Availability

The data used to support the findings of this study are included within the article. Further data or information is available from the corresponding author upon request.

Conflicts of Interest

The authors declare that there are no conflicts of interest regarding the publication of this paper.

Acknowledgments

The authors appreciate the supports from Arba Minch University, Ethiopia, for providing help during the research and preparation of the manuscript.

References

[1] S. Mohanavel Vinayagam, M. M. Suresh Kumar, S. M. Ravikumar, and T. Raja, "Feasibility and emission study on employing MgO nanoparticle as oxygenated additive in neat biodiesel," *International Journal of Ambient Energy*, vol. 42, no. 14, pp. 1629–1634, 2021.

[2] S. Komarneni, H. Katsuki, and S. Furuta, "Novel honeycomb structure: a microporous ZSM-5 and macroporous mullite composite," *Communication*, vol. 8, no. 11, pp. 2327–2329, 1998.

[3] Z. Shan, W. E. J. van Kooten, O. L. Oudshoorn et al., "Optimization of the preparation of binderless ZSM-5 coatings on stainless steel monoliths by in situ hydrothermal synthesis," *Microporous and Mesoporous Materials*, vol. 34, no. 1, pp. 81–91, 2000.

[4] "Substrate heating method for coating metal surfaces with high-silica zeolites: ZSM-5 coatings on stainless steel plates," *Microporous and Mesoporous Materials*, vol. 101, no. 3, pp. 374–380, 2007.

[5] B. Ganemi, E. Björnbom, B. Demirel, and J. Paul, "Zeolite Cu-ZSM-5: material characteristics and NO decomposition," *Microporous and Mesoporous Materials*, vol. 38, 2000.

[6] R. Moreno-tost, "Selective catalytic reduction of nitric oxide by ammonia over Cu-exchanged Cuban natural zeolites," *Applied Catalysis*, vol. 50, no. 4, pp. 279–288, 2004.

[7] K. Okada, Y. Kameshima, C. D. Madhusoodana, and R. N. Das, "Preparation of zeolite-coated cordierite honeycombs prepared by an in situ crystallization method," *Science and Technology of Advanced Materials*, vol. 5, no. 4, pp. 479–484, 2004.

[8] B. K. Cho, "Nitric oxide reduction by ethylene over Cu-ZSM-5 Under lean conditions: Study of Reaction Dynamics by

Transient Experiments," *Applied Catalysis*, vol. 155, no. 2, pp. 184–195, 1995.

[9] Faros, *Selective catalytic reduction of nitrogen oxide using an iron impregnated zeolite catalyst*, United states patent, 1995.

[10] O. Krocher, "Investigation of the selective catalytic reduction of NO by NH_3 on Fe-ZSM5 monolith catalysts," *Applied Catalysis*, vol. 66, no. 3-4, pp. 208–216, 2006.

[11] R. M. Heck and R. J. Farrauto, "Automobile exhaust catalysts," *Applied Catalysis*, vol. 221, no. 1-2, pp. 443–457, 2001.

[12] Schneider, *Catalyst for reducing the nitrogen oxide content of flue gases*, United States patent, 1987.

[13] B. Louis, P. Reuse, L. Kiwi-Minsker, and A. Renken, "Synthesis of ZSM-5 coatings on stainless steel grids and their catalytic performance for partial oxidation of benzene by N_2O," *Applied Catalysis*, vol. 210, 2001.

[14] Y. Traa, B. Burger, and J. Weitkamp, "Zeolite-based materials for the selective catalytic reduction of NO with hydrocarbons," *Microporous and mesoporous materials*, vol. 30, 1999.

[15] M. Wallin, "Selective catalytic reduction of NO $_{x}$ with NH_3 over zeolite H-ZSM-5: influence of transient ammonia supply," *Journal of Catalysis*, vol. 218, no. 2, pp. 354–364, 2003.

[16] D. Florea, *Zeolite catalyst for the purification of automotive exhaust gases*, Surface scienceand catalysis, 1995.

[17] C. D. Madhusoodana, R. N. Das, Y. Kameshima, and K. Okada, "Preparation of ZSM-5 zeolite honeycomb monoliths using microporous silica. Obtained from metakaolinite," *Journal of Porous Materials*, vol. 12, 2005.

[18] M. Cheralathan and G. Balaji, "Experimental investigation to reduce exhaust emissions in a single cylinder CI engine fuelled with methyl ester of neem oil using antioxidant (L-ascorbic acid)," *Journal of biofuels*, vol. 7, no. 3, pp. 305–312, 2016.

[19] M. Cheralathan and G. Balaji, "The effect of antioxidant additives with methyl ester of neem oil on the oxidation Stability," *Energy Sources, Part A: Recovery, Utilization, and Environmental Effects*, vol. 38, no. 16, pp. 2454–2461, 2016.

[20] G. Balaji and M. Cheralathan, "Influence of alumina oxide nanoparticles on the performance and emissions in a methyl ester of neem oil fuelled direct injection diesel engine," *Thermal science*, vol. 21, no. 1 Part B, pp. 499–510, 2017.

Hindawi
International Journal of Photoenergy
Volume 2022, Article ID 9353470, 12 pages
https://doi.org/10.1155/2022/9353470

Research Article

Artificial Deep Neural Network in Hybrid PV System for Controlling the Power Management

Satyajeet Sahoo,[1] **T. M. Amirthalakshmi**,[2] **S. Ramesh**,[3] **G. Ramkumar**,[4] **Joshuva Arockia Dhanraj**,[5] **A. Ranjith**,[6] **Sami Al Obaid**,[7] **Saleh Alfarraj**,[8] **and S. S. Kumar**[9]

[1]*Department of Electronics and Communication Engineering, Vignan's Foundation for Science, Technology and Research (Deemed to Be University), Vadlamudi, Guntur, Andhra Pradesh 522213, India*
[2]*Department of Electronics and Communication Engineering, Vel Tech Multi Tech Dr. Rangarajan Dr. Sakunthala Engineering College, Avadi, Chennai-600062, Tamil Nadu, India*
[3]*Department of Electronics and Communication Engineering, St. Mother Theresa College of Engineering, Vagaikulam, 628102 Tamil Nadu, India*
[4]*Department of Electronics and Communication Engineering, Saveetha School of Engineering, SIMATS, Chennai, 602 105 Tamil Nadu, India*
[5]*Centre for Automation and Robotics (ANRO), Department of Mechanical Engineering, Hindustan Institute of Technology and Science, Padur, Chennai, 603103 Tamil Nadu, India*
[6]*Department of Electronics and Communication Engineering, St. Joseph University in Tanzania, Dar es Salaam, Tanzania*
[7]*Department of Botany and Microbiology, College of Science, King Saud University, P.O. Box 2455, Riyadh 11451, Saudi Arabia*
[8]*Zoology Department, College of Science, King Saud University, Riyadh 11451, Saudi Arabia*
[9]*Department of Bioenvironmental Energy, College of Natural Resources & Life Science, Pusan National University, Miryang-si 50463, Republic of Korea*

Correspondence should be addressed to G. Ramkumar; pgrvlsi@gmail.com and A. Ranjith; ranjith.arumugam@sjuit.ac.tz

Received 18 January 2022; Revised 29 January 2022; Accepted 5 February 2022; Published 10 March 2022

Academic Editor: V. Mohanavel

Copyright © 2022 Satyajeet Sahoo et al. This is an open access article distributed under the Creative Commons Attribution License, which permits unrestricted use, distribution, and reproduction in any medium, provided the original work is properly cited.

The analysis of different components of a grid-linked hybrid energy system (HES) comprising a photovoltaic (PV) system is presented in this work. Due to the increase of the population and industries, power consumption is increasing every day. Due to environmental issues, traditional power plants alone are insufficient to supply customer demand. In this case, the most important thing is to discover another approach to meet customer demands. Most wealthy countries are now concentrating their efforts on developing sustainable materials and investing considerable amounts of money in product development. Wind, solar, fuel cells, and hydro/water resources are among the most environmentally benign renewable sources. To control the variability of PV generation, this sort of application necessitates the usage of energy storage systems (ESSs). Lithium-ion (Li-ion) batteries are the most often used ESSs; however, they have a short lifespan due to the applied stress. Hybrid energy storage systems (HESSs) started to evolve as a way to decrease the pressure on Li-ion batteries and increase their lifetime. This study represents a great power management technique for a PV system with Li-ion batteries and supercapacitor (SC) HESS based on an artificial neural network. The effectiveness of the suggested power management technique is demonstrated and validated using a conventional PV system. Computational models with short-term and long-term durations were used to illustrate their effectiveness. The findings reveal that Li-ion battery dynamical stress and peak value are reduced, resulting in longer battery life.

1. Introduction

In today's world, energy is critical to industrialization, urbanization, and a country's economic progress. According to the US EIA report, worldwide energy consumption is increasing at a rate of about 2.3 percent each year. According to the analysis, gasoline will be in short supply around the planet soon. Energy sources are the primary source of pollutants in the environment, including air and water contamination. As a result, renewable energy (RE) resources such as groundwater, air, photovoltaic, biofuels, and others have gotten more attention as potential energy individual behavioral. Renewable technologies, according to Kumar's research, are ubiquitous and affordable and polluted air [1]. Hybrid power systems are used to deliver loads and ensure load demand without the need for human involvement. People can use a variety of sources, including conventional sources such as coal, natural gas, and fossil fuels, as well as renewable technologies such as solar, wind, and hydroelectric. In addition to energy, a hybrid system includes DC or AC converters, a storage capability, and a process control enabling energy monitoring. A fuel cell functions as a battery, storing energy in the form of hydrogen [2]. It produces water and electricity by reacting hydrogen with atmospheric oxygen. However, multiple energy sources are required, such as the use of batteries in a rechargeable battery to harvest oxygen from the water or air, which results in a greater hydrogen storage price.

The goal of optimization algorithm-based strategies is to minimize an optimal solution. In general, the goal of reduction of this objective function is to lower the operational cost over a given period or to extend the lifespan of the HESS pieces. There are two sorts of strategies in this classification: optimization algorithm strategies and real-time optimization techniques. Based on a past understanding of future operational conditions, optimization algorithm strategies are devised to produce the best global solution [3]. Because of the higher processing expenses, this theory's real-time use has been restricted; this is generally only used to obtain a standard response to assess and change. Mathematical model, dynamic software, evolutionary algorithms, optimal controllers, and particle swarm optimization are some of the global optimization methodologies (PSO). Real-time optimization algorithms, on either extreme, use power supply choices to minimize an optimization problem. In particular, in both processing capacity and memory capacity, the mathematical modeling of this method must be appropriate for real-time implementation [4]. Pontryagin minimum principle (PMP), equivalent cost minimization strategy (ECMS), adaptive dynamic programming (ADP), model predictive control (MPC), extreme search (ES), artificial neural networks (ANNs), and robust control (RC) are all real-time optimizing methodologies.

An independent system with a HESS comprising Li-ion battery and SC, as well as a secondary storage resource, a fuel cell, was demonstrated with such a variable power control technique. Using a rolling average filter, the voltage regulation approach produces real-time values to the converters' speed controller connected with fuel cell, Li-ion batteries, and SC [5]. The simple moving machine's effectiveness is reinforced by simulation study experiments, which divide the average current reference between Li-ion batteries and fuel cells while efficiently distributing the rapid and oscillating demand elements to the SC. To manipulate the SOCs of the battery and the SCs and maintain it being within norms, an MPC voltage regulation approach was employed [6]. Given the complexity of using discrete modeling techniques and the high processing expense, this is a viable technique.

Photovoltaic technology is an excellent RES for controlling electromagnetic energy production from such a large centralized facility to a large number of tiny decentralized and distributed systems, reducing environmental impact and increasing resource production in remote places. The costs of photovoltaic components are rapidly decreasing, enabling photovoltaic systems more affordable than traditional energy sources [7]. Lithium battery packages and an energy storage stack make up the powerful engine of a typical proton electrolyte membrane hybrid hydrogen fuel cell. In this paper, a multiobjective optimum including fuel efficiency and system reliability is discussed for this commercial vehicle engine and transmission concept [8]. Given the complexity of using discrete modeling techniques and the high processing expense, this is a viable technique. A soft-run technique is given for the real-time and the interpredictive control method, based on the optimal results achieved by nonlinear optimization. The capacity of the lithium battery is taken into account to improve the soft-run method, which is carried out using two real-time algorithms. The energy requirement produces the best strategy which has proven to be the most suitable for power transit systems equipped with a bigger capacity battery, resulting in improved nonlinear programming results.

Classical control systems, such as RBC and frequency-based approaches, are still more susceptible to variable fluctuation and require an exact parametric representation, whereas optimization algorithm-based techniques are much more accurate and efficient [9]. As a result, artificial neural network-(ANN-) based optimization procedures are being designed to lessen the influence of parameter changes and to improve control methods. Due to its excellent generalization capabilities and nonlinear and adaptable architecture, which can improve the system dynamics without needing an accurate model, they can be successfully employed in process control.

An off-grid PV energy infrastructure with such a HESS comprised of a special type cell and lead-acid batteries was suggested using ANN-based power control. The proposed power requires managers to maintain a consistent battery SOC by controlling the electrolytes and hydrogen fuel outputs. In particular, compared to other approaches, simulated studies revealed that the suggested system has a fast response capability [10]. The high-frequency and low-frequency elements of a microgrid with such a HES made of Li-ion batteries and SC were separated using a wavelet treatment. To provide a better DC link voltage, a backpropagation ANN was also used to determine the current source of the Li-ion battery. The simulation experiments showed that the suggested power management can compensate for power variations from renewable electricity while keeping the DC voltage steady.

For powered mobility, an ANN-based power management technique was presented. A HES is used in the device, with Li-ion batteries permanently attached to the DC bus and SCs linked via a DC/DC conversion. The purpose of the installed ANN is to manage the SC DC/DC limit in addition to supporting Li-ion packs and increasing their lifetime. In comparison to battery-only ESSs, the simulations revealed a 64.8 percent increase in the lifetime of Li-ion batteries [11]. This presents a novel power strategic approach for HESSs based on ANN with low operating complexity, capable of managing the energy flow of all HESS components and extending the life of Li-ion battery systems by reducing dynamic strain and peak market requirements while consistently providing the stress only with demanded strength [12]. To maintain the protection and longevity of every ESS, the suggested energy management approach evaluates its SOC in real time and alters its charge/discharge commands. A typical standalone PV system with DC coupling and centralized control design was generated and constructed to test the effectiveness of the suggested battery management technique.

2. Related Works

A method for operating a grid-connected hybrid approach is presented in this study [13]. A control scheme with a photovoltaic (PV) array and a proton exchange membrane fuel cell (PEMFC) is being studied. When fluctuations in temperature and irradiance happen, the PV array usually employs a maximum power point tracking (MPPT) approach to continually send the greatest energy to the system, making it an uncontrolled source. The hybrid system's input voltage is controlled thanks to the PEMFC. Unit-power control (UPC) and feeder-flow control (FFC) are different operating methods that can be used with a hybrid system. The presentation covers the coordinating of two input modes, the synchronization of the PV system as well as the PEMFC within a hybrid power system, and also the derivation of estimate. The suggested operating strategy with variable operation mode shift always maintains the PV module at peak voltage and the PEMFC through its highly efficient performing band, resulting in improved performance and reliability, increased stability of the system, and fewer operating mode transitions.

A technology known as maximum power point tracking (MPPT) is used to improve photovoltaic (PV) power-generating efficiency. For quick climate changes and partial shade circumstances, this work offers a hybrid MPPT algorithm combining the modified invasive weed optimization (MIWO) and perturb and observe (P&O) techniques for effective removal of peak power from such a freestanding PV-based hybrid model. To obtain speedy global peak (GP) and maximal PV power, MIWO manages the earliest phases of MPPT and tests the effectiveness of the P&O algorithm in the latter stages. The PV system, batteries, accumulator, hydrogen fuel, and demand are all part of the microgrid under investigation. To protect the batteries from unwanted charging/discharging operations, a synchronized DC voltage-regulating and voltage control technique is

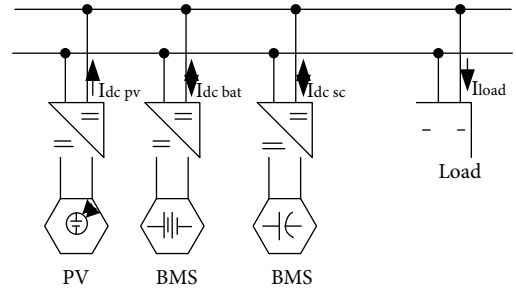

Figure 1: Implemented system block diagram.

established between every component of the hybrid power system. Furthermore, with the measurement of DC voltage, the DC/DC converter connected to the battery and DC link functions as an MPPT circuit for the PV, eliminating the need for an additional specialized circuit. The Takagi-Sugeno (TS) fuzzy controller is used to suppress/mitigate microgrid energy oscillations caused by changes in solar irradiation and power consumption. When compared to a few of the existing methodologies, the findings clearly show that the proposed approach outperforms them [14].

Solar energy creation is sporadic. A photovoltaic (PV) system's ability to produce power constantly and reliably to a fluctuating load is practically impossible. Paralleling a controlled source, such as a fuel cell, with PV could be a method for supplying electricity to changeable loads. A power management solution for the microgrid network is necessary to manage the power source between fuel cells and PVs. This work provides a remote monitoring system for such a grid-connected PV and solid oxide fuel cell (SOFC) that takes a load and direct solar variations into account. The suggested system's goal is to draw as little electricity from the grid as possible while operating the SOFC within a certain range. Because the PV is operating at maximum output, the power management requires using a proportional and integral (PI) system to control the power factor of the SOFC. The genetic algorithm (GA) and simplex approach are used to estimate the parameter settings of a PI controller K_p (proportional constants) and T_i (essential time continual). In addition, to produce suitable control variables for the PI controller, a fuzzy controller is constructed. The sum of the advanced process by standard deviation (ITAE) criteria is used to measure the controls' effectiveness. The fuzzy-based PI controller beats the PI controller adjusted by GA and linear approach in regulating the energy first from mixed source efficiently under demand and solar irradiance fluctuations, according to numerical simulations [15].

Today, consumption is growing at a rapid rate, highlighting the need for renewable resources. Among the several sources of renewable energy, power through solar cells is found to be an excellent source. However, one disadvantage of renewable radiation is that it was not available at that time, necessitating the use of additional sources in conjunction with solar fuel to produce the process more accurately and effectively. So, when power generated from the sun is insufficient to fulfill the necessary load, a solar energy system is integrated with a diesel power system developed to supply

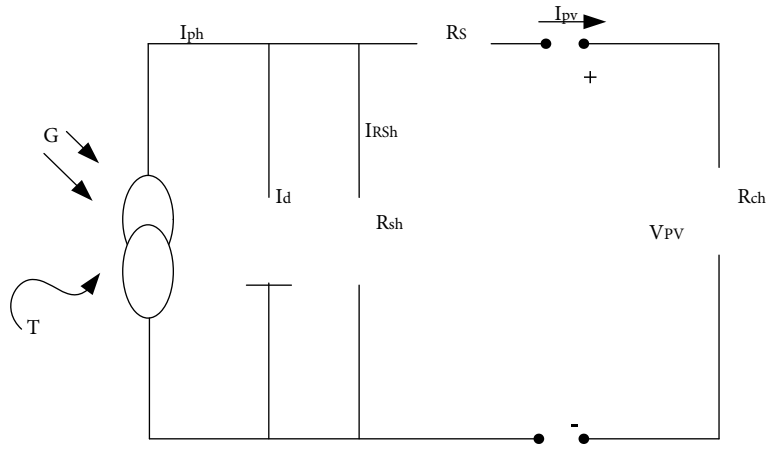

Figure 2: Boost converter.

the required. The battery energy storage technology is used as a backup device in this case (BESS). The PV-battery diesel combo is exported to the electrical to reach the necessary power consumption [16].

This research offers an energy management system (EMS) centered on artificial neural networks (ANNs) for regulating power in AC–DC hybrid distribution channels. The suggested ANN-based EMS gathers information like distributed generation (DG) energy, power system, and status of charge to determine the best operating mode (SOC). Profile information also on power conversion quantity of ESS for different distribution system energy scenarios was generated for learning the ANN, and also, the ANNs were educated with such a failure rate of less than 10%. In a grid-connected hybrid manner, the suggested EMS uses an already taught ANN to operate every voltage regulator in the best mode of operation. A modest hybrid AD/DC microgrid was built for model validation of the recommended EMS, and calculations and tests were conducted for each operating condition [17].

3. Materials and Methods

The equivalent circuit of the developed system is shown in Figure 1: a freestanding photovoltaic system using DC couplings and a logically centralized structure, composed of a PV unit, Li-ion battery, and SC. A buck-boost converter connects the PV unit's configurable sources and solar photovoltaic profile virtualization software configuration to the DC bus. Using the maximum power point tracking (MPPT) method, the buck-boost converter extracts the output power of the PV unit [18]. Two converters, DC/DC buck-boost converters, provide electron flow between its ESSs as well as the DC link. The system's major objective is to collect the highest available generated by the PV module to a DC bus at every given time, as well as capacity to control the energy flow among all HESS components while meeting the demand at any given time.

A Texas Electronics (Dallas, TX, USA) microprocessor TMS320F28069 serves as the actual control unit. This 32-bit fixed-point microcontroller is competent in parallel computing and is employed in mathematical applications of increasing difficulty. It operates at 90 MHz and has 100 kb and 2 kb of RAM and ROM memory, correspondingly, as well as 256 kb of flash memory. It also has 16 pulse width modulation (PWM) channels and 16 ADC channels with 12-bit precision and obtained using difference of roughly 333 nanoseconds. It also supports 12C, CAN, and SPI connectivity. Li-ion batteries and SC make up the HESS. Each of these ESSs is made up of several 12 units.

3.1. PV Energy System. To examine the nonlinear properties of PV generators related to semiconductor technology, different mathematical methods have been constructed [19]. The following model was proposed for this research:

PV current:

$$I_{\mathrm{pv}} = I_{\mathrm{ph}} - I_{\mathrm{d}} - I_{\mathrm{Rsh}}. \tag{1}$$

Then, the equation of current is given by

$$I_{\mathrm{pv}} = I_{\mathrm{sc}}\left\{1 - Q_1\left[\exp\left(U_2, R_{\mathrm{mpu}} - 1\right)\right]\right\}, \tag{2}$$

where U_1, U_2, and r are the coefficients given by

$$\begin{aligned} U_1 &= 0.01175, \\ U_2 &= \frac{U_4}{V_{\mathrm{oc}}\, r}, \\ U_2 &= \ln\left[\frac{I_{\mathrm{sc}}(1+U_1) - I_{\mathrm{mpp}}}{U_1 + I_{\mathrm{sc}}}\right], \\ U_4 &= \ln\left[\frac{1+U_1}{U_1}\right], \\ r &= \frac{\ln\left[U_2/U_4\right]}{\ln\left[V_{\mathrm{mpp}}/V_{\mathrm{oc}}\right]}. \end{aligned} \tag{3}$$

For standard test conditions (STP) of GSTC = 1000 W/

Table 1: ESS charge or discharge.

	Boost converter		Buck converter		Buck-boost converter	
	Charge	Discharge	Charge	Discharge	Charge	Discharge
1	0	Pulse widthmodulation	$\overline{\text{Pulse width modulation}}$	0	0	Pulse width modulation
2	1	$\overline{\text{Pulse width modulation}}$	Pulse width modulation	1	Pulse width modulation	1
3	$\overline{\text{Pulse width modulation}}$	1	1	Pulse width modulation	1	Pulse width modulation
4	Pulse width modulation	0	0	$\overline{\text{Pulse width modulation}}$	Pulse width modulation	0

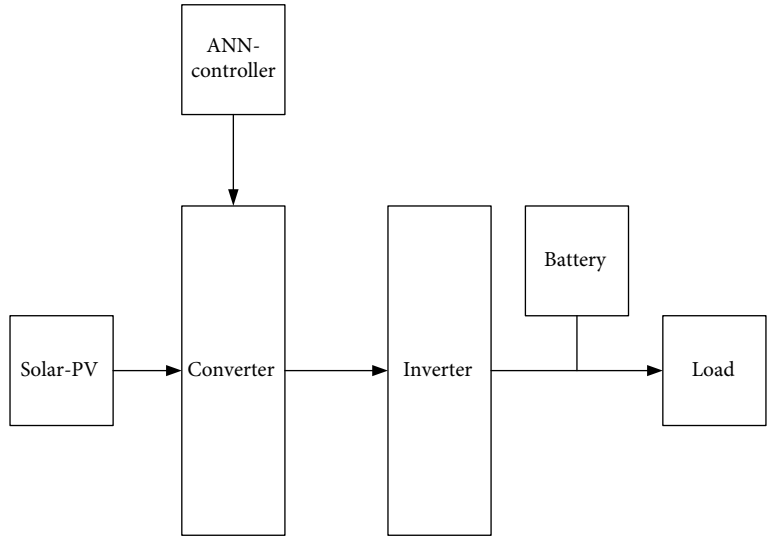

Figure 3: Configuration of the power management system.

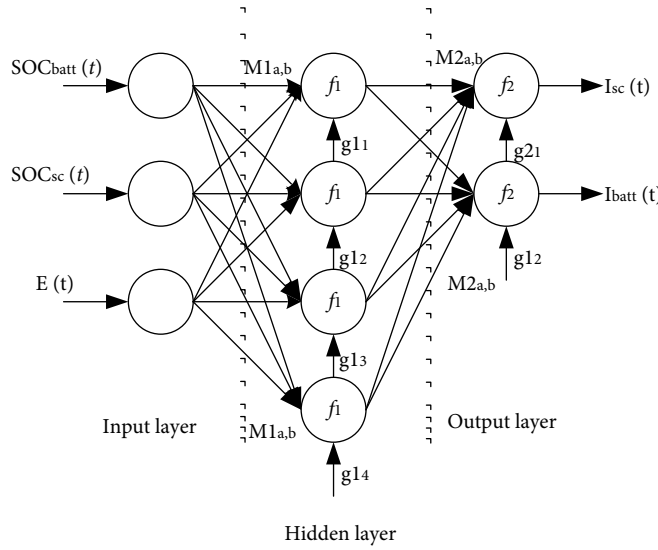

Figure 4: The architecture of a neural network.

m^2 and TSTC = 250 C, Equation (2) is only applicable for one irradiation level G with module temperature T_m. According to the formulae, as temperatures and isolated change, other parameters change as well:

$$\Delta T_m = T_m - T_{STC},$$
$$\Delta I_{pv} = \alpha_{sc}\left(\frac{G}{G_{STC}}\right)\Delta T_m + \left(\frac{G}{G_{STC}} - 1\right)I_{sc,STC}. \quad (4)$$

Voltage of PV:

$$\Delta V_{pv} = -\beta_{oc}\Delta T_m - R_s\Delta I_{pv}. \quad (5)$$

3.2. Boost Converter. A boost converter in Figure 2 seems to be a DC to DC switching mode conversion with a higher output voltage than that of the input power. It was also known as a step-up converter. The inductance within the input signal resists abrupt fluctuations in input current, which boosts the converter's function [20]. It is stored in the inductor power in the induced electromagnetic force while switch S is open and releases it because when switching S is shut. The output circuit's capacitance is large enough because the outputs track's RC circuit's sampling frequency is high. When compared to the switching cycle, the sampling frequency is large, resulting in minimal output power.

$$V_o(t) = V_0(\text{constant}). \quad (6)$$

Duty cycle:

$$D = \frac{1 - V_{in(min)} \times \eta}{V_{out}}. \quad (7)$$

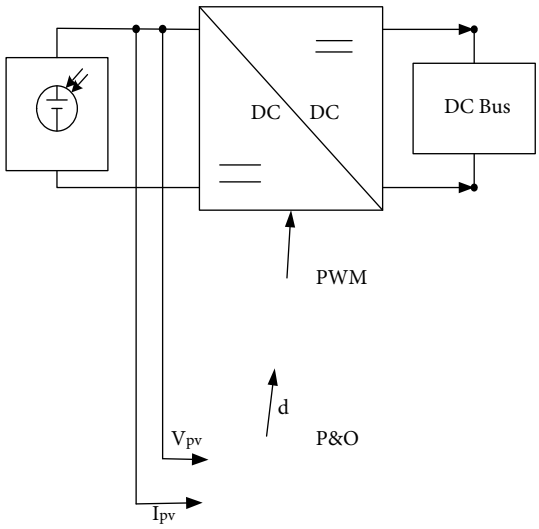

Figure 5: Control system of P&O.

Table 2: Parameter of PI controller.

Controller	Parameter	Closed-loop current	Closed-loop voltage
$PI_{battery}$	K_i	0.0043075	0.0207
	K_p	1.7813	0.0515
PI_{SC}	K_i	0.0001	0.0001
	K_p	0.7788	0.9378
$PI_{reference}$	K_i	0.005965	0.042
	K_p	0.4	4.6145

Voltage output:

$$V_{\text{out}} = \frac{V_{\text{in}}}{1-D}, \qquad \Delta I_L = \frac{V_{\text{in(min)}} \times D}{f_s \times L}. \tag{8}$$

Current output:

$$I_{\text{max out}} = \left(I_{\text{lim(min)}} - \frac{\Delta I_L}{2}\right) \times (1-D). \tag{9}$$

3.3. Inverter. An inverter is a power electronic system that transforms DC electricity into AC power while also regulating the signal's amplitude, current, and speed. The DC power from a solar panel is sent to an inverter that transforms it to AC and delivers it to the demand in photovoltaic systems.

Voltage output:

$$V(t) = V_0 \cos(\omega t). \tag{10}$$

Current output:

$$I(t) = I_0 \cos(\omega t - \Psi). \tag{11}$$

Table 1 shows the difficult switching options for each ESS discharge and charge method of operation.

3.4. Power Management System. The benefits of the proposed PV hybrid power system using battery storage are dependent on several significant criteria, including the form and type of the load, speed, solar irradiation, cost of energy, and accessibility. For low-power applications, photovoltaic systems seem to be more cost-effective. The cost of electricity storage is an essential parameter to consider in the development of PV power systems using renewable power in automated vehicles [21]. To do so, one must analyze several different economic theories for each PV system separately. The fundamental rationale for PV systems would be to reduce the volume and cost of inventory. The suggested power generation system, as depicted in Figure 3, combines multiple sources of energy: PV as well as a battery as a backup. The ANN manager is in charge of managing natural resources. PV is considered a main/primary supplier by ANN-based power management controller (PMC) generator which is considered a supplementary source by ANN-based voltage regulation controller (PMC). The primary goal of a PMC for an autonomous combination is to meet load requirements in climatic variations while also managing power flow to ensure reliable functioning. Three control phases are recommended to complete the entire energy consumed by the load and recharge the batteries based on variations in irradiance, temperatures, and speed to determine the PV hybrid renewable energy system's capability.

The required control scheme and controlling techniques of a hybrid energy management system can vary considerably or even theoretically from those of conventional energy systems, depending on the classification and severity of available renewable energy component propagation, load behavior, and voltage stability restrictions. Because energy resource components, especially digitally coupled equipment, have distinct steady-state and dynamic properties than typical large turbine generating units [22], the intelligent control scheme for the proposed HES is depicted as a block diagram. For such specified solar irradiance and speed, a feed-forward ANN is used to calculate the operational maximum power point of hybrid power management. The training is performed using test data collected at various radiation levels.

As shown in Figure 4, the developed architecture employs a multilayer feed-forward neural network (FFNN). The information is transmitted without reflection in the interconnected neurons in this structure, i.e., the number of emissions does not quite have valuable feedback to all the other neural sources. Equations (12) and (13) can be used to depict the output layer which generates the reference signal ($I_{\text{ref bat}}$ and $I_{\text{ref SC}}$) in Figure 4:

$$I_{\text{ref bat}}(t) = f_2\left[\sum_b \left[\text{Rw}_{b,1} \times f_1\left[\sum_a Iw_{a,b} \times \begin{bmatrix} u_a \\ \text{SOC}_{\text{bat}}(t) \\ \text{SOC}_{\text{SC}}(t) \\ E(t) \end{bmatrix} + g_b\right]\right] + g_{2,1}\right], \tag{12}$$

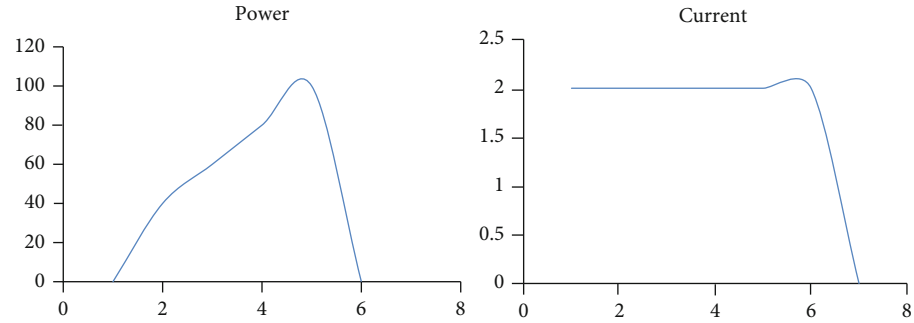

Figure 6: The curves of power voltage and the current voltage.

$$I_{\text{ref SC}}(t) = f_2\left[\sum_b \left[\text{Rw}_{b,2} \times f_1\left[\sum_a Iw_{a,b} \times \begin{bmatrix} \overset{u_a}{\widehat{\text{SOC}}}_{\text{bat}}(t) \\ \text{SOC}_{\text{SC}}(t) \\ E(t) \end{bmatrix} + g_b\right]\right] + g_{2,2}\right], \tag{13}$$

where i is the number of iterations, u_a is the data input matrix, b is the number of hidden neurons, and f_1 and f_2 are the activation functions. The values of the connections between both the encoder and decoder layers are represented by Rw; the masses of the connections between both the hidden layer and output layer are represented by Lw, and the bias of a transistor in the corresponding layers is represented by g_1 and g_2. The Heaviside value, the symmetrical saturated function with respect, the sigmoid component, the Gaussian feature, the logistic sigmoid operation, and also the spline feature are some of the regularly utilized training algorithms that must be selected suitably for every layer [23]. The symmetrical saturated linear model was applied in both stages in this research. The training technique, which may be classified into two basic classes: supervised learning techniques and unsupervised training techniques, is among the most significant elements of an ANN. The Levenberg-Marquardt learning algorithm was utilized to optimize the FFNN emotional experiences in the developed learning approach, which was an offline required guidance. In an attempt to optimize ANN learning accuracy and generalization capacity, input samples were constructed using artificial information while following numerous principles.

To maintain adequate use across manufacturer's standards, the regulations used in the development of ANN for adjusting the power were predicated on the authorized rated capacity of the Li-ion battery [24]. To reduce Li-ion battery real situation and peaking currents, limits were set for the maximum batteries current flowing ($I_{\text{mc battery}}$) and maximum Li-ion battery discharging current ($I_{\text{md battery}}$). These restrictions were calculated as a fraction of the Li-ion batteries' maximum design power. To ensure the safety and quality of Li-ion batteries and increase their lifetime, a functional range of SOC was developed ($\text{SOC}_{\text{min battery}}$ and $\text{SOC}_{\text{max battery}}$). The SOC operating range for Lion packs is now to be set between 20% and 90%, which was defined as the optimal frequency. Due to the fundamental properties of SCs, there is no such limiting problem about the SOC operating range; thus, the established limits of $\text{SOC}_{\text{min SC}}$ and $\text{SOC}_{\text{max SC}}$ were set at 20% and 100%, accordingly.

Table 3: PV system values.

Short-circuit power (A) (I_{SC})	4.96 A
Voltage coefficient of temperature (β_{OC})	-150 mV/°C
Coefficients Q_1	0.01175
Short-circuit temperature coefficient (α_{SC})	3.00 mA/°C
Standard conditions of test (T_{STC})	25°C

3.5. Control System. Closed-loop power converter and closed-loop voltage regulation are two types of techniques for the specified control strategy. Before turning on the machine, the operating settings were chosen [25]. A voltage regulation approach and three error signal processors with mechanisms are among the deployed control schemes (PI-awu). The power management approach among ESSs is executed with an FFNN which defines the current references ($I_{\text{ref bat}}$ and $I_{\text{ref sc}}$) in real-time information while taking into account the state of charge of a two parental, which is determined using the charge density method of counting, which quantifies this same charging/discharging current of such a battery/SC bundle and combines current over the period.

The result from PI_{ref} a controller is another FFNN input. It works to eliminate the error signal between the reference voltage $I_{\text{ref bat}}$ and the DC bus voltage (V_{dc}) in the closed-loop voltage control scheme, and it functions to eliminate the error signal between the reference current ($I_{\text{dc bat}}$) and the load current in the closed-loop current control method I_{load}. The 2 different control systems (PI_{bat} and PI_{SC}) perform by adapting the PWM duty cycle of such DC/DC adapters to calculate the output load of each inverter and remove the input signals in between time constants ($I_{\text{ref bat}}$ and $I_{\text{ref SC}}$) and the ESS current flow once currents ($I_{\text{ref bat}}$ and $I_{\text{ref SC}}$) have already been calculated through all the ANN.

3.6. Algorithm of MPPT. Thus, perturb and observe (P&O) technique was used to implement the MPPT algorithm, as shown in Figure 5. Low computing cost, simplicity of

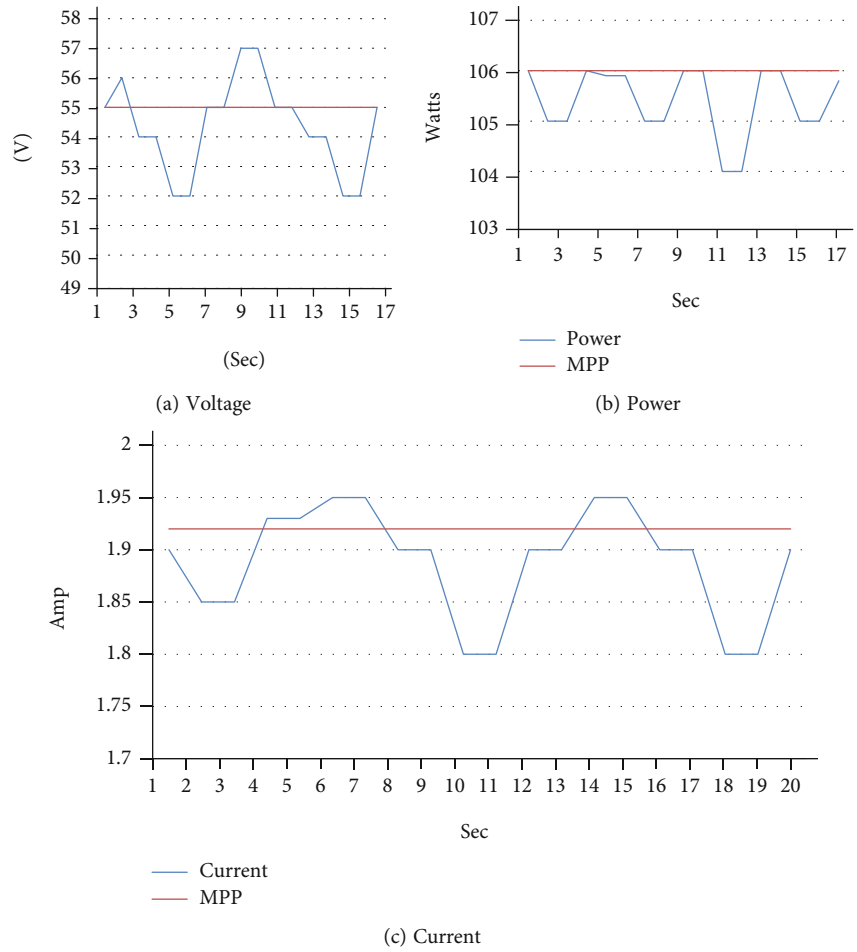

Figure 7: During all the system's operations, MPPT P&O algorithm signals were employed.

construction, and control are all characteristics of this approach [26]. It entails detecting the amount of electricity produced from the PV unit (P_k) at a specific time (t_k) and perturbing the DC/DC converter's PWM duty cycle (Δd). The quantity of energy collected (p_{k+1}) is then evaluated at the instant (t_{k+1}) and contrasted to the level of voltage recovered at an instant (t_k). If the perturbations lead to high voltage, the algorithms modify the converter's traditional operating frequency in the same manner as disturbance; otherwise, it alters the orientation of the disturbance. This is done until the peak power is attained.

3.7. Optimization of PI Control. Particle swarm optimization (PSO) was utilized with both control systems to identify the best settings of the PI controllers. The concepts of collaboration and behavior in society influenced the particle swarm algorithm. The method has a population of particles (n_p), each of which symbolizes a potential response. The goal is to make the nanoparticles examine the multivariate state space (d) to discover the best solution [27]. Equations (14) and (15) alter the speed (v_i) and location (x_i) from each I particle in the populations n_p, respectively. The program analyzes each molecule's efficiency using a predetermined objective function (OF) and alters the speed of each particle (v_i) as a result of three parts of equations at every iteration t. The photon's inertia (component of weight w) in retaining its current velocity is represented by the first component [28]. The second election adjusts each photon's efficiency towards its latest (p_{best}) so far, taking into consideration the cognitive variable (s_1). Finally, the final term directs the electron to the greatest performance of the other particles in the group (g_{best}), while accounting for the social variable (s_2). The results of optimizing the parameters connected with each controller are shown in Table 2.

$$v_{i,d}(t+1) = wv_{i,d}(t) + s_1 r_1 \left(p_{\text{best}\,i,d}(t) - x_{i,d}(t)\right) + s_2 r_2 \left(g_{\text{best}\,d} - x_{i,d}(t)\right), \tag{14}$$

$$x_{i,d}(t+1) = x_{i,d}(t) + v_{i,d}(t+1). \tag{15}$$

4. Result and Discussion

Modern computing analyses were carried to assess the performance of the system depicted in Figure 1. All equipment analyses were carried within standard conditions (irradiation of 1000 W/m^2 at 25°C) on an emulated PV with a PMPP of 106 Wp. The system's HESS was made up of 12 Li-ion battery

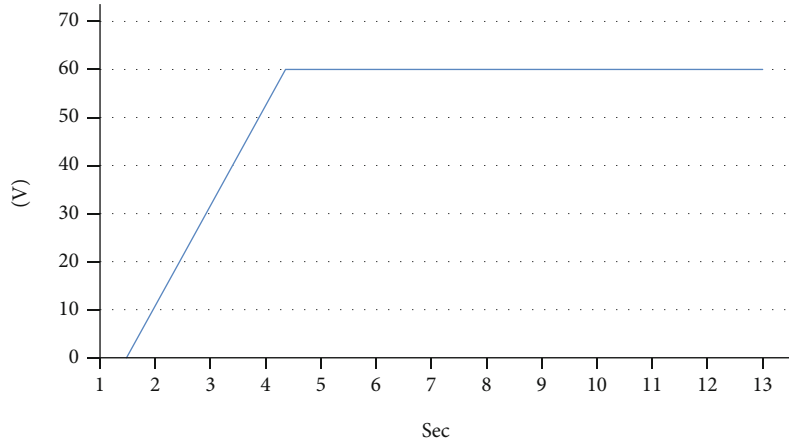

(a) The voltage at a constant state

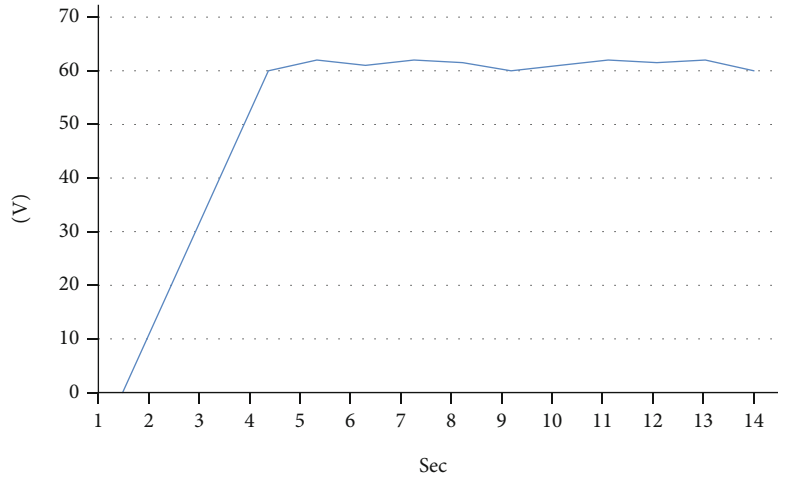

(b) The voltage at variable state

Figure 8: A voltage of DC bus.

cells that are connected and have a notional capacity of 2 Ah, as well as 12 SC cells in series connection and having a conventional capacitor of 500 F.

4.1. Results of Photovoltaic Energy. This employed a configurable source from Magna current, the DC SL 500-5.2, and its software configuration, solar photovoltaic curve emulation, to evaluate the MPPT algorithms for PV production. Figure 6 illustrates the *P-V* and *I-V* curves of the simulated PV, which are defined by $V_{oc} = 63$ V, $I_{SC} = 2$ A, $V_{MPP} = 55.53$ V, and $I_{MPP} = 1.911$ A, which equates to $P_{MPP} = 106$ Wp during standardized test circumstances ($1000\ W/m^2$ and 25°C). The values in Table 3 should be utilized in the mathematical modeling of a photovoltaic system.

The incredible system of PV is shown in Figure 7(b), with the MPP lines in orange. As can be seen, the energy collected from the PV is extremely near to the maximum power attainable in the PV throughout the test. This MPPT has a fast response time, only taking a few seconds to locate the MPP. This could attest to the outstanding results of the MPPT algorithm in use, and the DC/DC converters it is connected to. Figures 7(a) and 7(c) show the retrieved power of PV generation for the test. It could be observed that its MPPT P&O method implemented is just a basic, reliable, and efficient technique.

(a) Voltage
(b) Power
(c) Current

4.2. Performance Test of HESS Control. The testing used a voltage closed-loop control to simulate a realistic standalone operation. In this method, consistent power on the DC bus could be guaranteed throughout the system's operations. The test scenarios that were run concentrated on two parts of the power strategic approach that had been implemented: PV generation was less than the required load power ($P_{load} - P_{dc\,pv} < 0$); PV generation was higher than the required power system ($P_{load} - P_{dc\,pv} > 0$). As a result, it was feasible to evaluate the system's behavior whether the DC bus had an excess or deficiency of energy. Finally, two further situations were run to verify the state's opportunity to follow a control signal on the DC bus. During normal conditions, a DC bus voltage standard was implemented for the purpose, while in normal operation the system followed a dynamic DC bus voltage comparison. This research examines whether the system could

sustain a reference signal in the DC bus independent of PV generation power or the loads attached to that though.

Each ESS had a SOC of around 50% in the tests that were conducted. The maximum Li-ion battery charge/discharge mostly during realized testing was set to 0.4 A associated with system limits in terms of energy and to guarantee the program's stability.

The electricity taken from PV generation was larger than the requested load power in the first situation. As a result, excess HESS power would have to be assigned. However, because the current during the experiment surpassed the high voltage authorized for charging the Li-ion batteries, the surplus current had to be sent to the SCs, which assisted the Li-ion battery packs in accepting the additional current.

The power retrieved from PV generation would be less than the required peak load in the second example ($P_{\text{load}} - P_{\text{dc pv}} < 0$). As a result, the Li-ion batteries had to be discharged to supplement the PV generation and meet the load. However, the current required to fulfill the demand during testing surpassed the maximum current allowed for Li-ion battery degradation. As a result, the SCs had to be depleted in needed to aid PV generation the Li-ion battery in meeting the load demand.

The DC-link voltage even during an experiment using a closed-loop reference voltage is shown in Figure 8(a). All throughout the experiment, the DC-link voltage remained maintained at the predetermined value (60 V), demonstrating the energy management technique and controllers' high stability. The current development on the DC bus during perfect knowledge with changing power supply is shown in Figure 8(b). As can be observed, the system had a decent capability to follow a control voltage, indicating that the control method had a larger bandwidth.

(a) The voltage at a constant state

(b) The voltage at variable state

The results of the experimental testing confirmed the results of the earlier computational simulations, demonstrating the good response of the applied power management approach and the accompanying power management system. Scheme of control of the power management approach effectively demanded the SC within following circumstances, as in preceding computer analysis: (i) during the transient and steady-state responses and (ii) when the required power surpassed the Li-ion batteries' maximum output. As a result, the Li-ion batteries' dynamical load and peak market requirements were reduced, and their life was prolonged. Finally, the computational calculations and experimental setup demonstrated that the model battery management technique performs better.

5. Conclusion

The energy management controllers for a photovoltaic hybrid power system with such a power supply are presented in this research, which is developed on an artificial neural network. In hybrid renewable energy systems, the ANN controller may scale up enough energy and preserve sustainable management. This research proposes a unique HESS voltage regulation technique based on such an artificial neural network only intending to reduce Li-ion battery pressure in standalone renewables microgrids in switching device exchange situations. The suggested energy management method is capable of regulating the ESSs' flow of energy, controlling their charge or discharge power based on their SOC state and meeting the load requirements all across the system's operations. To demonstrate the practical information that can be extracted from a battery management technique, the provided system was constructed in hardware platforms, and realistic tests have been carried out. The conclusions back up the graph-theoretical experiments and ensure that the Li-ion cells are effectively protected as well as that the integrated controllers respond quickly. This shows that by implementing the proposed approach, the lifetime of Li-ion batteries could be extended.

Data Availability

The data used to support the findings of this study are included within the article.

Conflicts of Interest

The authors declare that there is no conflict of interest regarding the publication of this article.

Acknowledgments

The authors would like to express their gratitude towards Saveetha School of Engineering, Saveetha Institute of Medical and Technical Sciences (formerly known as Saveetha University), for providing the necessary infrastructure to carry out this work successfully. This project was supported by Researchers Supporting Project number (RSP-2021/315), King Saud University, Riyadh, Saudi Arabia.

References

[1] M. Boussetta, S. Motahhir, R. El Bachtiri, A. Allouhi, M. Khanfara, and Y. Chaibi, "Design and embedded implementation of a power management controller for wind-PV-diesel microgrid system," *International Journal of Photoenergy*, vol. 2019, 16 pages, 2019.

[2] A. Abusorrah, M. M. al-Hindawi, Y. al-Turki et al., "Stability of a boost converter fed from photovoltaic source," *Solar Energy*, vol. 98, pp. 458–471, 2013.

[3] P. Nirmala, G. Ramkumar, S. Sahoo et al., "Artificial intelligence to analyze the performance of the ceramic-coated diesel engine using digital filter optimization," *Advances in Materials Science and Engineering*, vol. 2021, Article ID 7663348, 10 pages, 2021.

[4] C. Ma, C. Li, X. Zhang, G. Li, and Y. Han, "Reconfiguration of distribution networks with distributed generation using a dual hybrid particle swarm optimization algorithm," *Mathematical Problems in Engineering*, vol. 2017, 10 pages, 2017.

[5] M. M. Rahman, M. Shakeri, S. K. Tiong et al., "Prospective methodologies in hybrid renewable energy systems for energy prediction using artificial neural networks," *Sustainability*, vol. 13, no. 4, p. 2393, 2021.

[6] J. A. Dhanraj, A. Mostafaeipour, K. Velmurugan et al., "An effective evaluation on fault detection in solar panels," *Energies*, vol. 14, no. 22, p. 7770, 2021.

[7] I. Aboudrar, S. El Hani, M. S. Heyine, and N. Naseri, "Dynamic modeling and robust control by ADRC of grid-connected hybrid PV-wind energy conversion system," *Mathematical Problems in Engineering*, vol. 2019, 19 pages, 2019.

[8] G. Ramkumar, S. Sahoo, T. M. Amirthalakshmi et al., "A short-term solar photovoltaic power optimized prediction interval model based on FOS-ELM algorithm," *International Journal of Photoenergy*, vol. 2021, Article ID 3981456, 2021.

[9] A. A. M. Nureddin, J. Rahebi, and A. Ab-BelKhair, "Power management controller for microgrid integration of hybrid PV/fuel cell system based on artificial deep neural network," *International Journal of Photoenergy*, vol. 2020, 21 pages, 2020.

[10] J. Faria, J. Pombo, M. Calado, and S. Mariano, "Power management control strategy based on artificial neural networks for standalone PV applications with a hybrid energy storage system," *Energies*, vol. 12, no. 5, p. 902, 2019.

[11] T. M. Amirthalakshmi, S. Ramesh, R. T. Prabu et al., "A novel approach in hybrid energy storage system for maximizing solar PV energy penetration in microgrid," *International Journal of Photoenergy*, vol. 2022, Article ID 3559837, 7 pages, 2021.

[12] X. Zhang, L. Liu, and Y. Dai, "Fuzzy state machine energy management strategy for hybrid electric UAVs with PV/fuel cell/battery power system," *International Journal of Aerospace Engineering*, vol. 2018, 16 pages, 2018.

[13] L. N. Khanh, J.-J. Seo, Y.-S. Kim, and D.-J. Won, "Power-management strategies for a grid-connected PV-FC hybrid system," *IEEE Transactions on Power Delivery*, vol. 25, no. 3, pp. 1874–1882, 2010.

[14] C. Pradhan, M. K. Senapati, S. G. Malla, P. K. Nayak, and T. Gjengedal, "Coordinated power management and control of standalone PV-hybrid system with modified IWO-based MPPT," *IEEE Systems Journal*, vol. 15, no. 3, pp. 3585–3596, 2021.

[15] S. Sukumar, M. Marsadek, A. Ramasamy, H. Mokhlis, and S. Mekhilef, "A fuzzy-based PI controller for power management of a grid-connected PV-SOFC hybrid system," *Energies*, vol. 10, no. 11, p. 1720, 2017.

[16] P. Sivasankari, S. Padmini, and R. C. Ilambirai, *Modelling control power management of grid connected hybrid PV battery diesel system*, *AIP Conference Proceedings 2112, 020103*, 2019.

[17] K.-M. Kang, B. Y. Choi, H. Lee et al., "Energy management method of hybrid AC/DC microgrid using artificial neural network," *Electronics*, vol. 10, no. 16, p. 1939, 2021.

[18] H. H. Ammar, A. T. Azar, R. Shalaby, and M. I. Mahmoud, "Metaheuristic optimization of fractional order incremental conductance (FO- INC) maximum power point tracking (MPPT)," *Complexity*, vol. 2019, 13 pages, 2019.

[19] O. O. Mengi and I. H. Altas, "A new energy management technique for PV/wind/grid renewable energy system," *International Journal of Photoenergy*, vol. 2015, 19 pages, 2015.

[20] V. Fulmali, S. Gupta, and M. F. Khan, "Modeling and simulation of boost converter for solar-PV energy system to enhance its output," in *2015 International Conference on Computer, Communication and Control (IC4)*, pp. 1–4, Indore, India, 2015.

[21] S. Kumaravel and S. Ashok, "Optimal power management controller for a stand-alone solar PV/wind/battery hybrid energy system," *Energy Sources, Part A: Recovery, Utilization, and Environmental Effects*, vol. 37, no. 4, pp. 407–415, 2015.

[22] S. Das and A. K. Akella, "A control strategy for power management of an isolated micro hydro-PV-battery hybrid energy system," in *2018 4th International Conference on Electrical Energy Systems (ICEES)*, pp. 397–401, Chennai, India, 2018.

[23] O. Charrouf, A. Betka, S. Abdeddaim, and A. Ghamri, "Artificial neural network power manager for hybrid PV-wind desalination system," *Mathematics and Computers in Simulation*, vol. 167, pp. 443–460, 2020.

[24] N. Mhusa, G. Nyakoe, and E. Mgaya, "Power management in photovoltaic-wind hybrid system based on artificial intelligence," *Journal of Multidisciplinary Engineering Science and Technology*, vol. 2, no. 1, 2015.

[25] S. Kumaravel and S. Ashok, *Adapted multilayer feedforward ANN based power management control of solar photovoltaic and wind integrated power system*, ISGT2011, India, 2011.

[26] M. Orabi, F. Hilmy, A. Shawky, J. A. A. Qahouq, E.-S. Hasaneen, and E. Gomaa, "On-chip integrated power management MPPT controller utilizing cell-level architecture for PV solar system," *Solar Energy*, vol. 117, pp. 10–28, 2015.

[27] V. Rashtchi, H. Kord, and A. Rohani, "Application of GA and PSO in optimal design of a hybrid photovoltaic/fuel cell energy system," *Fuel Cells*, vol. 3, p. 7, 2009.

[28] B. Benlahbib, N. Bouarroudj, S. Mekhilef et al., "Experimental investigation of power management and control of a PV/wind/fuel cell/battery hybrid energy system microgrid," *International Journal of Hydrogen Energy*, vol. 45, no. 53, pp. 29110–29122, 2020.

Hindawi
International Journal of Photoenergy
Volume 2022, Article ID 9491808, 12 pages
https://doi.org/10.1155/2022/9491808

Research Article

Hybrid Renewable Power Generation for Modeling and Controlling the Battery Storage Photovoltaic System

Mohd Mustafa,[1] **G. Anandhakumar**,[2] **Anju Anna Jacob**,[3] **Ngangbam Phalguni Singh**,[4] **S. Asha**,[5] **and S. Arockia Jayadhas**[6]

[1]*Department of Electrical and Electronics Engineering, Saveetha School of Engineering, Saveetha Institute of Medical and Technical Sciences, Chennai, 602 105 Tamil Nadu, India*
[2]*Department of Energy and Environmental Engineering, Saveetha School of Engineering, Saveetha Institute of Medical and Technical Sciences, Chennai, 602 105 Tamil Nadu, India*
[3]*School of Engineering, Emirates Aviation University, Dubai, UAE*
[4]*Department of Electronics and Communication Engineering, Koneru Lakshmaiah Education Foundation, KL Deemed to be University, Vaddeswaram, Andhra Pradesh, India*
[5]*Department of Electronics and Communication Engineering, Saveetha Engineering College, Chennai, 602 105 Tamil Nadu, India*
[6]*Department of EECE St. Joseph University in Tanzania, Tanzania*

Correspondence should be addressed to Mohd Mustafa; mustafakmcet@gmail.com
and S. Arockia Jayadhas; arockia.jayadhas@sjuit.ac.tz

Received 22 January 2022; Revised 4 February 2022; Accepted 7 February 2022; Published 27 February 2022

Academic Editor: V. Mohanavel

Copyright © 2022 Mohd Mustafa et al. This is an open access article distributed under the Creative Commons Attribution License, which permits unrestricted use, distribution, and reproduction in any medium, provided the original work is properly cited.

A major portion of the global energy demand was likely to be fulfilled by an extensive supply of renewable power. Renewable energy outputs, on the other hand, are changeable due to the dynamic nature of their sources. The integration of these variable sources of power into current power grids is proving difficult for electrical power system operators all around the world. The fundamental issue with renewable energy systems is that, due to the stochastic nature of renewable power, electricity production varies from period to period. Recent research and development on renewable technologies can ensure the islands' long-term electricity supply. Renewable energy sources, on the other hand, are limited by their unpredictable nature and significant reliance on weather conditions. To offset this disadvantage, several renewable energy sources and converters must be joined. To balance the power generation and load power, a hybrid renewable power generation for standalone application is proposed. The solar plant model is made up of a 170 W photovoltaic (PV) panel connected in series, and conversion of energy is done using the maximum power point tracking (MPPT) algorithm, which regulates a buck-boost converter modulation. The MPPT method used in the converter's control step is based on perturb and observe (P&O) and enhanced with a PI controller. The bidirectional buck-boost DC-DC converters (BBDC) are utilized to preserve a DC-link voltage stable. This is also storing additional hybrid energy in a large battery and is distributed to the system load; then there is a shortage of hybrid power. The load current power is regulated in terms of the frequency and enables it to be achieved using three vector control technique voltage source inverters (VSI). The results were offered to demonstrate a hybrid performance of this organization.

1. Introduction

Hybrid renewable power generation is becoming increasingly versatile and appealing to meet load in both standalone and grid-connected modes. The predictable power generation resources were finite and will be consumed in the next years [1]. In the current context of increased power generation needs, leading to the advancements of sophisticated digital technology and a much more pleasant lifestyle, it is critical to produce more energy to close a significant gap between generation and transmission requirements. When the system has a power shortage, embedded production in distribution systems compensates for it. Fossil fuels presently account for the majority of the world's energy sources.

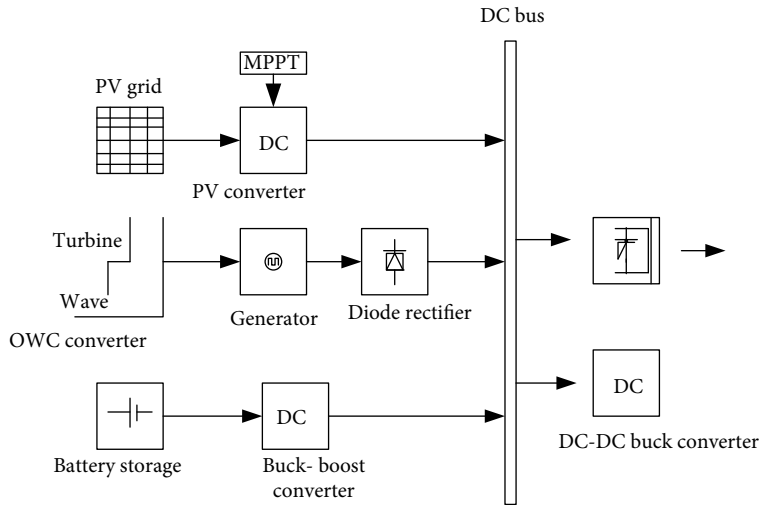

Figure 1: PV-wave proposed hybrid system block diagram.

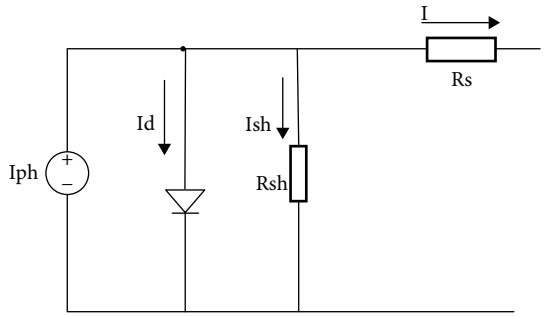

Figure 2: PV single-diode model.

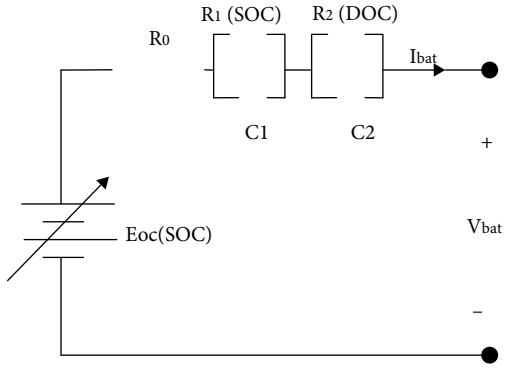

Figure 3: Model of battery.

Table 1: PV panel description.

Description	Parameter
I_{sc}	5.97 A
I_{MP}	5.59 A
V_{OC}	64.3 V
V_{MP}	54.8 V
N_S	97
T	25
$P_{\max}$	305 W
K_I	$3.6\,\frac{\text{mA}}{^\circ\text{C}}$
K_V	$-176.7\,\frac{\text{mV}}{^\circ\text{C}}$
N_{Ser}	05
N_{par}	67

One of the benefits of fossil fuels is the ability to generate hydroelectric power from a single source. However, as fossil fuels are not renewable and therefore will eventually run out, they pose a threat to energy stability [2]. Even while the costs of energy generated from fossil fuels are inexpensive in comparison to other possibilities, the transformation of such materials into electricity causes substantial pollution issues, such as the release of greenhouse gases into the atmosphere, which contributes to present global warming.

For decades, hybrid systems combining wind and PV energy sources have consumed a lot of attention. A hybrid organization may additionally incorporate a DC or AC converter, a packing area, filters, and a load management process control in addition to the energy sources [3]. All of these elements can be linked in a variety of ways. In renewable energy source applications, data-acquisition systems are commonly utilized to gather data on the deployed system's routine and estimation purposes. The information is initially conditioned with precise electronic circuits before being interfaced with a computer via a data achievement card. Solar energy is the most ecofriendly and speediest green energy source among some of the renewable energy sources [4]. However, the PV system's biggest disadvantage is that even the power it generates is greatly dependent on climatic circumstances. A PV system, for example, may not be able to generate any electricity at night or even during overcast times. As a result, the PV system generates power periodically, which implies that it may not be able to fully supply

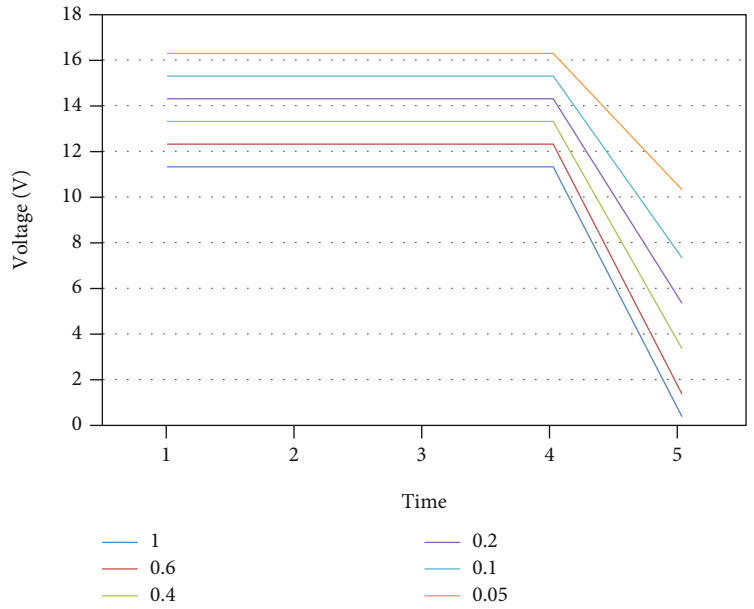

Figure 4: Characteristics of battery discharge.

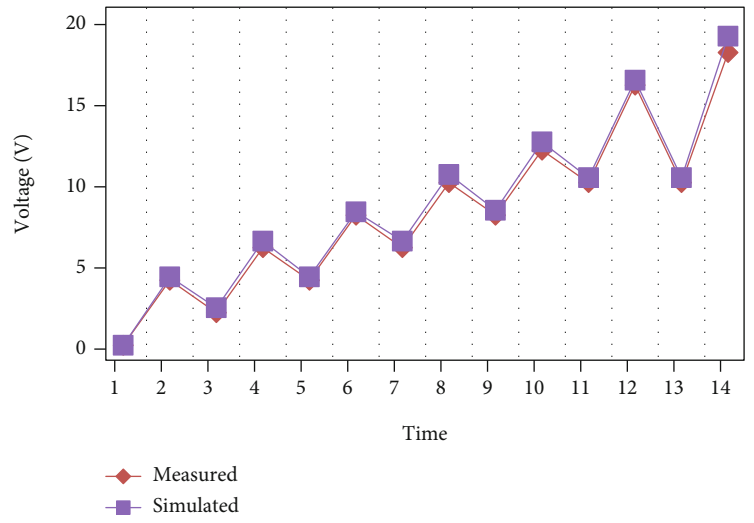

Figure 5: Yuasa NP18-12 battery, 0.2 pulse charge.

the power at any one time [5]. In an appropriate hybrid framework, this challenge is fixed by a PV integrating systems by some other energy storage technologies.

The ability to combine renewable sources of energy to form a hybrid system, on either side, is an ideal alternative for distributed energy-producing systems. As a result, alternative energy sources may be extra to the energy system to assure a long-term supply of electricity to the demand whenever the wind is inadequate. Solar energy, in addition to wind, is a frequently used renewable energy source [6]. It is also a reliant energy source, comparable to wind because the amount of energy created is based on numerous seasonal factors like irradiation angle, panel temperatures, and irradiance levels. As a result, the extra energy can be stored and used to charge equipment. The research can be carried out after simulating three distinct solar farms with such a rated output of 15 kW that are believed to be located in remote locations. The DC-DC converter system uses buck conversions with the perturb and observe (P&O) MPPT control algorithm, which ensures that the power produced for each solar plant is stable [1]. Between the storage battery as well as the DC-link, a BBDC is used to construct controller parameters, and a switching power inverter is used at the load-side end. To reduce the undesirable high-frequency vibrations caused by a load current of VSI depending on an inverter operating frequency, a humble passive L-C filter is put after the inverter at the load-side end [7]. The numerical solution can be used not only to evaluate the performance of the battery storage generated in PV-wave hybrid

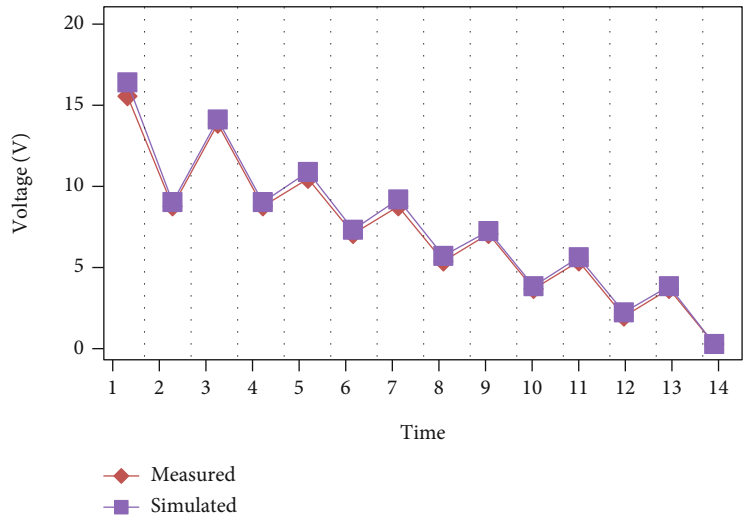

Figure 6: Yuasa NP18-12 battery, 0.2 pulse discharge.

Table 2: Modified P&O algorithm's different control operations.

Case	(ΔV)	(ΔP)	(ΔI)	TD	G	d
1	Positive	Positive	Positive	Correct	High	$d = d + \Delta d$
2	Positive	Positive	Negative	Correct	Constant	$d = d - \Delta d$
3	Positive	Negative	Positive	Incorrect	High	$d = d - 2\Delta d$
4	Positive	Negative	Negative	Incorrect	Constant	$d = d + 2\Delta d$
5	Negative	Positive	Positive	Correct	Constant	$d = d + \Delta d$
6	Negative	Positive	Negative	Correct	Low	$d = d - \Delta d$
7	Negative	Negative	Positive	Incorrect	Constant	$d = d - 2\Delta d$
8	Negative	Negative	Negative	Incorrect	Low	$d = d - 2\Delta d$

systems, but also to generate the amount of network hybrid renewable power output that meets the consumer load requirements in any situation. In this research, the proposed standalone PV-wave hybrid system model design was modeled and developed. The results are provided to demonstrate that the proposed system is effective.

2. Related Works

Grid extension to remote areas is fraught with technical and financial challenges. It has promoted the exploration and usage of renewable energy sources (RES) for decentralized power generation. The usage of renewable energy sources necessitates the use of a power source that is not always available. This difficulty has been mitigated to some extent by the installation of an energy storage unit (ESU) integration. The procedural review of a hybrid wind and PV production in a standalone method is presented in this study. The entire generation is influenced by associated components such as converters, storage units, controllers, and optimization strategies. Wind and solar energy are widely available, ubiquitous, and likely to show a significant role in a future energy market. To solve the problem of global warming caused by emissions from fossil-fuel-based thermal power stations, the analysis of the advancement of standalone renewable power units based upon PV and wind microgrids is included in this article [8].

A multi-input converter (MIC) is suggested, constructed, evaluated, simulated, and implemented to develop wind-PV power. The MIC is capable of processing both solar and wind energy, with its construction developed from the forward DC/DC conversion to a step-down/up power for a charger device, DC circulation uses. The MIC consists of a DSP-based control system, a higher adapted double-ended forward, a mutual output inductance, a lower altered double-ended forward, and an above altered double-ended forward. The two redesigned double-ended converters can work independently or in tandem to handle the hybrid renewable energy's variance under diverse air conditions. Improved results and lower volume can be obtained when the MIC is integrating the operation. The suggested MIC can recycle the energy held in the leaking inductance while achieving a high step-up voltage output. To attain a MPPT, the perturb and observe technique is used to pull a maximum output from wind turbines and solar panels. The MIC is built, examined, simulated, and put to the test. The possibility and

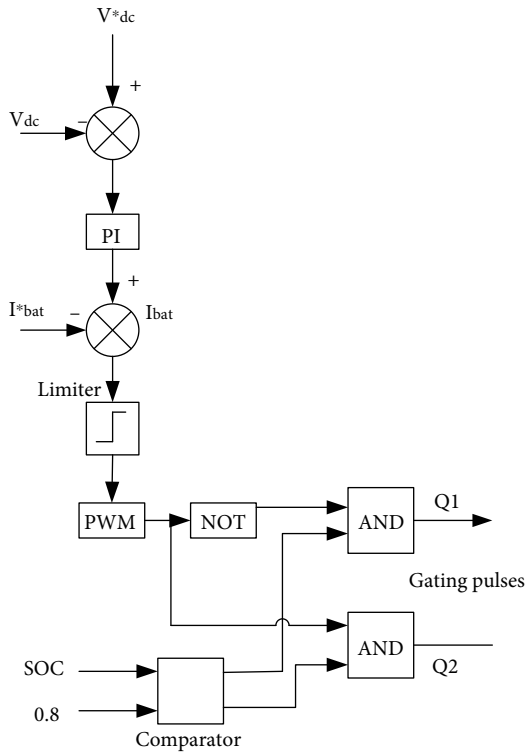

Figure 7: The DC-DC converter controller's diagram.

efficiency of a proposed multiconverter are shown through simulations or hardware tests [9].

An effective DC bus voltage parameter technique for a grid-connected photovoltaic (PV) system with a battery-energy storage (BES) is evaluated in this research. A DC/DC buck-boost converter connects a BES to the PV system's DC bus. During extreme disturbance circumstances, the converter enables the power of BES charge or discharge to adjust for a voltage of DC bus variance. In this method, the PV/BES system's DC bus voltage control can be improved over the traditional regulation, which is purely reliant on the voltage-sourced converter (VSC). The two control approaches, namely voltage-mode and current-mode controls, are used on the grid side VSC (G-VSC). For G-VSC voltage- and current-mode controls, as well as the BES DC/DC buck-boost converter regulators, the basic optimization method is used to optimize control parameters. For comparison, a new set of performance characteristics is generated for each of the power converters. The implementation of the developed improved control technique in comparison to existing methods is evaluated using PSCAD/EMTDC-based simulated research studies [10].

The goal is to prevent load shedding and a difficult blackout while still providing a cheap and reliable electricity supply for both big and minor consumers. The additional advantage is that renewable energy supplies can be more efficiently and cost-effectively integrated into the existing national grid. Solar PV use has increased in recent years due to an increase in demand for renewable energy. Because of the solar PV production in a DC and maximum household appliances can run on DC, this article proposes an AC-DC hybrid distribution network with a power management. EMS aids in the shifting of control of auxiliary loads, as well as forcing people to operate specified loads at specific times. These methods also aid in the management of overload during peak and off-peak hours. This explains how to build a DC-AC network using PV-solar and battery banks that integrate with a current organization. The outcome suggests that employing a hybrid AC-DC framework improves effectiveness and stability significantly. All of this working together improves overall efficiency, resulting in a power grid that is safe, cost-effective, dependable, and smart [11].

The supply of electricity could have a significant positive effect on reducing feelings of alienation and insecurity that orphanages often experience. The mathematical optimization analysis of a standalone photovoltaic electricity scheme that provided the required power requirements of an orphanage was given in this work. The National Aeronautics and Space Administration (NASA) surface meteorological and particularly a solar website provided solar sources for the software architecture at a location of $6^\circ\,51'$ N latitude and $7^\circ\,35'$ E longitude, with a yearly average of solar radiation of $4.92\,\text{kWh/m}^2/\text{d}$. This research is centred on the modeling, simulations, and improvement of the orphanage's power system. The orphanage's consumption of load habits is investigated and appropriately modeled for improvement. The suggested standalone solar power system analysis was performed and designed using the Hybrid Optimization Model for Electric Renewables (HOMER) software. The design was created to give the best configuration settings depending on hour-by-hour energy requirements and market data. This report included a full design, specification, and anticipated effectiveness of the software [12].

3. Materials and Methods

This study briefly explains the basic schematic plan of a hybrid PV-wave renewable power technology. Figure 1 depicts an entire block figure of a standalone PV-wave HRES. The proposed system involves of a PV system, a pulse width modulation (PWM), an OWC scheme, a BBDC with even a proportional-integral-derivative (PI) ratio of control duty, a storage battery, and insulated-gate bipolar transistor (IGBT) VSI located on the demand side [13]. A solar PV system consists of a PV grid as well as a DC-DC transmitter with the MPPT technique. In a photovoltaic panel, MPPT is utilized to raise system performance by controlling the DC-DC converter. The Darrieus turbine-driven permanent-magnet oscillator is bidirectional [14], and an AC-DC three-phase converter was used to build the OWC technology.

To satisfy the load need, the HRES uses a renewable photovoltaic and a wave-energy system as a major power generating source, with a battery bank serving as a backup energy storage device. As a result, if the HRES-generated power is insufficient to change the system load requirements, the battery storage will provide energy to equalize the system power requirement. The DC-link voltage has to be constant to connect a PV-wave, and the battery bank in hybrid architecture

Table 3: OWC parameter.

Length of chamber OWC		1.6 m	
Area of water surface inside a chamber		1.5 m^2	
Area of inlet turbine		0.013 m^2	
	Height of wave (m)	Period of wave (s)	Depth (m)
Depth of water	0.97	4.8	16.48
	0.97	4.78	15.76
	0.87	4.76	15.74

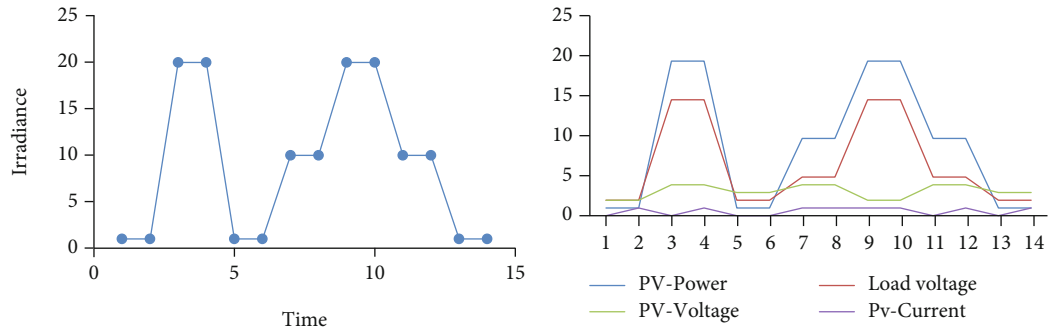

(a) (b)

Figure 8: (a) An illumination profile of MPPT. (b) Matching results.

[15]. To retain a voltage DC-link constantly, the HRES uses a BBDC with a PI controller. To manage the voltage demand side in terms of an occurrence and breadth, a three-phase VSI with a very composite vector control method is employed at the demand side. The next sections provide a detailed summary of each aspect of organizational HRES and controllers.

3.1. PV Module Modeling. A PV-cell is made up of a p-n junctional semiconducting material; then its equivalent circuit is revealed in Figure 2. This paper [16] refers to the mathematical analysis of PV systems. When solar energy falls upon that PV panel's surface, the PV process utilizes MPPT to get the most electricity. The formulas from the study referenced [17, 18] were used to create the PV system. Table 1 shows the PV array characteristics. The power of the solar SRP-305-WHT panel is simulated in a suggested hybrid renewable power generation using Matlab-2019 SIMULINK. I-V parameters of a photovoltaic panel are not linear. The experimental solution for the current would be as follows.

$$I = I_{PV} - I_o\left[\exp\left(\frac{V + R_s I}{V_t x}\right) - 1\right] - \frac{V + IR_s}{R_p}, \quad (1)$$

where $V_t = \mathrm{KTN}_s/q$.

As a result of the incident light, the current created is as follows:

$$I_{PV} = (I_{PVn} + K_I \Delta_T)\frac{G}{G_m}, \quad (2)$$

where $\Delta_T = T - T_n$ and $I_{PVn} = (R_p + R_s)/R_p I_{sc_n}$.

The diode leakage current is stated as

$$I_o = \frac{I_{sc_n} + K_I \Delta_T}{\exp\left((V_{oc} + K_I \Delta_T)/nV_t\right) - 1}, \quad (3)$$

A perfect photovoltaic cell's current is given as

$$I = I_{PV} N_{Par} - I_0 N_{Par}\left[\exp\left(\frac{V + R_s\left(N_{ser}/N_{par}\right)I}{V_t x N_{ser}}\right) - 1\right] - \frac{V + R_s\left(N_{ser}/N_{par}\right)I}{R_p\left(N_{ser}/N_{par}\right)}. \quad (4)$$

3.2. Oscillating Wave Column (OWC). This segment contains measured formulae that demonstrate the energy produced by the OWC scheme. The power produced at a wave turbine is made up of two terms: P_r (pressure of air) and P_V (velocity of air) [19]. As a result, the total energy of the chambers will be expressed to use the calculation

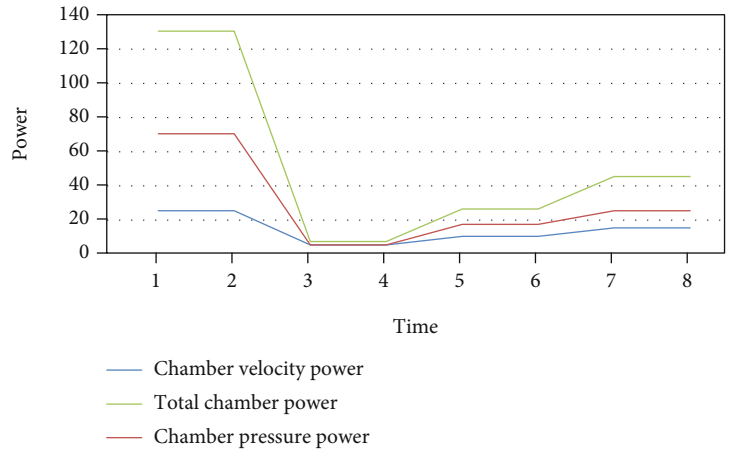

Figure 9: Ocean wave chamber.

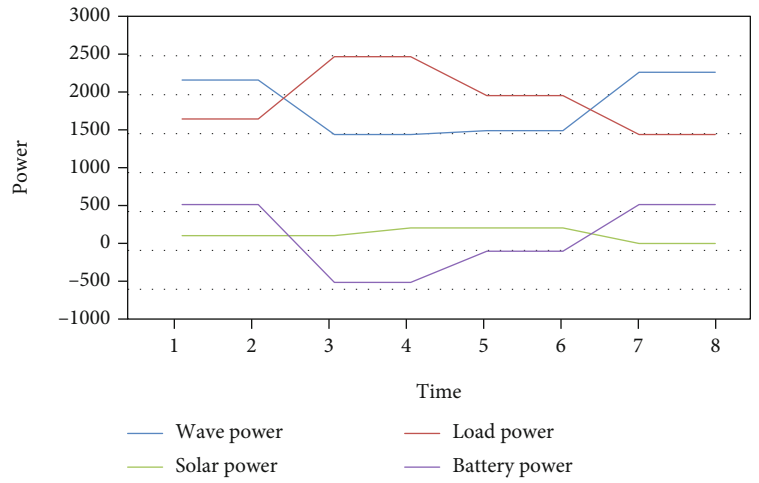

Figure 10: Distributed power by a hybrid PV-wave system.

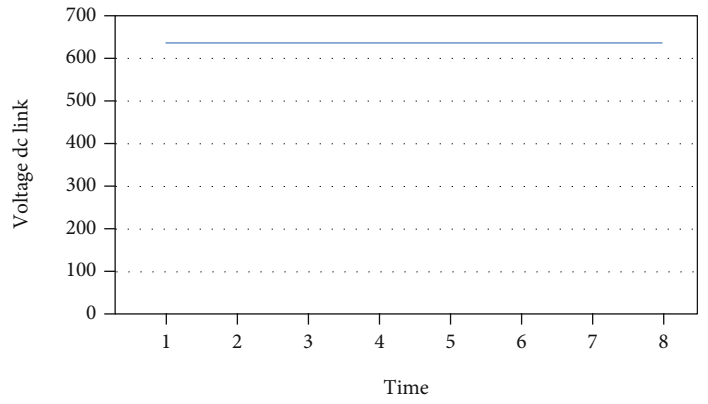

Figure 11: Voltage of DC-link.

below.

$$\text{Power of Chamber}: P_c = P_V + P_r, \tag{5}$$

where due to atmospheric velocity term, the power P_V operating on the turbine is

$$P_V = \rho A_2 \frac{(V_2)^3}{2}. \tag{6}$$

And, because of the air pressure condition, the power P_r

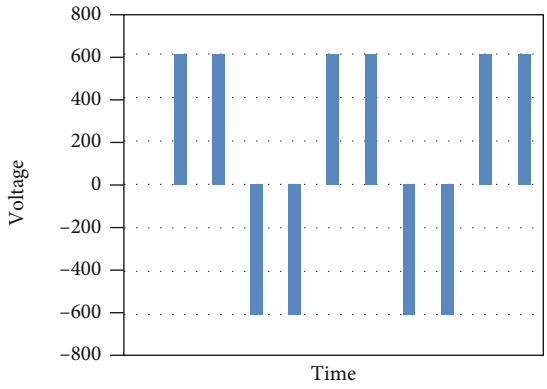

Figure 12: Output voltage of inverter.

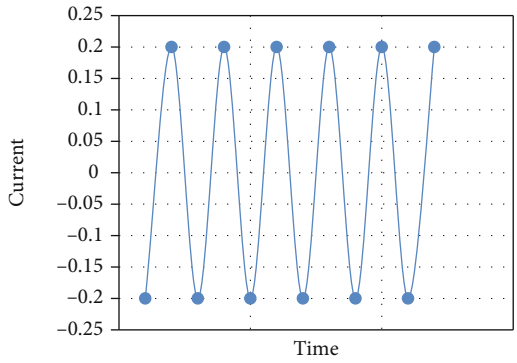

Figure 13: Three-phase current.

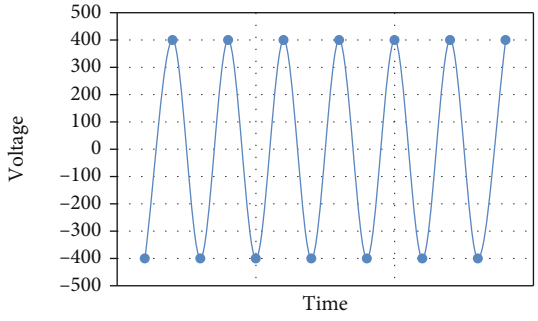

Figure 14: Three-phase voltage.

attainable to the turbine is

$$P_r = \left[-\frac{X_1}{X_2}\frac{W_{\text{in}}^2}{\theta^2}\omega^2\left\{2\cos(\omega t)^2 - 1\right\} \times Sin^2\left(\frac{\theta}{2}\right) + \frac{Q_X}{A_2}(V_2 - V_1)\right] \times Q_x \times \rho. \tag{7}$$

Because the OWC's independent power is the product of a generator coefficient power C_O, the overall power output is produced by an OWC that equals

$$P_{total} = (P_v + P_r) \times C_O. \tag{8}$$

3.3. Battery Storage System. In PV systems, batteries are also the primary storage technique. The model of battery is utilized to investigate the impacts of a different rate of charge, as well as the battery's state of charge (SOC) and state of health (SOH) [20]. Various test scenarios can be used to determine the best battery size for a specific application. Without any need for costly staging areas, simulations are utilized to compare alternative storage methods.

Figure 3 depicts a simple transmission line battery concept. The model of battery considers the battery's state of charge (SOC) and depth of charge (DOC). With a rising current discharge, the battery's serviceable capacity decreases; the DOC of the battery monitors the segment of the battery's capacity to a functioning capacity [21]. An open-circuit battery voltage E_{oc}, internal resistance R_0, and two RC-parallel branching are included in the model. The formulas for the system are displayed on the following equations.

$$\begin{aligned} E_{oc} &= E_0 - K_e(1 - SOC), \\ R_1 &= R_{10}e(-K_1(1 - SOC)), \\ R_2 &= \frac{R_{20}}{DOC}, \\ SOC &= 1 - \frac{1}{C_n}\int i_{batt}d\tau, \\ DOC &= 1 - \frac{1}{C(i_{avg})}\int i_{batt}d\tau, \end{aligned} \tag{9}$$

where SOC is the battery's condition of state charge, DOC is the battery's condition of deep charge, C_n is the capacity of a battery, $C(i_{avg})$ is the current-dependent capacity of a battery, E_0, when the batteries are fully charged, is the open-circuit voltage, K_e is a constant, K_1 is constant, R_{10} is a 1st constant RC branch in Ω, R_{20} is a 2nd constant RC branch in Ω, τ_1 is the 1st the time constant RC branch in Ω, and τ_2 is the 2nd the time constant RC branch in Ω.

For various C-rates, Figure 4 displays the modeled characteristics of discharge curves for the Yuasa Np18-12 lead-acid batteries. $E_0 = 12.84$, $K_e = 1.7$, $R_0 = 0.12\,\Omega$ for charge and 0.057 for discharge, $R_{10} = 0.16\Omega$ for charge and 0.02 for discharge, $K_1 = 7$, and $R_{20} = 0.0055\Omega$ in both charging and discharging, according to testing on the Yuasa Np18-12 battery. The battery's $0.2C$ pulse charging and discharging is shown in Figures 5 and 6, correspondingly.

A solar panel, conversion, loads, and battery bank are the most frequent components of freestanding photovoltaic systems. When there are differences between accessible and necessary energy, the energy formed by a photovoltaic module is retained in a rechargeable battery to satisfy the requirements of demand [22]. Charge-discharge devices have wider sheets than vehicle batteries and are designed to be continually drained to that more at 80% depth of discharge (DOD), providing them a good alternative for PV storage. The unit is normally designed to power a capacity for 2-3 days, resulting in a great rechargeable battery which will have to be changed every several decades.

The energy transfer from a PV module to the battery and a demand is controlled by a battery management system (BMS). Measuring the battery SOC, adjusting the DC-DC

converter pulse width, and applying the charging method are all tasks performed by the BMS. The BMS is based on an estimate of the SOC. The battery charge and discharge are affected by the current battery SOC [23]. The DC-DC inverter is utilized to convert MPPT tracking to charge the battery and power the demand. Sensors and measuring circuits measure the photovoltaic panel, battery, load voltage, and current, as well as the solar panel and battery condition [24]. The control algorithm uses these analytics to enhance the system's activity to make the effective use of existing energy to keep a battery at such a maximum SOC while also guaranteeing the demand requirements are fulfilled throughout all times.

3.4. Modified P&O MPPT. The standard P&O is not ideal for tracking changeable radiation levels since it also oscillates frequently about the MPP whenever the PV system's peak power is generated at a specific operational point and deviates from MPP if solar irradiation changes [25]. The divergence is caused by a shift in the level of irradiation. As a result, both of the aforementioned factors result in energy losses in the PV module, as well as limitations in typical P&O solutions. To circumvent these limitations, a modified P&O approach is assigned. By changing the current (I) variable in the algorithm, the improved P&O improves the network efficiency.

The proposed MPPT algorithm behaves like classic P&O under constant irradiance. When the irradiance changes, the MPPT algorithm behaves differently than the conventional P&O algorithm. The number of iterations is increased for velocity tracking during poor tracking periods [26]. This MPPT algorithm can distinguish between power fluctuations caused by solar illumination and measured voltage disruptions. As a result, according to the cited article, MPP deviation can be ignored. Table 2 details the different control measures of the improved P&O algorithm, and it may cover up to eight different scenarios. The tracking motion and controlling success are determined by the power differential (P). There are two types of cases that can be explored.

Case 1. The PV panel is in continuous irradiation if the changes in voltage (ΔV) and current (ΔI) have opposite signs.

Case 2. If the (ΔV) and (ΔI) take almost the same sign, the PV array gets irradiated differently.

3.5. DC-Link Voltage Control. A planned PV-wave hybrid standalone system's circuit layout is presented in this section. A neutral device is connected among the capacitors attached even before VSI enabling supplying single-phase and three-phase applications to the present scheme. The DC-link portion of a BBDC is linked to the battery bank in this research; the major goal of the BBDC's management is to keep a continual voltage DC-link as a standard value, as well as discharge or charge power from or to the batteries reserve according to with an essential load power [27]. Figure 7 shows a schematic representation of the battery system BBDC controller. By employing BBDC, the value of a large battery can indeed be considered lower than the standard DC-link voltage (V_{dc}^{*}), resulting in fewer batteries needing to be synchronized. The battery capacity voltage is maintained around 300 V in the planned standalone systems, while $V_{dc}^{*} = 650$ V.

The battery's bank of depletion is assumed to be 60% in this work, and it is created on the idea it should deliver an electric power of up to 2.5 kW, and demand is around an hour whenever the produced energy wave is zero.

The value of the inductance in a BBDC is critical for it to operate in the charging process. In addition, the presence of an inductor on the battery bank side leads to decreased ripple current, resulting in a longer lifetime and improved efficiency [28]. The operation of the charging process is also influenced by the incoming and outgoing currents, the value of the capacitors, and the switching speed. The inductance and capacitor values are as follows:

$$\begin{aligned}
\text{Inductance } L_2 &= \frac{V_{\text{Battery}} \times \left(V_{\text{DClink}} - V_{\text{Battery}}\right)}{I_{\text{Battery}} \times V_{\text{DClink}} \times f_w}, \\
\text{Buck mode capacitance } C_2 &= \frac{I_{\text{Battery}} \times K_L}{f_w \times 8 \times V_{\text{Battery(ripple)}}}, \\
\text{Boost mode capacitance } C_3 &= \frac{I_{\text{DClink}} \times D_{\text{Boost}}}{V_{\text{DClink(ripple)}} \times f_w},
\end{aligned} \tag{10}$$

where V_{Battery} is the energy of battery voltage, V_{DClink} is the voltage DC-link, I_{DClink} is the current DC-link, I_{Battery} is the current of battery storage, $V_{\text{Battery(ripple)}}$ is the output of buck side preferred a ripple voltage, $V_{\text{DClink(ripple)}}$ is the boost-side output preferred a ripple voltage, K_L is the approximate coefficient of measurement current ripple at the backside, and f_w is a scaling factor.

3.6. VSI Monitoring on the Load Side. A three-phase control technique VSI has utilized an interface device among a user load as well as the DC link voltage at a load end. The speed and amplitude only at the user load end are controlled by the load-side VSI controller. Since there is no electricity generation that developed a sense in the suggested HRES technology, its maximum output voltages should be managed in terms of primary frequency magnitude [29]. The output voltage is regulated using the state space modulation technique as the necessary hybrid or loading power varies.

The vector control method is adopted in this study, which depends on the simultaneously rotating scheme presented. Using the selected maximum output voltages electrical frequencies, the three-phase V_x, V_y, and V_z voltages and I_x, I_Y, and I_z currents should be translated and monitored from a standard stationary frame $a - b - c$ to a comparison by a rotating frame of $d - q$. 220 V and 50 HZ are the defined root mean square (RMS) values for the output voltage waveform and load voltage rate in this research.

The following are the voltage formulas by using references rotating $d-q$ frame transition:

$$V_d = V_{di} - H_f \frac{di_d}{dt} + H_f \omega i_q,$$
$$V_q = V_{qi} - H_f \frac{di_q}{dt} - H_f \omega i_d. \tag{11}$$

The active and reactive power is calculated using the $d-q$ reference rotational frame conversion.

$$\text{Active power } P = \frac{3}{2}\left(i_d v_d + i_q v_q\right),$$
$$\text{Reactive power Q} = \frac{3}{2}\left(i_q v_d + i_d v_q\right). \tag{12}$$

If the standard rotational frame is $v_q = 0$ and $v_d = |V|$, the power of active and reactive formulas is as follows:

$$P = \frac{3}{2} i_d v_d = \frac{3}{2} |V| i_d,$$
$$Q = \frac{3}{2} i_q v_d = \frac{3}{2} |V| i_q. \tag{13}$$

As a result, regulating direct and quadrature current components can regulate real and reactive power, correspondingly. Case V_d^* could also be controlled by it for resistors.

$$V_d^* = \sqrt{2} V_{RMS}^* \tag{14}$$

The output RMS phase reference voltage value is V_{RMS}^*. PI controllers manage the capacity voltage output in internal control loops and a charge output waveform in external monitoring loops in this control technology [30]. The Ziegler Nichols tuning approach is utilized to adjust all of the PI controllers in this article.

4. Result and Discussion

In the OWC system, battery storage, PV system, and BBDC with a PI control duty cycle, a voltage regulator is positioned at a lateral loading that makes up the proposed hybrid model. PV array and DC-DC converters with an MPPT algorithm make up a PV-solar system. The bidirectional turbine was powered by an asynchronous generator (SG) and an AC-DC three-phase rectification in OWC systems. The PV-renewable and wave-energy systems are employed as the major power generating source to satisfy systems demand requirement in hybrid renewable energy source (HRES), while stored energy is being used as a standby energy storage system. The DC-link voltage should be constant to interface PV-wave and a battery system in hybrid architecture. To keep a DC-link voltage steady, the HRES uses a BBDC with a PI controller.

The simulations were divided into four sections. The model of an ocean wave power converter was completed first, followed either by simulation of a photovoltaic system. The model is then run using a combination of ocean wave and PV systems, as well as a battery-energy storage system. Finally, the whole modeling of a hybrid power system, which would be founded on grid connectivity, has been completed. The simulation parameters are listed in Tables 3.

A strict profile for fluctuating solar radiation is utilized to demonstrate the usefulness of the suggested method. As suggested by the efficiency test, *EN* 50530, this profile includes several geometries such as step-up, step-down, ramp-up, and ramp-down. Two different slopes are chosen, with values of 1875 W/m^2/s and 2500 W/m^2/s, respectively, as shown in Figure 8(a). The suggested tracker may be thoroughly tested under intermittent and stable situations using this profile. The time of a test was prolonged by 4 seconds, while the temperature remained constant at 25 degrees Celsius. For both the P&O method and its version, the switching frequency step size is $\Delta d = 0.0002$.

To begin, the suggested P&O sensor was tested under a certain irradiance profile, with the simulated results shown in Figure 8(b). PV grandeurs including voltage (V), current (I), load voltage (V_0), and power (P) have their waveforms shown. The various grandeurs have acquired the same levels as the photovoltaic curve, as may be observed. It may be proven that the conversion utilized is a voltage step by comparing the behaviors of V and V_0. Moreover, the development of irradiance has a greater impact on the morphologies of I and P than on V, which will only be marginally influenced.

4.1. Ocean Wave Chamber Results. Figure 9 depicts the energy produced as a result of the airspeed and pressure of the chamber, respectively. The output total power is calculated using Equation (4), as shown in the figure. According to Figure 9, the chamber has a maximum power output of 8500 W. Figure 9 depicts the entire power output of the ocean wave system.

Figures 10 and 11 demonstrate the output of a buck-boost bidirectional DC-DC converter regulator. Figure 10 depicts the distribution of the power chart of produced solar power, load power, wave power, and battery-energy power. Figure 10 depicts how, when wave power, solar power, and necessary demand vary, the power first from the battery system varies (discharged/charged) to preserve a total power consistency. As shown in Figure 10, when the produced fusion power is greater than the needed load power, the regulator can charge a battery bank; when the necessary load power is greater than the produced hybrid power, the regulator can drain the battery bank. Furthermore, when the hybrid power and load demand fluctuate, it can preserve a continuous voltage DC-link at 650 V, as demonstrated in Figure 11. Figure 10 shows that the lack of solar power after 12 seconds indicates a foggy or evening phase. In this situation, both wave-energy and battery-energy power match the load requirements in every direction. As a result, the efficiency of the buck-boost DCDC multilevel inverter controller both in rapid and steady-state hybrid energy and state of charge conditions is quite excellent.

Finally, the DC-link is linked to a three-phase VSI. Figures 12–14 illustrate the results achieved after attaching

a hybrid approach to a three-phase grid. The load voltage depicted in Figure 14 is completely sinusoidal in a waveform.

5. Conclusion

Renewable energy resources are inconsistent, and designing a solar PV power producing system is difficult. An innovative freestanding PV-wave control scheme is conceived and modeled, complete with appropriate energy flow controllers. In this difficult situation, this study is aimed at constructing a hybrid power production system consisting of energy battery storage PV-wave renewables and an effective power control method to fulfill the load requirements. The results show that a controller can keep the voltage DC-link steady despite variations in produced hybrid power and necessary load power. Moreover, the controller is designed in such a way that battery storage can collect surplus energy produced by the combination organization and send it to the load demand throughout a hybrid network outage by managing the BBDC. The suggested hybrid system performs effectively in steady-state energy and also intermittent load power, solar, and wave circumstances. This study can be viewed as a first step in developing a standalone PV-wave hybrid model.

Data Availability

The data used to support the findings of this study are included within the article.

Conflicts of Interest

The authors declare that there is no conflict of interest regarding the publication of this article.

Acknowledgments

The authors would like to express their gratitude towards the Saveetha School of Engineering (SIMATS), Chennai, for providing the necessary infrastructure to carry out this work successfully.

References

[1] P. Rathod, S. K. Bhuyan, and S. K. Mishra, "Power management system using modified control strategy in hybrid renewable generation system connected to grid," *International Journal of Renewable Energy Research*, vol. 11, no. 3, pp. 1189–1204, 2021.

[2] T. M. Amirthalakshmi, S. Ramesh, R. T. Prabu et al., "A novel approach in hybrid energy storage system for maximizing solar PV energy penetration in microgrid," *International Journal of Photoenergy*, vol. 2022, Article ID 3559837, 2022.

[3] E. Kabalci, "Design and analysis of a hybrid renewable energy plant with solar and wind power," *Energy Conversion and Management*, vol. 72, pp. 51–59, 2013.

[4] G. Ramkumar, S. Sahoo, T. M. Amirthalakshmi et al., "A short-term solar photovoltaic power optimized prediction interval model based on FOS-ELM algorithm," *International Journal of Photoenergy*, vol. 2021, Article ID 3981456, 2021.

[5] N. H. Samrat, N. B. Ahmad, I. A. Choudhury, and Z. B. Taha, "Modeling, control, and simulation of battery storage photovoltaic-wave energy hybrid renewable power generation systems for island electrification in Malaysia," *The Scientific World Journal*, vol. 2014, 21 pages, 2014.

[6] L. Bernal-Agustín and R. Dufo-López, "Simulation and optimization of stand-alone hybrid renewable energy systems," *Renewable and Sustainable Energy Reviews*, vol. 13, no. 8, pp. 2111–2118, 2009.

[7] S. Das and A. K. Akella, "Power flow control of PV-wind-battery hybrid renewable energy systems for stand-alone application," *International Journal of Renewable Energy Research*, vol. 8, no. 1, pp. 36–43, 2018.

[8] P. Kumar and D. K. Palwalia, "Decentralized autonomous hybrid renewable power generation," *Journal of Renewable Energy*, vol. 2015, 18 pages, 2015.

[9] C.-L. Shen and S.-H. Yang, "Multi-input converter with MPPT feature for wind-PV power generation system," *International Journal of Photoenergy*, vol. 2013, 13 pages, 2013.

[10] M. Z. Daud, A. Mohamed, and M. A. Hannan, "An optimal control strategy for DC bus voltage regulation in photovoltaic system with battery energy storage," *The Scientific World Journal*, vol. 2014, Article ID 271087, 2014.

[11] S. Rauf and N. Khan, "Application of DC-AC hybrid grid and solar photovoltaic generation with battery storage using smart grid," *International Journal of Photoenergy*, vol. 2017, Article ID 6736928, 2017.

[12] V. A. Ani, "Feasibility and optimal design of a stand-alone photovoltaic energy system for the orphanage," *Journal of Renewable Energy*, vol. 2014, Article ID 379729, 2014.

[13] A. Martinez, D. Abbes, and G. Champenois, "Eco-design optimisation of an autonomous hybrid wind–photovoltaic system with battery storage," *IET Renewable Power Generation*, vol. 6, no. 5, pp. 358–371, 2012.

[14] A. Jemaa, O. Zarrad, M. A. Hajjaji, and M. N. Mansouri, "Hardware Implementation of a fuzzy logic controller for a hybrid wind-solar system in an isolated site," *International Journal of Photoenergy*, vol. 2018, Article ID 5379864, 2018.

[15] G. N. L. P. Raj and V. Kirubakaran, "Energy efficiency enhancement and climate change mitigations of SMEs through grid-interactive solar photovoltaic system," *International Journal of Photoenergy*, vol. 2021, Article ID 6651717, 2021.

[16] A. Laudani, F. R. Fulginei, and A. Salvini, "Identification of the one-diode model for photovoltaic modules from datasheet values," *Solar Energy*, vol. 108, pp. 432–446, 2014.

[17] M. G. Villalva, J. R. Gazoli, and E. Ruppert Filho, "Modeling and circuit-based simulation of photovoltaic arrays," in *2009 Brazilian Power Electronics Conference*, pp. 1244–1254, Bonito-Mato Grosso do Sul, Brazil, 2009.

[18] S. K. Bhuyan, P. K. Hota, and B. Panda, "Modeling and simulation of hybrid energy system supplying 3Ø load and its power quality analysis," *International Journal of Renewable Energy Research*, vol. 8, no. 1, pp. 592–603, 2018.

[19] S. Ahmad, M. J. Uddin, I. H. Nisu, M. M. Ahsan, I. Rahman, and N. H. Samrat, "Modeling of Grid Connected Battery Storage Wave Energy and PV Hybrid Renewable Power Generation," in *2017 International Conference on Electrical, Computer and Communication Engineering (ECCE)*, pp. 375–380, Cox's Bazar, Bangladesh, 2017.

[20] M. Nayeripour, M. Hoseintabar, and T. Niknam, "Frequency deviation control by coordination control of FC and double-

layer capacitor in an autonomous hybrid renewable energy power generation system," *Renewable Energy*, vol. 36, no. 6, pp. 1741–1746, 2011.

[21] J. Mudi, C. K. Shiva, B. Vedik, and V. Mukherjee, "Frequency stabilization of solar thermal-photovoltaic hybrid renewable power generation using energy storage devices," *Iranian Journal of Science and Technology, Transactions of Electrical Engineering*, vol. 45, no. 2, pp. 597–617, 2021.

[22] M. E. Glavin, P. K. W. Chan, S. Armstrong, and W. G. Hurley, "A stand-alone photovoltaic supercapacitor battery hybrid energy storage system," in *2008 13th International Power Electronics and Motion Control Conference*, pp. 1688–1695, Poznan, Poland, 2008.

[23] S. Moghaddam, M. Bigdeli, M. Moradlou, and P. Siano, "Designing of stand-alone hybrid PV/wind/battery system using improved crow search algorithm considering reliability index," *International Journal of Energy and Environmental Engineering*, vol. 10, no. 4, pp. 429–449, 2019.

[24] F. L. Tofoli, D. de Castro Pereira, and W. J. de Paula, "Comparative study of maximum power point tracking techniques for photovoltaic systems," *International Journal of Photoenergy*, vol. 2015, Article ID 812582, 2015.

[25] M. A. Abdourraziq, M. Ouassaid, M. Maaroufi, and S. Abdourraziq, "Modified P& O MPPT technique for photovoltaic systems," in *2013 International conference on renewable energy research and applications (ICRERA)*, pp. 728–733, Madrid, Spain, 2013.

[26] B. Bhandari, S. R. Poudel, K.-T. Lee, and S.-H. Ahn, "Mathematical modeling of hybrid renewable energy system: a review on small hydro-solar-wind power generation," *International Journal of Precision Engineering and Manufacturing-green Technology*, vol. 1, no. 2, pp. 157–173, 2014.

[27] M. Merai, M. W. Naouar, and I. Slama-Belkhodja, "An improved DC-link voltage control strategy for grid connected converters," *IEEE Transactions on Power Electronics*, vol. 33, no. 4, pp. 3575–3582, 2018.

[28] L. Shen, J. Chen, Z. Jin, Z. Liu, D. Zhou, and C. Wu, "Resonating power decoupling using multifunctional bidirectional DC/DC converter in hybrid railway traction application," *IEEE Transactions on Power Electronics*, vol. 37, no. 1, pp. 404–415, 2022.

[29] D. Jing, J. Shi, P. Meyrueis, and H. Zhou, "Semiconductor-based photocatalytic, photoelectrochemical, and photovoltaic solar-energy conversion," vol. 2014, Article ID 695204, 2014.

[30] E. K. Anto, J. A. Asumadu, and P. Y. Okyere, "PID control for improving P&O-MPPT performance of a grid-connected solar PV system with Ziegler-Nichols tuning method," in *2016 IEEE 11th Conference on Industrial Electronics and Applications (ICIEA)*, pp. 1847–1852, Hefei, China, 2016.

Hindawi
International Journal of Photoenergy
Volume 2022, Article ID 5473266, 9 pages
https://doi.org/10.1155/2022/5473266

Research Article

The Numerical Algorithms and Optimization Approach Used in Extracting the Parameters of the Single-Diode and Double-Diode Photovoltaic (PV) Models

R. Thandaiah Prabu,[1] **S. Parasuraman**,[2] **Satyajeet Sahoo**,[3] **T. M. Amirthalakshmi**,[4] **S. Ramesh**,[5] **S. Agnes Shifani**,[6] **S. Arockia Jayadhas**,[7] **M. Indra Reddy**,[8] **Sami Al Obaid**,[9] **Saleh Alfarraj**,[10] **and S. S. Kumar**[11]

[1]*Department of Electronics and Communication Engineering, Saveetha School of Engineering, SIMATS, Chennai, 602 105 Tamil Nadu, India*
[2]*Department of Electronics and Communication Engineering, Karpaga Vinayaga College of Engineering and Technology, Chennai, 603308 Tamil Nadu, India*
[3]*Department of Electronics and Communication Engineering, Vignan's Foundation for Science, Technology and Research (Deemed to be University), Vadlamudi, Guntur, 522213 Andhra Pradesh, India*
[4]*Department of Electronics and Communication Engineering, Rajalakshmi Institute of Technology, Chennai, Tamil Nadu, India*
[5]*Department of Electronics and Communication Engineering, St. Mother Theresa College of Engineering, Vagaikulam, 628102 Tamil Nadu, India*
[6]*Department of Electrical and Electronics Engineering, JP College of Engineering, Tenkasi, 627852 Tamil Nadu, India*
[7]*Department of EECE St. Joseph University in Tanzania, Tanzania*
[8]*Department of Mechanical Engineering, SRKR Engineering College, Bhimavaram 534204, India*
[9]*Department of Botany and Microbiology, College of Science, King Saud University, PO Box 2455, Riyadh 11451, Saudi Arabia*
[10]*Zoology Department, College of Science, King Saud University, Riyadh 11451, Saudi Arabia*
[11]*Department of Bioenvironmental Energy, College of Natural Resources & Life Science, Pusan National University, Miryang-si 50463, Republic of Korea*

Correspondence should be addressed to Satyajeet Sahoo; satyajeetsahoo.eltc@gmail.com and S. Arockia Jayadhas; arockia.jayadhas@sjuit.ac.tz

Received 22 December 2021; Revised 14 January 2022; Accepted 17 January 2022; Published 22 February 2022

Academic Editor: V. Mohanavel

Copyright © 2022 R. Thandaiah Prabu et al. This is an open access article distributed under the Creative Commons Attribution License, which permits unrestricted use, distribution, and reproduction in any medium, provided the original work is properly cited.

The current-voltage association of the single-diode photovoltaic (PV) cell comparable circuit system was characterized by its nonlinear implicit logical equation that would be hard to be resolved numerically. Because of the difficulty, various strategies for explaining this equation by using numerical approaches have been developed. The double-diode model is used to depict the PV cell in this research. This design is more accurate at the low irradiance levels, allowing for an extra accurate estimate performance of the PV system. The number of input variables is decreased to four to save time, and the values of R_p and R_s are calculated using an effective iterative technique. This research analyzes and compares three commonly used strategies for explaining the current-voltage equation parameter of a single-diode solar PV model. The chaotic optimization approach (COA) is used to evaluate the single-diode and double-diode solar cell characteristics. The suggested method relies on experimentally established current-voltage (I-V) characteristics. The suggested approach uses the curves of I-V characteristics obtained in the research laboratory for several standards of the solar temperature and the radiation and demonstrates its applicability in terms of efficacy, accuracy, and the simplicity of execution in an extensive range of real-world situations. As a conclusion, COA-based restriction approximation is beneficial to photovoltaic power generator manufacturers that want a timely and efficient PV cell/module model. It demonstrates that no single approach performs the best among all parameters and the method selection is always a trade-off depending on the user's focus.

1. Introduction

Solar energy's contribution to the total production of electric energy is steadily increasing. The solar inverter and panel costs continue to fall; many countries were focusing on their energy policies to increase the usage of solar energy. Electric network research, particularly testing the integration sources of solar energy into a power grid, necessitates a precise estimate of a solar maximum output and also correct modeling of solar cells. There are two primary models of PV solar cell equivalent circuits in works: the single-diode model (SDM) and the double-diode model (DDM). DDM takes into an account the complex result of the junction's impartial area; as a result, it correctly simulates solar cells more. It is, nevertheless, distinguished by seven unknown properties. Because DDM is complex, some writers limit the number of unknown factors, which can have a significant impact on model accuracy [1].

In recent years, the desire to boost energy supply security, reduce the ecological pollution, and adopt job possibilities via emerging a new green technology makes clean and sustainable energy sources an unavoidable alternative to consider [2]. There are several sorts of renewable energy sources, each with its own set of conversion processes. However, a significant rise in research and growth activity in the domain of photovoltaic (PV) networks are increased to the world's most populous renewable energy technologies for power production. The accuracy of the model's characteristics improves as the number of diodes rises; but, the math formulation necessary to produce the feature outcome becomes increasingly difficult. The single-diode model of 5 parameters is a good compromise, although it is necessitating to solving several equations to obtain the initial values used by the model. This problem is exacerbated by the manufacturer datasheet's lack of information [3].

Some studies compared the algorithms used to extract parameters from solar PV simulators. Identification of parameters of the single-diode model of solar cell, for example, has been conducted by using an experimental characteristics as I-V of Si and the multijunction of the solar cells. The extraction was performed using three different optimization strategies to determine which strategy outperforms the others in relation to the information-to-fitting scheme. Their findings exposed that a Newton–Raphson approach is the commonly used for the extraction of the parameter. Another study evaluated the I-V and P-V curves for a generic PV panel at varied temperatures and irradiation using five different algorithms. The double-diode design is suggested for better accuracy [4].

Adding a second diode to upgrade the variables, the main problem is in estimating the parameters of all design parameters while keeping the number of iterations reasonable. Several computing methods are proposed; however, all of them incorporate an additional coefficient into the calculations, enhancing their computational loads. Furthermore, identifying the parameters' starting values is difficult; Heuristic methods must be considered in some cases [5].

Physical variables including the electron diffusion rate, minority charge lifetime, and intrinsic charge density, as well as other material parameters, can also be used to characterize the double-diode model [6]. While all these simulations can help you understand the physical behavior of a cell, it is essential to understand semiconductors that are not often found in photovoltaic datasheets. As a result, developing a usable PV model using such a concept is not practical because majority of the cases on PV designers lack detailed knowledge of semiconductor processes. Through a chaotic optimization approach, offer both exact and an effective variable solar cell optimization of SDM and DDM. COA has recently been used to solve a variety of the optimization problems, including an identification of the parameter of the model of Jiles-Atherton hysteresis, array antenna reflection coefficient synthesis, calculation of single-phase converter characteristics, and parameter development of PID for the automatic voltage control of a synchronous generators [7]. COA's key advantages over other optimization approaches are its ease of implementation and quick execution time. The ratios of the parallel and serial resistances are computed using a simple and fast iterative approach. Designers of PV power converters and circuit simulators require a simple, fast, and realistic photovoltaic module model.

2. Related Work

The five design variables of a single-diode photovoltaic (PV) model are extracted using a hybrid method presented in this study. Only two parameters, series (R_s) and shunt resistance (R_{sh}), are evaluated using metaheuristic algorithms in the proposed technique, which is a blend of analytical and optimization procedures. The sum of the squared error is calculated using information from three primary critical points in datasheets provided by manufacturers. The remaining unknown parameters, such as the diode ideality factor (D), photo-generated current (I_{ph}), and dark saturation current (I_0), can be determined analytically. To demonstrate the effectiveness of the method, achievement indices include PV features, the standard error, normalized root mean square error (nRMSE), power factor, and comparative maximum power error from various technologies. The new approach was proven to be reasonably accurate after comparison with experimental data contained in the module specification as well as the previous method [8].

Photovoltaic (PV) cells/modules are widely used in power generation as renewable radiation becomes a prominent renewable energy source. A variety of PV modules from various manufacturers are used to evaluate the performance of the models, and the findings are evaluated to all those produced using similar predictive methods published in the literature. By comparing experimental I-V curves provided by the supplier, the current-voltage (I-V) properties of the photovoltaic panels reviewed here are also modeled. The parameters acquired for the PV modules are compatible with those found to use other analysis methods, according to the findings. The curves are also demonstrating a maximum degree of the agreement with those generated using the literature's ideal parameters for double-diode models. Furthermore, the suggested model has a significant benefit in

predicting control limitations in terms of convenience of use, demands of input information, dependence on preliminary situations, and consideration of characteristics that are overlooked in existing methods [9].

In this study, the whale optimization technique (WOA) is employed that predicts the design of single-, double-, and triple-diode PV modules. The simulation results, which were carried out using MATLAB programmed under various climatic conditions, validate the WOA-based PV models. The effectiveness of the WOA-based PV models is measured by reviewing the outcomes of the WOA-based PV models to those obtained using other optimization methodologies. To provide a genuine evaluation, these simulated outcomes are based on experimental results of a Kyocera KC200GT PV module. By comparing the relative confidence interval of the WOA-based PV model to the maximal error signal of other PV models, the absolute confidence interval of the WOA-based photovoltaic module was effectively examined. The implementation of the metaheuristic technique yields an efficient PV model. [10].

This research is offering a new hybrid method for calculating the properties of a double-diode photovoltaic (PV) module. It accomplishes the statistical approach's efficiency by relying purely on documentation knowledge, unlike previous methods. Four of the characteristics get determined analytically, and then, the enduring three are enhanced by using an evolutionary algorithm. A method for steering the Newton–Raphson iteration's initial conditions is presented. By comparing it to other well-known computing methodologies for crystalline silicon, polycrystalline, and thin-film components, the methodology is proven. When contrasted to empirical observations, the mean absolute error is reduced by a factor of two magnitudes and the speed is improved by three to four times. The standard error of the advances is less than 0.1 after 100 runs, showing that the improved technique is fairly consistent. Because of its accuracy and specificity, the technique is predicted to be very useful as a computational motor in PV simulations. [11].

This study uses the artificial immune system (AIS), a metaheuristic technique, to predict solar PV characteristics. The new technique is used to predict a variable of the double-Schottky diode. PV (solar power) characteristics are calculated by inserting estimated parameter values into a MATLAB model. For a performance study, the results obtained using AIS were associated with the results obtained using the genetic algorithm (GA) and a particle swarm optimization (PSO). To further confirm the recommended method, error graphs were created for two panels using AIS, GA, and PSO. The data reveal that the suggested AIS method outperforms GA and PSO in terms of factors which have the potential and standard deviation [12].

3. Materials and Methods

The modeling and evaluation of a PV system was a critical connection to an increase in PV system features, which in turn led to a development in the features of energy harvested from such systems. As a result, in the current work, the method for modeling and the characterization of PV systems was described and validated with measurement values. For the PV system, an accurate forecast model was developed and the outcomes were evaluated using comprehensive features resulting from simple computations.

3.1. PV Cell Modeling

3.1.1. Single-Diode PV Model. As exposed in Figure 1, the single-diode PV module formed the foundation for a PV model that was implemented. The step computations of current-voltage (I-V) and a power-voltage (P-V) parameters, depending on a specific equation, are included in the modeling of every PV cell. Meanwhile, creating a PV model that simulated various weather conditions and assisted in predicting the parameters of PV using a demonstrated manner is a significant undertaking [13]. Furthermore, the precision of the measurement characteristics of I-V and P-V was directly related to improving the level of solar panels and monitoring the effectiveness of PV systems.

Various strategies for applying numeric amounts of PV variables to PV modeling were reported in the literature. Following this trend, other researchers developed PV models based on five factors, while others developed PV products based on four, three, two, or even one parameter [14]. The five-parameter approach, on the other hand, had superior accuracy than other models and was more widely used, especially in outdoor situations. As a result, the five-parameter model is exact when all relevant DC variables are taken into account.

$$I = I_L - I_0\left[\exp\left(\frac{(IR_s)}{a}\right) - 1\right] - \frac{(IR_s)}{R_p}, \tag{1}$$

where I_L is represented as lighting diode current, I_0 is represented as diode's reverse saturation current and is indeed the adjusted effective area, R_s is represented as series resistance, R_p is the parallel resistance, and a is the changed factor of ideality. The major PV characteristics, as shown by the I-V characteristic curve, are described by equation (1). In the next part, look at the proposed equations for the existing parameters.

3.1.2. Double-Diode Model. The PV cell is represented by the double-diode model (DDM) in this research as shown in Figure 2, and the current-voltage (I-V) parameters can be determined as specified:

$$I = I_{ph} - I_{c1} - I_{c2} - I_{sh}. \tag{2}$$

The relationship between a diffusion diode current $I(I_{c1})$ and the voltage (V) across the cell is defined by

$$I_{c1} = I_{r1}\left[\exp\left(\frac{V + IR_s}{V_t a_1}\right) - 1\right]. \tag{3}$$

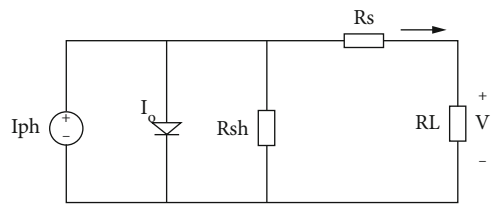

Figure 1: Single-diode PV model.

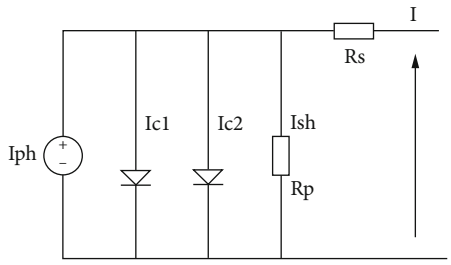

Figure 2: Double-diode PV model.

Similarly, the connection between diode 2's recombination current (I_{c2}) and V is as follows:

$$I_{c2} = I_{r2}\left[\exp\left(\frac{V + IR_s}{V_t a_2}\right) - 1\right]. \tag{4}$$

In addition, the following expression could be used to characterize the leakage current I_{sh} and then its connection to V throughout the cell.

$$I_{sh} = \frac{V + IR_s}{R_p}, \qquad V_t = \frac{TK}{q}, \tag{5}$$

where I_{sh} is represented as photogenerated current, I_{r1}, I_{r2} are the first and second diode reverse saturation currents, K is the Boltzmann constant $(K = 1.38 \times 10^{-23}\text{J/°K})$,$q$ is the electron charge $(q = 1.6 \times 10^{-19}\text{C})$,$(a_1 \& a_1)$ are the first and second diode ideality factors, V is node voltage, I is node current, T is the ambient temperature, R_s is the series resistance, R_p is the shunt resistance, and V_t is the thermal voltage. Many external circumstances have an impact on the PV unknown model parameters $(I_{r1}, I_{r2}, I_{ph}, R_s, R_p, a_2, \text{and } EG)$. The ideality factors a_1 and a_2 are often 1.5 and 2 in classical semiconductor and p-n circuit physics, according to previous research [15]. The saturation currents I_{s1} and I_{s2} may be deemed equal, although a_2 is more than 1.2. Some approaches set R_s and R_p to zero for mathematical convenience, whereas others fix a_1 and a_2. Furthermore, the incorrect selection of ideality factors has been linked to inaccuracies in computing output results. Ignoring R_s, on the other hand, has a significant impact on the PV model's reliability, particularly for datasets at the open-circuit voltage (V_{oc}) area. These connections, however, are not always reliable and have no structural function [16]. These variables will be computed in this research depending on genuine data, with the material energy bandgap EG set to 1.12 for the two components under consideration.

3.1.3. Computational Improved Method. The simplification of the current saturation formula is as follows: the current PV formula as a function of the irradiation and temperature is as follows:

$$I_{\text{PV}} = (I_{\text{PV\_STC}} + K_1 \Delta T)\frac{G}{G_{\text{STC}}}, \tag{6}$$

where $I_{\text{PV\_STC}}$ (in Ampere) represents the light-produced current at STC, $\Delta T = T - T_{\text{STC}}$ (in Kelvin, $T_{\text{STC}} = 25°\text{C}$), G represents a cell's surface of irradiance, and GSTC $(1000\,\text{W/m}^2)$ represents the irradiance at STC [17]. K_i is the short circuit of the current parameter, which is frequently supplied by the manufacturer. The well-known applied current formula for diodes is follows:

$$I_0 = I_{0,\text{STC}}\left(\frac{T_{\text{STC}}}{T}\right)^3 \exp\left[\frac{E_s q}{ka}\left(\frac{1}{T_{\text{STC}}} - \frac{1}{T}\right)\right], \tag{7}$$

where E_g is the semiconductor's bandgap energy and $I_{0,\text{STC}}$ is the nominal saturation current. $[x]$ is a better equation for describing the saturation current that takes temperature change into account:

$$I_0 = \frac{(I_{sc\_\text{STC}} + K_1 \Delta T)}{\exp\left[(V_{oc,\text{STC}} + K_v \Delta T)/aV_T\right] - 1}. \tag{8}$$

The open-circuit voltage ratio is represented by the constant K_v. This value can be found in the documentation. To make the model even more simple, both inverse saturation currents I_{01} and I_{02} are set to be comparable in magnitude in this study.

$$I_{01} = I_{02} = \frac{(I_{sc\_\text{STC}} + K_1 \Delta T)}{\exp\left[(V_{oc,\text{STC}} + K_v \Delta T)/\{(a_1 + a_2)/p\}\, V_T\right] - 1}. \tag{9}$$

Analytically, equation (8) can be evaluated. This is a benefit over other processes that involve mathematical computation to compute I_{01}, I_{02}. According to detailed investigations of (8), if $(a_1 + a_2)/p = 1$, the following expression for I_{01}, I_{02} is obtained:

$$I_{01} = I_{02} = \frac{(\text{I}_{sc\_\text{STC}} + K_1 \Delta T)}{\exp\left[(V_{oc,n} + K_v \Delta T)/V_T\right] - 1}. \tag{10}$$

The uncertainty in selecting the parameters of a_1 and a_2 can be removed with this generalization. Five parameters of this model, $I_{\text{PV}}, I_{01}, I_{02}$, a_1, and a_2, maybe easily found using (3) and (7). In addition, the iterative step for computing I_{01} and I_{02} is omitted, resulting in a shorter computation time.

3.1.4. R_s and R_p Determination Values. Iteration is used to determine the last two values, R_s and R_p. Several scholars have separately approximated these two factors, but the findings have been disappointing. R_s and R_p are determined simultaneously in this paper, following the approach proposed [18]. For the double-diode model, this method has not been used. The is goal to combine a predicted peak power ($P_{mp,C}$) and an observed peak power ($P_{mp,E}$) by raising the parameter of R_s repeatedly although computing the value of R_p. The equation for R_p can be adjusted and recast as follows from (1) at maximum power point condition:

$$R_p = \frac{V_{mp}\left(V_{mp}, +, R_s, I_m\right.}{\left[V_{mp}\{I_{\mathrm{PV}} - I_{c1} - I_{c2}\} - P_{E,\max}\right]}. \tag{11}$$

The technique of iteration to achieve the correct R_s value is depicted in Figure 3. For this example, KC200GT and MSX-60 PV modules were applied. In each example, R_s is enhanced until $P_{C,\max}$ and $P_{E,\max}$ are identical. Meanwhile, the value of R_p is determined simultaneously for each iteration. The output cell current may be computed by using a usual Newton–Raphson approach which has all seven variables available.

3.2. Modeling of Single- and Double-Diode PV Cells. The analogous circuit of the DM system for solar cell modeling is depicted in Figure 4. The following expression can be used to define the relationship curves of I-V for this model:

$$I = I_{\mathrm{PV}} - I_0\left(e^{(V+R_sI)/V_{\mathrm{th}}.n} - 1\right) - \frac{V + R_sI}{R_p}. \tag{12}$$

Figure 4 depicts the solar cell's equivalent resistance with DDM. As a result, unlike the model of SDM, the DDM PV design of the PV solar cell includes one extra diode which is parallel to the diode rectifier that accounts for the space-efficient charge current. DDM's I-V feature is listed as follows.

$$I = I_{\mathrm{PV}} - I_{01}\left(e^{(V+R_sI)/V_{th}.n_1} - 1\right) - I_{02}\left(e^{(V+R_sI)/V_{th}.n_2} - 1\right) - \frac{V + R_sI}{R_p}. \tag{13}$$

The propagation and saturation oscillations are I_{01} and I_{02}, respectively, and the propagation and recombination diode ideality ratios are n_1 and n_2, respectively. The ideality factor is explored, and an equation for calculating the ideality component is presented.

3.3. Objective Function and COA. Chaos is a type of nonperiodic long-term behavior which arises in nonlinear predictable schemes with a sensitive dependence on the preliminary circumstances when specific circumstances are met. This is concerned with the stable equilibrium of system dynamics that are described by a partial differential equation or an iterative map. The system's behavior is determined by

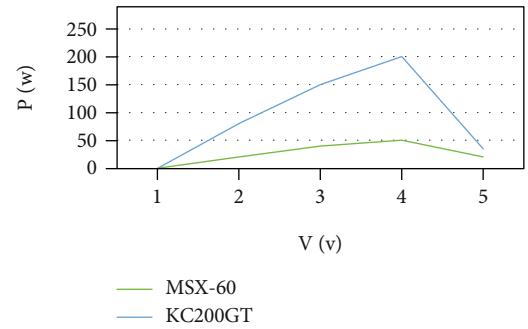

Figure 3: Methodology of PV curves for two PV modules.

the values of its characteristics. The bifurcation parameter is a variable that can be adjusted [19]. Bifurcations, or qualitative alterations in the structure of the network, occur when the bifurcation parameter is changed. As a result, the system displays a variety of dynamic behavior, such as trajectories convergent to the equilibrium position, border ring, or confused attraction.

The sensitive dependency on the beginning conditions is a typical attribute of the chaotic dynamical system. If certain systems evolve from two nearest points, after a sufficient amount of time, they would be infinitely far apart. The chaotic attractor's time patterns are entirely irregular, with no recurrence in any monitoring period of the final length [20]. Although the state is generated by a deterministic equation, there is arbitrariness in the temporal domain and long-term uncertainty in the state. The chaotic time signal has a power spectral density that looks like noise.

The Lorenz system is one of the most well-known chaotic systems. While simulating an atmospheric scheme, meteorologist is Edward Lorenz uncovered a sensitive requirement on beginning conditions by accident. Lorenz uses three equations to explain this complex system, which has subsequently become known as the three-dimensional Lorenz system:

$$\begin{aligned} \frac{dx}{dt} &= \sigma(y - x), \\ \frac{dy}{dt} &= -xz + rx - y, \\ \frac{dz}{dt} &= xy - bz, \end{aligned} \tag{14}$$

with the solution of chaotic for $\sigma = 10$, $r = 28$, and $b = 8/3$.

Iterative maps with the Tent map, Lozi map, logistic map, and others exhibit chaotic behavior. The chaotic sequence was constructed in this article by using a well-known Logistic map provided by

$$y_{i+1} = ey_i(1 - y_i), \tag{15}$$

where i is denoted as the number of iterations and e is represented as the repetition rate. The stochastic equation represents a process that begins with exponential growth but

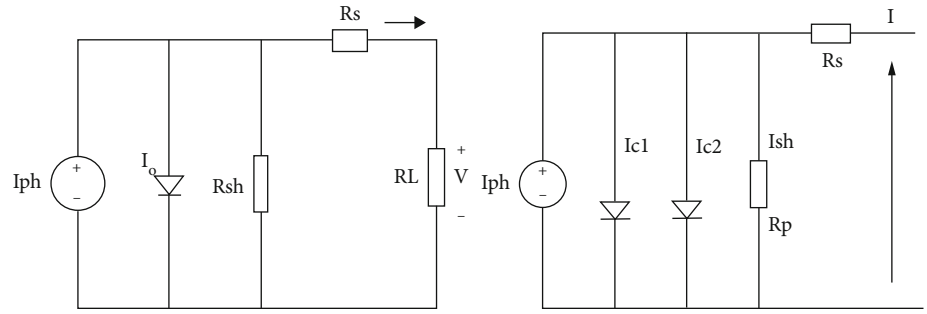

Figure 4: SDM and DDM of a PV cell.

eventually ceases due to nonlinearity. In this simple example, most of the common characteristics of chaos are present. COA's goal is to find an estimate for a set of unknown variables V that reduces the objective function (OF). In some cases, for a SDM, $V = [R_s, R_p, I_{pv}, I_0, n]$, and then DDM, $V = [R_s, R_p, I_{pv}, I_0, n_1, n_2]$.

As a result, vector $V = [v_1, v_2, \cdots, v_n$ contains parameters that are confined to the lowest (LV) and highest (UV) permissible values, i.e., $v_i \in [L_i, U_i]$. The OF for SDM, on either hand, is

$$\text{Objective function (OF)} = \sum_{t=1}^{p}\left(I_{pv} - I_0\left(e^{(V_t+I_tR_s)/n.V_{th}} - 1\right) - \frac{V_t + I_tR_s}{R_p} - I_t\right). \tag{16}$$

Whereas for DDM, it reads

$$\text{Objective function (OF)} = \sum_{t=1}^{p}\left(I_{pv} - I_{01}\left(e^{(V_t+I_tR_s)/n_1.V_{th}} - 1\right) - I_{02}\left(e^{(V_t+I_tR_s)/n_2.V_{th}} - 1\right) - \frac{V_t + I_tR_s}{R_p} - I_t\right), \tag{17}$$

where P denotes the number of I-V pairs determined from the features of I-V, V_t and I_t are denoted as the voltage or current quantity of the pair t, respectively. The COA flowchart, shown in Figure 5, depicts the search procedure. The COA flowchart's detailed overview can be obtained.

The following COA variables were utilized in this study: $M = 1000$, $N = 50{,}000$. The root mean square error (RMSE) is used to compare COA-based estimation to other methodologies. It is specifically defined:

$$\text{RMSE} = \sqrt{\frac{\sum_{k=1}^{p}\left(I_{est,k} - I_{meas,k}\right)^2}{P}}, \tag{18}$$

where $I_{est,k}$ and $I_{meas,k}$, with point k, reflect the predicted and observed values of the solar irradiance current, respectively.

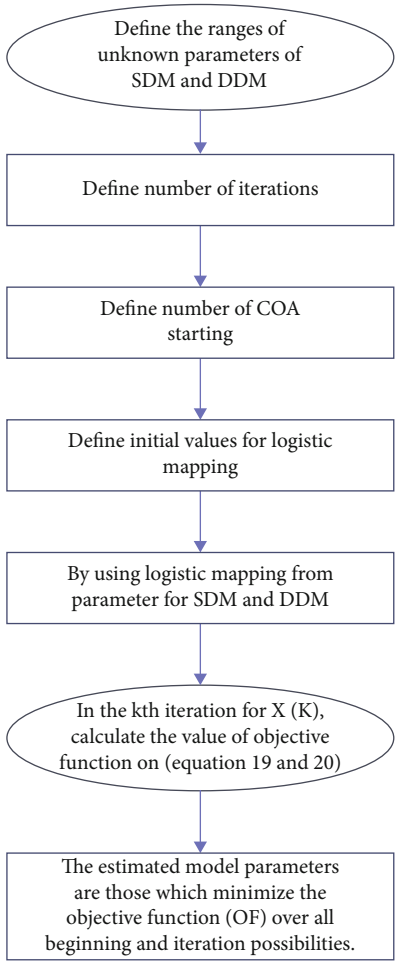

Figure 5: Flowchart of COA.

4. Results and Discussion

The accuracy test determines how closely the produced results correspond to the manufacturer's published experimental values. Three common statistical techniques are used to assess the algorithms' accuracy: the mean absolute percentage error (MAPE), mean absolute bias error (MABE), and root mean square error (RMSE). The arithmetical assessments can be stated accurately as (18), (19),

and (20), respectively.

$$\text{MABE} = \frac{1}{p}\sum_{k=1}^{p}\left|I_{est,k} - I_{meas,k}\right|, \tag{19}$$

$$\text{MAPE} = \frac{1}{p}\sum_{k=1}^{p}\left|\frac{I_{est,k} - I_{meas,k}}{I_{est,k}}\right|, \tag{20}$$

where $I_{est,k}$ and $I_{meas,k}$, with point k, reflect the predicted and observed values of solar irradiance current, respectively. p is the number of modules considered at the specified operational point among measured I-V pairs. Recover single-diode PV sample parameters for selected PV modules in STC rated by three algorithms. After that the limitations were acquired, the techniques are utilized to forecast the PV modules' electrical characteristics. Figure 6 shows the comparison of the IV properties from one of the photovoltaic panels, the Kyocera Solar KD210GX-LPU, to the experimental data. The experimental and simulated results found better agreement.

Measured values of the chosen PV modules validate the double-diode model provided in this research. Table 1 summarizes the specs of these modules. The results of the computations were associated to the R_s and R_p models. The variables for the suggested double-diode model are listed in Table 2. Although the model has more variables, only four parameters were calculated because $I_{01} = I_{02}$, whereas a_1 and a_2 can be picked at random. Only the MSX-60 and KC200GT are used in the validation of the model for the sake of brevity. The verification of partial shading modeling will incorporate the SM55. For varying degrees of irradiation, the I-V curves for a single KC200GT component are shown in Figure 7.

The curves of I-V for the KC200GT module are displayed in Figure 7 for various amounts of irradiation. The proposed model of double-diode and R_p models' computed values are compared to measurement values from the datasheet of the manufacturer. At STC, the proposed hybrid model and the R_p model both produce the same results. This is to be predicted, given that both algorithms analyze the parameters of the model at STC using the same peak power similarity measure. However, as irradiance decreases, the double-diode model produces more accurate findings, particularly near the open voltage sensor. The R_p design deviates from the experimental results at V_{oc} implying that the R_p model is insufficient when compared with similar irradiance levels. This is expected to have a major effect when a partial shading is used. Following that, the models' efficiency when exposed to temperature variations is examined. All tests are carried out with a 1000 W/m^2 STC irradiance. An evaluation is made among the suggested model and the R_s model. The comparison was chosen expressly to demonstrate the R_s serious model's flaws when exposed to changes in temperature. The KC200GT and MSX-60 components were put to the test. The curves I-V created using the two-diode model fit the test data accurately for all humidity conditions, as shown in Figure 8. At a maximum temperature, however, the model R_s findings depart significantly from a measured data.

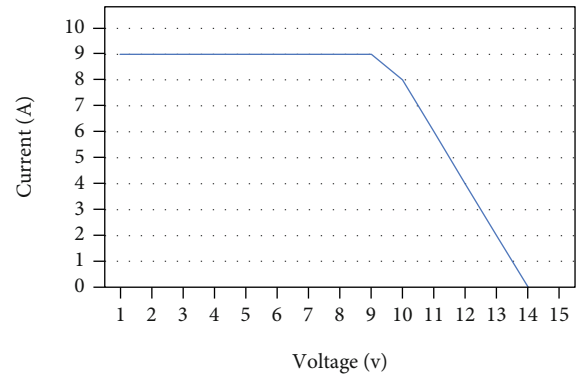

Figure 6: Kyocera Solar KD210GX-LPU at STC.

Table 1: Specification of the model.

Parameter	KC200GT	MSX-60
I_{mp}	7.62 Amp	3.5 Amp
I_{sc}	8.22 Amp	3.8 Amp
V_{oc}	32.8 vol	21.1 vol
V_{mp}	26.3 vol	17.1 vol
K_i	318 mA/°C	3 mA/°C
N_s	55	37
K_v	−124 mV/°C	−80 mV/°C

Table 2: Parameter of the double-diode model.

Parameter	KC200GT	MSX-60
I_{mp}	7.62 Amp	3.5 Amp
I_{sc}	8.22 Amp	3.8 Amp
V_{oc}	32.8 vol	21.1 vol
V_{mp}	26.3 vol	17.1 vol
I_{pv}	8.23 Amp	3.808 Amp
$I_{01} = I_{02}$	4.218×10^{-10} Amp	4.704×10^{-10} Amp
R_s	0.32 Ω	0.34 Ω
R_p	146 Ω	152.6 Ω

Users also examined solar cells from the renewable energy training setup to test the usability and effectiveness of COA for photovoltaic estimation methods. The main reason for using these photovoltaic panels is that it allows for variable solar insolation, data tracking for a PC-assisted information collecting for analysis, and highly complex didactic application for control system and the real-time data monitoring. To start, we examined the I-V parameters at a temperature of 42°C and insolation of 1285 W/m^2. Thus, calculate THE single- and double-diode solar cell characteristics using the measured I-V pairings. The parameter ranges for the estimation of SDM are $R_s(\Omega) \in [0.4, 0.1]$; $I_{pv}(\text{Amp}) \in [0.4, 0.2]$; $I_0(\text{Amp}) \in [15 \times 10^{-8}, 5 \times 10^{-8}]$;

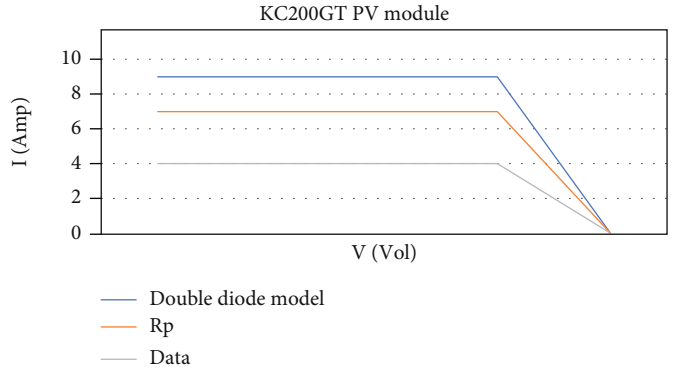

Figure 7: KC200GT PV module curves of I-V.

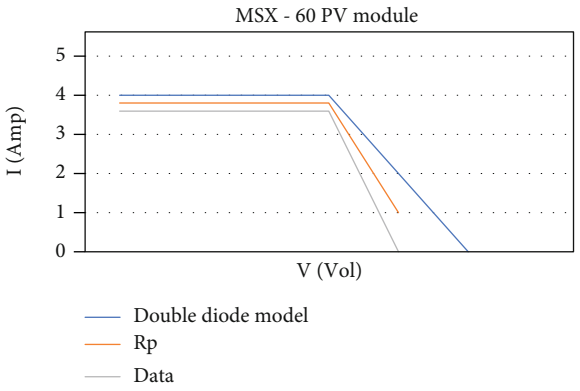

Figure 8: MSX-60 PV module curves of I-V.

Table 3: An estimated parameter value of the solar PV module.

SDM		DDM	
$R_s(\Omega)$	0.2284	$R_s(\Omega)$	0.2514
$R_p(\Omega)$	438.56	$R_p(\Omega)$	782.9912
I_{pv}(Amp)	0.2988	I_{pv}(Amp)	0.2973
I_o(Amp)	10.57×10^{-8}	I_{o1}(Amp)	6.8453×10^{-8}
		I_{o2}(Amp)	6.0644×10^{-8}
n	0.3442	n_1	0.3343
		n_2	1.9907
RMSE	4.3419×10^{-4}	*RMSE*	4.147×10^{-4}

$R_p(\Omega) \in [600, 200]$; and $n \in [1, 0.2]$, whereas DDM is $R_s(\Omega) \in [0.4, 0.1]$; $R_p(\Omega) \in [900, 600]$;

$I_{pv}(\text{Amp}) \in [0.4, 0.2]$; $I_{o1}(\text{Amp}) \in [15 \times 10^{-8}, 5 \times 10^{-8}]$; $I_{o2}(\text{Amp}) \in [15 \times 10^{-8}, 5 \times 10^{-8}]$; $n_1 \in [1, 0.2]$; and $n_2 \in [2, 1.95]$.

The I-V and P-V properties were then measured for various insolation and humidity data. The required simulated features were calculated by taking into account the change of variables with solar irradiance and humidity. The calculated and measured curves of I-V and P-V for various amounts of solar output and temperatures were shown. There is a clear correlation between both the measured and estimated features. Finally, we ran the estimating technique on all of the I-V characteristics that had been measured. The calculated values of the parameters were within 4% of the measured data, indicating that we can predict parameters using any of the measurable properties. On either hand, enough for a module, it is clear that the DDM was more efficient than the SDM which is based on the information in Table 3.

5. Conclusion

This research suggested that models of single diode and double diode can be improved. The number of input parameters is decreased to four to save time, and the values of R_p and R_s are calculated using an efficient iterative technique. Actual data from the producers confirm the accuracy of the proposed double-diode model. The double-diode model is found to be superior to the R_p and R_s models. COA is proposed as a very successful strategy for this aim in this research. The proposed method has been tested with real-world data from a variety of manufacturers. Its accuracy is verified by comparing its root mean square error (RMSE) to a variety of metaheuristics and a nonmetaheuristic approach for a different solar cell. COA's usefulness for parameter estimation was also tested experimentally in a laboratory setting. A high level of accuracy is proven in all of the circumstances evaluated. Besides that, the excellent match between the simulated curves of I-V and P-V and the observed features further validates the COA precision and usefulness for estimation methods.

Data Availability

The data used to support the findings of this study are included within the article.

Conflicts of Interest

The authors declare that there is no conflict of interest regarding the publication of this article.

Acknowledgments

The authors would like to express their gratitude towards Saveetha School of Engineering, SIMATS, for providing the necessary infrastructure to carry out this work successfully. This project was supported by Researchers Supporting Project number (RSP-2021/315) King Saud University, Riyadh, Saudi Arabia.

References

[1] M. Ćalasan, D. Jovanović, V. Rubežić, S. Mujović, and S. Đukanović, "Estimation of single-diode and two-diode solar cell parameters by using a chaotic optimization approach," *Energies*, vol. 12, no. 21, p. 4209, 2019.

[2] T. R. Ayodele, A. S. O. Ogunjuyigbe, and E. E. Ekoh, "Evaluation of numerical algorithms used in extracting the parameters of a single-diode photovoltaic model," *Sustainable Energy Technologies and Assessments*, vol. 13, pp. 51–59, 2016.

[3] S. J. Yaqoob, A. L. Saleh, S. Motahhir, E. B. Agyekum, A. Nayyar, and B. Qureshi, "Comparative study with practical validation of photovoltaic monocrystalline module for single and double diode models," *Scientific Reports*, vol. 11, no. 1, p. 19153, 2021.

[4] A. M. Humada, S. Y. Darweesh, K. G. Mohammed et al., "Modeling of PV system and parameter extraction based on experimental data: review and investigation," *Solar Energy*, vol. 199, pp. 742–760, 2020.

[5] T. Sudhakar Babu, J. Prasanth Ram, K. Sangeetha, A. Laudani, and N. Rajasekar, "Parameter extraction of two diode solar PV model using fireworks algorithm," *Solar Energy*, vol. 140, pp. 265–276, 2016.

[6] H. M. Waly, H. Z. Azazi, D. S. M. Osheba, and A. E. El-Sabbe, "Parameters extraction of photovoltaic sources based on experimental data," *IET Renewable Power Generation*, vol. 13, no. 9, pp. 1466–1473, 2019.

[7] N. Pourmousa, S. M. Ebrahimi, M. Malekzadeh, and M. Alizadeh, "Parameter estimation of photovoltaic cells using improved Lozi map based chaotic optimization algorithm," *Solar Energy*, vol. 180, pp. 180–191, 2019.

[8] M. R. Arabshahi, H. Torkaman, and A. Keyhani, "A method for hybrid extraction of single-diode model parameters of photovoltaics," *Renewable Energy*, vol. 158, pp. 236–252, 2020.

[9] B. K. Atay and U. Eminoğlu, "A new approach for parameter estimation of the single-diode model for photovoltaic cells/modules," *Turkish Journal of Electrical Engineering and Computer Sciences*, vol. 27, no. 4, pp. 3026–3039, 2019.

[10] O. S. Elazab, H. M. Hasanien, M. A. Elgendy, and A. M. Abdeen, "Parameters estimation of single- and multiple-diode photovoltaic model using whale optimisation algorithm," *IET Renewable Power Generation*, vol. 12, no. 15, pp. 1755–1761, 2018.

[11] V. J. Chin, Z. Salam, and K. Ishaque, "An accurate and fast computational algorithm for the two-diode model of PV module based on a hybrid method," *IEEE Transactions on Industrial Electronics*, vol. 64, no. 8, pp. 6212–6222, 2017.

[12] B. Jacob, K. Balasubramanian, S. Babu T, S. M. Azharuddin, and N. Rajasekar, "Solar PV modelling and parameter extraction using artificial immune system," *Energy Procedia*, vol. 75, pp. 331–336, 2015.

[13] M. S. Rasheed and S. Shihab, "Modelling and parameter extraction of PV cell using single-diode model," *Advanced Energy Conversion Materials*, vol. 1, no. 2, pp. 70–104, 2020.

[14] E. I. Batzelis and S. A. Papathanassiou, "A method for the analytical extraction of the single-diode PV model parameters," *IEEE Transactions on Sustainable Energy*, vol. 7, no. 2, pp. 504–512, 2016.

[15] K. Ishaque, Z. Salam, H. Taheri, and Syafaruddin, "Modeling and simulation of photovoltaic (PV) system during partial shading based on a two-diode model," *Simulation Modelling Practice and Theory*, vol. 19, no. 7, pp. 1613–1626, 2011.

[16] S. Kumar, H. S. Sahu, and S. K. Nayak, "Estimation of MPP of a double diode model PV module from explicit i–v characteristic," *IEEE Transactions on Industrial Electronics*, vol. 66, no. 9, pp. 7032–7042, 2018.

[17] Z. Salam, K. Ishaque, and H. Taheri, "An Improved Two-Diode Photovoltaic (PV) Model for PV System," in *2010 Joint International Conference on Power Electronics, Drives and Energy Systems & 2010 Power India*, pp. 1–5, New Delhi, India, Dec 2010.

[18] L. M. P. Archila, J. D. B. Rodríguez, and R. Correa, "Implicit modelling of series-parallel photovoltaic arrays using double-diode model and its solution," *Solar Energy*, vol. 214, pp. 131–137, 2021.

[19] M. Abdel-Basset, R. Mohamed, A. El-Fergany, M. Abouhawwash, and S. Askar, "Parameters identification of PV triple-diode model using improved generalized normal distribution algorithm," *Mathematics*, vol. 9, no. 9, p. 995, 2021.

[20] J. Gálvez, E. Cuevas, H. Becerra, and O. Avalos, "A hybrid optimization approach based on clustering and chaotic sequences," *International Journal of Machine Learning and Cybernetics*, vol. 11, no. 2, pp. 359–401, 2020.

Hindawi
International Journal of Photoenergy
Volume 2022, Article ID 8755464, 9 pages
https://doi.org/10.1155/2022/8755464

Research Article

Ultrasensitive and Selective Electrochemical Detection of Dopamine Based on CuO/PVA Nanocomposite-Modified GC Electrode

A. Mohamed Azharudeen,[1] **Arpita Roy**,[2] **R. Karthiga**,[3] **S. Arun Prabhu**,[4] **M. G. Prakash**,[5] **A. Mohamed Ismail Badhusha**,[6] **Huma Ali**,[7] **Khadijah Mohammedsaleh Katubi**,[8] **and Md. Rabiul Islam**[9]

[1]*Department of Chemistry, M.S.S. Wakf Board College, Madurai - 625020, India*
[2]*Department of Biotechnology, School of Engineering & Technology, Sharda University, Greater Noida 201310, India*
[3]*PG & Research Department of Chemistry, C.P.A. College, Bodinayakanur - 625513, India*
[4]*Department of Chemistry, National College, Tiruchirappalli, Tamilnadu - 620001, India*
[5]*Department of Chemistry, University of Witwatersrand, Johannesburg - 2050, South Africa*
[6]*Research Department of Chemistry, Sadakathullah Appa College, Tirunelveli - 627011, India*
[7]*Department of Chemistry, Maulana Azad National Institute of Technology Bhopal, India*
[8]*Department of Chemistry, College of Science, Princess Nourah bint Abdulrahman University, P.O. Box 84428, Riyadh 11671, Saudi Arabia*
[9]*Department of Pharmacy, University of Asia Pacific, Dhaka, Bangladesh*

Correspondence should be addressed to A. Mohamed Azharudeen; azhar5406@gmail.com, Arpita Roy; arbt2014@gmail.com, and Md. Rabiul Islam; robi.ayaan@gmail.com

Received 16 January 2022; Accepted 5 February 2022; Published 22 February 2022

Academic Editor: V. Mohanavel

Copyright © 2022 A. Mohamed Azharudeen et al. This is an open access article distributed under the Creative Commons Attribution License, which permits unrestricted use, distribution, and reproduction in any medium, provided the original work is properly cited.

At present, the determination of dopamine (DA) is enormously necessary for the human body. Since then, it has played a crucial role in the brain that affects mood, sleep, memory, learning, and concentration. Dopamine insufficiency is a threat to human health. Dopamine recognition is important to avoid this problem. Copper oxide (CuO) nanoparticles are one of the potentials which can be used in the detection of dopamine level in the sample. In this work, CuO was synthesized by a simple chemical precipitation technique and modified by polyvinyl alcohol (PVA) as a capping agent. The nanomaterials manufactured are used for the detection of dopamine in 0.1 M PBS medium at room temperature. The CuO/PVA-modified electrode shows better electrocatalytic activity than CuO/GCE (glassy carbon electrode). The constructed dopamine biosensor of copper oxide-PVA nanocomposites also has extraordinary selectivity, stability, sensitivity (183.12 μA mM^{-1} cm^{-2}), and a minimum level detection limit of 0.017 μM, is inexpensive, and has minimal effort and rapid detection of dopamine.

1. Introduction

The biomolecules are playing a significant role in the human body. They are involved in metabolic processes, and some of them act as neurotransmitters, neuroactive molecules, etc. Among the biomolecules, dopamine is one of the predominated ones, which is located naturally in the human body. It is a catecholamine neurotransmitter that directs the signal from the body to the brain. It controls the movement and emotional responses of humans. When dopamine levels are diminished in the human body, it causes Parkinson and schizophrenic diseases [1]. Furthermore, dopamine regulates all brain functions; it may protect the human heart racing and widen blood vessels in the viscera, which is effective in

the treatment of cardiogenic shock and kidney failure [2]. Therefore, measurement of dopamine level in the human body is necessary.

Recently, in the realm of biomolecule detection such as dopamine, the electrochemical sensor has become one of the most essential detection technologies. It has small smart equipment and real-time monitoring. Moreover, immunoassays, biosensors, and other disciplines of research use the electrochemical sensors for various applications. Nowadays, metal oxide based on electrochemical sensors received huge attention towards dopamine detection [2]. Among the metal oxide, CuO semiconductors are excellent candidates for dopamine detection. Owing to their unique properties, such as electrocatalytic catalytic activity, antipoisoning of chloridion, and small band gap, they show a magnificent quality. For instance, Reddy coworkers reported that CuO nanoparticles have sensor characteristics for determining dopamine electrochemically [3]. Furthermore, Li et al. [4] reported Ag-doped CuO nanoparticles for the electrochemical determination of DA in human serum, Zhuang et al. [5] synthesized Co_3O_4/CuO nanocage for dopamine biosensing, and Zou et al. accounted for g-C3N4/CuO nanocomposites for the evaluation of dopamine [6].

Electrical, optical, heterogeneous catalysis, photovoltaic devices, FE emitters, gas sensing, Li ion electrode materials, and magnetic storage media have all been successfully made with copper oxide nanoparticles [7]. Though there are several attempts for preparing homogeneous nanoparticles and nanostructured metal oxides (NMOs) applied in the field of dopamine sensor, owing to their elevated oxidation potential, trivial sensitivity, and fouling of the oxidation signals, the researchers nowadays develop nanocomposite materials to resolve these problems [8].

A polymer-incorporated nanomaterial is frequently utilized to ameliorate the conductivity and catalytic tendency of sensors and to drastically increase the strength of the electrochemical transmission when developing nanocomposites based on metal oxide/copper oxide [9]. For instance, polymers such as PEG [10], PVP [11], PVA [12], PAA [13], and polyaniline (PANI) [14] are effectively used in the fabrication of a biosensor. The polymer plays a huge attention in electrochemical sensor because of the unique characters of polymer such as conductive nature, compatibility, electron supporter, and inexpensive [15, 16]. As a result, dopamine levels have been linked to the sensitivity and advancement of neurological disorders such as Parkinson's and Alzheimer's diseases. The ability to detect DA in a sensitive and selective manner is critical for diagnosing neurological illnesses. To the best of our knowledge, no study has reported the synthesis of CuO-modified PVA nanocomposite for the detection of dopamine. In this study, a CuO/PVA-modified GCE-based electrochemical sensor was established for the detection of dopamine.

2. Materials and Methods

2.4 g of 0.1 M copper nitrate trihydrate was dissolved in 100 mL of distilled water (DW), and 0.8 g of 0.2 M NaOH was dissolved in 100 mL of DW separately. The copper nitrate trihydrate solution was taken in a flask, and the NaOH solution was added dropwise under continuous magnetic stirring for 2 h. The precipitate was then filtered off and heated in a hot air oven at 120°C for 1 hr. The product was finely crushed and calcinated at 500°C for 2 hrs in a muffle furnace, and the obtained product was black in colour. Then, the PVA was incorporated on the CuO nanoparticles through the chemical impregnated method. The synthesized nanocomposite was characterized using FT-IR, XRD, SEM, and EDS. The prepared CuO/PVA nanocomposite was employed as a dopamine (DA) sensor.

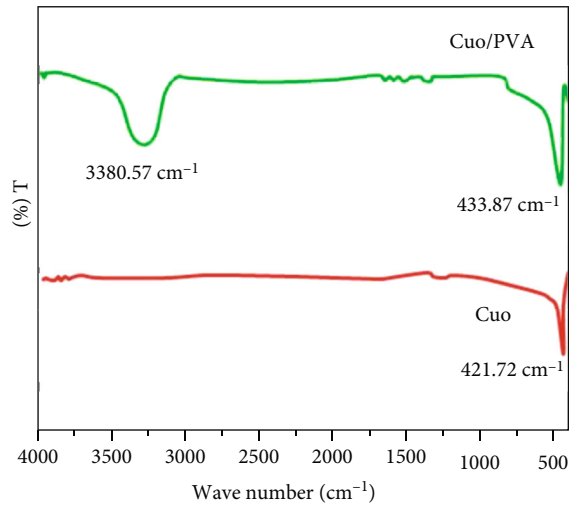

Figure 1: FT-IR spectrum of (a) CuO and (b) CuO/PVA nanocomposites.

3. Result and Discussion

3.1. FT-IR. The tentative frequency assignment of arranged spectra for pure and PVA-coated CuO nanoparticles is shown in Figure 1. The major characteristic peaks at ~3380.57 cm^{-1} for O-H stretching mode of PVA [17]. There are sharp characteristic vibrational bands (Figures 1(a) and 1(b)) observed at 421.72 and 433.87 cm^{-1} in the spectrum of pure and PVA-incorporated CuO NPs which are corresponding towards the Cu-O bond formation and vibrations of CuO monoclinic phase [18]. This affirmed the formation of CuO nanoparticle, and no impurity peaks was found in the sample as well.

3.2. Raman Analysis. Figure 2 visualizes the Raman spectrum of CuO, PVA-coated CuO NPs. In Figure 3(a), the Raman peaks observed at 291.71, 332.38, and 629.23 cm^{-1} are related to the Ag, B_g^1, and B_g^2 mode of CuO [19]. Then, Raman bands are positioned at 300.54, 347.27, and 632.54 cm^{-1} in the PVA-modified CuO NPs (Figure 2(b)) sample. The intensity of the Raman peaks expanded in the PVA-incorporated CuO NPs renders to the CuO modified with PVA.

Moreover, the Raman bands located at 2948.63, and 3418.84 cm^{-1} are relevant to the elongated mode of C-C and O-H in PVA [20, 21]. This reveals the capping action

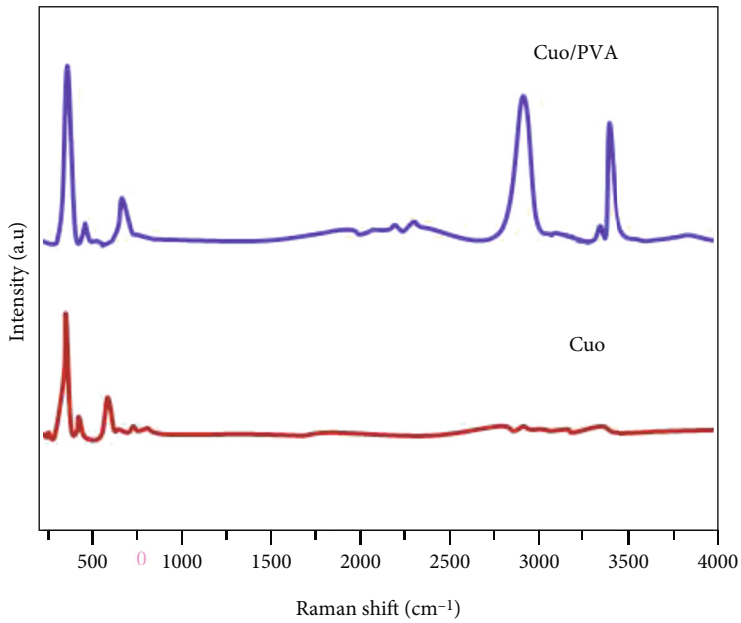

Figure 2: Raman spectrum of (a) CuO and (b) CuO/PVA nanocomposites.

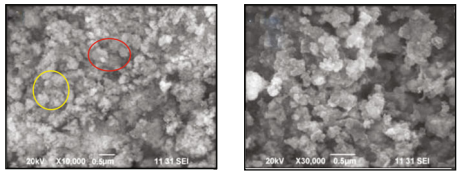

(a) (b)

Figure 3: SEM images of (a) CuO and (b) CuO/PVA nanocomposites.

of PVA on the CuO surface. Further, the Raman bands are red shifted in the Raman spectrum of PVA-coated CuO NPs showing the surface enhancement effect.

3.3. Crystal Structure. Figure 4 visualizes the XRD pattern of synthesized CuO and PVA-coated CuO NPs. The formation of CuO phase in 700°C annealed samples was confirmed by an X-ray diffractometer. The average crystallite sizes (D) were calculated by Scherrer's formula (eqution (1)) given below.

$$D = \frac{K\lambda}{\beta \cos \theta}, \quad (1)$$

where λ is the X-ray wavelength, β stands for FWHM, K is equals to 0.89, and θ is the Bragg diffraction angle. The average particle sizes of the nanoparticles were calculated to be 30.78 and 15.16 nm for CuO and PVA-coated CuO, respectively. The diffraction peaks were matched using JCPDS software, and it was well-matched with the CuO of file no. JCPDF 89-5899 (Figure 4(a)) acquired at 35.3°, 38.5°, 48.6°, 58.1°, 61.8°, 66.4°, and 68.5° can be assigned to the (−111), (111), (−202), (−113), (−311), and (220) planes of CuO [22] phase: monoclinic, lattice: end-centered, ($a = 4.68$, $b = 3.42$, and $c = 5.13$). There are no debasement peaks in the patterns, indicating that the produced CuO samples are pure, and the crisp diffraction peaks reveal a magnificent crystal structure of the created CuO. Moreover, the XRD pattern of CuO compared with PVA-incorporated CuO NPs (Figure 4(b)) can keep the typical CuO crystal structure afterward incorporating with PVA.

There is a trivial alteration in crystallite size while there is intercalation of PVA. This reduction of crystallite size is chiefly due to the alteration in the host CuO by the doping/capping agent. This reveals the incorporation of PVA on the surface of CuO. Hence, construction of a nanocomposite is confirmed. The FT-IR and Raman results corroborate very well with the XRD result.

3.4. Morphological Study. Figure 3 visualizes the SEM images of CuO PVA-modified CuO NPs. The SEM image of CuO (Figure 3(a)) shows small rods/ball-like structure, and the surface is rough. However, PVA-coated CuO NPs (Figure 3(b)) exhibit small hallow nanoflake-like morphology, and the size of the PVA-coated CuO NPs is smaller than CuO. This illustrates the doping/capping happening on the surface of CuO. Consequently, the PVA dramatically change the cryogenically fractured surface of the PVA-incorporated CuO NPs.

The elemental distributions of prepared nanomaterials were determined by EDS measurement. The EDS spectrum of CuO and PVA-coated CuO NPs was presented in Figures 5(a) and 5(b). The fundamental peaks of Cu and O are observed in the EDS spectrum. The uncoated sample exhibits the purity of the CuO nanoparticle. The fabricated nanomaterials display decent stoichiometry and profoundly porous nature. The sensor's very porous surface of PVA-modified CuO NPs is a key feature. Furthermore, the intensity of Cu increases from 1490.18 to 2487.72 in the EDS spectrum of PVA-coated CuO NPs (Figure 5(b)). This is

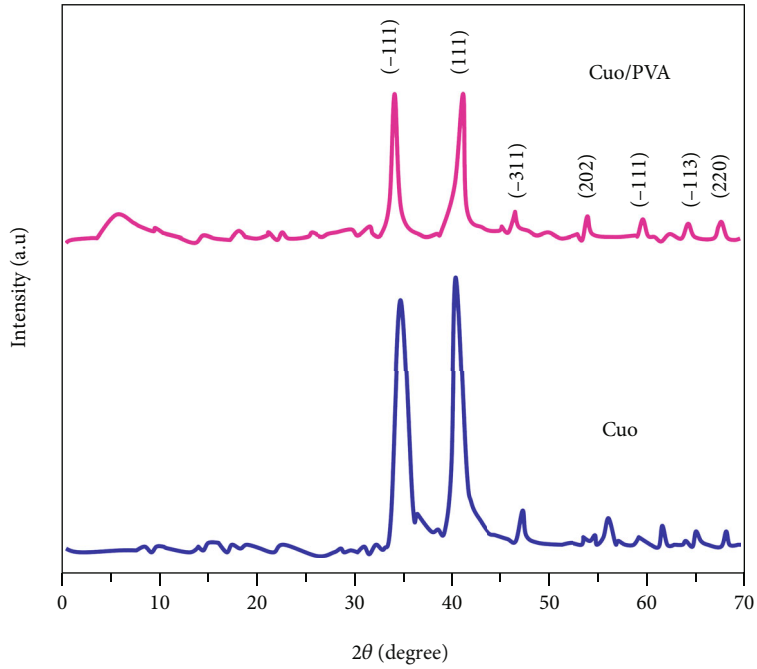

Figure 4: XRD patterns of (a) CuO and (b) CuO/PVA nanocomposites.

because the surface modifier of PVP enlarges the intensity of the Cu. It corroborates the PVA present on the surface of CuO.

3.5. Application. The neurotransmitters are endogenous substances that allow nerve impulses to be transmitted between neurons via the synapse. It also relaxes the brain while stimulating excitatory neurotransmitters. In neurotransmitter progression, DA acts as a messenger molecule, binding to neurotransmitter receptors and transporters by magnitude of distribution between the synaptic fissures [23]. DA, on the other hand, is a rare neurotransmitter in that it is classified as both excitatory and inhibitory. It regulates attention, cognition, pleasure, movement, and hormonal functions, among other things. It is also found in the CNS, hormonal, urinary system, and heart-circulatory systems [24]. The quantity of dopamine that is abnormally formed in the CNS is a symptom of a fundamental neurological problem in the body of the person. As a result, DA monitoring takes precedence.

3.5.1. Study of Dopamine Sensing on a CuO/PVA-Modified GC Electrode. The electrocatalytic activity of CuO/GCE and CuO/PVA/GCE nanocomposites was examined by cyclic voltammetry (CV) studies in 1 mM of $K_3[Fe(CN)_6]$, under 0.1 M of PBS (pH = 7.0). Figure 6 shows couple of distinct redox peak seemed to bare GC electrode. This demonstrates that the redox behavior of DA may be accomplished using a two electrons and two protons method, which is possible since electrons transfer at the base GCE electrode in a quasireversible and sluggish manner. Several anodic and cathodic curves were seen at 0.23 and −0.11 V for CuO/GCE, respectively, as well as a redox peak at 0.20 and −0.14 V for CuO/PVA/GCE. Among these modified electrodes, the anodic peak current of CuO/PVA/GCE has been increased. This shows the high surface area and promotes more conducting electron transfer from $K_3[Fe(CN)_6]$ to the CuO/PVA/GC electrode.

The higher anodic curve potential is due to the excellent electrooxidation of Cu (II)/Cu (III) towards DA. The redox behavior of CuO/PVA/GCE revealed the brilliant electrocatalytic activity and enormous surface area provided by PVA.

3.5.2. Amperometric Detection of Dopamine at CuO/PVA-Modified GC Electrode. The detection limit and concentration range are crucial factors to consider when evaluating the performance of an electrochemical sensor. CuO/PVA/amperometric GCE's reaction to DA in 0.1 M PB solution was measured. The potential anodic peak was observed in the range of +0.1 to +0.3 V in Figure 7. As a result, the best applied potential may be found between +0.1 and +0.3 V. The effect of applied potential on amperometric measurements was inspected by adding 2 μM of dopamine every 50 seconds at varied potentials of +0.1, +0.2, and +0.3 V.

The current responsiveness of 2 μM DA hiked dramatically as the applied potential was increased from +0.1 to +0.3 V, as shown in Figure 7. At +0.2 V, the current response was 1-fold larger than that of +0.1 V and 1-fold smaller than that of +0.3 V. As a result, the ideal constant applied potential for amperometric detection of DA was determined to be +0.2 V. $I_{pa}(A) = 7.34 + 0.56\, C_{dopamine}$ with correlation coefficient (R^2). 0.9914 is calculated from the calibration plot (not shown) of the optimal applied potential at +0.1 V with the linear regression formula. With a sensitivity of 183.12 μA mM^{-1} cm^{-2}, the sensor has a small detection limit of ($S/N = 3$) of 0.017 μM.

Table 1 compares the results of the current DA sensor to those of other DA sensors that have been reported. CuO/

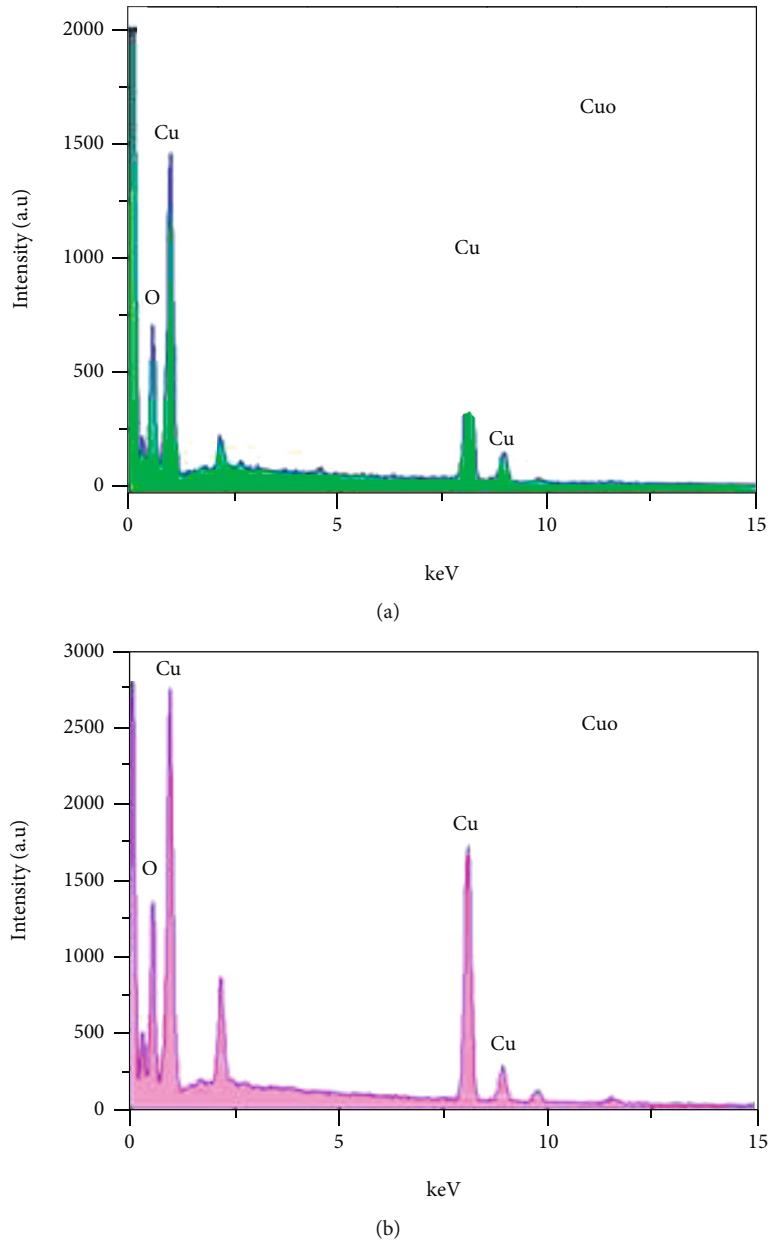

Figure 5: EDX images of (a) CuO and (b) CuO/PVA nanocomposites.

PVA/GC electrode, among the many modified electrodes, offers greater sensitivity, an extensive linear range, a lower detection limit, and speedy detection of DA, making it a promising choice for the dopamine sensor.

3.5.3. Interference Analysis. To examine the selectivity of the sensor towards dopamine, an interference study was analyzed. The interference species such as 100 μM of fructose, 100 μM of sucrose, 100 μM of lactose, 100 μM of glucose, 100 μM ureic acid (UA), 100 μM of ascorbic acid (AA), 100 μM of urea, and 100 μM of hydrogen peroxide as well as the common ionic species such as potassium chloride in biological media were added to the electrolyte solution during the amperometric analysis of DA. As shown in Figure 8, none of these species disclose any important manipulate on the DA oxidation current even at high concentration (100 μM) indicates the stupendous selectivity of the CuO/PVA/GC electrode towards DA detection.

3.5.4. Stability and Reproducibility. The electrochemical sensor performance is primarily evaluated by the steadiness and reproducibility of the produced sensor. For 0.5 μM of DA in 0.1 M of PBS (pH = 7), the CVs of the CuO/PVA/GCE-modified electrode were recorded. For 20 repeated trials, the oxidation peak potential of DA stayed constant with a relative standard deviation of 1.3 percent and 1.1 percent, respectively. To test the modified electrodes' repeatability,

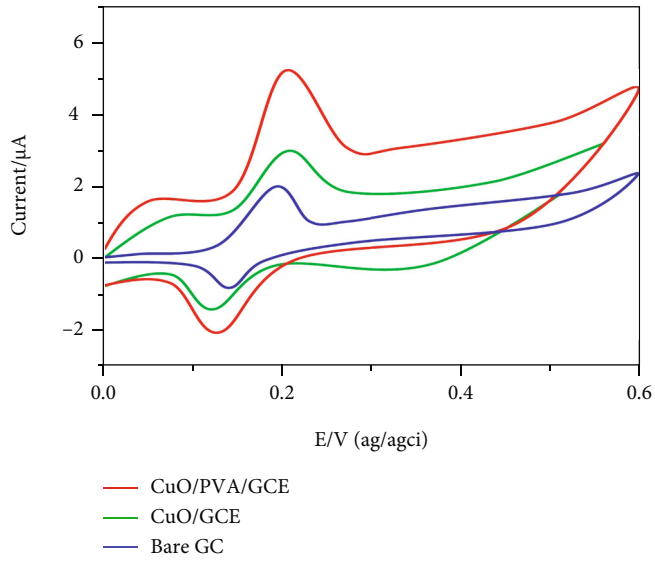

Figure 6: CV curve of CuO/GCE and CuO/PVA/GCE in a 0.1 M PB solution at the scan rate of 50 mV s^{-1}.

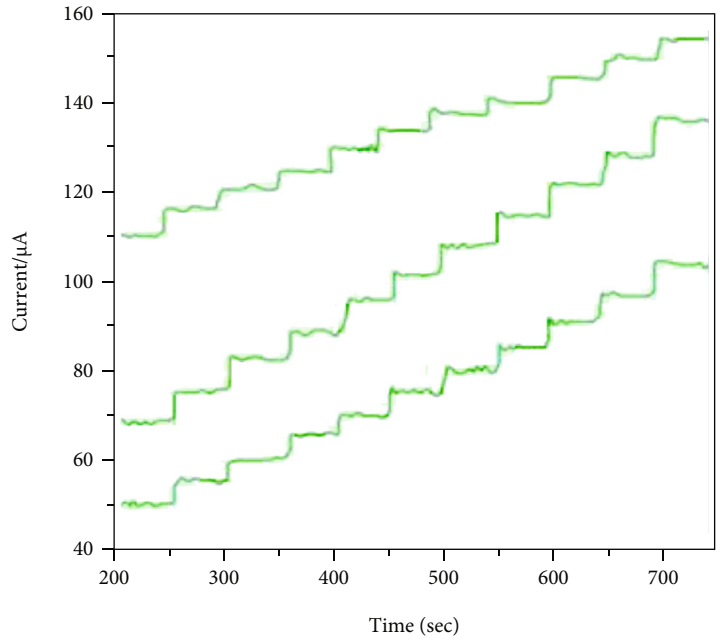

Figure 7: Amperometric measurement of CuO/PVA/GCE biosensor with the addition of each 2 μM dopamine in 0.1 M of PBS analyzed at 0.1, 0.2, and +0.3 V.

10 CuO/PVA/GCE sensors were fabricated identically for the monitoring of DA, and their electrocatalytic current signal was established with RSD of 5.09 percent. These findings show that the suggested modified electrode can function as a stable biosensor for DA with elevated sensitivity and selectivity.

3.6. Real Sample Analysis. The urine samples from the male patient were accumulated at the Tirunelveli Medical College Hospital, Tirunelveli. Primarily, the urine sample was diluted 10 times before using a medium for dopamine analysis. The DA was calculated by the SA method. The analytical outcomes are displayed in Table 2. All samples show a retrieval of more than 100%, which may be due to the inherent dopamine present in biological samples or complex matrix effects of the medium. However, the recovery was noticed to be very close to 100%; this discloses the appropriateness and selectivity of CuO/PVA/GCE sensors for the discovery of DA in biological samples.

Table 1: Assessment of sensing action of the CuO/PVA/GC electrode with other fabricated electrodes.

S. no	Electrodes	LOD (μM)	Reference
1	Au/Pt/GCE	24	[25]
2	Pd_3Pt_1/RGO/GCE	0.04	[26]
3	Ag NPs/P (Arg)-GO/GCE	0.01	[27]
4	Ni- ZIF-8/N S–CNTs/GCE	0.93	[28]
5	Pd NPs/GR/CS/GCE	0.1	[29]
6	PdAg NFs/rGO/GCE	0.048	[30]
7	Ni-meso-PANI/GCE	9.6	[31]
8	Ni/C/GCE	0.05	[32]
9	GP-MWCNTs-Au NCs/GCE	0.77	[33]
10	CuO/PVA/GCE	0.017	**This work**

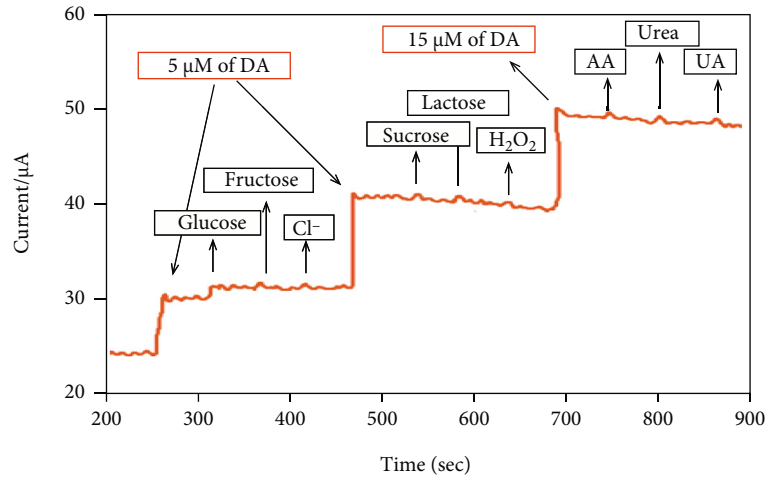

Figure 8: Amperometric detection of interfering species of the sensor in 0.1 M PBS with 100 μM of fructose, 100 μM of glucose, 100 μM of lactose, 100 μM of sucrose, 100 μM ureic acid (UA), 100 μM of ascorbic acid (AA), 100 μM of urea, and 100 μM of hydrogen peroxide as well as the common ionic species potassium chloride.

Table 2: Determination of DA in human urine samples using the CuO/PVA/GCE sensor (practical application of the proposed method $n = 3$).

Urine sample	Added (μM)	Found (μM)	RSD (%)	Recovery (%)
A	5	4.13	2.69	98.50
B	5	4.54	2.45	98.89
C	5	4.13	2.39	98.79
D	5	4.49	1.94	99.43
E	5	4.67	2.23	99.63

4. Conclusion

We were able to successfully produce copper oxide using a simple chemical precipitation process and a surface modification of PVA (wt%). By using a simple chemical precipitation procedure, the p-XRD analysis verified that the sample generated with and without PVA had a monoclinic arrangement. The production of nanoballs/nanorods can be seen in morphological studies of the produced nanocomposite. The presence of copper and oxygen was validated by EDX. CuO/PVA/GCE has been created as a biosensing material. The performance of PVA, which serves as a medium for electron transport among the modified electrode and dopamine, increases the electrocatalytic activity of CuO. For dopamine determination, the suggested and produced structural compound CuO/PVA/GCE demonstrated great electrochemical stability, excellent selectivity, increased sensitivity ($183.12\,\mu A\,mM^{-1}\,cm^{-2}$), and a lower detection limit of 0.017 μM ($S/N = 3$). This information is applicable to the examination of human real-life samples as well.

Data Availability

The data used to support the findings of this study are included within the article.

Conflicts of Interest

The authors declare no conflict of interest.

Acknowledgments

Princess Nourah bint Abdulrahman University Researchers Supporting Project number (PNURSP2022R26), Princess Nourah bint Abdulrahman University, Riyadh, Saudi Arabia.

References

[1] A. Manbohi and S. H. Ahamadi, "Sensitive and selective detection of dopamine using electrochemical microfluidic paper based analytical nanosensor," *Sensing and Bio-Sensing Research*, vol. 23, p. 100270, 2019.

[2] C. Zhang, Z. Cao, G. Zhang et al., "An electrochemical sensor based on plasma-treated zinc oxide nanoflowers for the simultaneous detection of dopamine and diclofenac sodium," *Microchemical Journal*, vol. 158, 2020.

[3] S. Reddy, B. E. K. Swamy, and H. Jayadevappa, "CuO nanoparticle sensor for the electrochemical determination of dopamine," *Electrochimica Acta*, vol. 61, pp. 78–86, 2012.

[4] Y. Y. Li, P. Kang, S. Q. Wang, Z. G. Liu, Y. X. Li, and Z. Guo, "Ag nanoparticles anchored onto porous CuO nanobelts for the ultrasensitive electrochemical detection of dopamine in human serum," *Sensors and Actuators B: Chemical*, vol. 327, p. 128878, 2021.

[5] Y. Zhuang, X. Zhang, Q. Chen, S. Li, H. Cao, and Y. Huang, "Co_3O_4/CuO hollow nanocage hybrids with high oxidase-like activity for biosensing of dopamine," *Materials Science and Engineering: C*, vol. 94, pp. 858–866, 2019.

[6] J. Zou, S. Wu, Y. Liu et al., "An ultrasensitive electrochemical sensor based on 2D g-C_3N_4/CuO nanocomposites for dopamine detection," *Carbon*, vol. 130, pp. 652–663, 2018.

[7] T. Wen, W. Zhu, C. Xue et al., "Novel electrochemical sensing platform based on magnetic field-induced self- assembly of Fe_3O_4@Polyaniline nanoparticles for clinical detection of creatinine," *Biosensors & Bioelectronics*, vol. 56, pp. 180–185, 2014.

[8] A. M. Azharudeen, T. Suriyakala, M. Rajarajan, and A. Suganthi, "An improved sensitive and selective non-enzymatic dopamine biosensor based on PEG assisted CuO nanocomposites," *Egyptian Journal of Chemistry*, vol. 62, pp. 487–500, 2019.

[9] B. Li, Y. Zhou, W. Wu et al., "Highly selective and sensitive determination of dopamine by the novel molecularly imprinted poly(nicotinamide)/CuO nanoparticles modified electrode," *Biosensors & Bioelectronics*, vol. 67, pp. 121–128, 2015.

[10] N. Kohler, C. Sun, A. Fichtenholtz, J. Gunn, C. Fang, and M. Q. Zhang, "Methotrexate-immobilized poly (ethylene glycol) magnetic nanoparticles for MR imaging and drug delivery," *Small*, vol. 2, no. 6, pp. 785–792, 2006.

[11] H. Y. Lee, S. H. Lee, C. Xu et al., "Synthesis and characterization of PVP-coated large core iron oxide nanoparticles as an MRI contrast agent," *Nanotechnology*, vol. 19, 2008.

[12] R. Hariharan, S. Senthilkumar, A. Suganthi, and M. Rajarajan, "Photodynamic action of curcumin derived polymer modified ZnO nanocomposites," *Materials Research Bulletin*, vol. 94, pp. 454–459, 2005.

[13] X. Mo, C. Y. Wang, M. You, Y. R. Zhu, Z. Y. Chen, and Y. Hu, "A novel ultraviolet-irradiation route to CdS nanocrystallites with different morphologies," *Materials Research Bulletin*, vol. 36, no. 13-14, pp. 2277–2282, 2001.

[14] A. M. Azharudeen, R. Karthiga, M. Rajarajan, and A. Suganthi, "Fabrication, characterization of polyaniline intercalated NiO nanocomposites and application in the development of non-enzymatic glucose biosensor," *Arabian Journal of Chemistry*, vol. 13, no. 2, pp. 4053–4064, 2020.

[15] O. Rezaee, H. M. Chenari, F. E. Ghodsi, and H. Ziyadi, "Preparation of PVA nanofibers containing tungsten oxide nanoparticle by electrospinning and consideration of their structural properties and photocatalytic activity," *Journal of Alloys and Compounds*, vol. 690, pp. 864–872, 2017.

[16] T. Jan, J. Iqbal, V. Farooq et al., "Structural, Raman and optical characteristics of Sn doped CuO nanostructures: a novel anticancer agent," *Ceramics International*, vol. 41, no. 10, pp. 13074–13079, 2015.

[17] F. Bayansal, O. Sachin, and H. W. Cetikare, "Mechanical and structural properties of Li-doped CuO thin films deposited by the successive ionic layer adsorption and reaction method," *Thin Solid Films*, vol. 697, p. 137839, 2020.

[18] Y. F. Zhang, M. M. Guo, Y. Zhang et al., "Flexible, stretchable and conductive PVA/PEDOT: PSS composite hydrogels prepared by SPIN strategy," *Polymer Testing*, vol. 81, 2020.

[19] H. Zhang and J. Zhang, "The preparation of novel polyvinyl alcohol (PVA)-based nanoparticle/carbon nanotube (PNP/CNTs) aerogel for solvents adsoption application," *Journal of Colloid and Interface Science*, vol. 569, pp. 264–266, 2020.

[20] M. Sun, Y. Lei, H. Cheng et al., "Mg doped CuO-Fe_2O_3 composites activated by persulfate as highly active heterogeneous catalysts for the degradation of organic pollutants," *Journal of Alloys and Compounds*, vol. 825, p. 154036, 2020.

[21] M. A. Kurian, P. Gissen, M. Smith, S. J. Heales, and P. T. Clayton, "The monoamine neurotransmitter disorders an expanding range of neurological syndromes," *The Lancet Neurology*, vol. 10, no. 8, pp. 721–733, 2011.

[22] S. S. Castro, R. J. Mortimer, M. F. De Oliveira, and N. R. Stradiotto, "Electrooxidation and determination of dopamine using a Nafion®-cobalt hexacyanoferrate film modified electrode," *Sensor*, vol. 8, no. 3, pp. 1950–1959, 2008.

[23] M. M. Ardakani, H. Rajabi, H. Beitollahi, B. Mirjalili, A. Akbari, and N. Taghavinia, "Voltammetric determination of dopamine at the surface of TiO_2 nanoparticles modified carbon paste electrode," *International Journal of Electrochemical Science*, vol. 5, pp. 147–157, 2010.

[24] A. Galvan and T. Wichmann, "Pathophysiology of parkinsonism," *Clinical Neurophysiology*, vol. 119, no. 7, pp. 1459–1474, 2008.

[25] S. Thiagarajan and S. Chen, "Preparation and characterization of PtAu hybrid film modified electrodes and their use in simultaneous determination of dopamine, ascorbic acid and uric acid," *Talanta*, vol. 74, no. 2, pp. 212–222, 2007.

[26] J. Yan, S. Liu, Z. Zhang et al., "Simultaneous electrochemical detection of ascorbic acid, dopamine and uric acid based on graphene anchored with Pd-Pt nanoparticles," *Colloids and Surfaces B: Biointerfaces*, vol. 111, pp. 392–397, 2013.

[27] G. Tığ, "Development of electrochemical sensor for detection of ascorbic acid, dopamine, uric acid and L-tryptophan based on ag nanoparticles and poly(l-arginine)-graphene oxide

composite," *Journal of Electroanalytical Chemistry*, vol. 807, pp. 19–28, 2017.

[28] W. Yao, H. Guo, H. Liu et al., "High electrochemical performance of Ni-ZIF-8/N S–CNTs/CS composite for simultaneous determination of dopamine, uric acid and L-tryptophan," *Microchemical Journal*, vol. 152, p. 1043357, 2020.

[29] X. Wang, M. Wu, W. Tang et al., "Simultaneous electrochemical determination of ascorbic acid, dopamine and uric acid using a palladium nanoparticle/graphene/chitosan modified electrode," *Journal of Electroanalytical Chemistry*, vol. 695, pp. 10–16, 2013.

[30] L. X. Chen, J. N. Zheng, A. J. Wang, L. J. Wu, J. R. Chen, and J. J. Feng, "Facile synthesis of porous bimetallic alloyed PdAg nanoflowers supported on reduced graphene oxide for simultaneous detection of ascorbic acid, dopamine, and uric acid," *Analyst*, vol. 140, no. 9, pp. 3183–3192, 2015.

[31] M. U. A. Prathap and R. Srivastava, "Tailoring properties of polyaniline for simultaneous determination of a quaternary mixture of ascorbic acid, dopamine, uric acid, and tryptophan," *Sensors and Actuators B: Chemical*, vol. 177, pp. 239–250, 2013.

[32] W. He, Y. Ding, W. Zhang, L. Ji, X. Zhang, and F. Yang, "A highly sensitive sensor for simultaneous determination of ascorbic acid, dopamine and uric acid based on ultra-small Ni nanoparticles," *Journal of Electroanalytical Chemistry*, vol. 775, pp. 205–211, 2016.

[33] X. Liu, S. Wei, S. Chen, D. Yuan, and W. Zhang, "Graphene-multiwall carbon nanotube gold nanocluster composites modified electrode for the simultaneous determination of ascorbic acid, dopamine, and uric acid," *Applied Biochemistry and Biotechnology*, vol. 173, no. 7, pp. 1717–1726, 2014.

Hindawi
International Journal of Photoenergy
Volume 2022, Article ID 6711300, 9 pages
https://doi.org/10.1155/2022/6711300

Research Article

Utilization of Sustainable Resources for Promoting Energy Efficiency in Environment Using Smart Technologies

V. Vedanarayanan,[1] Chirag Vibhakar,[2] A. Sujaatha,[3] Jiten K. Chavda,[4] M. Karthik,[5] P. V. Pramila,[6] and Ishwarya Komalnu Raghavan[7]

[1]*Department of Electronics and Communication Engineering, Sathyabama Institute of Science and Technology, Chennai, 600 119 Tamil Nadu, India*
[2]*Department of Electrical Engineering, Gujarat Power Engineering & Research Institute, Mehsana, 382710 Gujarat, India*
[3]*Department of Civil Engineering, Sri Sairam Engineering College, Chennai, 600044 Tamil Nadu, India*
[4]*Department of Electrical and Electronics Engineering, LD College of Engineering, Navrangpura, Ahmedabad 380015, India*
[5]*Department of Electronics and Electronics Engineering, Kongu Engineering College, Perundurai, Erode, 638060 Tamil Nadu, India*
[6]*Department of Computer Science and Engineering SIMTAS, Saveetha University, Chennai, Tamil Nadu, India*
[7]*Department of Electromechanical Engineering, Faculty of Manufacturing, Institute of Technology, Hawassa University, Ethiopia*

Correspondence should be addressed to Ishwarya Komalnu Raghavan; ishwarya138@hu.edu.et

Received 10 November 2021; Accepted 27 December 2021; Published 21 February 2022

Academic Editor: V. Mohanavel

Copyright © 2022 V. Vedanarayanan et al. This is an open access article distributed under the Creative Commons Attribution License, which permits unrestricted use, distribution, and reproduction in any medium, provided the original work is properly cited.

Smart technology has potential in tracking the key challenges based on population based on the sustainable future. In today's cultures, a smart approach enables for the integration of information needed to address crucial concerns. The critical challenge is to limit the effects of global warming while maintaining a balanced economic growth. The impact of global warming mitigates the fundamental problem while ensuring the balance economic development. Intense research efforts should be directed toward balanced resource utilization, renewable energy system integration, efficient energy conversion technologies, effective process integration, effective techniques to enable a circular economy framework, and other issues that are important to the population. This paper finds the latest technology in the field of smart grid technologies which focused on the effective enhancement and efficient utilization of resource. The issues and challenges in using sustainable future are discussed and bring new ideas towards the sustainable future base on the application of smart technologies.

1. Introduction

Global energy demand is the worldwide concern, which is rapidly growing and satisfies the energy demand in the future. Economic growth, modernization, and automation are mainly depending on the energy supply. The carbon dioxide emission causes greenhouse effect and environmental degradation which threatened the global environment. Worldwide greenhouse gas emissions are steadily increasing on a global scale, where climate change concerns are becoming increasingly prevalent and wreaking havoc on the people. CO_2 emissions have grown by around 2.7 percent, making them the most dominant emissions. This recent surge in CO_2 emissions is very alarming, especially given that CO_2 levels were nearly steady. CO_2 levels are currently at 411 ppm, although they were below 400 ppm just five years ago. Methane (CH_4) is the more dangerous greenhouse gas, as it is over 30 times more effective as a heat-trapping gas than CO_2. Large amounts of CH_4 are stored in ice sheets, where they are progressively released into the atmosphere when the ice sheets melt owing to climate change concerns. It is obvious that current measures are insufficient and that strong and timely global actions are required to attain this aim and, as a result, to limit the adverse effects of anthropogenic activities on the environment. It is the requirement for long-term development that leads to the integration of cost-

effective ways based on interdisciplinary knowledge. Globally, fossil fuels are still used to generate power to a great level, accounting for more than half of all electricity generation, mostly coal, and natural gas. One of the major problems with current fossil fuel energy systems is their low conversion efficiency, which results in a high rate of thermal energy waste [1].

The renewable energy generation level increases as the energy development, which relies on the reduction of fossil fuel generation. The fossil fuel is taken as a primary source of energy to satisfy the supply of energy demand. This fossil fuel emits greenhouse gases and create hazard to environment and affect the future generation. So, the sustainable energy resource is of great significance to reduce the fossil fuel consumption. The renewable energy resources are free from emission. The renewable energy with smart technology provides an idea for the emission problem and contributes significantly in generating power with less emission of greenhouse gases. Increased energy demand, along with the depletion of fossil fuels, has heightened the need for rapid development of renewable energy (RE) sources to meet demand. However, the use of renewable energy as a percentage of total energy consumption in many nations is still at a low level [2]. RE is needed for a variety of activities, including lighting, heating, and cooking, and it may originate from a variety of sources, including biomass, solar, wind, and hydropower. The costs of developing various alternative energy sources to meet the energy needs of a certain location are varied [3].

The costs of developing various alternative energy sources to meet the energy needs of a certain location are varied. The challenge in energy resource management is deciding how to effectively employ available renewable energy resources to satisfy power demand [4]. Energy efficiency is widely acknowledged as a critical tactic in energy and climate change policy. Energy efficiency advantages include decreased greenhouse gas emissions and local air pollution, as well as fewer energy infrastructure expenditures, lower fossil fuel reliance, better competitiveness, and improved customer welfare [5].

For coal-based power plants, an average energy conversion efficiency of 35 percent to 45 percent is appropriate, with the latter number for state-of-the-art facilities, but for natural gas combined cycle plants, the efficiency can reach 60 percent. As a result, the operation of present fossil fuel-based technologies is accompanied by a high rate of emitted waste heat, ranging from 60% to 70% on average, which is mostly unutilized. In order to make better use of discharged waste heat, more efficient energy ideas are required, particularly in industrial applications.

Renewable energy technologies now available provide a viable alternative to fossil fuels, but with limits, owing to poor energy conversion efficiency and power generating nondispatchability. Photovoltaics (PV) and wind generators have dominated the market in the previous decade, with substantial growth, while the capacities of large hydroelectric plants have grown at a slower pace, since their potential has been fully used for decades, especially in developed nations.

Meanwhile, emission-free energy sources such as solar, wind, hydro, geothermal, biomass, and others exist across the world. Renewable energy technologies are an excellent alternative since they can considerably contribute to global power generation while emitting less greenhouse emissions. According to the International Energy Agency's (IEA) "sustainable future" scenario, renewable energy sources would generate 57 percent of global power by 2050. To attain this ultimate goal, long-term forecasting and planning are essential. For a given zone, renewable energy-based power generation and delivery to the national grid are required. The traditional grid connects several networks, and the regulatory system is made up of different layers of communication and coordination, with the majority of the systems being regulated manually. A smart grid is a novel idea that enables the transmission and distribution grids to be improved. The smart grid system is the digitalization of transmission and the creation of new markets for renewable energy generation. In today's energy generating and distribution business, smart grid is frequently used [6].

A smart grid is a novel idea based on smart technology that allows the transmission and distribution system to be modernized. The smart grid technology is the digitalization of transmission and the creation of new markets for renewable energy generation. In today's energy generating and distribution business, the phrase "smart grid" is frequently used. The smart grid, when combined with distributed power generation, creates a new platform that dramatically improves electric energy security and quality [7]. As more energy sources become accessible, such as wind, hydropower, solar, and biomass, this approach becomes more feasible and trustworthy. Renewable and nonconventional energy sources are allowed to connect to a smart grid-connected distributed power generating connection. This paper explores the role of renewable energy sources in power generation and their integration with the smart grid system.

2. Related Work

Renewable energy sources must be integrated into the power system to achieve a variety of socioeconomic and environmental benefits, as well as to minimise greenhouse gas emissions from traditional power plants. PV power generation, on the other hand, is unpredictable and intermittent, putting significant pressure on the system and causing energy supply instability. Intermittent energy sources, to be more specific, may fail to assure the power supply's continuity and stability. Apart from the aforementioned concerns with PV integration, power system back-feeding poses substantial operational hurdles [8].

PV power producing equipment can cause reverse power flow, high voltage levels, and an increase in the number of tap operations. To cope with reverse power flow, dispersed PV power generation units have been proposed instead of centralised generating units. Furthermore, the integration of renewable power generation units as new distributed generations, encompassing large scale at the transmission level, medium scale at the distribution level, and small scale on

commercial or residential buildings, can pose challenges for resource dispatch and control, as well as system operation [9].

The traditional approach to evaluating electric utility energy efficiency and smart-grid programmes, as well as an agent-based end-use modelling strategy that addresses many of the shortcomings of previous techniques, are also reviewed. Over a fifteen-year period, data from a representative sample of utility customers is utilized to evaluate energy efficiency and smart grid programme objectives. According to model analysis, combining the two least stringent efficiency and smart grid programme scenarios reduces peak hour demand by one-third more than the most stringent smart grid programme. This suggests that peak demand reductions are more feasible when both efficiency and smart grid programmes are considered [10].

Smart technology and energy approaches are being industrialized to enhance energy efficiency and decrease greenhouse gas emissions. Additionally, suggestions for incorporating energy-efficient and zero-carbon approach for lighting, air cooling, and conditioning, as well as sustainable energy consumption in office buildings around the country, are offered. The present policies and strategic energy of renewable energy technologies (RETs) are highlighted. The pronged method of lowering energy use, implementing RETs, and monitoring greenhouse gas emissions is used to decrease greenhouse gas emissions and enhance energy efficiency. Policy enactment, in addition to energy advocacy, has the potential to reduce greenhouse gas emissions, energy consumption, and efficiency of energy, all of which are important for humanity's future to be clean and sustainable [11].

Energy extraction, conversion, and usage processes are all prone to waste. Environmental deterioration, quicker depletion of energy supplies, and higher costs of energy products and services are all consequences of such waste. As a result, the notion of sustainable development requires a concerted effort to enhance energy efficiency in the production, conversion, and usage of energy. Energy resources and their use are inextricably linked to long-term development. Increasing the energy efficiency of operations that use sustainable energy resources is critical to achieving sustainable development [12].

The environment is another source of worry in the continuous use of fossil fuels, in addition to their limited nature and lack of viable replacement. Climate change and the environmental externalities linked with energy usage have emerged as a major global concern. The contribution of the industrial sector to greenhouse gas (GHG) emissions has been shown to be large, suggesting that reducing GHG emissions from the industry is one of the greatest approaches to address the climate change challenge. In this aspect, energy efficiency is critical. By enhancing the efficiency of energy usage in the sector, an estimated 10-30% decrease can be accomplished at little or no expense [13].

Low-carbon technology, environmental protection, renewable energy, and green development have been at the forefront of global power system reform. New electricity market and power sector changes are being investigated, and renewable energy market mechanisms are being explored across the world to address climate change and emission reduction. Because the usage of hydropower production resources in industrialized nations has already reached a high level, renewable energy sources such as biomass, geothermal, win, and solar are being explored [14].

The majority of study on energy utilization has been concentrated on the residential sector. Energy behaviours in the residential sector are large field experiments assessing instruments to encourage more effective energy behaviours and seeking to discover behavioural drivers for energy use. In the last decade, psychology research has dominated the bulk of energy behaviour studies. It comprises a detailed investigation of the factors that influence proenvironmental behaviour in the residential sector, as well as the sorts of involvements that may be utilized to encourage it. Local and national governments utilize energy organisations that have employed energy restrictions, behavioural change programmes, and demand side management, to encourage more efficient energy behaviour. Despite significant investments in these programmes over the past few decades, more important energy utilization changes are necessary.

3. Smart Grid Technology

A smart grid is a solution for improving the infrastructure and electrical energy system in order to create a more intelligent environment. A smart grid is a method for modernizing the electrical power infrastructure and services so that a more smart and dependable power grid can be presented [15]. Traditional grids offer a number of benefits that smart grids do not. Smart grids improve the economic and physical operation of the grid and improve the sustainability and reliability. The market or a smart grid determines an intelligent self-response by integrating sophisticated sensing, measurement and control approaches, and two-way communication into the recent energy system, according to the US Government of Energy's advancing technology grid project. The smart grid concept is depicted in Figure 1 as a block diagram. By establishing a smart power grid, energy security and resource optimization can be improved.

The smart grid system is built to deal with unpredictable events. The smart grid technology is used to maintain power distribution availability based on consumer demand. The major goal of the smart grid is to improve total management that entails gaining direct monitoring of the system and thereby increasing reliability of the system. Despite its low energy efficiency, this approach offers significant advantages in terms of frugality. By utilizing flexible transmission systems, smart grid technologies can assist the system operator in better managing and controlling the energy streams on the grid [16].

The smart grid's distribution network automation enables utility companies to improve the distribution network's strong communication and prevents supply interruptions to end users in the occurrence of unexpected events including an environmental problem that destroys power poles or damages the substation's facilities. Using distribution channel automation also helps to control end-user load. The smart grid's basic mission is to deliver better and more

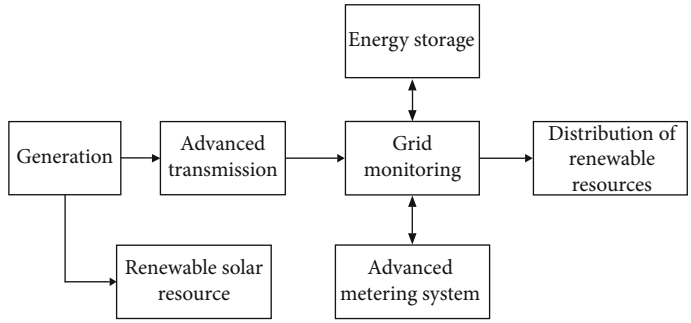

Figure 1: Block diagram of smart technology for sustainable resources.

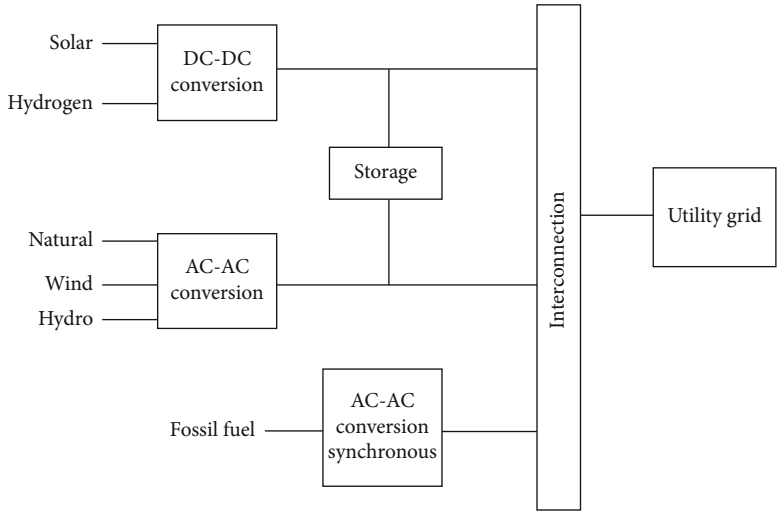

Figure 2: Integration of renewable energy resource in grid.

reliable services to end users by integrating current communication systems with diverse grid segments [17].

3.1. Renewable Energy Source Integration in Smart Grid. Renewable energy resources are more efficient and convenient, especially in increasing the energy prices and the greenhouse effect. Solar technology is the most perfect system for reducing greenhouse gas emissions and managing energy consumption; it represents a watershed moment in the development of clean and green energy. The most impressive approach is utilized wind generators, solar energy, hydroelectric, and biofuels to generate electricity. The widespread adoption of these types of innovations and technology is contingent on three critical variables connected to future energy supply and grid multiapplication: demand-side capacity planning, distributed energy storage (DES), and DG (DSLM). DG connects multiple energy sources to the electricity grid [18].

Figure 2 reveals the integration of renewable energy resource in grid. In order to establish the smart grid, local power generation from renewable energy is critical. Handling renewable sources of energy necessitate meticulous planning and execution based on technological concepts. A more adaptable, efficient, and smarter grid is required for large-scale distributed renewable energy systems. Energy storage is also a key component of the smart grid. The growth of renewable energy sources is aided by the developed system. This system aids in the development of renewable energy sources. The whole renewable energy integration and storage system is depicted in Figure 3. Energy storage will become increasingly important as renewable energy becomes more integrated into the electricity supply system. The usage of a big amount of electrical power storage might be difficult and result in system losses. The usage of DES is a feasible solution since it mitigates the drawback of the smart grid's energy backup requirements [19].

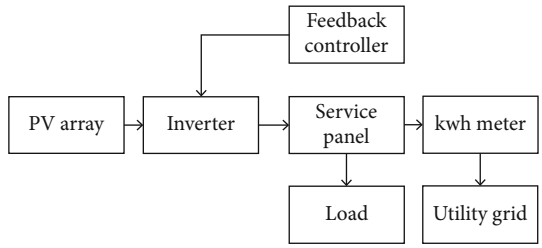

Figure 3: Solar energy integration in PV system.

3.2. Solar Energy Utilization. Solar energy is now mostly used to generate electricity using photovoltaic (PV)

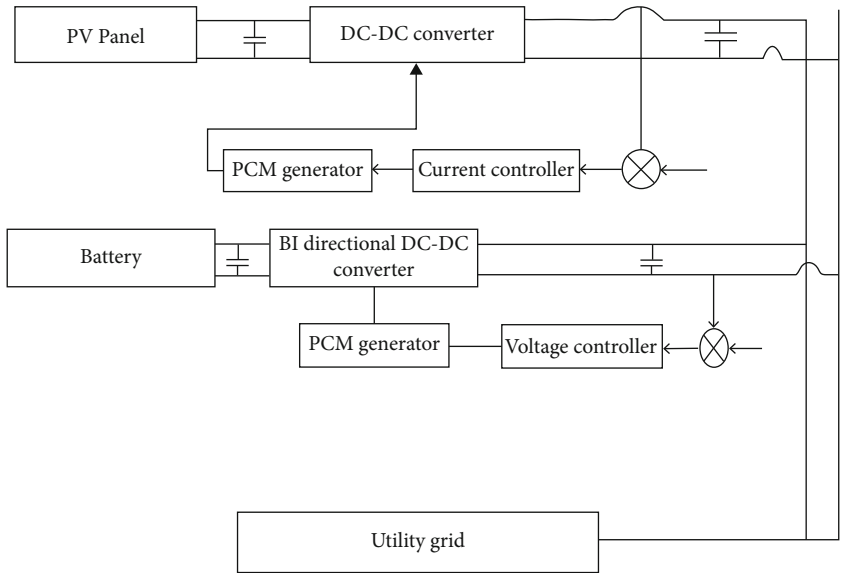

Figure 4: Control scheme connected to renewable resource.

Table 1: Energy demand using renewable resource.

Energy source	Demand (%)
Coal	22
Gas	24
Oil	35
Hydro	2
Nuclear	5
Biomass	10
Other renewable	1.12

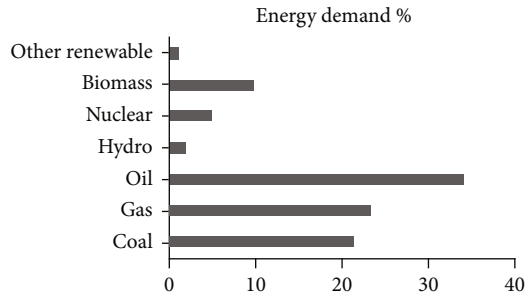

Figure 5: Energy demand for various sources.

Table 2: Energy consumption of renewable resources.

Renewable energy source	Energy consumption
Biomass	13%
Traditional biomass	61%
Wind	8%
Hydro	13%
Biofuel	5%

technology or heat using various solar-thermal systems. There are other linked photovoltaic-thermal technologies that can produce both thermal and electrical energy, although they are currently less marketable due to the comparatively high total asset cost. The creation of hybrid power systems, depending on the use of solar energy, could be a viable solution for integrating multiple market-available renewable energy sources. The unique control technique allows for the connection of real-time field data with previous usage patterns, resulting in a decrease in energy to imbalance as well as administrative expenses [20].

On a worldwide scale, efficiency improvements of PV systems and their mechanisms lead to increased PV capacity. PV system performance could be improved with correct maximum power point (MMPT) techniques. Solar energy consumption necessitates solar collection and transformation, as well as solar storage. Photovoltaic systems can be used to collect and convert solar energy (PVs). The goal is to decrease the cost per watt of provided solar energy by a factor of ten. Solar energy is diffused associated with fossil energy; thus, material prices must be low to make a photovoltaic process economically viable. If the irradiance striking that area over a time is known, it is quite straightforward to compute the sale price of converted energy that is necessary to pay back at least the original cost of covering a section of the earth with solar energy systems [21].

Because of the variability in local solar irradiance, renewable power will never be a primary energy source for humanity in the lack of expense storage. In theory, batteries might be used to store electricity, but no battery is currently cheap enough to meet the required cost per W requirements for the entire system when amortised over the 30-year lifetime of a solar unit. Electricity might be utilized to power turbines that pump water difficult. This method is comparatively cheap for storage of huge expanses of energy at low adsorption and desorption rates and to charged and discharged every 24 hours to account for the daytime cycle.

The conversion of sunlight into a "wireless current" is one of the most important phases in photosynthesis. In all cases, O_2 must be converted into a usable fuel before being released into our oxygen-rich atmosphere or used as an oxidation reagent for other fuels. The reduced fuel might be hydrogen produced from water reduction or an organic species such as methanol or methane derived from ambient CO_2 fixation. The carbon-neutral cycle would subsequently be completed by recombination of the reduced fuel with freed O_2. However, considerable advances in basic research are necessary for this technology to attain its full potential.

3.3. Energy Efficiency. Energy sources and supplies are critical for social and economic development. The most important goal is to improve the energy supply system. To improve energy efficiency and technological innovations and capture the dynamic must be to achieve general sustainability objectives for various engineering applications, increased efficiency of efficient estimation available technologies, structures, procedures, or individual components has become a necessity. The continuation of this review paper will present a summary of current breakthroughs in improved efficiency for diverse industrial applications and effective management, as they are critical population issues. Because the topic of efficiency is so broad, the overview offered here is restricted to specific technological difficulties and implementations in general [22].

The effectiveness of different technologies and process elements in energy systems is a prominent research area with substantial implications for sustainability and resource usage. Economic expansion, rising living standards, and societal development in general all come at a cost to the ecosystem, and it is becoming clear that this cost is causing a natural equilibrium to be disrupted. Anthropogenic activities are to a large measure the cause of these problems, and human actions will be required to solve it. Sustainability is a realistic objective that requires a clear vision, meticulous preparation of focused activities, and timely and effective implementation [23].

3.4. Reliability of the Smart Grid. In today's electrical networks, reliability issues are getting more difficult to solve. Grid congestion is worsening, greater transfers are being made over greater distances, variability is rising, and dependability margins are shrinking. The effective information system of islanding coupled to DG has the potential to improve the local energy supply's dependability and quality of service. The user can benefit from an electricity charge based on real-time sensing, which is made feasible by applying advance measuring. The smart grid has features such as self-healing from power outages, allowing end-user contribution in demand managing, cyber-attacks, and physical damage, providing the required power quality in the twenty-first century, flexibility in all generation and storage, and the ability to introduce new products and services [24].

In grid-connected mode, the renewable energy system is illustrated in Figure 4, which must be overseen by certain power converter control schemes to regulate the voltage and power. System synchronisation and management of the quality of power put into the grid are the foundations of grid control. The grid functionalities are inserted into Converter Control, which guides the various operating modes, manages the energy stored in the batteries, and provides references for the active and reactive powers.

Smart grid technology controls appliances by delivering power from suppliers to customers via robust two-way digital connections. It is also the integration of communications networks with the electrical power grid in such a way as to create an electricity communications superhighway capable of continuously monitoring its own health, alerting the utility immediately if any problems arise, and automatically taking corrective actions that can allow the grid to fail gracefully and prevent a local failure from spreading out of control. The traditional grid has centralised power generation, unidirectional power flow, and poor market integration at the distribution level. Smart grid technology encompasses both centralised and distributed power generation, with renewable energy sources playing a large role. The system incorporates

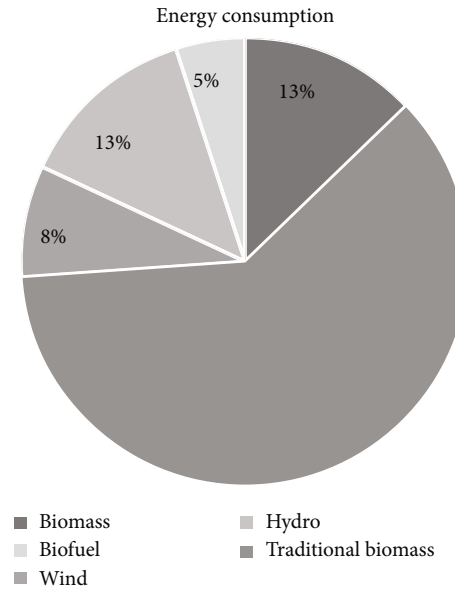

Figure 6: Global energy consumption of renewable energy resource.

Table 3: Annual load distribution for a building for various electrical sources.

	Energy consumption (%)	
	Energy resource	Utilizing renewable energy resources
Lighting	18	3
Water heating	5	5
Space heating	65	22
Fan and pump	12	12
General purpose	7	7

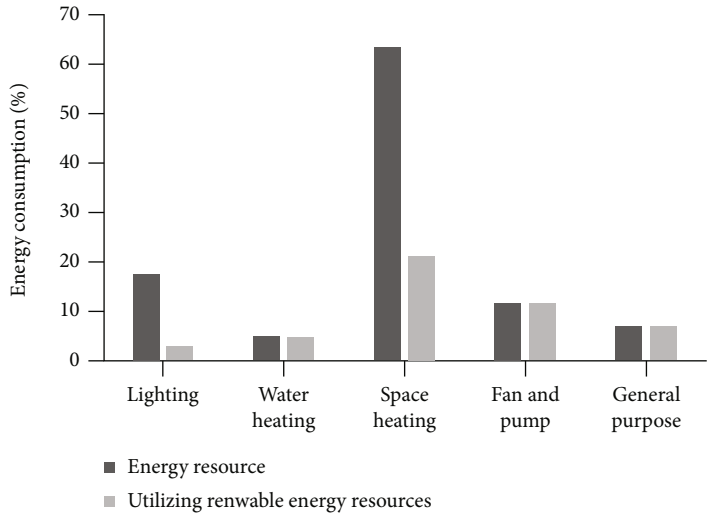

Figure 7: Energy efficiency in utilizing renewable resources.

dispersed and active resources such as generation, loads, and storage. It is the electrical network that intelligently connects producers and consumers to effectively supply power that is safe, economical, dependable, efficient, and sustainable. One of the two main objectives for boosting electric power intercommunication for both energy suppliers and end users tends to push smart grid technologies.

Due to ever-increasing energy demand and the objective of reducing greenhouse gas emissions, the world's energy output is changing, necessitating the extensive utilization of renewable energy sources. The renewable energy sources are frequently intermittent and unpredictable, and energy storage is the only answer to this problem. Energy storage is a major aspect in the integration of renewable energy sources, as it helps to increase energy production efficiency while also ensuring a stable and dependable contemporary power grid. It can increase the electric system's flexibility, dependability, and stability by reducing power fluctuations [25].

3.5. Smart Grid Technology and Applications. To construct the smart grid, modern tools and techniques are necessary. To fully comprehend the application of smart grid, it is required to integrate information technology, a robust monitoring system, and a practical strategic strategy. The notion of meeting power demand with a centralised and distributed generation (DG) system using smart grid is a fairly contemporary and trustworthy. Recent technologies and information control the smart grid's system performance and control system, allowing the operator to exercise demand monitoring and conveniently supply dependable and high-quality service. Through a two-way communication network based on client answers, the smart grid offers the efficient electrical distribution network. Power companies around the world are unpredictably confronted with significant difficulties. Existing grids are also under pressure to operate securely and reliably. In addition, the social and political benefits of electricity generation and use, as well as their environmental consequences, are significant. Developing countries need to develop policies based on the need for a more advanced smart grid: a massive oversupply and efficient provision of dependable and high-quality service [26].

Table 4: Comparison of smart grid technology with traditional power grid.

Criteria	Traditional power grid	Smart grid
Metering	Inadequate	Wide
Power flow control	Limited	Automated
Efficiency	Poor	Excessive
Electricity generation	Central	Distributed
Restoration	Physical	Self-healing
Environmental pollution	High	Low

4. Result and Discussion

Natural gas has a good influence on the environment since it is a cost-effective and efficient source of power. The greatest factor of demand in the energy market will be electric power, indicating an increase in living standards as more individuals and companies have access to safe and dependable electricity. Table 1 reveals the energy demand using renewable resource.

Figure 5 reveals the energy demand for various sources. The world primary energy demand is increasing based on the population rate. The energy consumption shows the increasing of energy demand. The demand of gas is increasing tremendously. The natural renewable resources remain as a fuel for the power generation as it provides more efficiency. The intensities may vary because of differences in economic growth, energy usage, energy rate, location, climate, and culture. Table 2 reveals the energy consumption of renewable resources.

Figure 6 depicts the overall energy contribution of various sectors of energy sources, with a focus on renewable energy sources contribution to total world energy consumption. The renewable energy technology is positive and

extensive. It is analysed that energy consumption is more in traditional biomass and biofuel provide less energy consumption. The energy consumption profiles for a residential building which have low energy consumption are defined primarily. A number of design factors can impact each primary end use that creates the demand on energy and design variables of building has the possible range of values. Table 3 reveals the annual load distribution for a building for various electrical sources.

Figure 7 shows the annual demand of energy for the building. Various components of the building are used to estimate the total power consumption based on the utilization factor, size, and maintenance factors.

Table 4 reveals the comparison of smart grid technology with the traditional power grid. It is analysed that the smart grid technique is more reliable and flexible and performs better compared to a traditional power grid. The generated power is distributed and provides less pollution to the environment.

5. Conclusion

Economic expansion, rising living standards, and societal progress in general all come at a cost to the environment, and it has become clear that this cost is causing a natural equilibrium to be disrupted. Providing energy that is dependable, efficient, and inexpensive is a huge task. Using renewable energy sources to generate power can bring immediate and indirect economic advantages that outweigh the expenses, as well as environmental benefits. Recent advancements in solar energy use have focused on improving existing PV technologies as well as investigating new PV technologies. Improvements in efficiency and the continued expansion of control mechanisms for PVs and energy systems were also explored. A smart strategy enables the integration of data needed to address crucial difficulties in today's societies. The main contest is to limit the properties of global warming while maintaining a healthy economic growth. The smart grid system enhances the efficiency of electricity distribution by addressing the deterioration of energy sources and contemporary information technologies for communication. A smart grid can change the electrical grid of the twentieth century into a network that is more intelligent, adaptable, dependable, self-balancing, and interactive, allowing for economic development, monitoring, energy security, and operational efficiency.

Data Availability

The data used to support the findings of this study are included within the article.

Conflicts of Interest

The authors declare that they have no conflicts of interest.

References

[1] D. Gielen, F. Boshell, D. Saygin, M. D. Bazilian, N. Wagner, and R. Gorini, "The role of renewable energy in the global energy transformation," *Energy Strategy Reviews*, vol. 24, pp. 38–50, 2019.

[2] M. Bilgili, A. Ozbek, B. Sahin, and A. Kahraman, "An overview of renewable electric power capacity and progress in new technologies in the world," *Renewable and Sustainable Energy Reviews*, vol. 49, pp. 323–334, 2015.

[3] W. Strielkowski, E. Volkova, L. Pushkareva, and D. Streimikiene, "Innovative policies for energy efficiency and the use of renewables in households," *Energies*, vol. 12, no. 7, p. 1392, 2019.

[4] Y. Meng, Y. Yang, H. Chung, P.-H. Lee, and C. Shao, "Enhancing sustainability and energy efficiency in smart factories: a review," *Sustainability*, vol. 10, no. 12, p. 4779, 2018.

[5] I. Vigna, R. Pernetti, W. Pasut, and R. Lollini, "New domain for promoting energy efficiency: energy flexible building cluster," *Sustainable Cities and Society*, vol. 38, pp. 526–533, 2018.

[6] M. L. Tuballa and M. L. Abundo, "A review of the development of smart grid technologies," *Renewable and Sustainable Energy Reviews*, vol. 59, pp. 710–725, 2016.

[7] F. M. Bhutta, "Application of smart energy technologies in building sector—future prospects," in *2017 International Conference on Energy Conservation and Efficiency (ICECE)*, pp. 7–10, 2017.

[8] M. A. Mac Kinnon, J. Brouwer, and S. Samuelsen, "The role of natural gas and its infrastructure in mitigating greenhouse gas emissions, improving regional air quality, and renewable resource integration," *Progress in Energy and Combustion science*, vol. 64, pp. 62–92, 2018.

[9] T. R. Matsumoto, S. I. Nabeta, I. E. Chabu, S. Nagao, N. R. Santos, and A. Dominice, "Induction voltage regulator performance in primary distribution networks with a high degree of distributed generation," *IEEE Transactions on Power Delivery*, vol. 36, no. 3, pp. 1837–1846, 2020.

[10] J. Jackson, "Improving energy efficiency and smart grid program analysis with agent-based end-use forecasting models," *Energy Policy*, vol. 38, no. 7, pp. 3771–3780, 2010.

[11] A. S. Isa, Y. A. Dodo, H. Ojobo, and I. A. Alkali, "Deployment of smart technologies for improving energy efficiency in office buildings in Nigeria," *Journal of Multidisciplinary Engineering Science and Technology*, vol. 3, no. 1, 2016.

[12] A. Chel and G. Kaushik, "Renewable energy technologies for sustainable development of energy efficient building," *Alexandria Engineering Journal*, vol. 57, no. 2, pp. 655–669, 2018.

[13] A. Kalair, N. Abas, M. S. Saleem, A. R. Kalair, and N. Khan, "Role of energy storage systems in energy transition from fossil fuels to renewables," *Energy Storage*, vol. 3, no. 1, p. e135, 2021.

[14] N. Gaurav, S. Sivasankari, G. Kiran, A. Ninawe, and J. Selvin, "Utilization of bioresources for sustainable biofuels: a review," *Renewable and Sustainable Energy Reviews*, vol. 73, pp. 205–214, 2017.

[15] M. N. Dudin, E. E. Frolova, O. V. Protopopova, O. Mamedov, and S. V. Odintsov, "Study of innovative technologies in the energy industry: nontraditional and renewable energy sources," *Entrepreneurship and Sustainability Issues*, vol. 6, no. 4, p. 1704, 2019.

[16] M. Saunila, M. Nasiri, J. Ukko, and T. Rantala, "Smart technologies and corporate sustainability: the mediation effect of

corporate sustainability strategy," *Computers in Industry*, vol. 108, pp. 178–185, 2019.

[17] G. Dileep, "A survey on smart grid technologies and applications," *Renewable Energy*, vol. 146, pp. 2589–2625, 2020.

[18] X. Du, Y. Qi, B. Chen, B. Shan, and X. Liu, "The integration of blockchain technology and smart grid: framework and application," *Mathematical Problems in Engineering*, vol. 2021, Article ID 9956385, 12 pages, 2021.

[19] G. L. P. Raj and V. Kirubakaran, "Energy efficiency enhancement and climate change mitigations of SMEs through grid-interactive solar photovoltaic system," *International Journal of Photoenergy*, 2021.

[20] C. Ocampo-Martinez, "Energy efficiency in discrete-manufacturing systems: insights, trends, and control strategies," *Journal of Manufacturing Systems*, vol. 52, pp. 131–145, 2019.

[21] M. J. Khan and Pushparaj, "A novel artificial intelligence based hybrid maximum power point tracking technique for solar photovoltaic system," *Journal of Electrical Engineering & Technology*, vol. 16, pp. 1879–1889, 2021.

[22] S. Nižetić, N. Djilali, A. Papadopoulos, and J. J. Rodrigues, "Smart technologies for promotion of energy efficiency, utilization of sustainable resources and waste management," *Journal of Cleaner Production*, vol. 231, pp. 565–591, 2019.

[23] M. A. Ahad, S. Paiva, G. Tripathi, and N. Feroz, "Enabling technologies and sustainable smart cities," *Sustainable Cities and Society*, vol. 61, p. 102301, 2020.

[24] R. Sharma and H. Kamth, "Reliability analysis for smart grid challenges in India," in *2018 International Conference on Circuits and Systems in Digital Enterprise Technology (ICCSDET)*, pp. 1–3, 2018.

[25] E. Iacovidou, P. Purnell, and M. K. Lim, "The use of smart technologies in enabling construction components reuse: a viable method or a problem creating solution?," *Journal of Environmental Management*, vol. 216, pp. 214–223, 2018.

[26] B. K. Bose, "Power semiconductor devices for smart grid and renewable energy systems," *Power Electronics in Renewable Energy Systems and Smart Grid: Technology and Applications, IEEE*, pp. 85–152, 2019.

Hindawi
International Journal of Photoenergy
Volume 2022, Article ID 7276670, 9 pages
https://doi.org/10.1155/2022/7276670

Research Article

Effect of 3-Nitroacetophenone on Corrosion Inhibition of Mild Steel in Acidic Medium

Sani Ibrahim,[1,2] R. Sanmugapriya,[1] J. Arockia Selvi,[1] T. Pushpa Malini,[1] P. Kamaraj,[3] P. A. Vivekanand,[4] Govindasami Periyasami,[5] Ali Aldalbahi,[6] Karthikeyan Perumal,[5] J. Madhavan,[7] and Santosh Khanal[8]

[1]*Department of Chemistry, SRM Institute of Science & Technology, Kattankulathur, 603203 Tamil Nadu, India*
[2]*Zamfara State College of Education Maru, P.M.B 1002 Maru, Zamfara, Nigeria*
[3]*Department of Chemistry, Bharath Institute of Higher Education and Research, Chennai 600073, India*
[4]*Department of Chemistry, Saveetha Engineering College, Thandalam, Chennai 602105, India*
[5]*Department of Chemistry, College of Science, King Saud University, P.O. Box 2455, Riyadh 11451, Saudi Arabia*
[6]*Department of Chemistry and Biochemistry, The Ohio State University, 151 W. Woodruff Ave, Columbus, OH 43210, USA*
[7]*Department of Chemistry, Thiruvalluvar University, 632115, Vellore, India*
[8]*Central Department of Chemistry, Tribhuvan University, Kirtipur Kathmandu, Nepal*

Correspondence should be addressed to J. Arockia Selvi; arockiaselvi29@yahoo.co.in
and Santosh Khanal; santoshkhanal2003@yahoo.com

Received 27 November 2021; Revised 12 January 2022; Accepted 17 January 2022; Published 16 February 2022

Academic Editor: Bharath Govindan

Copyright © 2022 Sani Ibrahim et al. This is an open access article distributed under the Creative Commons Attribution License, which permits unrestricted use, distribution, and reproduction in any medium, provided the original work is properly cited.

Acetophenone derivatives are eco-friendly corrosion inhibitors to prevent corrosion of mild steel (MS) in acidic medium. In this work, the inhibition effect of 3-nitroacetophenone (3-NA) on the corrosion of MS in acidic medium (1 N HCl) was investigated using weight loss measurements, electrochemical measurements, scanning electron microscopy, energy-dispersive X-ray spectroscopy, and quantum chemistry analysis. The studies were performed using different concentrations of inhibitors and at different temperatures. The results indicated that the inhibition efficiency of 3-NA increases with an increase in inhibitor concentration and reaches to a maximum of 64% at inhibitor concentration of 250 ppm at 30°C. The potentiodynamic polarization measurement indicated that 3-NA acts as mixed category of interdict. The adsorption of 3-NA on MS surface followed the Langmuir adsorption isotherm. The mode of adsorption of 3-NA on MS surface was further studied by quantum chemical calculations based on density functional theory (DFT). The results plainly revealed that 3-NA performs fairly as corrosion interdict for MS in acidic medium.

1. Introduction

Mild steel (MS) is widely used in infrastructural construction and has gained popularity due to its mechanical properties, malleability, toughness, availability, and low cost. It is substantially applied in different industries for different purposes which comprise production of pipelines, metal tanks, gas cylinders, and heat exchangers. MS plays a significant role in human civilization and sustainable development, so undesirable degradation due to corrosion is a big issue. Corrosion of MS considerably affects the industrial and natural environments, and development of suitable methods for corrosion control is necessary. The use of organic and inorganic inhibitors is the finest approach to shield mild steel from corrosion, specifically in acidic conditions. Inhibitors are chemical substances that can successfully impede the metal corrosion in a corrosive environment, and several organic and inorganic compounds with electron-donating substituents are used as an effective corrosion inhibitor in various industries [1].

Acetophenone is used in industry as a solvent for plastics and resins, as a catalyst for polymerization of olefins and as a photosensitizer in organic synthesis. Acetophenone is also used as an anesthetic agent to induce analgesia and also as a hypnotic agent [2]. Acetophenone compounds are a

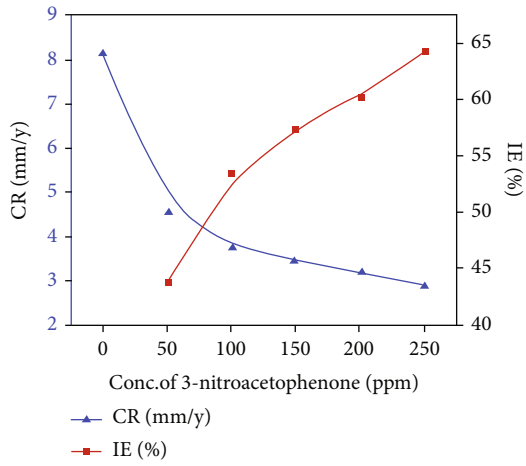

Figure 1: Corrosion rates and inhibition efficiencies of 3-NA from weight loss measurements.

successful class of compounds for bioreduction using CRED enzymes [3]. Also, acetophenones and their derivatives are known to act as corrosion inhibitors in aggressive media [4–7].

Acetophenone derivative was chosen for this study due to electron density and electron withdrawing and donating nature of the substituent group. To control corrosion of the metal, its surface needs to be masked significantly with an organic or an inorganic interdict material to be segregated from corrosive territory or domain [8–10]. Application of molecules as an interdict species is the finest and most reliable practical technique to shield the metal from dissipation in an acidic medium [11–13]. It was reported that 4-aminoacetophenonepyridine 2-aldehyde (4AAPA) inhibits the corrosion of the mild steel in 1 N HCl and maximum inhibition of 91% was achieved at a concentration of 60 ppm [14].

In this study, the inhibition effect of 3-nitroacetophenone (3-NA), as an organic inhibitor on MS in 1 N HCl, was studied via weight loss measurement, open circuit potentials, potentiodynamic polarization studies, and electrochemical impedance spectroscopy (EIS). The hydrophobicity of the MS specimen was determined through contact angle measurement, and molecular parameters were studied by quantum chemical calculations based on density functional theory (DFT). Surface morphologies and elemental composition of MS were investigated by scanning electron microscopy (SEM) and energy-dispersive X-ray spectroscopy (EDX), respectively.

2. Experimental

2.1. Materials. MS sample specimen was purchased from the local market in Chennai. The composition of the MS was carbon (0.160%), manganese (0.845%), sulphur (0.007%), silicon (0.050%), phosphorus (0.024%), and iron (98.7%). 3-NA and hydrochloric acid were supplied by Sigma-Aldrich. Different concentrations of 3-NA (50 ppm, 100 ppm, 150 ppm, 200 ppm, and 250 ppm) were prepared in deionized water, and 1 N HCl solution was used as corroding electrolyte.

2.2. Surface Preparation of MS Specimen. The MS ($1 \times 1\ cm^2$) specimens were abraded successfully with an emery sheet of different grades (600-1200 grade) until the surface was mirror polished, degreased with trichloroethylene, dried, and placed in a desiccator. Finally, the smooth and clean specimen was immersed in the solution.

2.3. Weight Loss Measurements. The inhibition efficiency of 3-NA was investigated by weight loss measurement. The weight of abraded MS sample was recorded with four-digit analytical balance before and after immersion in 100 mL of 1 N HCl and 1 N HCl+different concentrations of 3-NA for 1 h. The effect of temperature on corrosion inhibition was studied using 250 ppm 3-NA at 303 K, 313 K, 323 K, and 333 K, respectively. MS samples were washed with water, rinsed with acetone, dried in air, and weighed after each measurement. Corrosion rate (CR), surface coverage (θ), and inhibition efficiency (IE %) were calculated using the following formula. The experiments were performed in triplicate, and average values are reported.

$$\mathrm{CR} = \frac{87.6\,W}{A \cdot d \cdot t}, \tag{1}$$

where W, A, d, and t represent weight loss in mg, surface area in cm^2, and density in $g\,cm^{-3}$ of MS sample, and time of immersion in hour, respectively. The geometric surface coverage (θ) is given by

$$\theta = \frac{W_1 - W_2}{W_1}, \tag{2}$$

where W_1 and W_2 are weight loss of the MS sample in 1 N HCl and 1 N HCl+3-NA, respectively. Finally, inhibition efficiency is calculated as

$$\mathrm{IE}\,(\%) = \frac{W_1 - W_2}{W_1} \times 100. \tag{3}$$

2.4. Electrochemical Measurements. The electrochemical measurements were carried out in Ivium Vertex potentiostat/galvanostat/ZRA with Ivium soft electrochemistry software, using an electrochemical cell assembled with three electrode cells. All measurements were performed with 300 mL of solution using a three-electrode system. A polished MS sample with surface area 1 cm^2 was employed as working electrode, the saturated calomel electrode (SCE) as reference electrode, and platinum electrode as counter electrode. The MS samples were immersed in the test solution for 15 min to attain a stable open circuit potential (OCP) before each polarization measurement. Potentiodynamic polarization (PDP) was recorded from −250 mV to +250 mV vs. OCP with a scan rate of 1 mV s^{-1}. The cathodic and anodic slopes were determined from corresponding polarization curves. The corrosion potential (E_{corr}) and corrosion current (i_{corr}) were determined from Tafel extrapolation method, and corrosion inhibition efficiency (IE) was calculated by using the formula

$$\mathrm{IE}\,(\%) = \frac{i^{\circ}_{corr} - i_{corr}}{i^{\circ}_{corr}} \times 100, \tag{4}$$

Table 1: Corrosion rate (mm/y) and inhibition efficiency obtained from weight loss measurements for MS specimen in the absence and presence of 0-250 ppm concentrations of 3-NA inhibitor in acidic medium (1 N HCl).

Conc. (ppm)	Blank (1 N HCl)	50	100	150	200	250
Weight loss (g)	0.0073	0.0041	0.0034	0.0031	0.0029	0.0026
Corrosion rate (mm/y)	8.1259	4.5695	3.7893	3.455	3.2321	2.8977
Surface coverage (θ)	—	0.4384	0.5342	0.5753	0.6027	0.6438
Inhibition efficiency (%)	—	43.84	53.42	57.53	60.27	64.38

where i°_{corr} and i_{corr} are the corrosion current densities in the absence and presence of inhibitors, respectively.

The electrochemical impendence measurements were carried out using an AC signal of 10 mV amplitude in a frequency range 100 kHz to 0.01 Hz. The value of charge transfer resistance (R_t) was obtained from the diameter of Nyquist plots, and IE was calculated using the following relation:

$$\text{IE}\,(\%) = \frac{R_t - R^{\circ}_t}{R_t} \times 100, \tag{5}$$

where R°_t and R_t are the charge transfer resistance for MS sample in the absence and presence of inhibitors, respectively.

2.5. SEM-EDX Analysis. MS specimens were exposed to 1 N HCl in the absence and presence of 3-NA inhibitor for 1 h. The MS samples were eroded, degreased with trichloroethylene, and dried, and surface morphology and elemental composition were carried out by a scanning electron microscope (SEM) coupled with an energy-dispersive X-ray spectrometer (SNE 3200M, SEC).

2.6. Contact Angle Measurements. The water contact angles (WCA) of the MS surface were measured by contact angle meter KYOWA DMs-40, following sessile drop method using half-angle fitting method and FAMAS (interFAce Measurement and Analysis System) software. The volume of water droplet of 2 μL was placed on MS surfaces. The measurements were repeated 10 times.

2.7. Computational Studies. Corrosion inhibition efficiency (%) is more correlated with the molecular structure of the inhibitors. Thus, the molecular structure of 3-nitroacetophenone was optimized by the density functional theory (DFT) with B3LYP correlation functional [15, 16] and the 6-31 G (d, p) basis set. Quantum chemical calculations were carried out using Gaussian 16 software [17]. The ionization potential (I) and electron affinity (A) are defined by $I = -E_{HOMO}$ and $A = -E_{LUMO}$, respectively. The electronegativity $\chi = I + A/2$ and global hardness $\gamma = I - A/2$ are calculated. Then, the ΔN value can be calculated according to [18]

$$\Delta N = \frac{\chi_{Fe} - \chi_{inh}}{2(\gamma_{Fe} + \gamma_{inh})}, \tag{6}$$

where $\chi_{Fe} = 7.0$ eV and $\gamma_{Fe} \approx 0$ for iron are quoted from literature.

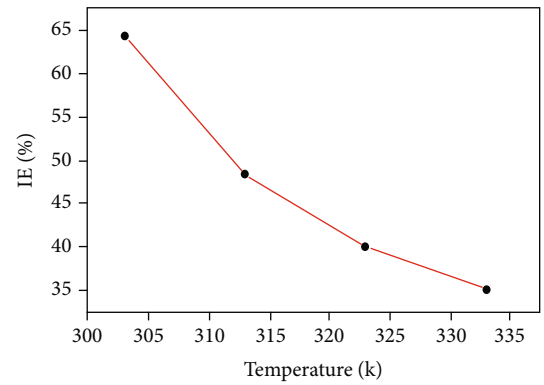

Figure 2: Inhibition efficiency of 250 ppm of 3-NA in 1 N HCl for MS in temperature ranging from 303 to 323 K.

3. Results and Discussion

3.1. Weight Loss Measurements. The abraded MS specimens were immersed in the solution (1 N HCl with various concentrations of the inhibitor) for 1 hour, and corrosion rate (CR) and inhibition efficiency (IE) were calculated and the results are shown in Figure 1 and Table 1. It is evident that the corrosion rate decreases with an increase in the concentration of the 3-NA and the inhibition efficiency increases with an increase in the concentration of the inhibitors which indicated that there is a substantial surface coverage by the interdict and strong bonding to surface of the mild steel.

3.1.1. Effect of Temperature. It is well known that the rate of chemical reaction increases with the increase of temperature, and then, desorption of 3-NA on MS surface occurs on increasing temperature [14]. It is also revealed that the propensity of an organic corrosion inhibitor to shield MS is via the formation of an adherent common monomolecular layer of the metal surface [14]. The effect of temperature on corrosion rate and inhibition efficiency is shown in Figure 2, and data are tabulated in Table 2. The results suggested that the inhibition efficiency of 3-NA gradually decreased on increasing temperature from 303 K to 333 K in an inhibitor concentration of 250 ppm. This is due to desorption of 3-NA from the MS surface.

3.2. Electrochemical Impedance Spectroscopy (EIS). The electrochemical impedance spectroscopy technique was used to find the inhibition efficiency of acetophenone derivatives

Table 2: Corrosion rate and inhibition efficiency obtained from weight loss measurements for MS specimen at different temperatures in the absence and presence of 250 ppm concentration of 3-NA inhibitor in an acidic medium (1 N HCl).

Temperature (K)		303	313	323	333
Blank (1 N HCl)	CR (mm/y)	8.1259	14.1542	16.1695	22.1221
3-Nitroacetophenone (250 ppm)	CR (mm/y)	4.5694	5.4610	7.0214	8.2473
Inhibition efficiency (%)	IE (%)	64.34	48.42	40.00	35.08

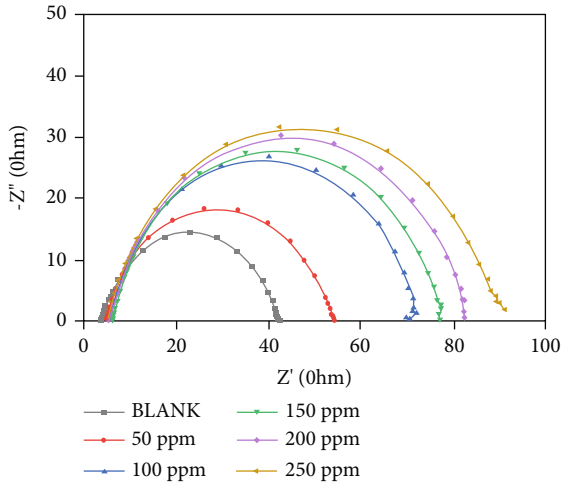

Figure 3: Nyquist plot for MS obtained with the absence and presence of 50-250 ppm of 3-NA in 1 N HCl.

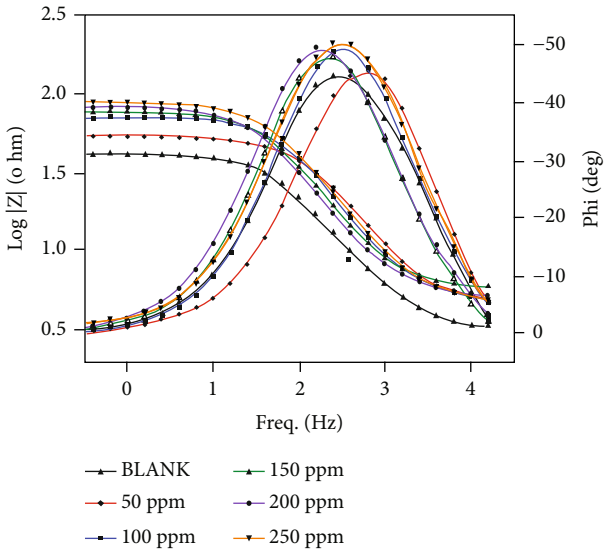

Figure 4: Bode plot for MS obtained with the absence and presence of 50-250 ppm of 3-nitroacetophenone in 1 N HCl.

and was accomplished in the frequency span of 100 kHz to 0.01 Hz. Nyquist plots and Bode plots for the MS in the absence and presence of 3-NA inhibitor at 50-250 ppm concentration in 1 N HCl are shown in Figures 3 and 4, respectively. Table 3 shows the impedance parameters comprise of charge transfer resistance (R_{ct}), double layer capacitance (C_{dl}

Table 3: The EIS parameter for MS in 1 N HCl in the presence and absence of 3-NA.

Conc. of inhibitor (ppm)	R_{ct} (ohm·cm^2)	C_{dl} (F cm^{-2})	IE (%)
Blank 1 N HCl	38.45	2.6129×10^{-5}	—
50 ppm	49.08	2.0468×10^{-5}	21.7
100 ppm	64.64	1.5542×10^{-5}	40.5
150 ppm	71.99	1.3955×10^{-5}	46.58
200 ppm	77.58	1.2950×10^{-5}	50.43
250 ppm	86.13	1.1664×10^{-5}	55.36

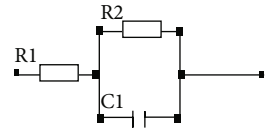

3-Nitroacetophenone in 1 N HCl

Figure 5: Equivalent circuit for EIS spectra of the studied system.

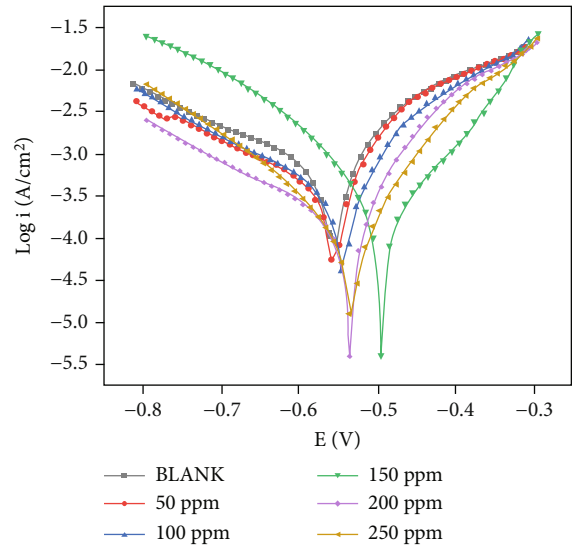

Figure 6: Tafel plot for MS obtained with the absence and presence of 50-250 ppm of 3-NA 1 N HCl.

), and inhibition efficiency, respectively. The increase in charge transfer resistance (R_{ct}) from 38.45 ohm·cm^2 (blank) to 86.13 ohm·cm^2 (250 ppm) revealed the formation of a

Table 4: The polarization parameters for mild steel in 1 N HCl in the presence and absence of 250 ppm of 3-nitroacetophenone.

Conc. of inhibitor (ppm)	E_{corr} (V vs. SCE)	i_{corr} (A/cm^2)	R_p (ohm)	β_a (V dec^{-1})	β_c (V dec^{-1})	CR (mm/y)	IE (%)
Blank	-0.571	14.02×10^{-4}	35.7	0.214	0.262	16.49	—
50	-0.573	11.63×10^{-4}	43.0	0.211	0.223	13.68	17.04
100	-0.560	9.59×10^{-4}	52.1	0.161	0.214	11.28	31.60
150	-0.498	5.71×10^{-4}	87.6	0.085	0.158	6.71	59.27
200	-0.556	5.04×10^{-4}	99.2	0.130	0.216	5.926	64.05
250	-0.545	3.81×10^{-4}	131.3	0.100	0.148	4.478	72.82

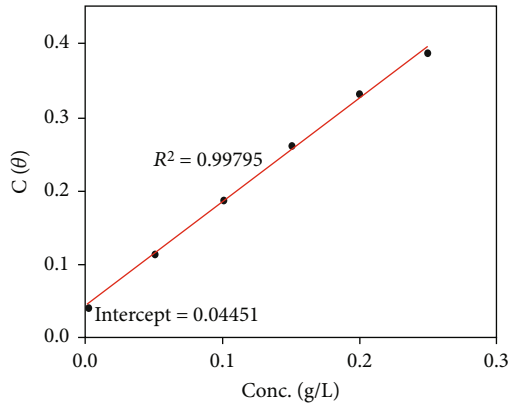

Figure 7: Linearized Langmuir adsorption isotherm plots of mild steel in 1 N HCl.

defensive film of 3-NA on the surface of MS by adsorption. The maximum inhibition efficiency reaches 58.5% in 3-NA concentration of 25 ppm. The adsorption of 3-NA inhibitor on the metal surface leads to the formation of double layer, which could form a barrier between the metal surface and the corrosive medium. This is further confirmed by the decrease in the double layer capacitance (C_{dl}) from 2.6129 $\times 10^{-5}$ F cm^{-2} (blank) to 1.1664×10^{-5} F cm^{-2} (250 ppm of 3-NA). The impedance increases with an increase in the concentration of 3-NA. Nyquist and Bode plots confirmed the single charge transfer process in corrosion inhibition mechanism. The EIS spectra obtained for mild steel were best fitted with the equivalent circuit as shown in Figure 5, where $R1$ is the solution resistance, $R2$ is the polarization resistance, and $C1$ is the double layer capacitance. The R (CR) model is used for the protective isolated layer formed at the metal surface and that provides a protective performance by 3-NA.

3.2.1. Potentiodynamic Polarization Study. The potentiodynamic polarization measurements were studied to investigate the effect of 3-NA on the anodic and cathodic reactions on corrosion phenomenon. The saturated calomel electrode (SCE) was used as reference electrode, mild steel with a surface area of 1 cm^2 was used as working electrode, platinum electrode was used as counter electrode, and 3-nitroacetophenone inhibitor in 1 N HCl was used as electrolyte mixture. The polarization curves for MS in 1 N HCl solution containing different concentrations (50-250 ppm) of 3-NA are shown in Figure 6. The different parameters obtained from polarization measurements such as corrosion potentials (E_{corr}) as well as kinetic values like corrosion current density (i_{corr}), cathodic and anodic Tafel slopes (β_c and β_a), and polarization resistance (R_p) are presented in Table 4. There are little changes in parameters for β_a and β_c upon addition of the inhibitors as compared to blank value which indicates that the inhibitor gets adsorbed on mild steel surface controlling both anodic and cathodic reactions. The inhibitor 3-NA is a mixed type of inhibitor as the difference in corrosion potential, E_{corr}, between inhibitor and that of blank is less than 80 mV. The decrease in corrosion current, i_{corr}, from 14.02×10^{-4} (blank) to 3.81×10^{-4} (250 ppm of 3-NA) is observed and exhibits 72.82% IE.

3.3. Adsorption Isotherms. The adsorption isotherms are numerical utterances which give clear information on the mutual effect of the surface of the metal and adsorbing species at a constant temperature. Though there are many adsorption isotherms that give the correlation between metal surface coverage and concentration of the adsorbed species [19], the prominent adsorption isotherm is Langmuir adsorption isotherm and can be expressed via the following [19, 20]:

$$\frac{C}{\theta} = \frac{1}{K_{ads}} + C, \tag{7}$$

where C is the concentration of the inhibitor, θ is the standard degree of the surface coverage on the MS (from electrochemical impedance and polarization studies), and K_{ads} is the equilibrium constant for the adsorption. The plot of C/θ vs. C, shown in Figure 7, gives a straight line with a high correlation coefficient of the nearest unity and an intercept of 0.04451, suggesting the Langmuir adsorption isotherm for adsorption of 3-NA on the MS surface. It should be noted that the adsorbed 3-NA lined up on the surface of MS to give a monolayer. K_{ads} of the inhibitor was calculated using an intercept of the C/θ vs. C plots and was used to calculate the free energy of adsorption (ΔG^0_{ads}) via the following:

$$\Delta G^0_{ads} = -RT \ln (55.5 K_{ads}), \tag{8}$$

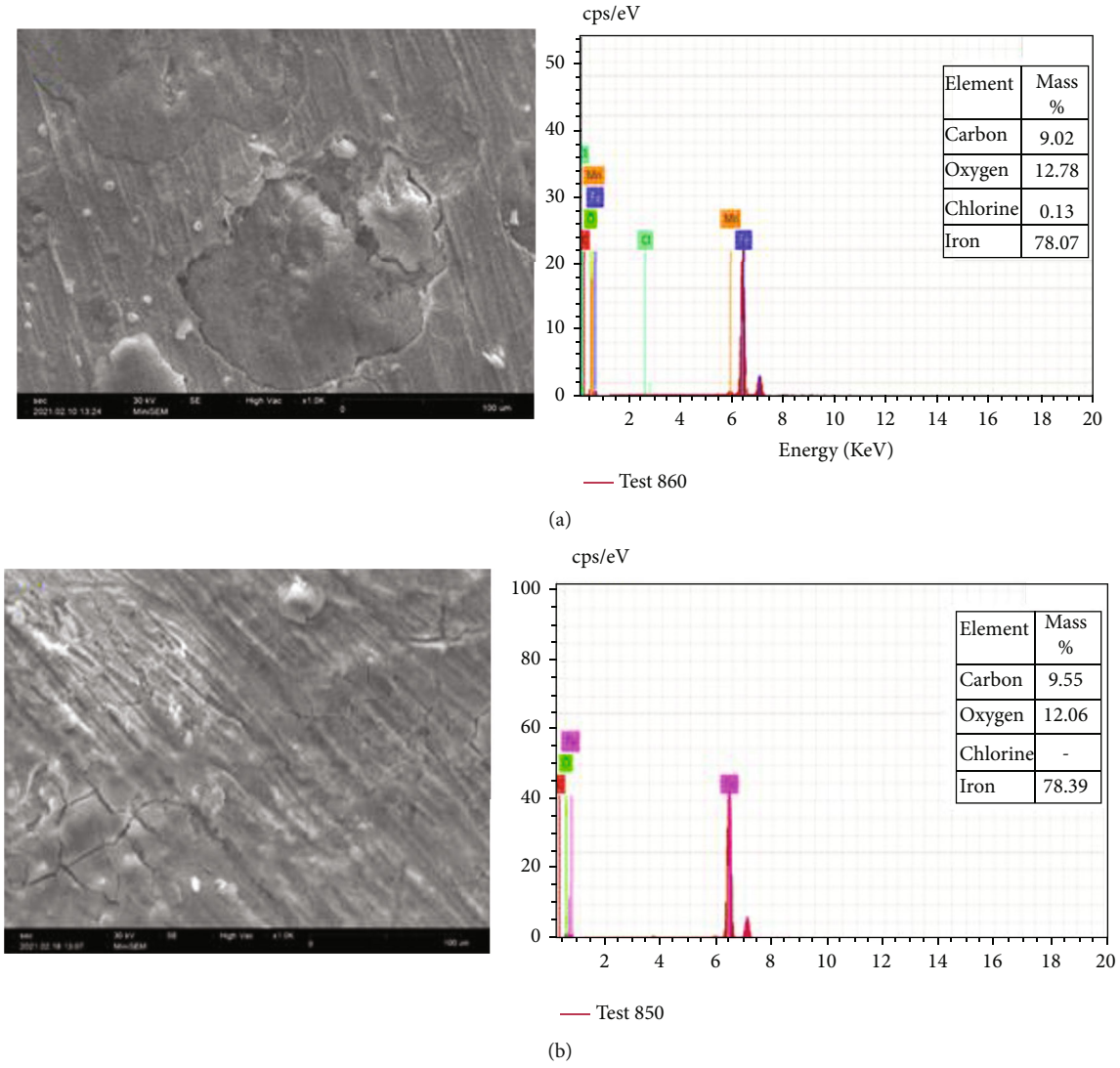

Figure 8: SEM-EDX micrographs of the mild steel surface: (a) in 1 N HCl solution and (b) in 1 N HCl solution with 250 ppm of 3-NA.

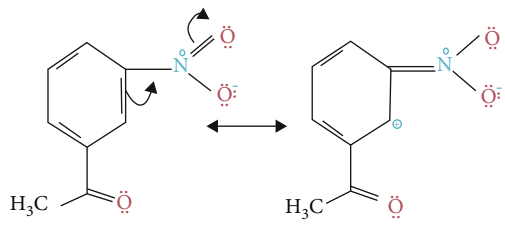

Figure 9: Resonance structures of 3-nitroacetophenone.

where R was the gas constant (8.3142 J $K^{-1}Mol^{-1}$), T is the absolute temperature (K), and 55.5 was the molar concentration of water. The adsorption parameters K_{ads} and free energy of adsorption (ΔG^0_{ads}) are 22.47 Lg^{-1} and -17.96 kJ mol^{-1}, respectively. The negative value of the standard free energy of adsorption indicates that the adsorption of 3-NA molecule on the MS surface is spontaneous. The values of ΔG^0_{ads} obtained (-17.96 kJ mol^{-1}) are less than 20 kJ mol^{-1} which reveals the physical adsorption of 3-NA due to electrostatic communication between charged particles and charged metal.

3.4. SEM-EDX Analysis. The surface morphology of the MS specimen was evaluated by a scanning electron microscope, which gives the nature of the film formed on the MS surface. It is suggested that surface roughness is increased on attacking metal surface by aggressive media [21, 22]. SEM images are shown in Figure 8. It is observed that the MS surface is uniform before the immersion in 1 N HCl and the surface is damaged after immersion in acid solution (Figure 8(a)). However, in the presence of 3-NA at a concentration of 250 ppm, the surface of MS is smooth and less damaged (Figure 8(b)), which suggests that the surface of the MS is shielded and protected by 3-NA and a good corrosion inhibition efficiency is increased. The absence of chlorine in EDX of the inhibited metal surface suggests the formation of a protective layer by the inhibitor, which prevents the

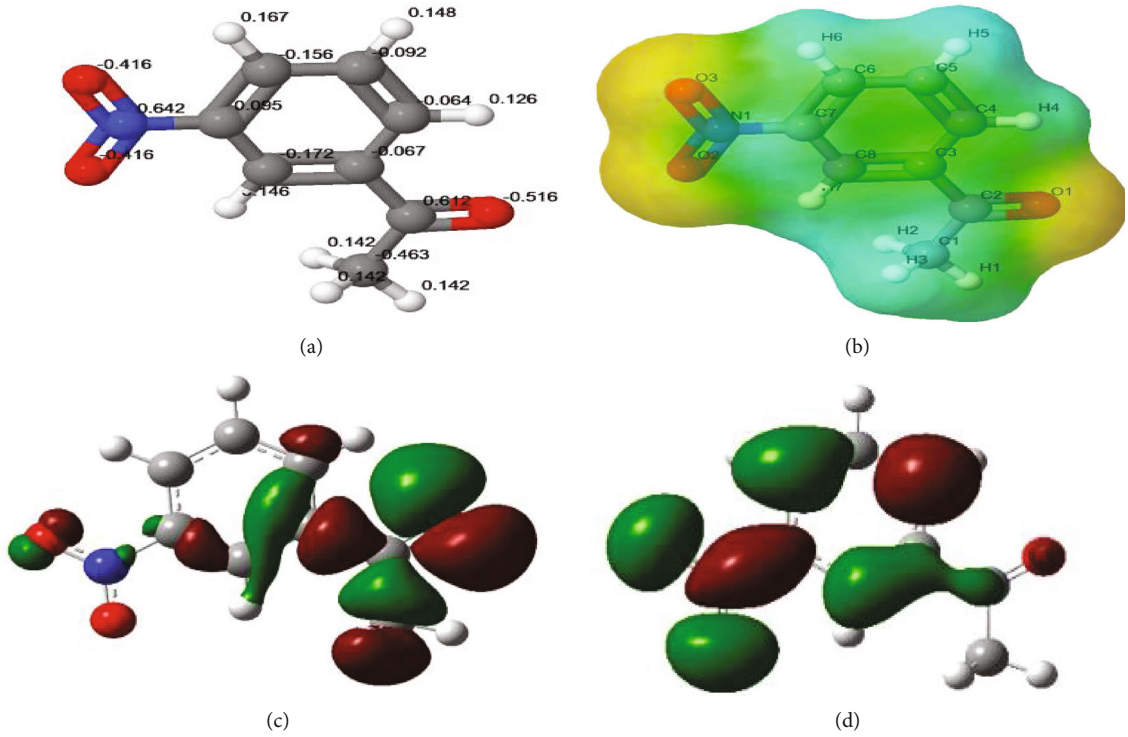

Figure 10: (a) Optimized structure, (b) electrostatic potential, (c) HOMO, and (d) LUMO of 3-nitroacetophenone.

attack of Cl^- towards the metal surface. However, the surface of the metal is not fully covered by the inhibitor, as is evident from the higher mass % of Fe as shown in the table.

3.5. Computational Studies. The resonance structure of 3-NA is shown in Figure 9, and the optimized molecular structure, electronic structure, and molecular orbital energy of 3-NA are shown in Figure 10. The quantum chemical parameters, such as the energy of the highest occupied molecular orbital (E_{HOMO}, -6.2767 eV), energy of the lowest unoccupied molecular orbital (E_{LUMO}, -3.8771 eV), energy gap ($E_{LUMO} - E_{HOMO}$, 2.3996 eV), dipole moment (1.6871 D), and ionization potential (6.2765 eV) and electron affinity (3.8771 eV), are obtained for 3-NA. The higher values of E_{HOMO} denote the electron-donating abilities of the molecule. Also, the molecule with lower energy gap value in the range of 6.40 to 3.38 eV shows higher inhibition efficiency [23–26]. However, the energy gap calculated in 3-NA is 2.3996 eV, which is not in the range required for better IE %. The measure of electron transfer from inhibitor molecule to metal is favored, if $\Delta N > 0$ [27]. Thereby, the calculated value of $\Delta N = 0.8014$ for 3-NA reveals the electron-donating ability of the inhibitor at the metal surface. The Mulliken charges on the atoms are used to analyze the adsorption center of the inhibitor; it is observed that if the atom has more negative charge, then the adsorption is more on the surface. The optimized structure of 3-NA with charges is shown in Figure 9(a). It is inferred that adsorption of inhibitor on the metal surface is through O atom rather than N atom, as greater negative charge is observed on O atoms. π-electrons also interact with the vacant d-orbital of metal. However, the presence of electron-withdrawing nitro group attracts the π-electrons of the aromatic ring. Thereby, this leads to a decrease in the electron density of the aromatic ring and thus shows lower inhibition efficiency of 3-NA. The inhibition efficiency of 3-NA is compared with corrosion inhibition performance of other inhibitors as given in Table 5. The DFT study revealed that the nitration of corrosion inhibitor molecules led to the decrease in inhibition efficiency as the $-NO_2$ group is a strong electron acceptor [28].

3.6. Contact Angle Measurement. The sessile drop contact angle measurements are shown in Figure 11 for (a) polished metal surface, (b) surface of mild steel immersed in 1 N HCl, and (c) an inhibited metal surface with 250 ppm of 3-NA in 1 N HCl. The water wetting nature of the metal surfaces was carried out on all the three metal surfaces. Generally, if WCA is smaller than 90°, the metal surface is hydrophilic, and if WCA is greater than 90°, then the metal surface is hydrophobic [31, 32]. The WCA for polished metal sample is observed at 102°, and since WCA is greater than 90°, it is hydrophobic. Furthermore, WCA of the metal surface immersed in 1 N HCl is found at 41.2°. This confirms the wettability of the uninhibited metal surface and its hydrophilic nature. However, for inhibited metal surface using 250 ppm of 3-NA, WCA is seen at 64.2° and a slight increase in WCA relatively shows the protective layer formed on the metal surface by the inhibitor. The decrease in wettability and increase in hydrophobicity confirm the protective nature of the mild steel surface from wetting.

Table 5: Comparison of nitro compounds on inhibition efficiencies of steel in acid medium.

S.N.	Inhibitor	Medium	Performance	Reference
1.	4-Nitrobenzofuroxan	1M HCl	200 ppm/55% IE at 30°C for carbon steel	[29]
2.	4-Nitro-2-mercaptobenzimidazole	Acidic medium	Quantum mechanical assignment, 80.52%	[28]
3.	4-Nitro-2-methylbenzimidazole	Acidic medium	Quantum mechanical assignment, 66.80%	[28]
4.	4-Nitrobenzimidazole	Acidic medium	Quantum mechanical assignment, 64.01%	[28]
5.	2-Nitroacridone	1M HCl	5 mM/94.96% at 25°C for low carbon steel	[30]
6.	3-Nitroacetophenone	1N HCl	250 ppm/64.34% at 30°C for mild steel	This study

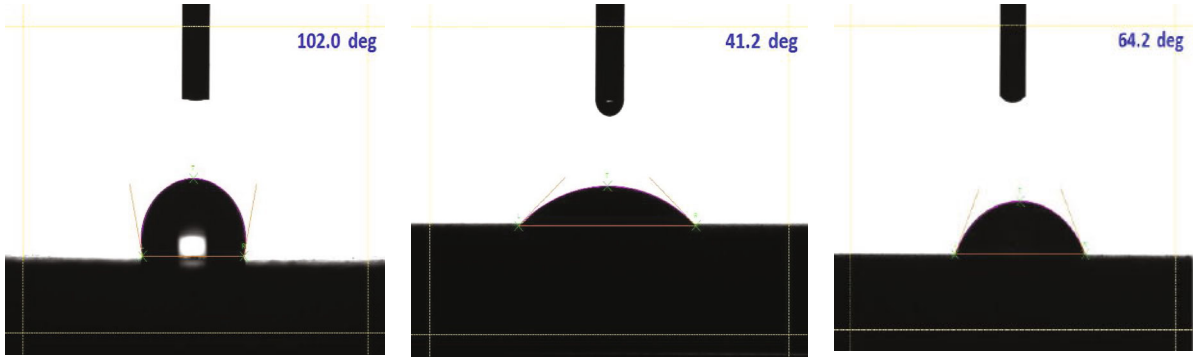

(a) (b) (c)

Figure 11: Sessile drop method: contact angle of (a) polished mild steel, (b) mild steel immersed in 1 N HCl, and (c) mild steel immersed in 250 ppm of 3-nitroacetophenone.

4. Conclusions

In this study, the inhibition effect of 3-nitroacetophenone (3-NA) on the corrosion of MS in an acidic medium (1 N HCl) was investigated using weight loss measurements, electrochemical measurements, and computational studies using density function theory. The results showed that 3-NA acts as mild corrosion inhibitors for MS in 1 N HCl solution. The inhibition efficiency (IE) increases with the increase in concentration of 3-NA, giving maximum inhibition efficiency in 250 ppm of 3-NA. The adsorption of 3-NA on the MS surface follows Langmuir adsorption isotherm; the value of ΔG^0 (-17.96 kJ mol^{-1}) indicates spontaneous adsorption of 3-NA by physical interaction. Polarization studies suggest that 3-NA acts as an assorted type of inhibitors. EIS studies reveal the single charge transfer process in corrosion inhibition mechanism. SEM and EDX analysis conform the formation of a protective film of 3-NA on the MS surface that inhibits the corrosion. Computational studies suggest remarkable inhibition efficiency of 3-NA and adsorption of inhibitor on the MS surface is through oxygen atom rather than nitrogen atom. However, the presence of an electron-withdrawing nitro group in 3-NA attracts the π-electrons of the aromatic group leading to a decrease in electron density and thereby shows lower inhibition efficiency.

Data Availability

The data used to support the findings of this study are available upon request.

Conflicts of Interest

All authors declared that they have no conflicts of interest.

Acknowledgments

The authors are immensely thankful and acknowledge the Nanotechnology Research Centre (NRC), SRMIST, for providing the research facilities, SEM. We thank Dr. K.K. Ramanatha Datta, SRM IST, Functional Nanomaterials Laboratory, for contact angle measurements. They also acknowledge Dr. Renjith S. Pillai, SRM IST, for the computational studies. The authors acknowledge King Saud University, Riyadh, Saudi Arabia, for funding this work through Researchers Supporting Project number RSP-2021/30.

Supplementary Materials

Supplementary 1: the graphical abstract summarizes the entire manuscript. *(Supplementary Materials)*

References

[1] I. G. Mamedov, I. M. Shikhaliyeva, Y. V. Mamedova, S. Z. Gasimova, and A. M. Maharramov, "Some acetophenone derivatives as corrosion inhibitors," *Chemical Problems*, vol. 17, no. 2, pp. 302–309, 2019.

[2] N. V. Soucy, "Acetophenone," in *Encyclopedia of Toxicology [Third Edition]*, P. Wexler, Ed., pp. 43–45, 2014.

[3] Thomas S. Moody and J. David Rozzell, "Modern biocatalytic ketone reduction„" in *Organic Synthesis Using Biocatalysis*

[First Edition], A. Goswami and J. Stewart, Eds., pp. 149–185, Elsevier, 2016.

[4] M. Bouklah, B. Hammouti, A. Aouniti, M. Benkaddour, and A. Bouyanzer, "Synergistic effect of iodide ions on the corrosion inhibition of steel in 0.5M H2SO4 by new chalcone derivatives," *Applied Surface Science*, vol. 252, no. 18, pp. 6236–6242, 2006.

[5] J. Y. Hu, X. O. Song, Z. Zhang, D. Z. Zeng, T. H. Shi, and I. F. Gao, "The corrosion inhibition behaviors of 2′-hydroxy-acetophenone for AZ91D magnesium alloy," *Materials and Corrosion*, vol. 66, no. 4, pp. 396–404, 2015.

[6] A. S. Fouda, K. Shalabi, G. Y. Elewady, and H. F. Merayyed, "Chalcone derivatives as corrosion inhibitors for carbon steel in 1 M HCl solutions," *International Journal of Electrochemical Science*, vol. 9, pp. 7038–7058, 2014.

[7] Y. Zhu, L. Zhao, P. Liu, P. Chen, and W. Tao, "Corrosion and inhibition of P110 steel in 20% HCl solution by Mannich base inhibitor," *International Journal of Electrochemical Science*, vol. 14, pp. 1331–1341, 2019.

[8] P. Singh, M. A. Quraishi, E. E. Ebenso, and C. B. Verma, "Ultrasound assisted synthesis of chalcones as green corrosion inhibitors for mild steel in 1M hydrochloric solution," *International Journal of Electrochemical Science*, vol. 9, pp. 7446–7459, 2014.

[9] H. El Attari, S. Mengouch, M. Siniti, E. Zahidi, L. Khamliche, and A. Kheribech, "Quantum chemical studies and adsorption characteristics of 4-hydroxy-3-[1-(2-phenylhydrazinylidene) ethyl] 2H-1-benzopyran-2one on mild steel in hydrochloric acid," *Journal of Materials and Environmental Science*, vol. 2508, pp. 689–700, 2018.

[10] S. Cao, D. Liu, P. Zhang et al., "Green Bronsted acid ionic liquids as novel corrosion inhibitors for carbon steel in acidic medium," *Scientific Reports*, vol. 7, no. 1, pp. 1–14, 2017.

[11] Y. Meng, W. Ning, B. Xu et al., ""Inhibition of mild steel corrosion in hydrochloric acid using two novel pyridine Schiff base derivatives": a comparative study of experimental and theoretical results," *RSC Advances*, vol. 7, no. 68, pp. 43014–43029, 2017.

[12] M. A. Deyab, A. S. Fouda, M. M. Osman, and S. Abdel-Fattah, "Mitigation of acid corrosion on carbon steel by novel pyrazolone derivatives," *RSC Advances*, vol. 7, no. 71, pp. 45232–45240, 2017.

[13] H. B. Sehmi, A. Ouici, M. F. Guendouzi, O. Benali, and F. Boudjellal, "Corrosion inhibition of mild steel by newly synthesized pyrazole carboxamide derivatives in HCl acid medium," *Journal of the Electrochemical Society*, vol. 167, no. 15, p. 155508, 2020.

[14] R. Karthik, G. Vimaladevi, A. Shen-Ming Chen, B. J. Elangovan, and P. Prakash, "Corrosion inhibition and adsorption behaviour of 4–amino acetophenone pyridine 2-aldehyde in 1 M hydrochloric acid," *International Journal of Electrochemical Science*, vol. 10, pp. 4666–4681, 2015.

[15] A. D. Becke, "Density-functional thermochemistry. III. The role of exact exchange," *The Journal of Chemical Physics*, vol. 98, pp. 5648–5652, 1993.

[16] C. T. Lee, W. T. Yang, and R. G. Parr, "Development of the Colle-Salvetti correlation-energy formula into a functional of the electron density," *Physical Review B*, vol. 37, no. 2, pp. 785–789, 1988.

[17] M. J. Frisch, G. W. Trucks, H. B. Schlegel et al., *Gaussian 16, Revision B.01*, Gaussian, Inc., Wallingford CT, UK, 2016.

[18] V. S. Sastri and J. R. Perumareddi, "Molecular orbital theoretical studies of some organic corrosion inhibitors," *Corrosion*, vol. 53, no. 8, pp. 617–622, 1997.

[19] A. A. Farag, A. S. Ismail, and M. A. Migahed, "Environmental-friendly shrimp waste protein corrosion inhibitor for carbon steel in 1 M HCl solution," *Journal of Petroleum*, vol. 27, no. 4, pp. 1187–1194, 2018.

[20] T. K. Bhuvaneswari, C. Jeyaprabha, and P. Arulmathi, "Corrosion inhibition of mild steel in hydrochloric acid by leaves extract of Tephrosiapurpurea," *Journal of Adhesion Science and Technology*, vol. 34, pp. 2424–2427, 2020.

[21] V. Saraswat and M. Yadav, "Computational and electrochemical analysis on quinoxalines as corrosion inhibitors for mild steel in acidic medium," *Journal of Molecular Liquids*, vol. 297, p. 111883, 2020.

[22] M. M. El-Naggar, "Corrosion inhibition of mild steel in acidic medium by some sulfa drugs compounds," *Corrosion Science*, vol. 49, no. 5, pp. 2226–2236, 2007.

[23] M. Corrales Luna, T. le Manh, R. Cabrera Sierra, J. V. Medina Flores, L. Lartundo Rojas, and E. M. Arce Estrada, "Study of corrosion behavior of API 5L X52 steel in sulfuric acid in the presence of ionic liquid 1-ethyl 3-methylimidazolium thiocyanate as corrosion inhibitor," *Journal of Molecular Liquids*, vol. 289, p. 111106, 2019.

[24] C. Verma, L. O. Olasunkanmi, I. Bahadur et al., "Experimental, density functional theory and molecular dynamics supported adsorption behavior of environmental benign imidazolium based ionic liquids on mild steel surface in acidic medium," *Journal of Molecular Liquids*, vol. 273, pp. 1–15, 2019.

[25] E. A. M. Gad, E. M. S. Azzam, and S. A. Halim, "Theoretical approach for the performance of 4-mercapto-1-alkylpyridin-1-ium bromide as corrosion inhibitors using DFT," *Egyptian Journal of Petroleum*, vol. 27, no. 4, pp. 695–699, 2018.

[26] S. Fouda, M. M. Gouda, and S. I. Abd El-Rahman, "1, 2, 4-Triazole on carbon steel corrosion in hydrochloric acid," *Bulletin of the Korean Chemical Society*, vol. 21, no. 11, 2000.

[27] Z. Cao, Y. Tang, H. Cang, J. Xu, G. Lu, and W. Jing, "Novel benzimidazole derivatives as corrosion inhibitors of mild steel in the acidic media. Part II: theoretical studies," *Corrosion Science*, vol. 83, pp. 292–298, 2014.

[28] H. R. Obayes, G. H. Alwan, A. H. M. J. Alobaidy, A. A. Al-Amiery, A. A. H. Kadhum, and A. B. Mohamad, "Quantum chemical assessment of benzimidazole derivatives as corrosion inhibitors," *Chemistry Central Journal*, vol. 8, no. 1, pp. 1–8, 2014.

[29] M. Abdallah, B. H. Asghar, I. Zaafarany, and M. Sobhi, "Synthesis of some aromatic nitro compounds and its applications as inhibitors for corrosion of carbon steel in hydrochloric acid solution," *Protection of Metals and Physical Chemistry of Surfaces*, vol. 49, no. 4, pp. 485–491, 2013.

[30] J. Aslam, R. Aslam, I. H. Lone et al., "Inhibitory effect of 2-nitroacridone on corrosion of low carbon steel in 1 M HCl solution: an experimental and theoretical approach," *Journal of Materials Research and Technology*, vol. 9, no. 3, pp. 4061–4075, 2020.

[31] P. Singh, A. K. Singh, and V. P. Singh, "Synthesis, structural and corrosion inhibition properties of some transition metal(II) complexes with o-hydroxyacetophenone-2-thiophenoyl hydrazone," *Polyhedron*, vol. 65, pp. 73–81, 2013.

[32] H. Jafari, I. Danaee, H. Eskandari, and M. Rashvand Avei, "Electrochemical and theoretical studies of adsorption and corrosion inhibition of N, N-bis (2-hydroxy ethoxy acetophenone) 2-dimethyl-1, 2-propanediimine on low carbon steel (API 5L Geade B) in acidic medium," *Industrial and Engineering Chemistry Research*, vol. 52, no. 20, pp. 6617–663220, 2013.

Hindawi
International Journal of Photoenergy
Volume 2022, Article ID 5357053, 11 pages
https://doi.org/10.1155/2022/5357053

Research Article

Influence of Aluminum Silicate and Cerium (IV) Oxide Nanofluid on Pool Boiling Characteristics

Yoganand Kumaravelu,[1] Vasanthkumar Periyathambi,[1] Poongundran Udhayanan,[1] Mohanraj Murugesan,[2] R. Jothi Ramalingam,[3] Hamad Al-Lohedan,[3] Dhaifallah M. Al-dhayan,[3] and Ishwarya Komalnu Raghavan[4]

[1]*Department of Mechanical Engineering, SRM Institute of Science and Technology, Ramapuram, Chennai 600089, India*
[2]*Department of Mechanical System Design Engineering, Seoul National University of Science & Technology, Seoul-01811, Republic of Korea*
[3]*Chemistry Department, College of Science, King Saud University, P.O. Box. 2455, Riyadh 11451, Saudi Arabia*
[4]*Department of Electromechanical Engineering, Faculty of Manufacturing, Institute of Technology, Hawassa University, Hawassa, Ethiopia*

Correspondence should be addressed to Vasanthkumar Periyathambi; pvasanthme@gmail.com

Received 2 December 2021; Accepted 27 December 2021; Published 11 February 2022

Academic Editor: V. Mohanavel

Copyright © 2022 Yoganand Kumaravelu et al. This is an open access article distributed under the Creative Commons Attribution License, which permits unrestricted use, distribution, and reproduction in any medium, provided the original work is properly cited.

A study into pool boiling heat transfer with nanofluids particularly aluminum silicate and cerium (IV) oxide was used to prepare nanofluids. A review of existing nanofluid implementations done previously in multiple literature and research journals was taken into consideration while determining their effects as nanoparticles in necessary base fluids. The nanofluids were prepared with two-step method by dispersing Al_2SiO_5 and CeO_2 nanopowders in water and were analyzed at base temperatures of 50-75°C and peak flux readings taken at saturation temperature. An inference between these and surface modifications due to settlement of nanoparticles on heater surface was studied by SEM imaging, and dispersion was studied with TEM imaging. The volume concentrations of Al_2SiO_5 and CeO_2 nanofluids are varied from $0.1\% \le \varphi \le 0.3\%$. Readings taken at temperatures varied by 5°C between 50°C to 75°C and at 100°C. The improvement of q'' for Al_2SiO_5/H_2O and CeO_2/H_2O nanofluids is about $120.5 \pm 0.6\%$ in PHF over water as base fluids for 0.3% volume concentration solutions.

1. Introduction

Boiling heat transfer has always been a powerful energy extradition technology which persuades the way in achieving milestones in the advancement of the futuristic technologies. The ameliorations in the field of nanotechnology have gone hand-in-hand with almost all the fields, and the enhancement by implementing it in the boiling heat transfer has exhibited enormous increase in the efficiency of the process and has played a role in the elevation of the reliability of the process by increasing various factors that are need of the hour. Our experiments had us spectate that the PHF has inclined to a steep level upon addition of minimal quantity of nanoparticles. Nanofluids were prepared with the aid of dispersion of the nanoparticles of the order 10-50 nm which gave the increase of density of fluid and also high specific surface-area that paves the way to higher heat transfer between surface and fluids. It also grants acclimation of properties such as thermal conductivity and wettability by varying the concentrations. Our experiments were conducted based on pool boiling, and the results were focused mainly on uplifting of the PHF using nanofluids as the base fluid [1]. All these property enrichments are noticed because the high surface area of the nanoparticle and their enhanced thermal properties. Pool boiling is mode of the boiling phenomenon in which fluid is stationary with respect to heating surface in the beginning; vapor is spawned at a superheated wall that is

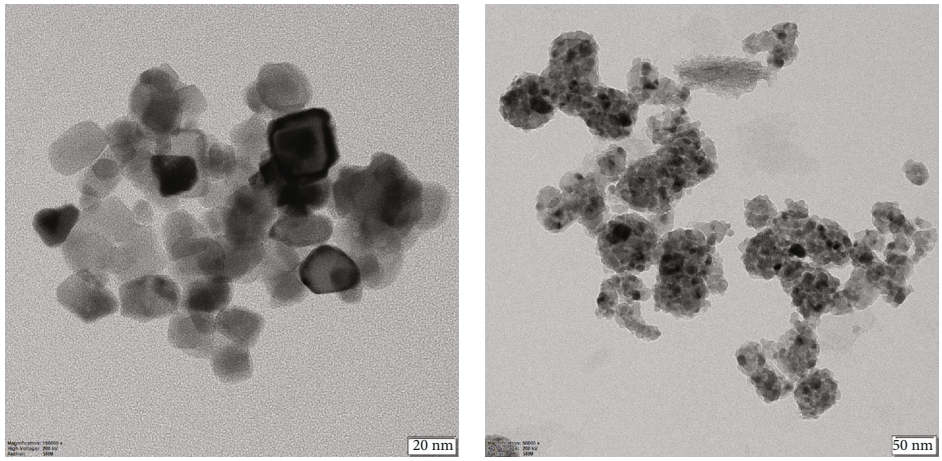

(a) (b)

Figure 1: HRTEM image of dried nanoparticles after dispersion in water: (a) CeO_2 nanoparticle and (b) Al_2SiO_5 nanoparticle.

tiny compared to the dimensions of the pool of ostensibly dormant liquid in which it is intent. In our experiments as cited in several papers, we use Ni-Chrome (80-20% composition) wire as the heating element through a set of platinum wire which has minimal resistance and anticorrosive in nature, and electricity is supplied. The bubbles formed by the cause are captured, and the certain parameters were calculated on the nucleation site, and the corresponding density with the diameter of the bubble that is formed when different nanofluid is applied [2, 3]. The existence of a vermicular structure in CuO nanoparticles contributes to the particles' wear resistance and improved lubrication [4].

The literature demonstrated that a variety of parameters could affect the performance of pool boiling of nanofluids as represented by the pool boiling heat transfer coefficient including the amount of nanoparticle loading, the size of nanomaterials, the roughness of the heater, the thickness of the thermally insulating nanolayer, and the time of boiling. A number of parameters may directly affect the behavior of bubbles, including the density of nucleation sites, bubble diameter, bubble frequency, bubble waiting time, and growth time, considered as essential boiling parameters that might influence the boiling performance of pools.

It has been determined that cerium oxide nanoparticles can be considered as an attractive nanomaterial based on the data from all published experimental studies. They are inexpensive, have excellent chemical and physical properties, are nontoxic compared to other metal oxide powders, and are available as a readily available material. As acclaimed in various papers that the alumina [5] and silica nanoparticles [6] tend to increase the peak heat flux of the heating element, we have proposed to use a complex aluminum silicate which has the properties, and in addition to that, cerium was also employed for exhibiting high electron conductivity and also has an increased thermal conductivity due to its valence of electrons.

Table 1: Volume concentration values with respective weights.

Vol. Conc., φ (%)	Material	Density, ρ_n (g/cc)	Weight, W_n (g/L)	Molecular weight (g/mol)
0.1	Al_2SiO_5	1.5	0.15	162.05
0.2	Al_2SiO_5	1.5	0.3	162.05
0.3	Al_2SiO_5	1.5	0.465	162.05
0.1	CeO_2	6.5	0.656	172.115
0.2	CeO_2	6.5	1.325	172.115
0.3	CeO_2	6.5	2.01	172.115

2. Materials and Methods

2.1. Chemical and Reagents. Aluminum silicate (Al_2SiO_5, 99.9% purity) and cerium (IV) oxide (CeO_2, 99.9% purity), which was purchased from Platonic nanotech, were used to prepare nanofluids with DI water used as base fluid. All chemicals were of analytical grade. The average sizes were found to be 50 nm and 40 nm for aluminum silicate and cerium (IV) oxide, respectively.

2.1.1. Characterization of Material. The nanoparticles were studied with FTIR, XRD, HRSEM, and HRTEM to get better understanding of material properties and compositions. HRSEM was taken with F E I Quanta FEG 200, HRTEM was taken with JEOL Japan, JEM-2100 Plus, and XRD was done using BRUKER USA D8 Advance, Davinci, with nanoparticles in powder form. HRTEM imaging of nanoparticles was taken after drying then once dispersed in DI water as shown in Figures 1(a) and 1(b).

2.1.2. Preparation of Nanofluids. Two methods are used for preparing nanofluids—one-step and two-step methods. Many researchers have reported that two-step method is most economical way to synthesize nanofluids. The advantage of two-step approach is it is cost-effective and able to produce large volumes of nanofluids. In this work, two-

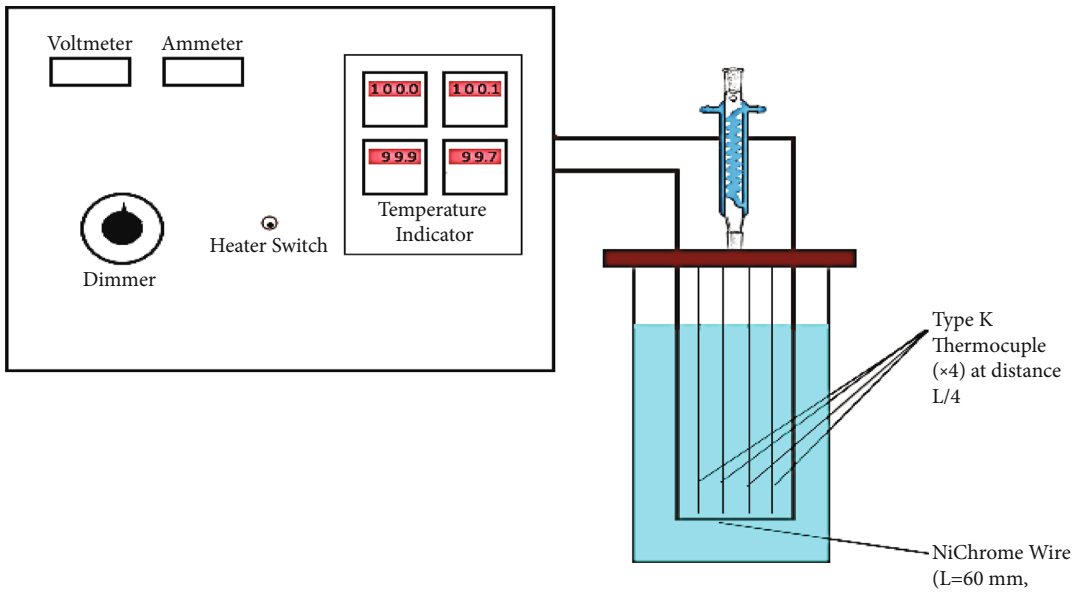

Figure 2: Experimental setup.

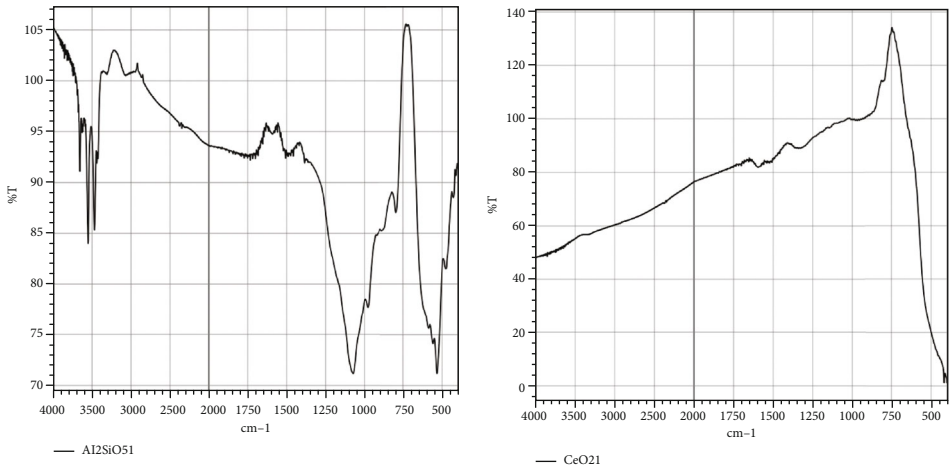

(a) (b)

Figure 3: FTIR spectroscopy: (a) Al_2SiO_5 nanoparticle and (b) C_eO_2 nanoparticle.

step method is adopted for preparing aluminum silicate (Al_2SiO_5) and cerium oxide (CeO_2) nanofluids. In this process, nanoparticles are prepared and dispersed in the base fluid (distilled water) with or without the help of surfactants by mechanical stirring or ultrasonication methods. The two-step method is widely chosen because the nanoparticles have high surface area and surface energy interactions which tend to aggregate the nanoparticles which are available in dried form.

The following steps are involved in preparation of Al_2SiO_5 and CeO_2 nanofluids:

Determination of volume concentration (φ) for adding to base fluid was done by using the following equation [7]:

$$\varphi = \left[\frac{(W_n/\rho_n)}{\{W_n/\rho_n + W_{\text{bf}}/\rho_{\text{bf}}\}}\right] * 100. \quad (1)$$

The above equation can be simplified as

$$W_n = \left(\frac{\varphi}{100-\varphi}\right)\left(\frac{\rho_n}{\rho_{\text{bf}}}\right) W_{\text{bf.}} \quad (2)$$

By using the above formula, the quantities of nanoparticles to be added are determined as follows in Table 1.

(i) The measured nanoparticle is added little by little into the base fluid and mechanically stirred for 2 hours. Despite of having extremely small sizes and relatively high kinetic energies resulting from Brownian motion, they do not remain in suspension. With time, nanoparticles settle out of solution under the influence of gravity [8]

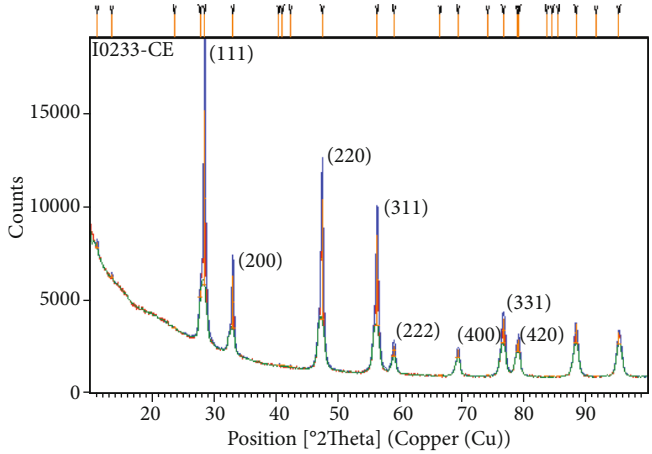

Figure 4: XRD of CeO_2 nanoparticle (JCPDS 898436).

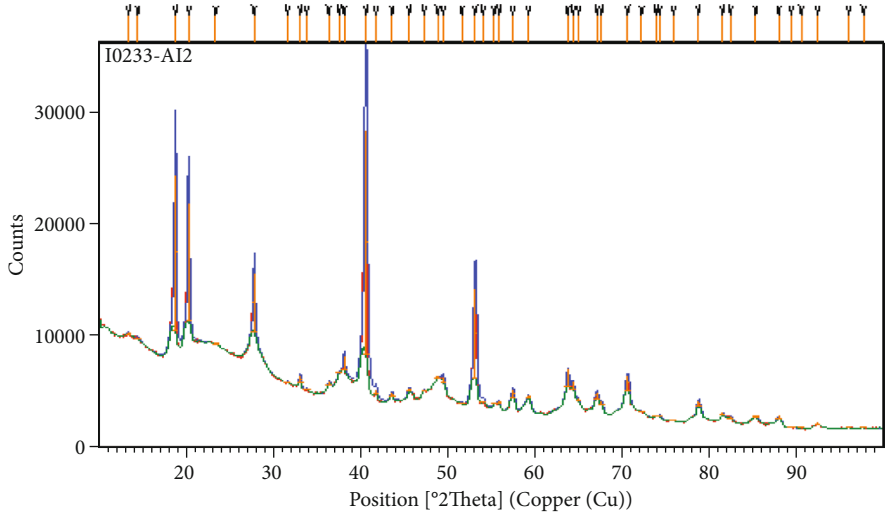

Figure 5: XRD of Al_2SiO_5 nanoparticle.

(ii) Hence, after stirring for 2 hours, the nanofluid is subjected to ultrasonication process for 4 hours to ensure uniform dispersion of nanoparticles as well as to prevent the nanoparticles from agglomerating in the base fluid. Many studies show that increase in sonication and stirring time reduces particle clustering

(iii) Nanofluids are considered stable only if no sedimentation takes place over time. Various sedimentation techniques are used to determine long-term stability of wide variety of nanofluids, and we considered simple 24-hour settlement under natural conditions for this study

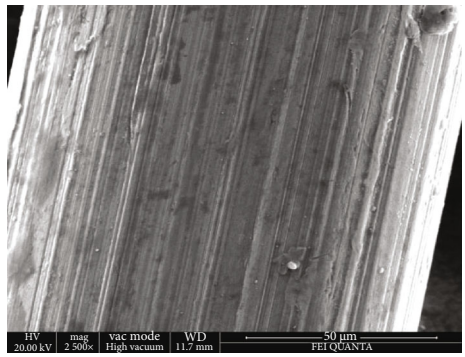

Figure 6: SEM image of Ni-Chrome wire (uncoated).

3. Experimental Details and Data Analysis

3.1. Experimental Setup. The setup as shown in Figure 2 consists of a 230 V AC power supply, hot plate, MI type K thermocouple (4 Nos.), temperature indicators (4 Nos.), jacketed condenser, and Ni-Chrome wire of diameter 40 SWG and 60 mm length which serves as the heater element. To demonstrate this concept, a custom-made glass beaker is made

(a) (b)

Figure 7: Surface morphology of heater surface: (a) 0.1% volume concentration Al_2SiO_5 and (b) 0.1% volume concentration CeO_2.

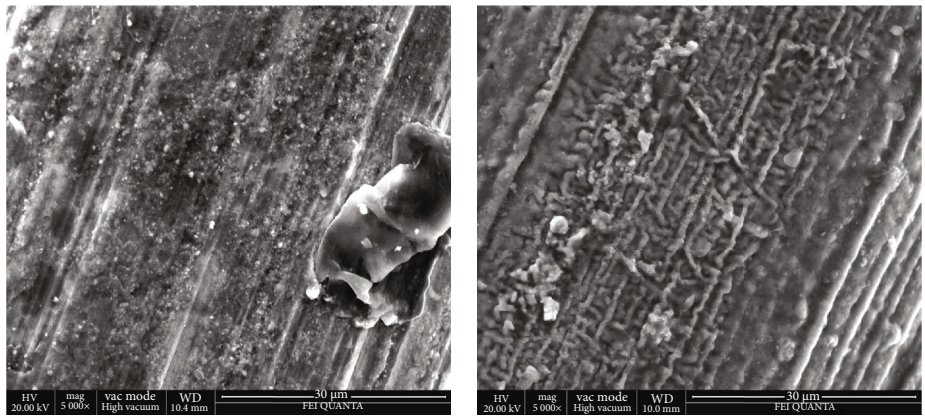

(a) (b)

Figure 8: Surface morphology of heater surface: (a) 0.2% volume concentration Al_2SiO_5 and (b) 0.2% volume concentration CeO_2.

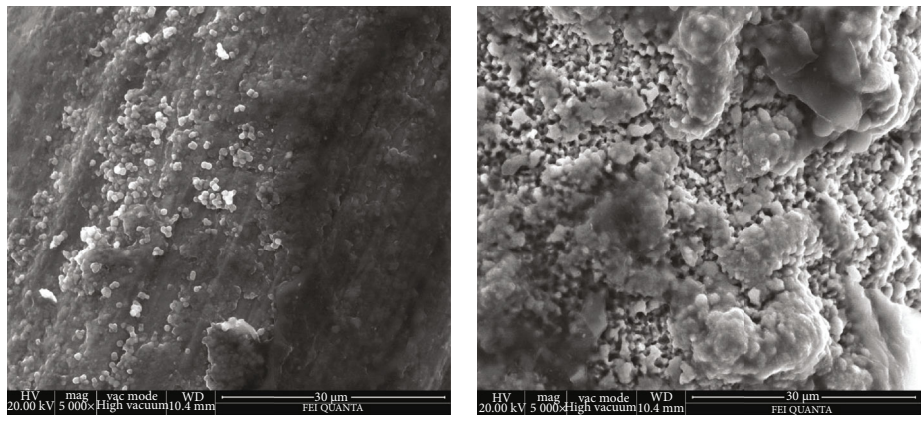

(a) (b)

Figure 9: Surface morphology of heater surface: (a) 0.3% volume concentration Al_2SiO_5 and (b) 0.3% volume concentration CeO_2.

for experimenting peak heat flux enhancement in nanofluid. Through the lid of the beaker, voltage sensing wires are connected to two platinum wires which are suspended at ends of the beaker in which the Ni-Chrome wire is connected and current is passed through platinum wire to avoid contact resistance with test specimen. Hot plate is used to heat up to the saturation temperature T_{sat} (100°C for water) of fluid, at 1 atm, while bulk temperature was being monitored with

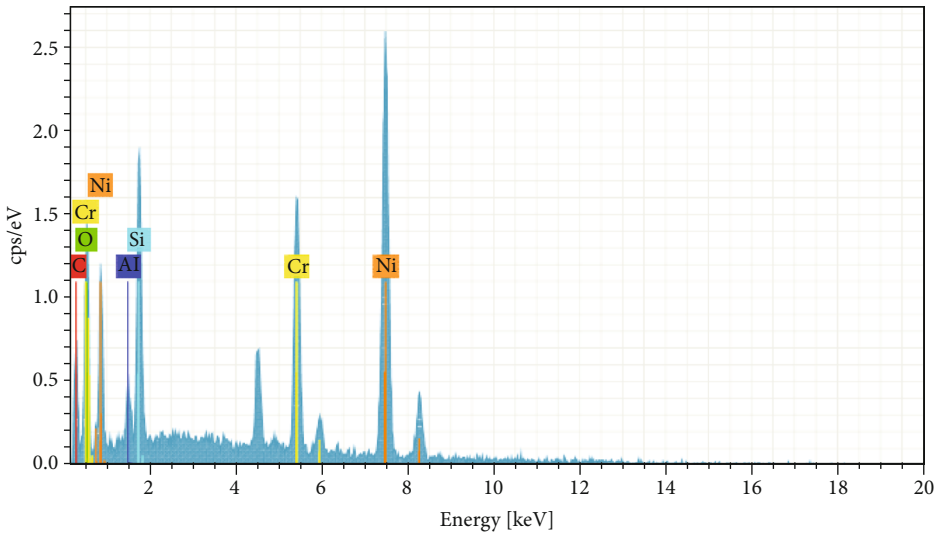

Figure 10: EDS for 0.3% volume concentration Al_2SiO_5.

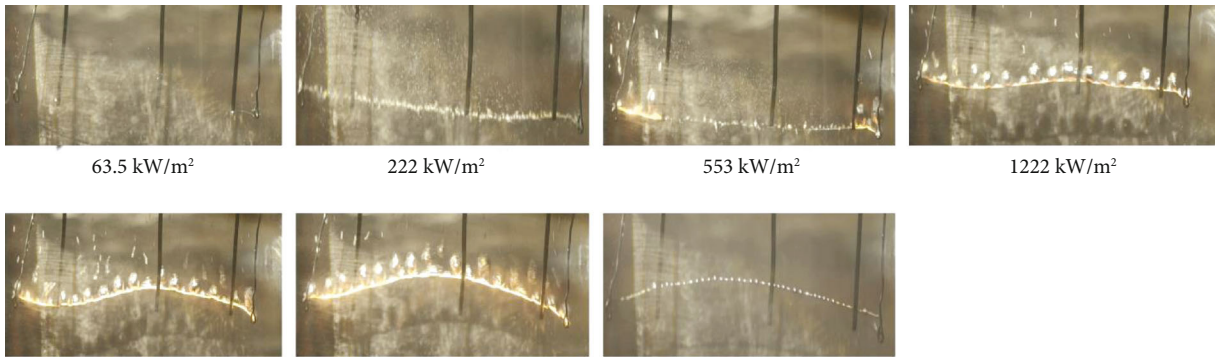

Figure 11: Bubble diameter variation with increase in heat flux for water.

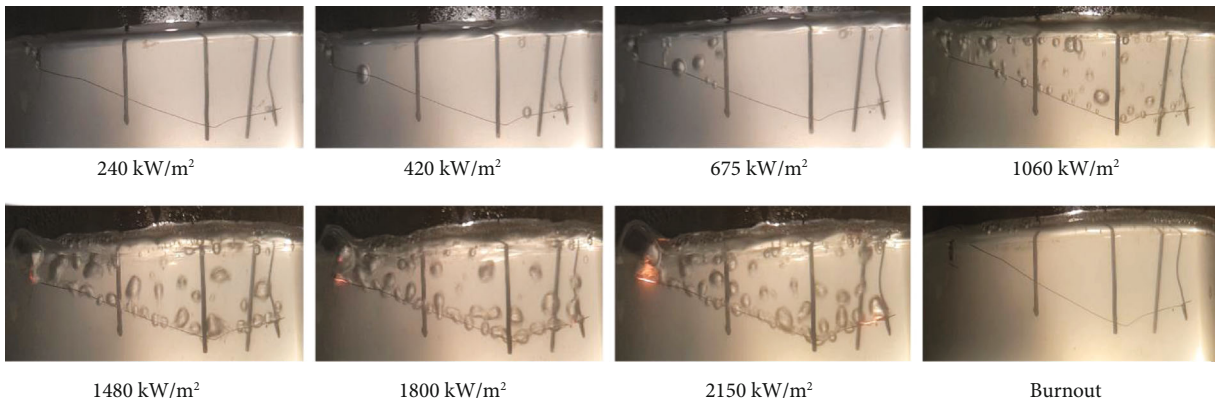

Figure 12: Bubble diameter variation with increase in heat flux for Al_2SiO_5.

thermocouples. Similarly, the four thermocouples are equipped in beaker through the lid and all are placed at equal distance to determine the average wire temperature. Since thermocouples are placed too close to the surface, along with the minimal contact resistance of the tiny gap between the thermocouple tip and the wire surface, it is assumed that the measured temperature represents the boiling surface temperature.

3.2. Experimental Procedure. Initially, the experiment is conducted in distilled water. The distilled water is heated on hot plate till its saturation temperature T_{sat} is 100°C, and temperature was being monitored by thermocouple. Current is applied to Ni-Chrome wire through platinum wires by regulating the variac. Voltage and ammeter readings are noted during burnout [9] of Ni-Chrome wire for heat flux measurement and for comparing with various nanofluids. Similarly, the nanofluid is heated on a hot plate to saturation temperature T_{sat} (100°C) of base fluid (distilled water) at atmospheric pressure 1 atm, while bulk temperature is monitored by thermocouples. Current is applied to Ni-Chrome wire that is regulated by variac for constant heat flux control, with increments of 0.5 A. The voltage measurements are noted at steady rate just after the current increase, and intervals are given after each increment to changes in system. Heat flux at any point is calculated by the following equation:

$$q'' = \frac{VI}{\pi DL}. \quad (3)$$

4. Results and Discussion

Figure 3(a) indicates presence of OH functional groups which might be due to the presence of moisture in the sample in the range around 3500 cm^{-1}. The peak at 1100 cm^{-1} indicates the Si-O-Si antisymmetry stretching. Figure 3(b) indicates no peaks which evidently shows the absence of organic compounds in the CeO_2 nanoparticle.

4.1. XRD Analysis of CeO_2. The crystal phase and the lattice constant of the nanocrystals were evaluated using XRD studies. Figures 4 and 5 show the XRD spectrum of the KBr-mediated synthesis of CeO_2 and Al_2SiO_5. The patterns in the figure CeO_2, comprising peaks at the 2 theta values of 28.46, 32.96, 47.39, 56.23, 59.03, 69.27, 76.71, and 79.04, respectively, correspond to the (1 1 1), (2 0 0), (2 2 0), (3 1 1), (2 2 2), (4 0 0), (3 3 1), and (4 2 0) planes, as depicted in Figure 4. All the diffraction patterns of CeO_2 harmonized with the JCPDS data card No. 898436, and this shows the cubic crystal structure of CeO_2 with a space group of Fm3m (225). In XRD patterns for Al_2SiO_5, the presence of moisture content of the sample showed a slight level of impurities in the prepared sample. No impurity peaks were observed indicating the high purity of the prepared samples. The existence of CeO_2 was further identified by SEM and EDAX studies.

4.2. SEM and EDX Analysis. Scanning electron microscopy (SEM) is a unique technology to characterize the morphology, defects, and structure of materials. The typical SEM images in Figure 6 show the morphology of pure Ni-Chrome wire, Figures 7(a), 8(a), and 9(a) show 0.1%-0.3% of Al_2SiO_5-doped Ni-Chrome, and Figures 7(b), 8(b), and 9(b) show 0.1%-0.3% of CeO_2-doped Ni-Chrome, respectively. It can be inferred from the SEM image in Figure 6 that pure Ni-Chrome wire has a smooth surface morphology as obtained while Figure 7(a) shows

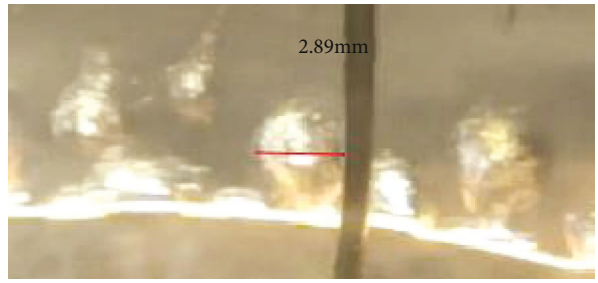

Figure 13: Bubble departure diameter for Al_2SiO_5 (0.3% vol) measured in Octave GNU.

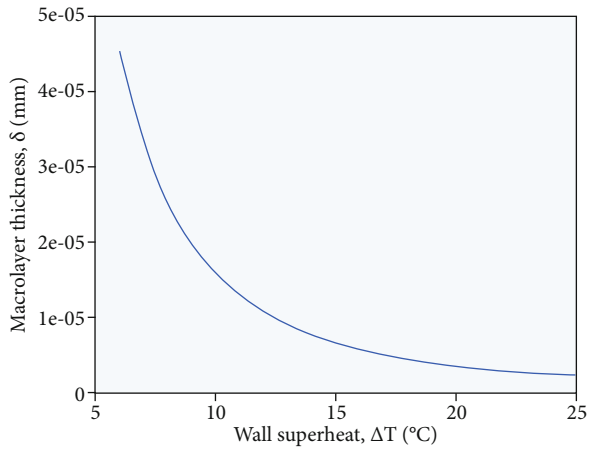

Figure 14: Heat flux variation with microlayer thickness.

the SEM images of 0.1% of Al_2SiO_5-doped Ni-Chrome; Al_2SiO_5 deposits are found on the Ni-Chrome wire, and with increasing concentration, there is a significant improvement observed. Figure 10 shows the elemental analysis of Ni-Chrome doped with Al_2SiO_5, in these compositions of Ni, Cr, Si, Al, and O that were present.

SEM imaging of Ni-Chrome wire-untreated (uncoated) was taken initially to study surface morphology and provide for a base to compare with wires used in experimentation. Figure 6 showcases a plain Ni-Chrome wire and can be seen to have no coatings and a simple plain structured morphology.

As noticed in Figures 7–9, a certain layer of coating tends to form on the wire during experimentation which clearly enhances the heat flux of wire as the excess heat dissipation due to this nanocoating [10] is enhanced when compared to uncoated wire and also becomes more efficient with increase in volume concentration of nanofluids; this is also evident in the respective EDS data as shown in Figure 10, which generated that with increase in volume concentration, the amount deposited onto the wire also increases.

The aluminum silicate and cerium oxide nanofluids were tested with the base-fluid water, and enhancements were observed that varied with change in volume fraction. The varying bubble diameter at increasing heat flux is portrayed in Figures 11 and 12 which show that the bubble diameter increases as the heat flux applied to the wire increases.

Table 2: Heat flux comparison to acclaimed studies.

Model	Form	Value
Zuber model	$q''_{\max} = 0.131\, h_{lv}\rho_v \left[\frac{\sigma(\rho_l - \rho_v)g}{\rho_v^2}\right]^{1/4}$	1.138×10^3 W/m^2
Rohsenow and Griffith bubble interface model	$q''_{\max} = 0.012\, \rho_g h_{fg} \left(\frac{\rho_f - \rho_g}{\rho_g}\right)^{0.6}$	1.353×10^3 W/m^2
Haramura and Katto model	$q''_{\max} = \rho_f h_{fg} \delta \left(1 - 0.0584 \left(\frac{\rho_g}{\rho_f}\right)^{1/5}\right) f$	1.286×10^3 W/m^2
This study	Experimental	1.781×10^3 W/m^2

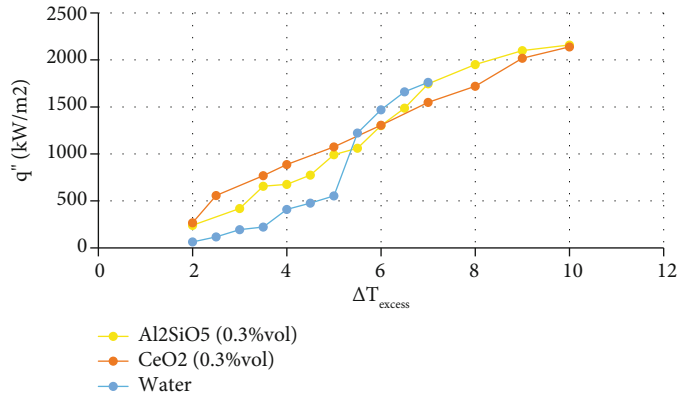

Figure 15: Heat flux comparison.

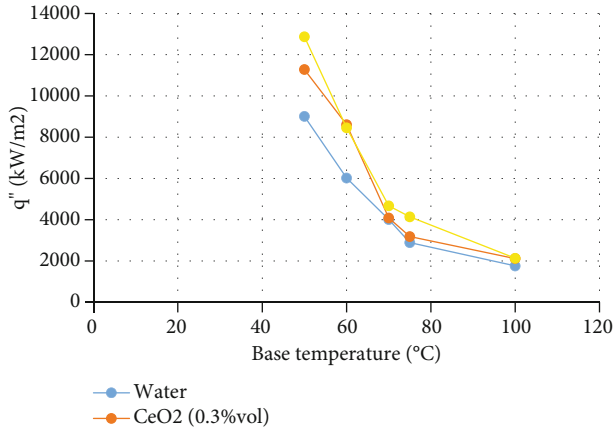

Figure 16: Heat flux variations based on base temperature.

It is observed that starting at lower base temperature, a higher value for peak heat flux can be achieved, as illustrated by the graph above. Theoretically, bubble diameter was calculated using Haramura relation.

Bubble departure diameter, D_b

$$\sqrt{\frac{\sigma}{g\left(\rho_l - \rho_g\right)}} = 2.77 \text{ mm for water.} \quad (4)$$

Experimentally, bubble diameter was calculated visually by using images captured during the experimentation process and using the Octave GNU software to attain exact values as shown in Figure 13.

Macrolayer thickness, δ, was calculated by the following formula, $\delta(t) = \sqrt{\delta_o^2 - 2(\lambda \Delta T/\rho_l h_{fg})t}$.

From the above formula, values where calculated using Octave GNU and it was inferred that the macrolayer thickness value decreases from the initial layer thickness as suggested by other literatures [11, 12], while an increase in initial macrolayer thickness is observed with increase in base temperatures for fluids. Graph in Figure 14 shows the values of macrolayer thickness varying with increase in wall superheat of fluid.

Use preestablished models where comparative study was done to determine variations with these and our experimental model [13]. Table 2 shows clear comparison of existing models for pool boiling.

Hence, from experimental data as shown in Figures 15 and 16, it is observed that both Al_2SiO_5 and CeO_2 show enhancements of about $120.5 \pm 0.6\%$ in PHF over water as base fluids for 0.3% volume concentration solutions. The reason for increase in PHF is also contributed by the macrolayer increase at higher temperatures [14]. Nucleation sites were determined using images captured from video taken during the experimentation process and were then fed into

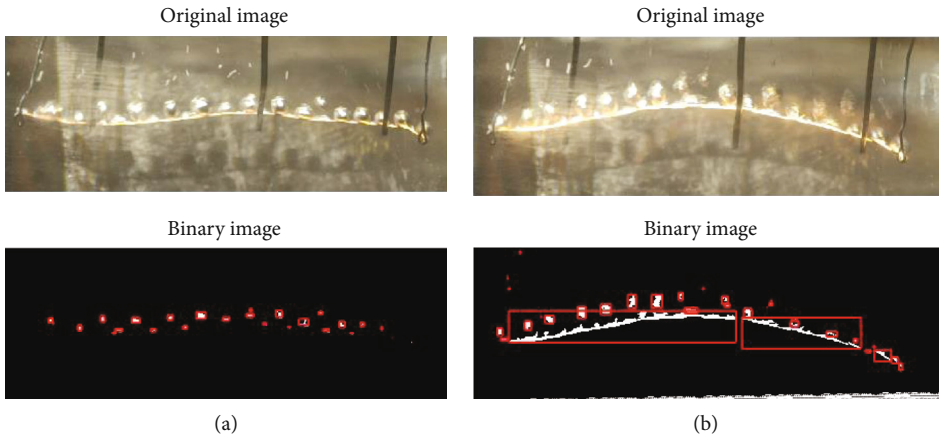

Figure 17: Nucleation sites on heater surface: (a) water and (b) water at higher PHF.

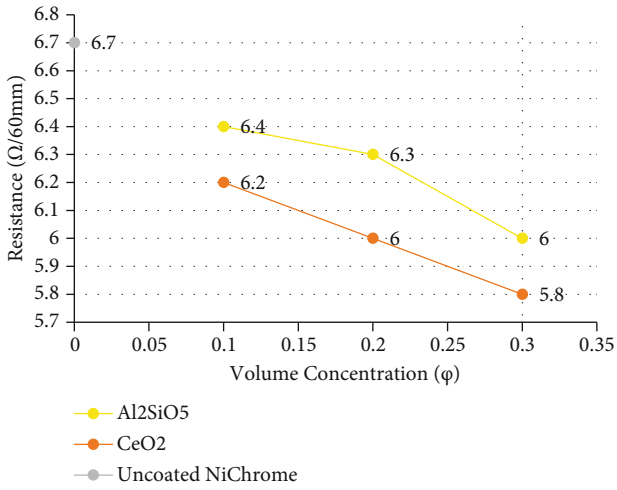

Figure 18: Influence of coating over Ni-Chrome wire on resistance of wire.

Octave GNU with algorithm created by author to determine number of sites as showcased in Figures 17(a) and 17(b).

Boiling has developed a great interest during the past few decades, as a method to increase the heat transfer rates with modest temperature differences. At high heat fluxes, heat transfer [15] by boiling is highly effective. Hence, find applications such coolants for nuclear reactors and also rocket engines where heat transfer rates are in high values (10^6 to 10^7 W/m^2). The probability to attain higher thermal energy conversion efficiency through boiling working fluid with heated surface is possible by these methodologies and has a large area of applications.

These coating of nanofluids over surface of wire or heater/heating surfaces tend to influence resistance which could be directly tracked to thermal conductance by inverse proportionality as shown in Figure 18 that when the coating increases, a decrease in resistance offered by wire is observed, and the values of resistance are for 60 mm of wire lengths as used in experimentation process for testing and generating direct relations. Nanofluids having high specific surface area serve to be better than other commercial fluids for heat transfer applications carrying more torridity between particles being the most important feature of nanofluids in heat carrying applications.

Using metallic fluids in heat carrying applications denotes significant difference when compared to commercial fluids for the same application. The hitch here being clogging of micrometer-sized particles in small passages and nanofluids being nanometer-sized can overcome this obstacle. Adding as low as 1-6 vol% of nanoparticle in a base fluid can enhance the heat carrying ability to a significant change of 20%. Usage of nanomaterials like Cu, Al, Si, Zn, Mg, and Se is advised on this prospect, and so a combination of aluminum and silicate forming aluminum silicate (Al_2SiO_5) and cerium oxide is tested upon with 0.1%, 0.2%, and 0.3% of both the nanofluids. The stability of oxide-based nanofluids is higher, and therefore, both are chosen to be oxide-based nanofluids. Table 3 clearly depicts the improvement in peak heat flux (PHF) in comparison with other reported results.

Alumina particles have the tendency to decrease the pool boiling heat transfer but it has improved the CHF by 20% [20]. The CHF enhancement is due to the surface modifications that happen in the wire surface due to deposition of nanoparticles [21, 22]. A main cost attributing factor for nanofluids is the use of stabilizers which increases the production cost of these nanofluids without which nanoparticles tent to settle over a period of time. So cheaper stabilizers or nanofluids which are more substantial without the use of stabilizers need to be invented. The stabilizers that are commercially used in nanofluids are proven to be unstable at high temperatures being a drawback for stability in heat carrying applications. Most nanofluids upon testing results have lower specific heat at their respective temperatures when compared to its base fluids. On production of nanofluids, the particles tend to agglomerate into larger particles resulting in limiting the main asset of nanoparticles' high surface area.

Table 3: Comparison with earlier literatures.

Literature	Nanofluids	PHF
Karima et al. [16], Liu et al. [17]	CuO in H_2O	Enhanced by 25–50%
Shi et al. [8]	Al_2O_3 & Fe in H_2O	Enhanced to ≈60%
Wen et al. [5]	γ-Al_2O_3 in H_2O	Enhanced to ≈40%
Milanova et al. [18]	Al_2O_3, SiO_2, & CeO_2 in H_2O	Deteriorated
Vassallo et al. [19]	SiO_2 in H_2O	Slight change
This study	Al_2SiO_5, CeO_2 in H_2O	Enhanced by ≈20%

5. Conclusion

In this study, the effects of nanoparticles in base-fluid water on heat transfer characteristics are conducted using a critical heat flux apparatus. The volume concentrations of Al_2SiO_5 and CeO_2 nanofluids are varied from $0.1\% \le \varphi \le 0.3\%$. Readings taken at temperatures varied by 5°C between 50°C to 75°C and at 100°C. The improvement of q'' for Al_2SiO_5/H_2O and CeO_2/H_2O nanofluids is about 1.781×10^3 W/m^2, which displays a lower improvement in heat transfer for lower volume fraction; however, the significant enhancement of q'' is observed for higher volume fraction. From the results arrived, for enhancement of PHF and HTC nanofluids and nanosurface modifications showcase as dominant tools, modifications to working fluid and/or heater surface high thermal energy conversion efficiency can be achieved for boiling.

Abbreviations

D_b: Bubble departure diameter (mm)
σ: Surface tension (N/m)
g: Gravity (m/s^2)
ρ_l: Density of liquid (kg/m^3)
ρ_g: Density of vapor (kg/m^3)
δ: Macrolayer thickness (mm)
h_{fg}: Latent heat of vaporization (kJ/kg)
t: Time (s
q'': Heat flux (W/m^2)
V: Potential difference (V)
I: Input current (A)
πD: Circumference of Ni-Chrome wire (m)
L: Length of Ni-Chrome wire (m)
φ: Volume concentration (%)
W_n: Weight of nanoparticle (g)
ρ_n: Bulk density of nanoparticle (g/cc)
W_{bf}: Weight of base fluid (g)
ρ_{bf}: Bulk density of base fluid (g/cc).

Data Availability

The data used to support the findings of this study are included within the article.

Conflicts of Interest

The authors declare that there is no conflict of interest regarding the publication of this article.

Acknowledgments

The authors acknowledge the HRTEM Facility at SRMIST setup with support from the Ministry of New and Renewable Energy India (Project No. 31/03/2014-15/PVSE-R&D). We also acknowledge Nanotechnology Research Centre (NRC), SRMIST, for providing the research facilities. The authors are thankful for the financial support by the Researchers Supporting Project Number (RSP-2021/54), King Saud University, Riyadh, Saudi Arabia.

References

[1] S. Lee, S. U.-S. Choi, S. Li, and J. A. Eastman, "Measuring thermal conductivity of fluids containing oxide nanoparticles," *Journal of Heat Transfer*, vol. 121, no. 2, pp. 280–289, 1999.

[2] P. Vetrivezhan, C. Ayyanar, P. V. Arunraj, P. Vasanthkumar, and D. Ganesan, "Electroless deposition of aluminium alloy LM25 by SiC and Ni-P nano coating," *Materials Today: Proceedings*, vol. 45, pp. 6449–6453, 2021.

[3] K. Arul and V. S. Senthil Kumar, "Effects of Nano additives in bio cutting fluid for turning of Monel K500 alloy," *Journal of the Balkan Tribological Association*, vol. 26, no. 3, pp. 589–600, 2020.

[4] K. Arul and V. S. Senthil Kumar, "Magnetorhelogical based minimum quantity lubrication (MR-MQL) with additive n-CuO," *Materials and Manufacturing Processes*, vol. 35, no. 4, pp. 405–414, 2020.

[5] D. Wen and Y. Ding, "Experimental investigation into the pool boiling heat transfer of aqueous based γ-alumina nanofluids," *Journal of Nanoparticle Research*, vol. 7, no. 2-3, pp. 265–274, 2005.

[6] S. Das, D. S. Kumar, and S. Bhaumik, "Experimental study of nucleate pool boiling heat transfer of water on silicon oxide nanoparticle coated copper heating surface," *Applied Thermal Engineering*, vol. 96, pp. 555–567, 2016.

[7] S. Mukherjee and S. Paria, "Preparation and stability of nanofluids-a review," *IOSR Journal of Mechanical and Civil Engineering*, vol. 9, no. 2, pp. 63–69, 2013.

[8] M. H. Shi, M. Q. Shuai, Z. Q. Chen, Q. Li, and Y. M. Xuan, "Study on pool boiling heat transfer of nano-particle suspensions on plate surface," *Journal of Enhanced Heat Transfer*, vol. 14, no. 3, pp. 223–231, 2007.

[9] T. G. Theofanous, T. N. Dinh, J. P. Tu, and A. T. Dinh, "The boiling crisis phenomenon: part II: dryout dynamics and burnout," *Experimental Thermal and Fluid Science*, vol. 26, no. 6-7, pp. 793–810, 2002.

[10] V. B. Khabensky, A. L. Sirotkina, V. I. Almjashev, E. D. Fedorovich, V. V. Sergeev, and V. V. Gusarov, "Experimental studies of impact on a critical heat flux the parameters of nanoparticle layer formed at nanofluid boiling," *Nanosystems: Physics, Chemistry, Mathematics*, vol. 9, no. 2, pp. 279–289, 2018.

[11] H. K. Forster and N. Zuber, "Dynamics of vapor bubbles and boiling heat transfer," *AICHE Journal*, vol. 1, no. 4, p. 531, 1955.

[12] Y. Haramura and Y. Katto, "Новая гидРодинамическая модель кРитического теплового потока, пРигодная для описания кипения как в Большом оБъеме, так и пРи вынужденной конвекции в случае тел, погРузенныч в насыженную зидкость," *International Journal of Heat and Mass Transfer*, vol. 26, no. 3, pp. 389–399, 1983.

[13] S. Nukiyama, "The maximum and minimum values of the heat Q transmitted from metal to boiling water under atmospheric pressure," *Journal of the Society of Mechanical Engineers*, vol. 37, no. 206, pp. 367–374, 1934.

[14] K. C. Udaiyakumar, U. Poongundran, K. Yoganand, and V. M. Kumar, "An experimental study and comparitive validation of macrolayer thickness in nucleate pool boiling for horizontal copper tube heater," *IOP Conference Series: Materials Science and Engineering*, vol. 402, 2018.

[15] X. Fang, Y. Chen, H. Zhang, W. Chen, A. Dong, and R. Wang, "Heat transfer and critical heat flux of nanofluid boiling: a comprehensive review," *Renewable and Sustainable Energy Review*, vol. 62, pp. 924–940, 2016.

[16] K. Boukerma and M. Kadja, "Convective heat transfer of Al2O3 and CuO nanofluids using various mixtures of water-ethylene glycol as base fluids," *Engineering, Technology & Applied Science Research*, vol. 7, no. 2, pp. 1496–1503, 2017.

[17] Z. Liu, J. Xiong, and R. Bao, "Boiling heat transfer characteristics of nanofluids in a flat heat pipe evaporator with micro-grooved heating surface," *International Journal of Multiphase Flow*, vol. 33, pp. 1284–1295, 2007.

[18] D. Milanova and R. Kumar, "Role of ions in pool boiling heat transfer of pure and silica nanofluids," *Applied Physics Letters*, vol. 87, no. 23, pp. 233107–233107-3, 2005.

[19] P. Vassallo, R. Kumar, and S. D. Amico, "Pool boiling heat transfer experiments in silica-water nano-fluids," *International Journal of Heat and Mass Transfer*, vol. 47, no. 2, pp. 407–411, 2004.

[20] I. C. Bang and S. H. Chang, "Boiling heat transfer performance and phenomena of Al_2O_3-water nano-fluids from a plain surface in a pool," *International Journal of Heat and Mass Transfer*, vol. 48, no. 12, pp. 2407–2419, 2005.

[21] H. S. Ahn and M. H. Kim, "The boiling phenomenon of alumina nanofluid near critical heat flux," *International Journal of Heat and Mass Transfer*, vol. 62, pp. 718–728, 2013.

[22] K. Arul and V. S. Senthil Kumar, "Effect of magneto rheological minimum quantity lubrication on machinability, wettability and tribological behavior in turning of Monel K500 alloy," *International Journal of Machining Science and Technology*, vol. 24, no. 5, pp. 810–836, 2020.

Hindawi
International Journal of Photoenergy
Volume 2022, Article ID 7065940, 9 pages
https://doi.org/10.1155/2022/7065940

Research Article

Experimental Analysis of the Thermal Performance of a Latent Heat Energy of Helical Coil for the Application of Solar Energy

T. Jayakumar[1], **S. Jaanaa Rubavathy**[2], **R. Karpagam**[3], **S. Diwakaran**[4], **S. Arockia Jayadhas**[5], **Maqusood Ahamed**[6] and **Shanmugam Sureshkumar**[7]

[1]*Department of Mechanical Engineering, AMET Deemed to be University, Chennai, Tamil Nadu, India*
[2]*Department of Electrical and Electronics Engineering, Saveetha School of Engineering, Saveetha Institute of Medical and Technical Sciences, Chennai, Tamil Nadu, India*
[3]*Department of Electrical and Electronics Engineering, Easwari Engineering College, Ramapuram, Chennai, Tamil Nadu, India*
[4]*Department of Electronics and Communication Engineering, Kalasalingam Academy of Research and Education, Krishnankoil, Srivilliputhur, Tamil Nadu, India*
[5]*Department of EECE, St. Joseph University in Tanzania, Tanzania*
[6]*Department of Physics and Astronomy, College of Science, King Saud University, Riyadh 11451, Saudi Arabia*
[7]*Department of Animal Resources Science, Dankook University, 119, Dandae-ro, Cheonan 31116, Republic of Korea*

Correspondence should be addressed to S. Jaanaa Rubavathy; jaanaarubavathys.sse@saveetha.com
and S. Arockia Jayadhas; arockia.jayadhas@sjuit.ac.tz

Received 13 December 2021; Revised 26 December 2021; Accepted 27 December 2021; Published 25 January 2022

Academic Editor: V. Mohanavel

Copyright © 2022 T. Jayakumar et al. This is an open access article distributed under the Creative Commons Attribution License, which permits unrestricted use, distribution, and reproduction in any medium, provided the original work is properly cited.

The latent thermal power storage system has more characteristics than the sensitive storage system. The heating system is a process of releasing and absorbing heat energy using phase transfer material (PCM) and it provides more efficient energy than sensible heat storage. This also consist of high energy storage and high density. It provides high heat transfer in low volume and thereby enhances heat transfer. This enhances the capacity and efficiency of the EFU while extending the service life. The coil tube is designed for latent thermal energy storage to implement and enhance thermal performance during the loading and unloading process. The offloading time, however, was not affected by the flows. Higher throughput has also been shown to improve the effectiveness of recovery. The direction of flow of the HTF did not affect the total time of loading and recharging but affected the temperature changes of the PCM in the energy storage element. It is intended to predict the ability to store maximum energy as higher energy efficiency during the phase shift process. Parameters such as the mean temperature of the PCM, the growth of the melting front, the energy efficiency, and the number of generations of entropy are studied.

1. Introduction

Renewable energies, such as wind and solar, are plentiful, but intermittent, and there is often a mismatch between market forces. It is critical to building effective energy loading devices that can store electricity harvested during periods of the highest production and afford it during times of high mandate to fully practice this renewable energy. In the domestic sector, conventional solar thermal water heaters are used; in addition, they have lower capacity and efficiency, particularly during periods of low sunlight. The use of phase switching materials (PCM) to conserve thermal energy is an option [1]. Because of the high energy density of PCM, thermal heat storage solutions using PCM have proven more productive than thermal energy storage methods. For various renewable energies, thermal systems, and energy efficiency of buildings, phase change-based storage solutions (PCM) with acceptable storage behavior and temperature gradient are attractive solutions. These heat transfer, storage (LHS) devices can meet constant thermal energy demand, eliminating problems caused by changes in power generation. The success of LHS systems is

influenced by the heat capacity of PCMs and the heat transport suitable interventions in storage technologies. The thermal efficiency of most LHS technologies is degraded by the huge, microscopic heated surface and low thermal expansion of PCM [2].

When the heated coolant (HTF), such as everything from a solar panel, passes through the PCM tank, it adds heat to the energy storage unit. In latent thermal exchangers, water is usually used as HTF. Recent research has suggested the use of liquid nanomaterials, which have superior thermal conductivity and a higher heat transfer rate than the basic liquid [3]. In their solid shape, liquid metals are good melting temperatures and are extremely tough. Due to its high melting and boiling points, inorganic MCPs are often used in high concentration applications. Previous research has demonstrated that inorganic MCCs have significant disadvantages, such as undercooling and degradation of containment materials. Because of its availability, high heat source of fusion, chemical resistance, and tolerance with a broad variety of materials with no degradation in the enclosure medium, wax is a good choice [4]. Despite this, paraffin has high thermal conductivity, resulting in slow heat transmission and extended charging or discharging durations. Different heat transfer augmentation approaches have been used to overcome this problem.

As a result, the solution has poor melt and crystallization, as well as considerable temperature differences. As a result, before commencement, the creation of effective storage systems as well as rigorous heat study is critical. Building heat pumps, solar thermal technologies, absorbing coolers, electronic element heat dissipation, battery heat dissipation, and photovoltaic thermal systems has all successfully used PCM-based energy storage devices [5]. Furthermore, the helical coil significantly improved heat transmission performance and reduced the overall freezing time of the storage system, according to the findings. The temp according to the findings, the helical coil considerably increased thermal transfer efficiency and decreased the overall melting time of the storage solution. Numerically and experimentally, the temperature distribution and thermal characteristics of paraffin in an indistinguishable and nonequidistant helical-coil storage facility were examined. Creature supply and thermal properties of paraffin in an indistinguishable and nonequidistant helical-coil storage facility were evaluated numerically and experimentally. The simulation demonstrated consistent temperature, and the nonequidistant alpha helix device outperformed the equal one in terms of results.

Because no type of substance can meet the requirements for all of the key qualities, no solitary PCM could be used for all applications. Consequently, selecting an ECHP for a given purpose requires careful consideration. Since it produces high heat, is noncorrosive, chemically stable, and nontoxic, beeswax was investigated as a PCM. Despite this, the thermal resistance of wax remains the major obstacle to its application as a PCM in latent thermal energy storage (LHTS) [6]. As a result, several recent studies have focused on optimizing the heat exchange process in the PCM by employing various approaches. The addition of fines to the pipe shell and storage to improve thermal efficiency and the addition of microphones to the PCM to improve thermal conductance are examples of these strategies. According to the literature, a traditional SAH is observed as a poor potential heater in practice due to significant heat losses and low heat storage capabilities. As a result, numerous modifications have been introduced to advance the quality and construction of solar thermal systems. Two strategies have been discovered to be far superior to others, including the use of rough surfaces, surface or stretched geometries, and the employment of a high-quality thermal power storage (TES) substance.

Various LHTES designs and expansion techniques, such as adding blades and nanomaterials. It was suggested that metallic foam be added to the primary material (MCF) to improve the efficiency of the LHTES. Due to the comparatively high thermal performance, which may be exploited as an annulus around two concentric circular tubes, dual-energy packing has effectively acquired high thermal efficiency among the various LHTES unit designs [7]. Furthermore, the power storage needs can be easily met by building and possibly installing a single unit or perhaps an array. Helical tubing is a design that can be used in the LHTS to improve thermal efficiency while loading and unloading. This project has several advantages over traditional designs, including ease of design and implementation, a high heat transfer surface in a slight capacity, and increased fluid mix across the tube due to secondary vortices created by the helical flow, which improves thermal performance [8].

During the melting process, the thermal performance of the innovative conical-shaped helical coiled LHSU design is studied and compared to that of a spherical coil with almost the same heat transfer under the same operating temperatures.

2. Related Works

To investigate the feasibility of storing solar energy in thermal energy storage (TES) tank employing different heat transfer fluids (HTF), the TES container is combined with a flat plate solar absorber and is meant to provide hot water for an average of four family people in India: a method on the performance of latent heat and solar thermal energy storage system [9]. The TES tank serves as a heat storage unit, with phase change materials (PCM) encased in metal tubes and stacked in three beds, all surrounded by heat storage material (SHS), which is water. The TES tank is filled when solar power is produced by passing variables HTF through the flat-plate solar collection. The HTF uses a helical copper coil heating element in the TES tank to transmit heat from the solar concentrator to the TES tank. The heat is stored as a mix of thermal energy, heat in the water, and PCM in the TES tank. The performance metrics of several HTFs, including such recharge time and immediate heat stored, are investigated.

The method of performance evaluation approach based on the solar heat storage system using phase change material is proposed by [10]. In comparison to thermal storage, latent heat storage with exchanger provides an alternate strategy with higher energy storage density and reduced area demand

Table 1: Specification of LHTS units.

Equipment			Unit
Helical (coiled) LHTS unit	Shell	Building material	Acrylic
		Measurement	49.5 cm
		Inner thickness	17.6 cm
		Shell thickness	0.6 cm
		Lagging	Glass wool of 4 cm thickness
	Coil	Construction material	Copper
		Number of turns	46 cm
		Pipe diameter	12.6 cm
		Height	17
		Diameter	4 cm
		Pitch length	0.954 cm
		Pipe length	0.08 cm
		Pipe thickness	700 cm

and has seen widespread use in recent years. To determine whether a system design is practical, a measuring performance approach is required. With one example of conventional solar latent storage systems, the suggested method was used to analyze five design instances with various mass transit efficiency of heat transferring fluid and solar collecting regions. A three-dimensional numerical model was also created and verified by experiment to replicate the transient thermal decomposition inside the latent heat storage unit. The analysis was used to predict the temporal connection between both the storing unit's intake and outlet temperatures. The proposed technique is able for performance assessment of solar thermal energy storage systems and aid relevant professionals in optimizing the system design, according to the findings of five designed examples.

The research presented a thermal performance assessment of an integrated solar water heater. This incorporates the phase change material-carrying helical tubes [11]. The goal of this study was to increase the performance of solar water heaters. There is a template SAH-A as well as a revised model SAH-B with wax as a reduced power backup system. The model SAH-B can also be transformed into a version SAH-C, and it has a unique wax and a particulate charcoal dioxide mixture. The use of a copper helical tube as a heat storage container for the abovementioned active materials has been investigated. According to the key factors of the present employment, the model SAH-C is an economical and excellent architecture for house heating, hardwood conditioning, drying activities, and other processes. The total cost of the greatest SAH-C model is only 68 dollars.

The usage of double-tube helical tubes as a single-performing phase change (PCM) material for low-temperature thermal energy storage (LHTES) systems is proposed in this work. The study effectively verified a three-dimensional mathematical method that tackles convective dynamics during PCM melting. The frozen trend of PCM in longitudinal and lateral linear double-pipe LHTES apparatus of the same surface area will be analyzed and compared with a new similar LHTES equipment to analyze the unique LHTES design. After that, the double-pipe spherical vault's thermal efficiency was put to the test in a variety of settings. The usage of a double piping helical coil tube energy storage device is offered as a method for improving PCM dissolving in energy storage systems [12]. With the double helical-coiled tube, the optimal coil pitch for PCM melting is 2 OD. According to the study, the ignition temperature and the radiation parameter (Re) of the heat transmission medium have a significant impact on the PCM crystallization process. The ideal coil pitch for PCM melting in a double-pipe helical-coiled tube is 2 OD. According to the findings, the combustion temperature and the heat transmission medium's radiation parameter have a substantial impact on the PCM crystallization process.

The method for the design and experimental analysis of a helical coil phase in which the phase change hears the exchange for thermal energy storage is expressed in the proposed system of [13]. Heat transfer power supply replaces traditional perceptual power storage technologies. At a practically precise temperature, a phase change material (PCM) with a high heat of fusion can collect and release a significant amount of thermal energy. This increases the energy-storage device's efficiency and scalability while also extending its service life. This study designs, fabricates, and tests a prototype PCM exchanger with a helical coil tube for heat storage performance under various operating conditions. Even though the PCM is wax, the heat transmission is a mixture of propylene glycol (EG) and alcohol (HTF).

3. Materials and Methods

3.1. Apparatus and Materials. The experimental analysis is carried out by using custom-built coiled LHTS units. To a 16-turn coil, a 7 m copper piper was wounded in it and with a 12.5 cm centerline diameter. To an acrylic shell of a diameter of 17.6 cm, the coil is embedded. The side of the shell is filled with 12 kilograms of P56-58 wax. In the container, a 4 cm thick coating of wool beaker with a laminate surface was used to insulate the shells outside the surface. Table 1: illustrates the specification of LHTS units [14]. This depicts the challenges being faced that were created, and the

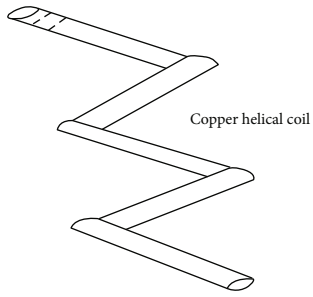

Figure 1: Copper helical coil.

following Figure 1 shows the copper helical coil. The heat transmission properties during the crystallization processes were evaluated using this setup. The LHTS was installed vertically, LHTS unit (coil and shell), 22 K-type heat temperature is linked to a information acquisition system and PC, and a 500 L electrical heating water tank, a compressor, ball joints, and an LZM calibrated flow meter (0.07 L/min uncertainties) were all included in the challenges being faced [15]. For both the crystallization procedures, tap water was utilized as the HTF, while P56-58 wax was employed as the PCM. The following Figure 1 represents the copper helical coil.

4. Experimental Setup Procedure

A TES tank with insulated spherical chaplets encased in PCM, a solar flat plate collector, a flow meter, and a rotating pump. The experimental set-up is seen via the lens of a camera. The carbon steel TES tank, which has a width of 455 meters and a thickness of 580 mm, has a volume of 95 L and can give hot water to a family of 58 people [2]. Glass wool, 50 millimeters thick, is used to protect the storage facility. The spherical container is composed of aluminum with a wall nominal thickness and a 45-millimeter internal diameter. Regarding the situation with porosity $\varepsilon = 0.49$, the overall number of carpets in the TES tank is 180. Three layers of spherical couplets are evenly packed, each held by wire mesh. When the PCM containers occupy 50% of the whole volume of the holding tank, with SHS substance occupying the remaining volume, the following Figure 2: thermal energy storage system shows the schematic diagram, and their specification is mentioned below.

4.1. Thermal Energy Storage Specification. The thermal energy storing tank was constructed based on the calculation and appropriate composition. From the copper tubes, the heat exchanger of the helical copper coil is constructed, and by using bull hose pipes, the solar collector is connected to the tank [8]. The TES tank was filled with glass wool and then covered with aluminum cladding after the leak performance test, and then the leak is arrested.

4.2. Selection of Phase Change Material. PCM Selection depends on the following parameters:

(i) Thermal assets

(ii) Physical assets

(iii) Kinetic assets

(iv) Chemical assets

Thermal assets are as follows:

(i) For a particular operation, a suitable melting point is selected

(ii) High latent melting heat per unit volume

(iii) To improve heat transfer, the thermal conductivity is high due to solid, and liquid phases are chosen

(iv) For additional sensible heat storage, higher specific heat is selected

Physical assets are as follows:

(i) Small container blocks with higher density were selected

(ii) During the phase transition, small volume is noted

(iii) To reduce the containment problems, low vapor pressure is used

Kinetic assets are as follows:

(i) During freezing no supercooling or little cooling

(ii) High nucleation and growth rates

(iii) Efficient heat transmission

Chemical assets are as follows:

(i) After a certain number of freeze/melt cycles, there is no degradation

4.3. Phase Change Material Selection. Based on the above characteristic, the wax is used as the PCM. Testing with a differential scanning calorimeter has confirmed the freezing point and thermal heat of reaction of the wax (DSC). This wax grade was chosen for the purpose, which is to supplying warm water for home use [16]. During the manufacturing of petroleum products, wax is extracted from crude oil. The oil extracted and refining level of such waxes is used to classify them. The wax offered is fully purified and includes less than 0.5 percent oil. Various characterization methods were designed to estimate the thermophysical parameters of the P56-58 wax utilized in the studies. The precision of the heat conductivity measurement was less than 5%.

The above Figure 3: DSC curve depicts the heat transfer of wax in the solid form at temperatures ranging from 25 to 45 degrees Celsius [17]. When the temperature is raised from 25-35 degrees Celsius, the heat transfer drops linearly. The curve result of the wax used in the studies may be seen here. The melting maximum temperature of the wax is between 48.3 and 62°C, with a melting energy of 114.5 kJ/kg.

By using a digital viscometer, the recommended thickness of the crude wax is measured. The liquid wax sample is then placed in a glass pipette that has been immersed in swirling boiling liquid to prevent overheating consistently

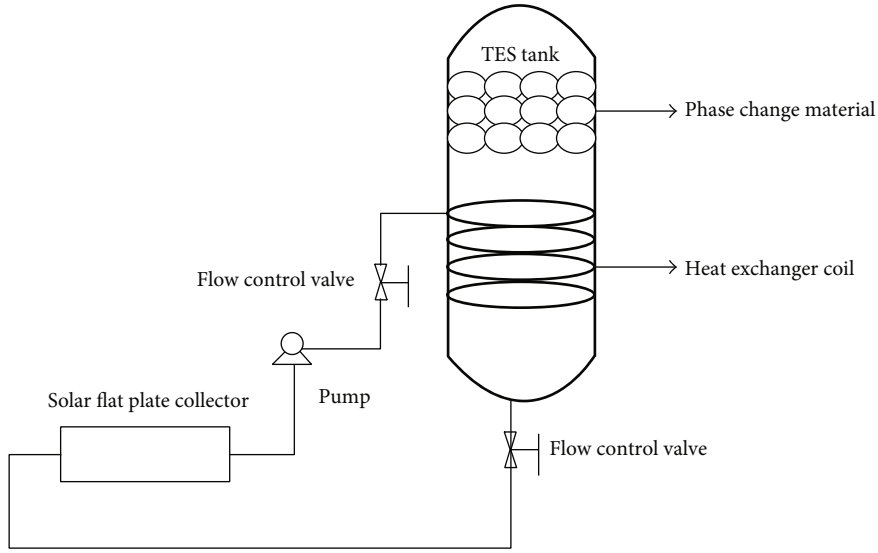

Figure 2: Thermal energy storage.

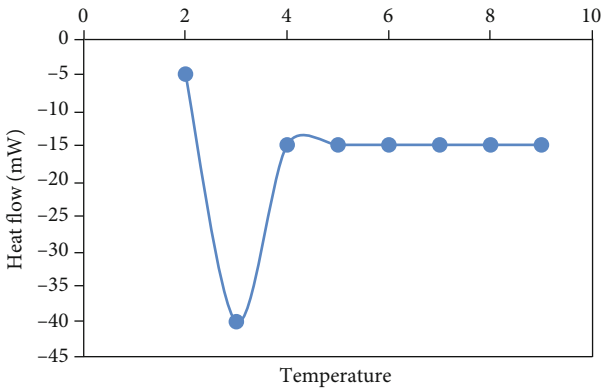

Figure 3: DSC curve.

throughout the investigation. The measurement was performed at a temperature of 53°C to 62°C at a speed of 100 revolutions per minute.

4.4. Experimental Procedure and Operating Conditions. The experimental procedure is used to investigate the temperature and flow rate of heat transfer fluid, and this affects the thermal behavior of the PCM; this is measured using the multiple heat transfer fluid. Each behavior is investigated using the phase change material and LHTS. To simulate the real-world operation of a household solar water heating system, where degrees can exceed 80°C, and to reduce water evaporation, three freezing temperatures were chosen: 65°C, 70°C, and 75°C. The crystallization method was performed out with tap water at 30°C. Multiple HTF flow rates were examined both for melting and solidification processes. For all of the testing runs, the PCM temperature was set to 30°C. Experiments were conducted in the setup depicted [18]. During the chilling phase, excess heat from the hot water was fed into the base of the Latent Heat thermal storage unit (i.e., charging). When all of the temperature measurements were above the high melting point of the phase

Table 2: Parameter of uncertainty.

Specification	Unit	Uncertainty (%)
Thermocouples	°C	±1.7
National Instrument cdaq-9175	°C	±0.080
Water volumetric flow rate	L/min	±0.26
Melting process effectiveness	*	±1.8
Solidification process effectiveness	*	±3.5

change material at the end of the recharge procedure, it was reasonable to conclude that solid PCM had already been totally changed to a liquid condition. The wax crystallization process was initiated by releasing the valves and allowing cool water to permeate the LHTS unit from the top. A digital camera was configured to detention a snapshot every single 10 minutes while the dielectric was modified to make concealing and revealing the coil LHTS unit easier during image collection. Every minute, the temperature and pressure of the crystallization operations were measured [19].

4.5. Uncertainty Analysis. In most cases, the precision of experimental results is determined by the measurement tools and techniques used. The following formula was used to analyze the uncertainty caused by several independent variables:

$$\sigma_M = \left[\left(\left(\frac{\partial M}{\partial A_1}\sigma_1\right)^2 + \left(\frac{\partial M}{\partial A_2}\sigma_2\right)^2 + \cdots\cdots \left(\frac{\partial M}{\partial A_n}\sigma_n\right)^2\right)\right]^{1/2}. \quad (1)$$

M stands for the dependent variables, which seem to be a purpose of a large number of independent variables () and is the uncertainty [20]. For this study, Eq. (1) was used to quantify the uncertainty in the efficacy of the solidification and melting process $(A_1, A_2, \cdots..A_n)$ as a purpose of time

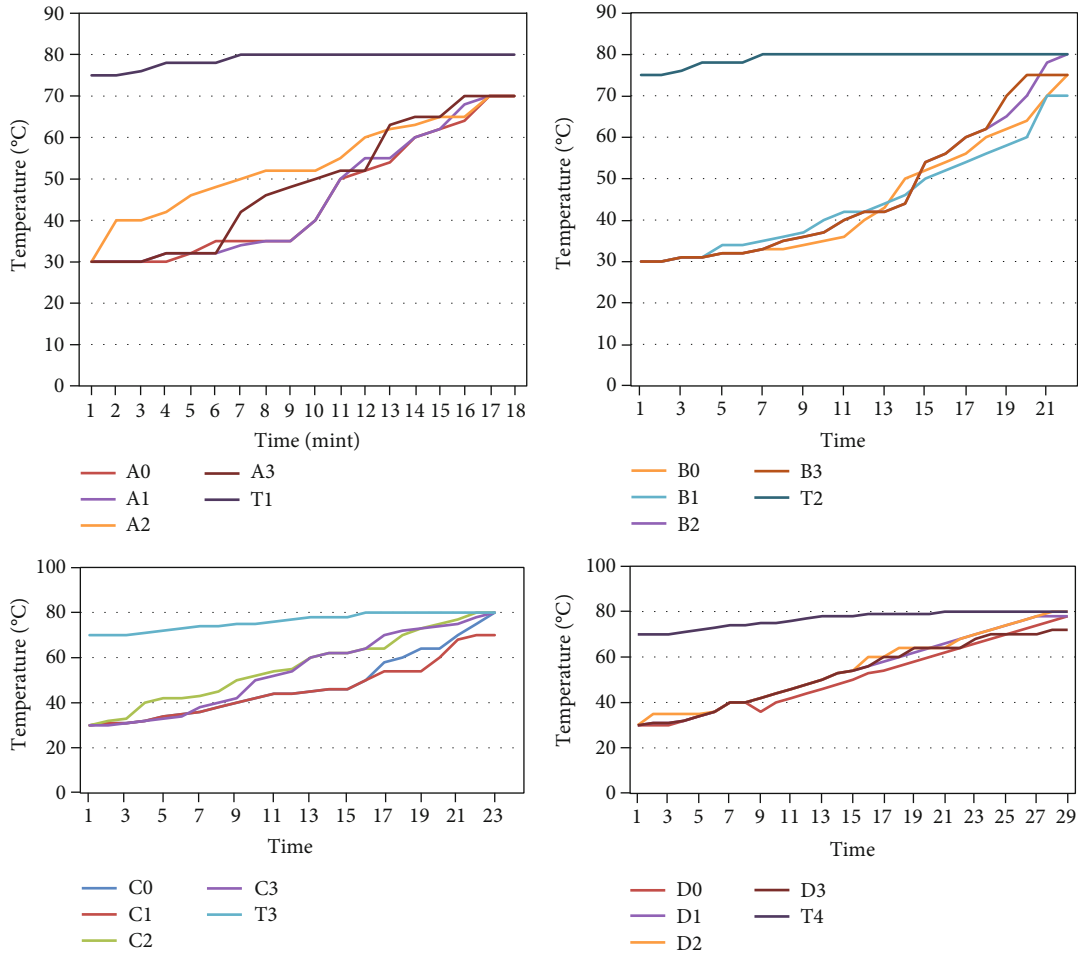

Figure 4: Phase change material temperature variation with time throughout melting time process based on different radial and axial locations along with the vertical latent heat thermal storage.

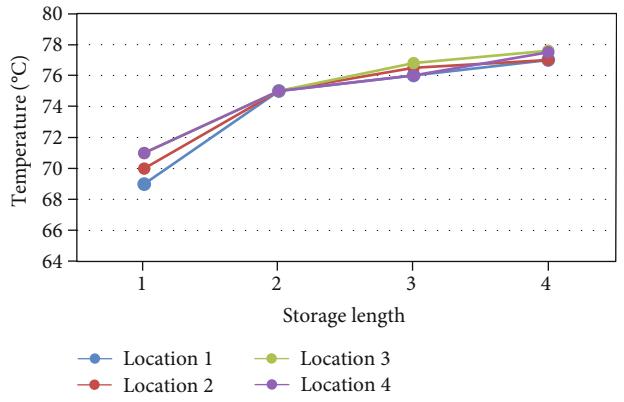

Figure 5: Local temperature.

and temperature (T), with the findings provided in Table 2: parameter of uncertainty.

$$\sigma_M = \left[\left(\left(\frac{\partial \varepsilon}{\partial T_{in}}\sigma_{Tin}\right)^2 + \left(\frac{\partial \varepsilon}{\partial T_{out}}\sigma_{out}\right)^2 + \cdots\cdots \left(\frac{\partial M}{\partial T_m}\sigma_{Tm}\right)^2\right)\right]^{1/2}, \quad (2)$$

where ε, T_{in}, T_{out}, and T_m denote the effectiveness, inlet temperature of heat transfer fluid and outlet temperature of heat transfer fluid, and finally the melting temperature of phase change material.

4.6. Melting Process. The temperatures of the PCM rise as the elevation of storing rises from the base to the tip, which is shown in the following seen graph. This has an outcome in organizations on the length of the localized crystallization process, shortening it [21]. In practice, the melted PCM rises from the bottom of the container under the force acting, generating a PCM liquid layer at the top. As a result, convection predominates at this layer compared to other regions of the store that are controlled by convection and conduction. As a result, near the top of the container, the PCM temperature rises noticeably with time, while the melting front consistently moves slowly lower, and the model provided the local PCM temperature. The time it took to complete PCM freezing at different rotational points along the storage varied between 185 minutes, 155 minutes, 125 minutes, and 90 minutes for positions L, M, N, and P correspondingly. The temperature of phase change material is visibly greater first from the centre outward, which is consistent with this

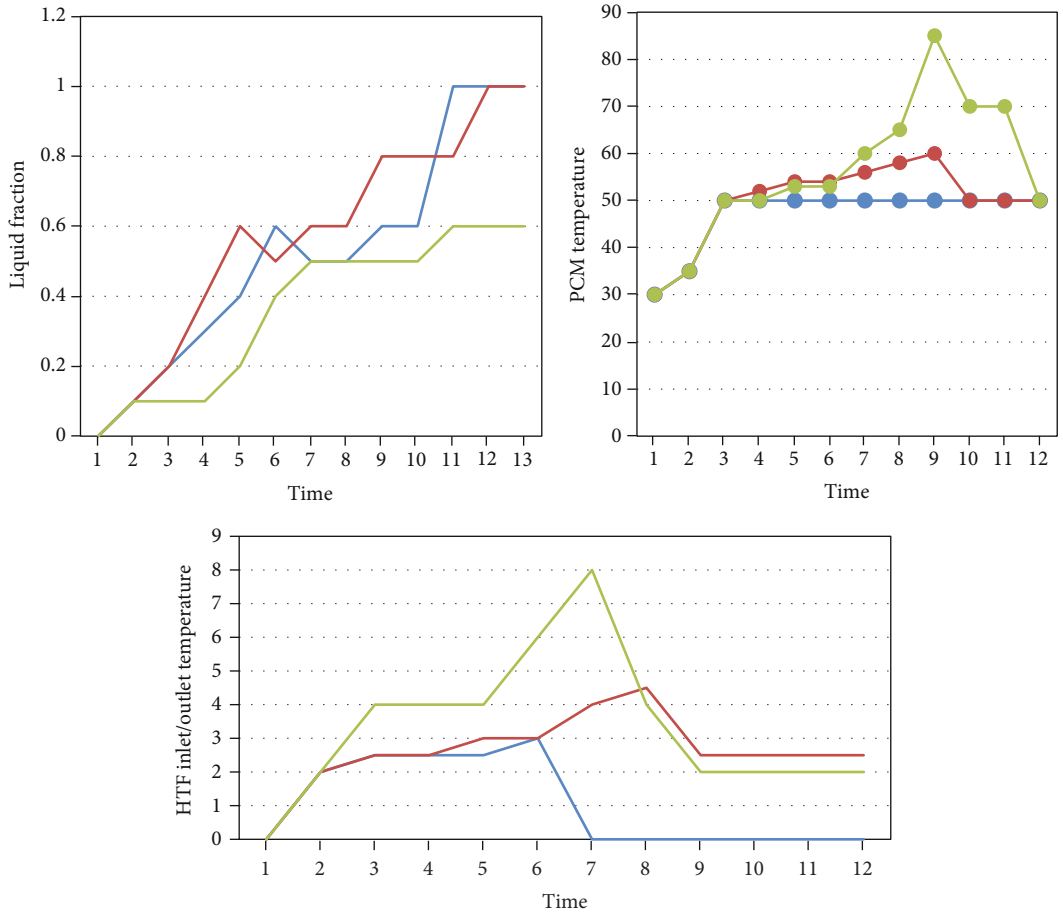

Figure 6: Mass flow rate evaluation of heat transfer fluid.

pattern [22]. The maximum PCM temperature was found near the helical surface (heat transmission surface) and the holding shell, resulting in the formation of radial dissolving fronts. Unexpectedly, when other places have fully melted, the observed temperatures of the PCM for the locations closest to the storing centre significantly increase. The high convection that accompanied the radial and axial two meltdown fronts may cause effect on the temperature. The coil turn at axial locations M, N, and P is closer to radial location 2 than site 3, resulting in inconsistencies in the observed PCM degrees at radial locations 2 and 3, as illustrated in subfigures M, N, and P.

4.7. Solidification Process. The feasibility of energy storage must be investigated during the charging and discharging periods. Using a steady HTF temperature (30) and various flow rates (1 L/min, 3 L/min, and 5 L/min), the discharging (solidification) phase is explored immediately after the conclusion of the blistering phase in this study. Throughout this section of the studies, the very same arrangement and several temperature sensors were used. Along with the storage, the temperatures of the PCM began to drop [21]. At the start of the solidifying process, the PCM temperatures along the radial and axial locations both dropped sharply and equally. As a result, the entire operation is governed by convective during this brief period. Following that, temperature variations become largely dependent on the thermocouple's radial position, indicating the creation of PCM solidifies. Along with the storage, the temperatures of the PCM began to drop [23]. At the start of the solidification process, the PCM temperature along the radial and axial locations both dropped sharply and equally. As a result, the entire operation is governed by convective during this brief period. Following that, temperature variations become largely dependent on the thermocouple's radial position, indicating the creation of PCM solidifies.

5. Result and Discussion

The experimental findings of the PCM crystallization process in a vertical helical type LHTS unit under various operating conditions are reported in this section. Figure 4: variation of temperature of PCM displays the value of PCM during the melting process at each radial distance (0, 1, 2, 3) and axial position (L, M, N, and P) all along the column at a consistent HTF rate of flow (3 L/min) and beginning temperature 80°C. Generally, the heating temperature of the PCM changes to increase throughout the melting process at all points along the storing elevation, with different behaviors according to the position. In all circumstances, the temperature goes up immediately at the start of the crystallization process and then gradually rises again until the

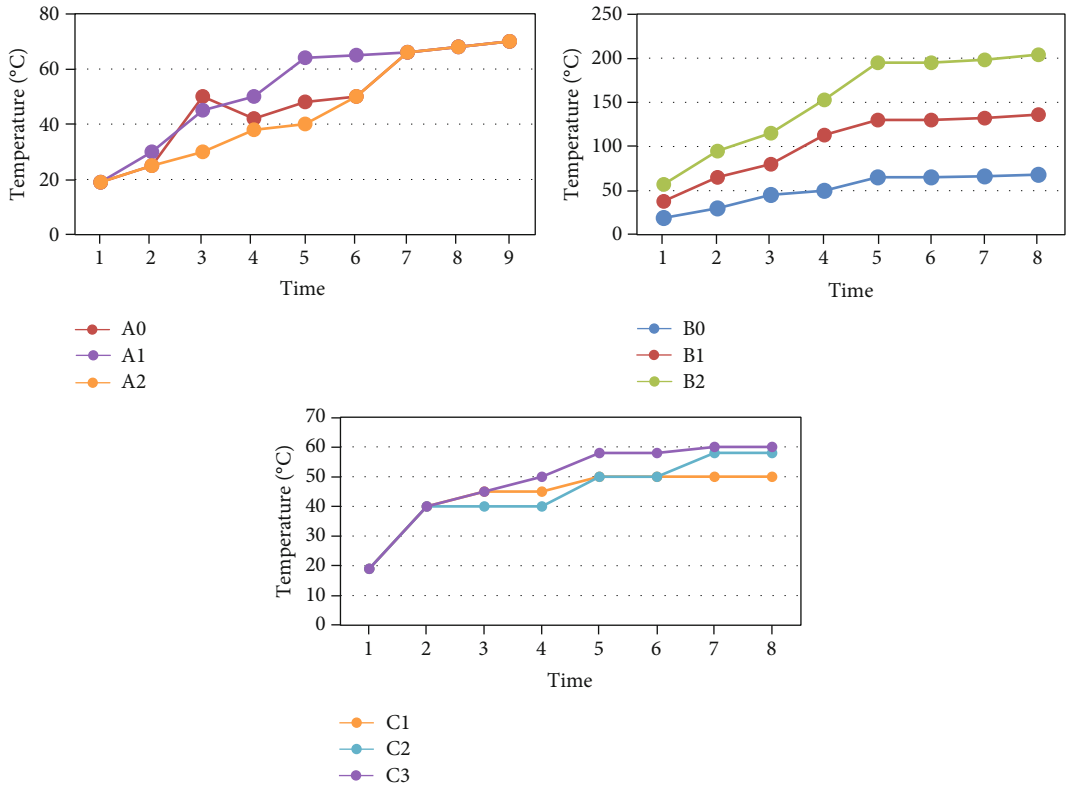

Figure 7: Temperature profile of helical coil latent heat storage.

phase is terminated. The degree of melting PCM, on the other hand, largely depends on the radius for a particular axial site. The greater the longitudinal position, the higher the temperature of PCM, according to consistent.

The following Figure 5: local temperature of PCM shows the temperature of a system of the PCM at the termination of the melting process about the storing elevation for just a temperature difference of 80°C and a rate of flow of 3 L/min. From the base of the container towards the high, it is evident that the heating of the PCM rises with elevation. This temperature rise, though, is large at the base and then increases slightly.

Moreover, the difference in temperature at different points all along storage elevation appears to be more pronounced at the bottom of the warehouse and afterward fades because as store length increased. The PCM local weather's action, on the other hand, is uniform throughout all radial sites.

5.1. Mass Flow Rate Evaluation of Heat Transfer Fluid. For each case, the entire charging process can be loosely broken down into four categories: For instance, in case 1 (mf = 0.028 kg/s), throughout the first stage (10 : 0012 : 00), when the cooling process did not take place and the PCM stored the power in the reasonable form, the liquid fraction remained zero, and the PCM heating rate increased rapidly from 30°C to 47.6°C, resulting in a low rate of heat transfer between both the HTF and PCM. The temperatures in the HTF intake rapidly climbed from 30°C to about 52.7°C (Figure 6: mass flow rate evaluation of heat transfer fluid). The temperature differential between the HTF input and output temperature grew from 0°C to 3.1°C when solar energy and ambient temperature were increased.

5.2. Comparison of Melting Behavior. Different calculated temperatures of the PCM during charging are monitored by a series of sensor thermocouples. Figure 7 shows only the outcomes found at a heat transfer fluid inlet temperature of 75°C for brevity. The charging period increased all of the temperature curves.

The curves' overall behavior entails a relatively straightforward rise in temperature at the beginning of the procedure. This observation indicates that the PCM was solid and heated by dispersion at the temperature needed to conduct, despite the PCM's weak heat capacity. The depending on the temperature fluctuations decreases as the freezing process begins once the temperature at that area approaches the PCM freezing maximum temperature of 48°C.

6. Conclusion

Experimentally, the thermal efficiency of helically coiled latent heat thermal energy storage was examined. The processes of melting and solidification were both explored. In both procedures, wax was used as a PCM, and tap water at various flow rates was employed, whereas three different HTF temperatures were used just in the melting phase. Only one HTF starting temperature is employed in the solidification process. The research defines the different processes involved in the solar energy application and their performance during the investigation process. To evaluate the

melting behavior of conical and helical coil LHSUs, they were tested concurrently. In addition, the influence of HTF inlet temperature was investigated. Temperature curves, heat outlines, and photos acquired to track its melting front while recharging has been used to evaluate their thermal efficiency.

Data Availability

The data used to support the findings of this study are included within the article.

Conflicts of Interest

The authors declare that there is no conflict of interest regarding the publication of this article.

Acknowledgments

The authors would like to express their gratitude towards Saveetha School of Engineering, Saveetha Institute of Medical and Technical Sciences (formerly known as Saveetha University) for providing the necessary infrastructure to carry out this work successfully. The authors are thankful to the Researchers Supporting Project (RSP-2021/129), King Saud University, Riyadh, Saudi Arabia.

References

[1] V. Saydam, M. Parsazadeh, M. Radeef, and X. Duan, "Design and experimental analysis of a helical coil phase change heat exchanger for thermal energy storage," *Journal of Energy Storage*, vol. 21, pp. 9–17, 2019.

[2] M. Fadl and P. Eames, "Thermal performance analysis of the charging/discharging process of a Shell and horizontally oriented multi-tube latent heat storage system," *Energies*, vol. 13, no. 23, p. 6193, 2020.

[3] E. Vengadesan and R. Senthil, "A review on recent development of thermal performance enhancement methods of flat plate solar water heater," *Solar Energy*, vol. 206, pp. 935–961, 2020.

[4] G. Ramkumar, S. Sahoo, T. M. Amirthalakshmi et al., "A short-term solar photovoltaic power optimized prediction interval model based on FOS-ELM algorithm," *International Journal of Photoenergy*, vol. 2021, Article ID 3981456, 12 pages, 2021.

[5] M. Delgado, A. Lázaro, J. Mazo, C. Peñalosa, P. Dolado, and B. Zalba, "Experimental analysis of a low cost phase change material emulsion for its use as thermal storage system," *Energy Conversion and Management*, vol. 106, pp. 201–212, 2015.

[6] V. Safari, H. Abolghasemi, and B. Kamkari, "Experimental and numerical investigations of thermal performance enhancement in a latent heat storage heat exchanger using bifurcated and straight fins," *Renewable Energy*, vol. 174, pp. 102–121, 2021.

[7] D. S. Mehta, K. Solanki, M. K. Rathod, and J. Banerjee, "Influence of orientation on thermal performance of shell and tube latent heat storage unit," *Applied Thermal Engineering*, vol. 157, article 113719, 2019.

[8] R. Anish, V. Mariappan, M. M. Joybari, and A. M. Abdulateef, "Performance comparison of the thermal behavior of xylitol and erythritol in a double spiral coil latent heat storage system," *Thermal Science and Engineering Progress*, vol. 15, article 100441, 2020.

[9] M. Ayyappan, M. Gajendran, A. Balasubramanian, J. Venkatesan, and N. Nallusamy, "Performance of latent heat soloar thermal energy storage system," *International Journal of Applied Engineering Research*, 2015.

[10] Y. Wang, X. Yang, T. Xiong, W. Li, and K. W. Shah, "Performance evaluation approach for solar heat storage systems using phase change material," *Energy and Buildings*, vol. 155, pp. 115–127, 2017.

[11] A. Saxena, N. Agarwal, and E. Cuce, "Thermal performance evaluation of a solar air heater integrated with helical tubes carrying phase change material," *Journal of Energy Storage*, vol. 30, article 101406, 2020.

[12] M. S. Mahdi, H. B. Mahood, J. M. Mahdi, A. A. Khadom, and A. N. Campbell, "Improved PCM melting in a thermal energy storage system of double-pipe helical-coil tube," *Energy Conversion and Management*, vol. 203, article 112238, 2020.

[13] I. Krupa, G. Miková, and A. Luyt, "Phase change materials based on low-density polyethylene/paraffin wax blends," *European Polymer Journal*, vol. 43, no. 11, pp. 4695–4705, 2007.

[14] S. K. Natarajan, S. K. Sahu, and A. Singh, "Thermal performance of a salt gradient non-convective solar pond in subtropical region climatic conditions," *IOP Conference Series: Earth and Environmental Science*, vol. 312, no. 1, article 012019, 2019.

[15] M. Rahimi, S. S. Ardahaie, M. Hosseini, and M. Gorzin, "Energy and exergy analysis of an experimentally examined latent heat thermal energy storage system," *Renewable Energy*, vol. 147, pp. 1845–1860, 2020.

[16] S. Salyan, B. Praveen, H. Singh, S. Suresh, and A. S. Reddy, "Liquid metal gallium in metal inserts for solar thermal energy storage: a novel heat transfer enhancement technique," *Solar Energy Materials and Solar Cells*, vol. 208, article 110365, 2020.

[17] S. H. Madaeni, R. Sioshansi, and P. Denholm, "How thermal energy storage enhances the economic viability of concentrating solar power," *Proceedings of the IEEE*, vol. 100, no. 2, pp. 335–347, 2012.

[18] I. Dincer and M. A. Rosen, *Thermal Energy Storage Systems and Applications*, John Wiley & Sons, 2021.

[19] F. Manenti and Z. Ravaghi-Ardebili, "Dynamic simulation of concentrating solar power plant and two-tanks direct thermal energy storage," *Energy*, vol. 55, pp. 89–97, 2013.

[20] S. Kuravi, J. Trahan, D. Y. Goswami, M. M. Rahman, and E. K. Stefanakos, "Thermal energy storage technologies and systems for concentrating solar power plants," *Progress in Energy and Combustion Science*, vol. 39, no. 4, pp. 285–319, 2013.

[21] N. Ridzuan, F. Adam, and Z. Yaacob, "Evaluation of the inhibitor selection on wax deposition for Malaysian crude oil," *Petroleum Science and Technology*, vol. 34, no. 4, pp. 366–371, 2016.

[22] K. Pielichowska and K. Pielichowski, "Phase change materials for thermal energy storage," *Progress in Materials Science*, vol. 65, pp. 67–123, 2014.

[23] M. Zaky, F. Soliman, and A. Farag, "Influence of paraffin wax characteristics on the formulation of wax-based binders and their debinding from green molded parts using two comparative techniques," *Journal of Materials Processing Technology*, vol. 209, no. 18–19, pp. 5981–5989, 2009.

Hindawi
International Journal of Photoenergy
Volume 2022, Article ID 3559837, 7 pages
https://doi.org/10.1155/2022/3559837

Research Article

A Novel Approach in Hybrid Energy Storage System for Maximizing Solar PV Energy Penetration in Microgrid

T. M. Amirthalakshmi,[1] **S. Ramesh**,[2] **R. Thandaiah Prabu**,[3] **G. Ramkumar**,[3] **Satyajeet Sahoo**,[4] **Prince Thomas**,[5] **R. Jothi Ramalingam**,[6] **Hamad Al-Lohedan**,[6] **Dhaifallah M. Al-Dhayan**,[6] **and Shanmugam Sureshkumar**[7]

[1]*Department of Electronics and Communication Engineering, Rajalakshmi Institute of Technology, Chennai, Tamil Nadu, India*
[2]*Department of Electronics and Communication Engineering, St. Mother Theresa College of Engineering, Vagaikulam, 628102 Tamil Nadu, India*
[3]*Department of Electronics and Communication Engineering, Saveetha School of Engineering, SIMATS, Chennai, 602 105 Tamil Nadu, India*
[4]*Department of Electronics and Communication Engineering, Vignan's Foundation for Science, Technology and Research (Deemed to Be University), Vadlamudi, Guntur, Andra Pradesh 522213, India*
[5]*School of Computing, Woldia Institute of Technology, Woldia University, Woldia, Ethiopia*
[6]*Chemistry Department, College of Science, King Saud University, P.O. Box. 2455, Riyadh 11451, Saudi Arabia*
[7]*Department of Animal Resources Science, Dankook University, 119, Dandae-ro, Cheonan 31116, Republic of Korea*

Correspondence should be addressed to T. M. Amirthalakshmi; amirthatm@gmail.com and Prince Thomas; prince.t@wldu.edu.et

Received 9 November 2021; Revised 14 December 2021; Accepted 17 December 2021; Published 22 January 2022

Academic Editor: V. Mohanavel

Copyright © 2022 T. M. Amirthalakshmi et al. This is an open access article distributed under the Creative Commons Attribution License, which permits unrestricted use, distribution, and reproduction in any medium, provided the original work is properly cited.

Nowadays, energy storage system is utilized in many countries for energy planning in the future. The changes in solar radiation lead to the overproduction of electricity in a solar photovoltaic generator. A hybrid energy storage system would play an important role in enhancing the reliability of power generation using the solar system. The microgrid is the indispensable infrastructure of the smart grid in photovoltaic systems. In this paper, the energy storage system within the microgrid of the PV system is analysed. The storage system configuration and topologies of the microgrid are analysed with power electronic interference, control scheme, and optimization of the renewable source and energy storage system. A general sizing technique for HESS in a PV system based on pinch analysis and design space. The size of HESS scales that connect generator ratings to storage capacity is created by utilizing the pinch analysis on load and resource data. The design space is a feasible combination of a short-, long-, and medium-sized energy storage system in a PV generator.

1. Introduction

Due to increasing fossil fuel shortage and environmental pressures, new generation high-efficiency sources such as fuel cells and microgas turbines, as well as renewable energy sources (RESs) such as wind and solar power, are rapidly becoming the most significant Distributed Energy Resources (DERs) today. Distributed and renewable energy sources will account for a growing share of total electric power generation [1]. With a growing trend, renewable energy sources have been widely employed to meet electrical energy demands and minimise greenhouse gas emissions. The intermittent nature of renewable energy sources has a negative impact on power generation, posing a problem for ensuring an uninterrupted and consistent supply of electricity to consumers and endangering grid operations in terms of many operational and technical aspects [2, 3].

The local reliability and flexibility of the electric power system is improved with the microgrid (MG), which includes the DER and energy storage unit [4]. A MG in

combination with renewable energy sources (RES) and distributed generation (DGs) sources might be a better answer to rising energy problems and accompaniment to today's centralized contemporary power grids. Due to their limited capacity, MGs' regular operation may be subject to random power exchange between the provider and the loads, making operational capability and power quality difficult to ensure [5, 6].

The RES energy output will fluctuate because to the strong reliance of many RES and DGs on climatic and meteorological conditions, particularly for a localised small-capacity MG with more than 10% of the RES occupation. ES is now the most important piece of equipment in an MG since it is a clever approach to mitigate potential power fluctuations and handle difficult demand-supply imbalance issues [7]. The term Distributed Energy Resources (DER) refers to nonrenewable and renewable energy systems. Distributed generation systems distribute electricity across the electrical network by using smaller generators that are closer to the loads. DER systems, unlike traditional distribution systems, use a variety of sources and loads to provide power which is required for the power network to deal with uncontrolled generators. When multiple uncontrolled sources are added to the electrical system, various technical issues, including power quality [8].

Solar PV electricity uses the sun as fuel, which, although abundant, is unpredictable. As a result, the output power of these systems fluctuates and is proportional to the sun's unpredictability [9]. The quantity of energy generated by a solar power system will change as the amount of sun radiation varies. Because the voltage on the medium-voltage network is always rigorously regulated, the concerns with PV and wind power penetration may be restricted to low-voltage networks [10]. This paper analyses energy storage system within the microgrid of the PV system. The storage system configuration and topologies of the microgrid are analysed with power electronic interference, control scheme and optimization of the renewable source and energy storage system. A general sizing technique for HESS in a PV system based on pinch analysis and design space.

2. Related Works

2.1. Technical Problem with Grid PV System. The power quality is the significant problem in the PV microgrid. From the customer's perspective as well as the utility's, power quality is critical. The power systems are made to run on a sinusoidal voltage with a certain voltage and frequency [8]. The issue in power quality is defined as any substantial change in the frequency, voltage magnitude, or purity of the waveform. The microprocessor-based controller is used in recent electrical equipment, and power electronic devices are more sensitive to voltage fluctuations [11].

Variations in solar radiation create variations in the operating point of solar cells, i.e., operating voltage and current. The voltage can be regulated because of power supply system with no current, every effort must be made to keep the voltage within a set and acceptable range to ensure that PV generators connected to distribution networks do not degrade power quality [12].

When there is a large concentration of roof-top PV systems, the instantaneous power output can occasionally surpass the immediate power consumption [13]. As a result of the power imbalance, power flows to the low voltage transformer, which forms the medium voltage transformer, suggesting that net power flows backwards to low-voltage transformers from the medium voltage. As a result, determining the maximum amount of PV penetration that can be delivered into a power network without generating power system difficulties is crucial [14].

Setting a limit to maximize possibilities is significant, and the production of harmonics by DER is another issue of concern. Solar PV systems produce direct current, which necessitates the installation of an inverter to connect to the electrical grid. Harmonic currents come from these inverters. Inverter technology has advanced substantially in recent years, and as a result, the number of harmonics produced by inverters has significantly decreased [15].

2.2. Advantage of Microgrid-Based Energy Storage System. The purpose of an ES element is to act as a buffer or backup in the event of a power discrepancy between both the upstream and downstream sides. This approach was first used in the early stages of power systems, such as when the DC electrical transmission system was implemented in New York City in the early 1800s. Lead-acid cells subsequently already provided energy for lighting bulbs, allowing the engines to be deenergized at night [16]. Grid-connected solar PV systems create power on demand, ensuring that electricity is delivered to the load in the most effective manner, and in many situations, the solar PV generating pattern matches the consumption pattern. The power providers and customers are attentive in dispersed generating systems, albeit from opposite perspectives, due to the benefits of the grid-connected PV. The grid-connected PV appeals to utilities because it allows them to create and sell power to their consumers over their current network. Some utilities consider large-scale grid-connected PV systems as a way to reduce the need for traditional network reinforcement. The benefit of having energy PV from the perspective of electricity consumers is that they can benefit from a standby power generation [17].

3. Materials and Methods

3.1. System Description. The microgrid with a renewable energy system consists of the DC bus and Power Electronic Converter (PEC), which is utilized to connect the microgrid subsystem. The ESS is utilized to conduct the load and power flow [16]. HESS is in the form of a battery and ultracapacitor. The voltage controller connects the microgrid with the PV panel. The layout of the microgrid system is shown in Figure 1.

The output power in PV system:

$$P_{pv} = V_{pv} \times I_{pv},$$
$$P_b = V_b \times I_b. \quad (1)$$

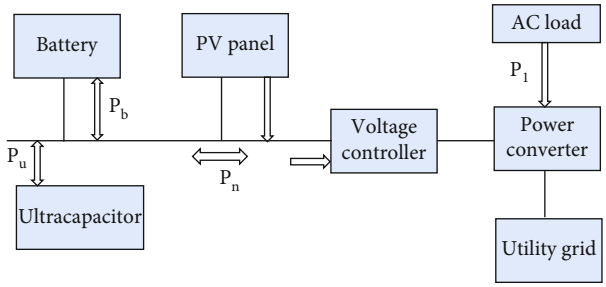

Figure 1: Layout of microgrid.

This indicates the output power and current of the battery:

$$P_c = V_c \times I_c. \quad (2)$$

This indicates the output power of the ultracapacitor. The power from the load is represented as P_l, and the power exchanged using the utility grid is P_u. The battery and ultracapacitor are utilized in the energy storage system, in which one component is not enough to conduct the changing power. The microgrid occupies little space and creates a low resistance of the line.

3.2. Hybrid Energy Storage Topologies. Different topologies can be used to link HESS to MG. To integrate HPS with HES, several topologies can be used. There are three types of power converter topologies: passive, semiactive, and active. Two storages with the same voltage are easily linked in a passive topology, which is an efficient, simple, and cost-effective architecture. The power distribution between HPS and HES units is mostly governed by internal resistances and the characteristic of voltage-current, as the storages' terminal voltage is not regulated. As a result, the HPS has a very limited amount of energy accessible, and it functions as a low pass filter for the HESS [18].

The power converter in semiactive topology is placed at the terminal of one storage system, and another storage system is connected directly to the DC bus. Although the addition of a converter increases installation space and costs, the architecture gives better controllability and dispatch capabilities. The additional converters in this architecture increase the HESS's operating range.

Active HESS topologies are made up of two or more energy storage units, connected to the storage system through a power converter separately. Although the system's losses, complexity, and cost rise, this type of topology offers certain benefits. The benefits of this setup are that all storage powers may be actively managed [19].

3.3. Energy Storage System Configuration. An ESS is an essential component of an MG's efficient operation. It provides the customer with dispatch capability of dispersed sources like solar panels and wind turbines. Along with generation sources, it is the primary contribution to balancing power demand. The collected power might be used to provide power during periods of high demand. As energy storage capacity is enhanced, manufacturing and controlling the

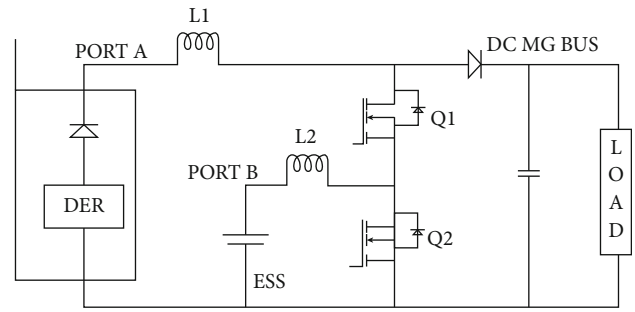

Figure 2: Power interface of energy storage system.

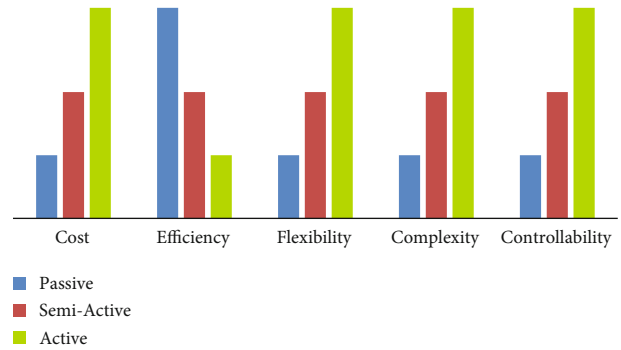

Figure 3: Comparison of HESS topologies.

ESS become more complicated and expensive. Small-scale and distributed energy storage can therefore be utilized to create flexible and efficient power control [20]. DER with various interfaces is linked with the ESS unit in the distributed ESS setup. The DC interface is required for solar PV. In general, a DC chopper is easier to use and less expensive than a DC converter. The advantage of connecting the grid with DER and ESS is that it increases the cost of electrical interference and increases efficiency. Because they only have to deal with one sort of source, these systems are usually straightforward. Before storing the electricity generated by the renewable resource, it is transported over the transmission line, offsetting the concentrated power flows on the line and the benefits of delayed line construction. Despite the fact that both the DER and ESS power electronics interfaces can be separately adjusted, with interfaces and line impedances which are connected to two facilities, losses are incurred in the storage process. MG, a combination of distributed and aggregated ESS, may be the greatest solution in the future [21].

3.4. Power Electronic Interface of Energy Storage System. Power interface of the energy storage system is shown in Figure 2. Unlike conventional converters, which only work when the primary source is accessible, the ESS interface will work continually to keep the MG operating for a long time. As a result, reliability and efficiency are the most important factors to consider while selecting converter topologies. High-frequency MG, line-frequency MG, and DC MG are the three most common forms of MG, and each requires a

Table 1: Evaluation of different HESS topologies.

Topology	Cost	Efficiency	Flexibility	Complexity	Controllability
Passive	Low	High	Low	Low	Low
Semiactive	Medium	Medium	Medium	Medium	Medium
Active	High	Low	High	High	High

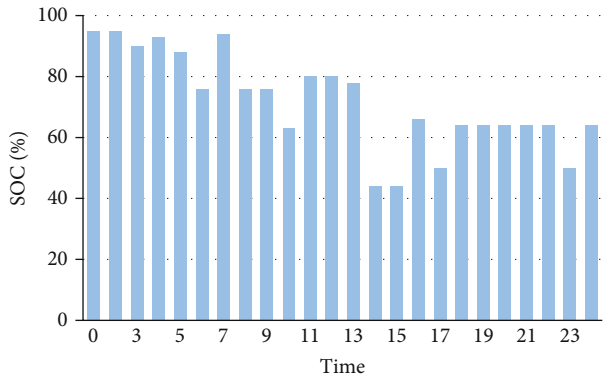

Figure 4: State of charge for ESS.

distinct approach to ESS access. For simplicity, all ESSs are considered to be DC sources because ESSs have a DC link or can be converted to DC [22].

Separate DC converters can be utilized to link DERs and ESS to the common DC bus. In comparison to the original separate converter system, the use of a combined multiport converter offers cheap cost, great efficiency, and dependability. A buck-boost converter is one of the multiport converter topologies that may be used for high-voltage ESS, whereas a boost converter can be used for low-voltage ESS. However, because the system is based on a mixture of original common elements, it is difficult to extend because there is no way to add more sources without redesigning it [23].

3.5. Hybrid Energy Storage System. Determining the right storage capacity is one of the most significant challenges in HESS applications. Various techniques for sizing storage capacity have been presented. Some techniques are created to assess the HESS capacity of a specific technology, while others may be used to size all sorts of storages independent of technology. The methodologies for sizing batteries and their applications in various RESs are examined. The overall cost of the system, as well as its dependability, should be addressed throughout the HESS sizing approach [24].

The most significant drawback of renewable energy sources is that, unlike traditional energy sources, they cannot be stored for later use. As a result, it is critical to extract as much energy as possible from them while they are still available. Furthermore, because they are dependent on the climatic conditions of the location, they cannot be guaranteed to remain constant and concentrated at all times. As a result, they are erratic and unreliable. The electricity supplied by solar PV is particularly susceptible to harmonic distortions and associated mistakes, which might impair the system's functioning, due to the highly unpredictable behaviour of solar [25].

Table 2: Impact of SOC on energy storage system.

SOC	3500 kW	10000 kW
35	0.42	0.27
45	0.42	0.29
55	0.42	0.35
65	0.42	0.45
75	0.42	0.51
85	0.442	0.53
90	0.448	0.54
95	0.45	0.55

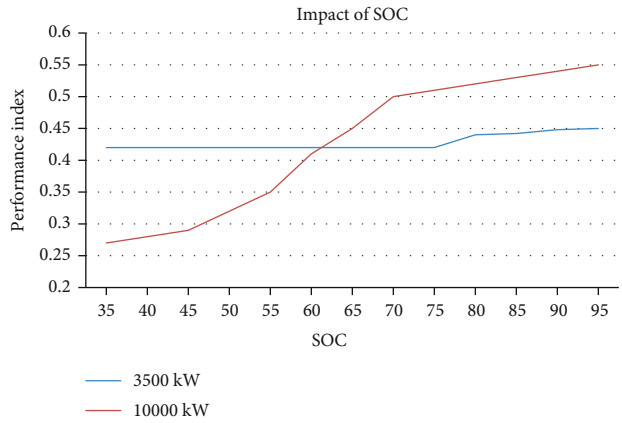

Figure 5: The performance comparison on impact of SOC with 3500 kW and 10000 kW.

In such circumstances, HESS is required to smooth out the anomalies and enhance the power quality. Controlling the power outputs and delivering ancillary services as needed are other important functions of ESS. As a result, they are an essential source of energy for achieving high levels of renewable system penetration. HESS may compensate for any power imbalance between the load and the generating units by acting as a buffer or backup. A microgrid in islanded mode will rely on HESS to maintain real and reactive power balance in the event that certain DGs fail [26].

Even if the situation is solved by load shedding or bringing up additional producing units, HESS is essential for quickly filling the power gap. ESSs are required while the MG is in grid-connected mode in order to preserve power quality and manage reactive power. The HESS scaling techniques may change depending on the HESS application's objective. The capacity size is determined using the pinch analysis approach.

Table 3: Comparison of ESS with power interface.

SOC	ESS		ESS with power interface	
	3500 kW	10000 kW	3500 kW	10000 kW
35	0.415	0.28	0.46	0.35
45	0.415	0.3	0.465	0.38
55	0.415	0.35	0.47	0.4
65	0.42	0.4	0.475	0.42
75	0.43	0.45	0.48	0.48
85	0.45	0.5	0.49	0.49
95	0.455	0.55	0.495	0.495

3.6. Pinch Analysis. Pinch analysis is a straightforward and adaptable technique for evaluating the lowest energy locations in a utility heat exchanger network. This technique is a substantially light technique that can be employed in a renewable microgrid [27]. In HESS implementations, pinch analysis is used. This strategy is based on variations in energy storage generation, load, and discharge times. Sizing curves for varying intervals scales are calculated by applying PAM to resource and load information. The produced curve denotes a set of data storage that is viable for the given time scale. Pinch analysis has proven to be effective in saving a variety of resources. Pinch analysis tools are used to develop isolated energy systems. The need of setting targets before designing is recognised by pinch analysis. This enables multiple process design objectives to be assessed before the process is designed in detail. Pinch analysis also provides diagrammatic tools to the system architect for easier visualisation and management over decision-making processes. Pinch analysis tools can be used to solve generalised resource conservation challenges by distributing generalised flows from various sources to various needs while satisfying generalised quality criteria [28].

3.7. Power Control System. A hybrid ESS's control method is substantially more difficult. Power system redistribution and ESS properties should be examined in relation to personal charge/discharge. When battery and supercapacitors are used to meet load requirements, for example, ultracapacitors can give faster response with peak power with than the battery, but they last less time. As a result, the batteries drain or charge slowly and surely, supercapacitors can control excess intermediate and strong and decisive battery current. Both the battery and the supercapacitors must be controlled by two separate loops in this situation. Batteries/supercapacitors must be recharged or drained according to the manufacturer's instructions in order to accomplish a long lifespan, maximum power, and maximum efficiency [29]. Traditional lead-acid batteries, for example, necessitate a lengthy low-current charge to eliminate sulfation from the lead plates. The rechargeable ESS can be recharged frequently while adjusting for MG Power fluctuations (SOC). When a device is less than totally depleted and so less than entirely recharged before even being drained again, it is known as the SOC operation with low output. The charge and discharge concerns are addressed by designing a sophisticated battery/supercapacitor management system. The two most common charge modes in energy storage devices are constant current and constant voltage. Constant power charging uses the periodic state-feedback control strategy, whereas constant power charging utilizes voltage or current double-loop control. A voltage or current double-loop technique is also required for ESS discharging control. Many advanced control approaches, including neural network, fuzzy control, and self-adaptive control which perform well for discharging and charging highly nonlinear behavior of the starting to charge process. Variation in cell parameters, uneven charging, connection between discharging process, ESS ageing problems, and other issues should all be carefully examined [30].

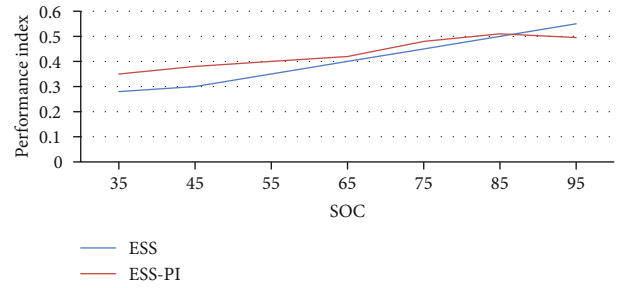

Figure 6: Performance comparison of energy storage system with power interface (10000 kW).

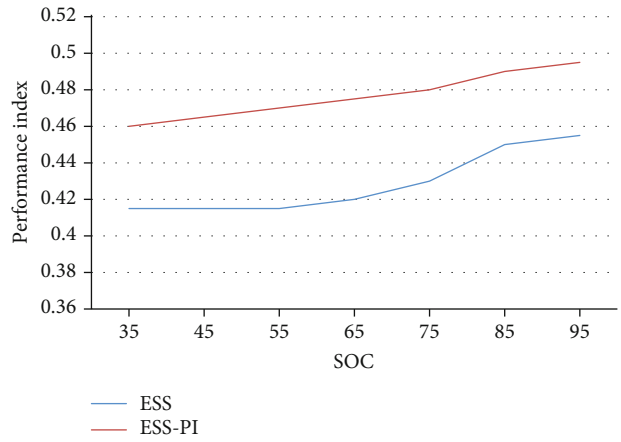

Figure 7: Performance comparison of ESS with power interface (3500 kW).

Table 4: Comparison of power capacity and confidence level.

Power capacity	Confidence level (%)
100	60
200	94
400	96
500	97
600	98

4. Result and Discussion

4.1. Comparison of HESS Topologies. The topology of the HESS has a direct influence on the energy storage approach.

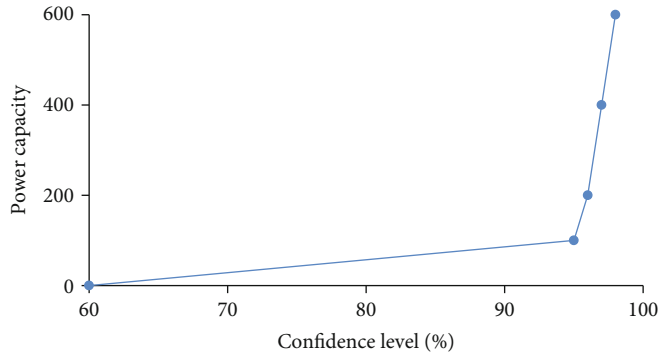

Figure 8: Power capacity of HESS at different confidence levels.

The power stored in a passive topology has no direct control. The storage of one output power is uncontrolled in the semi-active architecture. The active structure uses a rational control method to manage the outgoing or incoming power including both storages, albeit at the cost of lesser efficiency. Expenses, effectiveness, predictability, complexity, and adaptability should all be considered while choosing the right topology. The HESS topologies are compared in Figure 3 from various operational perspectives. The passive topology is modest and low cost, but it is uncontrollable. The active topology performs best at the moment of flexibility and controllability while taking into consideration inherent limitations such as SoC, but it comes with a high efficiency. Table 1 shows the evaluation of different HESS topologies.

Figure 4 illustrates the HESS's SOC and the storage scheduling system for the initial load requirement, which includes charging and discharging choices. With the availability of information, the energy storage problem is no longer dynamic, and each hour of the schedule period may be improved independently. Table 2 illustrates the impact of SOC on ESS.

Figure 5 illustrates the performance comparison on impact of SOC. The HESS performance is better with increase in the state of charge level. The system with a larger battery size had a performance index that was more sensitive to variations in SOC. Comparison of ESS with the power interface is shown in Table 3.

Figures 6 and 7 illustrate the variation in the size of battery and the initial state of charge which provide better performance in the energy storage system with power interference compared to the normal energy storage system. While initial SOC was raised, ESS-PI was able to achieve greater performance in a smooth and consistent manner. However, until the SOC level reached a specific amount, ESS did not work properly. Furthermore, as can be seen, the ESS-PI performance index when considering battery life is greater than the PI value, indicating that ESS-PI performs better while charging and discharging the battery, allowing the battery to survive longer. Comparison analysis result for various power capacities with confidence level is represented in Table 4.

The power capacities of HESS can be estimated by calculating the confidence level, in which the confidence level has a significant effect on the life cycle of the ES in the microgrid system which is shown in Figure 8.

5. Conclusion

In this paper, the energy storage system within the microgrid of the PV system is analysed. The storage system configuration and topologies of the microgrid are analysed with the power electronic interference, control scheme, and optimization of the renewable source and energy storage system. Typical sizing technique for HESS in PV system based on pinch analysis and design space. The sizes of HESS scales that connect generator ratings to storage capacity are created by utilizing the pinch analysis on the load and resource data. The energy storage system for the microgrid system is demonstrated, and the impact of the state of charge and power control system with the load demand is analysed. The energy storage system with power interference system in the microgrid provides better performance compared to the energy storage system without power interference. The performance of HESS is sensitive to change in the state of charge. The HESS with a higher battery size maintains the high performance of the microgrid.

Data Availability

The data used to support the findings of this study are included within the article.

Conflicts of Interest

The authors declare that there is no conflict of interest regarding the publication of this article.

Acknowledgments

The authors would like to express their gratitude towards Rajalakshmi Institute of Technology for providing the necessary infrastructure to carry out this work successfully. The authors are thankful for the financial support by the Researchers Supporting Project Number (RSP-2021/354), King Saud University, Riyadh, Saudi Arabia.

References

[1] E. Marrasso, C. Roselli, and M. Sasso, "Electric efficiency indicators and carbon dioxide emission factors for power generation by fossil and renewable energy sources on hourly basis," *Energy Conversion and Management*, vol. 196, pp. 1369–1384, 2019.

[2] R. M. Elavarasan, "The motivation for renewable energy and its comparison with other energy sources: a review," *European Journal of Sustainable Development research*, vol. 3, no. 1, article ???, 2019.

[3] S. Ramesh, P. Nirmala, G. Ramkumar et al., "Simulation process of injection molding and optimization for automobile instrument parameter in embedded system," *Advances in Materials Science and Engineering*, vol. 2021, Article ID 9720297, 10 pages, 2021.

[4] M. C. Pulcherio, A. A. Renjit, M. S. Illindala et al., "Evaluation of control methods to prevent collapse of a mixed-source microgrid," *IEEE Transactions on Industry Applications*, vol. 52, no. 6, pp. 4566–4576, 2016.

[5] B. Khan and P. Singh, "Optimal power flow techniques under characterization of conventional and renewable energy sources: a comprehensive analysis," *Journal of Engineering*, vol. 2017, Article ID 9539506, 16 pages, 2017.

[6] S. Sahoo, A. Gopalan, S. Ramesh et al., "Preparation of polymeric nanomaterials using emulsion polymerization," *Advances in Materials Science and Engineering*, vol. 2021, Article ID 1539230, 9 pages, 2021.

[7] G. Ramkumar, S. Sahoo, G. Anitha et al., "An unconventional approach for analyzing the mechanical properties of natural fiber composite using convolutional neural network," *Advances in Materials Science and Engineering*, vol. 2021, Article ID 5450935, 15 pages, 2021.

[8] N. A. A. H. M. Amleh, *Impacts of energy storage and smart restoration on the reliability of electric microgrid, [Ph.D. thesis]*, King Fahd University of Petroleum and Minerals (Saudi Arabia), 2016.

[9] P. Nirmala, G. Ramkumar, S. Sahoo et al., "Artificial intelligence to analyze the performance of the ceramic-coated diesel engine using digital filter optimization," *Advances in Materials Science and Engineering*, vol. 2021, Article ID 7663348, 10 pages, 2021.

[10] Y. Xing, H. Zhao, Z. Shen et al., "Optimal coordinated energy management in active distribution system with battery energy storage and price-responsive demand," *Mathematical Problems in Engineering*, vol. 2021, Article ID 6620550, 12 pages, 2021.

[11] T. Khatib and L. Sabri, "Grid impact assessment of centralized and decentralized photovoltaic-based distribution generation: a case study of power distribution network with high renewable energy penetration," *Mathematical Problems in Engineering*, vol. 2021, Article ID 5430089, 16 pages, 2021.

[12] B. Jain, S. Singh, S. Jain, and R. Nema, "Flexible mode control of grid connected wind energy conversion system using wavelet," *Journal of Energy*, vol. 2015, Article ID 152898, 12 pages, 2015.

[13] R. J. C. Pinto, S. J. Pinto Simões Mariano, and M. D. R. A. Calado, "Power quality experimental analysis on rural home grid-connected PV systems," *International Journal of Photoenergy*, vol. 2015, Article ID 791680, 8 pages, 2015.

[14] V. A. Ani, "Design of a reliable hybrid (PV/diesel) power system with energy storage in batteries for remote residential home," *Journal of Energy*, vol. 2016, Article ID 6278138, 16 pages, 2016.

[15] K. A. Alboaouh and S. Mohagheghi, "Impact of rooftop photovoltaics on the distribution system," *Journal of Renewable Energy*, vol. 2020, Article ID 4831434, 23 pages, 2020.

[16] O. O. Mengi and I. H. Altas, "A new energy management technique for PV/wind/grid renewable energy system," *International Journal of Photoenergy*, vol. 2015, Article ID 356930, 19 pages, 2015.

[17] D. Duncan, A. M. Zungeru, M. Mangwala et al., "Power-efficient hybrid energy storage system for seismic nodes," *Journal of Engineering*, vol. 2020, Article ID 3652848, 21 pages, 2020.

[18] O. Singh, A. Iqbal, S. Kumar, and S. K. Rajput, "Hybrid renewable energy system integration in the micro-grid: Indian context," in *2016 International Conference on Control, Computing, Communication and Materials (ICCCCM)*, pp. 1–5, Allahbad, India, 2016.

[19] T. Adefarati and R. Bansal, "Integration of renewable distributed generators into the distribution system: a review," *IET Renewable Power Generation*, vol. 10, no. 7, pp. 873–884, 2016.

[20] S. Singh, M. Singh, and S. C. Kaushik, "Optimal power scheduling of renewable energy systems in microgrids using distributed energy storage system," *IET Renewable Power Generation*, vol. 10, no. 9, pp. 1328–1339, 2016.

[21] R. Xiong, H. Chen, C. Wang, and F. Sun, "Towards a smarter hybrid energy storage system based on battery and ultracapacitor - A critical review on topology and energy management," *Journal of Cleaner Production*, vol. 202, pp. 1228–1240, 2018.

[22] T. Zimmermann, P. Keil, M. Hofmann, M. F. Horsche, S. Pichlmaier, and A. Jossen, "Review of system topologies for hybrid electrical energy storage systems," *Journal of Energy Storage*, vol. 8, pp. 78–90, 2016.

[23] Q. Li, F. Zhou, F. Guo, F. Fan, and Z. Huang, "Optimized energy storage system configuration for voltage regulation of distribution network with PV access," *Frontiers in Energy Research*, vol. 9, 2021.

[24] M. G. Molina, "Energy storage and power electronics technologies: a strong combination to empower the transformation to the smart grid," *Proceedings of the IEEE*, vol. 105, no. 11, pp. 2191–2219, 2017.

[25] J. Li, R. Xiong, Q. Yang, F. Liang, M. Zhang, and W. Yuan, "Design/test of a hybrid energy storage system for primary frequency control using a dynamic droop method in an isolated microgrid power system," *Applied Energy*, vol. 201, pp. 257–269, 2017.

[26] K. Wang, C. Liu, J. Sun et al., "State of charge estimation of composite energy storage systems with supercapacitors and lithium batteries," *Complexity*, vol. 2021, Article ID 8816250, 15 pages, 2021.

[27] N. R. Tummuru, M. K. Mishra, and S. Srinivas, "Dynamic energy management of renewable grid integrated hybrid energy storage system," *IEEE Transactions on Industrial Electronics*, vol. 62, no. 12, pp. 7728–7737, 2015.

[28] U. Manandhar, A. Ukil, H. B. Gooi et al., "Energy management and control for grid connected hybrid energy storage system under different operating modes," *IEEE Transactions on Smart Grid*, vol. 10, no. 2, pp. 1626–1636, 2017.

[29] J. Shen and A. Khaligh, "A supervisory energy management control strategy in a battery/ultracapacitor hybrid energy storage system," *IEEE Transactions on Transportation Electrification*, vol. 1, no. 3, pp. 223–231, 2015.

[30] A. S. Jacob, R. Banerjee, and P. C. Ghosh, "Sizing of hybrid energy storage system for a PV based microgrid through design space approach," *Applied Energy*, vol. 212, pp. 640–653, 2018.

Hindawi
International Journal of Photoenergy
Volume 2022, Article ID 7771607, 6 pages
https://doi.org/10.1155/2022/7771607

Research Article

Investigations of Optical Coulomb Blockade Oscillations in Plasmonic Nanoparticle Dimers

Lamessa Gudata,[1] Jule Leta Tesfaye,[1,2] Abela Saka,[1] R. Shanmugam,[3] L. Priyanka Dwarampudi,[4] Nagaraj Nagaprasad,[5] B. Stalin,[6] and Ramaswamy Krishnaraj[2,7]

[1]*Department of Physics, College of Natural and Computational Science, Dambi Dollo University, Ethiopia*
[2]*Centre for Excellence-Indigenous Knowledge, Innovative Technology Transfer and Entrepreneurship, Dambi Dollo University, Ethiopia*
[3]*TIFAC, CORE-HD, JSS College of Pharmacy, JSS Academy of Higher Education & Research, Ooty, Nilgiris, Tamil Nadu, India*
[4]*Department of Pharmacognosy, JSS College of Pharmacy, JSS Academy of Higher Education & Research, Ooty, Nilgiris, Tamil Nadu, India*
[5]*Department of Mechanical Engineering, ULTRA College of Engineering and Technology, Madurai, 625104 Tamil Nadu, India*
[6]*Department of Mechanical Engineering, Anna University, Regional Campus Madurai, Madurai, 625 019 Tamil Nadu, India*
[7]*Department of Mechanical Engineering, College of Engineering and Technology, Dambi Dollo University, Ethiopia*

Correspondence should be addressed to Ramaswamy Krishnaraj; prof.dr.krishnaraj@dadu.edu.et

Received 11 November 2021; Accepted 21 December 2021; Published 15 January 2022

Academic Editor: Bharath Govindan

Copyright © 2022 Lamessa Gudata et al. This is an open access article distributed under the Creative Commons Attribution License, which permits unrestricted use, distribution, and reproduction in any medium, provided the original work is properly cited.

The exploration of Coulomb blockade oscillations in plasmonic nanoparticle dimers is the subject of this study. When two metal nanoparticles are brought together at the end of their journey, tunnelling current prevents an infinite connection dipolar plasmon and an infinite amplification in the electric fields throughout the hot spot in between nanoparticles from occurring. One way to think about single-electron tunnelling through some kind of quantum dot is to think about Coulomb blockage oscillations in conductance. The electron transport between the dot and source is considered. The model of study is the linear conductance skilled at describing the basic physics of electronic states in the quantum dot. The linear conductance through the dot is defined as $G = \lim_{\to 0}(I/V)$ in the limit of infinity of small bias voltage. We discuss the classical and quantum metallic Coulomb blockade oscillations. Numerically, the linear conductance was plotted as a function gate voltage. The Coulomb blockade oscillation occurs as gate voltage varies. In the valleys, the conductance falls exponentially as a function gate voltage. As a result of our study, the conductance is constant at high temperature and does not show oscillation in both positive and negative gate voltages. At low temperature, conductance shows oscillation in both positive and negative gate voltages.

1. Introduction

Classical electromagnetism forecasts an infinite of the redshift hybridized noble metal nanoparticle plasmon polariton. The surface-to-surface distance approaches zero when there is a rapid increase in the field strength between the hotspot of two metallic nanopatrticles. One theory holds that quantum mechanical tunnelling of electrons prevents either type of deviations [1]. Additionally, the tunnelling current minimizes the accumulation of charge opposing surfaces. As a result, decreases in the electric field strength within the hotspot result in a seamless transition from either the dipolar bonding plasmon to the charge transfer plasmon. A high degree of agreement exists between quantum mechanical theories and experimental results [2]. Quantum tunnelling accounts for the vast majority of the optical response of couples of plasmonic nanoparticles along within close proximity [3]. Recently, tunnelling of electrons in quantum plasmonics

was thought to be a continuous phenomenon, when the conductivity across two nanoparticles increased progressively in decreasing range [4]. The development of charge transfer should be prevented by the Coulomb blockage of tunnelling current. The device should remain in the classical electromagnetism regime since a particular quantity of potential energy is achieved in the gap across plasmonic nanoparticles. With the emergence of supercomputers, numerical computations of electron transport across quantum dots have become increasingly essential in the field of physics. A computational approach allows for the derivation of the electronic characteristics and composition of a system of particles from the fundamental elements of the system and their interactions with one another. The quantum dot [5] is a system of particles that is presently receiving much attention. An artificial system made up of multiple interacting electrons that are constrained to limited regions among layers of metals is known as a quantum well.

In metal, a finite number of electrons are constrained. The possibility of evaluating and tuning features linked to quantum mechanical processes and charge quantization, as well as the ease with which such small devices may be constructed, encourages the interest in their fabrication. A very small capacitance is produced by a dot with a size that is in the region of the Fermi wavelength. Consequently, the electrons occupy separate quantum levels in dots, and the level spacing E is the spacing across neighbouring levels in a dot grid system. In a way to extend an electron to the dot or take an electron from the dot, a specific quantity of energy E_c is required, which varies based on the charging energy E_c. Atomic properties [6] are strikingly comparable to these features. As a result, quantum dots are considered "manufactured atoms" in some circles. The features of quantum dots, such as their spectrum, present a difficult advantage. It is possible to attach source and drain contacts to samples that are adjustable by an outside gate and that have source and drain contacts. As a result, it is possible to measure the transit through the dot. The tenability of variables has a significant impact on the amount of work that can be done in electron transport. With the addition of contacts to the dot, tunnelling of electrons away from and toward the dots becomes conceivable [7]. These result in a finite lifespan of the electron in the dot, producing a level broadening that is lower than the level spacing in the devices that we are interested in. A quantum dot is connected to three terminals by a quantum coupling. When the source and drain are in contact, particle exchange might occur. The third terminal, which is just electrically linked, is utilized as a gate electrode, shifting the energy spectrum of the dot as it passes through it. It is a quantum dot that has been attached to leads and the get capacitance that serves as the prototype for a solitary electron transistor. If we consider a realm in which temperature is substantially smaller than charging but still significantly greater than the level widening, the transport mechanism is controlled by a singular electron process. As with a transistor, the quantum dot operates similarly to a transistor in that the current flowing through it may be switched on and off by adjusting the gate voltage connected to it [8].

Quantum dots research embraces a variety of topics in physics, electrical and electronic engineering, chemistry, material science, biology, and medicine, where according to the demand of specific applications, different types of quantum dot structures are employed. Due to the fact that quantum dots could interconvert light and electricity in a controlled manner that is based on the size of the crystal, they can be used to inject directly charged particles [9]. One further use of quantum dots, and among the most intriguing interfaces of nanotechnology throughout the usage of a colloidal quantum dot in terms of speed and excitement, is in the field of biology [10]. There is a range of biological investigations in which typical fluorescent labels made from organic compounds fail to provide long-term sustainability or the ability to detect numerous signals at the same time. Their distinctive optical features made them appealing as fluorophores [11]. Applications of quantum in the area of biology are to investigate various cellular labelling mechanisms and develop drugs [12]. Generally, the applications of the quantum dots are diverse, and all could not be listed here in detail [13]. The confined electrons are held in place by a quantum dot, which would be a tiny area of a metal into which they might enter and exist due to tunnel contact. Charge transport through the quantum dots has been receiving significant theoretical and experimental interest. Research occurs on electron transport through the quantum dots in the noninteracting investigation to realize electron transport through the quantum dots at high temperature. On the other hand, there should be enough study for electrons to transport low temperature. The researcher is expected to fill this gap. The objective of the study is to investigate Coulomb blockade oscillations, conductance, and charge transport through the quantum dots and plot the normalized conductance as the function of gate voltage at nanoparticle plasmon dimers.

2. Materials and Methodology

The Coulomb barrier becomes significantly more visible as metallic nanoparticles within the sub-5 nm region become more readily available for manipulation. Scanning tunnelling microscopy [14] and electrochemistry with gold nanoparticles in the electrolyte [15] have both been used to observe Coulomb blockage occurring at ambient temperature. The quantum dot is perceived to be weakly coupled to two-electron reservoirs and to have a single electron energy level at $E_p(p = 1, 2, 3, \cdots)$; this is evaluated by handling the electron-electron interconnection in a mean-field (Hartee) approximation, which is a mean-field approximation of the electron-electron interaction [16]. In this chart, the stages are designated in ascending order and are evaluated in relation to the potential well's bottom. The location of the levels may be affected by the number of electrons in the molecule.

$$f_{\mathrm{l}}(E - E_{\mathrm{F}}) = \frac{1}{1 + e^{(E-E_{\mathrm{F}})/K_{\mathrm{B}}T_{\mathrm{l}}}},$$
$$f_{\mathrm{r}}(E - E_{\mathrm{F}}) = \frac{1}{1 + e^{(E-E_{\mathrm{F}})/K_{\mathrm{B}}T_{\mathrm{r}}}}, \quad (1)$$

where E_F is the Fermi energy, f is the Fermi-Dirac distribution, K_B is the Boltzmann constant, and T_l and T_r are the temperature of left and right reservoirs, respectively. Through applying a conceivable variation V between the left and right sides of the dot, a current I could be transmitted through it. It is indicated by Γ_p^l and Γ_p^r, respectively, that the tunnelling rate between level P to the left and right reservoirs is greater than zero. In the presence of a potential U imposed between both the source and drain reservoirs, the current will flow via the dot. The distribution of electrons in the quantum dot is altered as a result of this current. The stability distribution of electrons from between energy levels differs from the equilibrium distribution of electrons in the previous energy levels. The applied potential difference can now be considered a perturbation that can change the equilibrium distribution [17]. At $T = 0$, the position of the conductance peaks as a function of gate voltage can be evaluated from a consideration of the equilibrium characteristics of the system only [18]. In linear response theory, the response is a linear function of perturbation [19].

$$P(\{n_i\}) = P_{eq}(\{n_i\})\left[1 + \frac{eV}{KT}\psi(\{n_i\})\right]. \quad (2)$$

$\psi(\{n_i\})$ is the correction term due to the application of perturbation. The equilibrium distribution is shifted by the factor of $\psi(\{n_i\})$. The nonequilibrium probability evolves in time according to the master equation [20]. The master equation has gain terms and loses terms [21]. The (two-terminal) linear response conductance G of the quantum dot is characterized by the expression $G = I/V$ in the limit $V \longrightarrow 0$. The stationary current through the left equals the right barrier and is provided by

$$I = -e\sum_{p=1}^{\infty}\sum_{\{n_i\}}\Gamma_p^l P(\{n_i\})\left\{\sigma_{np,0} f\left(E^{i,l}(N) - E_F\right) - \sigma_{np,1}\left[1 - f\left(E^{f,l}(N) - E_F\right)\right]\right\}. \quad (3)$$

The first term expresses the chance of finding an electron with energy E upon on the left side of the graph and an emptiness state on the right side of the graph [22]. The second summation is based on the total number of occupations that have been realized $\{n_1, n_{2,\cdots,}\} = \{n_i\}$ from the energy levels in the quantum dot each with stationary probability $P_{\{\{n_i\}\}}$. The conductance through the quantum dot is for a given N:

$$G = \frac{e^2}{KT}\sum_{P=1}^{\infty}\sum_{N=1}^{\infty}\frac{\Gamma_p^l\Gamma_p^r}{\Gamma_p^l + \Gamma_p^r}P_{eq}(N)F_{eq}\left(E_{p|N}\right)\left[1 - f\left(E_p + U(N) - U(N-1) - E_F\right)\right]. \quad (4)$$

Specifically, this distribution function describes the tunnelling of an electron with an initial condition P in the dot [23]. When we are in the extreme temperature limit, we take the quantum into consideration and $K_B T \gg \Delta E$. The extreme temperature range intersect with lower temperature range [24].

The conductance of the particular barriers and quantum dots at higher temperatures is irrelevant, as the discreteness of neither the stages nor the charging energy is essential. The conductance does never fluctuate in response to the gate voltage [25]. For low-temperature characteristics, $KT \ll \Delta E$. All energy levels E_p are small that G is the highest if $1 - f$ is maximum. The charging energy $U(N)$ of the dot difference is discretely due to the variation in number N of electrons on the dot through tunnelling to or from the source leads, or it repeatedly varies due to the difference in the voltage on the external gate electrode [26]. In the low-temperature region, $KT \ll \Delta E$; the term with $P = N = N_{min}$ gives the dominant contribution to the sum over P and N in the conductance. Then, the equation of normalized conductance in the low-temperature boundary limit is given by

$$\frac{G}{G_o} = \frac{\sum_{N=1}^{\infty} e^{(N-N_{min})^2/2\sigma^2}\sum_{P=1}^{\infty} 1/1 + e^{-\beta\Delta}}{\sum_{N=1}^{\infty} e^{(N-N_{min})^2/2\sigma^2}}, \quad (5)$$

where $\Delta = NE_c + P\Delta E - (E_F + eV_g + E_c)$ and $G_0 = e^2\Gamma_p^r$ $\Gamma_p^l/KT(\Gamma_p^r + \Gamma_p^l)$. As temperature decreases, the width of Gaussian distribution σ_N decreases, and thus, $P(N)$ becomes sharply peaked around $N = N_{min}$.

3. Result and Discussion

The Coulomb blockade with resonant tunnelling and the optical field driving the plasmon leads to the equilibration of the Fermi Level of plasmonic nanoparticles and molecular levels of intertion [27]. The Coulomb blockade oscillations break down when thermal energy is equal to charging energy. The numerical computation of electron transport through the quantum dot is performed [28]. The graphs of the results are discussed using the equations that we use in the method. Conductance cannot be evaluated analytically but can be evaluated numerically [29]. The usefulness of numerical computation is more recognized, and today, it is used in many domains of research and development. The normalized conductance is shown as a measure of gate voltage on a graph.

Numerically equation (5) is solved for different values of thermal energy and plotted normalized conductance also as a variable of gate voltage [30]. The plot of equation (5) is shown in Figure 1. For negative gate voltage conductance shows no oscillations but rather has a constant positive value of 274.62. For ETH = $1.46\,x\,10^{-2}$ and negative gate voltage $V_g = -0.037$ V, the conductance falls from max to min ($G_{max} = 274.62$) to ($G_{min} = 12.05$) and oscillate between $G_{min} = 12.05$ and $G_{max} = 71.31$. The constant value of conductance in the positive gate voltage is less than the constant value in the negative gate voltage. Oscillations occur in the positive gate voltage [31].

The plotted graph for low temperature in Figure 2 is shown. For both negative and positive gates, voltage conductance shows no oscillation. For negative voltage $V_g = 0.5$ V, the conductance falls G_{max} to G_{min} ($G_{max} = 54.92$ to $G_{min} = 34.69$) for ETH = $1.82E^{-2}$ and shows no oscillations [32]. As gate voltage increases, conductance decreases—approaching

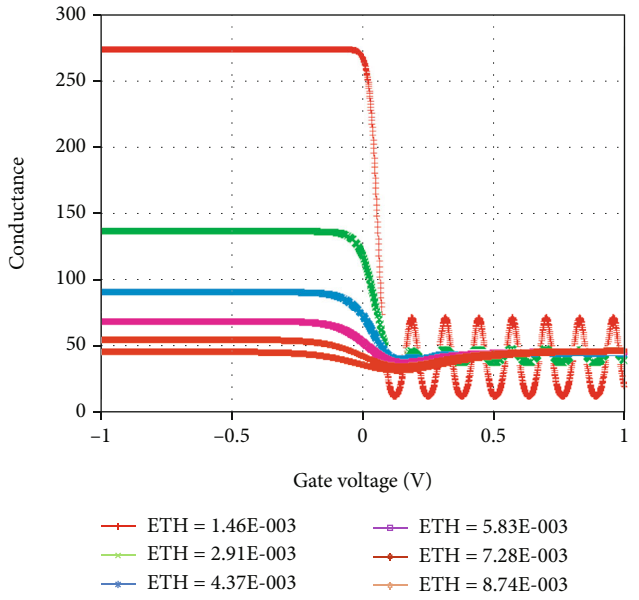

Figure 1: Normalized conductance versus gate voltage and plotted graph of equation (5).

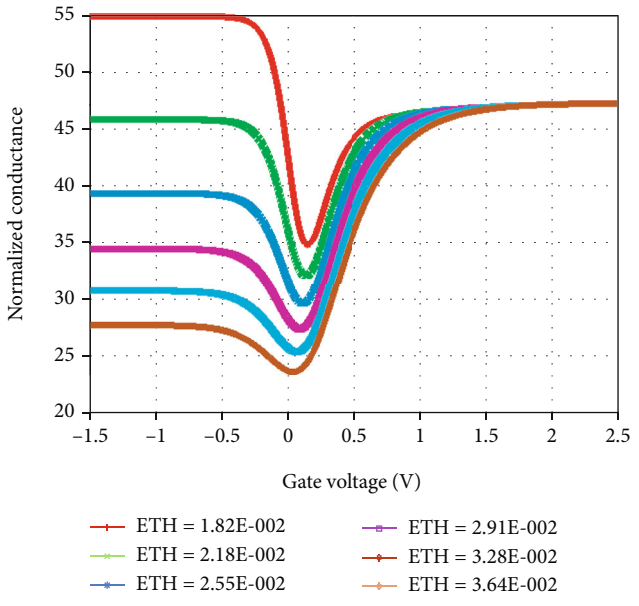

Figure 2: Blocking conditions. Normalized conductance versus gate voltage and a plotted graph of equation (5).

a minimum value in the positive gate voltage ($G_{max} = 34.69$)—and increases gradually becoming constant ($G = 46.70$). The conductance's blocking conditions (G is minimum) are fulfilled at different gate voltages [33]. As can be seen from the figure, at high temperature, the conductance does never exhibit oscillation as a variable of gate voltage. At a fixed gate voltage, the conductance valley (minima) through the dot is shifted to the right in energy proportional to the applied gate voltage. Transport blocked (Coulomb blockade) regions in

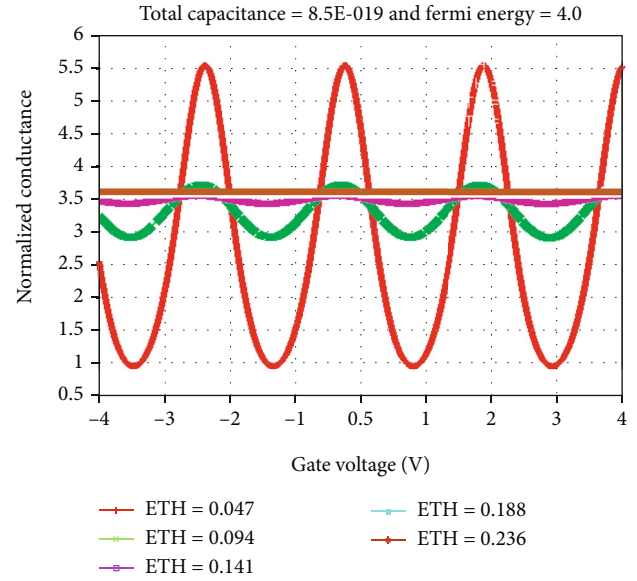

Figure 3: Normalized conductance versus gate voltage when $K_B T \ll \Delta E$ plotted using equation (5).

which no energy lies in the required energy window. No oscillations in both positive and negative gate voltages.

In Figure 3, we have plotted the normalized conductance as a variable of gate voltage for various capacitances with the same Fermi energy; the conductance becomes oscillatory for both negative and positive gate voltages [34]. For ETH $\approx$ 0.236 oscillation disappears, conductance becomes constant $G \approx 3.6$. Level spacing, capacitance, temperature, and chemical potential affect the oscillation nature of the conductance.

4. Inference

The close connections of our result and the objective of the study are in agreement with the theoretical explanation of the optical Coulomb blockade oscillations in plasmonic nanoparticle dimers. We briefly explained the appearances of the Coulomb blockade at high and low temperatures graphically.

5. Conclusion

Statistical computation of electron transport through the quantum dots is performed. The electron charge in the quantum dot is quantized. The conductance cannot be evaluated analytically but can be evaluated numerically. At high temperatures, the thermal energy is strong enough to overcome the repulsive of Coulomb force. The alternative pattern of peaks and suppressed region conductance as a variable of gate electrons are in the quantum dot. The normalized conductance is plotted as a variable of gate voltage for capacitance across the drain, capacitance across the gate voltage, capacitance across the source, charging energy, and the level spacing. The graphs of normalized conductance show a different behaviour, saturation, oscillation, oscillation depression, and varying amplitude of oscillation and period.

Data Availability

The data used to support the findings of this study are included within the article.

Disclosure

This study was performed as a part of the employment of the authors.

Conflicts of Interest

The authors declare that there are no conflicts of interest.

References

[1] S. Stewart, Q. Wei, and Y. Sun, "Surface chemistry of quantum-sized metal nanoparticles under light illumination," *Chemical Science*, vol. 12, no. 4, pp. 1227–1239, 2021.

[2] J. J. Cully, J. L. Swett, K. Willick, J. Baugh, and J. A. Mol, "Graphene nanogaps for the directed assembly of single-nanoparticle devices," *Nanoscale*, vol. 13, no. 13, pp. 6513–6520, 2021.

[3] Y. Yusof, S. Moosavi, M. R. Johan et al., "Electromagnetic characterization of a multiwalled carbon nanotubes–silver nanoparticles-reinforced polyvinyl alcohol hybrid nanocomposite in X-band frequency," *ACS Omega*, vol. 6, no. 6, pp. 4184–4191, 2021.

[4] V. I. Kleshch, V. Porshyn, A. S. Orekhov, A. S. Orekhov, D. Lützenkirchen-Hecht, and A. N. Obraztsov, "Coulomb-blockade-controlled single-electron point source," 2020, https://arxiv.org/abs/2005.02358.

[5] D. Pan, H. Song, S. Zhang et al., "In situ epitaxy of pure phase ultra-thin InAs-Al nanowires for quantum devices," 2020, https://arxiv.org/abs/2011.13620.

[6] P. Strasberg, C. W. Wächtler, and G. Schaller, "Autonomous implementation of thermodynamic cycles at the nanoscale," *Physical Review Letters*, vol. 126, no. 18, p. 180605, 2021.

[7] T. Kanne, D. Olsteins, M. Marnauza et al., "Double nanowires for hybrid quantum devices," 2021, https://arxiv.org/abs/2103.13938.

[8] Y. Chen, S. Huang, J. Mu, D. Pan, J. Zhao, and H. Q. Xu, "A double quantum dot defined by top gates in a single crystalline InSb nanosheet," *Chinese Physics B*, vol. 30, no. 12, p. 128501, 2021.

[9] N. Kavokine, R. R. Netz, and L. Bocquet, "Fluids at the nanoscale: from continuum to subcontinuum transport," *Annual Review of Fluid Mechanics*, vol. 53, no. 1, pp. 377–410, 2021.

[10] M. S. Anwar and J. C. Fenton, "Gate-controlled conductance of superconducting NbN nanowires: coherent quantum phase-slips or coulomb blockade?," 2021, http://arxiv.org/abs/2104.09331.

[11] C. J. Muller, "Decoupling environmental modes from tunneling electrons in a partially wet phase molecular mechanically contrallable break junction," 2021, http://arxiv.org/abs/2106.01716.

[12] M. Mirigliano and P. Milani, "Electrical conduction in nanogranular cluster-assembled metallic films," *Advances in Physics: X*, vol. 6, no. 1, p. 1908847, 2021.

[13] J. R. Bayogan, K. Park, Z. B. Siu et al., "Controllable p–n junctions in three-dimensional Dirac semimetal Cd3As2 nanowires," *Nanotechnology*, vol. 31, no. 20, p. 205001, 2020.

[14] I. S. Burmistrov, Y. Gefen, D. S. Shapiro, and A. Shnirman, "Mesoscopic stoner instability in open quantum dots: suppression of Coleman-Weinberg mechanism by electron tunneling," *Physical Review Letters*, vol. 124, no. 19, p. 196801, 2020.

[15] G. Scappucci, C. Kloeffel, F. A. Zwanenburg et al., "The germanium quantum information route," *Nature Reviews Materials*, vol. 45, pp. 1–18, 2020.

[16] F. Iachello and Y. Alhassid, "Nuclear Theory," Final Technical Report for DOE Grant DE-FG02-91ER40608 (No. DOE-YALE-40608), Yale Univ, New Haven, CT (United States), 2020.

[17] Y. W. Lu, J. F. Liu, Z. Liao, and X. H. Wang, "Plasmonic-photonic cavity for high-efficiency single-photon blockade," *Science China - Physics Mechanics & Astronomy*, vol. 64, no. 7, pp. 1–10, 2021.

[18] D. Sivun and T. A. Klar, "Optical coulomb blockade lifting in plasmonic nanoparticle dimers," *Optics Express*, vol. 28, no. 3, pp. 4115–4126, 2020.

[19] S. Kim, T. H. Le, Y. Choi et al., "Electrical monitoring of photoisomerization of block copolymers intercalated into graphene sheets," *Nature Communications*, vol. 11, no. 1, pp. 1–8, 2020.

[20] M. Mirigliano, S. Radice, A. Falqui, A. Casu, F. Cavaliere, and P. Milani, "Anomalous electrical conduction and negative temperature coefficient of resistance in nanostructured gold resistive switching films," *Scientific Reports*, vol. 10, no. 1, pp. 1–10, 2020.

[21] M. Tsutsui, S. Ryuzaki, K. Yokota et al., "Field effect control of translocation dynamics in surround-gate nanopores," *Communications Materials*, vol. 2, no. 1, pp. 1–9, 2021.

[22] A. Zalla, *Quantum chemical simulations of the interaction of polyynes with silver nanoparticles*, Europian Research Council, 2021.

[23] K. Willick, *Carbon nanotube electromechanical systems: nonlinear dynamics and self-oscillation, [Ph.D. thesis]*, University of Waterloo, Ontario, Canada, 2020.

[24] S. P. Madhusudanan, M. S. Kumar, K. Mohanta, and S. K. Batabyal, "Photoactive Cu_2FeSnS_4 thin films: influence of stabilizers," *Applied Surface Science*, vol. 535, p. 147600, 2021.

[25] M. Napari, T. N. Huq, R. L. Hoye, and J. L. MacManus-Driscoll, "Nickel oxide thin films grown by chemical deposition techniques: potential and challenges in next-generation rigid and flexible device applications," *InfoMat*, vol. 3, no. 5, pp. 536–576, 2021.

[26] A. W. Elshaari, E. Büyüközer, I. E. Zadeh et al., "Strain-tunable quantum integrated photonics," *Nano Letters*, vol. 18, no. 12, pp. 7969–7976, 2018.

[27] X. Zhang, M. Q. Le, V. C. Nguyen et al., "Characterization of micro-ZnO/PDMS composite structured via dielectrophoresis–toward medical application," *Materials & Design*, vol. 208, p. 109912, 2021.

[28] B. Wang, P. Nawarat, K. M. Lewis, P. Patsalas, and D. Gall, "Tunable infrared plasmonic properties of epitaxial Ti1–xMgxN(001) layers," *ACS Applied Materials & Interfaces*, vol. 13, no. 19, pp. 22738–22748, 2021.

[29] D. Sherman, J. S. Yodh, S. M. Albrecht, J. Nygård, P. Krogstrup, and C. M. Marcus, "Normal, superconducting

and topological regimes of hybrid double quantum dots," *Nature Nanotechnology*, vol. 12, no. 3, pp. 212–217, 2017.

[30] A. Avila-García, A. Chaudhary, and H. Rojas-Chávez, "Iridium oxide films as propane sensors," *Thin Solid Films*, vol. 724, p. 138617, 2021.

[31] A. M. Hassan, F. Diab, E. F. Kotp, G. Al-Kashef, E. R. Shaaban, and A. E. Metawa, "Implantation of Cu onto ZnTe thin film using plasma focus device for optoelectronic applications," *Optical Materials*, vol. 117, p. 111182, 2021.

[32] S. Vaitiekėnas, M. T. Deng, J. Nygård, P. Krogstrup, and C. M. Marcus, "Effective g factor of subgap states in hybrid nanowires," *Physical Review Letters*, vol. 121, no. 3, p. 037703, 2018.

[33] G. Badawy, S. Gazibegovic, F. Borsoi et al., "High mobility stemless InSb nanowires," *Nano Letters*, vol. 19, no. 6, pp. 3575–3582, 2019.

[34] R. L. O. Het Veld, D. Xu, V. Schaller et al., "In-plane selective area InSb-Al nanowire quantum networks," *Communications on Physics*, vol. 3, no. 1, pp. 1–7, 2020.

Hindawi
International Journal of Photoenergy
Volume 2022, Article ID 3519517, 8 pages
https://doi.org/10.1155/2022/3519517

Research Article

A Novel Approach on the Advancement in Polymer Phase Change Material in Solar Energy

G. Jegan[1], **P. Ramani**[2], **T. J. Nagalakshmi**[3], **S. Chitra**[4] and **T. Samraj Lawrence**[5]

[1]*Department of Electronics and Communication Engineering, Sathyabama Institute of Science and Technology, Chennai, Tamil Nadu, India*
[2]*Department of Electronics and Communication Engineering, SRM Institute of Science and Technology, Ramapuram, Chennai, Tamil Nadu, India*
[3]*Department of Electronics and Communication Engineering, Saveetha School of Engineering, Saveetha Institute of Medical and Technical Sciences, Chennai, 602 105 Tamil Nadu, India*
[4]*Department of Electronics and Communication Engineering, Rajalakshmi Engineering College, Chennai, Tamil Nadu, India*
[5]*Department of Information Technology, College of Engineering and Technology, Dambi Dollo University, Dambi Dollo, Oromia Region, Ethiopia*

Correspondence should be addressed to G. Jegan; gjegan.ece@sathyabama.ac.in and T. Samraj Lawrence; samraj@dadu.edu.et

Received 5 November 2021; Accepted 7 December 2021; Published 10 January 2022

Academic Editor: V. Mohanavel

Copyright © 2022 G. Jegan et al. This is an open access article distributed under the Creative Commons Attribution License, which permits unrestricted use, distribution, and reproduction in any medium, provided the original work is properly cited.

A wide interest has been shown in the application of solar energy in recent times. This motivated the researchers to make a development in the approach of solar energy, but there are different technologies like MPPT, CPG, and grid mode that have been used to maintain a constant temperature. Among these, phase change material has been used to regulate the temperature in the system. Solar energy is becoming an essential approach for increasing the efficiency of thermal energy conversion and utilizing polymeric step change composites, which have attracted extremely large interest in recent years due to their advantages of high energy density and powerful energy output stability. A plethora of reviews and reports have been published to compile the diverse range of PCMs made available for various applications. PCMs are created by improving thermophysical thermodynamic stability, latent heat, and heat capacity. Furthermore, the possible applications of polymer phase PCMs in a variety of fields, such as energy storage devices, thermal corrective action, and temperature-controlled drug carriers, are detailed. In this paper, a novel approach on the advancement of nanoconfined phase change material is defined along with the application of the solar energy system.

1. Introduction

The major issues that were faced in the world are environmental problems and the energy crisis, and this has to be addressed. The fuel price increases when there is a continuous rise in the power consumption level, and the main driving force of the emission of greenhouse gas is the effective use of renewable energy sources. Consumption of electricity increased by 1.5 percent globally in 2018 compared to 2017 [1]. Many studies have been undertaken on global power usage and production, and these topics have been extensively addressed. The consumption of renewable energy has become one of the answers to greenhouse emissions, and as a result, sustainable energy programs have been adopted in many areas. Professional possibilities include rapid commercial improvement for the advancement of societies around the world, which results in a rapidly rising energy consumption. The majority of power usage used coal and oil which are finite and cause significant carbon pollution.

As a result, efficient energy consumption has become a key concern, prompting a shift in the tendency towards the use of solar and wind resources. Energy production, for example, is unlimited, long-term available, readily available, and ecologically acceptable, making it a useful replacement

to coal and oil [2]. Heat transfer is more efficient than latent heat storage because it gives a significantly higher efficiency with a smaller temperature gradient while absorbing and releasing energy. Thermo-chemical, sensitive, and heating value storage is all types of TES that use the shift of stored energy inside the storage devices. Thermal energy storage (TES) is a viable way to solve this issue, and it is currently being developed at a rapid pace. The adoption of TES enhances the general performance and greatest degree possible of renewable energy power-producing applications [3].

The impacts of convective heat transfer during the phase separation of petroleum ether in a plate heat exchanger were experimentally studied. The dissolving front is developed at different periods near the HTF (heat transfer fluid) pipe and moved at varying rates outside, toward the shell, according to the researchers. They discovered that changing the inlet temperature of water from 70°C to 80°C closes out thermal decomposition time by 37%. The phase transition and crystallization of a wax in a shell and tube heat exchanger with HTF cycling within the tubes and PCM overlaying the shell side were investigated for various performance parameters and device characteristics.

When fossil fuels are used for energy, undesired chemicals are released into the atmosphere, resulting in increased fossil fuel emissions [4]. The long-term viability of energy production is jeopardized due to lack of resources and permanent fossil-fuel combustion. To address the concerns of rapidly rising consumption of nonrenewable fossil fuels and rising emissions while also ensuring the survival of life on earth, the researchers are working to develop new power generation, transformation, and storage systems. Because of changeable power production, environmental procedures, and large amounts of energy stores, regenerative techniques of energy storage applications have gotten a lot of interest in this area. Solar, wind, mechanical, hydrothermal, and other renewable resources are being used to replace traditional oil and coal sources of power [5]. Considering the lack of radiation from the sun during the nighttime and mother nature's transmission losses, the effectiveness of solar energy consumption is heavily reliant on the energy storage mechanism. Power in many kinds, such as wiring, robotic, and solar energy, can be maintained in a variety of ways.

Pumped hydropower storage (PHPS), flywheels, and storage systems can all be used to store mechanical energy (CAES). PHPS and CAES are the best pneumatic and hydraulic systems for large-scale facilities; nevertheless, flywheel energy can be employed for limitations or restrictions. This stored energy can be employed when the grid's power source is unavailable [6]. Thermal energy is then stored in a variety of ways, including heating, latent heat, thermochemical energy, or a mixture of these. Sensible radiant heat storing is a type of TES which shows the significant changes in heating between charging and discharging operations. Sensible radiant heat retention is a type of TES which shows the significant changes in thermostat between charging and discharging operations. The specific heat is an indicator of the amount of heat stored as a result of the accumulation of substance and temperature variations. PCM characterization for better usage in SWHs, establishment of a novel SWH that can be combined with the PCMs, long-term evaluation of the performance, and standardization of the SWHs for sale are all technical challenges [7]. It is worth noting that the economic viability includes expenditure analyses in various areas across the world, as well as the provision of subsidies, particularly in nations with plentiful solar radiation.

2. Literature Review

The crystallization operations of wax RT35 as phase transition materials in a finned tube are investigated in an experimental study. As a result, the impact of utilizing fins in this study, as well as several operational characteristics, is taken into account. The goal of this research is to design and build a unique shipping container that will be compared to a finless heat transfer. The effect of changing the inlet pressure and temperature rate on the charging and discharging processes of the exchanger is investigated in a series of experiments. It has been demonstrated that utilizing fins in the phase transition process improves the crystallization processes. This is defined as the investigation of phase change inside a finned-tube heat exchanger experiment proposed by [8]. The tendency of this fluctuation is various for heat pumps; for the bare tubular heat exchanger, boosting the temperature difference more efficiently reduces melting time.

The test of a phase change material in thermal performance is proposed by [9] with the cool roof system by a scaled model. Cool roofs in general are excellent at reducing thermal loads, but they have an issue with rising heating load. As a result, the purpose of this research is to use phase change features of phase change material to compensate for the shortcomings of the cool roof system (PCM). The investigation was conducted to verify the heat transfer performance of the PCM cool roof structure by monitoring the temperature on the horizontal and vertical of a tiny model (666 mm) [10]. PCM was added and not introduced, and the surface temperature between the cream-colored finish colors was evaluated. As a result, the degree of the surface of the plate when using PCM was lower than that when not using PCM, and there was a temporal lag in heat growth. When comparing temperature distributions based on finish color (brown vs. white), white demonstrated a low temperature profile of up to 16.35°C. White had a lower thermal performance of 5.40°C than brown even at ambient temperature. The employment of the PCM cool roof structure in roofing finishes might reduce the temperature rise and keep the interior temperature low.

There are different methods involved in the solar cells, and [11] proposed a method on recent advances in dye-sensitized solar cells. Energy production is a plentiful and freely obtainable renewable resource on the planet, and numerous types of photovoltaic (PV) devices, such as organic, inorganic, and hybrid cells, have been produced to harness it. Photovoltaic modules transform solar radiation to electricity without causing environmental harm. Despite the fact that hydrogel solar cells (inorganic cells) are normally strong and good, they are inflexible and expensive to manufacture. To circumvent these drawbacks, researchers

have concentrated on organic solar cells. The performance of DSSCs, which are made up of a sensitized transistor (photoelectrode) and a catalytic cathode (counter electrode) with a solution sandwiched across them, is determined by a variety of parameters. DSSCs have achieved a maximum electrical conversion efficiency of 11.1 percent so far, which would still be low for industrial use. The working concept, factors impacting performance, and main issues confronting DSSCs are all examined in this paper.

The environmental protection of the solar energy is proposed by [12]. People consumption of energy resource distribution has always been a core matter of all living beings, and attempting to obtain one immortal source of power has long been a human goal. Researchers and experts feel that using pure energies such as photovoltaic, turbine, and thermal ground energy, among others, rather than oil and coal technologies, will obstruct conservation efforts. In this way and around two decades after the introduction of the Photo voltaic cell into the public arena of producing energy, the close bond between strategy and resource utilization has led to the conclusion that there really is no place for financially explaining arguments and searching for ways to use sun's radiation and generated power.

An experiment study on the performance of a novel solar water heating system is proposed by [13] with and without PCM. By utilizing phase change materials (PCMs) for heat storage and inserted oscillation heat pipe (OHP) for improving performance, a unique solar water heating system (SWHS) effective in decreasing the influence of radiation from the sun intensity changes has been fabricated. Depending on the strength of solar irradiance in changing seasons and climate circumstances, several working styles can be chosen. A testing machine has also been built to evaluate the study's validity. For a few years in a row, full-year measurements in a variety of environmental situations have been taken out in Nanjing, China [14]. The performance of the system was tested and compared between the systems with and without PCM, including collecting efficiency (CE), mean collecting effectiveness (ACE), coefficient of performance (COP), and exit water temperature (EWT). Under comparable system parameters, the device with PCM is shown to perform significantly better. CE variation with PCM is over 30% lower during the day than that without PCM. EWT with PCM may maintain a temperature of above 50°C at night in the summer, whereas EWT without PCM has a noticeable drop. At night in the winter, COP with PCM is greater than 3.0, allowing EWT to reach 50°C in a substantially lesser duration than that without PCM.

3. Methodology

The research is about generating the power from the solar energy using the phase change material (PCM). Most of the research uses the CGPT and MPPT to generate the power from the solar energy, but they have several issues involved in generating the solar power; among these, the main issue is regulating the power. So, to overcome this issue, different research studies were developed; among these, PCM plays an important role in regulating the temperature. In this research, the advancement in the PCM method is used to regulate the temperature; hence, the power could be generated and used for the different purposes. Overview of PCM and power generation from the solar system is discussed in this section.

3.1. Advance Phase Change Material. Phase change material has expanded more interest over the research, and this produces the importance of the energy. The following is one of the categories, types, and approaches that will be covered. PCMs are divided into four main categories based on their phase transition: solid-liquid, solid-solid, liquid-gas, and solid-gas [15]. Solid-liquid PCMs are the best for storing heat energy between these four types, and they come in inorganic and eutectic forms, as illustrated in Figure 1.

Although it may be employed at a wide variety of climates and has a strong melting temperature, wax counts as a PCM. Paraffin can also be frozen without having to be supercooled. As a result, the most expensive, practical, and extensively utilized PCM is thermoset paraffin wax. Fatty acids are capable of replicating melting and being frozen with no or little crystallization [9]. The expense of saturated fats, which can be 2.0 to 2.5 twice those of petroleum ether, is one factor that prevents them from being used, since their heavy metals have not been a viable contender for PCM. Nevertheless, due to their strong heat conductivity and latent heat of reaction per cubic meter, metals are plausible rivals when quantity is considered.

Organic compounds, in their broadest sense, refer to any material found in nature. The majority of organic materials have carbon-hydrogen bond mixtures that are associated with living organisms. There are two types of organic PCMs: petroleum and nonparaffin. Organic compounds have a constant freezing characteristic, which means they may melt and freeze repeatedly without losing their hidden melting temperature. They are also highly stable, self-nucleating, and generally reusable.

Thermal properties of different kinds of organic and inorganic materials are listed in Table 1. The beneficial attributes and characteristics of the selected materials are as follows. However, the low thermal conductivity of organic PCMs in a solid form and the significant thermal expansion necessary during the solidification stage are disadvantages. The bulk thermal energy storage capacity of organic PCMs is poor; however, the flammable condition can generally be avoided by the well design. The paraffin fabrication process [16], on the other hand, is extremely costly [17]. Another disadvantage is that the manufacturers use paraffins, which are a structured paraffin mix that may be rather costly.

3.2. Solar Energy Production Using PCM. The solar energy is the most popular source which has been used in the household, and this offers certain benefits and annual investments. There are different types of solar energy such as photovoltaic, solar thermal, and solar organic system. In this study, the generation of power involves the use of phase change material (PCM) to store energy and regulate the temperature. Due to the potential of dispatchability, they are used on great demand, making them more competent and cost-

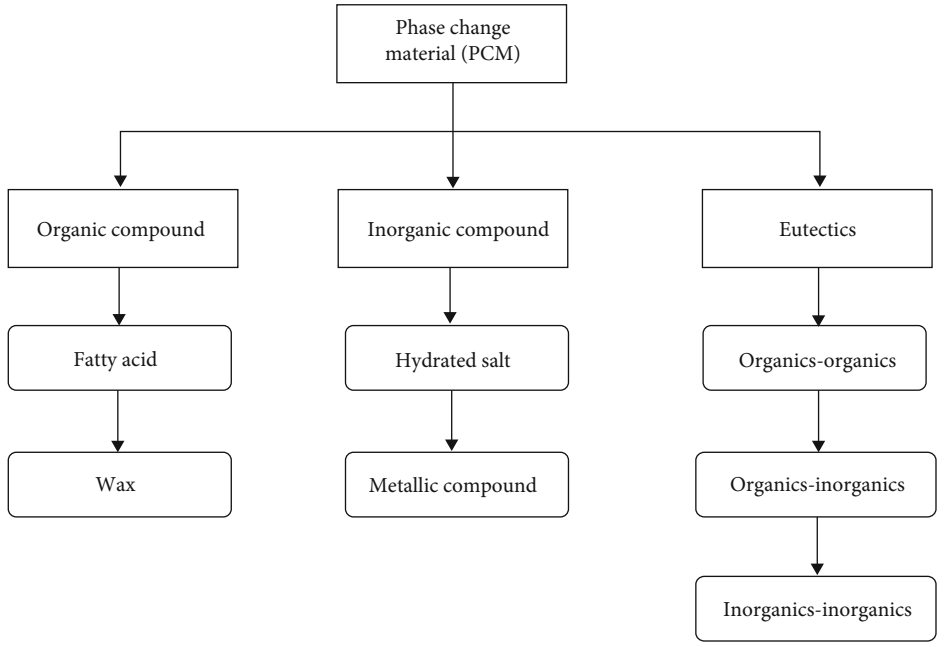

Figure 1: Classification of phase change material.

Table 1: Thermal properties of different kinds of organic and inorganic material.

Composition of heat storage	Composition type	Melting point (°C)	Sensible heat	Heat conductivity	Density solid
Acetamide	Chemical compound	83	2.5	—	1.159
Acetanilide	Chemical compound	119	2.00	—	—
Erythrol	Chemical compound	117	1.38	1.49	1.48
Trimethylolethane	Mixture	30	2.75	0.66	1.12
$Na_2S_2O_3 \cdot 5H_2O$	Hydrated salt	49	3.83	—	—

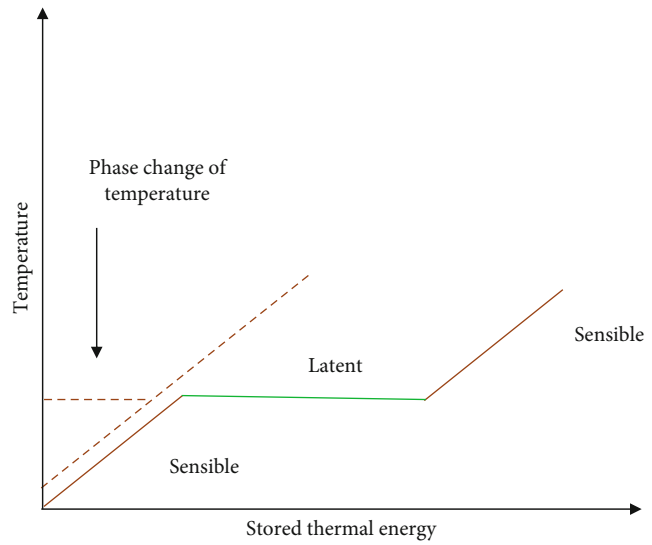

Figure 2: Measurement of increased thermal energy.

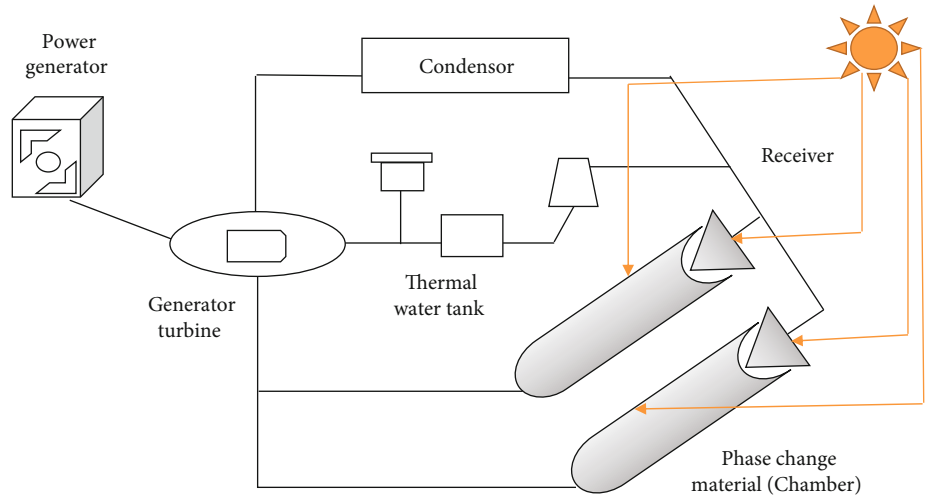

Figure 3: Schematic thermal energy storage using PCM.

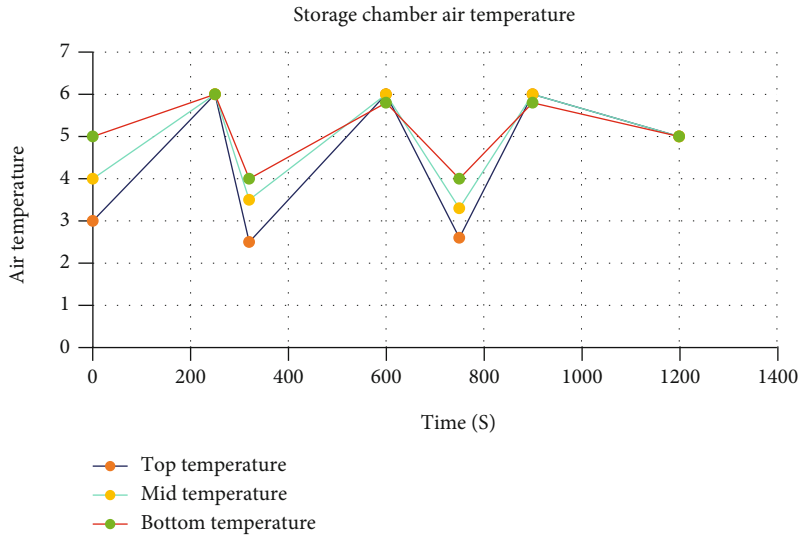

Figure 4: Storage chamber air temperature.

effective. Increased thermal energy storage (TES) systems are shown in Figure 2. Thermal energy, on the other hand, has not been proven safe; just a few generating facilities throughout the world have now been recognized as testing this method [18]. More modern SEGS prototypes have always used costly liquid fuel as a backup system, resulting in a temperature increase from 300 to 400°C; nonetheless, the technique is still financially unfeasible.

Phase change material is one type of heat trapping material utilized in solar energy generating system. Phase change material has not yet attained the desired economic level or substantial use due to the thermal conduction, which requires a long power conversion period, despite the fact that it presents a tremendous possibility to help the lowering of cost of power supplied by SEGS [6]. By adopting single-stage PCM storage, the heat exchange methodology for single-stage phase change material of various PCM salts may be studied. The findings demonstrated that PCMs are theoretically capable of achieving the necessary objectives, and they proposed a phase change material memory design with a vertically stacked heat pipe mentioned in Figure 3.

The interplay involving PCMs and the heat transfer fluid during charging and discharging is the most important part of utilizing latent heat storage in a highly focused solar thermal system. The CST plant could also be linked to a supercritical carbon cycle (s-CO2), in which it can be coupled to the Brayton cycle for energy production, and this works with thermal storage and the Rankine cycle [19]. A reflector field, center block (solar receiver), heat storage system, and energy block are all part of the political process. Reflector fields capture and focus sun power on the solar receiver. The heat transfer then circulates the heat generated through the process to a power block, where it is converted from heat to electric power. Thus, the solar energy is converted to power using the phase change material.

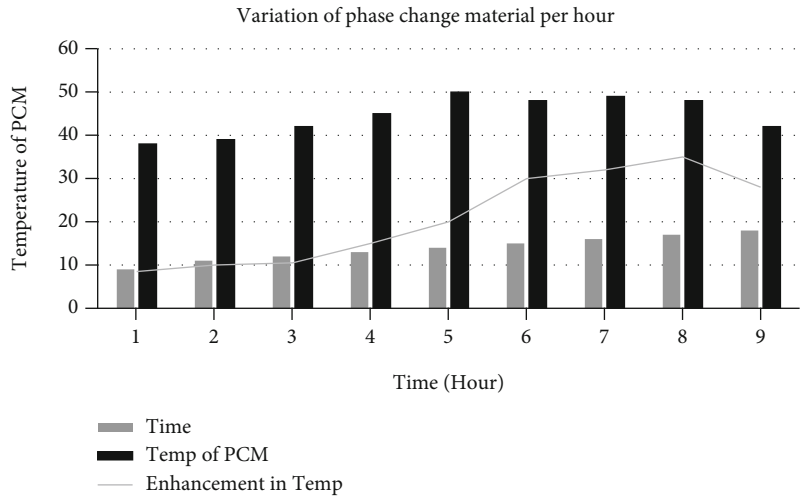

Figure 5: Variation of phase change material per hour.

Table 2: Comparison of PCM dealing in different sectors.

Set	Ratio	Sector
1	18%	PCM new development
2	21.5%	Treatment of existing PCM
3	15%	Specific application and technologies using phase change material
4	30%	Thermal properties of existing PCM and their studies
5	13%	Integration of PCM into building components

3.3. Application of PCM. Many applications for thermal storage have been developed using phase transition materials. PCM was housed in an aluminum box with a specific photovoltaic reflective coating on the front face to reflect a PV cell attached to the front [20]. The PCM was used in a carbon black to improve radiant heat evacuated by increasing heat capacity, and its model was evaluated to air spring blow chilling using a cold Li-particle batteries. Rising operating temperatures impact the efficiency of constructing photovoltaic devices as a source of electricity (BIPV). While their usefulness is limited by their reduced temperature conductivity and high crystallization separation during crystallization, PCMs can be utilized to actively restrict this temperature increase.

4. Result and Discussion

The following section shows the result obtained based on the conversion of solar energy to electric power using phase change material.

4.1. Selection of Phase Change Material. The limit of atmospheric temperature inside the cold storage area is acquired from the chart of temperatures against time for PCM selection.

The PCM is then chosen based on its melting point, which should be inside the air range of temperature, and this is shown in Figure 4. Figure 5 shows the temperature variations in the PCM as well as an enhancement in the heat of the phase change material.

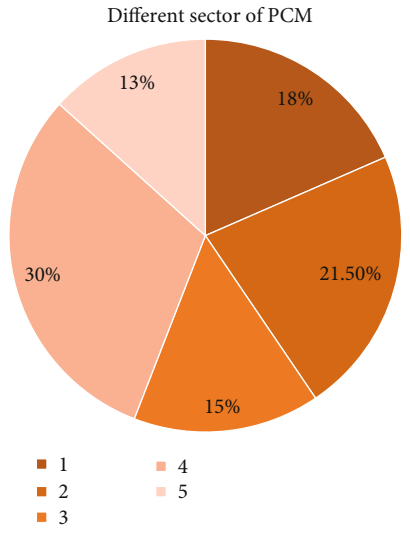

Figure 6: Comparison of PCM dealing in different sectors.

In each case, the average PCM temperatures per day were 41.10 and 48.10 degrees Celsius, respectively. Temperature increased by 17.1% according to the PCM. It has an ability to absorb heat quickly during sunrise hours and release the heat during sun set hours, and it outperforms CTSS and TSS in every way. This is noted based on Figure 5.

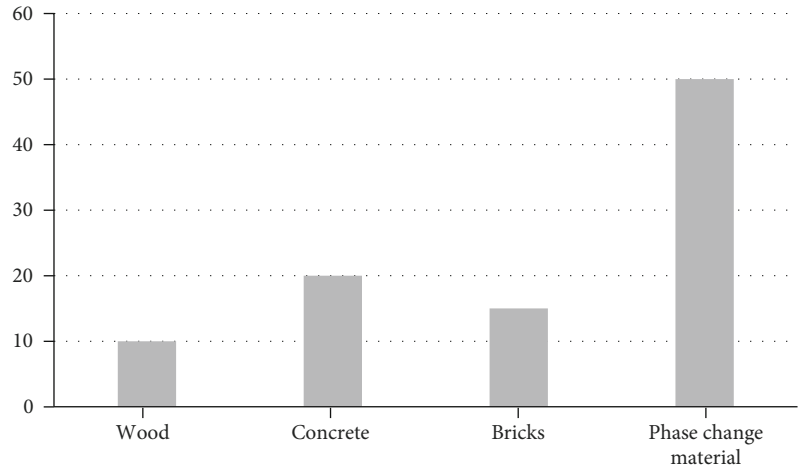

Figure 7: Density of energy storage.

4.2. Comparison of PCM Dealing in Different Sectors. The proportion of energy consumed in the building industry is utilized to power active heating and ventilation systems for interior air [21, 22].

Because the study themes in the literature include all aspects of phase change thermal applications, it is difficult to keep track of what is new, because some new findings may contradict old ones. Nonetheless, Table 2 and Figure 6 might provide an overview of the topics related to PCM in the industry.

4.3. Energy Consumption. Perishable food, medications, and pharmaceuticals are transported and stored. Building envelopes are more than just buildings; they do provide shelter from the elements while being sensitive to the cultural weather conditions, due to its considerably more heat transfer interaction and more straightforward application.

As shown in Figure 7, the building envelope is among the most researched parts of study and control, and it also offers a great possibility for energy reduction and the demand. It allows for the control of energy expenses and the enhancement of energy consumption, as well as economic and environmental effect.

5. Conclusion

A descriptive examination of the many technological solutions utilized in the modelling of PCM integration systems in building envelopes, as well as the simulation tools employed in this technique, is included in this paper. The researchers followed the technological methodologies utilized in solar energy storage system simulation. The study dedicated to the utilization of these approaches and methodologies in the application of solar management system techniques is continually growing, owing to the resource's potential, which has become an economic concern. Indeed, the retention of electrical energy using appropriate kinds of PCM is a continuing issue for building designers, and it has the potential to play a significant part in the upcoming power system. PCM has an efficiency of power absorption that is greater than that in other circumstances, making it the most effective in this situation. In the case of a one-hour power outage, PCM absorbs more energy than the others. When PCM absorbs energy at a faster pace, more power is saved; hence, in a 1-hour power outage, more energy is saved than in any other condition.

Data Availability

The data used to support the findings of this study are included within the article.

Conflicts of Interest

The authors declare that there is no conflict of interest regarding the publication of this article.

Acknowledgments

The authors would like to express their gratitude towards Sathayabama Institute of Science and Technology for providing the necessary infrastructure to carry out this work successfully.

References

[1] E. Koutroulis, K. Kalaitzakis, and N. C. Voulgaris, "Development of a microcontroller-based, photovoltaic maximum power point tracking control system," *IEEE Transactions on Power Electronics*, vol. 16, no. 1, pp. 46–54, 2001.

[2] Y. E. Abu Eldahab, N. H. Saad, and A. Zekry, "Enhancing the maximum power point tracking techniques for photovoltaic systems," *Renewable and Sustainable Energy Reviews*, vol. 40, pp. 505–514, 2014.

[3] S. Sahoo, A. Gopalan, S. Ramesh et al., "Preparation of Polymeric Nanomaterials Using Emulsion Polymerization," *Advances in Materials Science and Engineering*, vol. 2021, Article ID 1539230, 9 pages, 2021.

[4] B. Subudhi and R. Pradhan, "A comparative study on maximum power point tracking techniques for photovoltaic power

systems," *IEEE Transactions on Sustainable Energy*, vol. 4, no. 1, pp. 89–98, 2013.

[5] G. Edman Jonsson, H. Fredriksson, R. Sellappan, and D. Chakarov, "Nanostructures for enhanced light absorption in solar energy devices," *International Journal of Photoenergy*, vol. 2011, 11 pages, 2011.

[6] Nirmala, G. Ramkumar, S. Sahoo et al., "Artificial intelligence to analyze the performance of the ceramic-coated diesel engine using digital filter optimization," *Advances in Materials Science and Engineering*, vol. 2021, Article ID 7663348, 10 pages, 2021.

[7] P. D. Sonawane, V. Bupesh Raja, and M. Gupta, "Microstructure, mechanical, and electrical properties and corrosion analysis of lead-free solder CSI joints on Cu substrate using novel concentrated solar energy soldering (CSES) method," *Advances in Materials Science and Engineering*, vol. 2020, 16 pages, 2020.

[8] A. Váz Sá, R. Almeida, H. Sousa, and J. Delgado, "Numerical analysis of the energy improvement of plastering mortars with phase change materials," *Advances in Materials Science and Engineering*, vol. 2014, Article ID 582536, 12 pages, 2014.

[9] M. Rahimi, A. Ranjbar, D. Ganji, K. Sedighi, and M. Hosseini, "Experimental investigation of phase change inside a finned-tube heat exchanger," *Journal of Engineering*, vol. 2014, 11 pages, 2014.

[10] S. G. Yoon, Y. K. Yang, T. W. Kim, M. H. Chung, and J. C. Park, "Thermal performance test of a phase-change-material cool roof system by a scaled model," *Advances in Civil Engineering*, vol. 2018, Article ID 2646103, 11 pages, 2018.

[11] Y. Su, Y. Zhang, K. Lin et al., "Numerical study on resistance change characteristics of phase change materials," *Advances in Materials Science and Engineering*, vol. 2021, Article ID 7934173, 12 pages, 2021.

[12] U. Mehmood, S. Rahman, K. Harrabi, I. A. Hussein, and B. Reddy, "Recent advances in dye sensitized solar cells," *Advances in Materials Science and Engineering*, vol. 2014, Article ID 974782, 12 pages, 2014.

[13] A. Samimi, S. Zarinabadi, and M. Samimi, *Solar energy application on environmental protection*, International Journal of science and investigations, France, 2012.

[14] Ramesh, P. Nirmala, G. Ramkumar et al., "Simulation process of injection molding and optimization for automobile instrument parameter in embedded system," *Advances in Materials Science and Engineering*, vol. 2021, Article ID 9720297, 10 pages, 2021.

[15] A. H. N. Shirazi, F. Mohebbi, M. Azadi Kakavand, B. He, and T. Rabczuk, "Paraffin nanocomposites for heat management of lithium-ion batteries: a computational investigation," *Journal of Nanomaterials*, vol. 2016, 10 pages, 2016.

[16] F. O. Al Ghuol, K. Sopian, and S. Abdullah, "Enhancement of integrated solar collector with spherical capsules PCM affected by additive aluminum powder," *Journal of Thermodynamics*, vol. 2016, 7 pages, 2016.

[17] G. Peng, G. Dou, Y. Hu, Y. Sun, and Z. Chen, "Phase change material (PCM) microcapsules for thermal energy storage," *Advances in Polymer Technology*, vol. 2020, Article ID 9490873, 20 pages, 2020.

[18] F. S. Javadi, H. S. C. Metselaar, and P. Ganesan, "Performance improvement of solar thermal systems integrated with phase change materials (PCM), a review," *Solar Energy*, vol. 206, pp. 330–352, 2020.

[19] A. Ahmed, H. Baig, S. Sundaram, and T. K. Mallick, "Use of nanofluids in solar PV/thermal systems," *International Journal of Photoenergy*, vol. 2019, Article ID 8039129, 17 pages, 2019.

[20] G. Ramkumar, S. Sahoo, G. Anitha et al., "An unconventional approach for analyzing the mechanical properties of natural fiber composite using convolutional neural network," *Advances in Materials Science and Engineering*, vol. 2021, Article ID 5450935, 15 pages, 2021.

[21] I. R. Bellobono, F. Morazzoni, R. Bianchi et al., "Solar energy driven photocatalytic membrane modules for water reuse in agricultural and food industries. Pre-industrial experience using s-triazines as model molecules," *International Journal of Photoenergy*, vol. 7, no. 2, pp. 87–94, 2005.

[22] L. Coppola, D. Coffetti, and S. Lorenzi, "Cement-based renders manufactured with phase-change materials: applications and feasibility," *Advances in Materials Science and Engineering*, vol. 2016, Article ID 7254823, 6 pages, 2016.

Hindawi
International Journal of Photoenergy
Volume 2021, Article ID 3981456, 12 pages
https://doi.org/10.1155/2021/3981456

Research Article

A Short-Term Solar Photovoltaic Power Optimized Prediction Interval Model Based on FOS-ELM Algorithm

G. Ramkumar,[1] **Satyajeet Sahoo**,[2] **T. M. Amirthalakshmi**,[3] **S. Ramesh**,[4] **R. Thandaiah Prabu**,[5] **Kasipandian Kasirajan**,[6] **Antony V. Samrot**,[7] **and A. Ranjith**[8]

[1]*Department of Electronics and Communication Engineering, Saveetha School of Engineering, SIMATS, Chennai, 602 105 Tamil Nadu, India*
[2]*Department of Electronics and Communication Engineering, Vignan's Foundation for Science, Technology and Research (Deemed to be University), Vadlamudi, Andra Pradesh, 522213, Guntur, India*
[3]*Department of Electronics and Communication Engineering, Rajalakshmi Institute of Technology, Chennai, Tamil Nadu, India*
[4]*Department of Electronics and Communication Engineering, St. Mother Theresa College of Engineering, Vagaikulam-628102, Tamilnadu, India*
[5]*Department of Electronics and Communication Engineering, Jeppiaar Institute of Technology, Chennai, Tamil Nadu, India*
[6]*Faculty of Engineering and Built Environment, Mahsa University, Malaysia*
[7]*School of Bioscience, Faculty of Medicine, Bioscience and Nursing, MAHSA University, Jenjarom, 42610 Selangor, Malaysia*
[8]*Department of Electronics and Communication Engineering, St. Joseph University in Tanzania, Dar es Salaam, Tanzania*

Correspondence should be addressed to G. Ramkumar; pgrvlsi@gmail.com and A. Ranjith; ranjith.arumugam@sjuit.ac.tz

Received 18 October 2021; Accepted 7 November 2021; Published 29 November 2021

Academic Editor: V. Mohanavel

Copyright © 2021 G. Ramkumar et al. This is an open access article distributed under the Creative Commons Attribution License, which permits unrestricted use, distribution, and reproduction in any medium, provided the original work is properly cited.

Solar energy conversion efficiency has improved by the advancement technology of photovoltaic (PV) and the involvement of administrations worldwide. However, environmental conditions influence PV power output, resulting in randomness and intermittency. These characteristics may be harmful to the power scheme. As a conclusion, precise and timely power forecast information is essential for the power networks to engage solar energy. To lessen the negative impact of PV electricity usage, the offered short-term solar photovoltaic (PV) power estimate design is based on an online sequential extreme learning machine with a forgetting mechanism (FOS-ELM) under this study. This approach can replace existing knowledge with new information on a continuous basis. The variance of model uncertainty is computed in the first stage by using a learning algorithm to provide predictable PV power estimations. Stage two entails creating a one-of-a-kind PI based on cost function to enhance the ELM limitations and quantify noise uncertainty in respect of variance. As per findings, this approach does have the benefits of short training duration and better reliability. This technique can assist the energy dispatching unit list producing strategies while also providing temporal and spatial compensation and integrated power regulation, which are crucial for the stability and security of energy systems and also their continuous optimization.

1. Introduction

PV system research may bring solutions to the myriad difficulties confronting the location and the energy system itself. Trainings on improving the energy construction then enhancing the act of PV organization have been done [1]. Given the success mentioned previously, a PV system is especially sensitive to polluting and it has been disapproved for its instability, irregularity, and variable power generation. When the power supply was linked to the network, the situation of power fluctuations can threaten the network and endanger data security, making production scheduling much more challenging [2]. As a conclusion, reliable PV power production forecast is necessary in order to make improved generation suggestions, support temporal and spatial compensation, and provide synchronized control

scheme, lowering the requirement for power capacity and operational costs.

Many hybrid methods have been presented in recent years, combining the benefits of both methodologies. In reference, a hybrid technique depends on the wavelet transform (WT), and the radial basis function neural network (RBFNN) was created to anticipate short-term solar PV power. The annual autoregressive continuous simple moving approach was combined with the support vector machine (SVM) method by some researchers [3]. Given the fact that most of these methods, including the SVM and RBFNN designs, are significantly more challenging and informative for the network, they have been demonstrated to be real in the PV prediction.

The number of the approaches explored thus far ignored data time validation and presumed that the information does not seem out of date. In practice, training data must be updated in real time because it is time-dependent. So far, quite a few scientific papers have addressed this subject, among which was an online 24 hr forecasting method that employed RBF networks and classified input parameters depending on the type of weather [4]. Some of the academics have developed a two-stage process in which the solar power is statistically normalized first, and then, predictions of the standardized solar power were considered to anticipate PV power. Thus, we selected to use the extreme learning machine (ELM) method for the next reasons: ELM has a substantially lower computation complexion than many other machine learning techniques. ELM learns substantially quicker than most feed forward network learning techniques [5]. ELM outperforms many others in terms of generalization performance. The number of the hidden layer nodes is tiny and does not require tuning.

This study presents a novel strategy including the bootstrap technique, ELM, and improved DE (IDE) algorithm to generate optimum PIs for short-term PV power prediction [6]. The PIs addressed uncertainty in both predictive analysis and data disturbance at a quick rate, minimal computing burden, and good value for five-minute advanced PV power forecasts [7]. To begin, the bootstrap approach is being used to examine uncertainty in ELM models with the term of variance depending on ELM with PV power prediction. In addition, assumptions of data noises were the following: the frequency variation is evaluated but uses an ELM statistical model, the features of which have been optimized using an enhanced DE approach with a PI-based minimization problem.

Considering the variations of ELM equations, the information noise yields the optimum PIs with the coverage probability and the speed. Finally, the planned technique is shown through using an actual PV and atmospheric information from such a rooftop photovoltaic system [8]. The forecasting outcome shows that the suggested method is more dependable and effective than other ELM-based bootstrap methodologies. In order to anticipate PV power in various seasons, the ELM, OS-ELM, and FOS-ELM estimate models were tested. The results demonstrated that the FOS-ELM approach may expand accuracy while also reducing the training time.

2. Related Works

Ahn and Park provide a comprehensive RNN based on PV power estimate for the near future to identify the effect of climate deviations; the design employs an on-site climate IoT collection as well as actual power information. Thus, we investigated numerous limitations of the proposed deep RNN depending on prediction models; indeed, weather variables were grouped, in order to develop an effective predictive model. On the basis of the normalized RMSE, the accuracy rates of 5- and 15-minute forward solar PV power forecasts using three RNN networks with twelve time steps were 98.0 percent and 96.6 percent, consequently. Their individual R2 scores were 0.988 and 0.949. They performed 94.8 percent and 92.9 percent accuracy in studies 1 and 3 hours gaining the PV power predictions, correspondingly. Their R2 scores are 0.963 and 0.927, respectively. In these tests, the proposed deep RNN-based relatively brief prediction method outperformed the competition in terms of classification accuracy [9].

The purpose of this research is to employ intensity of light, air temperature, and humidity levels as input factors for determining solar output power. Considerations input data with wavelet soft beginning denoising to reduce noise and significantly increase the forecast model's adaptability in a variety of weather scenarios. Tented chaos patterning, asymmetric disturbances, and the multiple objective method were utilized to boost the whale algorithm's prediction performance; the revised whale algorithm was utilized to enhance the technique support vector machine (SVM) model for improving the forecast model's predictive performance. The study demonstrates that the symmetry-based long forecast model for solar panels achieves complete accuracy under a range of meteorological circumstances. The structured technique to predicting renewable output will promote the utilization of clean power and economic growth by reducing the burden of anticipating conversion efficiency [10].

One of the most critical concerns for the smart grid's effective and steady operation is solar photovoltaic fluctuations during the day. To adapt to PV power oscillations induced by climate changes, this work presents a short-term PV power forecasting method depending on the multilayer RNN. It is made up of multiple RNN layers that employ data from on-site IoT sensors to collect electricity and weather data. According to the normalized RMSE, the short-term PV power prediction accuracies of 5 minutes and 1 hour utilizing the 3 RNN layers with 12 time steps are 98.02 percent and 96.58 percent, respectively, according to empirical observations. The proposed short-term forecasting strategy based on the multi-RNN design was able to adjust the short-term PV power changes, as illustrated by these experimental results [11].

Solar power plants are a method of generating environmentally friendly renewable electricity, particularly in tropical areas where the sun shines all year. Rainfall, sun radiation, and clouds, on the other hand, can all have an effect on the maximum output of photovoltaic (PV) systems. Due to these considerations, establishing whether PV can

meet the current load's demands is challenging. This investigation advances a design to expect the output power of 160 × 285 W PV scheme in the topics when confident different situations are taken into account. To help forecast generation, the Python language is employed, together with one layer and multiple hidden layer multilayer perceptron, as well as typical multiple linear regression approaches. The simulation outcomes indicate that the neural network approach with two hidden layers surpasses one hidden layer and more linear regression in terms of reliability, as evaluated by R2, MSE, and MAE values [12].

Cervone et al. provide a method for creating 72-hour stochastic and deterministic estimates of the power produced by the photovoltaic (PV) power plants by utilizing input from the climate estimate, and quantifiable astronomical factors are based on Artificial Neural Networks (ANN) and Analog Ensemble (AnEn). ANN and AnEn are used to provide predictions for three photovoltaic panels in Italy, both separately and in combination. The computer flexibility of the planned method is assessed using synthetic data mimicking 4,450 PV power plants. The adequate manner of the suggested method is tested on the NCAR Yellowstone computer, which has nodes ranging from 1 to 4,450 [13].

3. Materials and Methods

3.1. Prediction Algorithm (Extreme Learning Machine (ELM)). The construction of ELM is displayed in Figure 1, and also, the procedure was explained below.

The ELM is an ANN with one hidden layer. The arbitrary hidden neuron quantity in the ELM design is assumed to be L, and distinct learning sample quantity (p, q) was supposed to be N [14]. Also, it is required which $p \in W^{d*N}, q \in W^{N}, x_k \in W^{1*d}, y_k \in W$, and x_k and y_k are both completely random arrays and vectors. The output function can then be rewritten:

$$f_H(p_n) = \sum_{k=1}^{H} \beta_k M(x_k, y_k, p_n) = q_n, \tag{1}$$

where β is the output weight matrix that links the randomized number of neurons to the output. G is the active purpose that joins the i^{th} arbitrary hidden neuron to the all-input nodes; then, this can be endlessly calculated as follows, such as the sigmoid function below:

$$M(x, y, p) = \frac{1}{1 + \exp\left(-(x \cdot p + y)\right)}. \tag{2}$$

Equation (1) can be expressed in the matrix form as

$$U \cdot \beta = P, \tag{3}$$

$$U = \begin{bmatrix} M(x_1, y_1, p_1) & \cdots & M(x_L, y_L, p_1) \\ \vdots & \ddots & \vdots \\ M(x_1, y_1, p_N) & \cdots & M(x_L, y_L, p_N) \end{bmatrix}, \tag{4}$$

$$\beta = [\beta_1 \ \beta_2 \quad \cdots \quad \beta_1]^T \ Q = [y_1 \quad y_2 \quad \cdots \quad y_N]^T.$$

The least-square approach to (1) is then

$$\beta = U^{+}Q = U^{T}\left(UU^{T}\right)Q, \tag{5}$$

which the matrix U represent the output hidden layer matrix, with i^{th} element (h_i) being the output hidden layer vector for the input p_i. Q is the vector containing training data's output. β is the only parameter that must be determined during the training procedure. The upper limit of the necessary number of distinct training models has several hidden nodes; the neurons in the hidden networks then will result in a lower subset of the training designs.

To applied regularization of parameter C to equation (5) to increase the stability and generalizability of the findings,

$$\beta = U^{T}\left(UU^{T} + \frac{1}{C}E\right)Q. \tag{6}$$

3.2. Online Sequential ELM (OS-ELM). The standard ELM implies that all information was being cast off for the training, whereas for estimate, information is sent chunk-by-chunk or one-by-one [15]. As a result, the traditional ELM must be modified to account for such circumstances. Historical climatic condition and PV power information were generated from the Supervisory Control and Data Acquisition (SCADA) structure on a regular basis and fed into the PV power forecast model. OS-ELM is better suited for PV power prediction because it refreshes the training data in real time. The algorithm is depicted below.

Step 1. Beginning—usage of a training data portion $\{(p_i, q_i)\}_{i=1}^{N_0}$ as initial information.

(i) Randomly produce p_j and q_j, where $j = 1, 2, \cdots, L$

(ii) Compute a primary hidden layer of the matrix output U_0:

$$U_0 = \begin{bmatrix} M(x_1, y_1, p_1) & \cdots & M(x_L, y_L, p_1) \\ \vdots & \ddots & \vdots \\ M\left(x_1, y_1, p_{N_0}\right) & \cdots & M\left(x_L, y_L, p_{N_0}\right) \end{bmatrix} \tag{7}$$

(iii) Approximation of the output initial weight vector:

$$\beta = U^{T}\left(UU^{T} + \frac{1}{C}E\right)Q, \tag{8}$$

Hindawi template version: may18

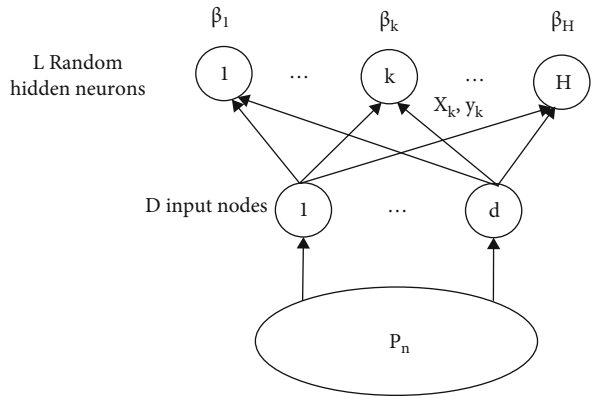

Figure 1: Extreme learning machine (ELM) architecture.

where

$$v_0 = \left(U_0^T U_0 + \frac{1}{C}E\right)^{-1},$$
$$Q_0 = \left[q_1 \cdots q_{N_0}\right]^T \tag{9}$$

(iv) Established $z = 0$

Online training.

(a) Once a $(z+1)^{\text{th}}$ new data portion $\{(p_i, q_i)\}_{i=(\sum_{j=0}^{z} N_j)+1}^{i=\sum_{j=0}^{z+1} N_j}$ is complete

(b) Compute the incomplete output hidden layer matrix U_{z+1} depending on the new data:

$$U_{z+1} = \begin{bmatrix} M\left(x_1, y_1, p_{\left(\sum_{j=0}^{z} N_j\right)+1}\right) & \cdots & M\left(x_L, y_L, p_{\left(\sum_{j=0}^{z} N_j\right)+1}\right) \\ \vdots & \ddots & \vdots \\ M\left(x_1, y_1, p_{z+1}\right)_{\sum_{j=0}^{} N_j} & \cdots & M\left(x_L, y_L, p_{z+1}\right)_{\sum_{j=0}^{} N_j} \end{bmatrix},$$
$$q_{z+1} = \begin{bmatrix} q_{\left(\sum_{j=0}^{z} N_j\right)+1} & \cdots & q_{\sum_{j=0}^{} N_j}^{z+1} \end{bmatrix}^T \tag{10}$$

(c) Evaluation of the new q_{z+1} and $\beta^{(z+1)}$ based on

$$v_{z+1} = v_z - v_z U_{z+1}^T \left(I + U_{z+1} v_z U_{z+1}^T\right)^{-1} U_{z+1},$$
$$\beta^{(z+1)} = \beta^{(z)} + v_{z+1} U_{z+1}^T \left(p_{z+1} - U_{z+1}\beta^{(z)}\right) \tag{11}$$

Set $z = z + 1$, then start from Step 2.

3.3. OS-ELM with Forgetting Mechanism (FOS-ELM). The training information must be accessed within a specific time frame. In other words, information is only valid for a limited time [16]. Data received before a particular time in the FOS-ELM process can be not extendedly used lower than the forgetting mechanism; the obsolete information may make the prognosis less correct. Because of solar energy and temperatures varying seasonally, FOS-ELM is the better model for predicting PV power. The FOS-ELM technique is shown below.

Step 1. Configuration; this corresponds to the OS-ELM from Step 1.

Step 2. This process of forgetting is used in online learning.

When the $(z+1)^{\text{th}}$ new data chunk $\{(p_i, q_i)\}_{i=(\sum_{j=0}^{z} N_j)+1}^{i=\sum_{j=0}^{z+1} N_j}$ is prepared,

(a) compute the partially output hidden units' matrix U_{z+1}, for the most recent data

$$U_{z+1} = \begin{bmatrix} M\left(x_1, y_1, p_{\left(\sum_{j=0}^{z} N_j\right)+1}\right) & \cdots & M\left(x_L, y_L, p_{\left(\sum_{j=0}^{z} N_j\right)+1}\right) \\ \vdots & \ddots & \vdots \\ M\left(x_1, y_1, p_{z+1}\right)_{\sum_{j=0}^{} N_j} & \cdots & M\left(x_L, y_L, p_{z+1}\right)_{\sum_{j=0}^{} N_j} \end{bmatrix},$$

$$q_{z+1} = \left[q \left(\sum_{j=0}^{z} N_j \right) + 1 \quad \cdots \quad \sum_{j=0}^{q_{z+1}} N_j \right]^T \tag{12}$$

(b) calculate the new q_{z+1} and β^{th} based on

$$v_{z+1} = v_z - v_z \begin{bmatrix} -U_{z-e-1} \\ U_{z+1} \end{bmatrix}^T \times \left(I + \begin{bmatrix} U_{z-e-1} \\ U_{z+1} \end{bmatrix} v_z \begin{bmatrix} -U_{z-e-1} \\ U_{z+1} \end{bmatrix}^{T^{-1}} \right) \times \begin{bmatrix} U_{z-e-1} \\ U_{z+1} \end{bmatrix} v_z,$$

$$\beta^{(z+1)} = \beta^{(z)} + v_{z+1} \begin{bmatrix} -U_{z-e-1} \\ U_{z+1} \end{bmatrix}^T \times \left(\begin{bmatrix} q_{z-e-1} \\ q_{z+1} \end{bmatrix} - \begin{bmatrix} U_{z-e-1} \\ U_{z+1} \end{bmatrix} \beta^{(z)} \right) \tag{13}$$

(c) set as $z = z + 1$, then go back to Step 2

The integration of the forgetting mechanism, which could not get rid of the obsolete prevent information of their involvement in opportunities online and also show the timeliness of the data, is the evident difference between FOS-ELM and OS-ELM.

3.4. PI Structure and Valuation

3.4.1. Formulation of PI. Assuming a training sample selected $S = \{(p_i, t_i)_{i=1}^N\}, p_i p_i$ is an input dataset containing historical data [6]. It is 5-minute gaining of PV power, which is used as the benchmark. PIs were built that contain the goal t_i with given assurance level $(1 - \alpha)$, known as PI nominal confidence (PINC) $100(1 - \alpha)\%$, percent, and PIs $M_t^\alpha(p_i)$ can be defined for the i^{th} target as

$$M(p_i) = [L(p_i), U(p_i)], \tag{14}$$

where $L(p_i)$ and $U(p_i)$ signify PI lower bounds and upper bounds, respectively. The PI attention amount can be defined as

$$x(t_i \in [L(p_i), U(p_i)]) = 100(1 - \alpha)\%. \tag{15}$$

t_i is the i^{th} target measured; this can be well defined as

$$t_i = q(p_i) + \mu(p_i) = f(p_i, \vartheta) + \varepsilon(p_i), \tag{16}$$

where $q(p_i)$ is the genuine regression average and $\varepsilon(p_i)$ is the mean noise with a zero mean. $f(p_i, \vartheta)$ is a mapping among the input p_i and exact regress value $q(p_i)$. The ELM technique is used as a regression design in this paper to approximate the true return value. As a result, the mean of the accurate regression $q(p_i)$ can be approximated by the output of the ELM model $f(p_i, \widehat{\vartheta})$:

$$\widehat{q}(p_i) = f(p_i, \vartheta) = E\left(\frac{t_i}{p_i}\right), \tag{17}$$

where $\widehat{q}(p_i)$ denotes a prediction target value; the prediction error can be defined as

$$t_i - \widehat{q}(p_i) = [q(p_i) - \widehat{q}(p_i)] + \varepsilon(p_i), \tag{18}$$

where $t_i - \widehat{q}(p_i)$ represents the overall error of prediction and reflects difference among the measured value t_i and value of real estimate $\widehat{q}(p_i)$. The error between the expected true regression output as well as the observed ELM output is denoted by $[q(p_i) - \widehat{q}(p_i)]$ denoting noise with such a mean of zero [17]. PIs are built to measure uncertainties in overall prediction, which consists of two independent statistical parts: $[q(p_i) - \widehat{q}(p_i)]$ and $\varepsilon(p_i)$. As a result, the total variance is defined as

$$\sigma_t^2(p_i) = \sigma_{\widehat{q}}^2(p_i) + \sigma_\varepsilon^2(p_i), \tag{19}$$

where $\sigma_{\widehat{q}}^2(p_i)$ is the model uncertainty variance and $\sigma_\varepsilon^2(p_i)$ is the information uncertainty variance. The low bound $L_t^\alpha(p_i)$ and upper bound $U_t^\alpha(p_i)$ can be rewritten as

$$L_t^\alpha(p_i) = \widehat{q}(p_i) - r_{1-\alpha/2}\sqrt{\sigma_{\widehat{t}}^2(p_i)}, \tag{20}$$

$$U_t^\alpha(p_i) = \widehat{q}(p_i) + r_{1-\alpha/2}\sqrt{\sigma_{\widehat{t}}^2(p_i)}, \tag{21}$$

where $r_{1-\alpha/2}$ is the $1 - \alpha/2$ standard normal quantile distribution.

3.4.2. PI Quality Metrics. The likelihood of PI coverage (PICP) and the breadth of PIs are two important indicators. The number of metrics and the indicators are presented to assess the quality of PIs [18]. The most essential metric for measuring the dependability of the PIs is PICP, which value reflects the likelihood that PIs will cover the upcoming objective. A greater value of PICP specifies that perhaps PIs are much more likely to accomplish the required area. For N labeled data, PICP is calculated as

$$\text{PICP} = \frac{1}{N}\sum_{t}^{N} \delta_t, \tag{22}$$

where δ_t is the Boolean value that can be given as

$$\delta_t = \begin{cases} 1, & t_i \in M_i^\alpha, \\ 0, & t_i \in M_i^\alpha. \end{cases} \tag{23}$$

Another essential metric for assessing the quality of the PIs is the interval breadth. If ignoring the interval width and only considering the PICP, and even if a high PICP

value is attained, it is difficult for decision-makers to gain relevant forecasting data. As a conclusion, better quality PIs must take PICP and PI quality into account totally. The brightness of PIs could be calculated using the mean prediction interval width (MPIW):

$$\text{MPIW} = \frac{1}{NE}\sum_{i=1}^{N}(U_t^{\alpha}(p_i) - L_t^{\alpha}(p_i)), \tag{24}$$

where E is a target variety and N is the number of datasets.

3.4.3. Model Uncertainty Variance. In 1979, the bootstrap technique is presented and named as a resampling methodology. Because of its simplicity and resilience, it is commonly used to predict a fundamentally unknown probability using a likelihood function. Bootstrap methods are used in regression applications to assess the uncertainty of regression models [19]. It is utilized in this study to quantify the uncertainty in the ELM model induced by the construction misspecification and arbitrarily assigned to the parameters of input. The variance is used to illustrate the uncertainty in the model.

An original training information model can be well defined as $D_{\text{orin}} = \{(p_i, t_i)\}_{i=1}^{N*}$ for the paired bootstrap approach, and the B training subdatasets $D_{\text{sub}} = \{(p_i, t_i)\}_{i=1}^{N*}$ are uniformly resampled using D_{orin} by replacing. Each ELM model's output is $\widehat{q}_s(p_i)$. The mean of the bootstrap ELM outputs can be used to estimate the genuine regression value. It can be represented as follows for B ELM models:

$$\widehat{q}(p_i) = \frac{1}{B}\sum_{s=1}^{B}\widehat{q}_s(p_i). \tag{25}$$

Depending on the B period ELM assessed findings, modification of design uncertainty is stated as

$$\sigma_{\widehat{q}}^2(p_i) = \frac{1}{B-1}\sum_{s=1}^{B}(\widehat{q}_s(p_i) - \widehat{q}(p_i)). \tag{26}$$

3.5. Architecture Model

3.5.1. Model. An array's PV output energy is measured as

$$p_s = \eta DR[1 - e(t_0 - 25)], \tag{27}$$

while η is the convert productivity, D is the array dimension PV (m^2), R is the solar energy (kW/m^2), e is the array effectiveness damage for every degree Celsius increase in the cell temperature, and t_0 is the ambient temperature (°C).

From equation (27), several parameters influence output power, including PV array dimensions, transform efficiency, ambient temperature, and solar radiation.

3.5.2. Input Vector. Based on its physical model offered, the elements that control output power are determined. As illustrated in the historical statistics, the effectiveness and dimensions of a multidimensional sequence are fixed. Ultraviolet irradiance and climatic parameters, on the other hand, change on a routine basis. As a consequence, as input parameters, choose time, radiation from the sun, and ambient temperature. A numerical weather prediction (NWP) technique is utilized to gather the input data [20]. It forecasts the temperature using computational equations of the composition of the atmosphere based on the changing meteorological conditions. The following is the source image:

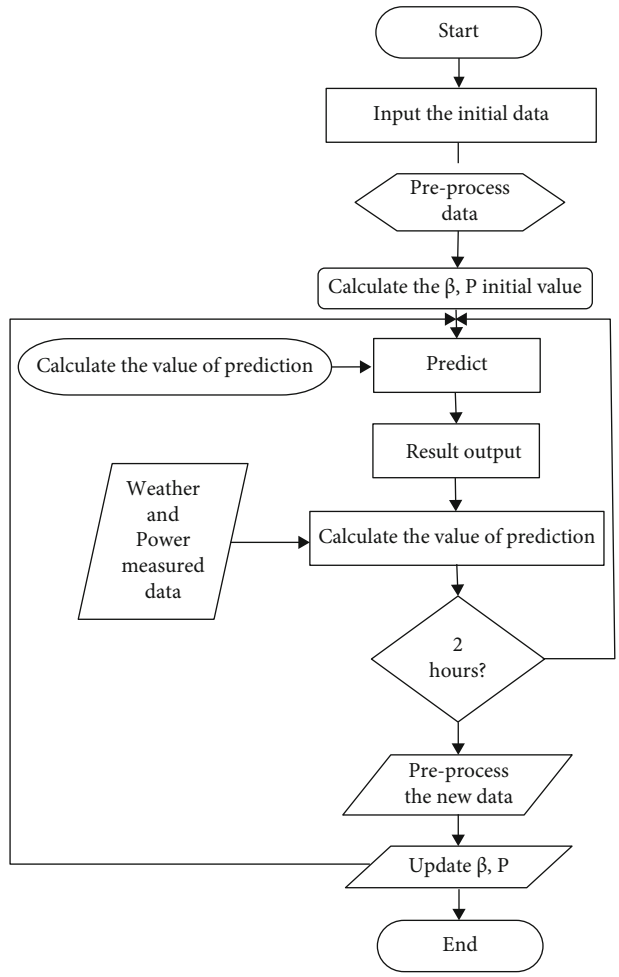

Figure 2: Flowchart prediction system for online sequential extreme learning machine with forgetting mechanism (FOS-ELM).

$$p_i = [\text{time temp } R]^T. \tag{28}$$

If temperature is the environmental temperatures, R seems to be the solar irradiance attainment region of the planet's surface closest to the PV cells.

3.6. Preprocessing Data. When standardizing various variables that adjust to the ELM in the following:

$$\overline{p_i} = \frac{p_i - p_{\min}}{p_{\max} - p_{\min}}, \tag{29}$$

where p_i denotes the input or output information and $p_{\max}$ and $p_{\min}$ denote the highest and smallest values. Since results

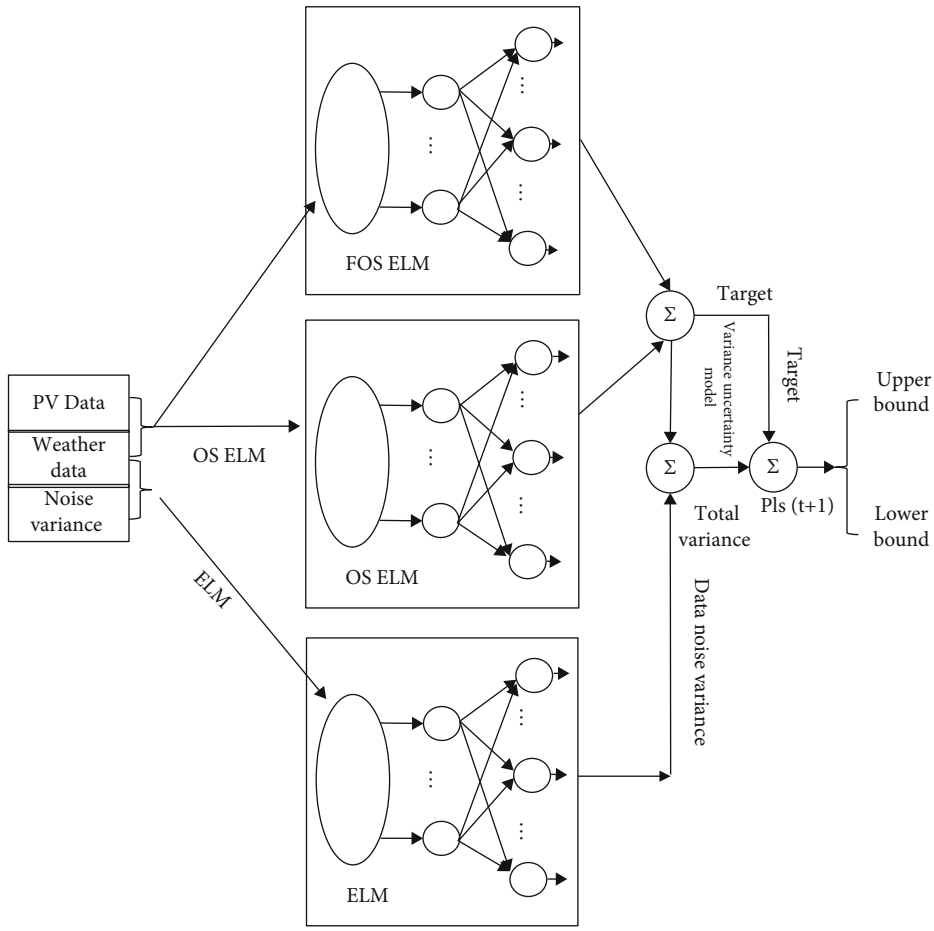

Figure 3: Proposed diagram.

obtained could be perfect, estimated power generation and direct solar information may possibly be below zero outstanding to statistical faults, which really was unachievable in the practice. In this case, change both to zero and also the corresponding expected data. After computing the faults, the data set shall be destroyed if the predicted and measured numbers are also both equivalent to 0.

3.7. Error Evaluation. The prediction algorithms were evaluated using the normalized Root Mean Square Error (nRMSE) and a Mean Absolute Percent Error (MAPE) [21]; these are evaluated as follows:

$$\text{nRMSE} = \frac{1}{V_{\text{rated}}} \sqrt{\frac{1}{n} \sum_{i=1}^{n} (V_{ui} - V_{vi})^2}, \tag{30}$$

$$\text{MAPE} = 100 \times \frac{1}{n} \sum_{i=1}^{n} \frac{|V_{mi} - V_{vi}|}{V_{mi}}, \tag{31}$$

where n represents the total number of power generation on the time periods, P_{rated} represents rated power, V_{vi} represents anticipated energy in the i^{th} time period, and V_{mi} represents the calculated influence in the i^{th} period. Researchers excluded the information established since together solar energy and PV power generated were equivalent to 0 by excluding night information.

3.8. Model Flowchart. The development of estimate is demonstrated in Figure 2. First, enter the early available information for preprocessing, then create the primary output hidden layer matrix H_0 and predict β_0 and P_0. Then, input forecasts over the next few days and calculate the predictive model [5]. When statistical information such as climate and electricity data come, they evaluate the forecast inaccuracy and save the data. Then take a glance at the moment. If it equals 1 h, inform the conditions H, β, and P; then, a preceding procedure was constant.

3.9. PI-Based Cost Function. The variance of noise is evaluated using the standard bootstrap approach under the presumption that information noise is dispersed generally with a zero mean. To train ELM parameters, the cost function of the maximum likelihood approximation is employed rather than one developed by employing assessment indicators of the complete PI presentation [22]. As a result, standard PIs are not always able to find the best PIs. To address this problem, this work proposes a new PI-based cost function that receives the PICP and the break length into a consideration to calculate data error variance.

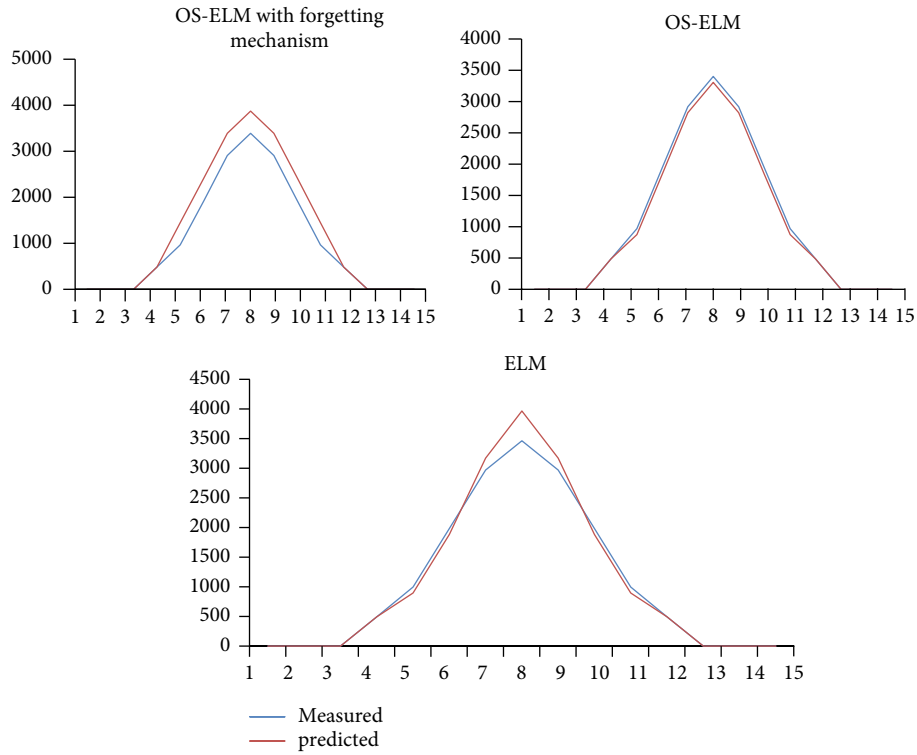

Figure 4: Sunny day three-model comparison.

PI performance should be evaluated in two ways: MPIW and PICP. It is pointless if only one component of PI performance is presented. A coverage width-based criterion (CWC) is specified as a PI-based cost function:

$$\mathrm{CWC} = \mathrm{MPIW} + \gamma \mathrm{PICP}^{\lambda} \times |\mu - \mathrm{PICP}|, \tag{32}$$

where m is the specified probability which is equivalent to the PI nominal confidence (PINC) level of $100(1-\alpha)\%$. l is a hyperparameter with a value among 10 and 100 that is used to penalize invalid PIs and γPICP. In this paper, the CWC value is normalized by nominal PV power and given as a percentage. A higher performing PI has been accomplished if a lower value of CWC is produced at the specified confidence level on $100(1-\alpha)\%$, which is the purpose of the PICP. If the rate of PICP is much added than m, γPICP worth is set to be 0, then the CWC rate is decided by the MPIW, which indicates that the breadth of the PIs must be preserved. Then, the PICP value was much fewer than m, the γPICP value is set to be 1, then the CWC is a total of the together MPIW then $\lambda * |\mu - \mathrm{PICP}|$, representing that broader PIs would be found to obtain an additional acceptable value of the PICP. In this paper, the CWC value was regularized by the minimal PV power and given as a percentage. A higher performing PI has been accomplished if a lower value of CWC is produced at the assumed assurance level on $100(1-\alpha)\%$.

Figure 3 depicts how the recommended fluctuation of unknown parameters and data disturbances is averaged to create PIs. This is vital to create an exact estimation modification of information disturbance in order to construct appropriate PIs. In this paper, an ELM model is constructed to predict the unpredictability of information disruption, so this improved DE (IDE) is used to enhance the ELM number of the criteria by diminishing a CWC [23]. As a result, as described by equation (32), the PI-based objective function for IDE is presented as follows:

$$F = \text{minimum}\,(\mathrm{CWC}). \tag{33}$$

The limitations can be well defined as

$$U(p) > L(p) \geq 0, \tag{34}$$

$$\begin{cases} \text{if } \alpha_i \leq \alpha_j, \\ L^{\alpha_i}(p) \geq L^{\alpha_j}(p),\ U^{\alpha_i}(p) \geq U^{\alpha_j}(p). \end{cases} \tag{35}$$

The first of the two restrictions are automatically fined with that as long as the computation is correct [24]. The other implies that given the identical datasets, a lower confidence level $(1\,a)$ should result in wider PIs.

3.10. Procedures. The proposed method can be separated into two sections in general. The following is a description of the detailed procedure. The bootstrap technique is used in the first stage to determine the modification of model uncertainty.

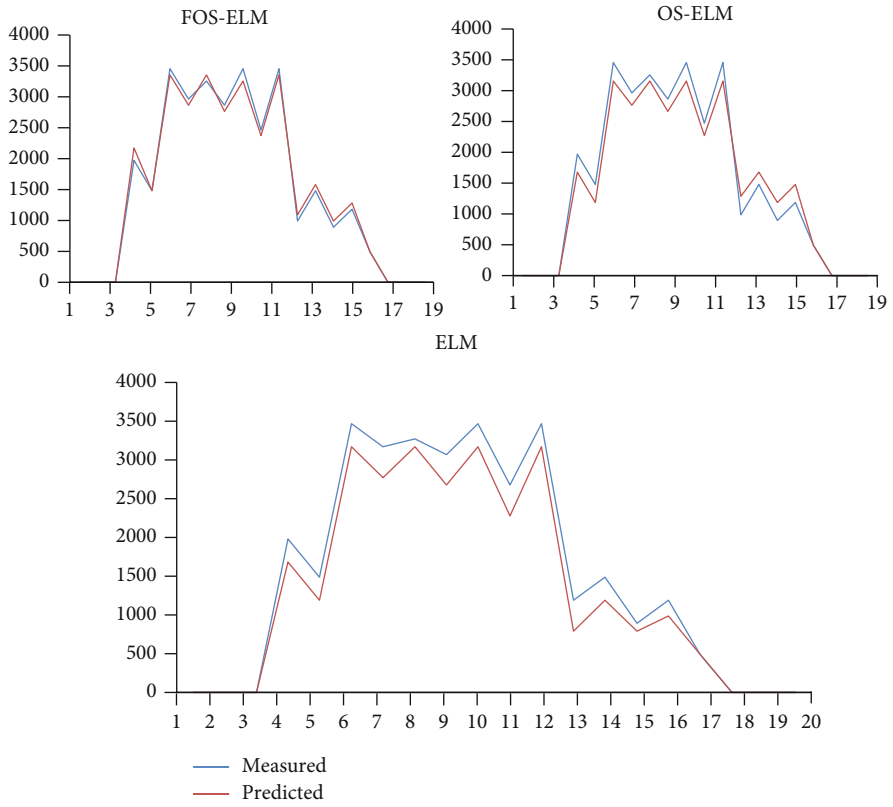

Figure 5: Cloudy/rainy day: three-model comparison.

Step 1. Resample $D_{\text{sub}} = \{(p_i, t_i)\}_{i=1}^{N*}$ B training models by the replacement from innovative PV training dataset $D_t = \{(p_i, t_i)\}_{i=1}^{N}$.

Step 2. Using the model of ELM regress, predict each trained model and produce $\{\widehat{q}_s(p_i)\}_{s=1}^{B}$.

Step 3. Equations (24) and (25) are used to calculate the mean output of the B ELMs models $\widehat{q}_s(p_i)$ and the alteration of the model uncertainty $\sigma_q^2(p_i)$ based on Step 2.

Step 4. $D_{r^2} = \{p_i, r^2(p_i)\}_{i=1}^{N}$ is the residual sample.

The 2nd stage's goal is to evaluate a modification of the information noise and build appropriate PIs.

To estimate variance of the data noise, an ELM approach was used [25]. Because ELM's input weight and hidden layers are generated at random, it is inescapable that most of them are the nonoptimal values. Furthermore, it has been demonstrated that the presentation of ELM is dependent on the excellence of the input masses and the concealed biases. The algorithm of IDE was utilized to identify the best ELM parameters by minimalizing the PI-based cost function in order to acquire the optimum PIs.

Step 1. The population is generated at random, and the applicant solution s_i is made up of a collection of input weights and hidden biases; i^{th} each can be expressed as

$$s_i = [C_{11}, \cdots, C_{1L}, C_{21}, \cdots, C_{2L}, \cdots, C_{n1,} C_{nL}, y_1, \cdots, y_n]. \quad (36)$$

Table 1: Evaluation of the monthly average accuracy comparison.

Climatic condition	Technique	nRMSE	MAPE
Winter season	ELM	0.984	1.770
	FOS-ELM	0.876	1.524
	OS-ELM	0.943	1.631
Autumn season	ELM	0.975	1.793
	FOS-ELM	0.893	1.528
	OS-ELM	0.934	1.632
Summer season	ELM	1.084	1.603
	FOS-ELM	0.893	1.432
	OS-ELM	0.934	1.584
Spring season	ELM	1.127	1.848
	FOS-ELM	0.952	1.549
	OS-ELM	1.042	1.673

Table 2: Comparison of test period and training period.

Technique	Training period (sec)	Test period (sec)
FOS-ELM	0.052	0.095
OS-ELM	0.052	0.049
ELM	0.076	0.076

Table 3: Comparison of different PIs on various climatic conditions.

Climatic condition	PINC(%)	Determination	Bootstrap-based traditional NNs (BNNs)	Double bootstrap method	Bootstrap MLE method	Bootstrap ELM method
Northeast monsoon	90%	19.06	15.19	14.32	14.25	13.76
Intermonsoon	90%	14.89	12.57	12.45	12.30	12.09
Southwest monsoon	90%	20.08	13.65	12.15	12.04	12.02
Intermonsoon	90%	26.55	15.89	13.14	13.03	12.65

Step 2. Each particular population is made up of a set of weights and hidden biases. Equation (2) is used to calculate the corresponding output weights, and $\delta_{\varepsilon}^{2}(p_i)$ is estimated.

Step 3. Use equation (19) to compute the total variance $\delta_{t}^{2}(p_i)$ and equations (20) and (21) to calculate the lower bound $\widehat{L}_{t}^{\alpha}(p_i)$ and upper bound $\widehat{U}_{t}^{\alpha}(p_i)$.

Step 4. The suitability of cost function, CWC, may be determined using equations (32), (22), and (24).

Step 5. An enhanced ID method is designed to alter ELM parameters in order to acquire the best s $\delta_{\varepsilon}^{2}(p_i)$ depending on the neutral function equation (33) and restriction equations (32) and (34).

Step 6. Steps 5 and 3 are used to construct the PIs.

4. Result and Analysis

Research emphasizes on the evaluation of the FOS-ELM, ELM, and OS-ELM because an ELM technique has a shorter development time and increased accuracy rate than BP neural nets, as shown in the research. The following are the specifics for the three models:

Model 1:(algorithm of FOS-ELM). the sigmoidal activation function is chosen as the method that can solve; results collected 48 hours prior to the current time were utilized as test examples to anticipate its energy production; the training model was adjusted every hour, but the information collected 48 hours prior got eliminated.

Model 2:(algorithm of OS-ELM). the exponent is being used as the dynamic variable; data received 48 hours prior to kick-off was used as the train approach to estimate electrical output; quality management was updated every hour utilizing the historic information that was still accessible.

Model 3:(ELM algorithm). the sigmoidal activation purpose is selected as greatly exceeding, and evidence gathered over the preceding month's past 48 hours was used to estimate power output. To put it another way, the algorithms were trained monthly.

Table 4: Comparison of test period and training period.

Technique	Training period (sec)	Test period (sec)
BNN bootstrap	0.0857	0.0574
MLE bootstrap	0.0138	0.0424
Double bootstrap	0.0147	0.0837
ELM bootstrap	0.0135	0.0422

4.1. Single-Day Accuracy Comparison. A three-model comparison predicted outcomes in a particularly sunny day in Figure 4. Figure 5 shows the three model comparison predicted outcomes in a Cloudy/rainy day.

Models 3, 2, and 1 have nRMSEs of 0.024, 0.036, and 0.054, respectively, and MAPEs of 9.708, 10.893, and 12.706. The precision of Prototypical 1 is clearly the best of the 3 models. Models 1, 2, and 3 have nRMSEs of 0.068, 0.075, and 0.083, correspondingly; the related MAPEs are 13.834, 14.304, and 15.112. Model 1's precision remains unquestionably the greatest of the three variants. Furthermore, by associating Figures 3 and 4, we can observe that the precision is higher when it becomes hotter than if it is foggy or wet.

4.2. Average Accuracy of Monthly Comparison. To assess the precision of three systems in various periods, data from the spring, summer, autumn, and winter seasons were used for the study. Table 1 summarizes the findings.

Table 1 demonstrates that the prediction correctness is better in the summers and the winters than in the autumn season in terms of nRMSE; the model has the best precision, while Model 3 has the lowest precision. In terms of MAPE, summer accuracy is better than winter accuracy; once again, Model 1 takes the precision value and Model 3 has the deepest. In conclusion, the strategy of FOS-ELM surpasses all others.

4.3. Training Time Comparison. In Model 1, startup takes 0.095 seconds and online training takes 0.052 seconds. Model 2 takes the same amount of time to initialize as Model 1, but only 0.049 seconds for online study. In Model 3, training takes 0.076 seconds each time as shown in Figure 5. As a result, it can be demonstrated that an online course saves approximately 30% of the retrain period. But, every time an online study is undertaken, Model 1 takes 6% longer than Model 3. Table 2 summarizes the comparison of test and training period.

The level of uncertainty in PV generation is strongly related to the chaotic nature of weather schemes. The

weather and solar radiation patterns change dramatically throughout the year. The warmer temperatures are considered by the two southwest monsoons divided by the intermonsoonal periods. Four seasons in Singapore are explored to validate the performance of the suggested approach: The northeast monsoon season (December to March), the intermonsoon period (April to May), the southwest monsoon season (June to September), and the intermonsoon period (October–November) were the four periods. The equivalent model is created for individual seasons. The equivalent model was created for each season. When the periodic differences and diversity are taken into account, the northeast monsoon, the intermediate monsoon, the southeastern monsoon, and the intermonsoon are chosen to generate test datasets to validate the proposed approach, and the remaining data are used as training datasets. Table 3 summarizes the findings with different PIs.

From Figure 2, the determination technique, the double bootstrap method, and MLK bootstrap technique are all outperformed by the approach. The nominal certainty increases as the PICP value rises. It means that the PIs have a better chance than the average profit of replacing the PV power in the next 5 minutes. When contrasted to the extra deadlifting models, the technique had the extreme value of PICP. Furthermore, the proposed approach's MPIW values are lower than those of previous benchmarking models. It demonstrates that the strategy resulted in smaller intervals. Comparison results shown in Table 4.

5. Conclusion

A new interim model of PV power forecast on the FOS-ELM approach is used in this work. To begin, they gave a fast summary of ELM, OS-ELM, and FOS-ELM theories, as well as the distinctions between the various theories to describe; FOS-ELM was the ideal approach that estimates generation of PV power. Now, this approach could be used for the practical purpose as a prediction device. Short-term forecasting of solar output is critical for power system functioning and economic cost. For quantifying the uncertainties in the PV power group, an extreme learning machine (ELM) and the model of bootstrap have been used along with the approach on the short-term PI forecasting method. Mutually, the data noise and the model of regression have been used to build the PI model. The bootstrap method is used to detect uncertainty of ELM systems, and a hybrid approach of the ELM and IDE with a PI optimal pricing purpose is built to estimate assumptions of the data noise. The suggested methodology could be more than 60 times nearer in training and 10 times nearer in evaluating than the BNNs, showing that the recent theories have great online possibility for the short-term power producing forecasts.

Data Availability

The data used to support the findings of this study are included within the article.

Conflicts of Interest

The authors declare that there is no conflict of interest regarding the publication of this article.

Acknowledgments

The authors would like to express their gratitude towards Saveetha School of Engineering, Saveetha Institute of Medical and Technical Sciences (formerly known as Saveetha University), for providing the necessary infrastructure to carry out this work successfully.

References

[1] M. Rana, I. Koprinska, and V. G. Agelidis, "Univariate and multivariate methods for very short-term solar photovoltaic power forecasting," *Energy Conversion and Management*, vol. 121, pp. 380–390, 2016.

[2] G. Ramkumar, S. Sahoo, G. Anitha et al., "An unconventional approach for analyzing the mechanical properties of natural fiber composite using convolutional neural network," *Advances in Materials Science and Engineering*, vol. 2021, Article ID 5450935, 15 pages, 2021.

[3] S. Mahesh and G. Ramkumar, "Smart face detection and recognition in low resolution images using Alexnet CNN compare accuracy with SVM," *Alinteri Journal of Agriculture Sciences*, vol. 36, no. 1, pp. 721–726, 2021.

[4] G. Ramkumar, M. Ayyadurai, and C. Senthilkumar, "An effectual underwater image enhancement using deep learning algorithm," in *2021 5th International Conference on Intelligent Computing and Control Systems (ICICCS)*, pp. 1507–1511, 2021.

[5] G. Ramkumar and E. Logashanmugam, "Study on impulsive assessment of chronic pain correlated expressions in facial images," *Biomedical Research*, vol. 29, no. 16, 2018.

[6] Q. Ni, S. Zhuang, H. Sheng, S. Wang, and J. Xiao, "An optimized prediction intervals approach for short term PV power forecasting," *Energies*, vol. 10, no. 10, p. 1669, 2017.

[7] Z.-H. Li, J.-J. Yang, H.-Q. Qin, Y.-W. Xia, and M. Zhuang, "A study of efficiency evaluation of national quality online courses during the epidemic: based on fuzzy logic calculation and bootstrap-DEA," *Mathematical Problems in Engineering*, vol. 2021, Article ID 5534583, 7 pages, 2021.

[8] H. Zhang, S. Zhang, and Y. Yin, "Online sequential ELM algorithm with forgetting factor for real applications," *Neurocomputing*, vol. 261, pp. 144–152, 2017.

[9] H. K. Ahn and N. Park, "Deep RNN-based photovoltaic power short-term forecast using power IoT sensors," *Energies*, vol. 14, no. 2, p. 436, 2021.

[10] Y.-W. Liu, H. Feng, H.-Y. Li, and L.-L. Li, "An improved whale algorithm for support vector machine prediction of photovoltaic power generation," *Symmetry*, vol. 13, no. 2, p. 212, 2021.

[11] N. Park and H. K. Ahn, "Multi-layer RNN-based short-term photovoltaic power forecasting using IoT dataset," in *2019 AEIT International Annual Conference (AEIT)*, pp. 1–5, Florence, Italy, 2019.

[12] R. Azka, W. Soefian, D. R. Aryani, F. H. Jufri, and A. R. Utomo, "Modelling of photovoltaic system power prediction based on environmental conditions using neural network single and

multiple hidden layers," in *IOP Conference Series: Earth and Environmental Science*, vol. 599, 2020.

[13] G. Cervone, L. Clemente-Harding, S. Alessandrini, and L. Delle Monache, "Short-term photovoltaic power forecasting using artificial neural networks and an analog ensemble," *Renewable Energy*, vol. 108, pp. 274–286, 2017.

[14] Y. Dash, S. K. Mishra, and B. K. Panigrahi, "Rainfall prediction for the Kerala state of India using artificial intelligence approaches," *Computers & Electrical Engineering*, vol. 70, pp. 66–73, 2018.

[15] W. Mao, J. Wang, and Z. Xue, "An ELM-based model with sparse-weighting strategy for sequential data imbalance problem," *International Journal of Machine Learning and Cybernetics*, vol. 8, no. 4, pp. 1333–1345, 2017.

[16] D. Xiao, B. Li, and S. Zhang, "An online sequential multiple hidden layers extreme learning machine method with forgetting mechanism," *Chemometrics and Intelligent Laboratory Systems*, vol. 176, pp. 126–133, 2018.

[17] W. Kong, Z. Y. Dong, Y. Jia, D. J. Hill, Y. Xu, and Y. Zhang, "Short-term residential load forecasting based on LSTM recurrent neural network," *IEEE Transactions on Smart Grid*, vol. 10, no. 1, pp. 841–851, 2017.

[18] I. Serykh and D. Sonechkin, "Nonchaotic and globally synchronized short-term climatic variations and their origin," *Theoretical and Applied Climatology*, vol. 137, no. 3, pp. 2639–2656, 2019.

[19] C. Wan, Z. Xu, P. Pinson, Z. Y. Dong, and K. P. Wong, "Probabilistic forecasting of wind power generation using extreme learning machine," *IEEE Transactions on Power Systems*, vol. 29, no. 3, pp. 1033–1044, 2013.

[20] J. Wang, P. Li, R. Ran, Y. Che, and Y. Zhou, "A short-term photovoltaic power prediction model based on the gradient boost decision tree," *Applied Sciences*, vol. 8, no. 5, p. 689, 2018.

[21] Z. Li, L. Ye, Y. Zhao, X. Song, J. Teng, and J. Jin, "Short-term wind power prediction based on extreme learning machine with error correction," *Protection and Control of Modern Power Systems*, vol. 1, no. 1, pp. 1–8, 2016.

[22] A. Khosravi, S. Nahavandi, D. Srinivasan, and R. Khosravi, "Constructing optimal prediction intervals by using neural networks and bootstrap method," *IEEE transactions on neural networks and learning systems*, vol. 26, no. 8, pp. 1810–1815, 2014.

[23] Q. Ni, S. Zhuang, H. Sheng, G. Kang, and J. Xiao, "An ensemble prediction intervals approach for short-term PV power forecasting," *Solar Energy*, vol. 155, pp. 1072–1083, 2017.

[24] N. Gustafsson, T. Janjić, C. Schraff et al., "Survey of data assimilation methods for convective-scale numerical weather prediction at operational centres," *Quarterly Journal of the Royal Meteorological Society*, vol. 144, no. 713, pp. 1218–1256, 2018.

[25] P. K. S. Sundar and P. C. Deka, *Spatio-temporal classification and prediction of land use and land cover change for the Vembanad Lake System, Kerala–a machine learning approach*, 2021, https://www.researchsquare.com/article/rs-581788/v1.